

UNIVERSITY OF BIRMINGHAM

THE DEVELOPMENT OF BIODEGRADABLE NANOPARTICLES FOR THE SYSTEMIC TREATMENT OF BRAIN TUMOURS

BY

BASANT SALAH ABDELMONEAM MAHMOUD

A thesis submitted to the University of Birmingham

For the degree of

DOCTOR OF PHILOSOPHY

The Institute of Clinical Sciences

School of Pharmacy

College of Medical and Dental Sciences

University of Birmingham

April 2022

UNIVERSITY OF
BIRMINGHAM

University of Birmingham Research Archive

e-theses repository

This unpublished thesis/dissertation is copyright of the author and/or third parties. The intellectual property rights of the author or third parties in respect of this work are as defined by The Copyright Designs and Patents Act 1988 or as modified by any successor legislation.

Any use made of information contained in this thesis/dissertation must be in accordance with that legislation and must be properly acknowledged. Further distribution or reproduction in any format is prohibited without the permission of the copyright holder.

ABSTRACT

The blood brain barrier (BBB) is a complex entity that restricts therapeutics from accessing the brain environment and reaching tumours in therapeutic doses. Development of polymeric nanoparticles (NPs) loaded with therapeutics could enhance the efficacy of the treatment. Polycaprolactone (PCL) is a biocompatible polymer that has a long-term degradation profile and does not lead to the production of acidic toxic products upon degradation. The aim of this thesis was to develop PCL NPs and PCL-PLGA blend NPs loaded with irinotecan hydrochloride (IRH) that can cross the BBB without impairing its integrity and be cytotoxic to high-grade glioma (HGG) cells. The results indicated that polymer amorphization and addition of electrolytes have resulted in enhanced encapsulation efficiency (EE) by the double emulsion solvent evaporation technique while maintaining the size of the NPs within an acceptable limit (<500 nm). By using Box-Behnken design (BBD) of experiments for further optimization, the most optimum conditions for producing the smallest size, lowest charge and highest EE% of PCL NPs were predicted to be achieved by using 61.02 mg PCL, 9 mg IRH and 4.82% PVA, which would yield 203.01 nm, -15.81 mV and 82.35% EE. Similarly, an optimum level of dependent factors of PCL-PLGA blend NPs would be achieved by using 162 mg polymer blend, 8.37 mg IRH and 8% PVA which would yield NPs with a size of 283.06 nm, a charge of -31.54 mV and a 70% EE. Blending PCL with PLGA has resulted in a reduced crystallinity and enhanced release of 69.39 ± 0.58 % over 16 days. Biological characterization of the NPs has revealed their haemocompatibility and their dose dependent cellular uptake in both HGG cells and endothelial cells. Additionally, the NPs were more cytotoxic than the free drug against HGG primary cells obtained from 3 different patients, where they induced

apoptosis *via* the extrinsic pathway. In the endothelial cells, the NPs were able to cross the BBB and impose a less cytotoxic effect on their viability compared to HGG cells. By analysing the expression of interleukin-6 (IL-6) as a marker of immunogenicity, both HGGs and endothelial cells treated with the NPs had less expression of IL-6 as compared to the free IRH. In conclusion, manipulating the formulation parameters could help design NPs with desirable properties able to cross the BBB and treat malignant brain tumours while reducing the toxic side effects produced by free chemotherapies.

This thesis is dedicated to my Parents; Hoda and Salah and to my brother Bassem

Acknowledgements

First and foremost, I would like to thank and praise Allah the Almighty, the most gracious, and the most merciful for blessing me during my PhD journey until completing this thesis.

Then, I would like to dedicate this PhD to my mother; Hoda, my late father; Salah and to my brother; Bassem. I would also like to seize this precious opportunity to express my deep love, appreciation, and gratitude for all their support, love, prayers and patience throughout my academic journey and my whole life.

I dedicate this PhD also to my supervisor Dr Christopher McConville for all his invaluable academic support, motivation, and belief in me as a researcher. Chris has always been understanding, patient and kind to me for which I am deeply and truthfully grateful and appreciative.

My appreciation also extends to Dr Marie-Christine Jones for her academic and personal support whenever needed. She has always been a good listener and wise advisor.

My gratitude and appreciation also go to the Egyptian ministry of higher education and scientific research for funding my PhD.

A massive thank you goes to my friends and colleagues who made this journey most enjoyable.

Publications

1. Mahmoud, B. S., Alamri, A. H. and McConville, C. (2020) 'Polymeric nanoparticles for the treatment of malignant gliomas', Cancers. MDPI AG, 12(1), p. 175.
2. Mahmoud, B. S. and McConville, C. (2021) 'Development and Optimization of Irinotecan-Loaded PCL Nanoparticles and Their Cytotoxicity against Primary High-Grade Glioma Cells', Pharmaceutics 2021, Vol. 13, Page 541. Multidisciplinary Digital Publishing Institute, 13(4), p. 541.

Conferences

1. Basant Salah Mahmoud, Chris McConville. Tiny but powerful: Nanomedicine with the potential of fighting malignant brain tumours. Poster presented at the University of Birmingham's 13th Annual Research Poster Conference; 2019 June 19th; Birmingham, England.

Table of Contents

Chapter 1 POLYMERIC NANOPARTICLES FOR THE TREATMENT OF MALIGNANT GLIOMAS ..1

1.1 Introduction 3

1.2 High Grade Gliomas 4

1.3 Treatment 5

1.3.1 Surgical Resection 5

1.3.2 Radiation Treatment 6

1.3.3 Chemotherapy 7

1.4 Postoperative Treatment 9

1.5 Prognosis 10

1.6 Glioblastoma Multiforme 11

1.6.1 Current Management 12

1.7 The Blood Brain Barrier 13

1.8 Drug Delivery to the Brain 15

1.9 Nanomedicine: A Non-Invasive Approach towards a Better Quality of Life 19

1.9.1 Physicochemical Properties of Nanoparticles 20

1.9.2 Nanoparticles as a Treatment for Malignant Gliomas 21

1.9.3 Routes of Administration of Nanoparticles in the Treatment of Malignant Gliomas 23

1.9.4 The Chemistry of Coating and Bioconjugation of Nanoparticles 24

1.9.5 Drug-Loading of Nanoparticles 29

1.10 Polymeric Nanoparticles for the Treatment of Malignant Gliomas 29

1.11 Targeted Polymeric Nanoparticles for the Treatment of Malignant Gliomas 31

1.12 Challenges Associated with Nanomedicine as a Treatment for Malignant Gliomas 35

1.12.1 Reticuloendothelial System 35

1.12.2 Renal System 36

1.12.3 BBB 37

1.12.4 Pathophysiological Barriers in Cancer 37

1.12.5 Multidrug Resistance 40

1.13 Clinical Transition of Polymeric Nanoparticles 41

1.14 Conclusions *43*

1.15 Aims and objectives *45*

Chapter 2 DEVELOPMENT AND OPTIMIZATION OF IRINOTECAN-LOADED PCL NANOPARTICLES AND THEIR CYTOTOXICITY AGAINST PRIMARY HIGH-GRADE GLIOMA CELLS *46*

2.1 Introduction *48*

2.2 Materials and Methods *53*

2.2.1 Chemicals **53**

2.2.2 IRH Solubility **53**

2.2.3 IRH Stability **54**

2.2.4 Solvent Evaporation Technique **54**

2.2.4.1 Single Emulsion (Oil in Water (O/W)) 54

2.2.4.2 Single Emulsion (Water in Oil (W/O)) 55

2.2.4.3 Single Emulsion (Oil in Oil (O/O)) 55

2.2.4.4 Double Emulsion (Water in Oil in Oil (W/O/O)) 56

2.2.4.5 Double Emulsion (Water in Oil in Water (W/O/W)) 56

2.2.4.5.1 The Influence of the Inclusion of Matrix Material in W/O/W 58

2.2.4.5.2 The Influence of Using Amorphized PCL W/O/W 58

2.2.4.5.3 The Influence of the Addition of Electrolytes to the Aqueous Phase W/O/W 58

2.2.5 The Influence of Different Parameters on Size, Charge and EE of Optimized NPs **58**

2.2.6 Collection and Lyophilization of NPs **58**

2.2.7 Morphology **59**

2.2.8 Measurement of Particle Size and Zeta Potential **59**

2.2.9 Measurement of EE **59**

2.2.10 Release Study **60**

2.2.11 IRH HPLC Methodology **60**

2.2.12 In Vitro Cell Culture and Cytotoxicity Study **60**

2.2.13 Statistical Analysis **61**

2.3 Results *62*

2.3.1 IRH Solubility and Stability **62**

2.3.2 Single Emulsion Optimization Parameters **63**

2.3.2.1 Parameters Influencing the Size, PDI and Surface Charge 63

2.3.2.2 Parameters Influencing EE 65

2.3.3 Double Emulsion Optimization Parameters **66**

2.3.4 Characterization of the Optimized IRH-Loaded PCL Nanoparticles **73**

2.4 Discussion *75*

2.4.1 Parameters Influencing Size, PDI and Surface Charge of Nanoparticle Formulations **76**

2.4.1.1 Sonication Time and Amplitude ... 76
2.4.1.2 Drug and Polymer Amount ... 77
2.4.1.3 Surfactant Concentration ... 78
2.4.1.4 Surfactant Type and Molecular Weight ... 78
2.4.2 Parameters Influencing EE ... 79
2.4.2.1 Single Emulsion Solvent Evaporation Technique ... 79
2.4.2.2 Double Emulsion Solvent Evaporation Technique ... 80
2.4.2.2.1 Matrix Material ... 80
2.4.2.2.2 The Use of Amorphous PCL and the Addition of Electrolytes ... 81
2.4.2.2.3 Amount of IRH ... 82
2.4.2.2.4 Solvent Evaporation Time ... 82
2.4.2.2.5 Surfactant Concentration ... 83
2.4.2.2.6 Surfactants with Different HLB Values ... 84
2.4.2.2.7 Aqueous Phase Volume ... 84
2.4.2.2.8 pH of the Aqueous Phase ... 85
2.4.3 Characterization of the Optimized IRH-Loaded PCL Nanoparticles ... 85
2.4.3.1 Morphology and *In Vitro* Drug Release ... 85
2.4.3.2 Cytotoxicity ... 87
2.5 Conclusions ... 87
Chapter 3 BOX-BEHNKEN DESIGN OF EXPERIMENTS OF DRUG-LOADED PCL NPS ... 89
3.1 Introduction ... 90
3.1.1 Design of Experiments ... 91
3.2 Materials and Methods ... 92
3.2.1 Materials ... 92
3.2.2 BBD ... 92
3.2.3 Yield Enhancement ... 93
3.2.4 Characterization of the NPs ... 94
3.2.5 Statistical Analysis ... 94
3.3 Results ... 94
3.3.1 BBD Predicted Model and Best Fit Regression Coefficient for Size ... 94
3.3.2 BBD Predicted Model and Best Fit Regression Coefficient for Zeta Potential 100
3.3.3 BBD Predicted Model and Best Fit Regression Coefficient for EE% ... 104
3.3.4 Yield of NPs ... 109
3.3.4.1 Characterization Of NPs Before and After Yield Enhancement ... 109
3.3.4.2 Initial and Enhanced Yield ... 110
3.4 Discussion ... 111
Chapter 4 BOX-BEHNKEN DESIGN OF EXPERIMENTS OF DRUG-LOADED PCL-PLGA BLEND NPS ... 116
4.1 Introduction ... 117
4.2 Materials and Methods ... 118

4.2.1 Materials 118
4.2.2 Development of PCL-PLGA Blend NPs. 118
4.2.3 BBD 119
4.2.4 Characterization of the NPs 119
4.2.5 Statistical Analysis 119
4.3 Results 119
4.3.1 Size, Charge and EE% of Drug Loaded PCL-PLGA NPs 119
4.3.2 BBD Predicted Model and Best Fit Regression Coefficient for Size 120
4.3.3 BBD Predicted Model and Best Fit Regression Coefficient for Zeta Potential 125
4.3.4 BBD Predicted Model and Best Fit Regression Coefficient for EE% 129
4.4 Discussion 134
Chapter 5 PHYSICO-CHEMICAL CHARACTERIZATION OF SELECTED PCL AND PCL-PLGA BLEND NPS 138
5.1 Introduction 139
5.1.1 Drug Release from Polymeric NPs 139
5.1.2 Thermal Analysis by DSC 142
5.1.3 Crystallinity Analysis by XRD 143
5.2 Materials and Methods 144
5.2.1 Materials 144
5.2.2 In Vitro Drug Release 144
5.2.3 DSC 145
5.2.4 XRD 145
5.2.5 Stability of NPs 145
5.2.6 Imaging of NPs 145
5.2.6.1 TEM Imaging 145
5.2.6.2 Scanning Electron Microscope (SEM) Imaging 146
5.2.7 Statistical Analysis 146
5.3 Results 146
5.3.1 Release of Selected Formulations in PBS 146
5.3.2 DSC 150
5.3.2.1 F2 PCL NPs (Individual Excipients, Physical Mixture and Overlay) 150
5.3.2.2 F18 blend NPs (Individual Excipients, Physical Mixture and Overlay) 155
5.3.3 XRD 161
5.3.4 Stability of NPs 164
5.3.5 Imaging of NPs 169

5.4 Discussion 171

Chapter 6 BIOLOGICAL CHARACTERIZATION OF THE PCL NPS FOR THEIR HAEMOCOMPATIBILITY, CELLULAR UPTAKE, AND CYTOTOXICTY AGAINST HGG PRIMARY CELLS 181

6.1 Introduction 182

6.1.1 Cellular Uptake of NPs and Free Drugs 182

6.1.2 NP-induced Apoptotic and Necrotic Cell Death 183

6.1.3 Haemocompatibility of NPs 186

6.1.4 IL-6 Protein Expression in Glioma Cells 187

6.2 Materials and Methods 188

6.2.1 Materials 188

6.2.2 Cell Culture of Primary HGG Cells 188

6.2.3 Flow Cytometry Analysis of Cellular Uptake In Primary HGG Cells 189

6.2.4 In Vitro Cytotoxicity and Morphology of Primary HGG Cells 189

6.2.5 Imaging of Internalized Nps in Primary HGG Cells by Confocal Microscopy 190

6.2.6 Flow Cytometry Analysis of Apoptosis And Necrosis in Primary HGG Cells 190

6.2.7 Caspase Luminescence Assay of Primary HGG Cells 191

6.2.8 ATP Luminescence Assay of Primary HGG Cells 192

6.2.9 Haemocompatibility of Selected NP Formulations 192

6.2.10 Interleukin-6 (IL-6) Protein Expression in Primary HGG Cells 193

6.2.11 Statistical Analysis 194

6.3 Results 194

6.3.1 Cellular Uptake 194

6.3.1.1 Analysis of Cellular Uptake by Flow Cytometry 194

6.3.1.2 Analysis of Cellular Uptake by Confocal Microscopy 202

6.3.2 Cytotoxicity 206

6.3.3 Optical Imaging of HGG Cells 229

6.3.4 Mechanism of Cell Death 238

6.3.5 Haemocompatibility 255

6.3.6 IL-6 Protein Expression 258

6.4 Discussion 262

Chapter 7 BIOLOGICAL CHARACTERIZATION OF AN ENDOTHELIAL CELL LINE TREATED WITH DRUG LOADED NPS 273

7.1 Introduction 274

7.1.1 BBB and Transendothelial Electrical Resistance (TEER) Measurement ...274
7.2 Materials and Methods ...276
7.2.1 Materials ...276
7.2.2 Cell Culture of Endothelial Cell Line ...276
7.2.3 Flow Cytometry Analysis of Cellular Uptake in Endothelial Cell Line ...276
7.2.4 In Vitro Cytotoxicity and Morphology of Endothelial Cell Line ...276
7.2.5 Flow Cytometry Analysis of Apoptosis and Necrosis in Endothelial Cell Line 276
7.2.6 BBB Permeability ...277
7.2.7 IL-6 Protein Expression in Endothelial Cell Line ...277
7.2.8 Statistical Analysis ...277
7.3 Results ...277
7.3.1 Cellular Uptake Analysis by Dot Plots and SSC Intensity Using Flow Cytometry ...277
7.3.2 Cytotoxicity ...285
7.3.3 Optical Imaging of Endothelial Cells ...293
7.3.4 Mechanism of Cell Death ...302
7.3.5 Permeability of BBB ...312
7.3.6 IL-6 Protein Expression ...315
7.4 Discussion ...320
Chapter 8 FINAL CONCLUSION, SUMMARY OF FINDINGS AND FUTURE RESEARCH ...324

List of Tables

Table 1.1. Examples of developed targeted polymer nanoparticles as targeted drug delivery system for treatment of malignant gliomas. 33

Table 2.1 Single emulsion process and formulation parameters using PVA (MW 13K) and PVP (MW 40K) surfactants. 54

Table 2.2. Double emulsion parameters of optimized formulations. 57

Table 2.3. Summary of EE% and the influencing parameters. 72

Table 2.4. The kinetic parameters from the different release models used for the optimized DE5 NPs. 74

Table 3.1. Box-Behnken coded 3-level factorial design 92

Table 3.2. Box-Behnken coded and actual values 93

Table 3.3. Summary of regression coefficient analysis for the response Y1 (Size). .. 96

Table 3.4. Experimental and theoretical values with residuals of the response Y1. .. 96

Table 3.5. Analysis of variance, degree of freedom (DF), sum of squares (SS), mean of squares (MS) and Fischer's ratio (F-value) for the size of the NPs. 96

Table 3.6. Summary of regression coefficient analysis for the response Y2 (Zeta potential). 101

Table 3.7. Experimental and theoretical values with residuals of the response Y2. 101

Table 3.8. Analysis of variance, DF, SS, MS and F-Value for the charge of the NPs. 101

Table 3.9. Summary of regression coefficient analysis for the response Y3 (EE%). 105

Table 3.10. Experimental and theoretical values with residuals of the response Y3. 105

Table 3.11. Analysis of variance, DF, SS, MS and F-Value for the EE% of the NPs. 106

Table 3.12. Mean size, PDI, zeta potential and EE% of NPs before yield enhancement 109

Table 3.13. Mean size, PDI, zeta potential and EE% of NPs after yield enhancement 109

Table 4.1. Box-Behnken coded and actual values..... 119

Table 4.2. Average particle size, PDI, Zeta potential and EE of IRH loaded blend NPs at various ratios of polymer amounts..... 120

Table 4.3. Summary of regression coefficient analysis for the response Y1 (Size). 121

Table 4.4. Experimental and theoretical values with residuals of the response Y1. 121

Table 4.5. Analysis of variance, DF, SS, MS and F-Value (F-value) for the size of the NPs. 122

Table 4.6. Summary of regression coefficient analysis for the response Y2 (Zeta potential)..... 125

Table 4.7. Experimental and theoretical values with residuals of the response Y2. 126

Table 4.8. Analysis of variance, DF, SS, MS and F-Value for the charge of the NPs. 126

Table 4.9. Summary of regression coefficient analysis for the response Y3 (EE%). 130

Table 4.10. Experimental and theoretical values with residuals of the response Y3. 130

Table 4.11. Analysis of variance, DF, SS, MS and F-Value for the EE% of the NPs. 131

Table 5.1. PCL, PLGA, IRH and PVA content of selected formulations 144

Table 5.2. Release models and mechanisms of selected NP formulations. 149

Table 5.3. Release mechanisms for spherical particles given by the n exponent (Sarker Apu et al., 2009) 173

List of Figures

Figure 2.1. Solubility (A) and stability of IRH in both dH20 (B) and PBS (C) over 16 days at 8, 25 and 37 °C (n=3).....62

Figure 2.2. The impact of sonication time (A), polymer amount (B), drug amount (C), sonication amplitude (D), surfactant type (E), pH and PVA concentration (F) on the average particle size, PDI and zeta potential of the nanoparticles manufactured using the single emulsion technique. 64

Figure 2.3. The impact of matrix material, PCL amorphization and electrolyte addition on the average particle size, PDI, zeta potential (B and D) and EE of nanoparticles (A and C) manufactured using the double emulsion technique. 67

Figure 2.4. The impact of drug amount (A and B), solvent evaporation time (C and D) and high-MW PVA (E and F) on the average particle size, PDI, zeta potential and EE of optimized nanoparticles manufactured using the double emulsion technique. 69

Figure 2.5. The impact of surfactant type (A and B), aqueous phase volume (C and D) and aqueous phase pH (E and F) on the average particle size, PDI, zeta potential and EE of optimized nanoparticles manufactured using the double emulsion technique..71

Figure 2.6. TEM image of DE5 showing average particle size of 149.2 ± 13.5 nm for 14 particles (A) and *in vitro* cumulative release of the IRH-loaded PCL nanoparticles (B) (n=3). 74

Figure 2.7. The cytotoxicity of free IRH and DE5 formulation on primary HGG cells (n=3).....75

Figure 3.1. Pareto chart expressing standardized effect of independent variables and their interaction on the size of the NPs. 97

Figure 3.2. Contour plot **(**A) and Surface plot (B) showing the effect of polymer amount (A) and drug amount (B) on the size of the NPs. 98

Figure 3.3. Contour plot and (A) Surface plot (B) showing the effect of polymer amount (A) and surfactant concentration (C) on the size of the NPs 99

Figure 3.4. Contour plot (A) and Surface plot (B) showing the effect of drug amount (B) and surfactant concentration (C) on the size of the NPs 99

Figure 3.5. Pareto chart expressing standardized effect of independent variables and their interaction on the charge of the NPs. 102

Figure 3.6. Contour plot (A) and Surface plot (B) showing the effect of polymer amount (A) and drug amount (B) on the charge of the NPs. 103

Figure 3.7. Contour plot (A) and Surface plot (B) showing the effect of polymer amount (A) and surfactant concentration (C) on the charge of the NPs 103

Figure 3.8. Contour plot (A) and Surface plot (B) showing the effect of drug amount (B) and surfactant concentration (C) on the charge of the NPs 104

Figure 3.9. Pareto chart expressing standardized effect of independent variables and their interaction on the EE% of the NPs. 106

Figure 3.10 Contour plot (A) and Surface plot (B) showing the effect of polymer amount (A) and drug amount (B) on the EE% of the NPs 107

Figure 3.11. Contour plot (A) and Surface plot (B) showing the effect of polymer amount (A) and surfactant concentration (C) on the EE% of the NPs 108

Figure 3.12. Contour plot (A) and Surface plot (B) showing the effect of drug amount (B) and surfactant concentration (C) on the EE% of the NPs. 108

Figure 3.13. Initial and enhanced yield percent of NP formulations 110

Figure 4.1. Pareto chart expressing standardized effect of independent variables and their interaction on the size of the NPs. 122

Figure 4.2. Contour plot and (A) Surface plot (B) showing the effect of polymer amount (A) and drug amount (B) on the size of the NPs. 123

Figure 4.3. Contour plot (A) and Surface plot (B) showing the effect of polymer amount (A) and surfactant concentration (C) on the size of the NPs. 124

Figure 4.4. Contour plot and (A) Surface plot (B) showing the effect of drug amount (B) and surfactant concentration (C) on the size of the NPs. 124

Figure 4.5. Pareto chart expressing standardized effect of independent variables and their interaction on the charge of the NPs. 127

Figure 4.6. Contour plot (A) and Surface plot (B) showing the effect of polymer amount (A) and drug amount (B) on the charge of the NPs. 128

Figure 4.7. Contour plot (A) and Surface plot (B) showing the effect of polymer amount (A) and surfactant concentration (C) on the charge of the NPs 128

Figure 4.8. Contour plot and (A) Surface plot (B) showing the effect of drug amount (B) and surfactant concentration (C) on the charge of the NPs 129

Figure 4.9. Pareto chart expressing standardized effect of independent variables and their interaction on the EE% of the NPs. 131

Figure 4.10. Contour plot and (A) Surface plot (B) showing the effect of polymer amount (A) and drug amount (B) on the EE% of the NPs 132

Figure 4.11. Contour plot and (A) Surface plot (B) showing the effect of polymer amount (A) and surfactant concentration (C) on the EE% of the NPs 133

Figure 4.12. Contour plot and (A) Surface plot (B) showing the effect of drug amount (B) and surfactant concentration (C) on the EE% of the NPs 133

Figure 5.1 Drug release from PCL and PCL-PLGA NPs in PBS: F2 (A) F3 (B) F4 (C) F10 (D) F12 (E) F15 (F) F18 (G) Overlay (H) (n=3). 148

Figure 5.2. DSC of Individual components of F2. PCL (A) IRH (B) PVA (C) Sucrose (D) 151

Figure 5.3. DSC of Physical mixture (A) Blank F2 (B) F2 (C) Overlay (D) 152

Figure 5.4. DSC of Dual mixes of F2 excipients PCL-IRH (A) PCL-PVA (B) PCL-Sucrose (C) IRH-PVA (D) IRH-Sucrose (E) 154

Figure 5.5. DSC of PCL (A) IRH (B) PLGA (C) PVA (D) 156

Figure 5.6. DSC of Sucrose (A) F18 blank (B) F18 (C) F2 (D) 157

Figure 5.7. DSC of Dual mixes of F18 excipients PCL- IRH (A) PCL-PLGA (B) PCL-PVA (C) PCL-Sucrose (D) 158

Figure 5.8. DSC of Dual mixes of F18 excipients PLGA- IRH (A) PLGA- PVA (B) PLGA-Sucrose (C) PVA- IRH (D) 159

Figure 5.9. DSC of Sucrose-IRH (A) Overlay F18 polymers (B) Overlay F18 (C) ... 160

Figure 5.10. XRD spectra of F2 and its blank NPs plotted with each individual excipient. PCL, Blank F2 and F2 (A) IRH, Blank F2 and F2 (B) PVA, Blank F2 and F2 (C) Sucrose, Blank F2 and F2 (D) Physical Mix, Blank F2 and F2 (E) PCL-IRH Physical mix, Blank F2 and F2 (F) 162

Figure 5.11. XRD spectra of F18 and its blank NPs plotted with each individual excipient. PCL, Blank F18 and F18 (A) IRH, Blank F18 and F18 (B) PVA, Blank F18 and F18 (C) Sucrose, Blank F18 and F18 (D) PLGA, Blank F18 and F18 (E) Physical Mix, Blank F18 and F18 (F) PCL-IRH Physical mix, Blank F18 and F18 (G) PLGA-IRH Physical mix, Blank F18 and F18 (H) PCL-PLGA Physical mix, Blank F18 and F18 (I) 164

Figure 5.12. Stability of NPs Size in PBS (A) pH 3 (B) pH 5.9 (C)Tissue Culture Media (D) (n=3) 167

Figure 5.13. Stability of NPs PDI in PBS (A) pH 3 (B) pH 5.9 (C) Tissue Culture Media (D) (n=3) 168

Figure 5.14. Stability of NPs Zeta Potential in PBS (A) pH 3 (B) pH 5.9 (C) Tissue Culture Media (D) (n=3) 168

Figure 5.15. TEM images of F2 taken at different scales 169

Figure 5.16. TEM images of F15 taken at different scales 170

Figure 5.17. TEM images of F18 taken at different scales. 170

Figure 5.18. SEM images of F2 taken at different scales 171

Figure 5.19. SEM images of F15 taken at different scales 171

Figure 5.20. SEM images of F18 taken at different scales. 171

Figure 6.1. HGG cellular uptake of low, medium, and high concentrations of free IRH and NPs after 1 day of treatment. 196

Figure 6.2. HGG cellular uptake of low, medium and high concentrations of free IRH and NPs after 3 days of treatment. 197

Figure 6.3. HGG cellular uptake of low, medium, and high concentrations of free IRH and NPs after 5 days of treatment. 198

Figure 6.4. HGG cellular uptake of low, medium and high concentrations of free IRH and NPs after 7 days of treatment. 199

Figure 6.5. HGG cellular uptake of low, medium, and high concentrations of free IRH and NPs after 9 days of treatment. 200

Figure 6.6. SSC intensity of HGG cells treated with low, medium, and high concentrations of free IRH and F2 over 9 days (n=3). 201

Figure 6.7. SSC intensity of HGG cells treated with low, medium, and high concentrations of free IRH and F18 over 9 days (n=3). 201

Figure 6.8. SSC intensity of HGG cells treated with low, medium, and high concentrations of free IRH and blank F18 over 9 days (n=3). 202

Figure 6.9. Volume view by confocal microscopy showing HGG cells after a 3-day treatment with F2 203

Figure 6.10. Volume view by confocal microscopy showing HGG cells after a 3-day treatment with F18 203

Figure 6.11. Volume view by confocal microscopy showing HGG cells after a 5-day treatment with F2 204

Figure 6.12. Volume view by confocal microscopy showing HGG cells after a 5-day treatment with F18 204

Figure 6.13. Volume view by confocal microscopy showing HGG cells after a 3-day treatment with Rhodamine-123 loaded NPs.....205

Figure 6.14. Volume view by confocal microscopy showing HGG cells after a 5-day treatment with Rhodamine-123 loaded NPs.....205

Figure 6.15. Cytotoxicity of free IRH and F2 on primary HGG cells compared to control cells in patient 1 (n=3). 206

Figure 6.16. Cytotoxicity of free IRH and F18 on primary HGG cells compared to control cells in patient 1 (n=3). 207

Figure 6.17. Cytotoxicity of free IRH and Blank F2 on primary HGG cells compared to control cells in patient 1 (n=3). 208

Figure 6.18. Cytotoxicity of free IRH and Blank F18 on primary HGG cells compared to control cells in patient 1 (n=3). 209

Figure 6.19. Cytotoxicity of Blank F2 and F2 on primary HGG cells compared to control cells in patient 1 (n=3). 210

Figure 6.20. Cytotoxicity of Blank F18 and F18 on primary HGG cells compared to control cells in patient 1 (n=3). 211

Figure 6.21. Cytotoxicity of F2 and F18 on primary HGG cells compared to control cells in patient 1 (n=3). 212

Figure 6.22. Cytotoxicity of Blank F2 and Blank F18 on primary HGG cells compared to control cells in patient 1 (n=3). 213

Figure 6.23. Cytotoxicity of free IRH and F2 on primary HGG cells compared to control cells in patient 2 (n=3). 214

Figure 6.24. Cytotoxicity of free IRH and F18 on primary HGG cells compared to control cells in patient 2 (n=3). 215

Figure 6.25. Cytotoxicity of free IRH and Blank F2 on primary HGG cells compared to control cells in patient 2 (n=3). 216

Figure 6.26. Cytotoxicity of free IRH and Blank F18 on primary HGG cells compared to control cells in patient 2 (n=3). 217

Figure 6.27. Cytotoxicity of Blank F2 and F2 on primary HGG cells compared to control cells in patient 2 (n=3). 218

Figure 6.28. Cytotoxicity of Blank F18 and F18 on primary HGG cells compared to control cells in patient 2 (n=3). 219

Figure 6.29. Cytotoxicity of F2 and F18 on primary HGG cells compared to control cells in patient 2 (n=3). 220

Figure 6.30. Cytotoxicity of Blank F2 and Blank F18 on primary HGG cells compared to control cells in patient 2 (n=3). 221

Figure 6.31. Cytotoxicity of free IRH and F2 on primary HGG cells compared to control cells in patient 3 (n=3). 222

Figure 6.32. Cytotoxicity of free IRH and F18 on primary HGG cells compared to control cells in patient 3 (n=3). 223

Figure 6.33. Cytotoxicity of free IRH and Blank F2 on primary HGG cells compared to control cells in patient 3 (n=3). 224

Figure 6.34. Cytotoxicity of free IRH and Blank F18 on primary HGG cells compared to control cells in patient 3 (n=3). 225

Figure 6.35. Cytotoxicity of F2 and Blank F2 on primary HGG cells compared to control cells in patient 3 (n=3). 226

Figure 6.36. Cytotoxicity of F18 and Blank F18 on primary HGG cells compared to control cells in patient 3 (n=3). 227

Figure 6.37. Cytotoxicity of F2 and F18 on primary HGG cells compared to control cells in patient 3 (n=3). 228

Figure 6.38. Cytotoxicity of Blank F2 and Blank F18 on primary HGG cells compared to control cells in patient 3 (n=3). 229

Figure 6.39. Optical imaging of untreated control of primary HGG cells over 11 days period. 230

Figure 6.40. Optical imaging of primary HGG cells exposed to 6 hours of 2 μM staurosporine and 20% DMSO. 230

Figure 6.41. Optical imaging of primary HGG cells exposed to low, medium and high concentrations of IRH for 11 days. 232

Figure 6.42. Optical imaging of primary HGG cells exposed to low, medium and high concentrations of F2 for 11 days with black areas showing sediments of NPs at high concentration. 233

Figure 6.43. Optical imaging of primary HGG cells exposed to low, medium and high concentrations of F18 for 11 days. 235

Figure 6.44. Optical imaging of primary HGG cells exposed to low, medium and high concentrations of Blank F2 for 11 days. 236

Figure 6.45. Optical imaging of primary HGG cells exposed to low, medium and high concentrations of Blank F18 for 11 days 238

Figure 6.46. Quantification of viable, apoptotic, and necrotic HGG cells exposed to 1-day treatment of IRH and F2 compared to negative and positive controls. 239

Figure 6.47. Quantification of viable, apoptotic and necrotic HGG cells exposed to 1-day treatment of IRH and F18 compared to negative and positive controls (n=3).... 240

Figure 6.48. Quantification of viable, apoptotic and necrotic HGG cells exposed to 1-day treatment of IRH and blank F2 compared to negative and positive controls (n=3). 241

Figure 6.49. Quantification of viable, apoptotic, and necrotic HGG cells exposed to 1-day treatment of IRH and blank F18 compared to negative and positive controls (n=3). 242

Figure 6.50. Quantification of viable, apoptotic, and necrotic HGG cells exposed to 3-day treatment with IRH and F2 compared to negative and positive controls (n=3). . 243

Figure 6.51. Quantification of viable, apoptotic and necrotic HGG cells exposed to 3-day treatment with IRH and F18 compared to negative and positive controls (n=3). 244

Figure 6.52. Quantification of viable, apoptotic and necrotic HGG cells exposed to 3-day treatment with IRH and blank F2 compared to negative and positive controls (n=3). 245

Figure 6.53. Quantification of viable, apoptotic, and necrotic HGG cells exposed to 3-day treatment with IRH and blank F18 compared to negative and positive controls (n=3).....246

Figure 6.54. Quantification of viable, apoptotic, and necrotic HGG cells exposed to 5-day treatment with IRH and F2 compared to negative and positive controls (n=3). .247

Figure 6.55. Quantification of viable, apoptotic, and necrotic HGG cells exposed to 5-day treatment with IRH and F18 compared to negative and positive controls (n=3). 248

Figure 6.56. Quantification of viable, apoptotic, and necrotic HGG cells exposed to 5-day treatment with IRH and blank F2 compared to negative and positive controls (n=3). 249

Figure 6.57. Quantification of viable, apoptotic, and necrotic HGG cells exposed to 5-day treatment with IRH and blank F18 compared to negative and positive controls (n=3).....250

Figure 6.58. Caspase levels induced in HGG exposed to low, medium and high concentrations of IRH compared to positive and negative control expressed by relative light units (RLU) luminescence assay (n=3).....251

Figure 6.59. Caspase levels induced in HGG exposed to low, medium and high concentrations of F2 compared to positive and negative control expressed by RLU luminescence assay (n=3). 251

Figure 6.60. Caspase levels induced in HGG exposed to low, medium, and high concentrations of F18 compared to positive and negative control expressed by RLU luminescence assay (n=3). 252

Figure 6.61. Caspase levels induced in HGG exposed to low, medium, and high concentrations of blank F18 compared to positive and negative control expressed by RLU luminescence assay (n=3). 252

Figure 6.62. ATP levels induced in HGG exposed to low, medium and high concentrations of free IRH and F2 compared to negative control expressed by RLU luminescence assay (n=3). 253

Figure 6.63. ATP levels in HGG cells exposed to low, medium and high concentrations of free IRH and F18 compared to negative control expressed by RLU luminescence assay (n=3). 254

Figure 6.64. ATP levels induced in HGG exposed to low, medium, and high concentrations of free IRH and blank F18 compared to negative control expressed by RLU luminescence assay (n=3). 254

Figure 6.65. ATP levels induced in HGG exposed to low, medium, and high concentrations of F2 compared to F18 expressed by RLU luminescence assay (n=3). 255

Figure 6.66. Haemolysis induced in RBCs by 0.5, 1, 10 and 100 μM of IRH (n=3). 256

Figure 6.67. Haemolysis induced in RBCs induced by low, medium and high concentrations of F2 (n=3). 256

Figure 6.68. Haemolysis induced in RBCs induced by low, medium, and high concentrations of F18 (n=3). 257

Figure 6.69. Haemolysis induced in RBCs induced by low, medium, and high concentrations of Blank F18 (n=3). 257

Figure 6.70. OD of IL-6 standard concentrations of human IL-6 (n=3). 259

Figure 6.71. Expression of IL-6 in primary HGG cells exposed to low, medium and high concentrations of free IRH and F2 for 3 and 5 days (n=3). 259

Figure 6.72. Expression of IL-6 in primary HGG cells exposed to low, medium and high concentrations of free IRH and F18 for 3 and 5 days (n=3). 260

Figure 6.73. Expression of IL-6 in primary HGG cells exposed to low, medium, and high concentrations of free IRH and blank F18 for 3 and 5 days (n=3). 260

Figure 6.74. Expression of IL-6 in primary HGG cells exposed to low, medium, and high concentrations of F18 and blank F18 for 3 and 5 days (n=3). 261

Figure 6.75. Expression of IL-6 in primary HGG cells exposed to low, medium, and high concentrations of F2 and F18 for 3 and 5 days (n=3). 261

Figure 7.1. Endothelial cellular uptake of low, medium and high concentrations of free IRH and NPs after 1 day of treatment. 280

Figure 7.2. Endothelial cellular uptake of low, medium and high concentrations of free IRH and NPs after 3 days of treatment. 281

Figure 7.3. Endothelial cellular uptake of low, medium and high concentrations of free IRH and NPs after 5 days of treatment. 282

Figure 7.4. SSC light intensity of endothelial cells treated with low, medium and high concentrations of free IRH and F2 over 5 days (n=3). 283

Figure 7.5. SSC light intensity of endothelial cells treated with low, medium and high concentrations of free IRH and F18 over a 5-day period (n=3). 283

Figure 7.6. SSC light intensity of endothelial cells treated with low, medium and high concentrations of free IRH and blank F2 over 5 days (n=3). 284

Figure 7.7. SSC light intensity of endothelial cells treated with low, medium and high concentrations of free IRH and blank F18 over 5 days (n=3). 284

Figure 7.8. SSC light intensity of endothelial cells treated with low, medium and high concentrations of F2 and F18 over 5 days (n=3). 285

Figure 7.9. Cytotoxicity of free IRH and F2 on endothelial cells compared to control cells (n=3). 286

Figure 7.10. Cytotoxicity of free IRH and F18 on endothelial cells compared to control cells (n=3). 287

Figure 7.11. Cytotoxicity of free IRH and blank F2 on endothelial cells compared to control cells (n=3). 288

Figure 7.12. Cytotoxicity of free IRH and blank F18 on endothelial cells compared to control cells (n=3). 289

Figure 7.13. Cytotoxicity of F2 and blank F2 on endothelial cells compared to control cells (n=3). 290

Figure 7.14. Cytotoxicity of F18 and blank F18 on endothelial cells compared to control cells (n=3). 291

Figure 7.15. Cytotoxicity of F2 and F18 on endothelial cells compared to control cells (n=3). 292

Figure 7.16. Cytotoxicity of blank F2 and blank F18 on endothelial cells compared to control cells (n=3). 293

Figure 7.17. Optical imaging of untreated control of endothelial cells over 11 days. 294

Figure 7.18. Optical imaging of endothelial cells exposed to low, medium and high concentrations of IRH for 11 days. 295

Figure 7.19. Optical imaging of endothelial cells exposed to low, medium and high concentrations of F2 for 11 days. 297

Figure 7.20. Optical imaging of endothelial cells exposed to low, medium and high concentrations of F18 for 11 days. 298

Figure 7.21. Optical imaging of endothelial cells exposed to low, medium and high concentrations of Blank F2 for 11 days. 300

Figure 7.22. Optical imaging of endothelial cells exposed to exposed to low, medium and high concentrations of Blank F18 for 11 days. 301

Figure 7.23. Quantification of viable, apoptotic and necrotic endothelial cells exposed to 1-day treatment with IRH and F2 compared to negative and positive controls (n=3). 303

Figure 7.24. Quantification of viable, apoptotic and necrotic endothelial cells exposed to 1- day treatment with IRH and F18 compared to negative and positive controls (n=3). 304

Figure 7.25. Quantification of viable, apoptotic and necrotic endothelial cells exposed to 1-day treatment with IRH and blank F2 compared to negative and positive controls (n=3). 305

Figure 7.26. Quantification of viable, apoptotic and necrotic endothelial cells exposed to 1- day treatment with IRH and blank F18 compared to negative and positive controls *(n=3)*. 306

Figure 7.27. Quantification of viable, apoptotic and necrotic endothelial cells exposed to 3-day treatment with IRH and F2 compared to negative and positive controls (n=3). 307

Figure 7.28. Quantification of viable, apoptotic and necrotic endothelial cells exposed to 3-day treatment with IRH and F18 compared to negative and positive controls (n=3). 307

Figure 7.29. Quantification of viable, apoptotic and necrotic endothelial cells exposed to 3-day treatment with IRH and blank F2 compared to negative and positive controls (n=3).....308

Figure 7.30. Quantification of viable, apoptotic and necrotic endothelial cells exposed to 3-day treatment with IRH and blank F18 compared to negative and positive controls (n=3).....309

Figure 7.31. Quantification of viable, apoptotic and necrotic endothelial cells exposed to 5-day treatment with IRH and F2 compared to negative and positive controls (n=3). 310

Figure 7.32. Quantification of viable, apoptotic and necrotic endothelial cells exposed to 5-day treatment with IRH and F18 compared to negative and positive controls (n=3). 310

Figure 7.33. Quantification of viable, apoptotic and necrotic endothelial cells exposed to 5-day treatment with IRH and blank F2 compared to negative and positive controls (n=3).....311

Figure 7.34. Quantification of viable, apoptotic and necrotic endothelial cells exposed to 5-day treatment with IRH and blank F18 compared to negative and positive controls (n=3).....312

Figure 7.35. Effect of free IRH on TEER of brain endothelial cells (n=3). 313

Figure 7.36. Effect of F2 on TEER of brain endothelial cells (n=3). 313

Figure 7.37. Effect of F18 on TEER of brain endothelial cells (n=3). 314

Figure 7.38. Effect of blank F2 on TEER of brain endothelial cells (n=3).....314

Figure 7.39. Effect of blank F18 on TEER of brain endothelial cells (n=3). 315

Figure 7.40. Expression of IL-6 in endothelial cells exposed to low, medium and high concentrations of F2 for 3 and 5 days (n=3). 316

Figure 7.41. Expression of IL-6 in endothelial cells exposed to low, medium and high concentrations of F18 for 3 and 5 days (n=3). 317

Figure 7.42. Expression of IL-6 in endothelial cells exposed to low, medium and high concentrations of blank F2 for 3 and 5 days (n=3).....317

Figure 7.43. Expression of IL-6 in endothelial cells exposed to low, medium and high concentrations of blank F18 for 3 and 5 days (n=3).....318

Figure 7.44. Expression of IL-6 in endothelial cells exposed to low, medium and high concentrations of F2 and blank F2 for 3 and 5 days (n=3). 318

Figure 7.45. Expression of IL-6 in endothelial cells exposed to low, medium and high concentrations of F18 and blank F18 for 3 and 5 days (n=3).....319

Figure 7.46. Expression of IL-6 in endothelial cells exposed to low, medium and high concentrations of F2 and F18 for 3 and 5 days (n=3).....319

List of Abbreviations

ABC	ATP-Binding Cassette
AMT	Adsorptive-Mediated Transcytosis
ANOVA	Analysis Of Variance
ARPE-19	Retinal Vascular Endothelial Cells
ATP	Adenosine Triphosphate
BBB	Blood Brain Barrier
BBD	Box-Behnken Design
BBTB	Blood Brain Tumour Barrier
BCNU	Bis-Chloroethylnitrosourea
BCRP	Breast Cancer Resistance Protein
BLB	Labyrinthine Barrier
CAT1	Cationic Amino Acid Transporter
CED	Convection Enhanced Delivery
CHO	Chinese Hamster Ovarian
ChT	Choline Transporter
CMT	Carrier-Mediated Transport
CNS	Central Nervous System
CSF	Cerebrospinal Fluid
DAPI	(4',6-Diamidino-2-Phenylindole)
DCM	Dichloromethane
DE	Double Emulsion

DF	Degrees Of Freedom
dH_2O	Deionized Water
DLS	Dynamic Light Scattering
DMAB	Didodecyl Dimethyl Ammonium Bromide
DMSO	Dimethyl Sulfoxide
DOE	Design Of Experiments
DSC	Differential Scanning Calorimetry
EE	Encapsulation Efficiency
EPR	Enhanced Permeability And Retention Effect
ESEM	Environmental Scanning Electron Microscope
F-Value	Fischer's Ratio
FACS	Fluorescence-Activated Cell Sorting
FBS	Foetal Bovine Serum
FDA	Food And Drug Administration
FEG	Field Emission Gun
GBM	Glioblastoma Multiforme
GLUT1	Glucose Transporter
HBRC	Human Biomaterials Resource Center
HCL	Hydrochloric Acid
HGG	High Grade Gliomas
HLB	Hydrophilic–Lipophilic Balance
HPLC	High Performance Liquid Chromatography
HRP	Horseradish Peroxidase
ICV	Intracerebroventricular

IDH	Isocitrate Dehydrogenase
IL-6	Interleukin-6
IMRT	Fixed Field Intensity Modulated RT
IRH	Irinotecan Hydrochloride Trihydrate
LAT1	L-Type Amino Acid Transporter
LDL	Low-Density Lipoprotein
MCT1	Monocarboxylate Lactate Transporter
MDR	Multidrug Resistance
MEM NEAA	Minimum Essential Medium Non-Essential Amino Acid Solution
MGMT	Methyl Guanine Methyl Transferase
MPS	Mononuclear Phagocyte System
MRI	Magnetic Resonance Imaging
MS	Mean Of Squares
MTT	3-(4,5-Dimethylthiazol-2-Yl)-2,5-Diphenyltetrazolium Bromide
NCCN	National Comprehensive Cancer Network
NPs	Nanoparticles
O	Organic Phase
O/O	Oil In Oil
O/W	Oil In Water
O1	First Oil Phase
O2	Second Oil Phase
OD	Optical Density

P-Gp	P-Glycoprotein
PBCA	Poly (Butyl-Cyanoacrylate)
PBS	Phosphate Buffer Saline
PCL	Polycaprolactone
PDI	Polydispersity Index
PEG	Polyethylene Glycol
PGA	Poly (Glycolic Acid)
PI	Propidium Iodide
PLA	Poly (Lactic Acid)
PLGA	Poly (Lactic-Co-Glycolic Acid)
PTS-6	Peptide Transport System-6
PVA	Polyvinyl Alcohol
PVP	Polyvinyl Pyrrolidone
RBCs	Red Blood Cells
RES	Reticuloendothelial System
RLU	Relative Light Units
RMT	Receptor-Mediated Transcytosis
ROS	Reactive Oxygen Species
RT	Radiation Therapy
RVEC	Retinal Pigment Epithelial Cells
SCF	Supercritical Fluid
SD	Standard Deviation
SE	Single Emulsion
SEM	Scanning Electron Microscope

SGLT	Sodium-Coupled Glucose Transporters
SRS	Stereotactic Radiosurgery
SS	Sum Of Squares Of The Model
SSA	Sum Of Squares for Each Individual Factor
SSC	Side Scattered Light
TEER	Transendothelial Electrical Resistance
TEM	Transmission Electron Microscope
Tg	Glass Transition Temperature
Tm	Melting Temperature
TMZ	Temozolomide
VEGF	Vascular Endothelial Growth Factor
VMAT	Volumetric-Modulated Arc Therapy
W/O	Water In Oil
W/O/O	Water In Oil In Oil
W/O/W	Water In Oil In Water
W1	Inner Aqueous Phase
W2	Outer Aqueous Phase
XRD	X-Ray Diffraction

Chapter 1 POLYMERIC NANOPARTICLES FOR THE TREATMENT OF MALIGNANT GLIOMAS

This chapter involves an open access publication cited as ***Mahmoud, B. S., Alamri, A. H. and McConville, C. (2020) 'Polymeric nanoparticles for the treatment of malignant gliomas', Cancers. MDPI AG, 12(1), p. 175***. Author Contributions: Design and writing of the publication were mainly done by the first author. The second author contributed with sections 1.10, 1.11 and 1.13. Reviewing of the publication was done by the third author.

Abstract: Malignant gliomas are one of the deadliest forms of brain cancer and despite advancements in treatment, patient prognosis remains poor, with an average survival of 15 months. Treatment using conventional chemotherapy does not deliver the required drug dose to the tumour site, owing to insufficient blood brain barrier (BBB) penetration, especially by hydrophilic drugs. Additionally, low molecular weight drugs cannot achieve specific accumulation in cancerous tissues and are characterized by a short circulation half-life. Nanoparticles can be designed to cross the BBB and deliver their drugs within the brain, thus improving their effectiveness for treatment when compared to administration of the free drug. The efficacy of nanoparticles can be enhanced by surface PEGylation to allow more specificity towards tumour receptors. This review will provide an overview of the different therapeutic strategies for the treatment of malignant gliomas, risk factors entailing them as well as the latest developments for brain drug delivery. It will also address the potential of polymeric nanoparticles in the treatment of malignant gliomas, including the importance of their coating and functionalization on their ability to cross the BBB and the chemistry underlying that.

Keywords: brain tumours; glioma; blood brain barrier; drug delivery; nanomedicine; polymeric nanoparticles; PEGylation

1.1 Introduction

In the past decade, there has been a great development in medicine and cancer treatment. However, cancer remains a challenging health issue owing to its complicated nature (Kaufmann and Chiocca, 2014; Silva et al., 2019). The number of cancer cases is expected to rise to 27.5 million in 2040, as stated by the American Cancer Society (Kaufmann and Chiocca, 2014). Among the most troublesome malignant cancers are the primary brain cancers that can rarely be cured, with a 5-year overall survival of only 35%. Gliomas count as the most common form of malignant primary brain tumours in adults (Lapointe et al., 2018).

The speed and ability to infiltrate and metastasize to nearby brain tissues are the main factors that determine if glioma cells are of low grade (WHO I and II) or high grade (WHO III and IV) (Paw et al., 2015). Gliomas have the ability to infiltrate to surrounding tissue and their margins are difficult to determine. This results in conventional treatment approaches being insufficient to produce a curative outcome. Also, the difficulty in achieving successful therapeutic approaches is caused by the physical and chemical barriers that exist, hampering drugs from reaching tumour sites (Cornago et al., 2014; De Boer and Gaillard, 2007; Parrish et al., 2015; Van Tellingen et al., 2015). The blood brain barrier (BBB) and blood brain tumour barrier (BBTB) represent the main barriers that stop drugs from entering the brain unless they possess certain characteristics. The BBTB represents a compromised BBB that varies in its level of disruption with patient-to-patient variability, tumour heterogeneity and tumour location within the brain (Sarkaria et al., 2018). Previous research has concluded that the majority of glioblastoma (GBM) features a highly resistant BBB despite showing a

significant tumour burden (Sarkaria et al., 2018). The multipotent stem cells that give rise to glioma cells, have the ability to self-renew and are responsible for glioma recurrence (Binello and Germano, 2011). Efforts have been extended towards overcoming physical hurdles by developing techniques that deliver therapeutics to the brain, however, most of these approaches are invasive and fraught with serious side effects, so curative measures should not be only based on extending survival, but also towards improving the quality of life of patients by reducing side effects. Among the advanced therapeutic strategies is using polymeric nanoparticles for drug delivery and targeting. As will be discussed later in this review, *in vitro* and *in vivo* studies have reported promising results for drug loaded nanoparticles targeted to gliomas. Therefore, more efforts should be made towards the betterment of these nanomedicines in terms of improving their loading efficiencies, coating and ability to target gliomas.

1.2 High Grade Gliomas

Primary malignant brain tumours in adults are mostly gliomas, 75% of which are high grade gliomas (HGG) diagnosed in the central nervous system (CNS). The rate of incidence is 3 to 5 per 100,000 every year, afflicting mostly men. HGG can occur at any age, however, they mainly occur in the 5th and 6th decades of life (Dolecek et al., 2012). Bailey and Cushing developed the seminal system for defining the morphology of glial tumours in the 1920s which is based on the glia stage of growth (MacKenzie, 1926). This system was used by the WHO in 2000 to classify Gliomas based on their morphology (Louis et al., 2016). Gliomas were further stratified based on genetic and molecular factors that were recognized and reported by the WHO in 2016. These

factors include isocitrate dehydrogenase (IDH) mutation status, the co-deletion status of 1p/19q and the mutation status of alpha thalassemia/mental retardation syndrome X-linked protein/gene (ATRX) (Louis et al., 2016). According to the 2016 WHO classification, grade III tumours which include anaplastic astrocytoma, anaplastic oligodendroglioma and mixed anaplastic oligoastrocytoma are among HGGs, in addition to grade IV GBM (Louis et al., 2016). GBM has the highest incident rate among HGGs with up to 60–70% of cases being a GBM. This is followed by anaplastic astrocytoma which makes up 10–15% of cases. Whereas, anaplastic oligodendrogliomas and anaplastic oligoastrocytomas have the least frequent incidence rate of only 10% (Sathornsumetee et al., 2007). Some other types of malignant gliomas, such as the WHO grade III gliomas, anaplastic ganglioglioma, anaplastic pilocytic astrocytoma and anaplastic pleomorphic xanthoastrocytoma and the grade IV gliomas, giant cell and small cell GBM, epithelioid GBM, and gliosarcoma are not very common. The main cause for HGGs is still enigmatic, with ionizing radiation only identified as a possible risk factor (Fischer and Meese, 2007).

1.3 Treatment

1.3.1 Surgical Resection

The site, grade and morphology of the tumour will determine if complete surgical resection of the tumour can be achieved. Patients with high grade tumours require near complete resection in order to reduce the burden of the tumour and pressure inside the skull, which in turn improves the survival rate (Fadul et al., 1988; Hentschel and Sawaya, 2003; Hess, 1999; Simpson et al., 1993). GBM cannot be fully cured with

surgical resection as it is invasive in nature and 80% of cases result in relapse within 2 to 3 cm of the original tumour margin (Iacob and Dinca, 2009).

1.3.2 Radiation Treatment

Radiation therapy (RT) can be administered internally or externally and is considered the standard treatment protocol for HGGs (Van Den Bent et al., 2005). The standard treatment using external RT involves 25 to 35 treatments on a daily basis for (5–7) weeks. Several factors control the total radiation dose to be administered which are: tumour site, grade, histology and the extent of resection (Chandana et al., 2008). A randomized trial conducted in the 1970s reported that whole brain irradiation with 60 Gy after surgical resection enhanced survival for patients suffering from HGG. This resulted in RT as being a standard therapy following tumour eradication for HGG (Walker, 1978). On the other hand, studies that investigated the difference between partial and whole brain irradiation for HGG treatment proved that whole brain irradiation did not provide extra benefit compared to partial irradiation of the brain (Shapiro et al., 1989). However, there was an improvement in the delineation accuracy that was achieved employing tomography and magnetic resonance for maintaining a partial irradiation of the brain for HGG cases (Heesters et al., 1993). The developments that have occurred in imaging and RT have enabled irradiation of tumour regions with higher doses while reducing the volume of normal brain tissue exposed to irradiation. Therefore, involved field RT was granted acceptance as the standard of care for HGGs. However, the issue of RT delivery for smaller surface areas remains debatable with efforts towards targeting infiltrating tumour cells (Saran et al., 2018). Some techniques that have been recognized for providing a more targeted irradiation towards

tumour tissues include fixed field intensity modulated RT (IMRT), dynamic arc IMRT, volumetric-modulated arc therapy (VMAT) and stereotactic radiosurgery (SRS). These techniques were reported to provide a more focused approach towards affected tissues while reducing toxicity to normal tissues (Scaringi et al., 2018). SRS is used to treat recurrent GBM and is used as a complementary treatment after external beam RT. However, the use of SRS for the treatment of recently diagnosed malignant gliomas is still under review (Chandana et al., 2008). Another approach for RT is interstitial RT or brachytherapy where radioactive material is implanted inside the tumour with the use of surgery. Proton therapy could also aid in targeting affected areas and may be used instead of photon irradiation (Scaringi et al., 2018). RT is associated with some limitations including necrosis of normal brain tissue, neuronal damage and radiation resistance of tumour cells (Iacob and Dinca, 2009).

1.3.3 Chemotherapy

The chemotherapeutic drug temozolomide (TMZ) is used in combination with RT in patients with HGG in order to improve the survival rate of patients. This protocol, known as the Stupp protocol, demonstrated a median survival rate of 14.6 month compared to 12.1 months (when RT alone was administered) in a phase III clinical trial. TMZ is initially administered at a daily dose of 75 mg/m^2 for 6 weeks, with a 1-month rest period upon the completion of RT treatment. TMZ treatment begins again with a daily dose of 150 mg/m^2 for 5 days in the first month. If this dose can be withstood by the patient, a higher daily dose of 200 mg/m^2 is administered for 5 consecutive days each month until the end of the treatment period. The Stupp protocol administers the TMZ therapy for 6 months following RT (Stupp et al., 2005). Synergistic effect of combined

therapy using RT and adjuvant chemotherapy with TMZ continued over a 5-year follow up treatment period. Also, the inclusion of TMZ was more beneficial for patients with a methylated gene promoter that encodes O-6-methylguanine-DNA methyltransferase (MGMT). This in turn had resulted in identifying MGMT as the first biomarker in brain tumours to help anticipate the responsiveness to the TMZ treatment and selection of patients accordingly (Stupp and Roila, 2009). However, MGMT is unreliable for patients who do not have a methylated promoter of MGMT except for elderly GBM patients (Vleeschouwer and Bergers, 2017). Some other chemotherapeutic drugs have shown efficacy against recurrent malignant gliomas. These drugs are non-methylating agents such as irinotecan or those that target the vascular endothelial growth factor (VEGF) such as bevacizumab. Other chemotherapy drugs such as gefitinib, erlotinib and imatinib target the epidermal and platelet-derived growth factor receptors (Stupp et al., 2006).

Among the latest therapeutic approaches is a device named Optune® that received approval by the U.S. Food and Drug Administration (FDA) in October 2015. This device allows for the delivery of electric fields that enable the treatment of tumours by interrupting the division of cells causing cell death. It is used as an adjuvant therapy with TMZ following surgical resection and is the standard of care for adults that have been recently diagnosed with supratentorial GBM. The Optune® treatment regimen alongside TMZ increased survival from 4 to 7 months when compared to treatment with TMZ alone (Stupp et al., 2015). Optune® was initially approved by the FDA in 2011 as a single treatment for recurrent GBM. Optune® is alternatively used as a treatment for primary GBM after surgery and RT have been shown to be ineffective. A

randomized clinical trial exhibited similar rate of survival and less side effects with a significant reduction in the infectious, gastrointestinal and hematologic complications for the Optune® treatment group compared to the standard chemotherapy group (Stupp et al., 2012). The reduced side effects and practicality of use encouraged the National Comprehensive Cancer Network (NCCN) to include Optune® as a treatment for recurrent GBM (Davis, 2013).

Other treatment approaches such as radioimmunotherapy, iodine-125 brachytherapy, hyperfractionation and SRS have been investigated for their ability to localize treatment and protect normal brain tissues. However, none have been shown to improve survival rates (Barani and Larson, 2015). Therefore, it was concluded that chemotherapy used concomitantly and adjuvantly with RT is the standard of care in current application for GBM patients until more effective treatments become available (Stupp and Roila, 2009).

1.4 Postoperative Treatment

Follow up is necessary to monitor the postoperative complications and control the disease symptoms, which include seizures, cerebral oedema, turbulences in the gastrointestinal tract, osteoporosis, venous thromboembolism, dysfunction of the cognitive abilities and mood deterioration (Norden and Wen, 2006). Magnetic Resonance Imaging (MRI) scans are used to monitor the size of the tumour and performed 3 days following the surgical operation to determine how much of the tumour was eradicated. Steroids are administered to patients suffering vasogenic edema. However, treatments based on steroids are associated with adverse side effects such as myopathy (Kostaras et al., 2014) which affects 10% of patients with HGGs with an

increased incidence rate in elderly patients that are administered corticosteroids for long time periods (Wen et al., 2006). Also, patients become vulnerable to mental impairment, hyperglycemic and gastrointestinal complications, in addition to opportunistic fungal infections such as *Pneumocystis jirovecii*. Dexamethasone is a more favourable corticosteroid as it is lower in activity and upon its discontinuation, myopathy can be reversed (Omuro and DeAngelis, 2013; Wen et al., 2006). Patients with GBM and CNS lymphoma are more susceptible to venous thromboembolism, especially after craniotomy. Treatment using warfarin or heparin of low molecular weight is more favourable than vena cava filters in controlling the anticoagulation and reducing the complications. Levetiracetam is usually administered to patients suffering seizures due to its low toxicity and the fact that it does not interact with the chemotherapy drugs (Omuro and DeAngelis, 2013).

1.5 Prognosis

Patient prognosis remains depressing with a 15-month median survival, despite the advancements in surgical resection of the tumours (Thakkar et al., 2014). Anaplastic astrocytoma afflicted patients average between 2 to 3 years survival (Wick et al., 2009). The best prognosis is shown in cases suffering anaplastic oligodendroglioma leaving them with expected average survival of 12 to 15 years (Cairncross et al., 2013). The prognostic factors involve: the extent of tumour resected, age of the patient and the Karnofsky Performance Status. Younger age and higher performance status could imply longer survival. Negative results have been linked to tumours larger than 5 to 6 cm (Ellor et al., 2014). Surgically curable tumours such as those that arise in the

cerebrum or cerebellum have a better prognosis than those that arise in the brainstem or diencephalon (Walid, 2008).

1.6 Glioblastoma Multiforme

GBM is a malignant tumour that arises in the brain and is known to be the most common form of brain tumours. It represents 16% of the tumours that originate in the brain and CNS (Thakkar et al., 2014). GBM has an incidence rate of 3.2 per 100,000 population in the united states (Ostrom et al., 2015, 2014). GBMs are mainly located in the brain but can also occur in the brain stem, cerebellum and spinal cord. Moreover, the four lobes of the brain (frontal, temporal, parietal and occipital) represent the main sites for the development of the primary gliomas, with an overall incidence rate of 61% and individual incidence rate of 25%, 20%, 13% and 3%, respectively (Lovely et al., 2014). Initially, glial cells were thought to be the only source of GBMs, however, it has been shown that several types of cells possessing the characteristics of neural stem cells, could give rise to GBMs. These cells vary in their differentiation stage where they start out as stem cells then give rise to neurons and glia. This is accompanied with changes in their phenotype, mainly caused by the variation in their signalling pathways instead of the differences in the origin of the cell type (Tomasetti et al., 2017). The average age in which GBMs develop is 64 (Thakkar et al., 2014). Nevertheless, GBMs can develop at any age including children. Men are more likely to develop a GBM than women with a rate of 1.6 for every woman. Caucasians are also more likely to be stricken with the disease than other ethnicities (Ellor et al., 2014).

GBMs can vary in their classification, for example a GBM would be classed as primary or de novo in origin if it has developed without a defined precursor. If a GBM develops

from a transformed low-grade tumour it will be termed secondary. Most GBMs are primary in nature and mainly afflict the elderly, who have a poorer prognosis than their counterparts who develop secondary GBM (Wilson et al., 2014). GBMs can be further classified into four subtypes which are, classical, pro-neural, neural, and mesenchymal. Each subtype varies in its mode of development and survival (Phillips et al., 2006; Verhaak et al., 2010). GBMs are invasive in nature and are difficult to completely remove by surgical resection. They often exist in sensitive areas of the brain which mainly control speech, movement or the senses. The tumour cells also possess the ability to infiltrate and remain in areas that surround the brain, which leads to further disease recurrence (Wilson et al., 2014).

1.6.1 Current Management

The current treatment regimen for GBM is the Stupp protocol which was discussed earlier as the standard of care for glioma management (Stupp and Roila, 2009). The main action of TMZ involves methylation of the DNA at the N7 and O6 positions on guanine which halts the DNA mismatch repair mechanism resulting in DNA nicks that halts the cell cycle at the G2-M level, causing apoptosis. However, the elevated level of MGMT activity which functions by protecting tumour cells against chemotherapeutic agents can negatively impact the TMZ response. Moreover, TMZ, is reported to be fraught with deleterious complications such as hematological issues, fatigue and susceptibility to infections (Hart et al., 2013). Another chemotherapeutic agent used to treat GBM is the Gliadel® Wafer, which is a disc shaped 200 mg wafer made of biodegradable copolymers that contain 3.85% *w*/*w* of the alkylating agent bis-chloroethylnitrosourea (carmustine, also known as BCNU). Carmustine was initially

approved by the FDA as a potent antineoplastic agent for the treatment of GBM by intravenous administration (Ashby et al., 2016). Gliadel® is used for local administration of carmustine, with up to 8 discs placed into the resection cavity during surgery. After treatment with Gliadel® Wafers, the median survival in a group of patients with malignant glioma (95% of which was GBM) was 42 weeks, eight patients survived one year, and four patients survived more than 18 months. Local treatment allows the chemotherapy to be concentrated at the site of the tumour while avoiding systemic side effects. However, patients suffered perioperative infections, seizures and required addition steroid treatment (Brem et al., 1995). Moreover, the drug penetration into tissues after diffusion from the implants does not exceed 1mm which limits its efficacy (Fung et al., 1998).

In summary, the drawback of these treatments is that they are associated with serious unwanted side effects in addition to the development of resistance, limiting their efficacy. Some patients do not respond to the TMZ or BCNU, therefore, there has been a second line of drugs developed which include carboplatin, oxaliplatin, etoposide and irinotecan. Additional chemotherapeutic agents for GBM include anti-angiogenic agents like anti-VEGF monoclonal antibodies (bevacizumab), anti-FGF antibodies, monoclonal antibodies targeting EGFR (erlotinib and gefitinib) and tyrosine kinase inhibitors (Chang et al., 2007; Friedman et al., 2000; Iacob and Dinca, 2009; Scott et al., 2011). Despite developments in tumour diagnosis and treatment using RT and concomitant chemotherapy with TMZ, nearly all GBM patients experience tumour recurrence.

1.7 The Blood Brain Barrier

One of the main limitations in the systemic treatment of malignant gliomas is the presence of the BBB, which is a complex structure that comprises endothelial cells, pericytes, astroglia and perivascular mast cells and acts as a barrier to most cells, pathogens and drugs circulating in the blood. The BBB is compact in nature due to the presence of tight junctions between the endothelial cells of the vascular layer that are closely stuck together. The BBB surrounds both the brain and spinal cord capillaries and its compactness halts small molecules and ions from passing through the BBB and into the brain. The tightness of the BBB stops integral membrane proteins from moving between the apical and basolateral membranes of the cell, thus protecting the cell membrane from loss of function (De Boer and Breimer, 1998; Petty and Lo, 2002; Wahl et al., 1988).

The tight junctions of the BBB have three fundamental proteins which are occludin, claudins, and junctional adhesion molecules. Occludin and claudins form the pillar of junction strands. Whereas, when there is an immunologic response in the brain, the junctional adhesion molecules function in the transport of lymphocytes, neutrophils, and dendritic cells from the vascular system. The tight endothelial junctions and adherens junctions are made of cadherins and catenin proteins that are responsible for the adherence of the BBB endothelial cells, forming a transelectrical resistance >1500 W cm^2. Although the BBB acts as a physical barrier, it still regulates the transport of metabolic molecules to the brain for nutrition. Small molecules such as glucose or amino acids have specific transporters that convey them to the brain. While, macromolecules such as cytokines and neutrophils enter the brain by receptor mediated endocytosis (Kastin et al., 1999b; Rabanel et al., 2012).

The BBB limits the passage of chemotherapeutic drugs with only low molecular weight, electrically neutral, hydrophobic drugs able to cross the BBB with a preference towards molecular weight less than 500 Da and lipophilicity expressed in log *P* as (2–3) (Habgood et al., 2000). Most chemotherapeutic drugs are large, ionically charged, hydrophilic molecules and thus cannot easily cross the BBB at the levels required for therapeutic effect, which means a large systemic dose is required. For example, irinotecan hydrochloride, which is a potent anionic chemotherapy drug, possesses a molecular weight of 623.1 Da and is hydrophilic in nature, therefore it will face difficulty crossing the BBB and accumulating in the tumour in its initial administered dose. Even if the drug crosses the BBB, it can very quickly diffuse back making it difficult to obtain constant drug levels in the brain after systemic administration.

1.8 Drug Delivery to the Brain

Two strategies, crossing the BBB and bypassing the BBB, are currently used for the delivery of drugs to the brain. Crossing the BBB can take place *via* six main pathways: paracellular transport, passive transcellular diffusion, carrier-mediated transport (CMT), receptor-mediated transcytosis (RMT), adsorptive-mediated transcytosis (AMT), and cell- mediated transport. The normal physiology of the BBB does not afford paracellular permeability (Hawkins and Davis, 2005a). However, it can take place when the BBB is compromised in CNS disorders such as GBM, which could facilitate drug delivery to the brain (Jain, 2012). Transmembrane diffusion allows for the intake of most of the compounds based on their molecular weight and lipid solubility. Influx and efflux transporters facilitate mediated transport, which relies on protein carriers that bind solutes and transport them from the luminal side of the BBB to the other side

of the membrane *via* passive or active transport mechanism (Hart et al., 2013). Among the influx transporters are l-type amino acid transporter (LAT1), glucose transporter (GLUT1), monocarboxylate lactate transporter (MCT1), cationic amino acid transporter (CAT1), choline transporter (ChT), sodium-coupled glucose transporters (SGLTs). Influx transporters facilitate particle uptake by the BBB. Efflux transporters, on the other hand, mediate molecules exclusion from the BBB. These transporters are like p-glycoprotein (P-gp), peptide transport system-6 (PTS-6), and breast cancer resistant protein (BCRP) (Yu et al., 2013; On and Miller, 2014; Shityakov and Förster, 2014; Miller, 2015). RMT involves the uptake of macromolecules by clathrin-mediated or caveolin-mediated endocytosis. This route has been previously used to deliver both free drugs and nanoparticles into the brain (Kreuter, 2001). RMT is the route by which actively targeted drugs are internalized. Receptors expressed on the surface of cells are recognized and bound by complementary ligands coating the drug loaded nanoparticles and this complex structure enters the cell in vesicles coated with clathrin. This process is 1000 times more efficient than pinocytosis (Bray et al., 1998). The size of clathrin-coated vesicles is determined by the size of the drug delivery vehicle which they carry (Ehrlich et al., 2004). Several receptors aid in transporting compounds across the BBB, such as the insulin receptor, low-density lipoprotein (LDL) receptor, transferrin receptor, neonatal Fc receptor and leptin receptor (Giddings et al., 1985; Skarlatos et al., 1995; Golden et al., 1997; Zhang and Pardridge, 2001; Schlachetzki et al., 2002). Whether internalization occurs by pinocytosis or RMT, the cargo is delivered to the early endosome, which is of slightly acidic pH (6–6.8). The endosome has a sorting function, where it either allows the recycling of molecules back to the plasma membrane or sends them to late endosome and lysosome for degradation

(Mellman, 1996). Whereas, caveolin-mediated endocytosis forms caveolae which are invaginations in the plasma membrane that take the shape of small flasks that engulf large molecules and transport them internally. AMT relies on the electrostatic interaction between positively charged substances and the plasma membrane, leading to internalization of molecules followed by their transport across the BBB. This pathway could be exploited by developing drugs or nanoparticles with positive charges or by conjugating the drug or nanoparticles with a positively charged ligand (Hervé et al., 2008; Wang et al., 2010). CMT exploits the natural mechanism involved in inflammation with drugs and nanoparticles engulfed by immune cells such as monocytes and macrophages (Batrakova et al., 2011; Masserini, 2013). In diseases such as neuroinflammation, or GBM, immune cells such as leukocytes are transported towards the brain parenchyma by chemotaxis and diapedesis processes. This process could be exploited in designing drugs or nanoparticles that can be phagocytosed by leukocytes and thus transported into the brain. The efficacy of free drugs and nanoparticles delivered by this natural mechanism, also known as the Trojan Horse mechanism has been shown to increase. This mechanism allows for larger sized particles to enter the brain, however, their larger size can result in increased toxicity (Rodrigueza et al., 1993; Jain et al., 2003; Qin et al., 2007). There are a number of options for bypassing the BBB. Intracerebroventricular (ICV) administration is performed through an invasive procedure of skull penetration and drug injection directly into the brain. An implantable reservoir or a pump is used to introduce the drug through an outlet catheter. The pump allows for a constant drug supply at high concentrations. The ICV process is extremely invasive and can lead to infections and increased intracranial pressure (Bennewitz and Saltzman, 2009).

Intracerebral/intraparenchymal administration involves the delivery of drugs directly into brain tissue either *via* stereotactic injection or by formulating into an implant that can be implanted during resection surgery (i.e., Gliadel®) or *via* stereotactic surgery. The issue with this type of delivery is that drug diffusion occurs slowly and allows drug to travel only 2 mm from the injection/implantation site (Bennewitz and Saltzman, 2009). Convection Enhanced Delivery (CED) is a slightly less invasive surgical procedure where catheters are placed inside the interstitial space of the brain parenchyma. A drug solution is administered into the brain under a positive pressure gradient using a pump, leading to a higher distribution volume compared to intracerebral/intraparenchymal administration (Bennewitz and Saltzman, 2009). This procedure is still, however, invasive in nature and could subject patients to the risk of infections, tissue injury and air bubbles. Furthermore, due to the high pressure used, the drug solution could leak into sensitive areas of the brain, such as subarachnoid space (Bennewitz and Saltzman, 2009). Intrathecal administration is considered one of the least invasive procedures, where drugs are injected into the subarachnoid space of the spinal cord *via* a lumbar puncture where they reach the CNS parenchyma in the cerebral spinal fluid (Yi et al., 2014). However, possible side effects such as infections and adverse immune response could occur due to this technique (Yi et al., 2014). In addition, although the ICV and intrathecal techniques can bypass the BBB and cerebrospinal fluid (CSF) hurdles, there remain the ependymal cell layer and glial cells which come in the way between the CSF and the brain parenchyma limiting the efficacy of drug diffusion to reach the brain parenchyma *via* these techniques (Blasberg et al., 1975). Intratympanic administration employs the route of the middle ear to administer drugs, which are transported *via* pinocytosis, eventually reaching the brain where they

bypass the labyrinthine barrier (BLB) which is similar to the BBB. This route can be suitable for therapeutics up to 1 μm size (Chen et al., 2010). Poly(d,l-lactide-co-glycolide) (PLGA) nanoparticles were used to administer drugs *via* this route with promising efficacy (X. Zhang et al., 2013). Intranasal delivery is a non-invasive route of administration for bypassing of the BBB through spraying drugs into the nasal cavity, where they diffuse extracellularly or *via* convection. Another route is through olfactory sensory neuron termed intraneuronal transport or through trigeminal nerve, termed intraneuronal transport (Lochhead and Thorne, 2012). The intranasal route is beneficial in terms of being convenient to patients, allowing for rapid absorption and avoiding first pass metabolism (Zhang et al., 2016). Some other methods for crossing the BBB have been investigated, most of which are invasive in nature, such as osmotic opening of the BBB (Bellavance et al., 2008). Other non-invasive methods have also been investigated, for example, the Trojan Horse technology which relies on coupling drugs to genetically engineered proteins that can cross the BBB by receptor mediated transport processes (Wilson, 2009). Such methods are also fraught with side effects and thus alternative more effective and less toxic methods for delivery of drugs to the brain are needed in order to improve the treatment of brain tumours (Busquets et al., 2015).

1.9 Nanomedicine: A Non-Invasive Approach towards a Better Quality of Life

Nanotechnology has provided us with a promising tool that can be used to enhance the uptake of drugs across the BBB (Holmes, 2013; Re et al., 2012). This is because nanoparticles have the ability to be loaded with therapeutic agents and functionalized with multiple ligands that enable targeting and crossing of the BBB. In this case, the

ability to cross the BBB will not be dependent on the structure of the drug, which cannot readily be altered, but on the physicochemical properties of the nanoparticles, which can be altered. Nanoparticles are proposed to perform their action in delivering drugs across BBB by concentrating the drug inside or at the surface of the BBB, which will result in a high concentration gradient between blood and brain, encouraging passive diffusion of the drug into the brain (Haque et al., 2012).

Nanoparticles have the ability to diffuse into the leaky vasculature of tumour tissues by the enhanced permeability and retention effect (EPR). This cancer-specific attribute is characterized by poor lymphatic drainage allowing the accumulation of nanoparticles to reach concentrations much higher than their concentrations in plasma (Wicki et al., 2015). The effective treatment of GBM can be accomplished by achieving three main goals: (1) Improving the ability of chemotherapeutic agents to cross the BBB, penetrate into brain tissue reaching the tumour tissue at therapeutic concentrations (2) Avoiding or reducing side effects and (3) Sustaining therapeutic concentrations of the drugs at the site of the tumour, increasing their half-life and avoiding rapid clearance (Wicki et al., 2015).

1.9.1 Physicochemical Properties of Nanoparticles

The different physicochemical properties of nanoparticles such as the particle size, surface charge, hydrophobicity and coating material have an impact on the targeting process. They also impact the interaction of particles with the cell membrane and passage through biological body barriers (Malikmammadov et al., 2018). Size is an important factor that allows transport of nanoparticles in the blood stream and enables delivery of nanoparticles to the site of the tumour. Small sized nanoparticles can easily

reach the leaky blood vessels of the tumour, however, they can extravasate into the normal tissues (Bregoli et al., 2016). Therefore, optimization of nanoparticles size can enhance their uptake into tumour tissues. The shape of nanoparticles is also of importance as it influences the fluid dynamics and thus particle uptake. The current trend is towards using spherical nanoparticles owing to the ease in their synthesis and application (Truong et al., 2015). In addition, the stability of nanoparticles is affected by their surface charge which also impacts their distribution in the bloodstream. Previous studies have shown that positively charged nanoparticles could be more effective in targeting tumour vessels. However, this has been replaced by neutrally charged nanoparticles which extravasate quicker into the tumour tissue (Stylianopoulos et al., 2010).

1.9.2 Nanoparticles as a Treatment for Malignant Gliomas

A range of different nanoparticle formulations have been investigated to deliver chemotherapeutic drugs to the brain. The majority of these formulations have utilized polymers that have met the strict requirements needed to be accepted for biological applications (Adabi et al., 2017). During recent years, nanoparticles for the treatment of CNS diseases such as GBM have received significant attention (Saraiva et al., 2016; Wong et al., 2012). With systemic administration of free drug, a small percentage of the drug crosses the BBB with non-specific accumulation in off target tissues resulting in serious unwanted side effects. Therefore, the use of nanoparticles for delivery to the brain has the potential to increase the percentage of drug that crosses the BBB while reducing non-specific accumulation in other tissues (Chapman et al., 2013; Koo et al., 2006). For example, gadolinium-loaded nanoparticles increased the level of

gadolinium 100 fold across the BBB when compared to free gadolinium (Koffie et al., 2011). The manufacture of nanoparticles has improved in the last few years with optimization of drug loading, encapsulation efficiency and release profile. Furthermore, improvements in the stealth capabilities of nanoparticles have increased their protection from agglutination with proteins in the blood, enabling them to avoid being cleared from the blood by the reticuloendothelial system (RES). Nanoparticles whose surface has been modified with ligands have been used to facilitate imaging of brain tumours nanoparticles (Kelkar and Reineke, 2011; Winer et al., 2011). PEGylation of nanoparticles has been widely used in drug delivery in order to protect nanoparticles from blood protein interaction and from the RES (Hadjidemetriou et al., 2015; Salvati et al., 2013). Dawson et al. demonstrated that the PEGylation of nanoparticles completely prevented their interaction with proteins in the plasma. However, other studies have shown that PEGlylation does not completely prevent the interaction between proteins and nanoparticles in the blood (Downs et al., 2015).

Nanoparticles offer a non-invasive method for drug delivery to the brain. However, they need to be optimized in relation to size, release kinetics, chemical properties, while modifying their surface could improve their ability to cross the BBB as well as protecting the drug from the biological environment and enhancing drug solubility (Meyers et al., 2013). Nanoparticles for drug delivery to the brain need to meet certain essential requirements to be most effective, with reduced toxicity. The requirements include non-toxic, biodegradable, prolonged circulation period, no aggregation in the blood, good encapsulation efficiency and the ability to cross the BBB (Tian et al., 2014).

1.9.3 Routes of Administration of Nanoparticles in the Treatment of Malignant Gliomas

There are three main routes of administration for nanoparticles designed to treat brain tumours: (1) direct delivery to the brain; (2) direct systemic delivery to the brain and (3) indirect systemic delivery to the brain.

Direct delivery to the brain offers a way of bypassing the BBB by direct injection of the nanoparticles into the brain. CED has been used to infuse a nanoparticle suspension directly into brain tissue. Lollo et al. used CED to deliver 10 µL of paclitaxel-loaded lipid nanocapsules directly into the brain of mice. The results showed that the overall survival of mice treated with the lipid nanocapsules was significantly increased in comparison with mice treated with free paclitaxel (Allard et al., 2010; Lollo et al., 2015). Fourniols et al. described the direct injection of a photopolymerizable hydrogel containing TMZ-loaded micelles to the brain using a syringe to inject through an incision drilled in the skull. The TMZ-loaded micelles and injection were well tolerated while the hydrogel improved the drug release profile (Fourniols et al., 2015). The major limitations of direct delivery to the brain are its invasive nature, the risk of infection and the need to control critical parameters such as pH and osmolarity which if not optimized may lead to brain damage (Huynh et al., 2012). Direct systemic delivery to the brain is where nanoparticles are directly administered into blood stream through carotid artery and transported to the brain avoiding the rest of the systemic circulation. This technique has shown improved survival compared to CED with reduced risk of brain damage (Laine et al., 2012). Huynh et al. administered ferrociphenol-loaded nanoparticles to the brain of GBM inflicted rats using both CED and direct systemic

delivery. Direct systemic delivery provided a survival of 28 days compared to 24 days for the CED group. The results indicated that direct systemic delivery could provide a modest increase in survival when compared to direct delivery to the brain (Huynh et al., 2012, 2011). Indirect systemic delivery involves the delivery of nanoparticles into the systemic circulation *via* routes of administration that require absorption such as oral, topical, nasal, and peritoneal administration. The major advantages of oral administration are the convenience, non-invasiveness, and patient compliance. Kumar et al. administered two curcumin formulations (nanoparticles and plain suspension) orally to a rat intestinal ex-vivo model. The results showed that the bioavailability of nanoparticles formulation was 12 times greater than the plain suspension (Kumar et al., 2016). Intraperitoneal administration is widely used as an indirect systematic delivery method by injecting the drug into peritoneal tissue. It is used when administering large doses or when it is difficult to locate a vein for direct systemic delivery (Verreault et al., 2015).

1.9.4 The Chemistry of Coating and Bioconjugation of Nanoparticles

Tumour tissues with their leaky vasculature allow the passive accumulation of particles from 10 to 200 nm in size by the EPR effect. However, chemotherapeutics penetration over time becomes challenging due to the increased interstitial pressure and the dense structure of the tumour tissues caused by hydrophobic regions in the brain extracellular space which block therapeutic particles, by steric hindrance, from accessing the tumour. Instead, chemotherapeutics diffuse towards the tumour edge and leak to blood vessels formed by angiogenesis. Additionally, nanoparticles are spotted by the RES

as foreign particles and cleared by phagocytosis (Gritsenko et al., 2012; Pluen et al., 2001).

Advanced nanomedicine research has focused on developing stealth nanoparticles, which are designed with special coatings such as polyethylene glycol (PEG) that mask them from the RES system allowing them to circulate for longer in the bloodstream increasing tumour penetration and physiological stability. Furthermore, the coating enables targeting of brain tumour tissues in a more specific manner than uncoated particles (Garcia-Garcia et al., 2005; Gelperina et al., 2010). Such coated nanoparticles are chemically and physically developed using different techniques which involve grafting, coprecipitation and surface adsorption (Esmaeili et al., 2008). Such bioconjugation involves using coatings that are either biological in nature or synthetic but specifically designed for biological applications (Hermanson, 2013).

Nanoparticles could have their surface modified through covalent and non-covalent ligand binding. Covalent binding takes place *via* either disulphide bonds, primary amines cross linking, primary amine-carboxylic acid reaction, maleimide-thiol reaction, aldehyde-hydrazide reaction and primary amine-free aldehyde reaction (Nobs et al., 2004). Bioconjugates are also formed by using reactive crosslinking agents or reactive groups that aid in the coupling reaction. Some secondary activating agents could act as intermediates in the coupling process that facilitate binding specific functional groups. This process is specific in nature and resembles the selection of building blocks in order to create the whole structure. Affinity molecules act as an important part in the functionalized entity and they aim at targeting biomolecules (Hermanson, 2013).

Non-covalent or physical interaction between targeting ligands and nanoparticles does not involve chemical bonds, however, it may not create as strong a binding as is the case in covalent binding (Koo et al., 2005). The process of PEGylation could take place by coupling with linear or branched PEG molecules which provides a more stable structure with enhanced water solubility and half-life while reducing cytotoxicity and adverse immune response (Jevševar et al., 2010; Webster et al., 2007).

Surfactants offer a major advantage for nanoparticles by helping them penetrate the BBB as well as enhancing their uptake by tumour cells. These surfactants could be polysaccharides, poloxamers or polysorbates. A study reported that Polysorbate 80 (p80) coated polymeric nanoparticles carrying paclitaxel had enhanced uptake by GBM cells due to the coating masking them from the P-gps, which are responsible for drug resistance, as well as by allowing their penetration of the BBB (Koziara et al., 2004). Previously published studies have demonstrated the beneficial role of p80 and Poloxamer 107 as surface ligands in facilitating transport across the BBB with proven efficacy in GBM rats (Hekmatara et al., 2009; Kreuter, 2001; Petri et al., 2007; Steiniger et al., 2004). However, the main issue with these particles is that they could only travel through endothelial cells to neurons in close proximity with the BBB, *via* cell to cell processes. As a result, the parenchyma barrier of the brain tumour will remain unpenetrated. Therefore, the focus on developing nanoparticles that can exceed this hurdle is necessary for a better treatment response. Another study used a similar approach of coating their PLGA nanoparticles with two different surfactants (p80 or poloxamer 188) for the intravenous delivery of two model drugs; loperamide and doxorubicin to the brain. Good efficacy was observed in rats containing an intracranial GBM when treated with doxorubicin loaded particles, while an analgesic effect was

observed in mice when treated with the loperamide loaded particles, which confirms successful transport across the BBB at therapeutic levels. On the other hand, uncoated nanoparticles used in the same study had no effect for either drugs (Gelperina et al., 2010).

Other targeting moieties have been investigated for the treatment of malignant gliomas. Kuo and Chen (2015) reported that using lactoferrin and folic acid as grafting ligands for PLGA nanoparticles were effective in crossing the BBB and delivering etoposide in GBM U87MG cells (Kuo and Chen, 2015). Lactoferrin and folic acid coated nanoparticles had aided in the permeability of etoposide by almost 2-fold as compared to the uncoated nanoparticles. This resulted in a two-fold tumour suppression by the etoposide-loaded nanoparticles when compared to the free etoposide over 48 h. Furthermore, these nanoparticles were prepared with a cationic surfactant, didodecyl dimethyl ammonium bromide (DMAB) which was previously reported to enhance the affinity of the nanoparticles to the walls of arteries allowing for their uptake *via* AMT (Labhasetwar et al., 1998; Zhang et al., 1998). Other studies also highlighted the role of lactoferrin and other blood proteins (transferrin, insulin and leptin) as surface ligands in traversing through the BBB by RMT (Golden et al., 1997; Huang et al., 2009; Kuo and Chen, 2015).

Another study demonstrated that a hydrogel made of polymeric micelles coated with PEG dimethacrylate could provide sustained release of TMZ over a 1-week period in GBM bearing mice. This study indicated a dramatic decrease in the tumour volume following treatment with the TMZ photopolymerized hydrogel as well as increased apoptosis as compared with the other groups (Fourniols et al., 2015).

Dual coating of polymeric nanoparticles is also an interesting therapeutic trend. A study investigating polymeric nanoparticles with PEG and a covalently attached ligand called peptide-22 was shown to enhance BBB permeability, recognition by LDL receptor on the surface of glioma cells and increased delivery of paclitaxel (B. Zhang et al., 2013). The benefit of dual coating was further investigated in a study that coated PEGylated PCL nanoparticles with angiopep-2 which is a peptide that facilitates BBB permeation and drug delivery in glioma cells. This study has also employed cell penetrating peptides to allow deep permeation towards glioma cells and delivery of docetaxel which improved the rate of survival in glioma afflicted mice (Gao et al., 2014).

Another targeting protein moiety named EGFP-EGF1 was bound to polymeric nanoparticles carrying paclitaxel to form a dual coating alongside PEG aimed at targeting glioma in mice. This targeting protein has specific affinity towards tissue factor over-expressed in glioma cells therefore provided better penetration than non-fused nanoparticles. This study has reported enhanced apoptosis and necrosis and extended time of survival for mice treated with PLA-PEG-EGFP-EGF1 compared to the other groups (Zhang et al., 2014).

An *in vitro* study using murine glioma cell lines C6 and F98 compared the cytotoxicity of etoposide loaded and unloaded PLGA nanoparticles with and without surface coatings. Their results have indicated enhanced cytotoxic effect on both glioma cell lines as compared to unloaded nanoparticles or free drug (Callewaert et al., 2013). Surface coating of PLGA nanoparticles with protamine, which is a cationic protein that enhances drug transport across BBB, also significantly improved the delivery of

cisplatin in bovine endothelial cells and also were cytotoxic in U87 GBM cells (Dhami et al., 2014).

1.9.5 Drug-Loading of Nanoparticles

Drugs employed in the treatment of cancer can be loaded either by entrapment within, adsorption on or by covalently bonding to the nanoparticle (Peer et al., 2007). The process of drug entrapment could take place either during or after the process of nanoparticles manufacture. Several factors, such as the solubility of the chemotherapy drug in the nanoparticles matrix, the molecular mass of the drug, the type of interaction between the drug and the nanoparticles and the functional groups on the surface of the nanoparticles influence their loading process (Peer et al., 2007).

The method of drug loading could result in drug within the core or on the surface of the nanoparticles. Drugs loaded on the surface by covalent bonding or physical adsorption as for example by electrostatic interactions between the nanoparticle and drug usually exhibit low stability and become pH-labile (Liu et al., 2011; West and Otto, 2005). Drugs entrapped within the nanoparticles usually have greater stability and tend be released over a sustained period of time.

1.10 Polymeric Nanoparticles for the Treatment of Malignant Gliomas

Polymeric nanoparticles are defined as submicron colloidal nanoparticles and are used as carriers for different drugs such as chemotherapeutic drugs which are either adsorbed on the surface or encapsulated within the nanoparticles (Pinto Reis et al., 2006). There are many types of polymers which have been used in the manufacture of nanoparticles, such as poly(lactic acid) (PLA), poly(ε-caprolactone) (PCL),

poly(butyl-cyanoacrylate) (PBCA), poly(glycolic acid) (PGA), PLGA and poly (amino acids). PLGA, PGA, PLA are the most extensively utilized polymers in drug delivery to the brain, because of their biocompatibility and low toxicity compared to other polymers (Béduneau et al., 2007). They all degrade into lactic acid and glycolic acid that enter into the Krebs cycle where their metabolites are eliminated as carbon dioxide and water from the body (Crotts and Park, 1998). Polymeric nanoparticles have advantages over other types of nanoparticles such as improved release kinetics, better compatibility with some active agents, no oxidation issues as with phospholipids and improved shelf-life (Drummond et al., 1999; Davis, 2009; Shi et al., 2011). The successful development of polymeric nanoparticles for drug delivery to the brain will require an understanding of the molecular weight, crystallinity and stability of the polymers as well as physicochemical properties of the drug (Masood, 2016). The first polymeric nanoparticles developed to deliver drugs to the brain was performed by Kreuter et al. The BBB penetration of dalargin was significantly increased by formulating it into PBCA nanoparticles (Kreuter et al., 1995). In 2001, Kreuter et al. used the same dalargin-loaded PBCA nanoparticles coated with p80, to increase penetration into brain tissue. This nanoparticle formulation was utilized for the delivery of other drugs, such as doxorubicin and loperamide into the brain (Kreuter, 2001). Calvo et al. prepared PEG-PHDCA (poly (hexadecyl cyanoacrylate)) nanoparticles which demonstrated a greater accumulation in the brain when compared to the p80 formulation, which may be due to passive diffusion or intake *via* macrophage (Calvo et al., 2001). The density of the PEG coating on the surface of the nanoparticles can affect the level at which they cross the BBB. Vila et al. produced PEG-PLA nanoparticles with different densities of PEG coating and demonstrated that the

smaller nanoparticles with the highest density of PEG had a greater accumulation in the brain (Gao et al., 2006).

1.11 Targeted Polymeric Nanoparticles for the Treatment of Malignant Gliomas

The active targeting of polymeric nanoparticles *via* surface modification with ligands that bind to target molecules on the surface of cancer cells or other cells within the body is a significant development in nanotechnology (Kamaly et al., 2012). Table 1.1 shows examples of developed targeted polymer nanoparticles as targeted drug delivery system for treatment of malignant gliomas. The affinity ligands bind directly to antigens that are differentially overexpressed on the plasma membrane of cells or to extracellular proteins on the target tissue (Kamaly et al., 2012). Active targeting of nanoparticles can be used for either extracellular or intracellular delivery of drugs. Nanoparticles are more effective if they are targeted to intracellular sites (Sugano et al., 2000; Shi et al., 2011). For example, Alexis et al. demonstrated increased cytotoxicity of paclitaxel-loaded nanoparticles using a ligand targeted to the extracellular domain of the trans-membrane human epidermal growth factor receptor 2 (HER-2) when compared with non-targeted nanoparticles. This increase in cytotoxicity was due to an increased cellular uptake by the targeted nanoparticles (Alexis et al., 2008a). Studies have confirmed that enhancing cellular uptake is the most important role of using targeted nanoparticles (Bartlett et al., 2007; Kirpotin et al., 2006). Targeted nanoparticles can have either single or multi ligands attached to their surfaces. To date, most researchers have preferred to use a single ligand as multi-ligands are associated with some disadvantages, particularly when used for

penetration of the BBB and tumour cells. For example, multi-ligands influence drug release as well as the mobility of the nanoparticles. Furthermore, competitive binding and/or an interaction between ligands may reduce the targeting efficiency of the nanoparticles (Jain et al., 2015).

Transferrin receptors and low density lipoprotein receptor related protein (LRP) are known to be overexpressed on glioma cells (Jain et al., 2015). These two receptors have been used to target polymeric nanoparticles to glioma cells by attaching the anti-transferrin and angiopep ligands to their surface. Anti-transferrin can cross the BBB through transferrin receptors while the angiopep ligand binds to LRP on the surface of glioma cells (Jain et al., 2015; Xin et al., 2012). The transferrin receptor is the most widely characterized receptor-mediated transport system, which provides an efficient cellular uptake and is over expressed in numerous tumour cells (Chang et al., 2009). The targeting of BBB of an *in vitro* model has increased 20-fold with transferrin-PLGA nanoparticles compared to non-coated PLGA nanoparticles. Chang et al. demonstrated, using an *in vitro* model of the BBB, that transferrin-PLGA nanoparticles had a 20 fold increase in uptake by the BBB when compared to un-coated PLGA nanoparticles. The uptake of the transferrin-PLGA nanoparticles by the BBB was by endocytosis (Chang et al., 2009). The major disadvantages of using transferrin as a ligand for nanoparticles is the competition with endogenous transferrin for receptor binding. This may result in reducing the cellular uptake and thus the effectiveness of the nanoparticles (Georgieva et al., 2014). An antibody directed against the transferrin has been used as an alternative ligand to the endogenous transferrin as it binds to an epitope of the transferrin receptor which is located at a different location from transferrin binding. Therefore, the nanoparticles have less binding competition as they

do not interfere with the transferrin intake mechanism. This will increase their cellular uptake and thus their effectiveness (Chen and Liu, 2012). Different antibodies such as OX26 (anti-rat TfR mAbs), R17-217 and 8D3 (both anti-mouse TfR mAbs) have been developed for enhancing brain uptake. OX26 mAbs has been shown to have a high affinity for cells that overexpress transferrin, including GBM cells (Calzolari et al., 2010; Loureiro et al., 2014). The level of brain uptake for each of the antibodies is different. For example, the brain uptake of 8D3 mAbs was relatively high compared to R17-217 mAbs. 8D3 and R17-217 mAbs were more selective for brain than liver and kidney (Lee et al., 2000). Ramalho et al. developed receptor mediated TMZ-loaded PLGA nanoparticles for GBM treatment functionalized with an OX26 mAbs. The cellular internalization of the OX26mAbs nanoparticles was significantly enhanced compared to the PLGA nanoparticles with no mAbs (Ramalho et al., 2018).

Table 1.1. Examples of developed targeted polymer nanoparticles as targeted drug delivery system for treatment of malignant gliomas.

Polymer type	Loaded	Size (nm)	Targeting strategy	Targeted site	Ref.
PLGA	Dil	90	Transferrin	Transferrin receptors	(Chang et al., 2009)
PMLA	Antisense ON	25	mAbs antisense oligonucleotides (AONs)	(proteins) laminin-411	(Ding et al., 2010)
PEG-PCL	Paclitaxel	<100	Angiopep	LRP	(Xin et al., 2011)
PEG-PLGA	Coumarin 6	125	Peptide (12 amino-acid)	Peptide	(Li et al., 2011)
PEG-PCL	Paclitaxel Rhodamine	90	Angiopep	LRP	(Xin et al., 2012)
PLGA	Methotrexate	85	Transferrin	Transferrin receptors	(Jain et al., 2015)
PEG-PLGA	Doxorubicin	100-300	Endogenous tripeptide thiol (glutathione)	Glutathione transporters	(Geldenhuys et al., 2015)

PLGA	Loperamide	100	mAbs (8D3)	Transferrin receptors	(Fornaguera et al., 2015)
PLGA	Curcumin	100	Magnetic guidance Peptide (T7)	Transferrin receptors	(Cui et al., 2016)
PLGA	Doxorubicin	120	poloxamer 188	LRP	(Malinovskaya et al., 2017)
PEG-PLGA	TMZ	19	mAbs (OX26)	Transferrin receptors	(Ramalho et al., 2018)
PLGA	Paclitaxel	230-255	Tripeptide (RGD) Superparamac iron oxide (SPIO)	αvβ3 integrin	(Ganipineni et al., 2019)

Another approach to enhancing the uptake of nanoparticles by the BBB is to coat them with a polymer that will facilitate cellular uptake. As discussed earlier about the role of surfactants in coating, Kreuter demonstrated that intravenously injected doxorubicin-loaded p80-coated nanoparticles had a 40% cure rate in rats with intracranially transplanted GBMs. Although not fully elucidated, he hypothesized that the most likely mechanism for transport of the nanoparticles across the BBB was endocytosis by the endothelial cells lining the brain blood capillaries. Coating the nanoparticles with p80 led to the adsorption of apolipoprotein E from blood plasma onto the nanoparticles' surface. The particles then mimicked LDL particles and could thus interact with the LDL receptor leading to their enhanced uptake by the endothelial cells (Kreuter, 2001). The first polymeric nanoparticles for penetration of the BBB were investigated by Schröder et al. in 1995. PBCA nanoparticle coated with p80 enhanced BBB penetration of hexapeptide dalargin-loaded nanoparticles (Schröder and Sabel, 1996). Wohlfart et al. demonstrated, using a rat glioma model, that poloxamer 188-coated PLGA nanoparticles enabled the delivery of doxorubicin across the BBB in the therapeutically effective concentrations. The basis for their transport across the BBB was

hypothesized to be adsorption of blood apolipoproteins (ApoE or ApoA-I) onto the nanoparticles surface due to the poloxamer 188 coating, followed by RMT of the nanoparticles (Wohlfart et al., 2011). Manlioovskaya et al. demonstrated that these same nanoparticles entered U87 human GBM cells *via* clathrin-mediated endocytosis. They also demonstrated that the nanoparticles released their doxorubicin *via* diffusion rather than by intracellular degradation (Malinovskaya et al., 2017). These studies prove that PLGA nanoparticles coated with poloxamer 188 could improve the delivery of doxorubicin and potentially other chemotherapeutic drugs into brain tumours.

Another promising LPR ligand for delivering nanoparticles to the CNS and BBB penetration is angiopep. It is from a peptide family that is derived from aprotinin and human proteins (Demeule et al., 2008b). The transcytosis capacity and parenchymal accumulation of angiopep-2 is much greater compared to transferrin (Demeule et al., 2008a). The ability of angiopep to facilitate penetration of the BBB of polymeric nanoparticles has been confirmed in a number of studies (Shao et al., 2010; Xin et al., 2011). Xin et al. fabricated dual targeting nanoparticles to improve the drug delivery of paclitaxel to glioma cells. Angiopep-PEG-PCL nanoparticles were highly endocytosed by U87 GBM cells compared with non-targeted PEG-PCL nanoparticles. These nanoparticles have also shown higher penetration, distribution, and accumulation in 3D glioma spheroids as well as increased efficacy in U87 tumour bearing mice (Xin et al., 2012, 2011).

1.12 Challenges Associated with Nanomedicine as a Treatment for Malignant Gliomas

1.12.1 Reticuloendothelial System

The RES also termed the mononuclear phagocyte system (MPS), possesses cellular and noncellular components. Phagocytes could cause the clearance of nanoparticles by binding to them and triggering cytokine cascade, which causes inflammation (von Roemeling et al., 2017). Moreover, macromolecules such as proteins and lipids and others could attach to the surface of the nanoparticles forming a biological corona that gets recognized by the immune system and cleared from the blood stream (Miele et al., 2009). This challenge could be overcome by surface modification of the nanoparticles that could conceal them from being recognized by the RES and allow their existence for longer periods in bloodstream. Surface modification is done using zwitterionic ligands such as cysteine, glutathione or by PEGylation (von Roemeling et al., 2017). In a study performed by Choi et al. using zwitterionic (cysteine) or neutral dihydrolipoic acid ((DHLA)-connected PEG; DHLA-PEG) coatings to coat quantum dots has prevented adsorption of serum proteins and enhanced their renal clearance (Soo Choi et al., 2007). An *in vivo* study showed that using nanoparticles of PEGylated human serum albumin loaded with paclitaxel accomplished long systemic circulation of more than 96 h and enhanced accumulation in the tumour providing high efficacy against cancer and extension in the life span of animals (Lee et al., 2018).

1.12.2 Renal System

The main obstacle facing nanoparticles with the renal system is the process of blood filtration. Nanoparticles will follow certain routes by passing through fenestrated endothelium that has 70–100 nm pores, then they will go through the capillary endothelium and podocytes that are programmed to clear particles sized between 2 and 8 nm, whereas nanoparticles >8 nm will face difficulty crossing the glomerular

filtration barrier. In addition, the fact that the glomerular basement membrane carries a negative charge, cationic nanoparticles (2–6 nm) will exhibit more renal clearance than neutral or anionic same sized nanoparticles (von Roemeling et al., 2017). The shape of a nanoparticle could also influence renal clearance, with enhanced clearance of rod shaped nanoparticles of size 0.8–1.2 nm diameters as reported by Ruggiero et al. (Ruggiero et al., 2010). Size exclusion is a major challenge that affects the overall benefit of using the nanoparticles. The solution to this problem could lie through developing nanoparticles of biodegradable materials that can break down into particles prone to renal clearance. However, this could result in premature release of the therapeutic agents before reaching their target site (Liu et al., 2013). Therefore, in designing nanomedicines for clinical applications, it is necessary to keep the balance between formulating nanoparticles that have renal clearance to avoid long term toxicity as well as maintaining the therapeutic levels of the drugs in the plasma (von Roemeling et al., 2017).

1.12.3 BBB

As mentioned previously, the BBB is a barrier consisting of tight junctions that limit the entry of nanoparticles into the brain. However, nanoparticles with ligands attached have been used to pass through the BBB by the receptor mediated endocytosis (von Roemeling et al., 2017).

1.12.4 Pathophysiological Barriers in Cancer

The composition and structure of the tumour extracellular matrix and its vasculature vary according to the nature of the cancer, its position and stage, alongside personal characteristics (von Roemeling et al., 2017).

Therefore, deep penetration of the nanoparticles could be difficult to achieve (Blanco et al., 2015). Three steps are involved in the transport of pharmaceutical agents to tumour cells. These involve flow of the nanoparticles through blood vessels, then passage through the walls of the blood vessels, eventually crossing the interstitial space to reach the tumour site. The morphological discrepancy between tumour and normal tissues affects the delivery of the therapeutic agents. The abnormal environment of tumourous tissues results in leaky vessels, abnormal blood flow, dysfunctional lymphatic vessels and vascular hyperpermeability that causes interstitial hypertension. The high pressure of the interstitial fluid and dense extracellular matrix hinder the process of diffusion (Boucher et al., 1990; Jain, 2005). Several strategies have been addressed to enhance drug delivery such as: (1) Normalization of tumour vasculature by using antiangiogenic agents that repair the imbalance that took place between the overexpressed proangiogenic and antiangiogenic factors in tumour tissues (Jain, 2005). This approach has rapidly normalized the tumour microenvironment and reduced vessel size and vascular permeability in GBM patients after receiving cediranib as an antiangiogenic therapy (Batchelor et al., 2007). In a preclinical study, surface modified nanoparticles (20–40 nm) could successfully penetrate into breast cancer tissues following vascular normalization therapy (Jiang et al., 2015). Nevertheless, normalized vasculature would not grant entry to extra large nanoparticles due to the reduced pore vessel size. In addition, vessel normalization is impermanent and requires drug administration within the normalization period (Jain,

2005). (2) Normalization of tumour matrix that is mainly composed of collagen and glycosaminoglycan. The normalization process is based on degrading such components to improve nanoparticles penetration. Bacterial collagenase treatment has been administered in high collagen containing tumours such as HSTS26T sarcoma and Mu89 melanoma and has improved penetration of IgG antibodies (4.5 nm size) by two fold (Alexandrakis et al., 2004). Also, interstitial distribution of herpes simplex virus (size 75 nm) was improved by three-fold upon using bacterial collagenase for matrix modification (McKee et al., 2006). Other strategies have been suggested to improve penetration of nanoparticles into cancerous tissues. Inhibiting growth factor-β in pancreatic adenocarcinoma was reported to enhance the penetration of polymeric nanoparticles 100 nm in size (Cabral et al., 2011). Alternatively, using multi-staged nanoparticles could enhance drug delivery in cancer. This involves using large nanoparticles that have longer half-life in the blood stream (Ferrari, 2010). These large particles dissociate upon entry into the tumour microenvironment and release smaller nanoparticles that diffuse on a deeper level into the tumour tissue. A multistage nanoparticle system (100 nm) was engineered with a gelatine core to dissociate and release nanoparticles (10 nm) when it comes in contact with matrix metalloproteinases, for a deeper tumour penetration (Wong et al., 2011).

Designing nanoparticles that can have deep penetration into tumour tissues are under development. Additionally, smart nanoparticles are being developed that can respond to the surrounding conditions and allow a better bioavailability for treatment (Huang et al., 2013).

1.12.5 Multidrug Resistance

Multidrug resistance (MDR), whether hereditary or gained by long term exposure to drugs, involves discharge of drugs outside the cells leading to reduced drug concentration and efficacy inside the cell lumen. Cancer cells can be resistant to chemotherapeutic drugs causing increased toxicity of healthy cells which get exposed to drugs that get ejected by cancer cells. Some chemotherapy drugs that cancer cells are resistant to include taxanes, anthracyclines and vinca alkaloids (Szakács et al., 2006). In cancer, MDR usually comes from overexpressed P-gp which is an adenosine triphosphate (ATP)-binding cassette (ABC) transporter that acts as an efflux pump with the ability of binding many various hydrophobic drugs (Aller et al., 2009). Such transporter is present in several organs such as brain, liver and placenta, for example and it functions by protecting organs from toxins (Gottesman et al., 2002). Some other MDR associated proteins involve MDR-associated protein-1 and the breast cancer resistance protein (BCRP) (Fletcher et al., 2010). Efflux pump inhibitors such as verapamil (covera) and cyclosporine have been investigated and are emerging as first-generation antagonists (Dean et al., 2005). Addressing MDR in cancer has involved the exploitation of nanoparticles drug delivery systems in encapsulating chemotherapy drugs. Liposomes nanoparticles encapsulating doxorubicin and verapamil have been formulated for the targeted inhibition of P-gp (Wu et al., 2007). Furthermore, hybrid nanoparticles of lipids and co-polymers were developed and loaded with doxorubicin and GG918 to target BCRP (Ho-Lun et al., 2006). Both of the previously stated studies have accomplished higher cytotoxicity against leukemia and breast cancer cell lines, respectively, compared to free drug administration. PCL polymer was also employed alongside other co-polymers in the development of micelle nanoparticles of siRNA to

target MDR-1 and perform silencing of the gene responsible for P-gp expression (Xiong and Lavasanifar, 2011).

1.13 Clinical Transition of Polymeric Nanoparticles

Polymeric nanoparticle formulations utilizing different polymers, coatings and targeting ligands have been introduced into the clinic. As can be seen from above a wide range of different nanoparticle delivery systems have been investigated pre-clinically, which may lead to more nanoparticles reaching the clinic. Furthermore, the FDA has approved a range of different routes of administration for nanoparticles, such as systemic, local, and oral administration (Anselmo and Mitragotri, 2019). The main route of administration used in most preclinical and clinical studies is intravenous administration due to the nanoparticles being able to reach all parts of the body giving them a high potential to influence clinical care by targeting both the primary cancer and any associated metastasis (Dobrovolskaia et al., 2008; Moghimi et al., 2001). All of the nanoparticle formulations approved for cancer treatment are liposomal formulations. The first approved nanoparticle formulation was PEG-functionalized liposomal doxorubicin (Doxil) in 1995, and the most recently approved nanoparticle is irinotecan liposomal formulation (Onivyde) (Barenholz, 2012; Carnevale and Ko, 2016). The majority of all approved liposomal nanoparticle formulations are not PEGylated except for Doxil and Onivyde, which have been shown to have advantages over non-PEGylated nanoparticle formulations even with their low amount of PEG (Anselmo and Mitragotri, 2019; Chang et al., 2015). Preclinical research performed in the 1970s, 1980s, and 1990s, using polymers as controlled release systems for drug delivery has led to a number of clinically approved products (Kamaly et al., 2012). The clinical

success of using polymers for controlled release, and the ability to manufacture polymeric formulations on the nanoscale have driven the research of polymeric depots away from the macro/micro scale to the nano scale (Kreuter, 1978). A Number of PEGylated polymeric nanoparticle formulations such as SP1049C, NK911, and Genexol-PM are in early phase clinical trials for various types of cancers (Ahn et al., 2014; Andrade et al., 2018; Kim et al., 2004; Matsumura et al., 2004; Valle et al., 2011). SP1049C is a pluronic polymeric micelle nanoparticle containing entrapped doxorubicin, that is currently evaluated for patients with oesophagus and oesophageal junction metastatic cancer in a phase II clinical trial (Valle et al., 2011) . The other two polymeric nanoparticles, K911 (doxorubicin-loaded PEG-poly(aspartic acid)) and Genexol-PM (paclitaxel-loaded PEG-PLA) are in phase II clinical trials for various cancers (Ahn et al., 2014; Andrade et al., 2018). These first generation, polymeric nanoparticles have shown promising effect for various cancers with wider therapeutic windows and lower side effects. However, these nanoparticles are associated with number of limitations related to targeting, therefore targeted polymeric nanoparticles are now under preclinical and clinical investigation (Kamaly et al., 2012). The first targeted polymeric nanoparticles to reach the clinic is BIND-014, which is composed of a prostate specific membrane antigen (PSMA) conjugated to a docetaxel-loaded PLGA nanoparticles (Ahn et al., 2014; Kamaly et al., 2012). There are only two other targeted polymeric nanoparticles currently in clinical trials, CALAA-01 (phase I), and SEL-068 (phase I) (Autio et al., 2018; Chakraborty et al., 2017; Giri et al., 2015). The synthesis of targeted nanoparticles is complex and is difficult to scale-up. The tuning of ligand density is very difficult because the target ligands attach to the surface of the pre-prepared nanoparticles through post-coupling processes. In order to achieve a

high efficiency of coupling of the ligands excessive amounts of reagents and purification techniques for removing unbound ligands are needed. These issues have led to batch-to-batch variability and difficulty in reproducing the surface properties. Consequently, the clinical transition for targeted nanoparticles will be difficult unless they are prepared using pre-functionalized polymeric materials and minimum number of components (Gu et al., 2008; Kamaly et al., 2012). However, this will require the development and registration of new polymeric excipients.

1.14 Conclusions

Malignant gliomas remain to be among the most aggressive forms of tumours that may not respond to most of the conventional treatments of chemotherapy and RT. This in fact is attributed to the selective nature of the BBB that prevents most particles from entry inside the brain including therapeutics. Moreover, conventional management strategies for glioma only allow patients some extra time to survive while struggling with deleterious side effects that develop mostly from the invasiveness of the treatment approaches. Nanomedicine is a flexible and non-invasive therapeutic field that allows the design of materials with nanometer size dimensions to act as drug carriers and delivery agents crossing the BBB *via* targeting ligands and special coatings. Such designed nanoparticles will aim only towards receptors of interest that are overexpressed on tumour tissues, for instance, while sparing normal tissues. The promising pre-clinical data have paved the way for more nanoparticles to be introduced in the clinic. The FDA has approved various routes of administration of nanoparticles with a preference towards the intravenous route which offers advantages towards treatment of metastasized tumours. Polymeric nanoparticles are gaining more

attention for the treatment of malignant gliomas owing to their biodegradable and biocompatible behaviour inside the human body and the unlimited designs and characteristics they can be manipulated into. Polymeric nanoparticles can be extra advantageous when PEGylated as discussed earlier in this review. However, further efforts are needed to optimize their size, drug loading capacity and release of hydrophilic and hydrophobic drugs, taking in consideration the different physicochemical properties of drugs and the physiological barriers that may hamper their success.

1.15 Aims and objectives

The main aim of this thesis was to develop sterically stable polymeric NPs with the smallest possible size (<500 nm), within a narrow size distribution and loaded with a reasonably therapeutic amount of IRH that has a sustained release overtime and can cross the BBB. This aim was achieved *via* the following objectives:

1. Conducting a Box-Behnken design (BBD) of experiments to optimize the independent factors that control all of the size, charge and EE of the PCL NPS.
2. Blending the PCL and PLGA polymers to obtain a polymeric blend of reduced crystallinity and enhanced release.
3. Conducting a BBD of experiments to optimize the independent factors that control all of the size, charge and EE of the PCL-PLGA blend NPs.
4. Physico-chemical characterizing of both PCL and PCL-PLGA blend NPs to determine their drug release, thermal properties, crystallinity, stability, and morphology.
5. Biological characterizing of HGG primary cells treated with PCL and PCL-PLGA blend NP formulations by examining their cellular uptake, morphological change, cytotoxicity, mechanism of cytotoxicity and immune response.
6. Biological characterizing of endothelial cells treated with PCL and PCL-PLGA blend NP formulations by examining their cellular uptake, morphology, cytotoxicity, mechanism of cytotoxicity, immune response, and BBB permeability.

Chapter 2 DEVELOPMENT AND OPTIMIZATION OF IRINOTECAN-LOADED PCL NANOPARTICLES AND THEIR CYTOTOXICITY AGAINST PRIMARY HIGH-GRADE GLIOMA CELLS

This chapter involves an open access publication cited as ***Mahmoud, B. S. and McConville, C. (2021) 'Development and Optimization of Irinotecan-Loaded PCL Nanoparticles and Their Cytotoxicity against Primary High-Grade Glioma Cells', Pharmaceutics 2021, Vol. 13, Page 541.*** **Multidisciplinary Digital Publishing Institute, 13(4), p. 541**. Author Contributions: Study design: B.S.M. and C.M. Preparation and characterization of nanoparticles: B.S.M. Data analysis: B.S.M. and C.M. Writing of paper: B.S.M. and C.M.

Abstract: Background: High-grade gliomas (HGGs) are highly malignant tumours with a poor survival rate. The inability of free drugs to cross the BBB and their off-target accumulation result in dose-limiting side effects. This study aimed at enhancing the encapsulation efficiency (EE) of irinotecan hydrochloride trihydrate (IRH) within polycaprolactone (PCL) nanoparticles with optimized size and charge. Materials and Methods: IRH-loaded PCL nanoparticles were formulated using either the single emulsion (O/W, W/O and O/O) or double emulsion (W/O/O and W/O/W) solvent evaporation techniques. The nanoparticles were characterized for their size, zeta potential and EE, with the optimized nanoparticles being characterized for their drug release and cytotoxicity. Results: The amorphization of PCL and the addition of electrolytes to the aqueous phases of the W/O/W emulsion produced spherical nanoparticles with a mean diameter of 202.1 ± 2.0 nm and an EE of 65.0%. The IRH-loaded nanoparticles exhibited zero-order release and were cytotoxic against primary HGG cells. Conclusion: The amorphization of PCL improves its EE of hydrophilic drugs, while the addition of electrolytes to the aqueous phases of the W/O/W emulsion enhances their EE further. IRH-loaded PCL nanoparticles have the potential to deliver

cytotoxic levels of IRH over a sustained period of time, enhancing the cell death of HGGs.

Keywords: nanoparticles; high-grade gliomas; polycaprolactone; irinotecan; emulsification; solvent evaporation; amorphization; electrolytes

2.1 Introduction

Malignant brain tumours are associated with high mortality and morbidity rates, owing to the lack of long-term disease control. The majority of malignant brain tumours that affect adults are gliomas, with high-grade gliomas (HGGs) accounting for 75% (Lapointe et al., 2018). For each 100,000 population, 3 to 5 persons develop gliomas annually, with a higher frequency in men. Although the fifth and sixth decades of life are the most prominent for glioma incidence, gliomas can develop at any age (Dolecek et al., 2012). In 2016, the WHO included genetic criteria in classifying gliomas, which resulted in identifying anaplastic astrocytoma, anaplastic oligodendroglioma and mixed anaplastic oligoastrocytoma (grade III) and glioblastoma (grade IV) as high-grade gliomas, accounting for the majority of cases, with a 60 to 70% incidence rate (Louis et al., 2016). Several hurdles limit the efficacy of glioma treatment: (1) glioma cells can metastasize to other tissues in the brain and their irregular margins make complete resection difficult; (2) the BBB prevents drug molecules from entering the brain at therapeutic concentrations (Parrish et al., 2015); (3) cancer stem cells contribute to tumour initiation and therapeutic resistance and (4) glioma cells are immortalized in nature and any cells left behind during surgery will develop into a new tumour (Binello and Germano, 2011).

The standard treatment for gliomas is the Stupp protocol, in which patients undergo surgical resection, followed by radiotherapy and subsequent treatment with

temozolomide. This treatment protocol has been shown to increase survival to 14.6 months, compared to 12.1 months with radiotherapy alone (Stupp et al., 2005). Other treatment options include Gliadel® wafers made of biodegradable polycarboxyphenoxy propane containing the chemotherapeutic drug Carmustine (Bis-chloroethylnitrosourea). However, a Cochrane report demonstrated that the Gliadel wafers provided no significant clinical benefit for newly diagnosed HGG patients, with a small but significant clinical benefit to recurrent HGG patients (Hart et al., 2011). Furthermore, the Gliadel wafers suffer from poor drug penetration into the brain parenchyma, which means that the drug does not reach the deep-seated tumour tissue and reoperation is needed to implant additional wafers once they have finished releasing the drug, which introduces further invasiveness to the patient (Chang et al., 2007; Friedman et al., 2000; Iacob and Dinca, 2009; Scott et al., 2011). The problem with alkylating agents such as temozolomide is the presence of methyl guanine methyl transferase (MGMT), which can counteract their mechanism of action, leading to multidrug resistance (MDR). Therefore, there has been some research into a second line of drugs such as Carboplatin, Oxaliplatin and Irinotecan hydrochloride trihydrate (IRH). However, the systemic delivery of these chemotherapeutic drugs results in serious unwanted side effects for the patient, such as vomiting, diarrhoea, hair loss, neutropenia, myelosuppression and pain (Moore, 2016). Traditional chemotherapeutic drugs also have poor *in vivo* stability, with off-target tissue accumulation, low bioavailability and an inability to cross the BBB, leading to larger doses being administered in order to achieve the therapeutic concentrations needed in the brain, resulting in the deterioration of the patient's overall health.

Encapsulating drugs within nanoparticles (NPs) can offer a wide range of benefits that overcome some of the issues of traditional chemotherapy and could help to improve cancer treatment (Mahmoud et al., 2020). Drug-loaded NPs can cross the BBB by passive diffusion and accumulate in the tumour via the enhanced permeability and retention (EPR) effect, where they release their drug in a sustained fashion by diffusion and biodegradation(Wicki et al., 2015). NPs can protect drugs against early metabolism and reduce off-target tissue accumulation, which in turn increases treatment efficacy and protects healthy tissues. Drug encapsulation can extend the half-life of drugs and reduce the frequency of administration (Wicki et al., 2015). Targeting NPs by surface coating of antigen-specific antibodies can enhance the endocytosis uptake of NPs, where drugs encapsulated within NPs can escape MDR regulated by P-gp transporters (Kreuter et al., 1995). Among NPs, biodegradable polymers of synthetic or natural origin are widely favored for drug loading and delivery, since they metabolize and require no surgical removal after drug release. Synthetic polymers are utilized in drug delivery due to their uniformity and ease of manufacture as well as scale-up. Unlike phospholipids, synthetic polymers are inert materials with no oxidative by-products released upon degradation and they possess versatile properties that can be manipulated to suit their intended use (Davis, 2009; Drummond et al., 1999; Shi et al., 2011). Several synthetic polymers have been shown to offer advantages in drug delivery, such as poly (lactic acid) (PLA), polycaprolactone (PCL), poly (butyl-cyanoacrylate) (PBCA), poly (glycolic acid) (PGA), poly (lactic-co-glycolic acid) (PLGA) and poly (amino acids) (Béduneau et al., 2007). The choice of polymer depends on the final application of the NPs and their behavior can be affected by their crystalline or amorphous nature, porosity, biocompatibility and degradation profile.

Depending on their chemistry, synthetic polymers tend to undergo swelling followed by erosion or degradation, with drug release taking place by both diffusion, during the early stages of release, and degradation, during the later stages of release (Masood, 2016).

Several techniques are used to manufacture drug-loaded polymeric NPs, such as solvent evaporation, nanoprecipitation, emulsification/solvent diffusion, salting out and supercritical fluid (SCF) technology (Mahapatro and Singh, 2011). Drugs can be formulated into NPs as either nanospheres or nanocapsules. Nanospheres are compact spheres where the drug is either dissolved or dispersed in a polymer matrix, with dissolved drugs forming homogeneous systems, while dispersed drugs tend to form heterogeneous systems. With nanocapsules, the drug is surrounded by a polymeric coat. Drugs can either be loaded onto pre-manufactured NPs by covalent or non-covalent interactions or loaded into the NPs during their manufacture. The efficiency of the drug loading is controlled by drug solubility, polymer molecular weight, functional groups and the type of interaction between the polymer and drug (Liu et al., 2011; Peer et al., 2007; West and Otto, 2005).

Hydrophilic drugs are difficult to formulate and encapsulate into the matrix of a hydrophobic polymer. This is because they have poor affinity towards hydrophobic polymers and they favor the water phase during the emulsification process, which results in poor encapsulation efficiency (EE). In addition, the large surface area of the NPs can lead to premature drug release due to a large amount of the drug being on the surface of NPs, instead of being encapsulated on the inside. PCL is a semi-crystalline and slow-degrading polymer, which can alleviate the issue of rapid drug release. However, there are no publications on manipulating PCL to increase its

efficiency in encapsulating hydrophilic drugs. PCL degradation is slower than PLGA, which enhances its application in extending drug release for periods exceeding one year. Moreover, it has the advantages of high permeability to small drug molecules. A study (V.R. Sinha et al., 2004) had previously reported sustained release of proteins using PCL. Other advantages of PCL that encourage its use over PLGA are: PCL is considered more economical than PLGA, it does not induce an acidic environment upon degradation, and it provides sustained release and biodegradation over longer periods of time, which would in turn have less impact on homeostasis (Tang et al., 2007).

Our preliminary studies demonstrate that the solvent evaporation technique is efficient in producing spherical and monodisperse PCL NPs with reasonable stability (Data not shown). Therefore, we selected this technique to develop PCL NPs with tailored mechanical properties to enable a high EE of IRH. IRH is a potent hydrophilic chemotherapy that inhibits topoisomerase, leading to the inhibition of DNA replication (Hsiang et al., 1(Ka. The mechanism of action of IRH is not limited by MGMT methylation. Additionally, IRH and its highly potent metabolite (SN-38) are not substrates of the p-glycoprotein transporter and therefore will not face the challenge of MDR (Hoki et al., 1997). However, IRH can face difficulty crossing the BBB by passive diffusion because its molecular weight is 677 Da, which is above the limit (160 Da) for a hydrophilic drug. Moreover, IRH undergoes hydrolysis at physiological pH (7.4), which converts the active lactone form (stable below pH 5) to its less active carboxylate form (stable above pH 8) (Ebrahimnejad et al., 2009; Mosallaei et al., 2013). Therefore, it is necessary to protect the active form of the drug by shielding it from the physiological conditions, until reaching the acidic environment of the tumour. This

study will investigate the influence of different parameters such as drug and polymer concentration; pH; type, molecular weight, and concentration of surfactants; PCL amorphization and use of electrolytes on the size, polydispersity index (PDI), surface charge and EE. The release profile and cytotoxicity will be evaluated for the optimized IRH-loaded PCL NPs.

2.2 Materials and Methods

2.2.1 Chemicals

PCL (14,000—50,000 g/mol), polyvinyl alcohol (PVA) (13,000–23,000; 89,000–98,000 g/mol), sucrose, olive oil, dioctyl-sulfo-succinate sodium, polyvinyl pyrrolidone (PVP) (40,000 g/mol), sodium chloride, paraffin oil, span-80, hydrochloric acid (HCL) and tween-20 were purchased from Sigma-Aldrich (Dorset, Gillingham, UK). IRH was purchased from LGM Pharma (Erlanger, Kentucky, USA). Acetonitrile and dichloromethane (DCM) were purchased from ThermoFisher Scientific (Loughborough, UK). Phosphate buffer saline (PBS) tablets were purchased from OXOID (Basingstoke, Hampshire, England).

2.2.2 IRH Solubility

An over-saturated solution was formed by dissolving 40 mg IRH in 1 mL of each of deionized water (dH_2O) (pH 5.9) produced using Avidity filtration system (Long Crendon, Buckinghamshire, UK) and PBS (pH 7.4) prepared by dissolving each PBS tablet in 100 mL dH_2O. After 48 h, samples were centrifuged (Beckman Coulter Centrifuge, Buckinghamshire, UK) and the supernatant analyzed by high performance liquid chromatography (HPLC) as described in section 2.2.11. Data were represented as mean (n = 3) ± standard deviation (SD).

2.2.3 IRH Stability

First, 1 mg of IRH was dissolved in 5 mL of dH_2O and 10 mL of PBS and the solutions stored at 8 °C, 25 °C and 37 °C for 16 days. Samples were taken after 1, 2, 4, 8, 12 and 16 days and analyzed *via* HPLC as described in section 2.2.11. Data were represented as mean (n = 3) ± SD.

2.2.4 Solvent Evaporation Technique

PCL-IRH NPs were prepared using both the single and double emulsion solvent evaporation techniques by optimizing different parameters that influence the size, surface charge and EE of the formulated NPs.

2.2.4.1 Single Emulsion (Oil in Water (O/W))

Briefly, the required amounts of PCL and IRH (Table 2.1) were dissolved in DCM, which was subsequently introduced dropwise into the aqueous phase containing varying concentrations (Table 2.1) of surfactant. The solution was then sonicated on an ice bath using a probe sonicator (ThermoFisher Scientific, Loughborough, UK) for various durations (Table 2.1), with solvent evaporation taking place for 4 h under gentle stirring at room temperature.

Table 2.1 Single emulsion process and formulation parameters using PVA (MW 13K) and PVP (MW 40K) surfactants.

Form. No.	pH	Sonication Time (minutes)	Sonication Amplitude (%)	PCL Amount (mg)	IRH Amount (mg)	Surfactant Type	Surfactant %
SE 1		10	60	60	2	PVA	4%
SE 2		15	60	60	2	PVA	4%

SE 3	20	60	60	2	PVA	4%
SE 4	10	60	120	2	PVA	4%
SE 5	10	60	240	2	PVA	4%
SE 6	10	60	60	6	PVA	4%
SE 7	10	60	60	18	PVA	4%
SE 8	10	60	108	6	PVA	4%
SE 9	10	50	108	6	PVA	4%
SE 10	10	50	60	2	PVA	8%
SE 11	10	50	60	2	PVA	0.4%
SE 12	10	50	60	2	PVP	4%
SE 13 3	10	50	60	2	PVA	4%
SE 14 3	10	50	60	2	PVA	8%

2.2.4.2 Single Emulsion (Water in Oil (W/O))

First, 6 mg of IRH was dissolved in dH_2O and emulsified *via* sonication in DCM containing 108 mg of dissolved PCL. Sonication was performed for 10 min on an ice bath and the solvent evaporated over 4 h at room temperature to produce SE15.

2.2.4.3 Single Emulsion (Oil in Oil (O/O))

IRH-loaded NPs were produced using a modified single emulsion method (SE16). First, 108 mg of PCL and 6 mg of IRH were dissolved in 10 mL of DCM to form the first oil phase (O1). Then, 0.3% of dioctyl-sulfo-succinate sodium was dissolved in olive oil (O2). O1 was emulsified into 25 mL of O2 with sonication performed for 10 min at 50% amplitude on an ice bath. Solvent evaporation took place at room temperature over a period of 3 h. The formulation was subsequently centrifuged at 9500 rpm for 20 min

and washed twice using n-hexane. The pellet was collected by drying overnight at room temperature (Vijaya Ramesh, 2009).

2.2.4.4 Double Emulsion (Water in Oil in Oil (W/O/O))

A modified double emulsion method was investigated for the production of IRH-loaded NPs (DE1). First, 12 mg of IRH was dissolved in 0.5 mL of dH_2O to form W1. Then, 108 mg of PCL was dissolved in 2 mL of DCM to form O1. W1 was added dropwise to O1 under gentle stirring. This first emulsion was subsequently added to 50 mL of liquid paraffin as the second organic phase (O2), which contained 0.3% span-80 as a surfactant. Sonication with 50% amplitude took place for 10 min on an ice bath. Then, the solvent was evaporated at room temperature over a period of 4 h. Centrifugation (Beckman Coulter Centrifuge, Buckinghamshire, UK) at 9500 rpm was used to collect the NPs, washing twice with n-hexane. The pellet was then collected by drying overnight at room temperature (Wu et al., 2009).

2.2.4.5 Double Emulsion (Water in Oil in Water (W/O/W))

DE2 was prepared by dissolving the required amount of IRH in dH_2O to form the aqueous phase (W1) and the required amount of PCL in DCM to form the organic phase (O). W1 was added dropwise to the organic phase, under gentle stirring, to form the first emulsion, which was subsequently added to the required volume of the external aqueous phase (W2) containing the required amount of PVA surfactant. Following the double emulsification process, sonication was performed on an ice bath, followed by solvent evaporation under gentle stirring at room temperature (Table 2.2).

Table 2.2. Double emulsion parameters of optimized formulations.

Form No.	pH	PCL Amount (mg)	IRH Amount (mg)	Aqueous Phase Volume (mL)	Surfactant Type	Surfactant %	Surfactant Average MW (g/mol)	Evaporation Time (hours)
DE 1		108	12	50	Span-80	0.3%	N/A	4
DE 2		108	6	25	PVA	4%	13K	4
DE 3		108	6	100	Span-80/Tween-80	1% Span-80 1.25% Tween-80	N/A	4
DE 4		108	6	25	PVA	4%	13K	4
DE 5		108	6	25	PVA	4%	13K	4
DE 6		108	6	25	PVA	4%	13K	4
DE 7		108	4	25	PVA	4%	13K	4
DE 8		108	6	25	PVA	4%	13K	7
DE 9		108	6	25	PVA	4%	13K	12
DE 10		108	6	25	PVA	4%	13K	24
DE 11		108	6	25	PVA	4%	89K	4
DE 12		108	6	25	PVA	8%	89K	4
DE 13		108	6	25	Span-80/Tween-20	4%	N/A	4
DE 14		108	6	25	Span-80/PVA	4%	N/A	4
DE 15		108	6	15	PVA	4%	13K	4
DE 16		108	6	50	PVA	4%	13K	4
DE 17	3	108	6	25	PVA	4%	13K	4
DE 18	3	108	6	25	PVA	4%	13K	4

2.2.4.5.1 The Influence of the Inclusion of Matrix Material in W/O/W

DE3 was prepared by dissolving 6 mg of IRH in 3 mL dH_2O containing 2% sodium alginate to form the inner aqueous phase (W1). W1 was emulsified into 10 mL of DCM containing 108 mg PCL and 1% span 80 as a surfactant to form the W/O emulsion. This emulsion was further emulsified into the outer aqueous phase (W2) containing 100 mL of dH_2O with 1.25% tween 80 (Pal et al., 2011).

2.2.4.5.2 The Influence of Using Amorphized PCL W/O/W

DE4 was prepared by using amorphous PCL and the same process parameters as DE2.

2.2.4.5.3 The Influence of the Addition of Electrolytes to the Aqueous Phase W/O/W

DE5 and DE6 were prepared using the double emulsion technique and the same process parameters as DE4. The first aqueous phase contained 10 mg/mL NaCl, while the second aqueous phase contained 2.5% NaCl (Pistel and Kissel, 2000).

2.2.5 The Influence of Different Parameters on Size, Charge and EE of Optimized NPs

Following the optimization of EE, other parameters were further investigated, as shown in Table 2.2, using 50% sonication amplitude for 10 min.

2.2.6 Collection and Lyophilization of NPs

NP formulations prepared by single emulsification were collected by centrifugation at 9500 rpm. Further optimization involved using a higher speed of 24,500 rpm to

enhance the yield of the nanoparticles. The nanoparticles were then washed twice with dH_2O to remove the free drug, frozen overnight at −80 °C in 5% sucrose solution and subsequently lyophilized at 0.01 mbar and −85 °C for 48 h using Labconco lyophilizer (Kansas city, Missori, USA).

2.2.7 Morphology

The morphology of the IRH-loaded PCL NPs was analyzed by transmission electron microscopy (TEM) with a JEM 1010 electron microscope at a voltage of 80kV. The NPs were suspended in dH_2O, deposited on a copper grid and dried before measurement.

2.2.8 Measurement of Particle Size and Zeta Potential

First, 2 mg of the lyophilized NPs was dispersed in 3 mL of dH_2O and analyzed for their hydrodynamic diameter, PDI and zeta potential using a dynamic light scattering (DLS) Zetasizer (Malvern, Worcestershire, UK). Data were represented as mean (n = 3) ± SD.

2.2.9 Measurement of EE

The supernatant for the different NP formulations was analyzed by HPLC to determine the un-encapsulated drug (free drug). EE was calculated using the following equation:

$$\text{EE (\%)} = \frac{\text{Initial drug amount} - \text{Drug in the supernatant}}{\text{Initial drug amount}} \times 100.$$

Equation (1)

2.2.10 Release Study

First, 25 mg of the IRH-loaded NPs was dispersed in 25 mL of PBS release media and stirred at 200 rpm at 37 °C. Then, 0.5 mL samples were removed at 0, 1, 3, 5, 7, 9, 14, 16 days and replaced with fresh media. The samples were centrifuged, and the supernatant analyzed for their IRH content using HPLC. The percentage of drug release was determined as mean (n = 3) ± SD using the following equation:

$$\text{Cumulative Drug release (\%)} = \frac{\text{Released IRH}}{\text{Total IRH}} \text{ X } 100.$$

Equation (2)

2.2.11 IRH HPLC Methodology

IRH was analyzed using Agilent HPLC (Agilent Technologies 1260 infinity II) with a quaternary gradient pump. The separation was performed using a C18 column (150 mm × 4.6 cm), particle size 5 µm (ThermoFisher Scientific, Loughborough, UK), at 25 °C. The injection volume was 20 µL, with a run time of 10 min and a flow rate of 1.00 mL/min. The mobile phase was composed of ion pair solution (solution A): 1.2 g octane-l-sulfonic acid in 500 mL dH_2O and solution B: 13.6 g potassium dihydrogen phosphate dissolved in 500 mL dH_2O. Solution A, solution B and acetonitrile were in the ratio of 30:30:40 *v*/*v*/*v*. The pH was adjusted to 3 using orthophosphoric acid. The detector UV wavelength was set at 265 nm.

2.2.12 *In Vitro* Cell Culture and Cytotoxicity Study

Unfixed tumour core tissue was collected directly from recurrent glioblastoma patients undergoing craniotomies at the Queen Elizabeth Hospital, in accordance with ethical approval (application number: 19-337) from the Human Biomaterials Resource Center (HBRC). The samples were immediately placed in collection fluid and transported to

the laboratory. Extraction of the tumour cells from the tissue and culturing of the subsequent cells were performed using standard operating protocol. Cells were maintained using Dulbecco's modified Eagle's medium/nutrient mixture F-12 ham supplemented with 10% FBS (foetal bovine serum), penicillin/streptomycin, sodium pyruvate (Sigma-Aldrich, Dorset, Gillingham, UK) and minimum essential medium non-essential amino acid solution (MEM NEAA) (ThermoFisher Scientific, Loughborough, UK). The cells were plated onto 96-well flat-bottomed microtiter plates at a density of 10,000 cells per well and cultured in the presence of free IRH (low, medium, and high concentrations equivalent to 1, 10 and 100 μM, respectively). The NP formulations were selected in low, medium, and high concentrations equivalent to 1, 10 and 100 μM of encapsulated drug, respectively. Cytotoxicity testing was performed using the standard 3-(4,5-Dimethylthiazol-2-yl)-2,5-Diphenyltetrazolium Bromide (MTT) assay after 1, 3, 5, 7, 9 and 11 days of treatment, with all experiments performed in replicates (n = 3) ± SD. MTT was purchased from Sigma-Aldrich (Dorset, Gillingham, UK).

2.2.13 Statistical Analysis

The statistical analysis was carried out with GraphPad Prism, version 9. Two-way ANOVA (Analysis of variance) was used for multiple comparisons between the similar concentrations of the free drug and the formulation over 11 days. Tukey's post hoc test was carried out in the analysis. The statistical significance was presented as: $p \leq 0.0001$, $p \leq 0.05$. Non-significance was presented for $p > 0.05$. Data were presented as mean (n = 3) ± SD.

2.3 Results

2.3.1 IRH Solubility and Stability

Figure 2.1A demonstrates that IRH is more soluble in dH_2O compared to PBS. IRH has a solubility of 13.34 ± 0.046 mg/mL and 1.15 ± 0.056 mg/mL in dH_2O (pH 5.9) and PBS (pH 7.4), respectively, which correlates with the literature (Wei et al., 2013). In water, IRH retains greater than 80% of its stability over 16 days, with temperature having no effect (Figure 2.1B). However, in PBS, IRH loses more than 70% of its stability within 24 h, which remains constant over 16 days, with temperature having no effect (Figure 2.1C).

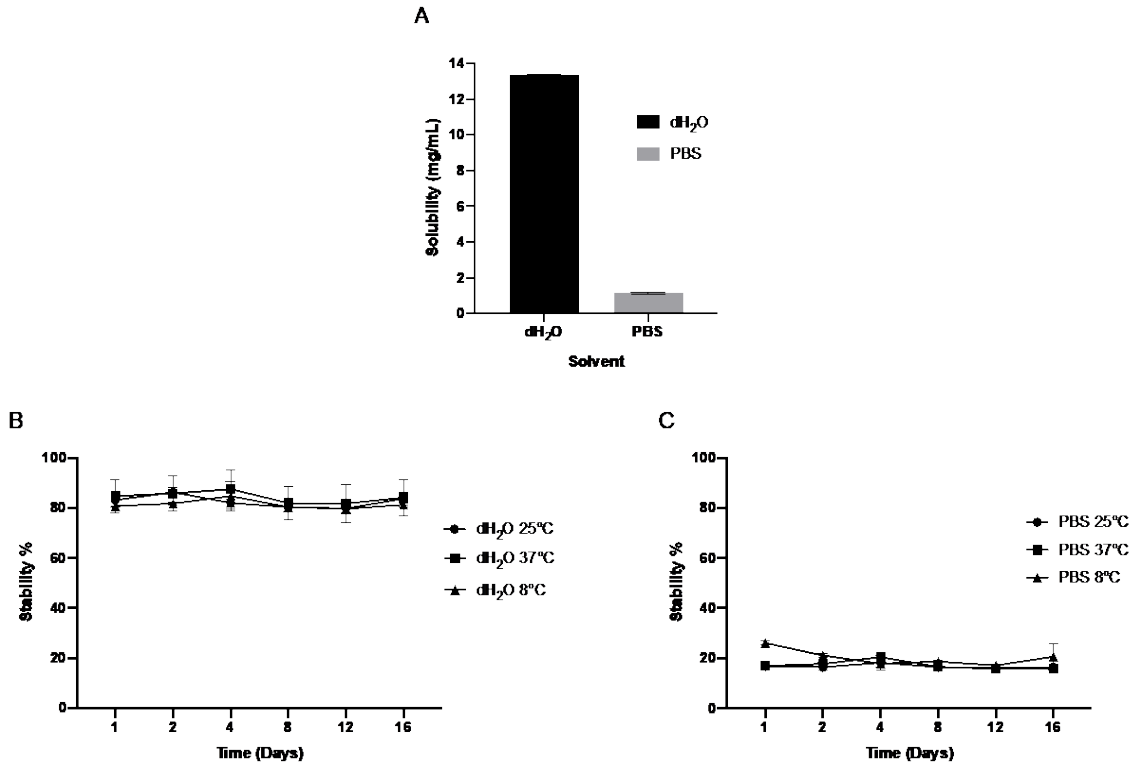


Figure 2.1. Solubility (A) and stability of IRH in both dH20 (B) and PBS (C) over 16 days at 8, 25 and 37 °C (n=3).

2.3.2 Single Emulsion Optimization Parameters

The aim of this study was to produce NPs with an average hydrodynamic diameter less than 500 nm, low PDI, an EE greater than 50% and high stability, which was based on their zeta potential. Small NPs are characterized by a large surface area, which could enhance drug dissolution and release (Sharma et al., 2016).

2.3.2.1 Parameters Influencing the Size, PDI and Surface Charge

Size optimization using the single emulsion technique was started by investigating three different durations of sonication (10, 15 and 20 min), as shown in Figure 2.2A. A duration of 10 min provided the most optimum results of monodisperse NPs (PDI < 0.5), with the smallest average hydrodynamic diameter of 290.90 ± 38.49 nm and a zeta potential of −23.7 ± 3.3 mV. The formulation parameters were then investigated for their impact on size and surface charge. Increasing the amount of PCL from 60 to 120 mg increased the particle size and PDI of the NPs, while a further increase in the amount of PCL reduced the particle size and PDI of the NPs (Figure 2.2B). Additionally, increasing drug loading from 2 to 18 mg resulted in an increase in particle size up to 554.3 ± 27.2 nm, with a zeta potential of −10.6 ± 0.5 mV (Figure 2.2C). Similarly, increasing the PVA concentration from 4 to 8% increased the size and PDI of the NPs (Figure 2.2F). PVP was investigated as a stabilizer (Coombes et al., 1998); however, it resulted in an increase in both size and PDI (Figure 2.2E). Additionally, a low PVA concentration of 0.4% increased the size of the NPs (Figure 2.2E).

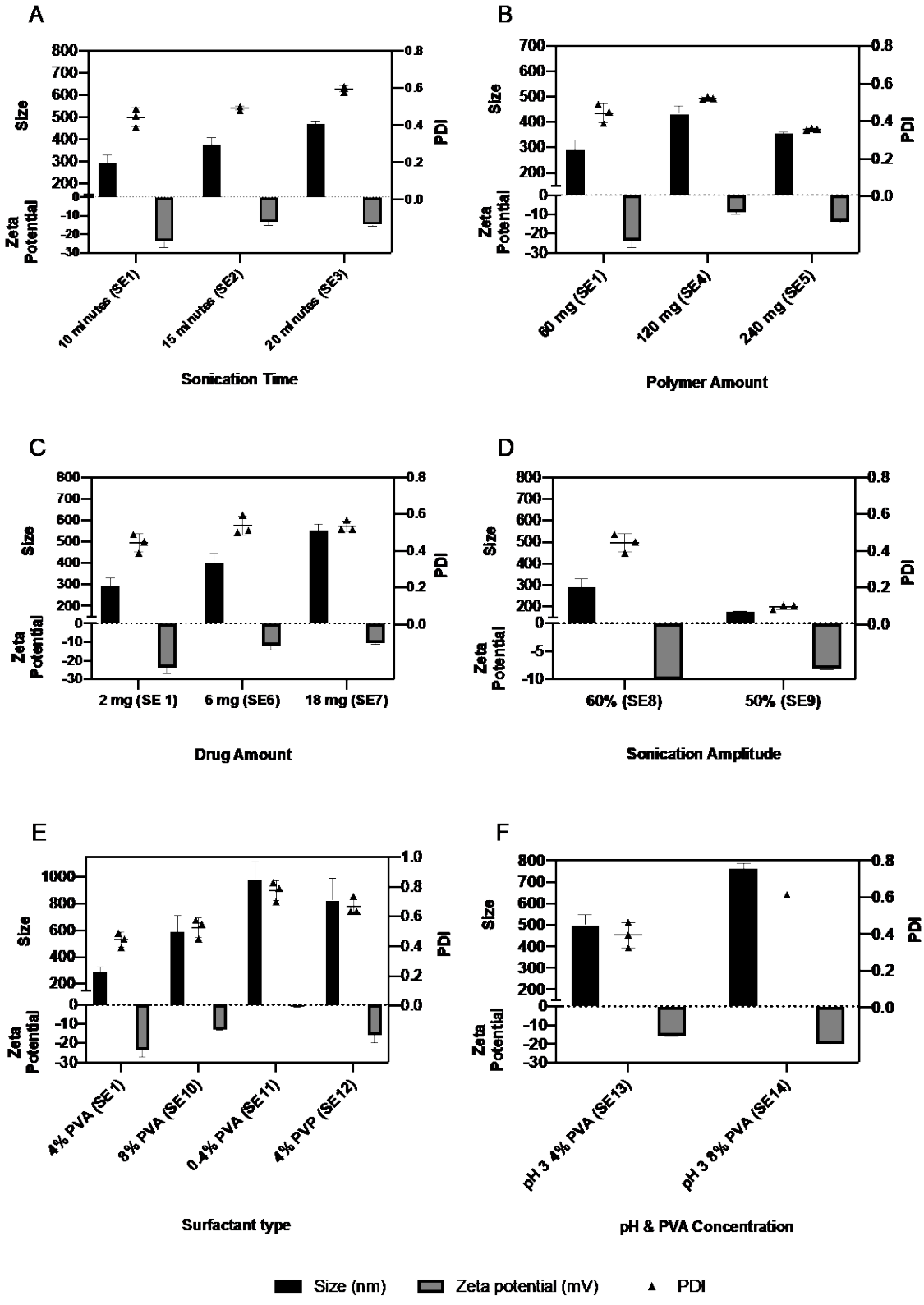


Figure 2.2. The impact of sonication time (A), polymer amount (B), drug amount (C), sonication amplitude (D), surfactant type (E), pH and PVA concentration (F) on the average particle size, PDI and zeta potential of the nanoparticles manufactured using the single emulsion technique.

The effect of acidic pH (pH 3) using 4% and 8% PVA is shown in Figure 2.2F, where there was an increase in size for both PVA concentrations at pH3 with the 8% showing a size bigger than 700 nm. Further optimization was performed by investigating the influence of sonication power on the size of the NPs. By switching from 60 to 50% sonication amplitude, the average hydrodynamic diameter of the NPs was reduced from 290.9 ± 38.5 nm to 178.6 ± 0.7 nm. Therefore, an amplitude of 50% was considered as the optimum sonication power for preparing the NP formulations (SE9), which was considered for further analysis by HPLC to determine the EE.

2.3.2.2 Parameters Influencing EE

Following size optimization, the drug content of SE9 was analyzed by HPLC and was very low (7.5%), which led us to investigate further parameters that could enhance the EE. By switching the emulsification process to water in oil as in SE15, the formulation stability was compromised, leading to the formation of irreversible aggregates.

Since IRH is a hydrophilic drug and tends to escape to the water phase, which limits its encapsulation, a method devoid of water was selected (O/O) to overcome this problem. SE16 was prepared using the O/O method, which was previously proven successful in encapsulating a water-soluble drug in PCL microparticles (Mei et al., 2018a). This method enhanced the EE to 40.5% when the parameters were adjusted in line with our optimized formulation parameters (SE9); however, the size was not in the nanometer range that could not be detected accurately by the equipment and the particles had poor stability, represented in the form of aggregates precipitating out of the emulsion. As a result, it was decided to focus on improving the EE of the O/W emulsion *via* lowering the pH of the aqueous phase and the addition of NaCl to the aqueous phase; however, both strategies resulted in no drug encapsulation. Finally,

the PCL polymer was converted to the amorphous form by heating to its melting point and subsequently quench cooling on dry ice until solidification (Angell, 1988; Turnbull, 1969). Using the amorphous PCL increased the EE to 12.1% (SE17), which was still considered low; however, it demonstrated that the amorphous PCL had a higher EE than the crystalline PCL. Based on the above observations, it has been concluded that the single emulsion technique is not suitable for the manufacture of IRH-loaded PCL NPs with an acceptable EE above 50%.

2.3.3 Double Emulsion Optimization Parameters

DE1 was prepared using the W/O/O emulsification technique, which produced an EE of 11.1%, but the size of the particles exceeded the nanometer range and thus it was excluded from the study. By using the W/O/W double emulsion technique, it was possible to achieve EEs greater than the acceptable 50%, proving that the double emulsification technique was more suited to the manufacture of IRH-loaded PCL NPs than the single emulsification technique, which is due to the hydrophilic nature of IRH. The W/O/W double emulsification produced NPs with EEs ranging from 18.7 to 73.7% depending on the process and formulation parameters (Figures 2.3 – 2.5).

Attempts to improve the EE started with the inclusion of a matrix material (Na alginate) to provide more matrix to entrap the drug. This approach (DE3) provided an EE of 18.7% (Figure 2.3A), which was considered too low, while increasing the particle size (Figure 2.3B). Based on the positive EE data for the amorphous PCL using the single emulsion technique, it was investigated using the double emulsion technique. The use of amorphous PCL (DE4) increased the EE to 34.8% (Figure 2.3C), while the addition of NaCl to both aqueous phases in combination with the amorphous PCL (DE5)

increased the EE to 65.0% (Figure 2.3C), which was higher than the use of amorphous PCL on its own or the addition of NaCl to W1 (DE6). Furthermore, neither approach increased the size of the NPs to above 324 nm (Figure 2.3D).

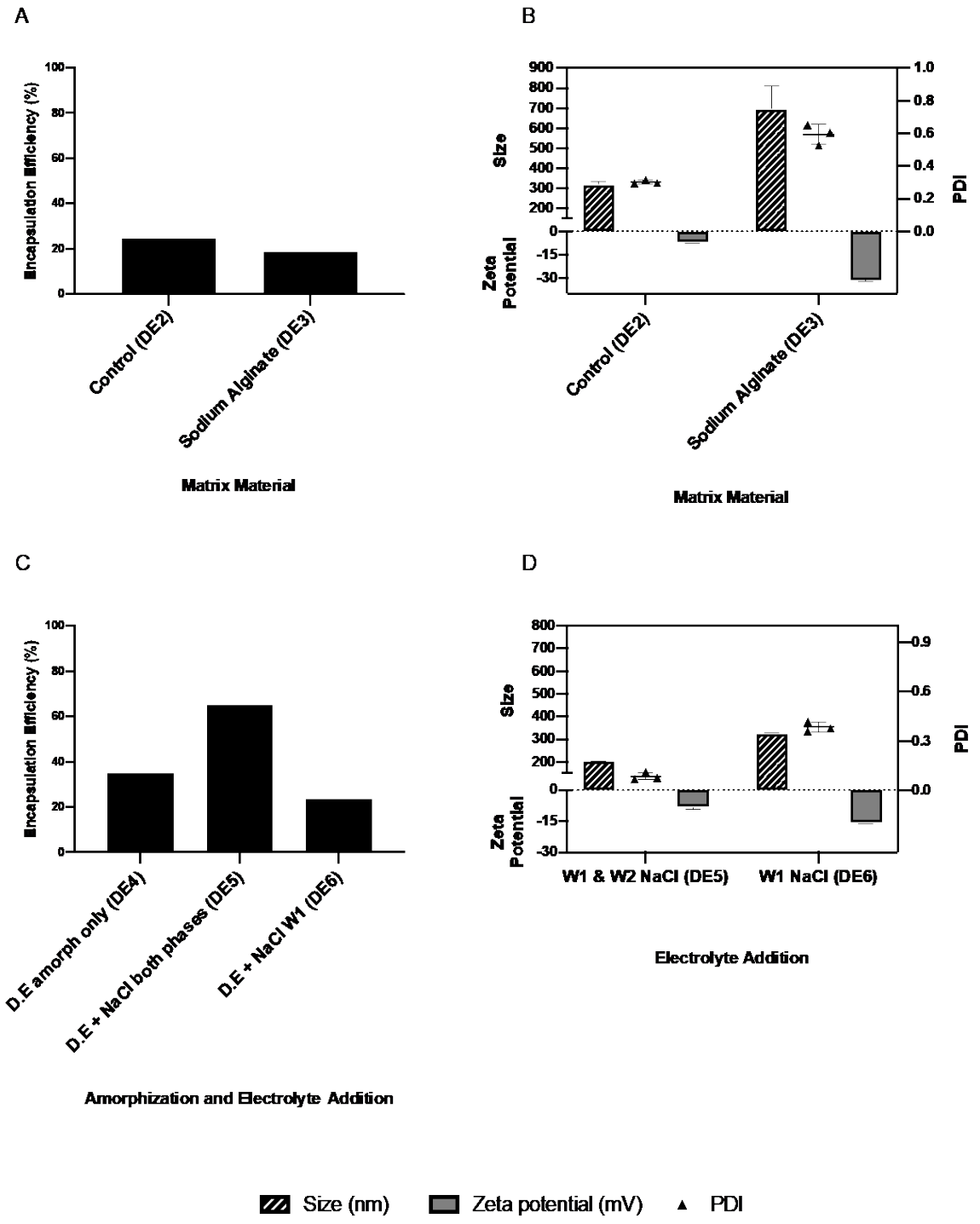


Figure 2.3. The impact of matrix material, PCL amorphization and electrolyte addition on the average particle size, PDI, zeta potential (B and D) and EE of nanoparticles (A and C) manufactured using the double emulsion technique.

After achieving an acceptable EE (65.0%), several other parameters were investigated for their influence on EE, size and charge (Figures 2.4 and 2.5). Reducing the amount of IRH from 6 to 4 mg decreased the EE to 56.0%, with limited impact on the size (Figure 2.4 A,B). Increasing the solvent evaporation time from 4 to 7 h improved the EE slightly from 65.0 to 69.2% (Figure 2.4C), with a slight increase in particle size and reduction in the negative charge magnitude (Figure 2.4D). A duration greater than 7 h (DE9 and 10) resulted in the formation of aggregated particles not in the nanometer range (data not shown). Therefore, an evaporation time of 4 h was selected as the optimum time for providing a suitable size, charge and EE. Using a PVA with a high average molecular weight (89,000 g/mol) (DE11 and 12) increased the EE to 73.2% (Figure 2.4E); however, the particle size was outside the nanometer range, with a high PDI (Figure 2.4F), and thus it was excluded from further study.

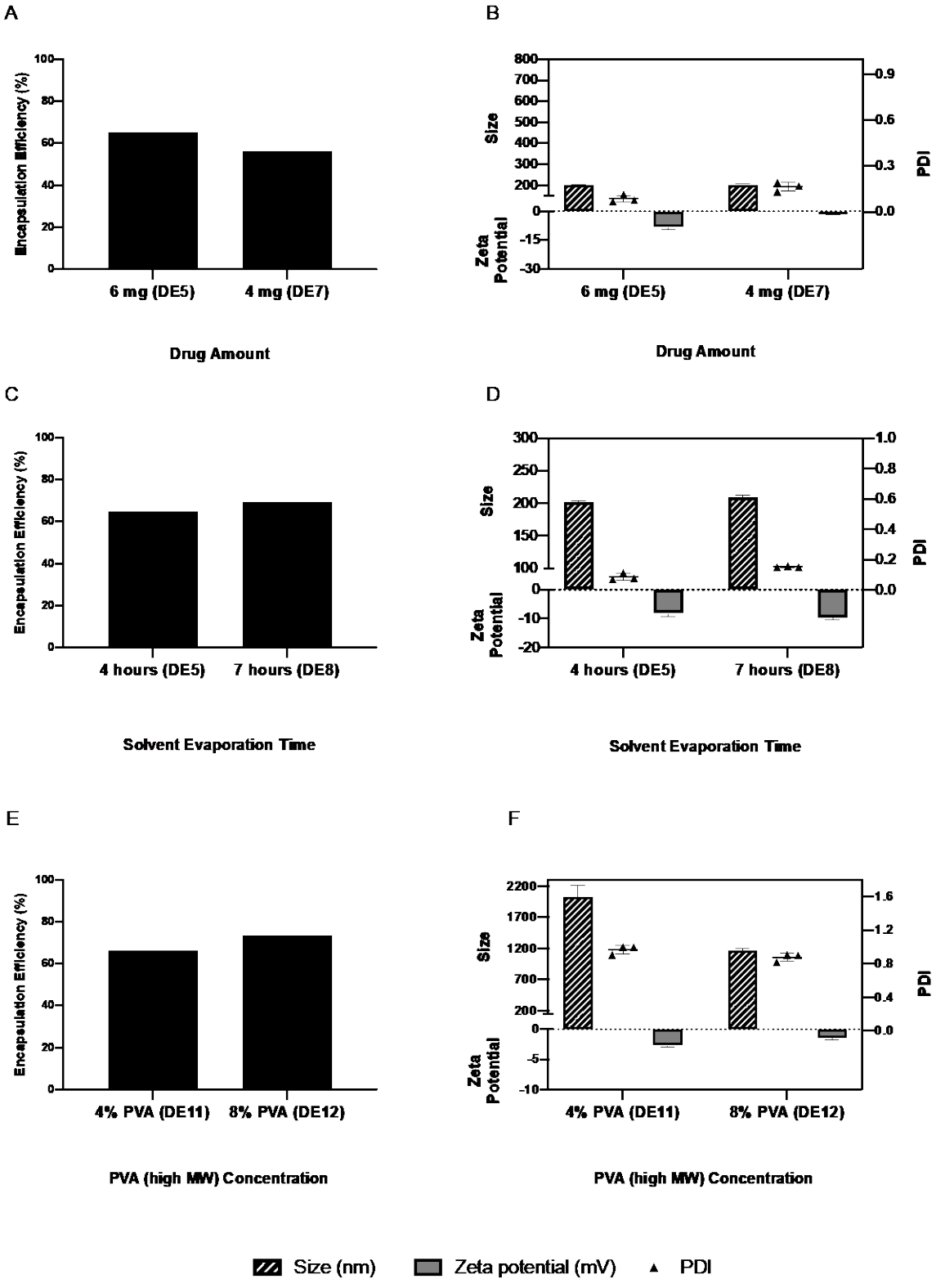


Figure 2.4. The impact of drug amount (A and B), solvent evaporation time (C and D) and high-MW PVA (E and F) on the average particle size, PDI, zeta potential and EE of optimized nanoparticles manufactured using the double emulsion technique.

The use of two surfactants with different hydrophilic–lipophilic balance (HLB) values (DE13 and 14) reduced the EE to 31.2 and 37.5% (Figure 2.5A) while increasing the size, PDI and zeta potential of the NPs (Figure 2.5B). Increasing or decreasing the volume of the aqueous phase to above or below 25 mL resulted in an increase in EE (Figure 2.5C); however, both particle size and PDI were also increased (Figure 2.5D) and thus 25 mL was selected as the optimum volume for the W2 aqueous phase. Decreasing the pH of either one or both of the aqueous phases reduced the EE (Figure 2.5E) while also increasing particle size, PDI and surface charge (Figure 2.5F). A summary of the EE% achieved using different methods and parameters is shown in table 2.3.

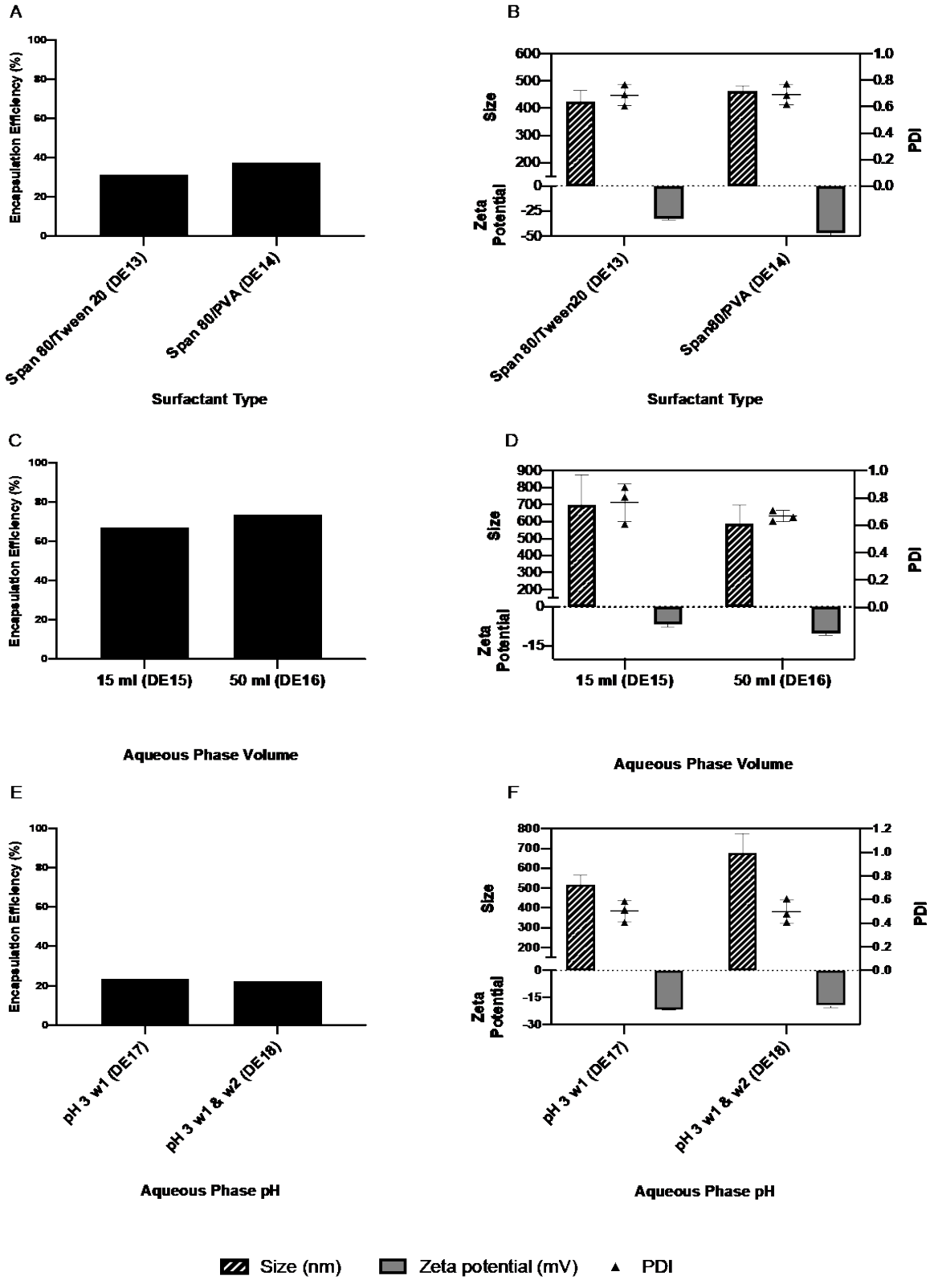


Figure 2.5. The impact of surfactant type (A and B), aqueous phase volume (C and D) and aqueous phase pH (E and F) on the average particle size, PDI, zeta potential and EE of optimized nanoparticles manufactured using the double emulsion technique.

Based on the optimization data above, it was decided that the double emulsion technique, using amorphous PCL with the addition of NaCl to both aqueous phases (DE5), was the optimum condition for the manufacture of IRH-loaded PCL NPs. The DE5 NPs were selected for further characterization of their morphology, drug release and cytotoxicity.

Table 2.3. Summary of EE% and the influencing parameters.

Formulation	EE%	Influencing Parameter
SE9	7.5	Emulsification Method (O/W)
SE16	40.5	Emulsification Method (O/O)
SE17	12.1	Amorphization
DE1	11.1	Emulsification Method (W/O/O)
DE2	24.6	Emulsification Method (W/O/W)
DE3	18.7	Inclusion of Matrix Material
DE4	34.8	Amorphization
DE5	65.0	Amorphization/Electrolyte Addition
DE6	23.6	Amorphization/Electrolyte Addition
DE7	56.0	Drug amount
DE8	69.2	Solvent evaporation time
DE11	66.1	Surfactant MW and concentration
DE12	73.2	Surfactant MW and concentration
DE13	31.2	Surfactant Type
DE14	37.5	Surfactant Type
DE15	67.3	Aqueous Phase volume
DE16	73.7	Aqueous Phase volume

DE17	23.6	Aqueous Phase pH
DE18	22.3	Aqueous Phase pH
DE19	29.0	Surfactant concentration and pH
DE20	43.3	Surfactant concentration and pH

2.3.4 Characterization of the Optimized IRH-Loaded PCL Nanoparticles

A TEM image of the optimized IRH-loaded PCL NPs (DE5) is presented in Figure 2.6A. It demonstrates that the nanoparticles are a group of uniform, spherical particles with smooth edges that are within the nanometer range, with an average particle size of 149.2 ± 13.5 nm, which is lower than the 202.1 ± 2.1 nm determined by DLS. This is due to DLS measuring the hydrodynamic diameter, which is the size of the NPs plus the liquid layer around them, while TEM is performed on dried NPs and gives the actual size of the NPs. However, TEM is an image of a much smaller sample size of the NPs compared to DLS. The TEM image suggests that the NPs are polydisperse, which does not agree with the PDI value of the DLS. However, the sample preparation for TEM can lead to the NPs forming layers on top of each other, which makes them resemble one large particle, giving the impression of a polydisperse system (Kaasalainen et al., 2017). The *in vitro* cumulative release demonstrates that the nanoparticles provide zero-order sustained release of IRH, releasing 40.4 ± 1.5% of their IRH content over the 16 days (Figure 2.6B). Table 2.4 shows the kinetic parameters for the zero-order, Higuchi and Korsmeyer–Peppas release models. The coefficient of determination (R^2) values demonstrate that the release fits all three models, with R^2 values of 0.9991, 0.9595 and 0.9958, respectively. This demonstrates that their release is zero-order and diffusion-controlled, while a diffusional exponent (n)

value of 0.6894 for the Korsmeyer–Peppas model suggests non-Fickian, anomalous diffusion, which is to be expected for NPs due to their small size and short diffusion pathway. Based on the diffusional exponents and release kinetic constants listed in Table 2.4, the mechanism of release is non-Fickian diffusion, with the IRH released *via* a combination of diffusion through the PCL and swelling of the PCL.

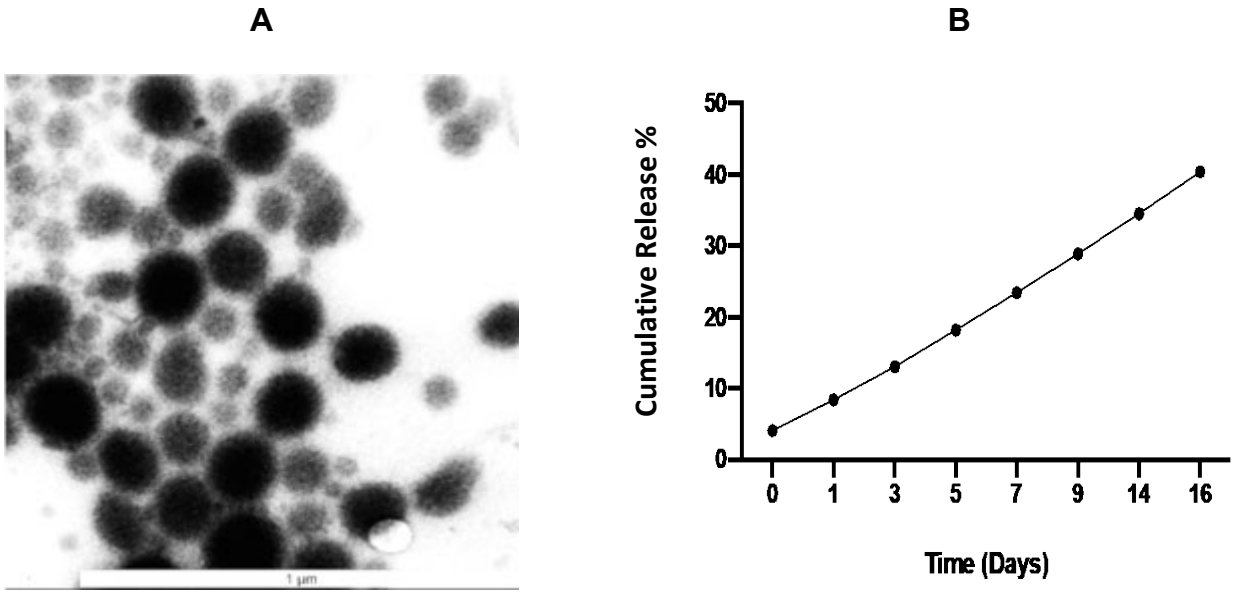


Figure 2.6. TEM image of DE5 showing average particle size of 149.2 ± 13.5 nm for 14 particles (A) and *in vitro* cumulative release of the IRH-loaded PCL nanoparticles (B) (n=3).

Table 2.4. The kinetic parameters from the different release models used for the optimized DE5 NPs.

Zero-Order		Higuchi		Korsmeyer–Peppas		
R^2	k (% h^{-1})	R^2	k (%$h^{-0.5}$)	R^2	k (%h^{-n})	n
0.9991	0.1071	0.9595	0.5093	0.9958	0.5269	0.6894

The cytotoxicity of the nanoparticles was compared to the unformulated IRH at three different doses over 11 days (Figure 2.7). The NPs were more cytotoxic than the unformulated IRH across all doses, with the highest cytotoxicity achieved at day 11. However, by day 5, there was no significant difference between the cytotoxicity of the

high-dose unformulated IRH and the high-dose IRH-loaded PCL NPs, while, by day 7, there was no significant difference across all doses up to day 11.

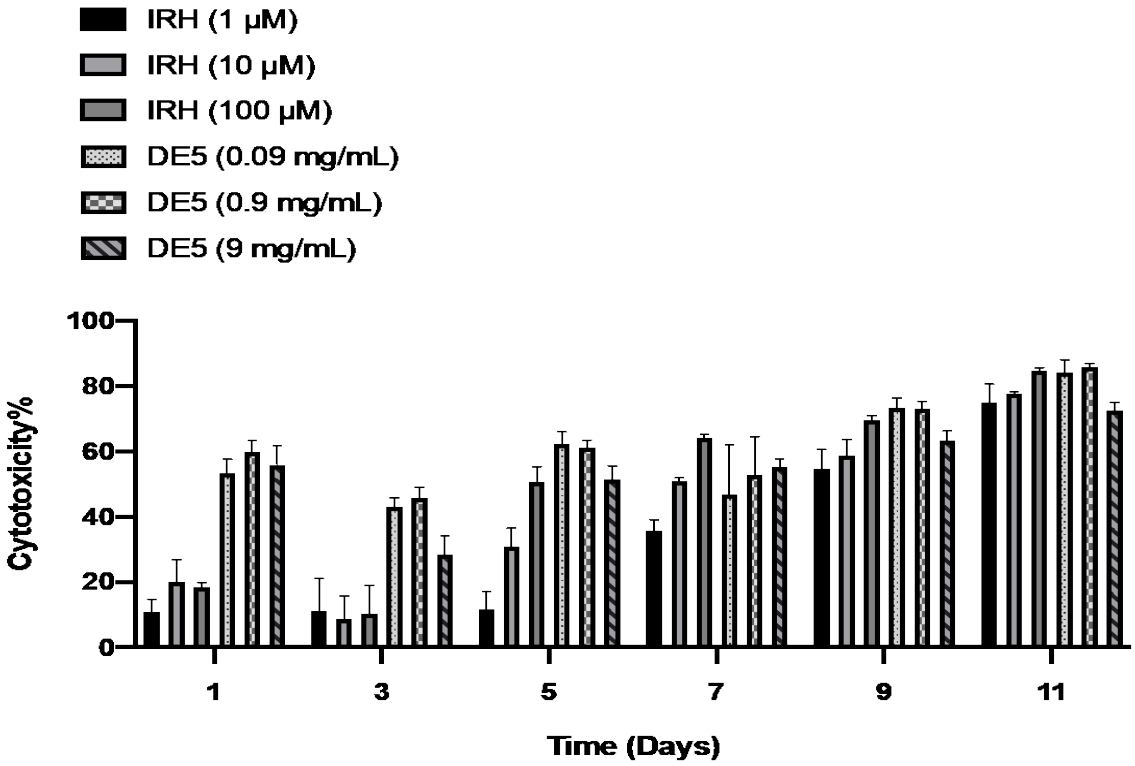


Figure 2.7. The cytotoxicity of free IRH and DE5 formulation on primary HGG cells (n=3).

2.4 Discussion

PCL NPs have great potential for drug delivery due to their slower biodegradation when compared to PLGA, which allows them to deliver drugs into cancerous tissue over a longer period of time, thus reducing the dosing interval. However, it is notoriously difficult to encapsulate drugs into PCL NPs due to its high crystallinity and the fact that drug entrapment occurs in the amorphous regions (Shuai et al., 2004). This was reported in a previous study where the percent EE of 5-fluorouracil in PCL NPs ranged from 4.3 ± 0.4 to 35.2 ± 3.1 (Ortiz et al., 2012). Another study reported low drug release of 5% over a period of one week from PCL NPs (Kirtane et al., 2018). These challenges

have led to limited publications on PCL NPs when compared to PLGA NPs. This chapter aimed to determine the most appropriate emulsification technique and formulation parameters to manufacture IRH-loaded PCL NPs with an acceptable EE, size and zeta potential. The optimum NPs were subsequently evaluated for their morphology, IRH release and cytotoxicity.

Both single and double emulsion techniques were evaluated using different process and formulation parameters to identify the optimum conditions for encapsulating the water-soluble IRH drug into PCL NPs.

2.4.1 Parameters Influencing Size, PDI and Surface Charge of Nanoparticle Formulations

2.4.1.1 Sonication Time and Amplitude

In Figure 2.2A, increasing the sonication time from 10 to 20 min resulted in an increase in the size of the NPs from 290.9 ± 38.5 nm to 471.1 ± 12.7 nm. This is due to overheating of the solution resulting in agglomeration, which has been previously reported (Al-Kaysi et al., 2005). Sonicator probes induce the formation of vapor cavities in the solution by the effect of mechanical vibration: this process is termed cavitation (Li and Fogler, 1978). This temporary acoustic cavitation can enhance emulsification. Cavitation can take place over two stages: 1. The low-frequency acoustic waves led to an unstable oil–water interface; 2. Temporary cavitation bubbles develop. The cavitation threshold is the minimum amount of energy required to generate cavitation. In order for the emulsification process to take place, the sonication power should be higher than the cavitation threshold (Mason, 1996). In our study, a sonication amplitude of 50% allowed for emulsification to take place and produce smaller NPs compared to

a higher sonication power. Previous studies had reported similar observations, where ultrasonication was effective in separating the agglomerated NPs, but further ultrasonication led to re-agglomeration of the NPs (Gokce et al., 2014). In another study, elevated levels of ultrasonication resulted in agglomerated NPs (Retamal Marín et al., 2018). This highlights that when the heating caused by sonication dominates over the cavitation power, it reduces the viscosity of the suspension and increases the thermal motion of the particles. This allows a higher collision rate between the accelerated particles, which results in increased particle interaction and agglomeration (Gokce et al., 2014). Agglomeration can also take place *via* the adhesion of particles if *van der Waals* attractive forces are predominant over the repulsive forces (Saltiel et al., 2004).

2.4.1.2 Drug and Polymer Amount

Increasing the amount of IRH from 2 to 18 mg using the single emulsion technique increased the size of the NPs from 290.9 ± 38.5 nm to 554.3 ± 27.2 nm. This is due to more drug particles accumulating on the surface of the polymeric NPs, as well as the low stability of the solution, leading to agglomeration of the NPs. Similar studies reported an increase in the particle size upon increasing the amount of drug (Khayata et al., 2012; Mohammady et al., 2016). Other research has suggested that increased phase viscosity occurs when the amount of drug is increased, leading to a larger particle size (Mao et al., 2008). Meanwhile, Chorny et al. (2002) reported no significant impact on particle size when the amount of drug was increased (Chorny et al., 2002). Increasing the amount of PCL to 240 mg reduced the particle size, which suggests that this polymer amount was sufficient to entrap more drug particles, preventing them from adsorbing on the surfaces of the nanoparticles and increasing their diameter.

2.4.1.3 Surfactant Concentration

Surfactants play an important role in reducing the surface tension between water and oil if used at the correct concentration. Low concentrations of surfactants do not reduce the surface tension as there is not enough surfactant to cover the interfacial surface between the organic and aqueous phases and thus are unable to stabilize the nanodroplets within the emulsion and prevent them from agglomerating (Sharma et al., 2016). The results demonstrate that 0.4% PVA (SE11) resulted in a large particle size (984.6 ± 129.6 nm) and a polydisperse formulation (PDI > 0.5), which is in accordance with a previous study that used 0.5% PVA for stabilizing PLGA NPs (Sharma et al., 2016). Furthermore, increasing the PVA concentration resulted in a decrease in the average size of the NPs produced by single emulsion (Figure 2.2E,F), which is in accordance with previous studies (Allémann et al., 1992; Lamprecht et al., 2001). However, others have reported an increase in the particle size upon using high concentrations of PVA (Arica and Lamprecht, 2005; Zweers et al., 2003). This discrepancy could be attributed to two different effects at high PVA concentrations: (1) increased stability between phases induced by the surfactant leads to a reduction in size; (2) increased viscosity of the aqueous phase results in poor mixing quality, thereby increasing size. The emulsification process and parameters used to produce the NPs would influence which of the above effects dominates over the other (Budhian et al., 2007).

2.4.1.4 Surfactant Type and Molecular Weight

Surfactants can impact particle size and are responsible for the overall formulation stability. PVA, when used as a single aqueous phase surfactant, produced smaller NPs

with better stability, when compared to the PVP used in the study. Another study obtained large particle sizes when using PVA (Van De Ven et al., 2012). In our study, the PVA with high molecular weight (89,000 g/mol) produced particles of a size outside the nanometer range due to its high viscosity. Other groups made similar observations, which demonstrate that too much emulsifier can cause particle aggregation as it adsorbs onto the surface of the NPs (Mohammady et al., 2016).

2.4.2 Parameters Influencing EE

2.4.2.1 Single Emulsion Solvent Evaporation Technique

The W/O single emulsion solvent evaporation technique produced unstable particles that contained aggregates. The O/W single emulsion solvent evaporation technique produced stable NPs within the nanometer range; however, the amount of IRH encapsulated was low, with a maximum of 12.1% achieved when amorphous PCL was used. The O/O single emulsion solvent evaporation technique produced particles outside the nanometer range, with an EE of 40.5%. Emulsions prepared using oil as the continuous phase provide better encapsulation for hydrophilic drugs by reducing the drug from partitioning into the external continuous phase (Vijaya Ramesh, 2009). A comparative study was conducted using both O/O and O/W solvent evaporation techniques to encapsulate the hydrophilic drug Rifampicin in PCL microspheres. Their results provided EEs of 43.5 to 61.9% and 12.3%, respectively (Mei et al., 2018b). The only disadvantage of using this method for the IRH-loaded PCL NPs is that it does not produce particles within the nanometer range but could be suitable for producing microspheres. The single emulsification technique has a poor record of encapsulation of hydrophilic drugs (Giri et al., 2013). Previous studies highlighted that the hydrophilic drugs such as caffeine, salicylic acid and theophylline could not be entrapped within

polylactic acid using the O/W single emulsification technique (Singh et al., 2014). Therefore, we investigated the double emulsification technique with different formulation parameters to identify those that produce optimum IRH-loaded PCL NPs in relation to EE, size, PDI and zeta potential.

2.4.2.2 Double Emulsion Solvent Evaporation Technique

The W/O/O double emulsion solvent evaporation technique has previously been used to increase the EE of a hydrophilic protein in PLGA microparticles (Wu et al., 2009). However, our results demonstrate that this technique achieved an EE of 11.1%, with a particle size outside the nanometer range, which suggests that the additional oil phase increases particle size and reduces drug entrapment. It is theorized that using a W/O/W double emulsion solvent evaporation technique leads to the formation of a semipermeable membrane, which permits water to migrate through the organic phase. This in turn leads the internal droplets to either swell or shrink, based on the direction of the osmotic gradient (Florence and Whitehill, 1982). Using this technique produced IRH-loaded PCL NPs with an acceptable particle size (less than 500 nm) and EE (greater than 50%); however, the parameters that reduce drug leakage into the aqueous phase had to be adjusted.

2.4.2.2.1 Matrix Material

The hydrophilic nature of IRH means that it readily moves into the aqueous phase, lowering its entrapment within the polymer matrix. Several studies on the emulsification of water-soluble drugs have reported low entrapment efficiency (Govender et al., 1999; Mandal, 1995; Niwa et al., 1994, 1993; Song et al., 1997), while other studies have

suggested that the use of a polymer matrix material, such as sodium alginate, can reduce the diffusion of the hydrophilic drug into the aqueous phase, increasing EE (Cui et al., 2001; Halder et al., 2005; Sriamornsak et al., 2007). The use of sodium alginate as a matrix material (DE3) produced IRH-loaded PCL NPs with an EE of only 18.7% and resulted in large particle size (>500 nm) and was thus discontinued. The large particle size could be due to the gelation of the sodium alginate, leading to high viscosity and incomplete emulsification. Additionally, the amount of sodium alginate could be insufficient to entrap the drug, as reported elsewhere (Rajinikanth et al., 2003).

2.4.2.2.2 The Use of Amorphous PCL and the Addition of Electrolytes

PCL with a crystallinity of up to 70% reduces the EE of drugs that generally favor more amorphous cores (Shuai et al., 2004). Semi-crystalline polymers such as PCL have a higher proportion of hydrophobic blocks, which increases core crystallinity and reduces their drug encapsulation capacity due to drugs favoring the amorphous blocks of the polymer (Chang et al., 2012). Using the double emulsion technique and amorphized PCL, IRH-loaded PCL NPs (DE4) with an EE of 34.8% were produced, which was enhanced to 65.0% with the addition of NaCl to both aqueous phases (DE5). However, the addition of NaCl to only aqueous phase W1 (DE6) resulted in a reduction in EE. Salts can enhance EE by producing an osmotic gradient and by forming porous particles. However, too many pores can lead to drug leakage. Similar to our results, the addition of NaCl with certain concentrations in both aqueous phases had previously improved the EE for protein-loaded microspheres (Pistel and Kissel, 2000). By increasing the NaCl concentration in the internal phase W1, it forces the water to migrate as a result of the osmotic pressure gradient from the outer to the inner phase,

causing swelling of the inner-phase droplets and the particles within. This swelling phenomenon causes breakage of the polymeric layer and release of the inner phase into the outer aqueous phase, which removes the drug during the encapsulation process. Therefore, at high salt concentrations, there is a possibility of damaging the double emulsion layer induced by the coalescence of the internal water droplets. On the other hand, the addition of NaCl to the external water phase could switch this phenomenon favorably. However, high salt concentrations in the external aqueous phase, regardless of the concentration of the salt in the W1 phase, could cause the water droplets to remain small in size, thereby keeping the porosity to a minimum. The results agree with these findings, with an improvement in the EE upon the addition of NaCl to both the internal (10 mg/mL) and external (2.5%) phases.

2.4.2.2.3 Amount of IRH

The reduction of the amount of IRH to 4 mg (DE7) reduced the EE of the NPs without much impact on the size. However, some studies suggest that the amount of drug does not play an important role in the EE as long as the polymer amount remains fixed and that the internal morphology of the particles is not affected by the drug loading (Mao et al., 2008; Sharma et al., 2016). Due to IRH being a hydrophilic drug, reducing the amount of IRH in the aqueous phase reduces its partitioning into the oil phase, which reduces the EE. Increasing the amount of IRH in the aqueous phase increases its partitioning into the oil phase, increasing EE (Itoh et al., 2015).

2.4.2.2.4 Solvent Evaporation Time

Increasing the solvent evaporation time from 4 (DE5) to 7 (DE8) hours had a slightly positive impact on EE, increasing it from 65.0 to 69.2%; however, there was also a

small increase in particle size from 202.1 ± 2.1 to 209.2 ± 3.3 nm, respectively. A duration longer than 7 h (DE9 and 10) reduced the stability of the formulations, leading to the formation of aggregates, with no NPs detected. The gradual decrease in the emulsion volume due to evaporation leads to an increase in viscosity, which impacts the electrostatic charge and equilibrium of the emulsion and leads to agglomeration during solvent removal (Sharma et al., 2016).

2.4.2.2.5 Surfactant Concentration

High concentrations of surfactants can increase the viscosity of the emulsion, leading to decreased stability, especially due to the gelatinization of PVA as a result of the formation of hydrogen bonds with the OH groups in the PVA during the formation of the NPs. Such a highly viscous emulsion could prevent the sonication energy from reaching all the droplets to shatter them into NPs. Moreover, the drug content of such viscous emulsions is usually high since the drug molecules have limited diffusion into the aqueous phase. Such opposing effects of the surfactant depend on the properties and concentration of the surfactant, as well as the formulation parameters, which will dictate which effect will dominate (Sharma et al., 2016). Maaz et al. improved the EE of the hydrophilic drug Gatifloxacin by increasing the surfactant concentration in the formulation (Maaz et al., 2015). It is theorized that increasing the surfactant concentration decreases the partitioning of a hydrophilic drug into the aqueous phase, thus enhancing its EE. Increasing the concentration from 4% (DE19) to 8% (DE20) for both the low- and high-MW PVA (DE11 and DE12) produced particles with EEs of 29.0, 43.3, 66.1 and 73.2%, respectively. Despite the high-MW PVA resulting in EEs above

50%, this formulation was abandoned due to the size of the particles being outside the nanometer range.

2.4.2.2.6 Surfactants with Different HLB Values

The oil layer of a W/O/W double emulsion sits between both aqueous phases and thus requires a minimum of two surfactants with different HLB values in order to form a stable emulsion. A surfactant with a low HLB value is required to emulsify the water in the oil (W/O) component, while a surfactant with a higher HLB value is required to further emulsify the W/O component into the water phase to form the W/O/W (Giri et al., 2013). Using tween-20 as the aqueous phase surfactant and span-80 as the organic phase surfactant (DE13) produced IRH-loaded PCL NPs with an EE of 31.2%, while using PVA as the aqueous phase surfactant and span-80 as an organic phase surfactant (DE14) achieved an EE of 37.5%. Although the NPs produced using this approach had an optimum size and high stability in terms of zeta potential, they did not achieve the optimum EE of greater than 50% and were therefore not investigated further.

2.4.2.2.7 Aqueous Phase Volume

Increasing or decreasing the volume of the aqueous phase to above or below 25 mL resulted in an increase in EE (Figure 2.5C) as well as particle size and PDI (Figure 2.5D). In addition, 15 and 50 mL of aqueous phase resulted in a particle size of 698.9 ± 175.8 and 587.1 ± 111.3 nm, respectively. This change in the ratio of aqueous and organic phases negatively impacts the emulsification shear force required for the formation of the NPs. By increasing the volume, the shear force of sonication will be distributed over the large volume and will not be sufficient to break down all the

particles to convert them to NPs. Likewise, a low aqueous phase volume will cause extra shear force and overheating of the small volume, leading to aggregation and a larger particle size (Sharma et al., 2016). Based on these results, 25 mL was confirmed as the optimum volume for the aqueous phase.

2.4.2.2.8 pH of the Aqueous Phase

Mohammady et al. found that by lowering the pH of the aqueous phase, the EE of IRH in PLGA NPs could be improved to above 50% (Mohammady et al., 2016). However, reducing the pH of only the inner aqueous phase (DE17) or both the inner and outer phases (DE18) to a pH of 3 produced IRH-loaded PCL NPs with EEs of only 23.6 and 22.3%, respectively; therefore, this approach was not investigated any further.

2.4.3 Characterization of the Optimized IRH-Loaded PCL Nanoparticles

IRH-loaded PCL NPs with an acceptable EE (>50%), size (<500 nm) and charge were produced using the double emulsion technique, 6 mg of IRH, amorphous PCL and the addition of NaCl to both aqueous phases (DE5). These NPs were subsequently characterized for their morphology, drug release and cytotoxicity against primary HGG cells.

2.4.3.1 Morphology and *In Vitro* Drug Release

TEM analysis demonstrated that the optimized IRH-loaded PCL NPs are a group of uniformly spherical particles with smooth edges that are within the nanometer range, with an average particle size of 149.2 ± 13.5 nm, which is lower than the 202.1 ± 2.1 nm determined by DLS. The *in vitro* drug release demonstrates a small burst on day 1 followed by slow and sustained release over a period of 16 days, with the NPs

releasing 40.4 ± 1.5% of their IRH content. The small burst on day 1 is due to the optimization process, which has resulted in more IRH being encapsulated in the NPs and less on the surface. The hydrophobic nature of the PCL delays the penetration of water into the matrix core, which means that IRH release is controlled solely by diffusion, with no polymer erosion. The small size of the nanoparticles results in a negligible diffusion pathway, resulting in the NPs having a zero-order release profile.

To better understand the drug release kinetics, the data were fitted to zero-order (cumulative percent of drug release versus time), Higuchi (cumulative percent of drug release versus square root of time) and Korsmeyer–Peppas release models (log cumulative percent of drug release versus ln time) (Table 2.4). The release data fitted all three models, as represented by high R^2 of 0.9991, 0.9595 and 0.9958, respectively. The correlation of the data to both the zero-order and Higuchi release models confirms that the release of the IRH is both zero-order and diffusion controlled. Drug release from polymeric NPs using the Korsmeyer–Peppas model can be described using the following equation: $Mt/M\infty = kt^n$ Equation (3) (Itoh et al., 2015).

($Mt/M\infty$) is the fraction of drug released at time t, k is the kinetic constant, and n is the exponent that correlates to a particular diffusion mechanism. Our results provided an n value of 0.6894, which corresponds to anomalous transport, which is non-Fickian diffusion. This is to be expected for NPs due to their small size and short diffusion pathway, while the inclusion of NaCl may have produced porous particles, which have been shown to have anomalous transport (Unagolla and Jayasuriya, 2018). In non-Fickian anomalous diffusion, tr ≈ td, where tr is the polymer relaxation time and td is the solvent penetration time (Grassi and Grassi, 2005). The release exponent n and K

values were calculated from the slope of the straight line for the plot of log cumulative percentage of drug released versus ln time.

2.4.3.2 Cytotoxicity

The initial cytotoxicity of the IRH-loaded NPs was significantly ($p < 0.0001$) higher than the unformulated IRH, which is due to the NPs penetrating the tumour cells faster than the free drug (Yan et al., 2020). Furthermore, nanoparticles are known to induce cytotoxicity by inducing apoptosis, depletion of ATP and necrosis(Unagolla and Jayasuriya, 2018). This may also be increasing their cytotoxicity at day 1 and day 3. By day 5, there was no significant difference in cytotoxicity between the high dose of the NPs and the high dose of the free IRH, and by day 7, there was no significant difference in cytotoxicity between all doses of the NPs and all doses of the free IRH. This is due to the IRH having now penetrated and diffused into the HGG cells. Additionally, the IRH-loaded NPs were significantly more cytotoxic ($p < 0.0001$) by day 11 compared to day 1, which is due to their slow release of IRH over the 11 days. However, there was no significant difference in the cytotoxicity of the high-dose NPs at day 1 and day 11, which may be due to the formation of a layer of NPs on top of the cells, preventing the release and uptake of the IRH over the 11 days.

2.5 Conclusions

Shielding drugs within NPs has the potential to improve how we treat brain tumours. PCL is a flexible polymer that has been often overlooked for the manufacture of NPs due to its poor EE. However, its slow degradation and ability to provide sustained release over a longer period of time when compared to PLGA makes investigating its

use for manufacturing NPs worthwhile. This research has covered a wide range of parameters and demonstrated that, through the use of amorphous PCL and the double emulsion technique, it is possible to encapsulate IRH into PCL NPs. The addition of electrolytes to both aqueous phases during the double emulsion process offers an additional benefit in encapsulating IRH by reducing its partitioning into the aqueous phase due to these phases being saturated with electrolytes. Furthermore, the IRH-loaded PCL NPs had an excellent morphology, provided zero-order sustained release of IRH for at least 16 days and are cytotoxic to primary HGGs cells over an 11-day period. This research demonstrates that IRH-loaded PCL NPs have the potential to be cytotoxic against primary HGG cells and their development should be further investigated.

Chapter 3 BOX-BEHNKEN DESIGN OF EXPERIMENTS OF DRUG-LOADED PCL NPS

3.1 Introduction

Hydrophilic drugs are difficult to formulate and encapsulate into a matrix of hydrophobic polymers. This is because they have limited affinity for hydrophobic polymers and thus favour the water phase during the emulsification process, which results in low EE. In addition, the large surface area of the NPs can lead to premature drug release due to a large proportion of the drug on the surface of NPs, instead of being encapsulated within the NPs (Mahmoud and McConville, 2021). Manipulating the different formulation parameters can influence the EE of hydrophilic drugs within the polymer as well as manipulating the size and charge of the NPs.

The size, PDI and surface charge of the NPs are critical factors that influence distribution, cellular uptake, membrane interactions, absorption and stability *in vivo* (Duan and Li, 2013). NPs can traverse through the endothelial fenestrations which vary in size depending on the organ or tumour (Gaumet et al., 2008). A desired size should be less than 500 nm to avoid phagocytosis of the NPs by macrophages (Vonarbourg et al., 2006). Smaller sized NPs favour uptake by non-phagocytic cells leading to an enhanced intracellular drug concentration (Champion et al., 2007). However, very small NPs can have minor ligand to receptor interaction (Shang et al., 2014). There is not a standard size for NPs that can reach and penetrate into tumours efficiently. Blood vessels obstruct particles of a large size, while small particles do not reside in tumours for long periods of time (Albanese et al., 2012a). Previous research suggested that 200 nm particles passed through normal blood vessels and were not filtered out in the kidneys but were able to penetrate through leaky blood vessels in the cancer environment by EPR effect (Ke et al., 2014).

The charge and hydrophobicity of the NPs can have an impact on the protein corona formed on their surface when administered intravenously. A neutral and hydrophilic surface is more favourable than a hydrophobic surface as it could accumulate plasma proteins (Cedervall et al., 2007). Additionally, a low negative net charge is reported to be more favourable than a positive charge due to better accumulation in tumours. On the other hand, positively charged NPs can lead to protein adsorption and adhesion to anionic polyelectrolytes of mucosal layers (Honary and Zahir, 2013; Liu et al., 2014).

3.1.1 Design of Experiments

The design of experiments (DOE) is a valuable statistical tool for developing a correlation between independent key parameters that control the manufacture of formulations. DOE determines the significant and insignificant factors that contribute towards an output of interest. This facilitates optimization of key factors using a limited number of runs designed with statistical foundation (Antony, 2014; Zhang and Mao, 2016). In a DOE, 2 or more independent variables are employed to develop a factorial design, through which the behaviour of the formulations can be interpreted and interactions between variables can be analysed (Lewis *et al*., 1998; Neves *et al*., 2014). NPs with favourable size, charge and EE can be achieved with a factorial design. The mixture of different variables with different levels could impact the interactions between molecules in the nano-formulations resulting in optimum properties (Wagner et al., 2013).

BBD of experiments is a response surface method used in DOE. It relies on the combination of a low, medium and high levels of variables. Compared to central composite design that requires 20 runs and 5 levels of factors, BBD requires a smaller

number of runs including 3 center points and 3 levels of variables where it does not take into account runs at the extreme level (Guterres et al., 2000). Therefore, a BBD was performed in this chapter, using the most optimum formulation parameters developed in chapter 2 as the center point, in order to examine the effect of the independent variables and their interaction on the characteristics of the PCL NPs. This chapter also aimed at developing NPs with various sizes, charges and EE at different levels of the independent parameters for further investigation of their release pattern.

3.2 Materials and Methods

3.2.1 Materials

The materials used in this chapter were the same as chapter 2, section 2.2.1.

3.2.2 BBD

15 drug-loaded NP formulations were developed by double emulsion modified method as described previously in section 2.2.4.5, chapter 2 using the parameters of the most optimum formulation (DE5). Table 3.1 presents the coded levels of the independent variables in BBD. Table 3.2 provides the actual levels corresponding to each of the codes in BBD.

Table 3.1. Box-Behnken coded 3-level factorial design

Experiment	Variable 1 (X1)	Variable 2 (X2)	Variable 3 (X3)
1	-1	-1	0
2	1	-1	0
3	-1	1	0
4	1	1	0
5	-1	0	-1
6	1	0	-1

7	-1	0	1
8	1	0	1
9	0	-1	-1
10	0	1	-1
11	0	-1	1
12	0	1	1
13	0	0	0
14	0	0	0
15	0	0	0

Table 3.2. Box-Behnken coded and actual values

Variable	**Coded Values**		
	-1 (low)	0 (medium)	1 (high)
X1= PCL Amount (mg)	54	108	162
X2= Drug Amount (mg)	3	6	9
X3= PVA Concentration (%)	2	4	6

3.2.3 Yield Enhancement

Different centrifugation approaches were used to enhance the yield of the NPs. The first approach involved repeated centrifugations at 9500 rpm (Beckman Coulter Centrifuge, Buckinghamshire, UK) for 20 minutes at 25°C. The second approach involved diluting formulations with dH_2O then centrifugation at 24,500 rpm for 30 minutes.

$$\%\ Yield = \frac{Mass\ of\ nanoparticles\ obtained}{Mass\ of\ polymer,drug\ and\ cryprotectant} \text{ x } 100 \qquad \text{Equation (4)}$$

3.2.4 Characterization of the NPs

The size, surface charge and EE of the NPs were analysed as described in section 2.2.8 and 2.2.9 in Chapter 2.

3.2.5 Statistical Analysis

Data produced from BBD were fitted using the Minitab software version 19.2020.2.0 to obtain the best fit model represented by the R^2. ANOVA was performed to ensure the model was a good fit. F-tests and P-values were employed to determine the significance of the regression coefficient. Data were expressed as the mean of 3 replicated measurements. A pareto chart was used to determine the significant variables. 2D and 3D plots were used to provide a graphical representation of the model.

3.3 Results

3.3.1 BBD Predicted Model and Best Fit Regression Coefficient for Size

The size (Y1) (dependent variable) obtained at 3 different independent variables (X1, X2 and X3 equivalent to A, B and C respectively as presented in the model) was subjected to multiple regression analysis to fit the response with the experimental data and produce a second order polynomial model as provided by equation 5.

$$\text{Size} = \text{Size} = 235.7 + 15.23\,\text{A} - 18.76\,\text{B} - 29.24\,\text{C} + 12.4\,\text{A}*\text{A} + 11.2\,\text{B}*\text{B} + 52.5\,\text{C}*\text{C} - 1.5\,\text{A}*\text{B} + 53.4\,\text{A}*\text{C} - 0.2\,\text{B}*\text{C}$$

Equation (5)

β0 represents the intercept with the y-axis, while β1 to β9 represent the regression coefficients for the linear, square and interaction effects as shown in table 3.3. The value for R^2 of equation (5) was found to be 0.94 which indicated a good correlation between the experimental and predicted data. R^2 values greater than 0.50 were considered reasonable as reported previously (Tinca et al., 2020). The adjusted R^2 was 0.83 which implied that 17.00% of the data were not explained by the model. A non-significant lack of fit (>0.05) indicated that the model is significant for the response. ANOVA was used to test the significance of the model and presented a significant model for describing the size of the NPs expressed in Prob > F value of 0.013. Probability of 0.05 or less is regarded as a significant effect for the independent factors on the response.

The size of the NPs for the different formulations ranged from 203.60 ± 1.04 to 388.10 ± 6.45. The model implies that the size of the NPs is significantly affected by the amount of drug and surfactant concentration which have an antagonistic effect on the response. Whereas the concentration of the surfactant square and interaction between the polymer and surfactant were shown to have a significant synergistic effect on the size of the NPs as shown in table 3.3. The main effects of A, B and C represent the average results for changing one variable at a time from its low to high level. The interaction terms AB, AC and BC represent the change in response when 2 variables are changed. The positive coefficients indicate the synergistic effect and the negative coefficients indicate an antagonistic effect on the response. The significance values for all contributing factors are provided in table 3.3. The theoretical and experimental values are presented in table 3.4.

Table 3.3. Summary of regression coefficient analysis for the response Y1 (Size).

Coefficient	β0	β1 (A)	β2 (B)	β3 (C)	β4 (A*A)	β5 (B*B)	β6 (C*C)	β7 (A*B)	β8 (A*C)	β9 (B*C)
Size (nm)	235.70	15.23	-18.76	-29.24	12.4	11.2	52.5	-1.5	53.4	-0.2
P value	0.000	0.086	0.047	0.009	0.290	0.337	0.004	0.886	0.003	0.985

Table 3.4. Experimental and theoretical values with residuals of the response Y1.

Formulation No.	Experimental (observed) value of Size	Theoretical (predicted) value of Size	Residuals	%Error
1	244.40	261.29	-16.89	-6.91
2	298.80	294.79	4.01	1.34
3	222.80	226.81	-4.01	-1.80
4	271.10	254.21	16.89	6.23
5	388.10	368.06	20.04	5.16
6	290.80	291.66	-0.86	-0.30
7	203.60	202.74	0.86	0.42
8	320.00	340.04	-20.04	-6.26
9	344.00	347.15	-3.15	-0.92
10	294.00	310.03	-16.03	-5.45
11	305.10	289.07	16.03	5.25
12	254.30	251.15	3.15	1.24
13	237.26	235.70	1.56	0.66
14	241.70	235.70	6.00	2.48
15	228.13	235.70	-7.57	-3.32

Table 3.5. Analysis of variance, degree of freedom (DF), sum of squares (SS), mean of squares (MS) and Fischer's ratio (F-value) for the size of the NPs.

Regression	DF	SS	MS	F value	P value
Size (nm)	9	33533.00	3725.90	9.15	0.01

The standardized effect of the independent variables and their interaction on the response is presented via the Pareto Chart (Figure 3.1) which ranks the effect of the variables on the output in terms of its significance. The pareto chart shows that the AC, C2 and C are the most significant factors in their effect on the size of the NPs (P= 0.003).

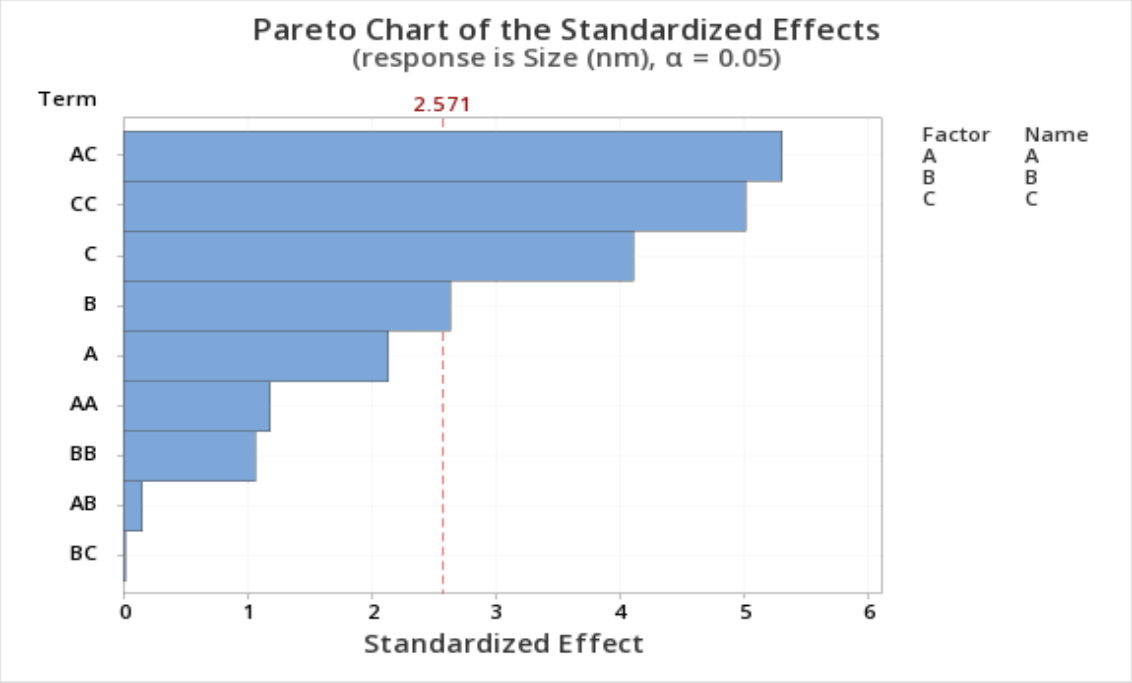


Figure 3.1. Pareto chart expressing standardized effect of independent variables and their interaction on the size of the NPs.

The relationship between the independent and dependent variables was further highlighted by plotting 2D contour and 3D surface plots. The effects of 2 variables and their interaction on the size of the NPs are expressed in figure 3.2, 3.3 and 3.4 at a fixed level of the third variable.It was determined from the contour and surface plots that a smaller NP size range from 203.60 to 210.00 nm could be obtained with an A range of -1 to -0.7 and C range from 1 to 0.4 (Figure 3.3). It is evident from the contour and surface plots that increasing the level of C while reducing the level of A results in reduction of the size of the NPs. The correlation between A and C show a significant

effect. On the contrary the relationship between A and B, and B and C was non-significant as shown from the circular contour plots in figures 3.2A and 3.4A and the saddle 3D plots (figures 3.2B and 3.4B).

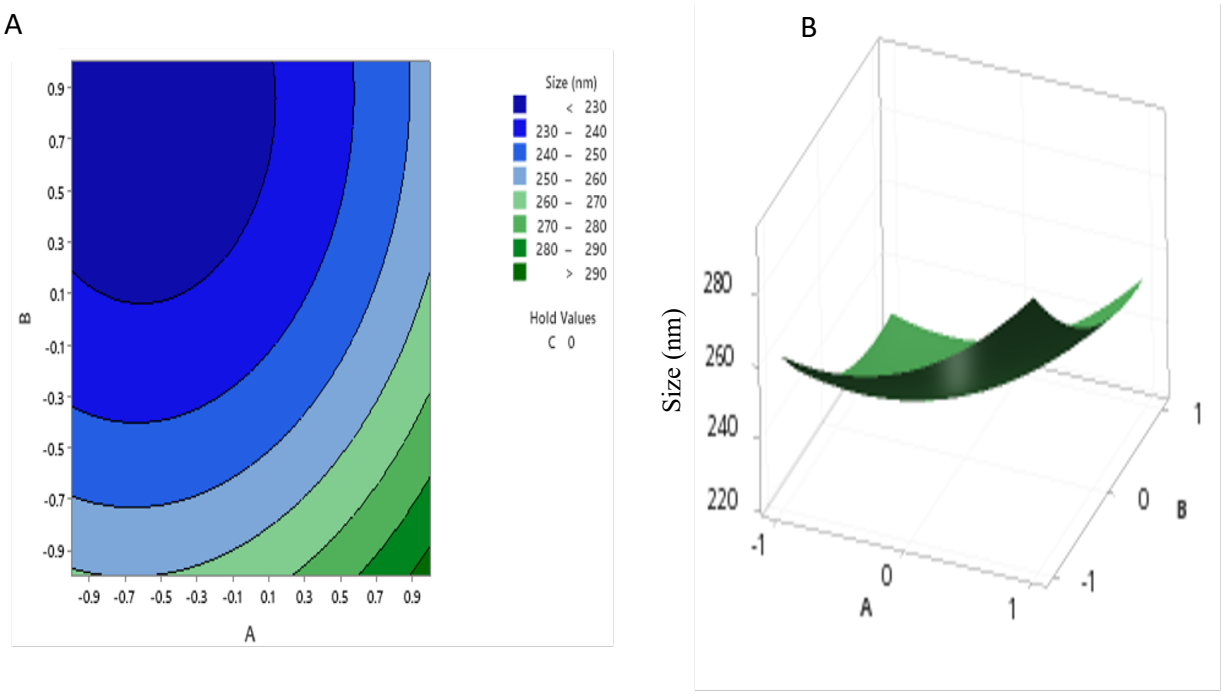


Figure 3.2. Contour plot **(**A) and Surface plot (B) showing the effect of polymer amount (A) and drug amount (B) on the size of the NPs.

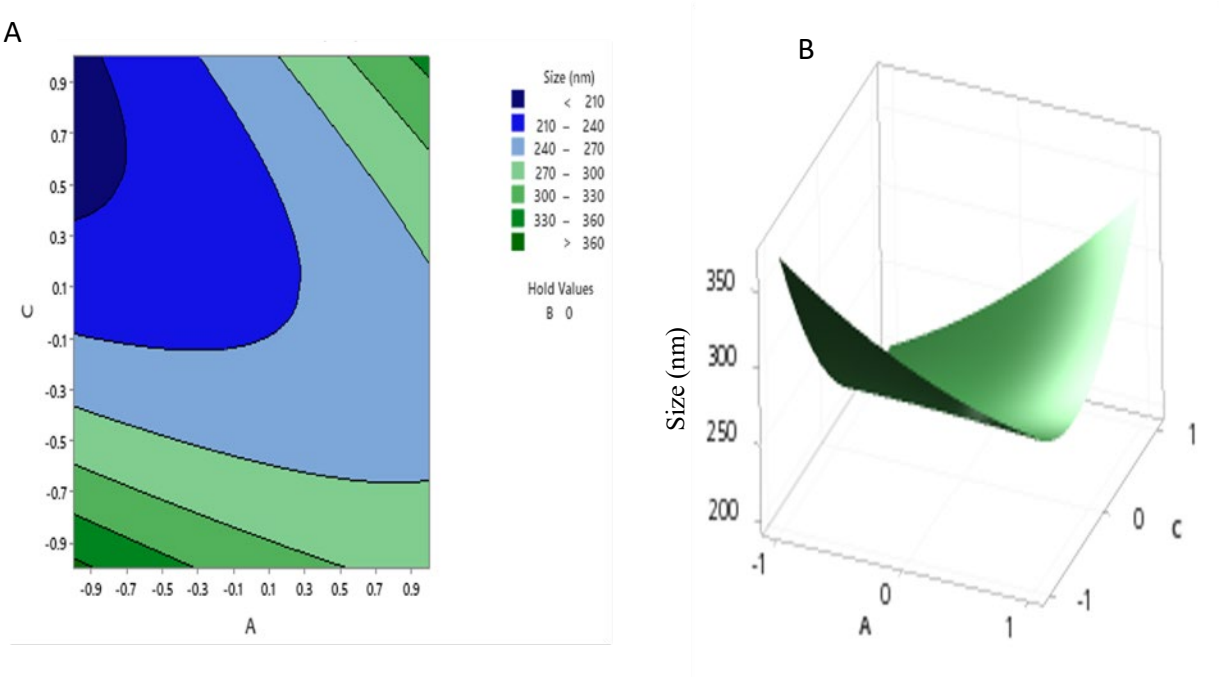


Figure 3.3. Contour plot and (A) Surface plot (B) showing the effect of polymer amount (A) and surfactant concentration (C) on the size of the NPs

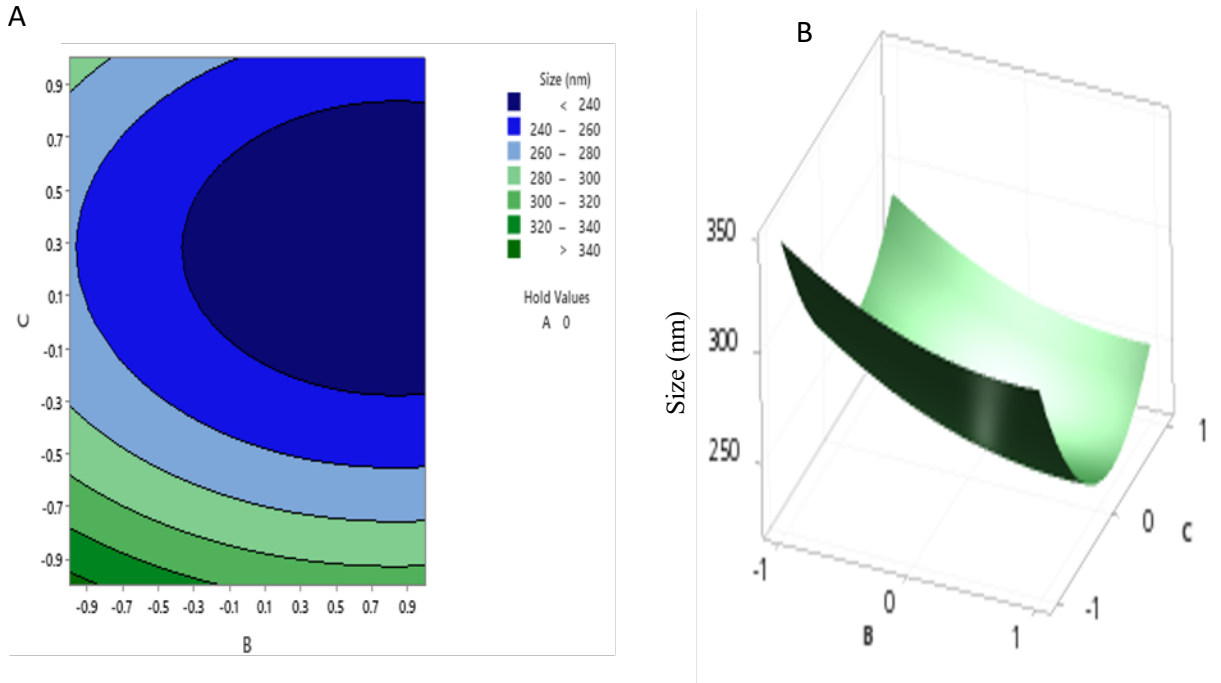


Figure 3.4. Contour plot (A) and Surface plot (B) showing the effect of drug amount (B) and surfactant concentration (C) on the size of the NPs

The highest significant effect was shown to be the interaction between the polymer and surfactant with a contribution of 34.04%. The contribution percent was calculated according to equation 6 (Khajeh and Ghanbari, 2011).

Contribution% = $\frac{SSA}{SS}$ X 100 Equation (6)

The SSA refers to the sum of squares for each individual factor, whereas SS refers to the sum of squares of the model.

3.3.2 BBD Predicted Model and Best Fit Regression Coefficient for Zeta Potential

The zeta potential (Y2) (dependent variable) obtained at 3 different independent variables (X1, X2 and X3) was subjected to multiple regression analysis to fit the response with the experimental data and produce a model of second order polynomial equation as follows:

Zeta Potential (mV) = -15.60 + 1.277 A + 1.754 B - 1.460 C + 1.94 A*A - 2.18 B*B + 2.59 C*C Equation (7)

The value for R^2 of equation 7 was found to be 0.78 and 0.61 for the adjusted R^2 with a non-significant lack of fit (0.06). The ANOVA represents a significant model for describing the charge of the NPs expressed in Prob > F value of 0.023.

The zeta potential of the NPs for the different formulations ranged from -7.63 ± 0.25 to -19.63 ± 2.56 mV. The model depicts that the charge of the NPs is significantly impacted by the amount of drug and squared concentration of the surfactant. This significant effect is shown to be a synergistic effect as shown in table 3.6. The

significant values for all contributing factors are provided in table 3.6. The theoretical and experimental values are presented in table 3.7.

Table 3.6. Summary of regression coefficient analysis for the response Y2 (Zeta potential).

Coefficient	β0	β1	β2	β3	β4	β5	β6
Zeta Potential (mV)	-15.60	1.27	1.75	-1.46	1.94	-2.18	2.59
P value	0.000	0.107	0.038	0.072	0.099	0.069	0.037

Table 3.7. Experimental and theoretical values with residuals of the response Y2.

Formulation No.	Experimental (observed) value of Charge	Theoretical (predicted) value of Charge	Residuals	%Error
1	-17.60	-17.91	0.31	-1.76
2	-19.23	-17.27	-1.95	10.14
3	-14.36	-16.32	1.95	-13.57
4	-12.16	-11.85	-0.31	2.54
5	-13.10	-11.20	-1.89	14.42
6	-7.63	-8.01	0.37	-4.84
7	-13.86	-13.48	-0.37	2.66
8	-9.68	-11.57	1.89	-19.52
9	-12.60	-14.17	1.57	-12.46
10	-13.33	-13.26	-0.06	0.45
11	-19.63	-19.69	0.06	-0.30
12	-15.16	-13.58	-1.57	10.35
13	-16.06	-15.60	-0.46	2.86
14	-14.96	-15.60	0.063	-4.21
15	-15.76	-15.60	-0.16	1.01

Table 3.8. Analysis of variance, DF, SS, MS and F-Value for the charge of the NPs.

Regression	Df	SS	MS	F value	P value
Charge	6	114.08	19.01	4.79	0.02

The standardized effect of the independent variables and their interaction on the response is presented *via* the Pareto Chart (figure 3.5) which ranks the effect of the variables on the outcome. As presented in the figure, the only significant factors are C^2 and B (P= 0.03).

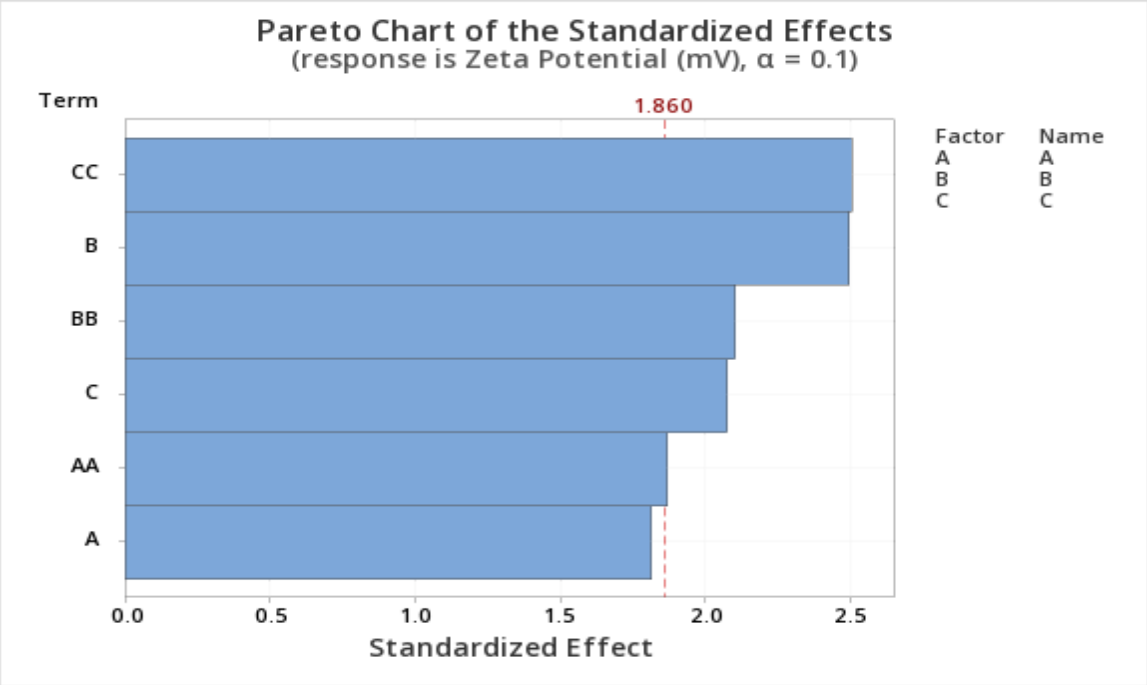


Figure 3.5. Pareto chart expressing standardized effect of independent variables and their interaction on the charge of the NPs.

The relationship between the independent and dependent variables was further highlighted by plotting surface and contour plots as expressed in figure 3.6, 3.7 and 3.8. As shown in the figures, there were no significant interactions between the independent parameters as expressed via the contour plots, quadratic (Figures 3.6B and 3.8B) and saddle surface plots (Figure 3.7B).

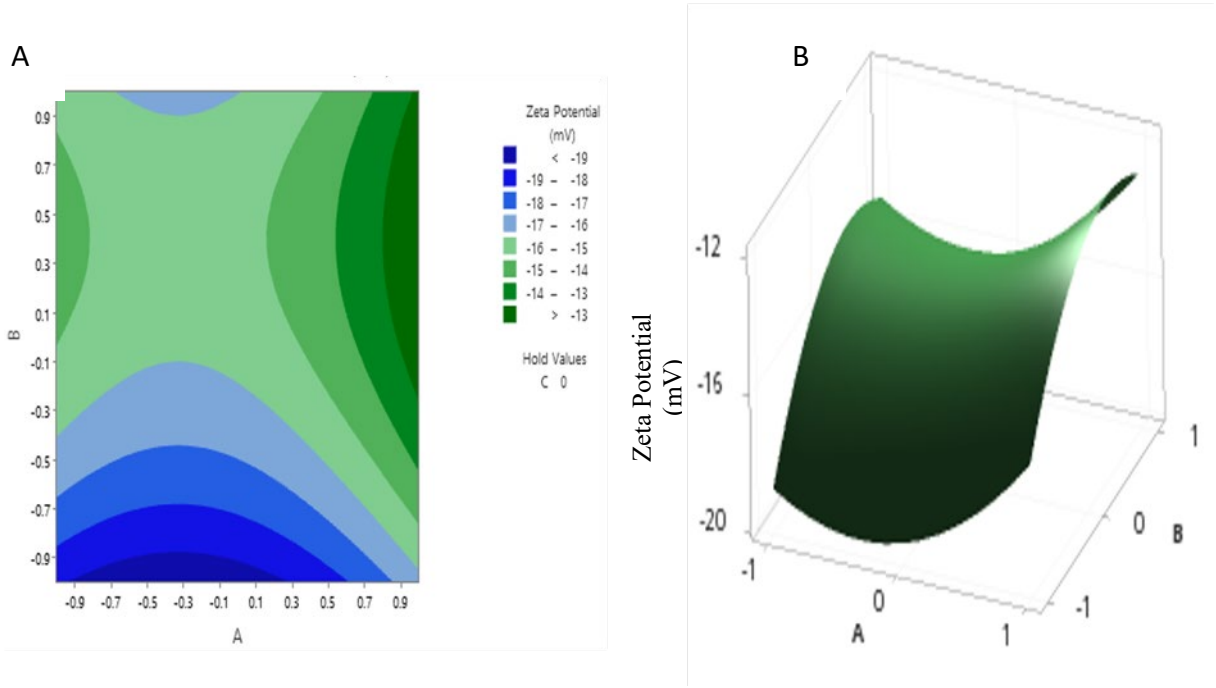


Figure 3.6. Contour plot (A) and Surface plot (B) showing the effect of polymer amount (A) and drug amount (B) on the charge of the NPs.

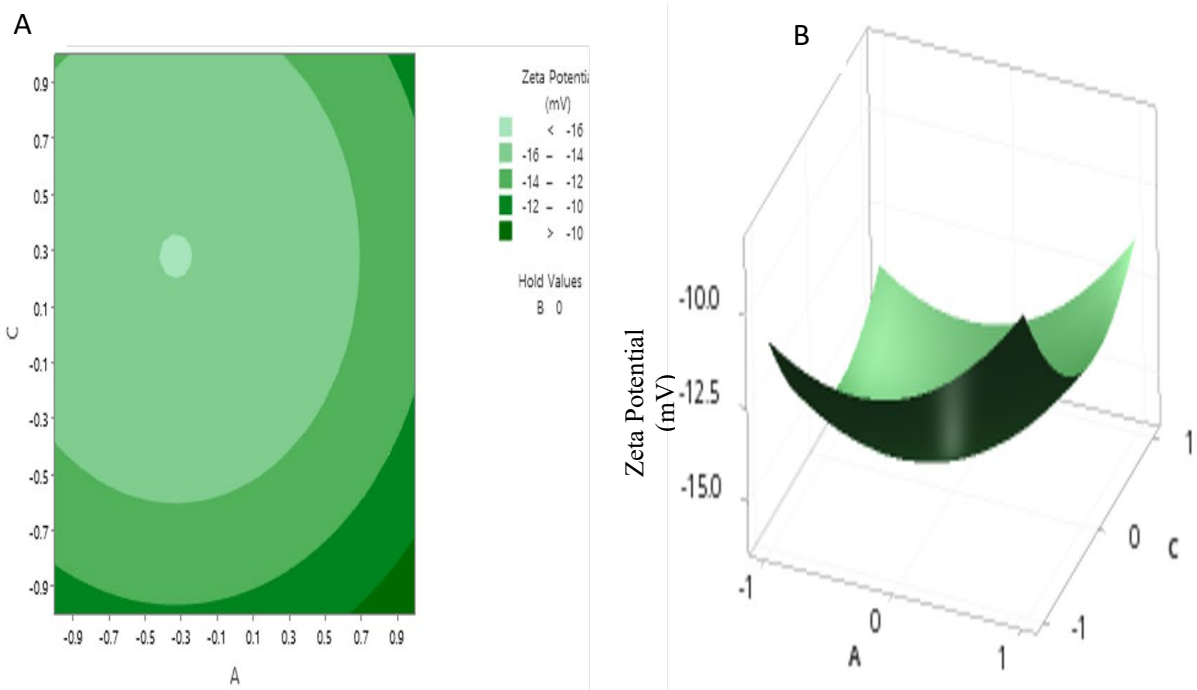


Figure 3.7. Contour plot (A) and Surface plot (B) showing the effect of polymer amount (A) and surfactant concentration (C) on the charge of the NPs

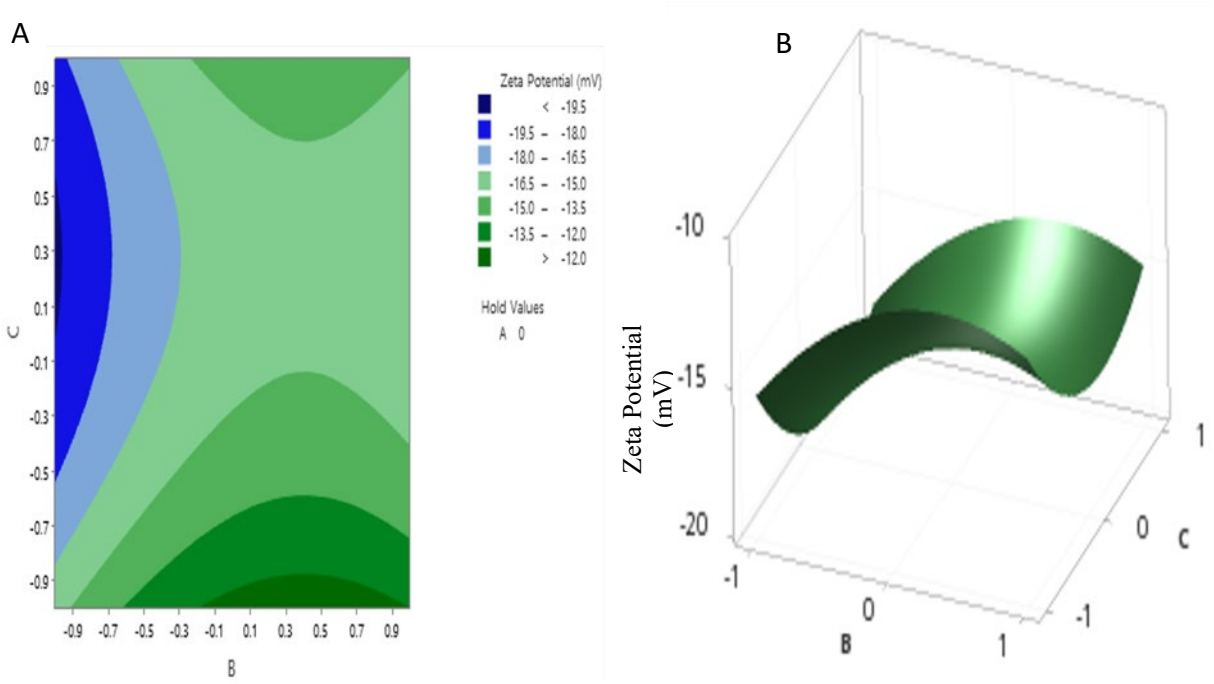


Figure 3.8. Contour plot (A) and Surface plot (B) showing the effect of drug amount (B) and surfactant concentration (C) on the charge of the NPs

The highest significant effect was shown to be the squared concentration of the surfactant (C^2) with 24.84% contribution.

3.3.3 BBD Predicted Model and Best Fit Regression Coefficient for EE%

The EE% (Y3) (dependent variable) obtained at 3 different independent variables (A, B and C) was subjected to multiple regression analysis to fit the response with the experimental data and produce a model of second order polynomial equation:

EE% = 64.40 - 2.914 A + 9.547 B - 2.919 C + 5.82 A*A + 2.12 B*B + 2.50 C*C + 1.19 A*B + 1.13 A*C + 3.59 B*C Equation (8)

The value for R^2 of equation 8 was found to be 0.97, adjusted R^2 was 0.94 with a non-significant lack of fit (0.08). The ANOVA represents a significant model for describing the EE% of the NPs expressed in Prob > F value of 0.001.

The EE% of the NPs for the different formulations ranged from 52.44% ± 0.10 to 82.42% ± 0.03. As shown in table 3.9, The model implies that EE% of the NPs is significantly influenced by the amount of drug, the interaction between the drug and surfactant and the amount of polymer squared which all have a synergistic effect on EE%. Whereas, the polymer amount and concentration of surfactant have antagonistic significant effects on the EE%. The theoretical and experimental values are provided in table 3.10.

Table 3.9. Summary of regression coefficient analysis for the response Y3 (EE%).

Coefficient	β_0	β_1	β_2	β_3	β_4	β_5	β_6	β_7	β_8	β_9
EE%	64.39	-2.91	9.54	-2.91	5.82	2.11	2.49	1.19	1.13	3.58
P value	0.000	0.011	0.000	0.011	0.003	0.111	0.072	0.308	0.331	0.019

Table 3.10. Experimental and theoretical values with residuals of the response Y3.

Formula-tion No.	Experimental (observed) value of EE%	Theoretical (predicted) value of EE%	Residuals	%Error
1	65.25	66.90	-1.65	-2.52
2	59.86	58.68	1.18	1.97
3	82.42	83.60	-1.18	-1.43
4	81.81	80.16	1.65	2.01
5	80.34	79.68	0.66	0.82
6	69.42	71.59	-2.17	-3.12
7	73.74	71.58	2.16	2.94
8	67.35	68.01	-0.66	-0.98

9	66.95	65.97	0.98	1.47
10	78.41	77.89	0.52	0.66
11	52.44	52.96	-0.52	-0.99
12	78.24	79.22	-0.98	-1.26
13	64.63	64.40	0.23	0.36
14	63.53	64.40	-0.87	-1.36
15	65.03	64.40	0.63	0.97

Table 3.11. Analysis of variance, DF, SS, MS and F-Value for the EE% of the NPs.

Regression	Df	SS	MS	F value	P value
EE%	9	1076.89	119.65	27.02	0.001

The standardized effect of the independent variables and their interaction on the response is presented *via* the Pareto Chart (figure 3.9) which shows that B, A^2 and C are the most significant factors (P= 0.000, 0.003 and 0.011 respectively).

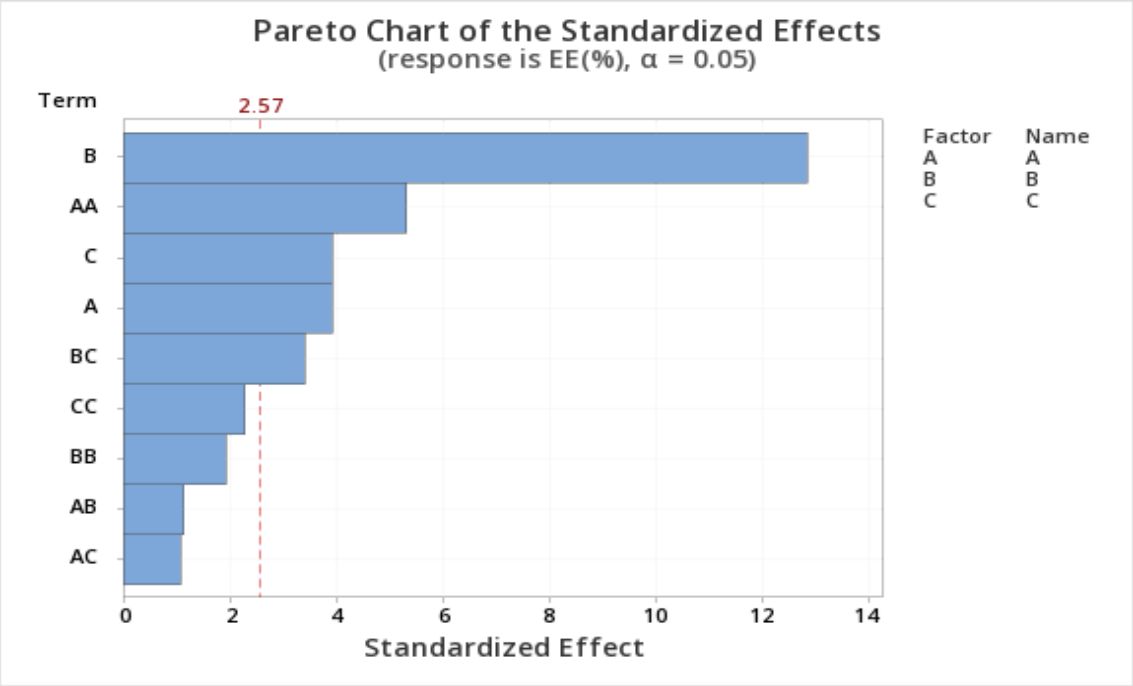


Figure 3.9. Pareto chart expressing standardized effect of independent variables and their interaction on the EE% of the NPs.

The relationship between the independent and dependent variables was further highlighted by plotting surface and contour plots. It was determined from the contour and surface plots (Figure 3.12) that an EE of 70.00% or higher could be obtained with a B range from -1 to 1 level and C range from -0.9 to 1 level. The highest significant effect was shown to be the amount of drug with the highest percent of contribution of 67.71%.

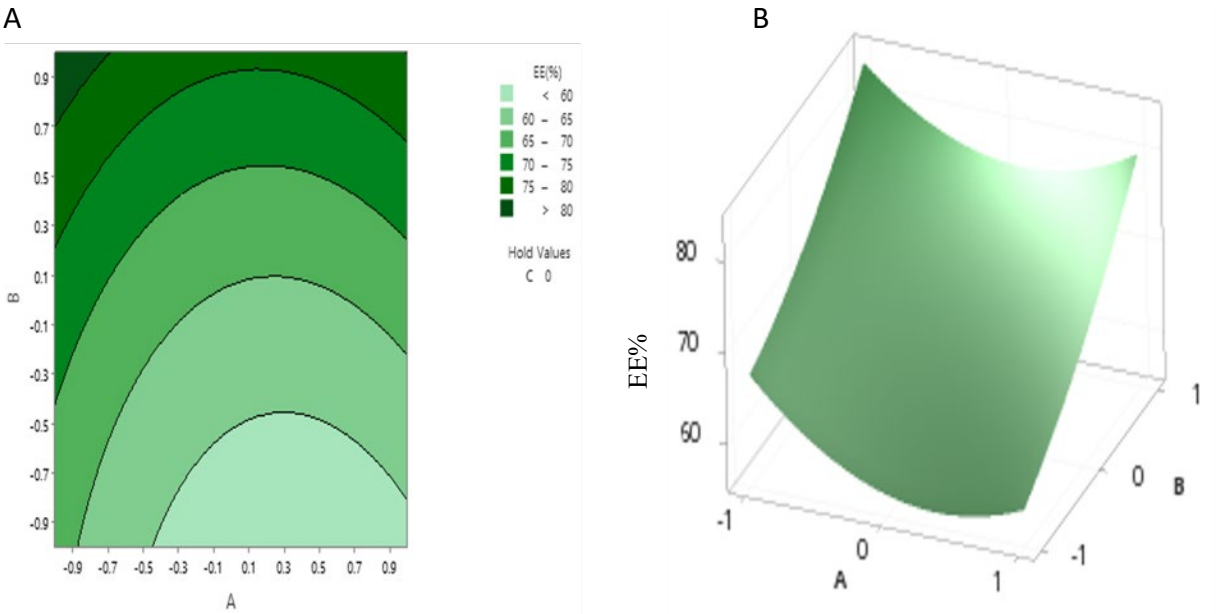


Figure 3.10 Contour plot (A) and Surface plot (B) showing the effect of polymer amount (A) and drug amount (B) on the EE% of the NPs

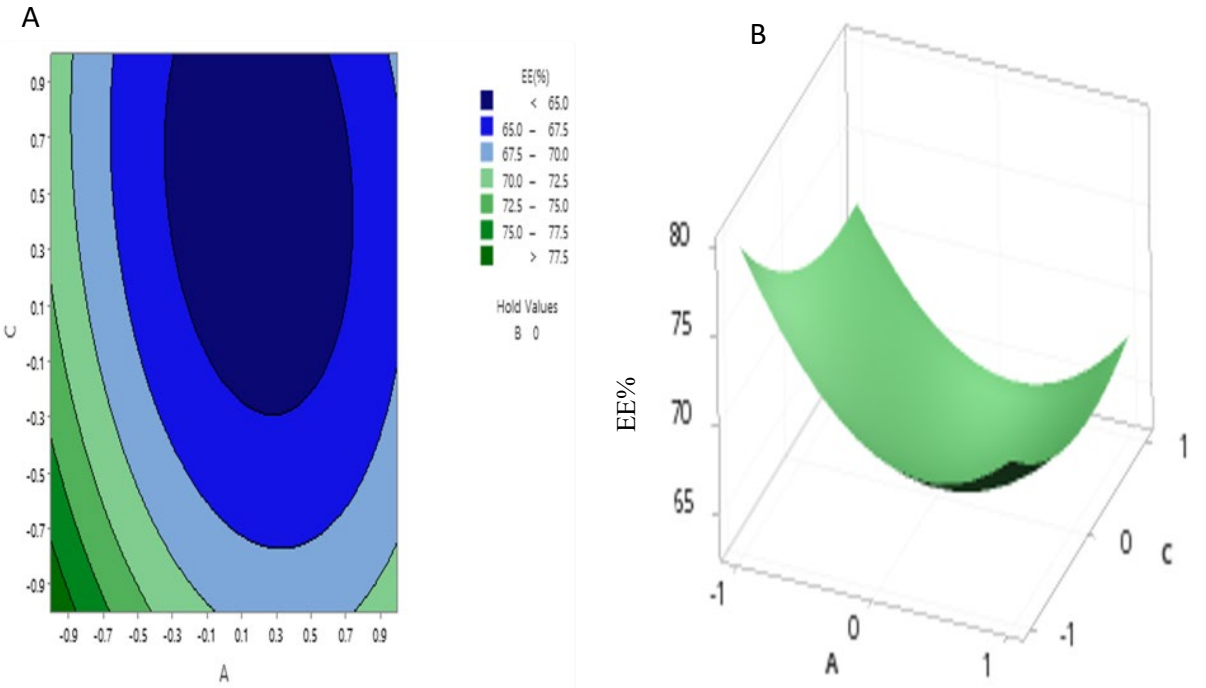


Figure 3.11. Contour plot (A) and Surface plot (B) showing the effect of polymer amount (A) and surfactant concentration (C) on the EE% of the NPs

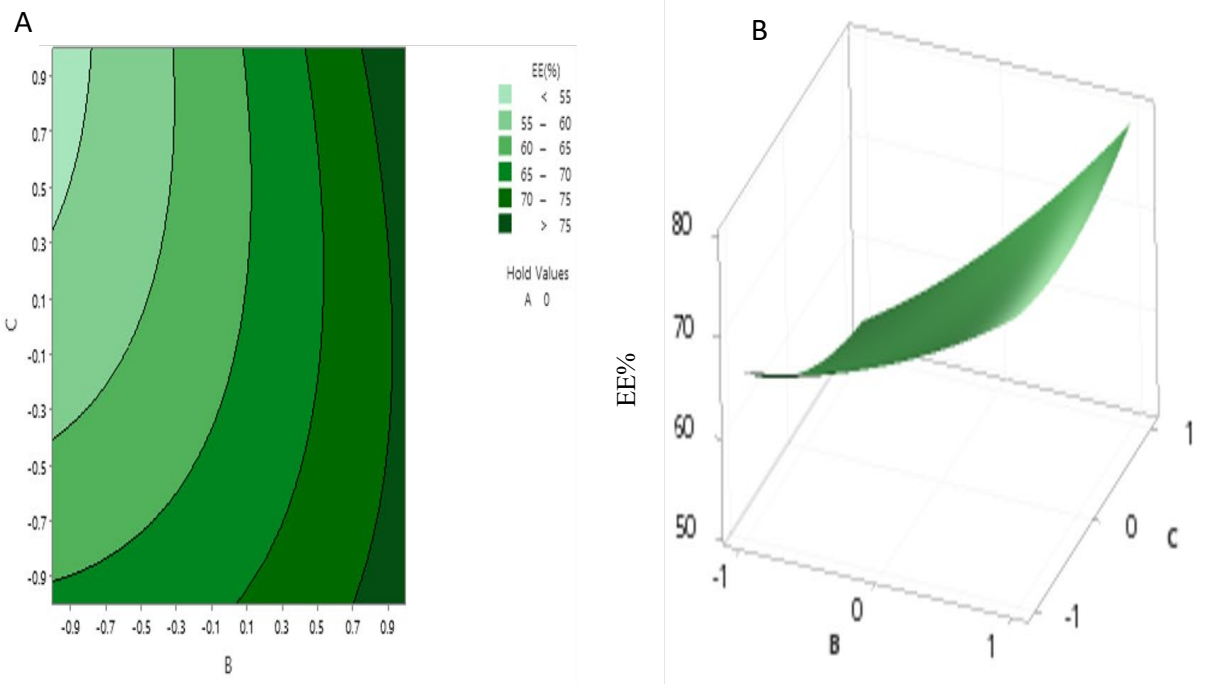


Figure 3.12. Contour plot (A) and Surface plot (B) showing the effect of drug amount (B) and surfactant concentration (C) on the EE% of the NPs

3.3.4 Yield of NPs

3.3.4.1 Characterization Of NPs Before and After Yield Enhancement

As shown in table 3.12, the charge of the NPs was impacted by the repeated centrifugation which is shown in the reduced values of the negative zeta potential. The size of the NPs, however, was not much impacted except for some formulations. While, in table 3.13, the surface charge of the NPs became more negative indicating more stability and less agglomeration with the higher speed centrifugation and reduced viscosity by water dilution. Figure 3.13 presents the difference in yield of NPs.

Table 3.12. Mean size, PDI, zeta potential and EE% of NPs before yield enhancement

Formulation	Size (nm)	PDI	Zeta Potential (-mV)	EE%
F1	281.63	0.30	-3.48	61.46
F2	288.83	0.38	-3.68	73.02
F3	708.93	0.52	-3.00	89.88
F4	268.43	0.33	-3.02	70.28
F5	373.43	0.48	-4.78	80.32
F6	476.70	0.55	-4.88	74.65
F7	378.47	0.18	-3.80	76.90
F8	250.37	0.43	-3.28	65.31
F9	294.03	0.44	-4.68	67.24
F10	520.80	0.55	-4.55	75.30
F11	351.20	0.51	-3.16	64.15
F12	1552.00	1.00	-2.69	84.11
F13	314.33	0.25	-3.32	74.60
F14	339.70	0.32	-3.593	70.89
F15	368.97	0.32	-3.09	67.83

Table 3.13. Mean size, PDI, zeta potential and EE% of NPs after yield enhancement

Formulation	Size (nm)	PDI	Zeta Potential (-mV)	EE%
F1	244.40	0.31	-17.60	65.25

F2	298.80	0.33	-19.23	59.86
F3	222.80	0.30	-14.36	82.42
F4	271.10	0.22	-12.16	81.81
F5	388.10	0.49	-13.10	80.34
F6	290.80	0.27	-7.63	69.42
F7	203.60	0.42	-13.86	73.74
F8	320.00	0.18	-9.68	67.35
F9	344.00	0.30	-12.60	66.95
F10	294.00	0.32	-13.33	78.41
F11	305.10	0.41	-19.63	52.44
F12	254.30	0.34	-15.16	78.24
F13	237.26	0.30	-16.06	64.63
F14	241.70	0.39	-14.96	63.53
F15	228.13	0.37	-15.76	65.03

3.3.4.2 Initial and Enhanced Yield

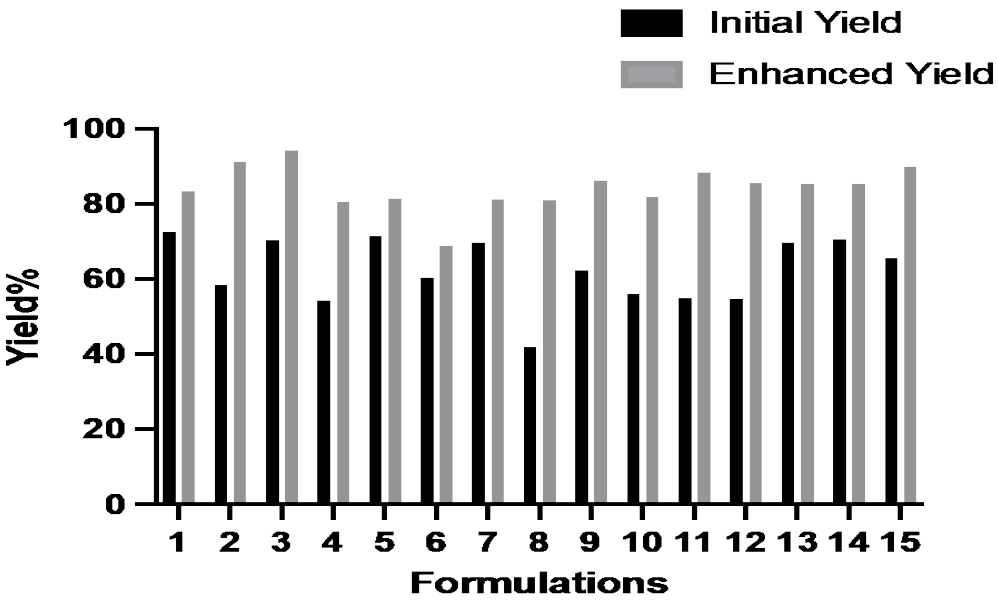


Figure 3.13. Initial and enhanced yield percent of NP formulations

3.4 Discussion

The purpose of using BBD of experiments was to examine the effect of different formulation variables on the characteristics of the NPs. The size, charge and EE of the NPs were evaluated by changing the concentrations of the formulation variables from low to high levels. The goal was to reduce the size and charge and to maximize the EE% of the NPs. It was found that a size ranging from 203.60 ± 1.04 to 388.10 ± 6.45 nm, a zeta potential ranging from -7.63 ± 0.25 to -19.63 ± 2.56 mV and EE% ranging from 52.44% ± 0.10 to 82.42% ± 0.03 were obtained *via* double emulsion solvent evaporation techniques using different amounts of polymer (54, 108 and 162 mg), drug (3, 6 and 9 mg) and surfactant concentration (2, 4 and 6%).

The BBD was conducted using 15 independent runs in random order at 3 different levels (low, medium and high). The polynomial equations, contour plots and 3D plots were used to determine the relationship between the independent variables and response. Multiple regression and ANOVA analyses were performed for the fitted polynomial model. The models were found to be a significant fit for size, charge and EE% responses. 2D contour and 3D surface plots provided a graphical view of the dependent and independent variables. Contour plots with elliptical shape indicate that the interaction between the independent variables were significant, whereas circular contour plots indicate a non-significant relationship (Arbab-Zavar et al., 2012; Fakheri and Alam, 2016). Through contour plots, optimum levels of the response could be easily detected.

The smallest size of the NPs was 203.60 ± 1.04 which was achieved by using -1, 0 and 1 levels equivalent to 54 mg, 6 mg and 6% of the polymer, drug and surfactant respectively. An average PDI of 0.18 to 0.49 substantiate a narrow size distribution. It

was previously reported that NPs up to 200 nm size were monodisperse, showed higher stability, and successfully crossed biological barriers. However, a larger size could allow for higher entrapment of the drug and enhance its release (Mallipeddi and Rohan, 2010; Vauthier and Bouchemal, 2009).

The model suggests that from 3 to 9 mg of drug, the higher amount of drug resulted in a significant size reduction which could imply that higher levels of drug were necessary to interact with the polymer and avoid agglomeration caused by excess drug concentration which helped in reducing the size (Mao et al., 2008). The concentration of the surfactant had a significantly antagonistic effect on the size, but when the concentration was squared it had an opposite effect leading to a larger particle size. Similar results were previously reported in which a high concentration of the surfactant increased the size of the NPs due to increased viscosity (Budhian et al., 2007). High stability is achieved in the presence of an adequate level of the surfactant which when increased beyond that level can lead to adverse effects on the size of the NPs (Budhian et al., 2007). Similarly, the interaction between the polymer and surfactant has increased the size significantly which is suggested to be due to increased hydrophobicity (Kuskov et al., 2010).

The lowest negative charge achieved in this model was -19.63 ± 2.56 mV by using 0, -1 and 1 levels equivalent to 108 mg, 3 mg and 6% of the polymer, drug and surfactant respectively. The negative charge of the NPs could be due to the carbonyl group of the PCL which creates a negative charge on the surface of the NPs. The shift in the values of the charge could be due to the different concentrations of the PCL as well as the shielding effect of the PVA as a result of its interaction with PCL or entrapped drug (Ajiboye et al., 2018). The negative charge of the NPs could also be due to the

interaction of the polymer with the hydrophobic region of the surfactant whereas the hydrophilic region of the surfactant is present in the aqueous phase. This interaction creates steric and electric stabilization (Mora-Huertas et al., 2010). The model suggests that the amount of drug and squared surfactant concentration has a significant impact on the charge of the NPs which could be explained by the high viscosity imposed by the high surfactant concentration in addition to the positively charged drug which could lead to an increase in the charge of the NPs. IRH is reported to have more positive charge in its lactone form than its carboxylate form (Casadó et al., 2016).

The stability of the NPs is achieved by maintaining a high value of negative zeta potential indicating a high level of repulsion between particles which is necessary to prevent aggregation of the particles (Zielińska et al., 2020). Also, there was no significant difference between the neutral and negative charged NPs in circulation half-life as previously demonstrated (Yamamoto et al., 2001). On the contrary, increasing the positive charge on PEGylated liposomes reduced their residence in the blood and enhanced their uptake by the liver in a previous study (Park et al., 2008). Moreover, the positively charged NPs were found to have enhanced interaction with the negatively charged cell membrane of the macrophages and phagocytosis than negatively charged or neutral NPs (Mutsaers and Papadimitriou, 1988).

The highest EE% in this BBD was found to be 82.42% ± 0.03 achieved with -1, 1 and 0 equivalent to 54 mg, 9 mg and 4% of the polymer, drug and surfactant respectively. A low level of PCL and high level of drug achieved the highest EE, which confirms that the amount of PCL was sufficient to entrap the drug and avoid agglomeration. PCL was reported to efficiently entrap drugs such as tamoxifen, dapivirine and docetaxel

and was dependent on the solubility of the drugs within the polymer (Das Neves et al., 2013; Q. Liu et al., 2012; Nandhakumar et al., 2017; Shenoy and Amiji, 2005).

The model implies that EE% of the NPs is significantly influenced by the amount of drug which is similarly proven in other research, where the concentration of cisplatin was directly proportional with EE% in PLGA-mPEG NPs (Gryparis et al., 2007). On the other hand, our results exhibited a significant decrease in EE% upon increasing the amount of polymer. However, the amount of polymer squared had a synergistic effect on EE%. The interaction between the drug and surfactant helped keep the drug entrapped in the NPs. However, with high levels of surfactant, the EE was negatively affected. This is due to the formation of hydrogen bonds between the hydroxyl groups of the PVA molecules leading to increased size and decreased EE% (Sharma et al., 2016).

A theoretical optimum condition could be achieved by setting the desired characteristics of minimum particle size and charge and maximum EE%. The optimum factors were predicted to be achieved by using -0.87 level of A, 1 level of B and 0.41 level of C which would yield 203.01 nm, -15.81 mV and 82.35% EE. The relation between the coded and actual values was provided according to the following equation:

$$x_i = \frac{X_i - x_0}{\Delta X_i} \qquad i = 1,2,3,\ldots,\mathrm{k} \qquad \text{Equation (9)}$$

Where xi is the coded value of an independent variable; Xi is the actual value of an independent variable; X0 is the actual value of an independent variable at the center point and ∆Xi is the step change (Tanyildizi et al., 2005).

According to equations 10, 11 and 12, the relationship between coded and actual values of independent variables for amount of polymer, drug and surfactant concentration respectively was calculated as follows:

$-0.87 = \frac{X_1 - 108}{54}$ X1 = 61.02 mg Equation (10)

$1 = \frac{X_2 - 6}{3}$ X2 = 9 mg Equation (11)

$0.41 = \frac{X_3 - 4}{2}$ X3 = 4.82% Equation (12)

The yield of the NPs was enhanced by reducing the viscosity of the solution by diluting the formulation with dH_2O before centrifugation. This also impacted their charge by protecting the stability of the NPs. A high magnitude of the negative charge indicated stability compared to the previous method of repeated centrifugation. It was evident that repeated spins have compromised the stability of the NPs represented in a lower value of negative zeta potential as expressed in table 17.

In conclusion, developing NPs with optimum properties is crucial for the design of nanomedical formulations. Therefore, BBD was employed in that regard to allow the investigation and selection of optimum values of the independent factors that result in the smallest size, lowest surface charge and highest EE which were found to be achieved by using 61.02 mg of PCL, 9 mg of drug and 4.82% of surfactant. This chapter highlighted that the size of the IRH loaded PCL NPs was mostly impacted by the interaction between the PCL and PVA. The charge of the NPs was mostly influenced by the squared concentration of the PVA and the highest influencing factor towards the EE was the amount of drug. The next chapter will investigate the optimum factors and their levels on developing PCL-PLGA blend NPs using BBD.

Chapter 4 BOX-BEHNKEN DESIGN OF EXPERIMENTS OF DRUG-LOADED PCL-PLGA BLEND NPS

4.1 Introduction

Polymer blends are favourable due to their mixed properties which are not usually present with the individual polymer (Paul, 1995). Blended polymers can have their properties tailored to overcome the limitations of the individual polymers used for drug delivery (Dash and Konkimalla, 2012).

The physicochemical characteristics of polymers such as their chemical and crystal structures, solubility, degradation, and hydrophobicity impact the surface charge, drug compatibility, and release patterns in pharmaceutical formulations. Such factors also influence the selection of a suitable polymer(s) for the intended application (Varma et al., 2004).

Blending hydrophobic polymers with hydrophilic polymers can be advantageous for enhancing drug release. The selection of a hydrophilic polymer such as PLGA can be influenced by the ratio of its glycolic and lactic acid monomers, which impacts its solubility and degradation (Zugasti et al., 2009). PCL is known to be suitable for blending with other polymers with three different types of compatibility (Koleske, 1978). PCL can either form a compatible blend with another polymer which can be confirmed by observing a single glass transition temperature (Tg). Another type of compatibility is the mechanical compatibility in which blended polymers show advantageous properties despite having two Tgs equivalent to the Tg of each polymer separately. The third type of compatibility is the crystalline interaction which happens when PCL is blended with other semi-crystalline polymers leading to enhanced crystallinity due to the interaction between the polymers (Koleske, 1978).

PLGA 50/50 was reported to have a better degradation and faster erosion rate compared to PLGA 75/25 because of greater rate of hydrolysis for the lactide/ glycolide monomers. PLGA chains also hydrolyse faster than PCL chains in PLGA/PCL/PLGA triblock copolymers as early reported (Choi and Park, 2002). Therefore, PLGA 50/50 was selected in this study to form blends with different ratios of PCL. Optimization of the formulation parameters of the blended polymers is required to obtain an effective formulation for drug delivery (Dash and Konkimalla, 2012). Therefore, a BBD was performed in this chapter to examine the effect of the independent variables and their interaction on the blended NP characteristics. This chapter also aimed at developing NPs with a different size, charge and EE range in order to select suitable formulations for further characterization and comparison with PCL NPs in terms of reduced crystallinity, enhanced drug release and cytotoxicity against glioma cells.

4.2 Materials and Methods

4.2.1 Materials

The DL-lactide/Glycolide copolymers; PURASORB® PDLG 5002A (50% Lactide, inherent viscosity of 0.2 dl/g) were purchased from Corbion Purac (Gorinchem, The Netherlands). The rest of the materials used were the same as chapter 2, section 2.2.1.

4.2.2 Development of PCL-PLGA Blend NPs.

Drug loaded PCL-PLGA blends were developed using the double emulsion method described in Chapter 2, section 2.2.4.5 with different amounts of PCL to PLGA at 25:75, 50:50 and 75:25 ratios. Initially the PCL was added to DCM and left until fully dissolved with agitation. Then, the required amount of PLGA was added and stirred

until fully solubilized. The rest of the method was completed using the parameters of the most optimum formulation described in chapter 2 but without amorphization of PCL.

4.2.3 BBD

15 drug loaded PCL-PLGA blend NP formulations were prepared using the double emulsion modified method as described previously. The coded levels of the independent variables used in BBD were described in Chapter 3, section 3.2.2. The actual levels of the independent variables are presented in table 4.1.

Table 4.1. Box-Behnken coded and actual values

Variable	**Coded Values**		
	-1 (low)	0 (medium)	1 (high)
X1= PCL-PLGA Amount (mg)	54 (27:27)	108 (54:54)	162 (81:81)
X2= Drug Amount (mg)	3	6	9
X3= PVA Concentration (%)	2	4	6

4.2.4 Characterization of the NPs

The size, surface charge and EE of the NPs were analysed as described in Chapter 2, section 2.2.8 and 2.2.9.

4.2.5 Statistical Analysis

Statistical analysis was performed as described previously in Chapter 3, section 3.2.5.

4.3 Results

4.3.1 Size, Charge and EE% of Drug Loaded PCL-PLGA NPs

Blended NPs made of PLGA and PCL had a more negative surface charge as shown in table 4.2 compared to the PCL NPs described in chapter 3. The highest EE efficiency (60.96 ± 6.62%) and smallest average size (234.26 ± 1.45 nm) was achieved with blend F18 (50:50 PCL: PLGA) (table 4.2). Therefore, it was selected and renamed to F2 for further optimization by BBD.

Table 4.2. Average particle size, PDI, Zeta potential and EE of IRH loaded blend NPs at various ratios of polymer amounts.

Formulation (PCL: PLGA)	Size (nm)	PDI	Zeta Potential (mV)	EE%
F17 (25:75)	350.23 ± 3.52	0.43 ± 0.01	-32.70 ± 0.34	59.69 ± 5.01
F18 (50:50)	234.26 ±1.45	0.36 ± 0.01	-32.50 ± 0.10	60.96 ± 6.62
F19 (75:25)	451.10 ± 8.35	0.42 ± 0.03	-27.13 ± 0.35	56.85 ± 8.30

4.3.2 BBD Predicted Model and Best Fit Regression Coefficient for Size

Three independent variables (X1, X2 and X3 equivalent to A, B and C of model terms respectively) were combined at 3 different levels provided the change in the dependent response of size (Y1). The response was fitted *via* multiple regression with the experimental data to produce a second order polynomial model in equation 13:

Size = 363.2 + 42.0 A + 26.9 B - 38.7 C - 60.0 A*A + 34.4 B*B - 37.8 C*C + 14.3 A*B - 29.5 A*C - 13.0 B*C Equation (13)

β0 implies the intercept with the y-axis, while β1 to β9 represent the regression coefficients. The value for R^2 of equation 13 was found to be 0.92. The adjusted R^2 was 0.77. An ANOVA was used to test the significance of the model and presented a

significant model for describing the size of the NPs expressed in Prob > F value of 0.027. A non-significant Lack of fit of 0.22 was also expressed by the model.

The size of the blended NPs ranged from 206.03 ± 2.95 to 461.33 ± 36.49. As presented by the model, the size of the NPs was significantly influenced by the polymer amount which had a positive effect on the size of the NPs. The surfactant concentration and the amount of polymer squared had a significantly negative impact on the size of the NPs as shown in table 4.3. The main effects of A, B and C represent the average results for changing one variable at a time from its low to high level. The interaction terms AB, AC and BC represent the change in response when two variables are changed. The theoretical and experimental values are presented in table 4.4.

Table 4.3. Summary of regression coefficient analysis for the response Y1 (Size).

Coefficient	β0	β1	β2	β3	β4	β5	β6	β7	β8	β9
Size	363.18	42	26.90	-38.70	-60	34.40	-37.80	14.30	-29.50	-13
P value	0.000	0.014	0.065	0.019	0.016	0.096	0.074	0.417	0.127	0.457

Table 4.4. Experimental and theoretical values with residuals of the response Y1.

Formulation No.	Experimental (observed) value of Size	Theoretical (predicted) value of Size	Residuals	%Error
1	313.80	282.86	30.94	9.86
2	350.23	338.39	11.84	3.38
3	296.37	308.21	-11.84	-4.00
4	389.90	420.84	-30.94	-7.94
5	221.60	232.61	-11.01	-4.97
6	383.73	375.65	8.08	2.11

7	206.03	214.12	-8.08	-3.92
8	250.26	239.24	11.02	4.40
9	338.63	358.56	-19.93	-5.88
10	461.33	438.48	22.86	4.95
11	284.27	307.12	-22.86	-8.04
12	354.93	335.01	19.93	5.61
13	380.87	363.19	17.68	4.64
14	341.37	363.19	-21.82	-6.39
15	367.33	363.19	4.14	1.13

Table 4.5. Analysis of variance, DF, SS, MS and F-Value (F-value) for the size of the NPs.

Regression	DF	SS	MS	F value	P value
Size (nm)	9	60682.40	6742.50	6.47	0.02

The standardized effect of the independent variables and their interaction on the response is presented *via* the Pareto Chart (Figure 4.1) which ranks the effect of the variables on the output in terms of its significance concluding that the top 3 significantly influencing factors are A, A^2 and C (P= 0.01).

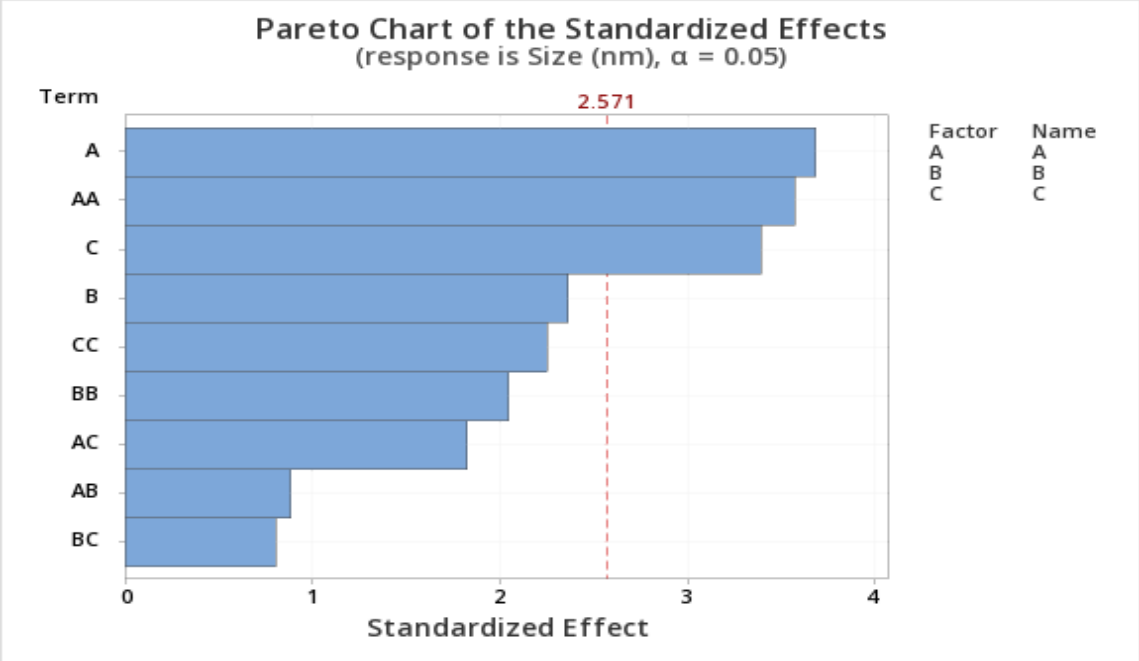


Figure 4.1. Pareto chart expressing standardized effect of independent variables and their interaction on the size of the NPs.

The relationship between the independent and dependent variables was further highlighted by plotting 2D contour and 3D surface plots. The effects of two variables and their interaction on the size of the NPs are expressed in figures 4.2, 4.3 and 4.4 at a fixed level of the third variable. A non-significant effect for the interaction between the independent variables is shown in the contour and 3D plots.

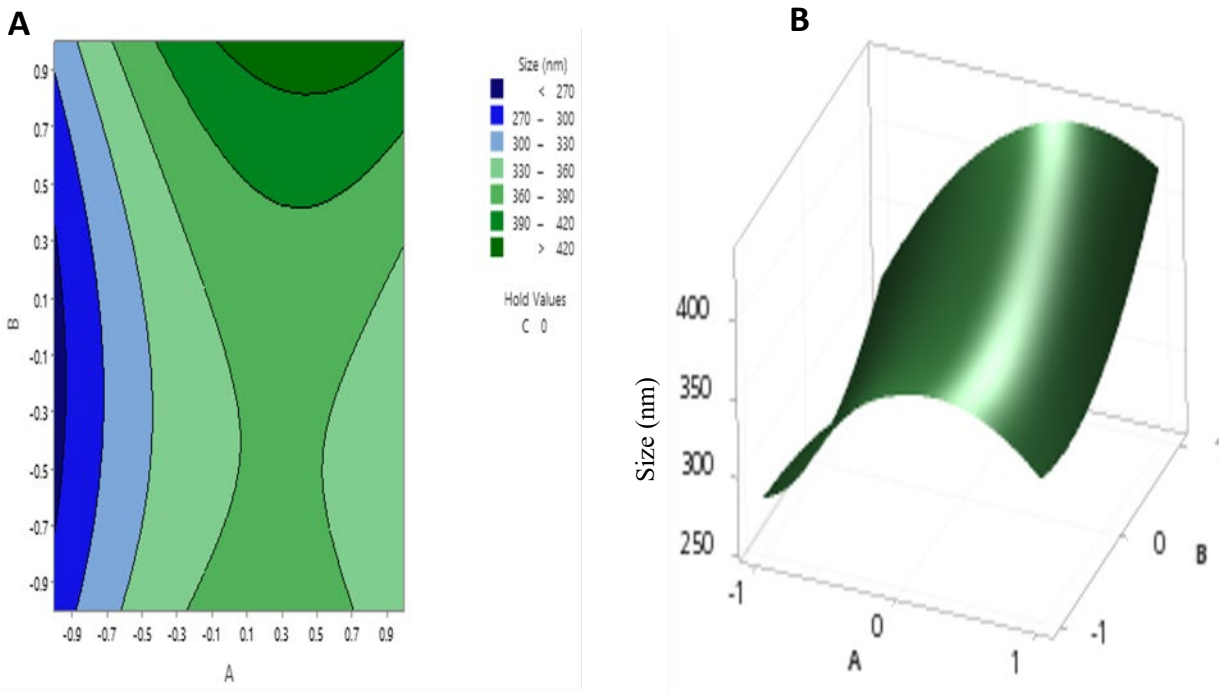


Figure 4.2. Contour plot and (A) Surface plot (B) showing the effect of polymer amount (A) and drug amount (B) on the size of the NPs.

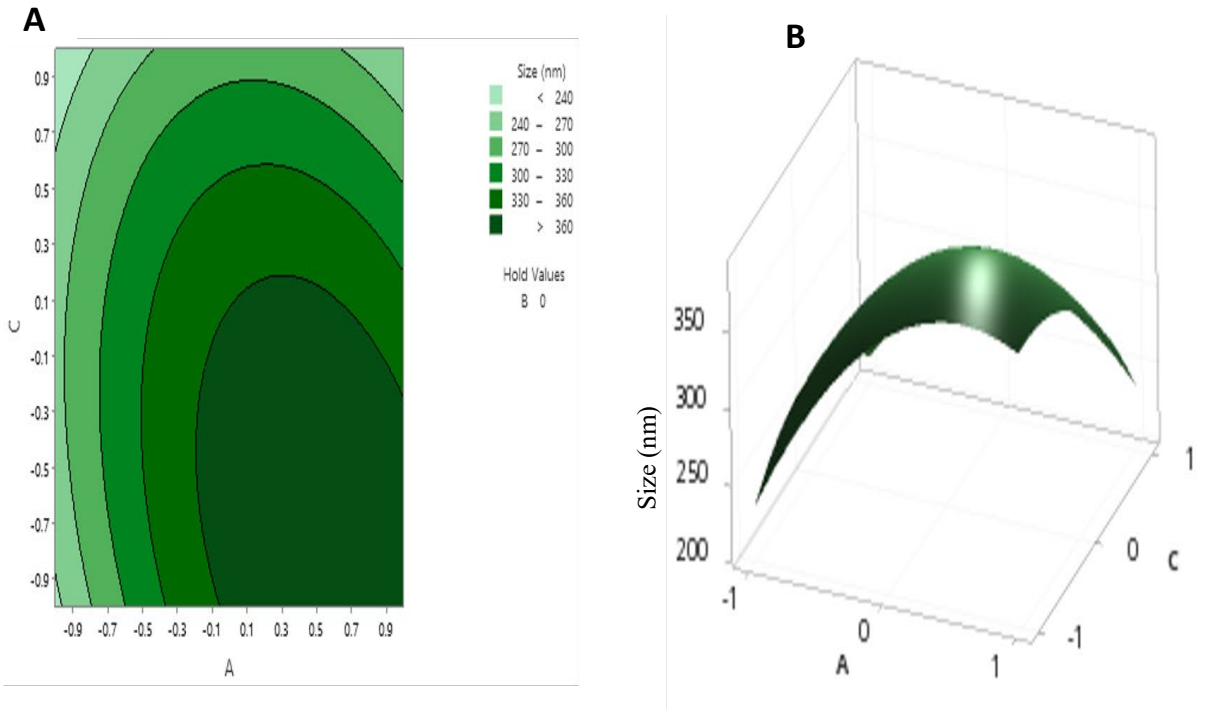


Figure 4.3. Contour plot (A) and Surface plot (B) showing the effect of polymer amount (A) and surfactant concentration (C) on the size of the NPs.

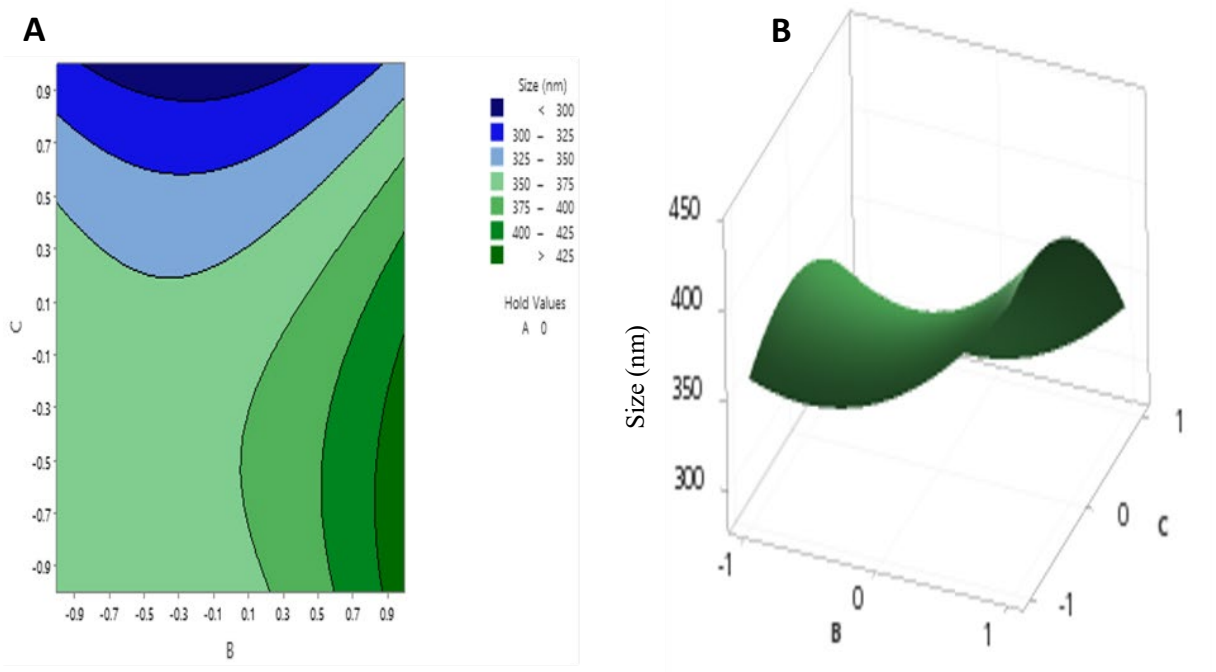


Figure 4.4. Contour plot and (A) Surface plot (B) showing the effect of drug amount (B) and surfactant concentration (C) on the size of the NPs.

The highest significant effect was shown to be the amount of polymer with contribution of 23.30 %.

4.3.3 BBD Predicted Model and Best Fit Regression Coefficient for Zeta Potential

Combination of the independent variables (X1, X2 and X3) at different levels from low to high resulted in different zeta potential responses which were fitted *via* multiple regression to yield a model of polynomial equation:

Zeta Potential (mV) = -26.205 - 4.196 A - 2.429 B + 2.550 C - 3.133 A*A + 1.717 B*C. Equation (14)

R^2 for equation 14 was found to be 0.90 with adjusted R^2 of 0.85 and a non-significant lack of fit (0.35). The ANOVA represents a significant model for describing the charge of the NPs expressed in Prob > F value of 0.000.

The zeta potential of the NPs for the different formulations ranged from -21.93 ± 0.55 to -36.70 ± 0.79 mV. The model depicts that the charge of the NPs is significantly impacted by the amount of polymer which had an antagonistic effect on the charge. The drug also exhibited an antagonistic effect on the charge. The concentration of the surfactant had a significantly positive effect on the charge. The amount of polymer squared was significantly antagonistic on the charge as shown in table 4.6. The theoretical and experimental values are presented in table 4.7.

Table 4.6. Summary of regression coefficient analysis for the response Y2 (Zeta potential).

Coefficient	β0	β1	β2	β3	β4	β5
Zeta Potential (mV)	-26.20	-4.19	-2.42	2.55	-3.13	1.71
P value	0.000	0.000	0.005	0.004	0.010	0.098

Table 4.7. Experimental and theoretical values with residuals of the response Y2.

Formulation No.	Experimental (observed) value of Charge	Theoretical (predicted) value of Charge	Residuals	%Error
1	-22.53	-22.71	0.18	-0.80
2	-32.50	-31.10	-1.40	4.29
3	-25.50	-27.57	2.07	-8.12
4	-36.70	-35.96	-0.74	2.01
5	-26.77	-27.69	0.92	-3.46
6	-35.30	-36.08	0.78	-2.22
7	-25.77	-22.59	-3.18	12.32
8	-29.63	-30.98	1.35	-4.56
9	-25.37	-24.61	-0.76	2.99
10	-34.93	-32.90	-2.03	5.82
11	-21.93	-22.94	1.01	-4.60
12	-24.63	-24.37	-0.27	1.08
13	-27.07	-26.20	-0.86	3.18
14	-24.97	-26.20	1.24	-4.96
15	-24.53	-26.20	1.67	-6.81

Table 4.8. Analysis of variance, DF, SS, MS and F-Value for the charge of the NPs.

Regression	Df	SS	MS	F value	P value
Charge	5	288.49	57.69	16.72	0.000

The standardized effect of the independent variables and their interaction on the response is presented *via* the Pareto Chart (Figure 4.5) which ranks the effect of the variables on the outcome. The most significant factors are shown to be A, C, B and A^2 as presented in table 4.6 by their corresponding coefficients.

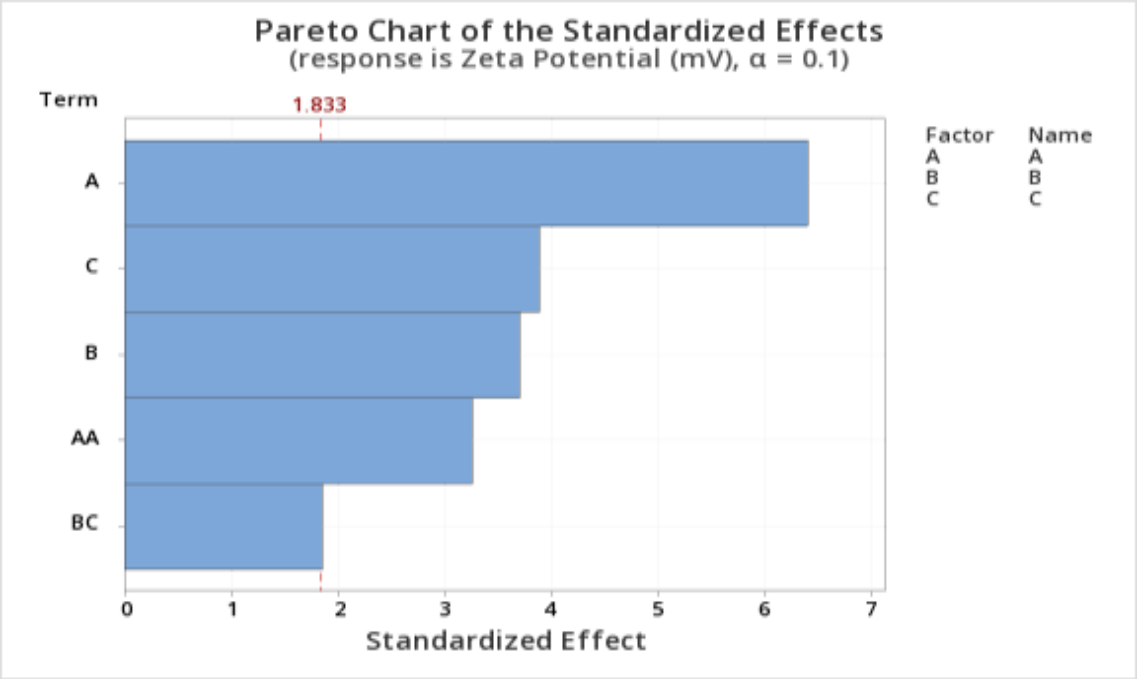


Figure 4.5. Pareto chart expressing standardized effect of independent variables and their interaction on the charge of the NPs.

The relationship between the independent and dependent variables was further highlighted by plotting surface and contour plots as expressed in figures 4.6, 4.7 and 4.8. The contour and quadratic 3D plots in figure 4.6 and 4.7 present a non-significant effect of the interaction between A and B, and A and C respectively. While figure 4.8 presents an elliptical contour plot and a twisted surface plot showing a significant effect on surface charge due to the interaction between B and C variables with highest negative charge achieved at B level of 0.8 to 1 and C level of -0.8 to -1.

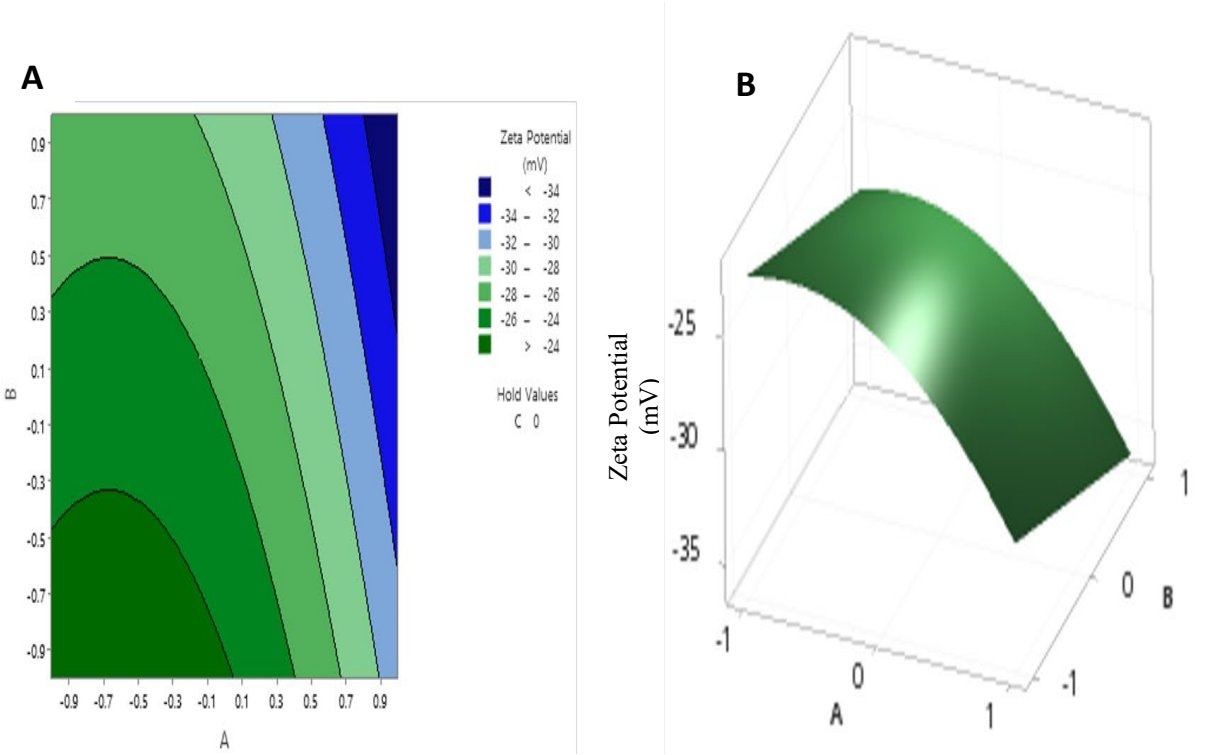


Figure 4.6. Contour plot (A) and Surface plot (B) showing the effect of polymer amount (A) and drug amount (B) on the charge of the NPs.

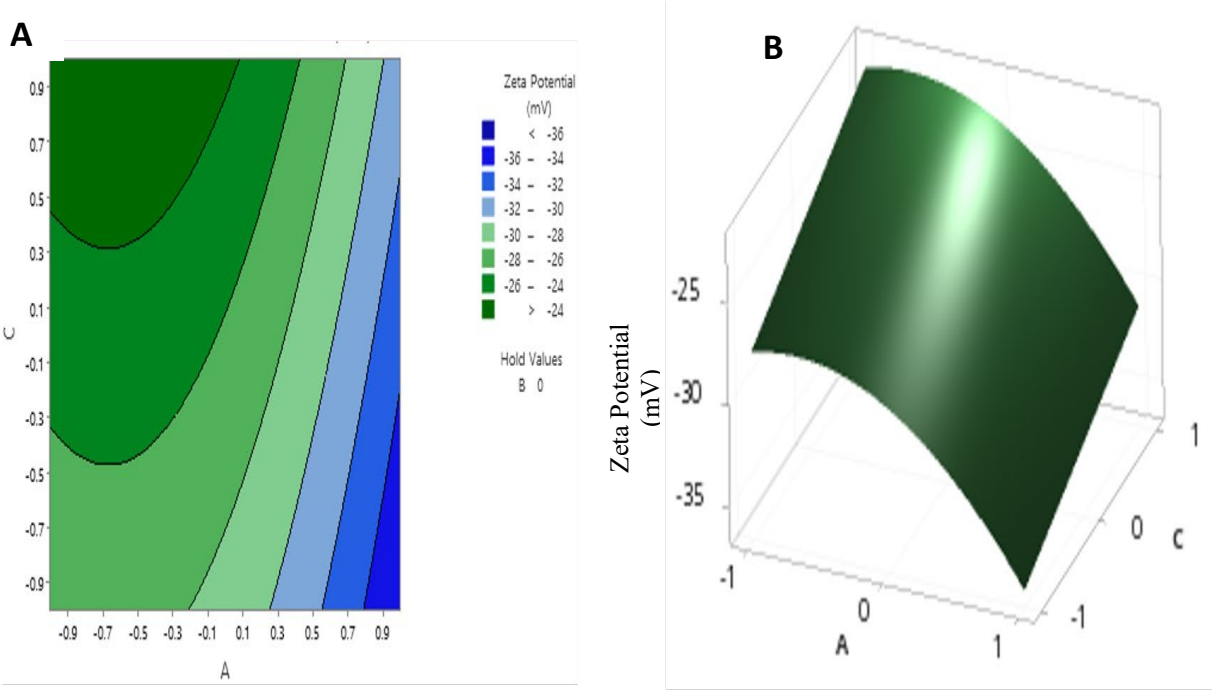


Figure 4.7. Contour plot (A) and Surface plot (B) showing the effect of polymer amount (A) and surfactant concentration (C) on the charge of the NPs

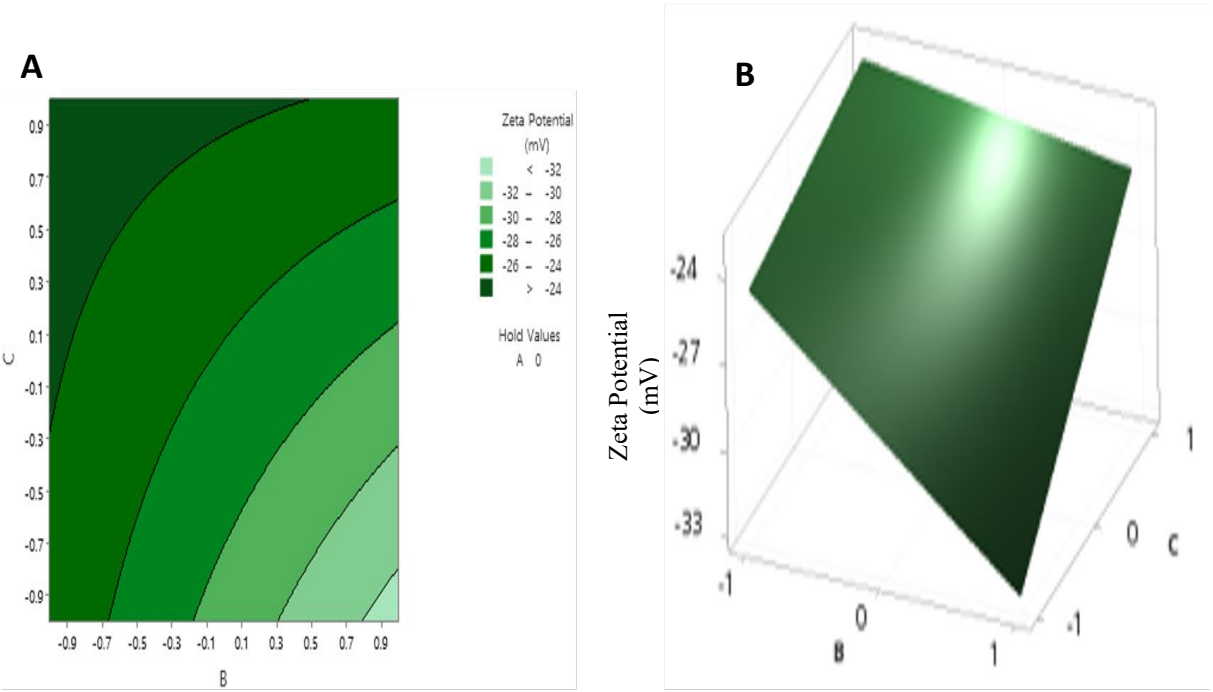


Figure 4.8. Contour plot and (A) Surface plot (B) showing the effect of drug amount (B) and surfactant concentration (C) on the charge of the NPs

The highest significant effect was shown to be the polymer amount with 48.81% contribution.

4.3.4 BBD Predicted Model and Best Fit Regression Coefficient for EE%

The EE% (Y3) (dependent variable) obtained at 3 different independent variables (A, B and C) was subjected to multiple regression to fit the response with the experimental data and produce a model of second order polynomial equation:

$$EE\% = 56.72 + 2.771\,A + 3.180\,B + 3.029\,C + 3.53\,A^*A + 3.69\,B^*B - 3.40\,A^*C + 3.19\,B^*C \quad \text{Equation (15)}$$

R^2 for equation 15 was 0.92 and adjusted R^2 was 0.85 with a non-significant lack of fit (0.62). The ANOVA represents a significant model for describing the EE% of the NPs expressed in Prob > F value of 0.002.

The EE% of the NPs for the different formulations ranged from 49.76% ± 0.19 to 70.01% ± 0.18. The variables that had a synergistic effect on EE were the amount of polymer, amount of drug, concentration of surfactant, amount of polymer squared, amount of drug squared and the interaction between the drug and surfactant. Whereas, the interaction between the polymer and surfactant had an antagonistic significant effect on the EE% (Table 4.9).

The significance values for all contributing factors are provided in table 4.9. The theoretical and experimental values are provided in table 4.10.

Table 4.9. Summary of regression coefficient analysis for the response Y3 (EE%).

Coefficient	β_0	β_1	β_2	β_3	β_4	β_5	β_8	β_9
EE%	56.72	2.77	3.18	3.02	3.53	3.69	-3.40	3.19
P value	0.000	0.007	0.004	0.005	0.014	0.011	0.014	0.018

Table 4.10. Experimental and theoretical values with residuals of the response Y3.

Formulation No.	Experimental (observed) value of EE%	Theoretical (predicted) value of EE%	Residuals	%Error
1	58.48	57.99	0.49	0.84
2	60.96	63.53	-2.57	-4.22
3	66.25	64.35	1.90	2.87
4	70.01	69.89	0.12	0.17
5	49.76	51.06	-1.30	-2.61
6	64.52	63.39	1.13	1.74
7	62.82	63.91	-1.09	-1.74
8	63.99	62.66	1.33	2.08
9	58.54	57.39	1.15	1.96
10	56.46	57.36	-0.90	-1.60
11	58.00	57.06	0.94	1.62

12	68.70	69.81	-1.11	-1.62
13	55.56	56.72	-1.16	-2.09
14	59.27	56.72	2.55	4.30
15	55.26	56.72	-1.46	-2.64

Table 4.11. Analysis of variance, DF, SS, MS and F-Value for the EE% of the NPs.

Regression	Df	SS	MS	F value	P value
EE%	7	393.19	56.17	12.84	0.002

The standardized effect of the independent variables and their interaction on the response is presented *via* the Pareto Chart showing that B, C and A are the highest significant factors that impacted the EE (Figure 4.9).

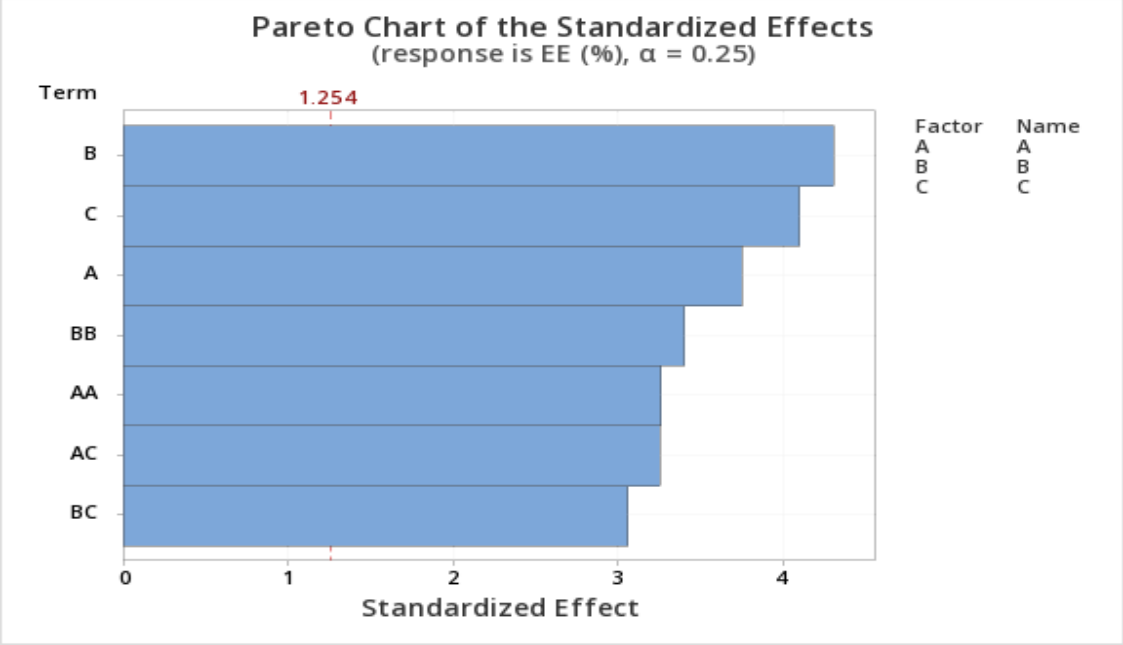


Figure 4.9. Pareto chart expressing standardized effect of independent variables and their interaction on the EE% of the NPs.

The relationship between the independent and dependent variables was further highlighted by plotting surface and contour plots (Figure 4.10, 4.11 and 4.12).

It was determined from the contour and surface plots that an EE higher than 62% could be obtained with an A range from 0.9 to 1 level and C range from -1 to 1 level (Figure

4.11). Figure 4.12 also presented a significant interaction effect of B and C. The optimum range of B was from 0.8 to 1 and that of C was from -0.7 to -1. Whereas there was no significant effect for the interaction between A and B as shown in figure 4.10. The highest significant effect on EE was shown to be the drug amount with the highest percent of contribution of 20.50%.

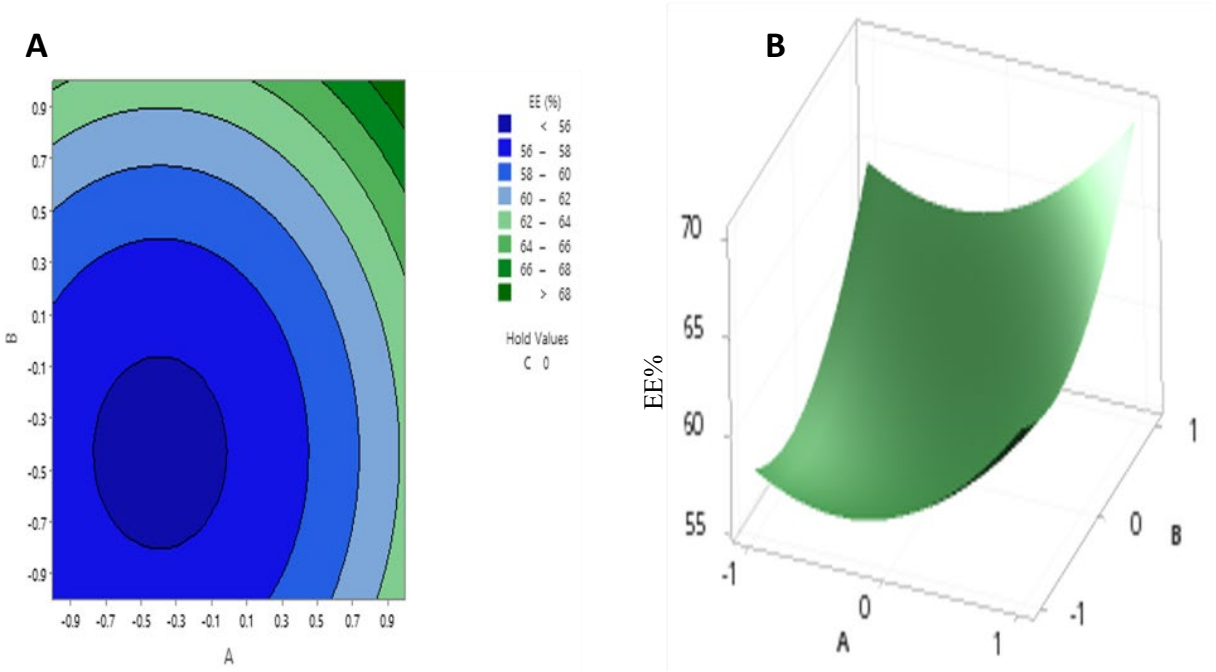


Figure 4.10. Contour plot and (A) Surface plot (B) showing the effect of polymer amount (A) and drug amount (B) on the EE% of the NPs

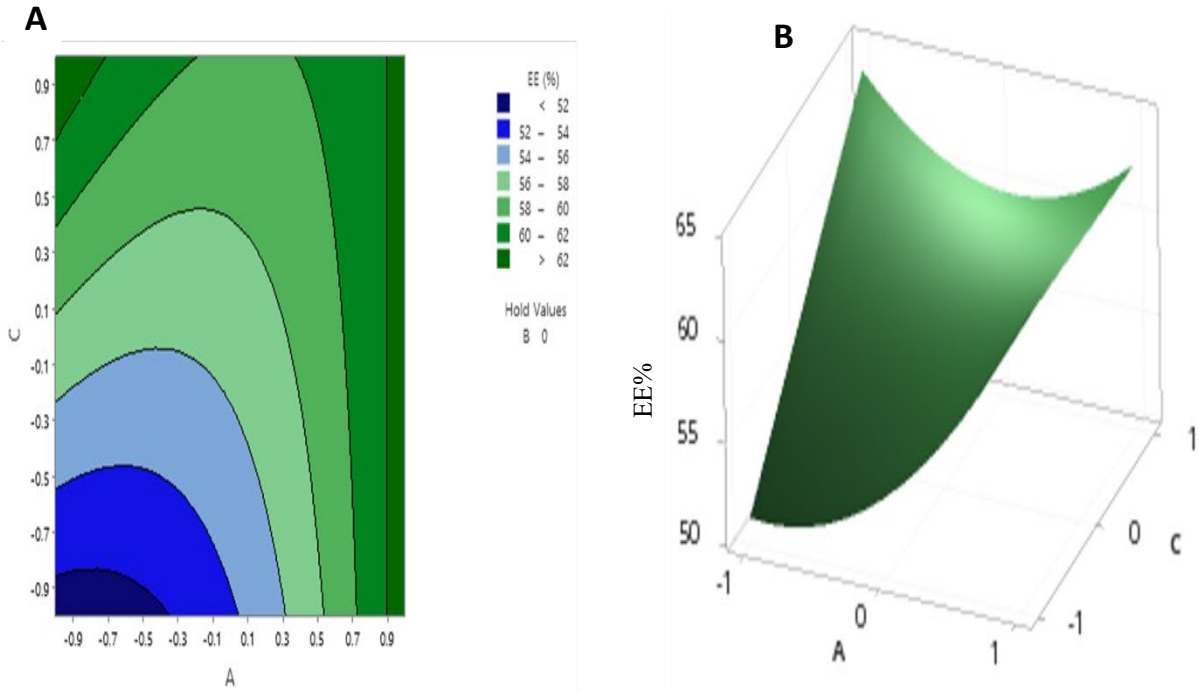


Figure 4.11. Contour plot and (A) Surface plot (B) showing the effect of polymer amount (A) and surfactant concentration (C) on the EE% of the NPs

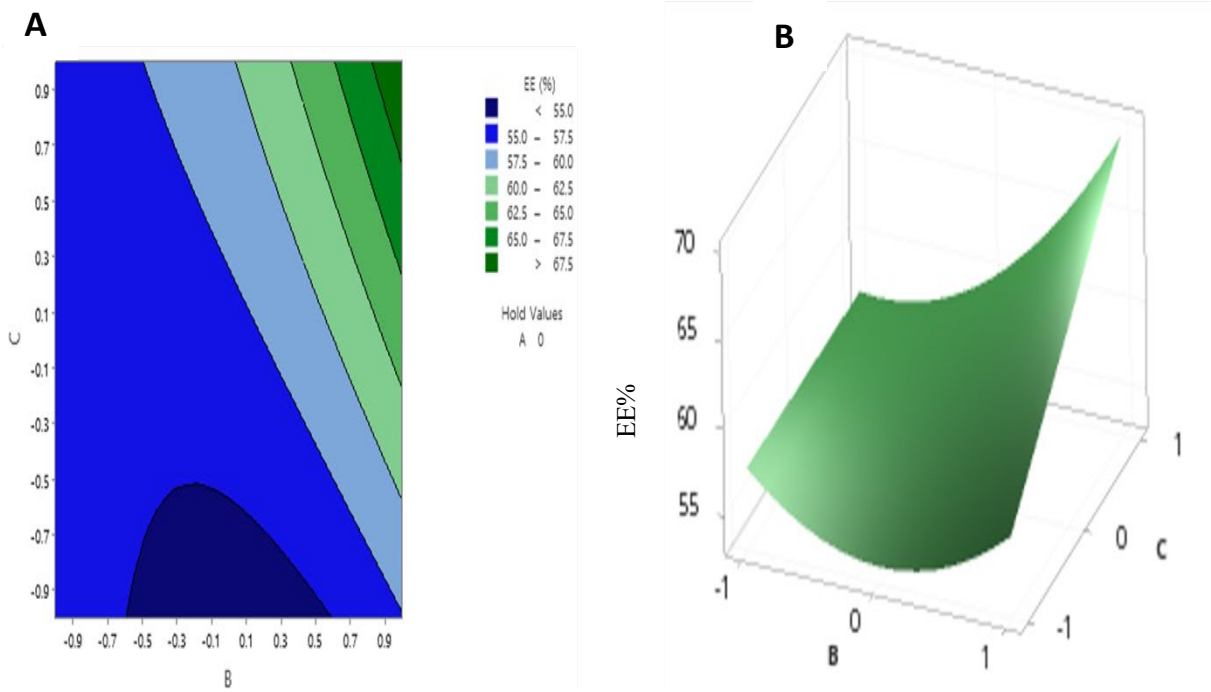


Figure 4.12. Contour plot and (A) Surface plot (B) showing the effect of drug amount (B) and surfactant concentration (C) on the EE% of the NPs

4.4 Discussion

Polymer blends are gaining interest for drug delivery application where the compatibility of the polymers and their interaction with drugs can be used to control drug release, which could be tailored depending on the ratios of polymers in the blend (Marks et al., 2014; Tipduangta et al., 2016).

PCL can form miscible blends with other polymers resulting in improved chemical characteristics as well as the solubility, degradation and crystallinity of the polymer. This could promote the use of PCL as a tailored drug delivery vehicle with improved EE and release profiles (De Jong and Borm, 2008; Mahapatro and Singh, 2011). The ratio of PCL with other polymers can be used to control their compatibility and drug permeability (Woodruff and Hutmacher, 2010). The degradation rate of PCL was enhanced and its hydrophobicity reduced when blended with PLGA and PLA (Abedalwafa et al., 2013).

Our results indicated that using a 50:50 ratio of PCL and PLGA blend produced monodisperse NPs with a higher EE (60.96 ± 6.62) compared to the 25: 75 (59.69 ± 5.01) and 75: 25 (56.85 ± 8.30) blends with an acceptable particle size of 234.26 ± 1.45 nm and charge of -32.50 ± 0.10. These results are in accordance with other research that reported the highest EE with equal ratios of PCL/PLGA. PCL increases the hydrophobicity of the blends helping to achieve higher EE of drugs. However, large particle sizes were reported when increasing the amount of PCL in the blend, which is likely due to certain chain organization and entanglement (Dimchevska et al., 2017a). This corroborates our result of a particle size of 451.10 ± 8.35 with the 75:25 PCL:PLGA ratio.

The goal of this study was to reduce the size and charge while maximizing the EE% of the NP blend. It was found that sizes ranging from 206.03 ± 2.95 to 461.33 ± 36.49 nm, zeta potentials ranging from 21.93 ± 0.55 to -36.70 ± 0.79 mV and EEs% ranging from 49.76% ± 0.19 to 70.01% ± 0.18 could be achieved using 54, 108 and 162 mg of the 50:50 polymer blends as well as different surfactant concentrations (2, 4 and 6%) and drug amounts (3, 6 and 9 mg).

The BBD was conducted using 15 independent runs in random order at 3 different levels (low, medium and high). The polynomial equations, contour plots and 3D plots were used to determine the relationship between the independent variables and response. Multiple regression and ANOVA analyses were performed for the fitted polynomial model. The models were found to be a significant fit for size, charge and EE% responses. 3D surface and 2D contour plots provided a graphical view of the dependent and independent variables.

The smallest size of the NPs was 206.03 ± 2.95 which was achieved by using -1, 0 and 1 levels equivalent to 54 mg, 6 mg and 6% of the polymers, drug and surfactant respectively. The size of the NPs was mostly influenced by the amount of polymers as a result of increased viscosity and chain entanglement induced by the higher concentration of polymers as previously discussed in chapter 3. However, the squared amount of polymers resulted in reduced particle size, while an increased surfactant concentration significantly reduced the size of the NPs due to a reduction in viscosity.

The highest negative charge achieved in this model was -36.70 ± 0.79 mV by using 1, 1 and 0 levels equivalent to 162 mg, 9 mg and 4% of the polymer, drug and surfactant respectively. PCL/PLGA blended NPs had higher negative zeta potential values

compared to PCL NPs as described in chapter 3. This can be attributed to the increased uncapped carboxylic groups of the PLGA leading to a high magnitude of the negative charge (Öcal et al., 2014).

The model depicts that the charge of the NPs was significantly impacted by the amount of polymer and its amount squared which had an antagonistic influence on the charge due to the increase in the carboxylic acid groups from the PLGA and PCL blend. The concentration of the surfactant had a significantly synergistic effect by reducing the magnitude of the negative charge due to the shielding effect of the surfactant on the negatively charged polymers. However, at high concentrations of PVA, some PVA molecules can interact with each other leading to reduced stability of the NPs (Ravi et al., 2015). Moreover, the traces of the PVA on the surface of the NPs can increase the size of the NPs (Ramalho et al., 2019).

The highest EE% in this BBD was found to be 70.01% ± 0.18 achieved with 1, 1 and 0 equivalent to 162 mg, 9 mg and 4% of the polymer, drug and surfactant respectively. It was determined from the contour and surface plots that an EE higher than 62% could be obtained with an A range from 0.9 to 1 level and C range from -1 to 1 level. A similar observation was reported in Chapter 3 for the level of surfactant required to achieve a high EE%.

The model implies that the EE% of the NPs is significantly influenced by the amount of drug which was previously reported in Chapter 3. A significant increase in EE was also noticed upon increasing the amount of blended polymers which is due to an increase in chain entanglement offering a larger matrix for EE. A high concentration of the surfactant also enhanced the EE. The interaction between the drug and surfactant

helped maintain the drug entrapped in the NPs with higher levels as reported in Chapter 3. Whereas, the interaction between the polymer and surfactant negatively impacted the EE. As previously reported, a high concentration of surfactant could lead to the formation of networks between molecules of the surfactant and the chains of the polymers leading to increased viscosity (Parikh et al., 2018). The amount of polymer squared and drug squared also enhanced the EE. In summary, a high level of the polymeric blend as well as a high level of drug achieved the best EE which confirms that the amount of blended polymers was sufficient to entrap a high amount of the drug.

A theoretical optimum condition could be achieved by setting the desired characteristics of minimum particle size and charge with a maximum EE. The optimum factors were predicted to be achieved by using 1 level of A, 0.79 level of B and 1 level of C equivalent to 162 mg, 8.37 mg and 8% respectively which would yield NPs with a size of 283.06 nm, a charge of -31.54 mV and a 70.00% EE.

In conclusion, the particle size, charge and EE of the blend NPs are dependent on the kinetics of the system which involve the behaviour of the polymers and their tendency to form aggregation or chain entanglement. Also, the interaction of the polymers with the surfactant and drug is an influential aspect in this regard. On the contrary, the amount of drug was not influential for the size and charge of NPs but significantly impacted the EE%.

The next chapter will investigate the physicochemical characteristics of F18 (F2 in BBD) blend NPs in terms of their release pattern, thermal profile, crystallinity, stability and morphology.

Chapter 5 PHYSICO-CHEMICAL CHARACTERIZATION OF SELECTED PCL AND PCL-PLGA BLEND NPS

5.1 Introduction

5.1.1 Drug Release from Polymeric NPs

Drug release from polymeric NPs is commonly a three-phase process, starting with the burst release of drug particles bound to the surface of the NPs which is the fastest step (Fredenberg et al., 2011). The second, slower, step involves the diffusion of drug particles, that are further from the surface, through the polymer. The third step involves the erosion and degradation of the polymer along with drug diffusion through the polymer. In matrix materials, drug release by diffusion is controlled by the polymer swelling, osmotic pressure and diffusion distance. Drug diffusion dominates erosion and biodegradation for more crystalline and hydrophobic polymers and depends on several factors such as the interaction between the drug and polymer, pKa of the drug, drug–drug interactions, water absorption and pore formation (Allen et al., 1999; Desai et al., 2010; Kang and Schwendeman, 2007). Different drug stabilities and solubilities also influence release (Fu and Kao, 2010a). Drug release from different systems of NPs vary by their shape, size and charge (Fredenberg et al., 2011). Another influencing factor is the ionic strength, pH, temperature and enzymes (if present) of the release medium.

The crystalline and hydrophobic nature of PCL could lead to the slow release of drugs (Shen et al., 2000). The PCL composition of five CH_2 moieties reduces the rate of its degradation compared to other polymers. This enhances it to be used as a long-term release vehicle (Bhattarai et al., 2006; V. R. Sinha et al., 2004). Degradation of semi-crystalline polymers occurs over two stages; 1. The infusion of water into the amorphous regions with random scission of bonds like the ester bonds and 2. The

degradation of the amorphous regions (Fu and Kao, 2010b). Drug diffusion from PCL depends on the distribution of the drug within the PCL matrix. Drug molecules covering the surface of the polymeric NPs tend to release faster than those immersed within the core of the NPs (Berkland et al., 2004; Pollauf and Pack, 2006; Shi et al., 2003). PCL has the advantages of being biocompatible and biodegradable with a high permeability for drugs, therefore tackling its hydrophobicity by blending it with more hydrophilic polymers could enhance its mechanical properties and improve its application in drug delivery (Balmayor et al., 2009; Sah et al., 1995; Seremeta et al., 2013). The advantage of using a hydrophilic polymer is enhanced release and faster degradation compared to using a hydrophobic polymer alone (Yuan et al., 2018). This property can be used to maintain a balance in drug release and can be tailored by managing the ratios of the different polymers according to the desired application. PLGA is an amorphous polymer with a faster degradation rate than PCL (Makadia and Siegel, 2011). Drug release from PLGA NPs follows the typical tri-phasic release associated with biodegradable polymers, beginning with drug diffusion as the initial stage, then polymer erosion followed by degradation stages (Blasi et al., 2005). In PLGA, pore formation occurs over time as the polymer is hydrated. This leads to the motion of the polymer chains by swelling and the pores formed allow the drug to traverse to the external media (Blasi et al., 2005). Degradation of the polymer occurs as soon as it absorbs water, leading to the hydrolysis of the ester bond and production of lactic and glycolic acid. These acidic by-products catalyse further hydrolysis of the polymer which is an autocatalytic process influenced by the concentration of the by-products (Fredenberg et al., 2011). As the hydration increases, bulk erosion increases and pores increase until full degradation of the polymer. The flexibility of the polymeric

chains leads the small pores to join together to form larger pores. This flexibility is dependent on the Tg of the polymer and its glasslike state. A higher glass-like state means slower hydration and hydrolysis (Blasi et al., 2005). Some polymers experience a slow and delayed second phase release due to factors such as blockage of the pores of the polymer or an interaction between the drug and polymer hindering the release, whereas a rapid third phase release for some polymers suggests an enhanced erosion or scissions in the polymeric matrix (Fredenberg et al., 2011). Several other factors govern drug release from PLGA NPs such as the molecular weight of the PLGA (50 to 150 kDa), the lactic acid (L) and glycolic acid (G) ratios and the end capping group. Other influencing factors include the pH and osmolarity of the release media; formulation excipients; physicochemical properties of the drug; presence of salts that affect the osmolarity force; size and shape of the NPs; the density and porosity of the system. A hydrophilic PLGA polymer is characterized by being uncapped with functional groups and by its low MW and low L:G ratio which helps enhance hydration, hydrolysis and erosion. Temperature is also a factor affecting the flexibility of the polymeric chains particularly at higher temperatures. However, in a biological environment, the conditions are different and other factors get involved in controlling the release mechanism such as the immunogenic response and the presence of esterase enzymes that catalyse the hydrolysis of the ester groups (Blasi et al., 2005; Pearson et al., 2014).

Differential scanning calorimetry (DSC) and X-ray diffraction (XRD) are informative techniques for analysing the molecular properties and possible interactions between drugs and polymers which could influence its release (Jeong et al., 2003; Zhang et al., 2007).

5.1.2 Thermal Analysis by DSC

DSC analyses the thermal characteristics of polymers by comparing the amount of heat required to increase the temperature of the sample and that of an empty reference pan. Then, a thermogram is plotted expressing the heat flux against temperature (Sindhu et al., 2015). Alteration in the physical properties of the sample is then monitored as a function of temperature by observing the endothermic and exothermic peaks which represent the amount of heat absorbed or released (Gill et al., 2010). Those peaks are representative of any interaction between the NP excipients or change in their crystalline and amorphous states (Ceschel et al., 2003). Among the applications of the DSC is measuring the melting temperature (Tm) and Tg of materials (Abraham et al., 2018). In solid states, polymers are rigid and have little energy to move their chains. Upon heating, they gain energy that renders them flexible and in a melted viscous state, whereas cooling removes the energy from the chains and the polymers become rigid. Amorphous materials exhibit only Tg, whereas semi-crystalline materials exhibit both Tm and Tg. At Tg, 30 to 50 carbon chains in amorphous polymers or amorphous regions of semi-crystalline polymers start moving around, transferring the compound from a rigid state to a more flexible rubbery state and the space between the chains of the molecules enlarges by 2.5 times. Flexible materials have low Tg whereas rigid materials have high Tg. Tg helps identify the transfer of state of materials (Nicholson, 2006). The Tm is a characteristic of the fluidity of the crystalline portions of polymers. Semi-crystalline polymers are soft above Tg but they are not in a fluid state unless they pass through their melting point. The temperature range between the Tg and Tm is known as the rubbery state temperature. In summary, above Tg the amorphous regions lose their integrity and the crystalline regions stay

stable until their Tm is achieved (Shrivastava, 2018). Materials with crystalline properties are characterized by regular arrangements of their molecular chains and exhibit sharp melting points. Crystallinity impacts the melting point of the polymers but no polymers have 100% crystallinity, some amorphous phases should also exist (Ebewele et al., 2000). On the contrary, amorphous polymers are irregular in the structure of their molecular chains that are randomly organized and they do not exhibit a sharp melting point. Whereas, semi-crystalline polymers share the properties of both the crystalline and amorphous polymers, where they exhibit Tm that represents the crystalline fractions and Tg that characterizes the amorphous portions of the polymer (Shrivastava, 2018). PCL as a semi-crystalline polymer exhibits a melting point of 58–64°C and Tg of –60°C (Douglas et al., 2016).

5.1.3 Crystallinity Analysis by XRD

XRD is an informative tool about the crystallinity of materials since the wavelength of the X-ray is in the range of 0.2 and 10 nm which is similar to the spaces between atoms of crystalline structures. This technique measures the average spaces between atoms organized in rows or layers (Salame et al., 2018). Diffraction of the X-ray happens when an interaction occurs between the photons and electrons of the material. Crystalline materials exhibit sharp peaks at certain scattering angles whereas amorphous materials have maximum intensity extending over several degrees (2θ) (Lamas *et al.*, 2017). The diffraction of the X-rays for crystalline materials is described by Bragg's law which correlates the wavelength of X-rays to the spaces between atoms represented by the following formula: $n\lambda=2d\sin\theta$. The distance between neighbouring planes is denoted by d, the incident ray angle is represented by θ, λ is the x-ray

wavelength and n is the wavelength between rays scattered by the coherent atomic planes (Salame et al., 2018).

This chapter aims to investigate the characteristics of the PCL and PCL-PLGA blend NPs, mainly their drug release, thermal properties, crystallinity, stability, and morphology.

5.2 Materials and Methods

5.2.1 Materials

Materials used in this chapter were the same as chapter 2, section 2.2.1.

5.2.2 *In Vitro* Drug Release

25 mg of each of the IRH-loaded PCL NPs (F2, F3, F4, F10, F12 and F15) and PCL-PLGA blend (F18) NPs, described in table 5.1, were dispersed in 25 mL of PBS (pH 7.4) release media and stirred at 200 rpm at 37 °C. 0.5 mL samples were removed at 0, 1, 3, 5, 7, 9, 14 and 16 days and replaced with fresh media. The samples were centrifuged and the supernatant analysed for their IRH content using HPLC. The percentage of cumulative drug release was determined as mean (n = 3) ± SD using the following equation:

Cumulative drug release (%) = $\frac{RELEASED\ IRH}{Total\ IRH}$ X 100. Equation (16)

Table 5.1. PCL, PLGA, IRH and PVA content of selected formulations

Formulation	PCL (mg)	PLGA (mg)	IRH (mg)	PVA (%)
F2	162	-	3	4
F3	54	-	9	4
F4	162	-	9	4
F10	108	-	9	2
F12	108	-	9	6
F15	108	-	6	4
F18	81	81	3	4

5.2.3 DSC

The thermal profile of the polymers, IRH, NP formulations and physical mixture of all the excipients were investigated using a Discovery DSC-25 (TA instruments Q200 DSC, Newcastle, UK). Approximately 2 mg of sample was heated to 300°C in a sealed aluminium pan at a rate of 15 °C/min under nitrogen at a flow rate of 50 mL/min. The polymeric blend NPs were subjected to a cooling cycle to -85°C, isothermal for 1 minute then heated to 300°C as above.

5.2.4 XRD

The molecular arrangements of the drug loaded NPs were analysed using an X-ray diffractometer (Rigaku Miniflex, Tokyo, Japan). The data was collected over an angular range from 3° to 90° in a continuous mode using a step size of 0.02° and step time of 10° per minute with 40 kv voltage and 15 mA current using Cu Kα radiation. The spin speed was 10 rpm.

5.2.5 Stability of NPs

25 mg of the IRH-loaded NPs was dispersed in 25 mL release media of either of PBS (pH 7.4), dH_2O (pH3), dH_2O (pH 5.9), tissue culture media (as described in chapter 2, section 2.2.12.) and stirred at 200 rpm at 37°C. Then, 0.5 mL samples were removed at 0, 1, 3, and 5 days to measure the size, PDI and surface charge. Then, the 0.5 mL was returned back to the solution.

5.2.6 Imaging of NPs

5.2.6.1 TEM Imaging

Images of PCL and PCL-PLGA blend NPs were acquired as described in chapter 2, section 2.2.7.

5.2.6.2 Scanning Electron Microscope (SEM) Imaging

A drop of the sample suspended in dH_2O was placed on a poly-lysine coated glass slide and allowed to dry. The slide was then mounted on a stub and sputter coated with platinum. The coating was 10 nm thick. The samples were then examined in a Philips XL30 field emission gun (FEG) environmental SEM (ESEM) operating in high vacuum mode at 20kV.

5.2.7 Statistical Analysis

The statistical analysis was carried out using GraphPad Prism, version 9. Two-way ANOVA (Analysis of variance) was used for multiple comparisons to determine the effect of incubation time and media on the stability of the NPs. Tukey's post hoc test was carried out in the analysis. The statistical significance was presented as: $p \leq 0.0001$, $p \leq 0.05$. Non-significance was presented for $p > 0.05$. Data were presented as mean (n = 3) ± SD.

5.3 Results

5.3.1 Release of Selected Formulations in PBS

Table 5.1 presents the amounts of the excipients used in the NP formulations. Four different models (zero order, first order, Higuchi and Korsmeyer-peppas) were fitted to the data and presented in table 5.2. The R^2 values for each model and the information about the release mechanism are also presented in the table. Drug release from the PCL and PCL-PLGA blend NPs was in the range of 15.66 ± 0.96 to 69.39 ± 0.58% as shown in Figure 5.1. All of the formulations used in the study exhibited anomalous

transport except F2 which had a high PCL content (162 mg), low drug amount (3 mg) and medium concentration of the surfactant (4%). By blending PLGA with PCL in F18 and using the same formulation parameters as in F2, the release mechanism changed to become anomalous release exhibiting enhanced release of 69.39 ± 0.58 % in 16 days.

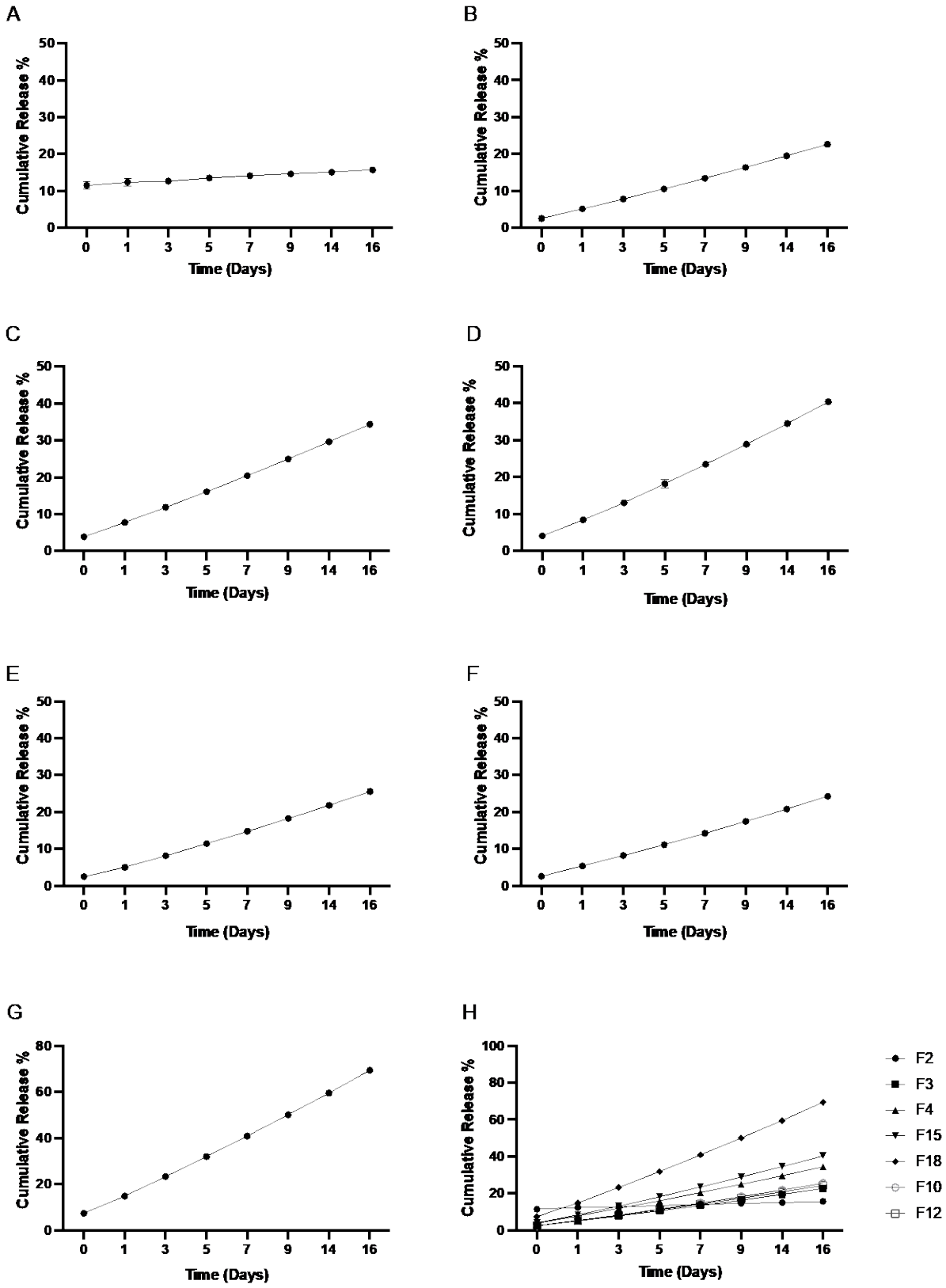


Figure 5.1 Drug release from PCL and PCL-PLGA NPs in PBS: F2 (A) F3 (B) F4 (C) F10 (D) F12 (E) F15 (F) F18 (G) Overlay (H) (n=3).

Table 5.2. Release models and mechanisms of selected NP formulations.

Form.	**Zero order** (Cumulative release% vs time)	**First Order** (Log remaining% vs time)	**Higuchi** (Cumulative release% vs square root time)	**Korsmeyer-Peppas** (Fraction of drug released vs time)	**n value**	**Release Mechanism**
-	**R^2**				-	-
F2	0.93	0.93	0.96	0.91	n= 0.08	Fickian Diffusion
F3	0.96	0.97	0.98	0.98	n=0.52	Anomalous Diffusion
F4	0.96	0.97	0.98	0.98	n=0.52	Anomalous Diffusion
F10	0.96	0.97	0.98	0.98	n=0.57	Anomalous Diffusion
F12	0.96	0.97	0.98	0.98	n=0.53	Anomalous Diffusion
F15	0.96	0.97	0.98	0.98	n=0.55	Anomalous Diffusion
F18	0.96	0.98	0.98	0.98	n=0.54	Anomalous Diffusion

Following the release study, F2 and F18 were selected for further characterization, and blank F2 and blank F18 were developed with the same parameters as their drug loaded counterparts. Blank F2 had a size of 246.03 nm, 0.28 PDI and -16.16 mV charge. Blank F18 had a size of 239.20 nm, 0.23 PDI and charge of -26.80 mV.

5.3.2 DSC

5.3.2.1 F2 PCL NPs (Individual Excipients, Physical Mixture and Overlay)

Figures 5.2 to 5.4 represent the DSC thermograms for individual excipients, physical mixtures, blank F2, IRH loaded F2, dual mixes and an overlay. PCL and IRH exhibited melting points of 64.03 °C and 276.66 °C respectively, while the melting points for PVA and sucrose were 217.62 °C and 192.00 °C respectively. In the physical mixture, the melting point of the PCL was not altered indicating no interaction or slight interaction involving PCL with the rest of the excipients. The presence of the sucrose in the physical mixture and its decomposition at 192.00 °C has masked the rest of the peaks; however, the IRH peak could be identified at the same region as in the individual thermogram.

In F2 and blank F2, there was a shift in PCL melting point down to 56.12 and 56.40 °C respectively, indicating both amorphization of the polymer and possible interaction with the drug in F2. Absence of the IRH melting peak confirms that the drug has lost its crystalline structure after being loaded into PCL, which would suggest that the IRH is dissolved in the PCL. The PVA maintained its melting point for both blank F2 and F2 NPs indicating no change in its crystallinity or interaction with the excipients. The dual excipients of F2 were physically mixed to indicate any interactions between each 2 excipients separately. As shown in figure 5.4, each individual component retained its thermal properties indicating no interaction *via* physical mixing or melting in the DSC.

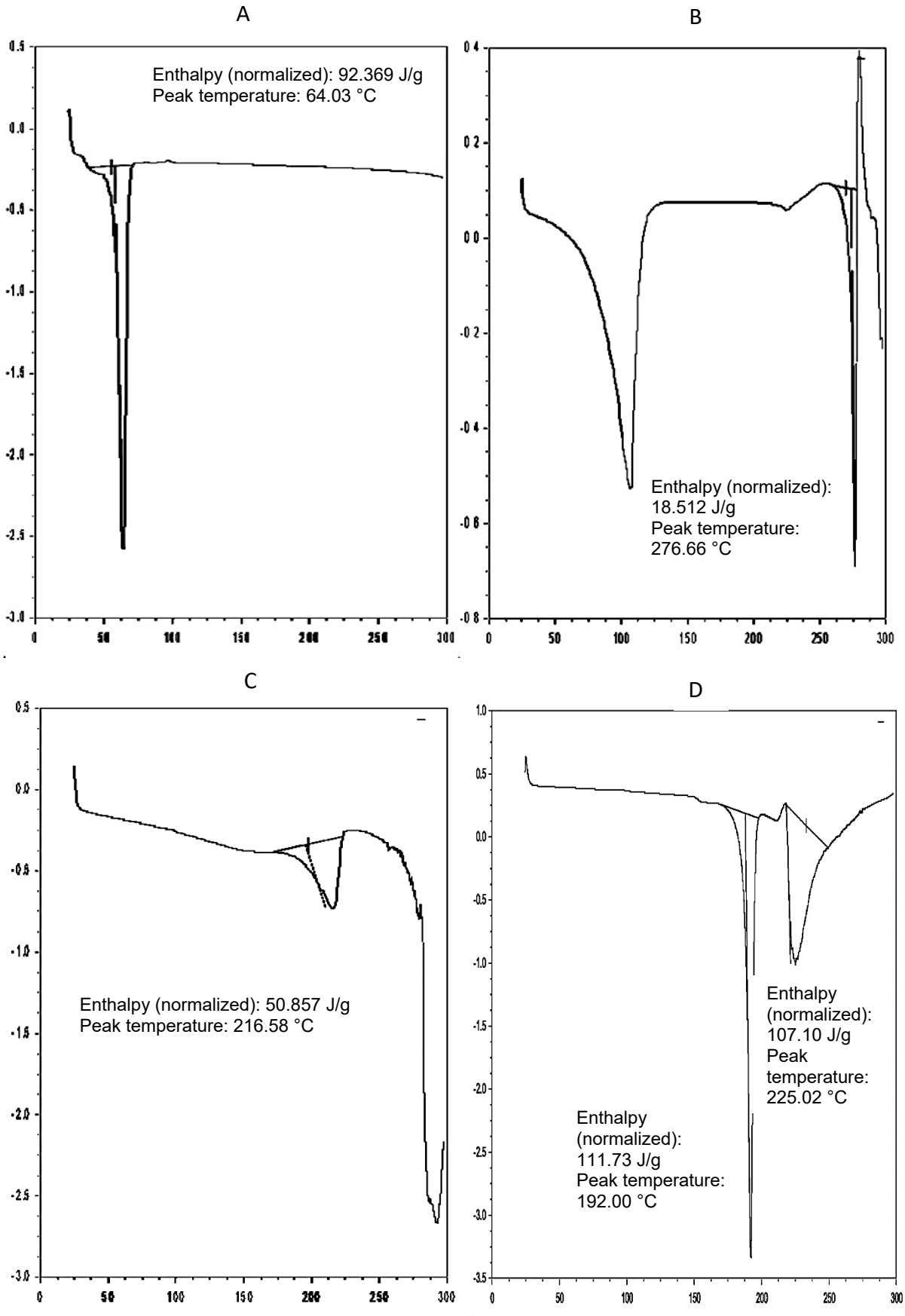


Figure 5.2. DSC of Individual components of F2. PCL (A) IRH (B) PVA (C) Sucrose (D)

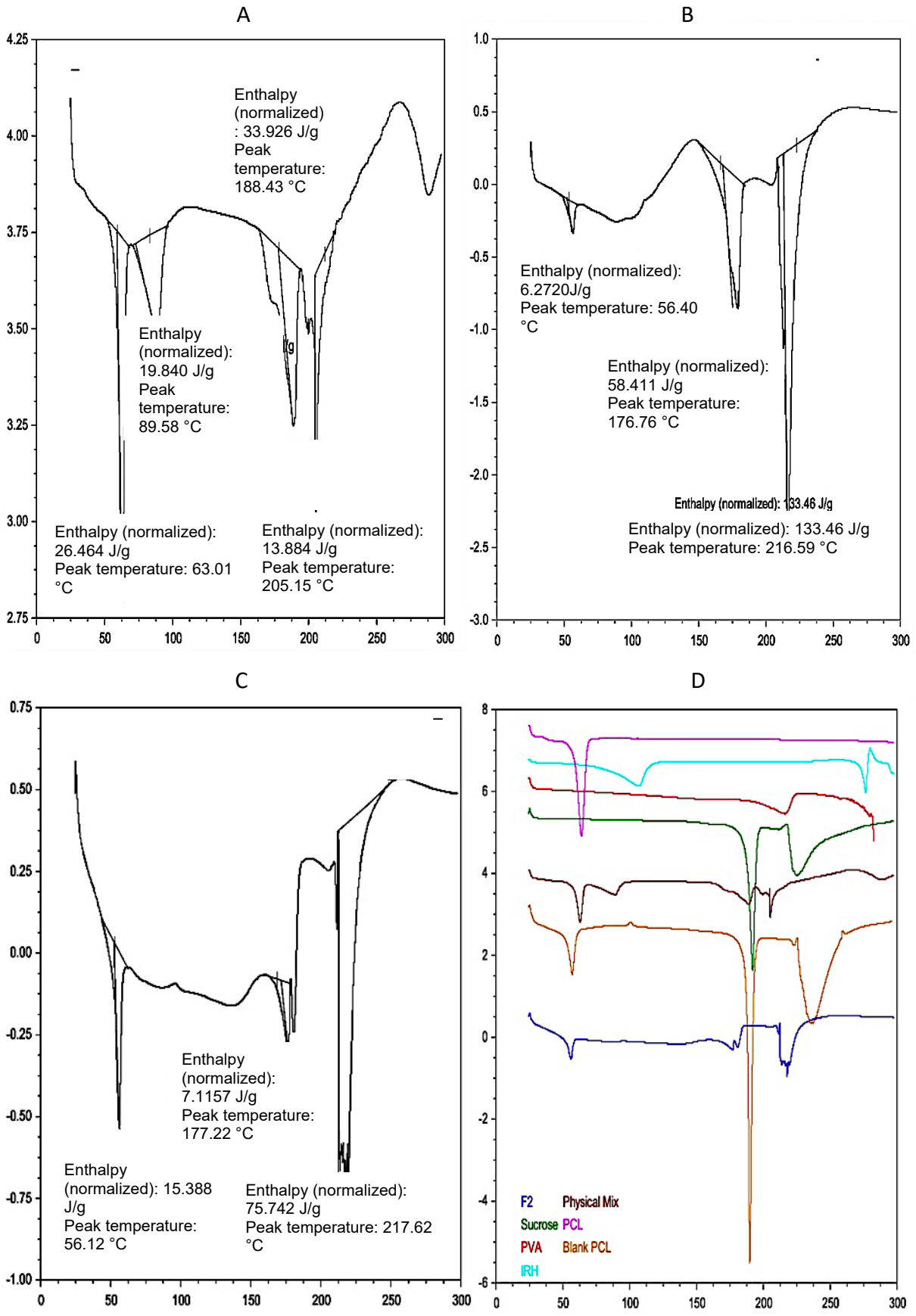
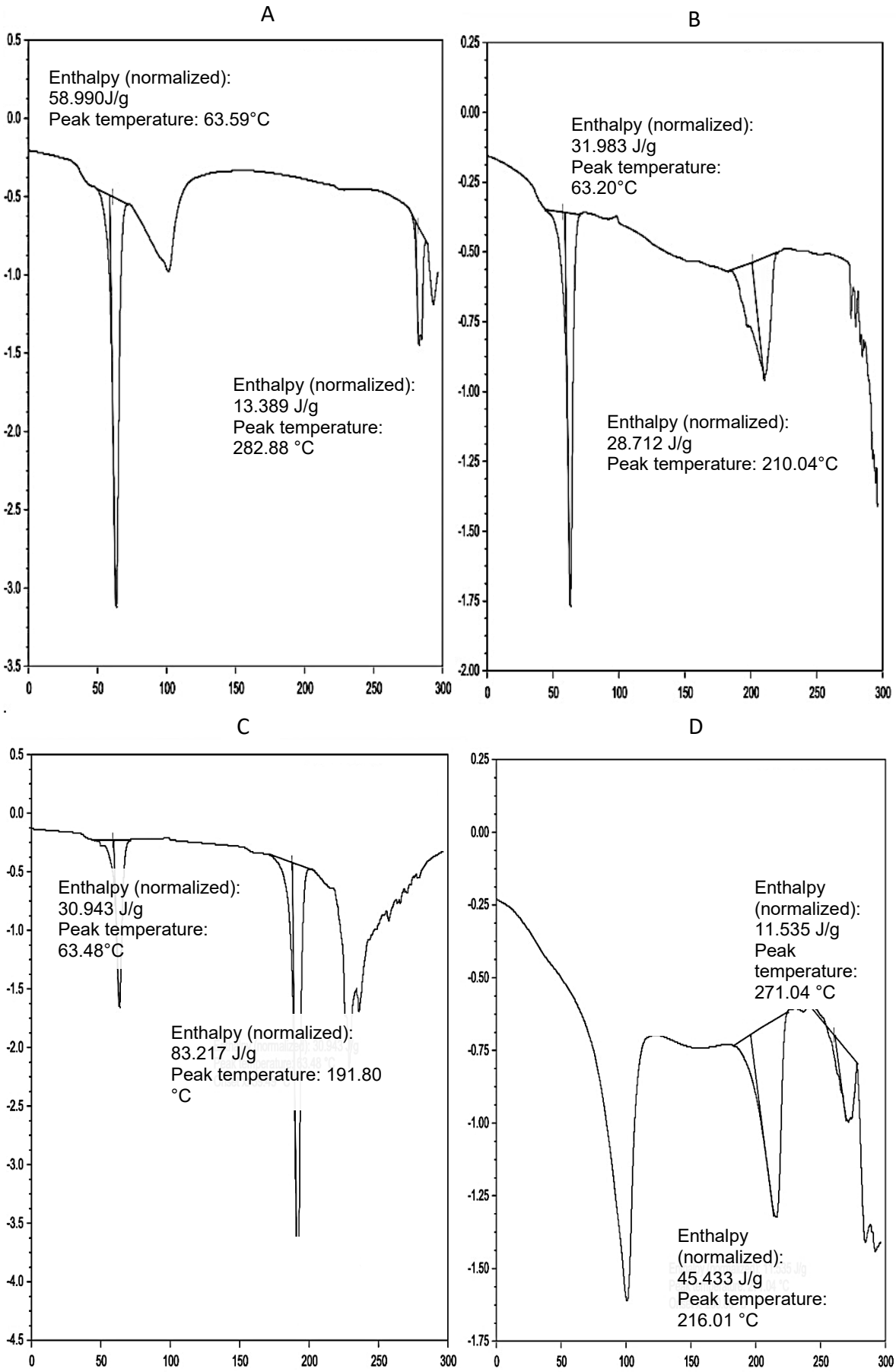


Figure 5.3. DSC of Physical mixture (A) Blank F2 (B) F2 (C) Overlay (D)


A
Enthalpy (normalized):
58.990J/g
Peak temperature: 63.59°C
Enthalpy (normalized):
13.389 J/g
Peak temperature:
282.88 °C
B
Enthalpy (normalized):
31.983 J/g
Peak temperature:
63.20°C
Enthalpy (normalized):
28.712 J/g
Peak temperature: 210.04°C
C
Enthalpy (normalized):
30.943 J/g
Peak temperature:
63.48°C
Enthalpy (normalized):
83.217 J/g
Peak temperature: 191.80
°C
D
Enthalpy
(normalized):
11.535 J/g
Peak
temperature:
271.04 °C
Enthalpy
(normalized):
45.433 J/g
Peak temperature:
216.01 °C

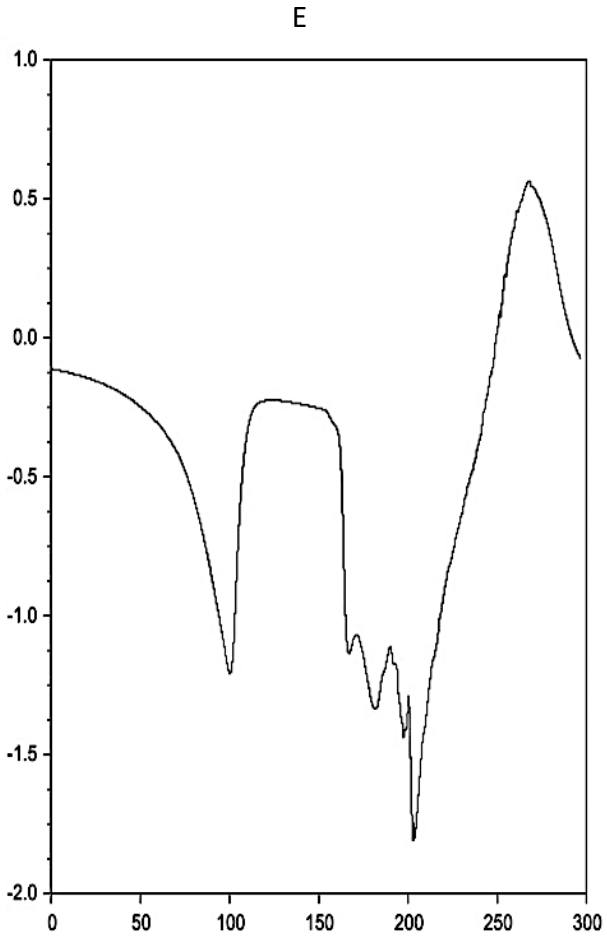


Figure 5.4. DSC of Dual mixes of F2 excipients PCL-IRH (A) PCL-PVA (B) PCL-Sucrose (C) IRH-PVA (D) IRH-Sucrose (E)

5.3.2.2 F18 blend NPs (Individual Excipients, Physical Mixture and Overlay)

Figures 5.5 to 5.9 represent the thermograms for individual excipients, physical mixture, blank F18, IRH loaded F18, dual mixes and an overlay. The thermograms exhibited similar melting points for individual excipients as in F2. Additionally, PCL exhibited a Tg of -63.03 °C, while PLGA exhibited a Tg of 39.03 °C. PLGA002 does not exhibit a Tm since it is an amorphous polymer, however, it does exhibit a Tg. In F18 and its blank, there was a single Tg at 8.43°C and 6.51°C respectively, indicating miscibility of the polymers to form blends. After blending the PLGA with PCL, the melting point of PCL was reduced from 64.03°C to 52.99°C and 53.05°C for both F18 and blank F18 respectively which confirmed the amorphization of PCL by the PLGA. Similar to F2, IRH did not exhibit a Tm suggesting its solubility in the polymer blend and thus loss of its crystallinity. Extra analysis of the individual excipients was followed by comparing each 2 separately as in figures 5.7 and 5.8 which indicated no change in Tg for the physical mixture of the blends.

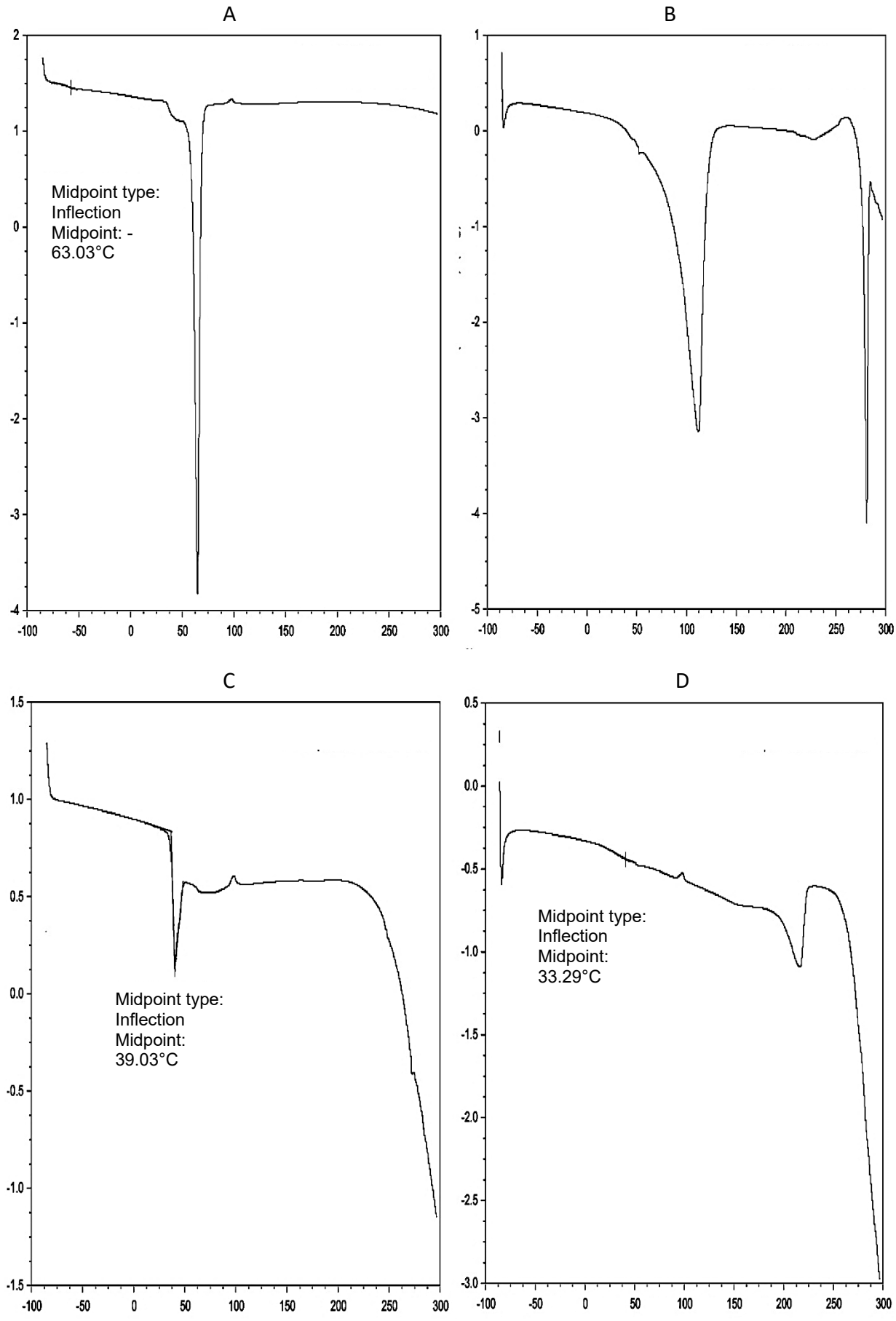


Figure 5.5. DSC of PCL (A) IRH (B) PLGA (C) PVA (D)

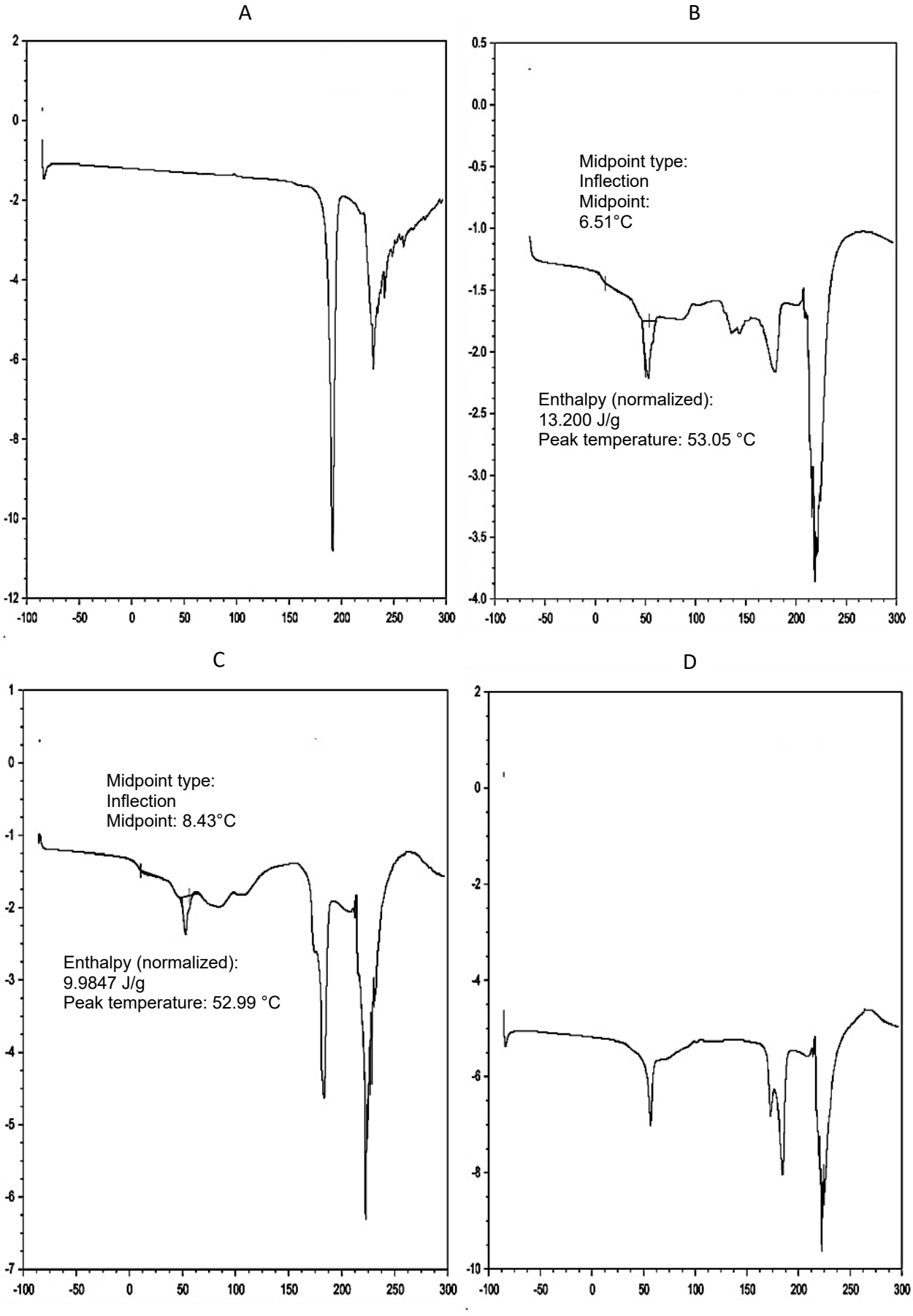


Figure 5.6. DSC of Sucrose (A) F18 blank (B) F18 (C) F2 (D)

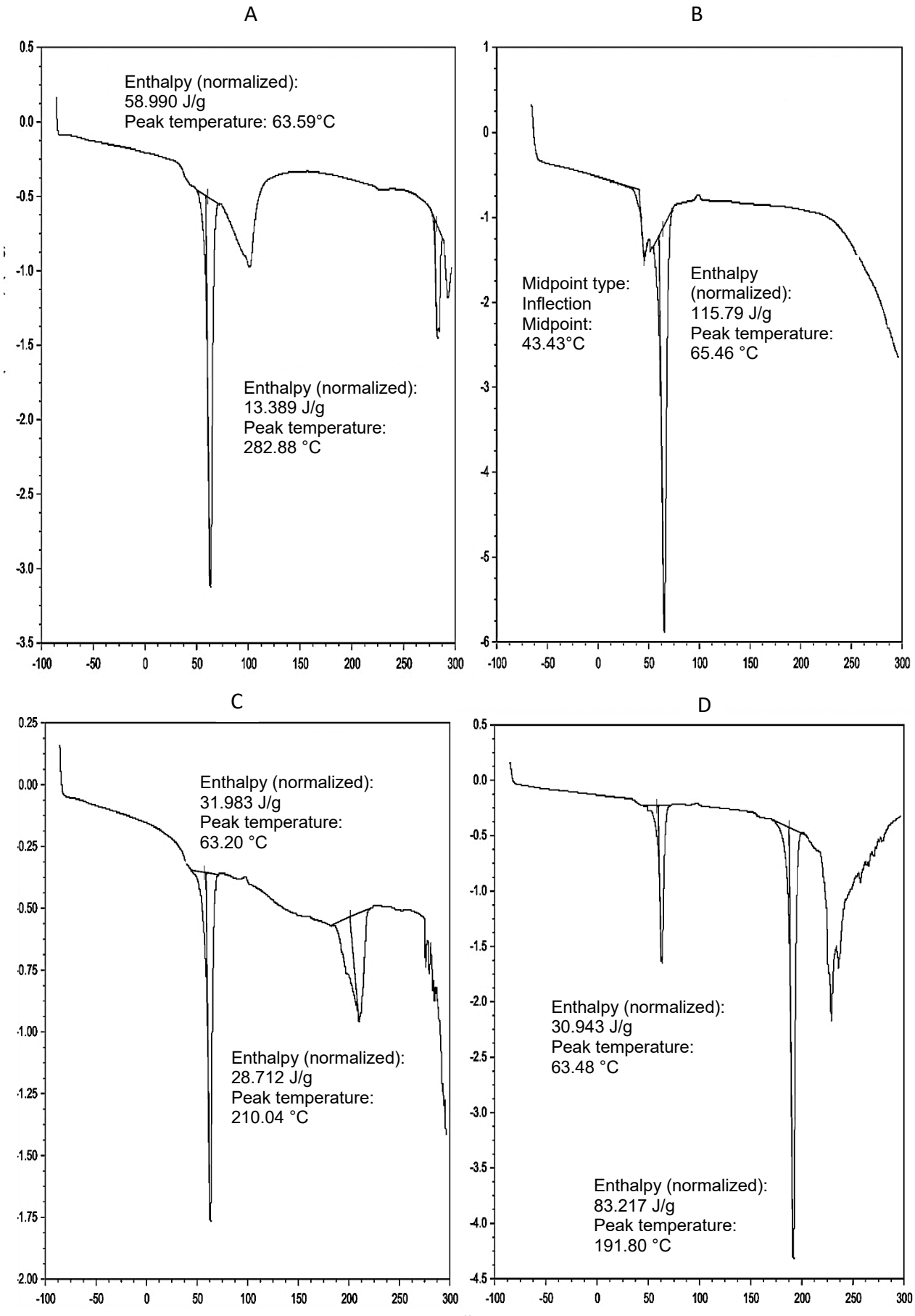


Figure 5.7. DSC of Dual mixes of F18 excipients PCL- IRH (A) PCL-PLGA (B) PCL-PVA (C) PCL-Sucrose (D)

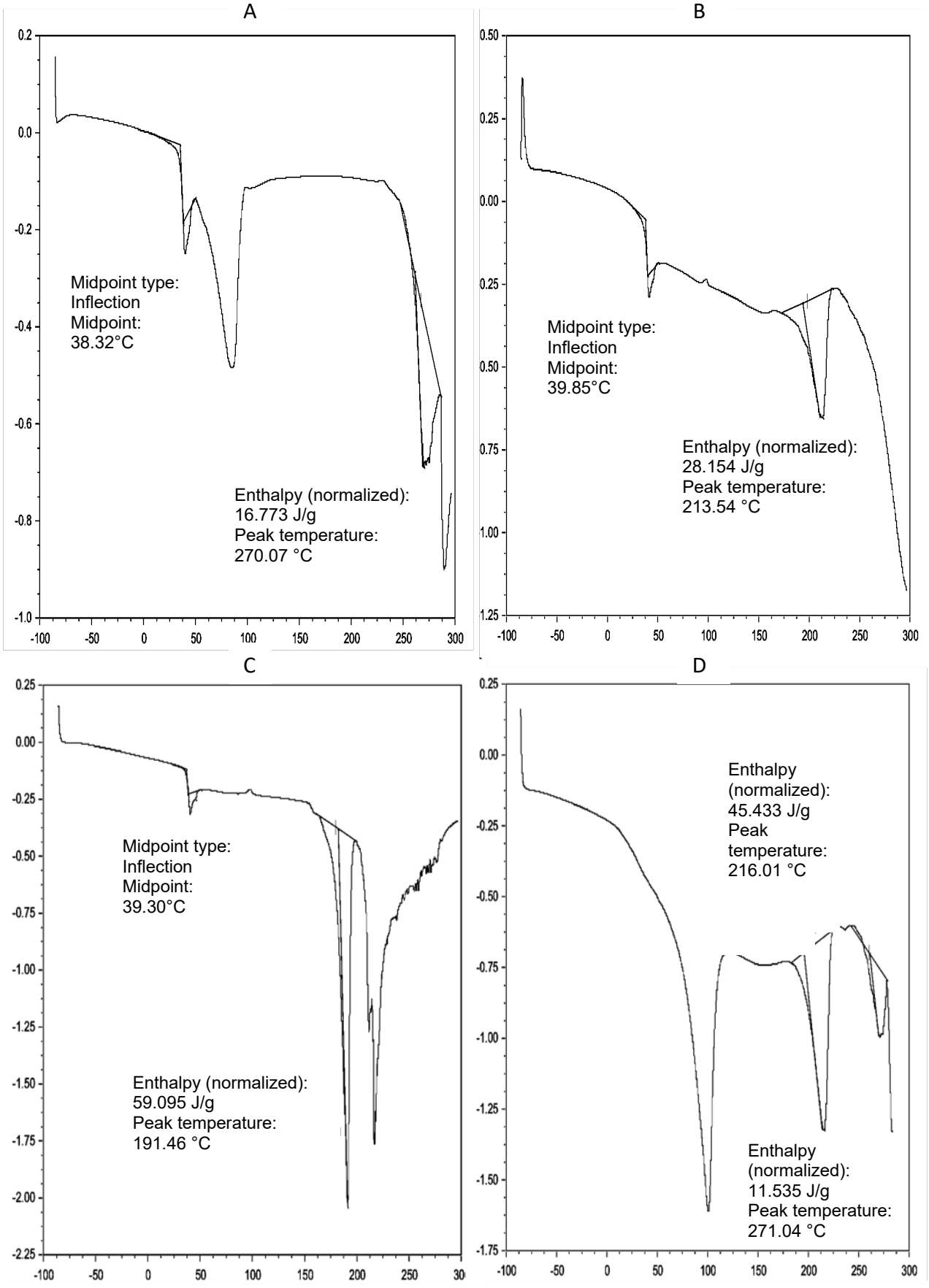


Figure 5.8. DSC of Dual mixes of F18 excipients PLGA- IRH (A) PLGA- PVA (B) PLGA-Sucrose (C) PVA-IRH (D)

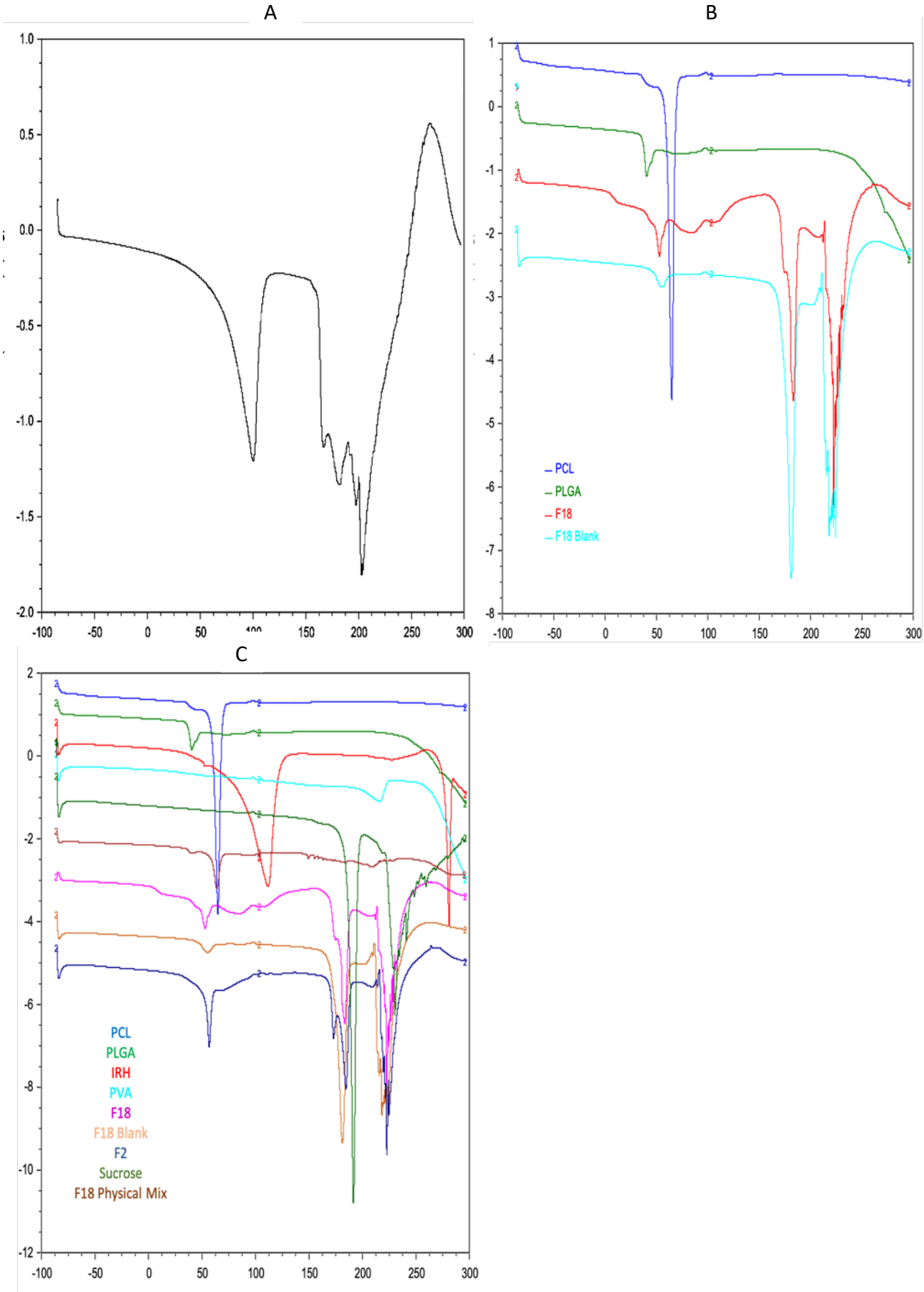


Figure 5.9. DSC of Sucrose-IRH (A) Overlay F18 polymers (B) Overlay F18 (C)

5.3.3 XRD

As shown in the XRD spectra presented in figure 5.10, the pure PCL, IRH, PVA and sucrose exhibited sharp peaks which indicated their crystalline structure. However, the NP formulations F2 and its blank exhibited broad low intensity peak within the 2θ range of 0 to 30 degrees, while the peak characteristics for the IRH has disappeared indicating solubility of the encapsulated IRH within the polymer and subsequent loss of its crystallinity. This phenomenon is favourable for the release and bioavailability of the drug. Also, the broad peak indicated a level of amorphization of the PCL. Some crystalline peaks belong to the PVA present in the formulation. The physical mixture of the formulation components exhibited sharp peaks for each of the individual excipients indicating no interaction or loss of crystallinity upon simple blending.

A similar trend was observed for F18 and its blank NPs as shown in figure 5.11 in which the PCL peaks exhibited broad structure from 0 to 30 degrees indicating amorphization by the hydrophilic PLGA. Also, no apparent peak for the IRH indicated its solubility in a non-crystalline form within the matrices of the polymers.

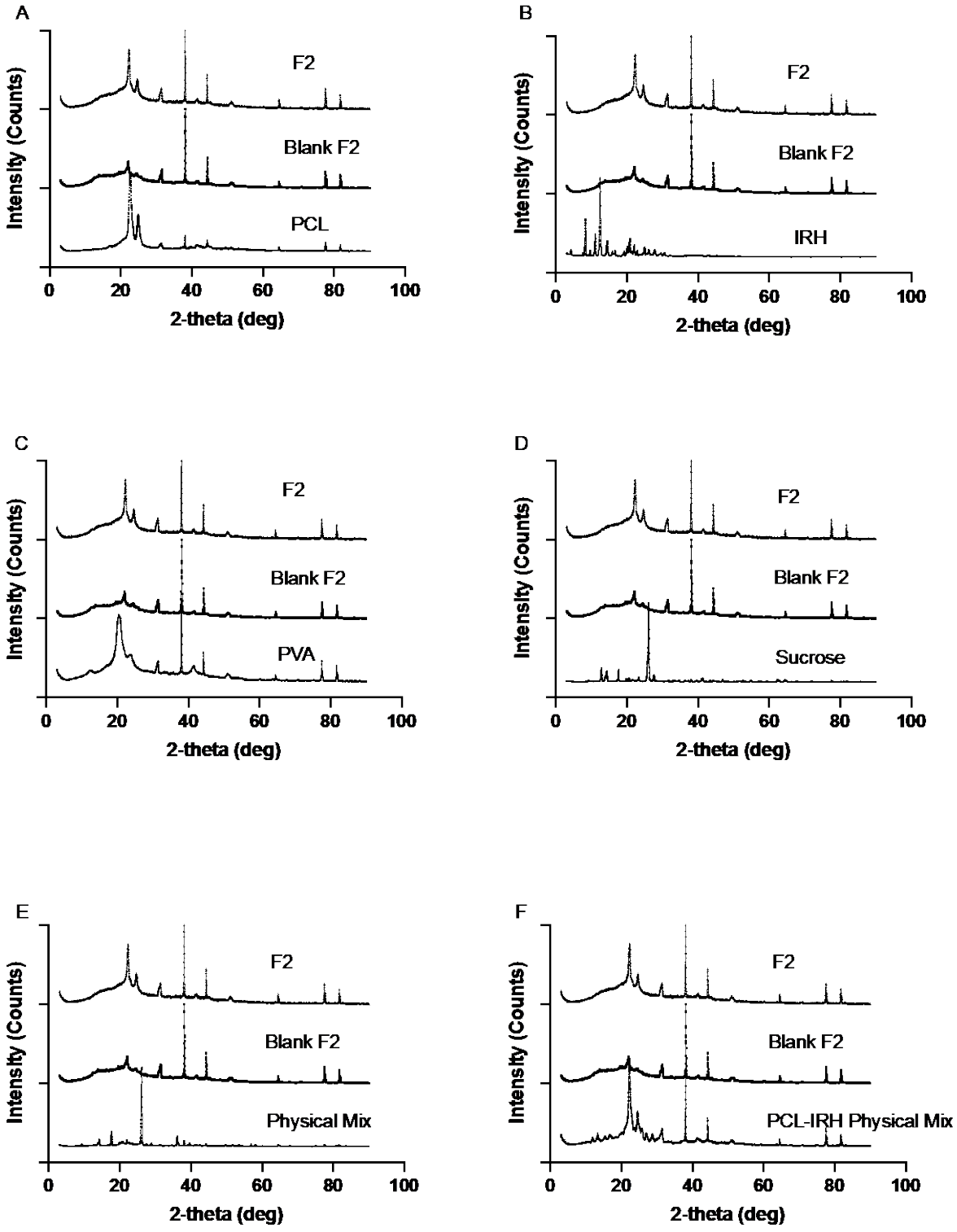
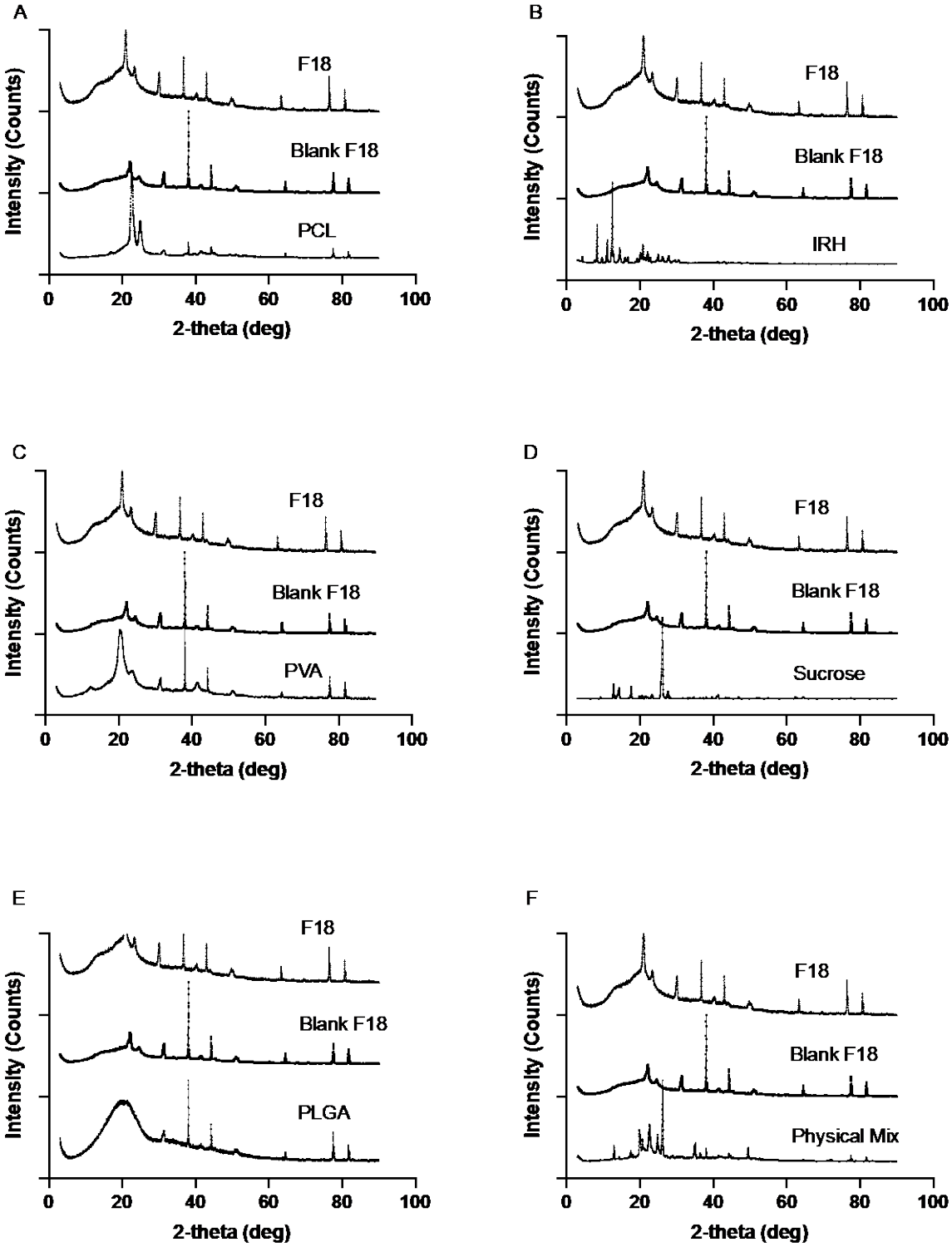


Figure 5.10. XRD spectra of F2 and its blank NPs plotted with each individual excipient. PCL, Blank F2 and F2 (A) IRH, Blank F2 and F2 (B) PVA, Blank F2 and F2 (C) Sucrose, Blank F2 and F2 (D) Physical Mix, Blank F2 and F2 (E) PCL-IRH Physical mix, Blank F2 and F2 (F)


A
F18
Blank F18
PCL
Intensity (Counts)
0
20
40
60
80
100
2-theta (deg)
B
F18
Blank F18
IRH
Intensity (Counts)
0
20
40
60
80
100
2-theta (deg)
C
F18
Blank F18
PVA
Intensity (Counts)
0
20
40
60
80
100
2-theta (deg)
D
F18
Blank F18
Sucrose
Intensity (Counts)
0
20
40
60
80
100
2-theta (deg)
E
F18
Blank F18
PLGA
Intensity (Counts)
0
20
40
60
80
100
2-theta (deg)
F
F18
Blank F18
Physical Mix
Intensity (Counts)
0
20
40
60
80
100
2-theta (deg)

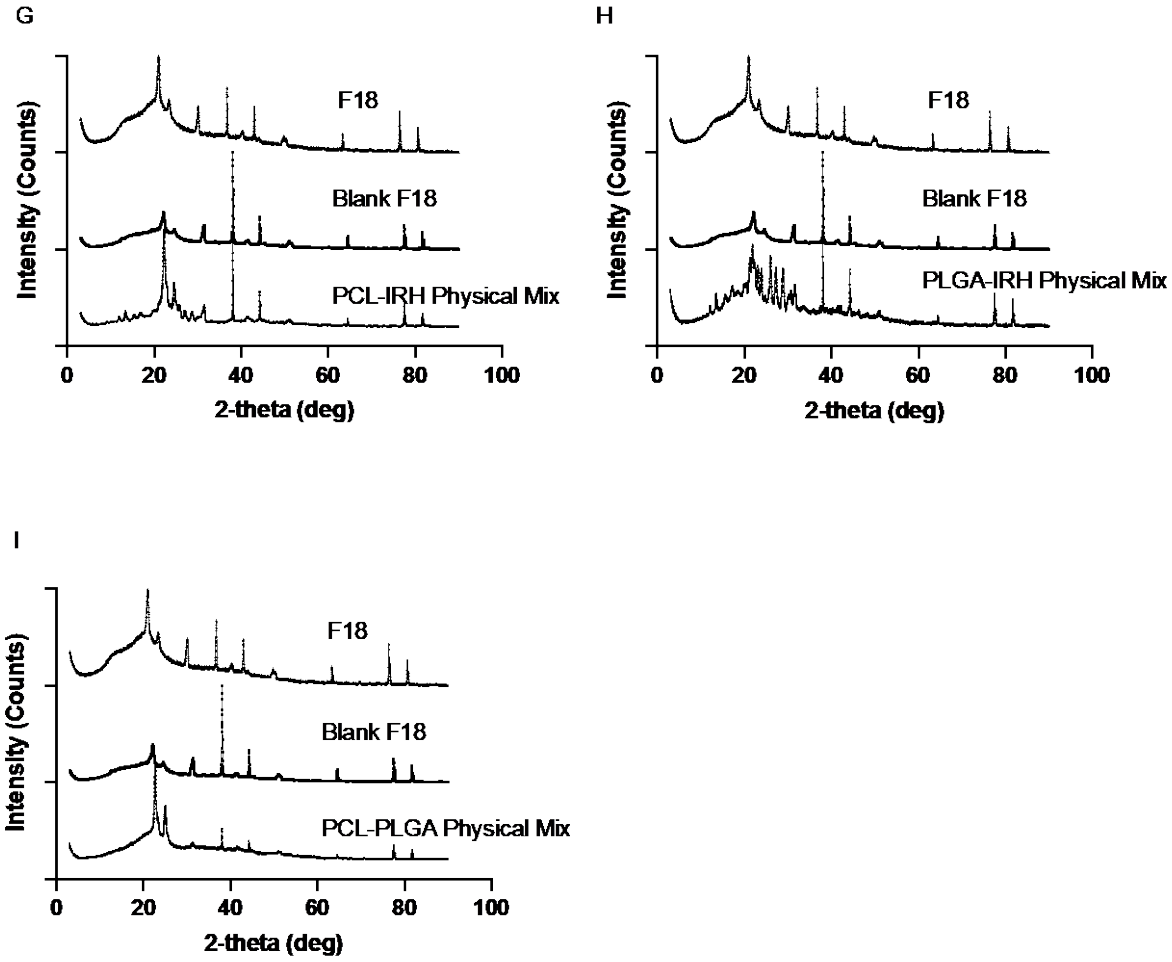


Figure 5.11. XRD spectra of F18 and its blank NPs plotted with each individual excipient. PCL, Blank F18 and F18 (A) IRH, Blank F18 and F18 (B) PVA, Blank F18 and F18 (C) Sucrose, Blank F18 and F18 (D) PLGA, Blank F18 and F18 (E) Physical Mix, Blank F18 and F18 (F) PCL-IRH Physical mix, Blank F18 and F18 (G) PLGA-IRH Physical mix, Blank F18 and F18 (H) PCL-PLGA Physical mix, Blank F18 and F18 (I)

5.3.4 Stability of NPs

Figure 5.12 to 5.14 exhibit the stability of selected NP formulations (F2, F3, F4, F12, F15, F18 and blank F18) in PBS, pH 3 and pH 5.9 over a period of 5 days. As shown in the figures, all the formulations underwent an increase in size and were less stable over time in PBS and at pH 3. While at pH 5.9, the formulations were significantly more stable when compared to pH 3 ($P < 0.0001$). In tissue culture media, the effect was

lower in relation to an increase in the size and stability compared to PBS and pH 3, with F18 retaining stability until the third day in tissue culture media.

In F2, the average particle size of the NPs has significantly increased ($P<0.0001$) by day 5 in PBS which also resulted in a higher PDI, and higher value of negative zeta potential compared to time 0. This is due to the swelling as well as agglomeration of the NPs that led to enlarging their size over time. The zeta potential ranging from -1.59 at time zero and -3.31 on day 5 is an indication of the instability of the NPs in PBS that compromises the stability of IRH as well. Similarly, a very low pH (pH 3) has negatively impacted the stability of the NPs providing a zeta potential of -0.06 at time zero and -0.20 on day 5. Also, the size at time zero in pH 3 was larger (631.03 nm) than the size of the NPs in PBS (355.66 nm) and pH 5.9 (359.10 nm). On the other hand, the charge at pH 5.9 (-10.36 mV at time zero and -13.10 on day 5) was more stable over time than in PBS and pH 3. However, the size continued to increase over time indicating swelling of the NPs and release of the drug but without loss of stability.

Similar trend was shown in F3 where there was a significant increase ($P<0.0001$) in size and PDI by day 5 in PBS and pH 3. A significant reduction in the magnitude of the negative charge was also shown in PBS and at pH 3 compared to pH 5.9 by day 5 ($P<0.0001$). However, the increase in size of the NPs was significantly less at pH 5.9 compared to PBS which indicates less agglomeration at the slightly acidic pH. In addition, at pH 5.9, the increase in size by day 5 was non-significant compared to time zero.

In F4, a significant ($P<0.0001$) increase in size was observed over time whereas the change in charge was not significant in PBS where it started with -1.17 at time zero

and changed to -2.73 on day 5 which continued similar trend of instability. Similarly, at pH 3, the size increased from 490.50 nm to 1067.60 nm by day 5 and the charge was -0.059 at time zero and -0.18 on day 5 indicating agglomeration of the NPs. At pH 5.9 the negative charge was significantly higher in magnitude than in PBS and pH 3 for all the days with an average of -20.4 ± 2.45 mV on day 5 indicating higher stability at that pH.

In F18, there was a significant ($P<0.0001$) increase in size over time in PBS which was significantly higher than the size of the NPs at pH 5.9 by the 5^{th} day. Also, at pH 5.9, the increase in size was non-significant indicating less agglomeration compared to the lower pH and PBS.

In F15, the size increased significantly ($P= 0.03$) at pH 3 but there was no significant increase in size at pH 5.9. While, in PBS the size was polydisperse at time zero with an average diameter of 1662 ± 263.64 nm which increased over time to 2219 ± 19 nm. Similar to the other formulations, the charge at pH 5.9 was significantly ($P<0.0001$) higher in magnitude and indicated more stability than it was in PBS and pH 3.

Similar trends were shown in F12 where there was an increase in size for PBS and a significant difference ($P<0.0001$) in zeta potential and PDI between PBS, pH 3 and pH 5.9.

Blank F18 NPs had the least average size at pH 5.9 on day 5 which was 229.03 ± 2.85 nm compared to 450.06 ± 65.90 nm in PBS and 1637.66 ± 29.02 nm in pH 3. In pH 3, blank NPs had a larger size (1637.667± 29.02 nm) compared to PBS and pH 5.9. The charge of the blank NPs was significantly ($P<0.0001$) more stable at pH 5.9 compared

to pH 3 and PBS. The size of the blank NPs was smaller compared to the rest of the formulations by day 5.

In tissue culture media, the average size of all the NP formulations increased by day 5, however, the increase in size was not as large as in PBS and pH 3.

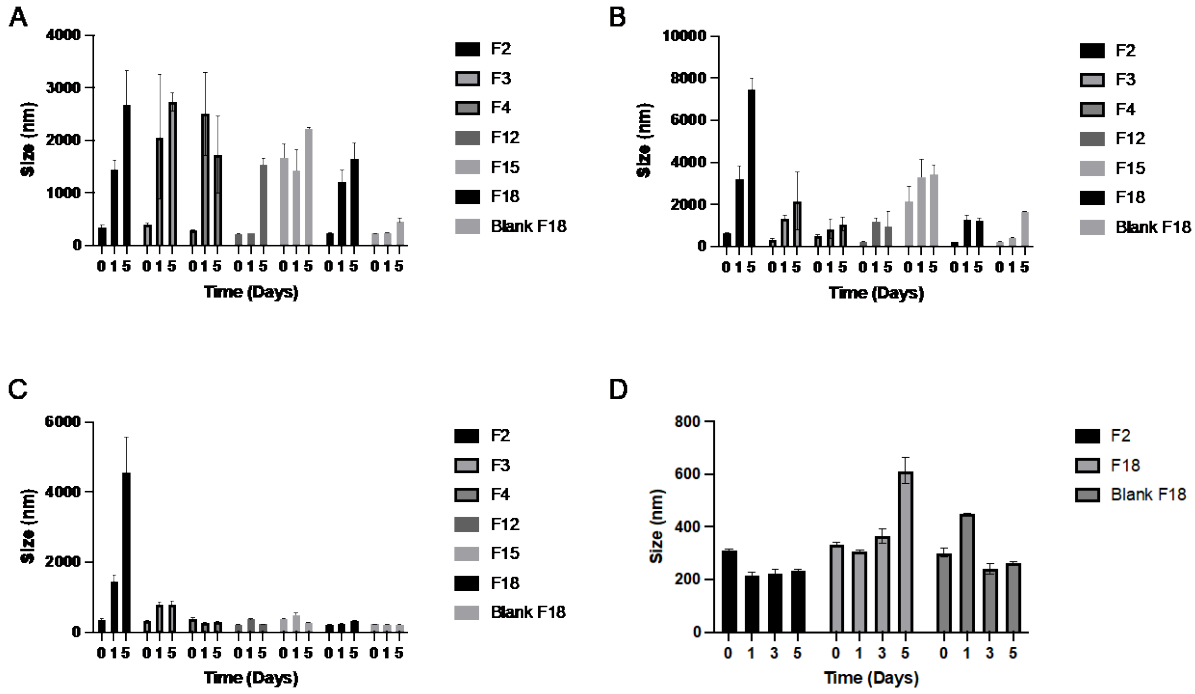


Figure 5.12. Stability of NPs Size in PBS (A) pH 3 (B) pH 5.9 (C)Tissue Culture Media (D) (n=3)

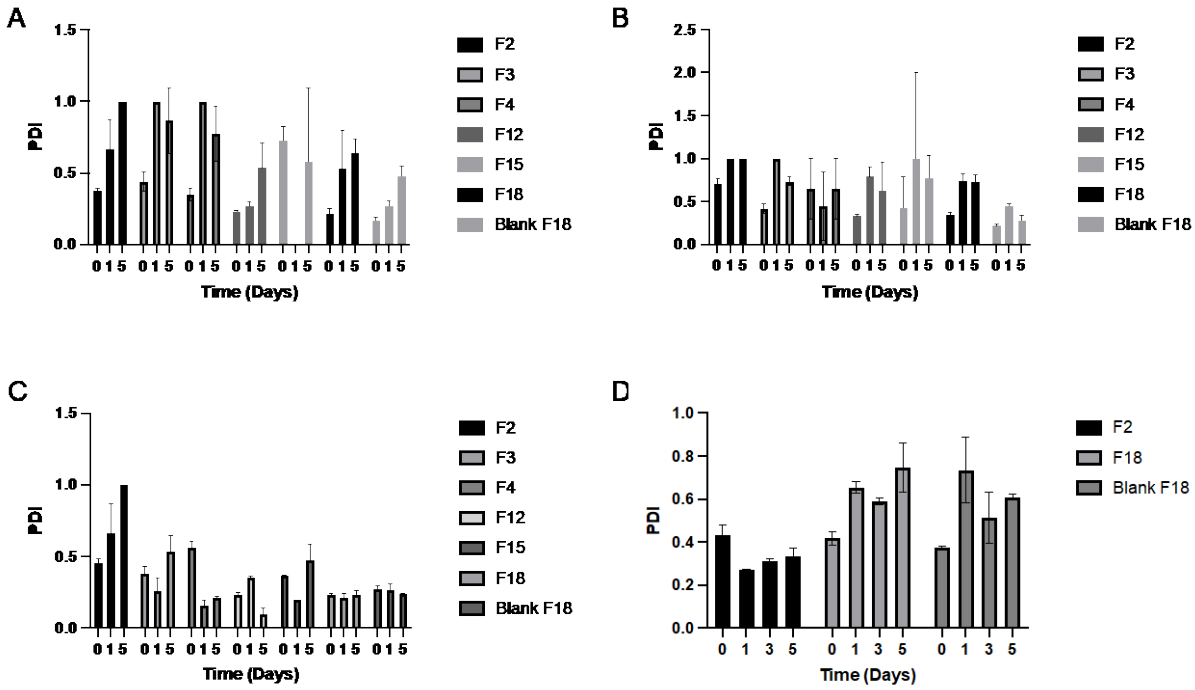


Figure 5.13. Stability of NPs PDI in PBS (A) pH 3 (B) pH 5.9 (C) Tissue Culture Media (D) (n=3)

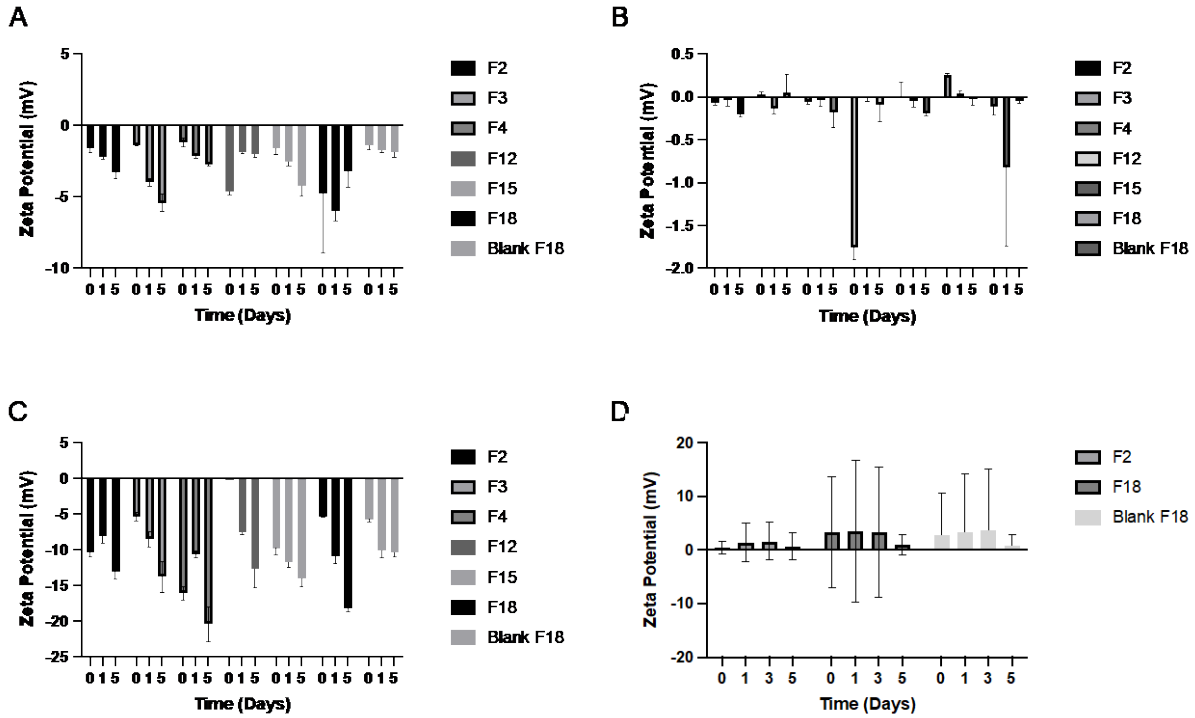


Figure 5.14. Stability of NPs Zeta Potential in PBS (A) pH 3 (B) pH 5.9 (C) Tissue Culture Media (D) (n=3)

5.3.5 Imaging of NPs

Figures 5.15 to 5.20 represent the TEM and SEM images of selected (F2, F15 and F18) NP formulations. The TEM and SEM images demonstrate that the NPs consist of a cluster of spherical particles with smooth edges. The F2, F15 and F18 NPs had average particle sizes of 85.83 ± 16.27 nm, 157.38 ± 26.74 nm and 134.23 ± 44.09 nm respectively which is a smaller particle size when compared to their hydrodynamic diameter measured by the DLS (298.80 ± 2.37 nm, 228.13 ± 2.19 nm, 234.26 ±1.45 nm respectively).

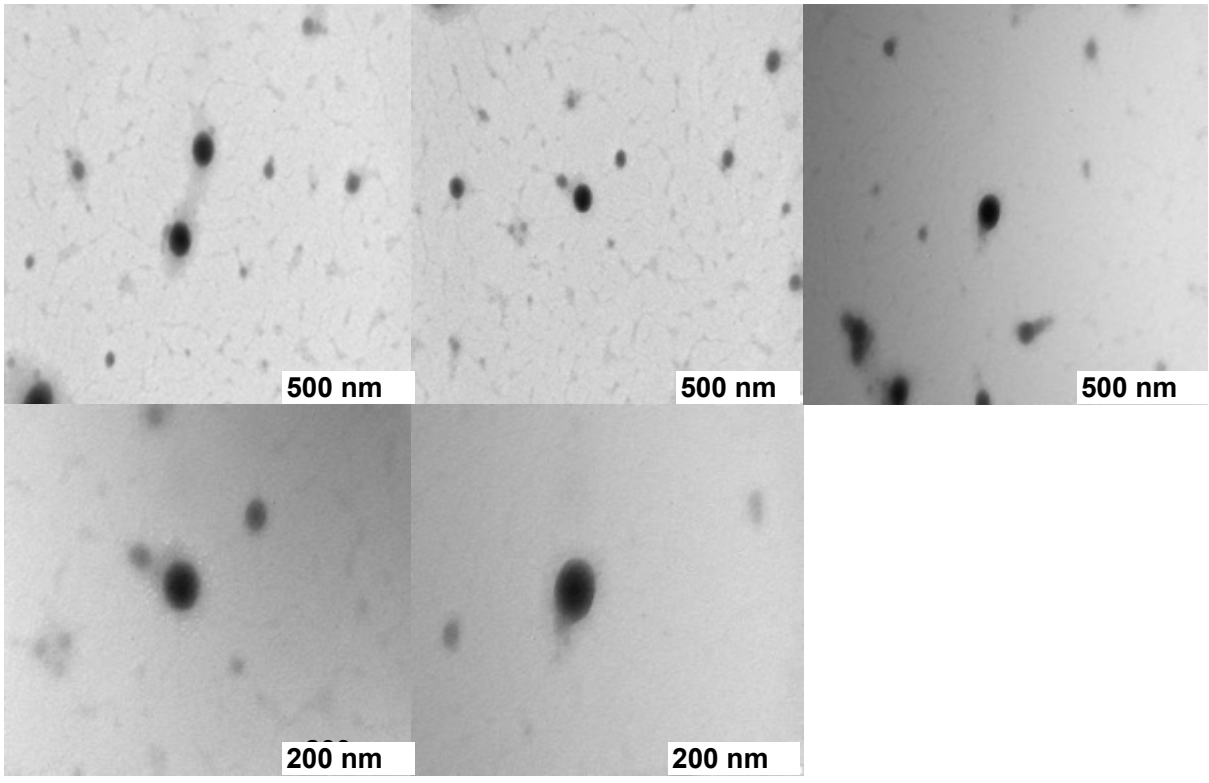


Figure 5.15. TEM images of F2 taken at different scales

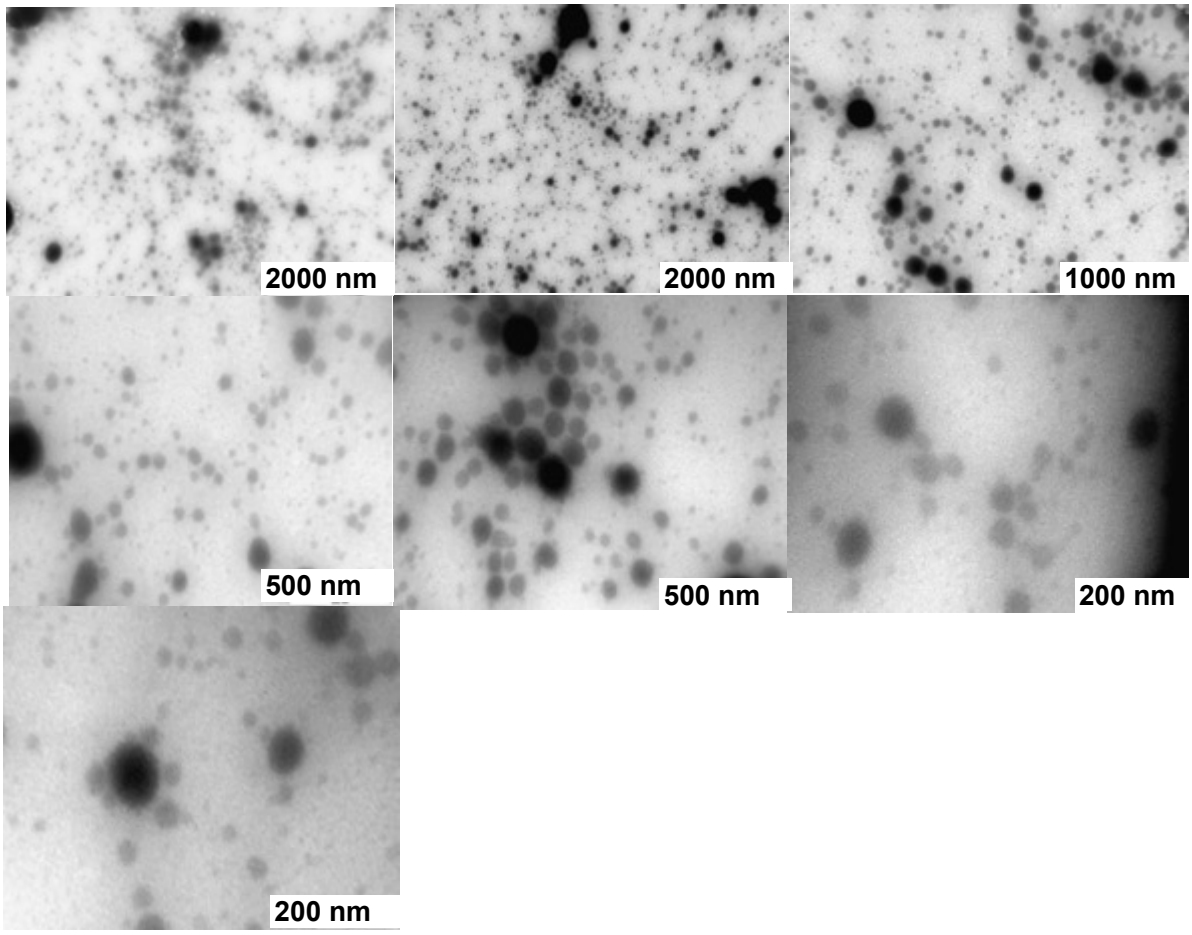


Figure 5.16. TEM images of F15 taken at different scales

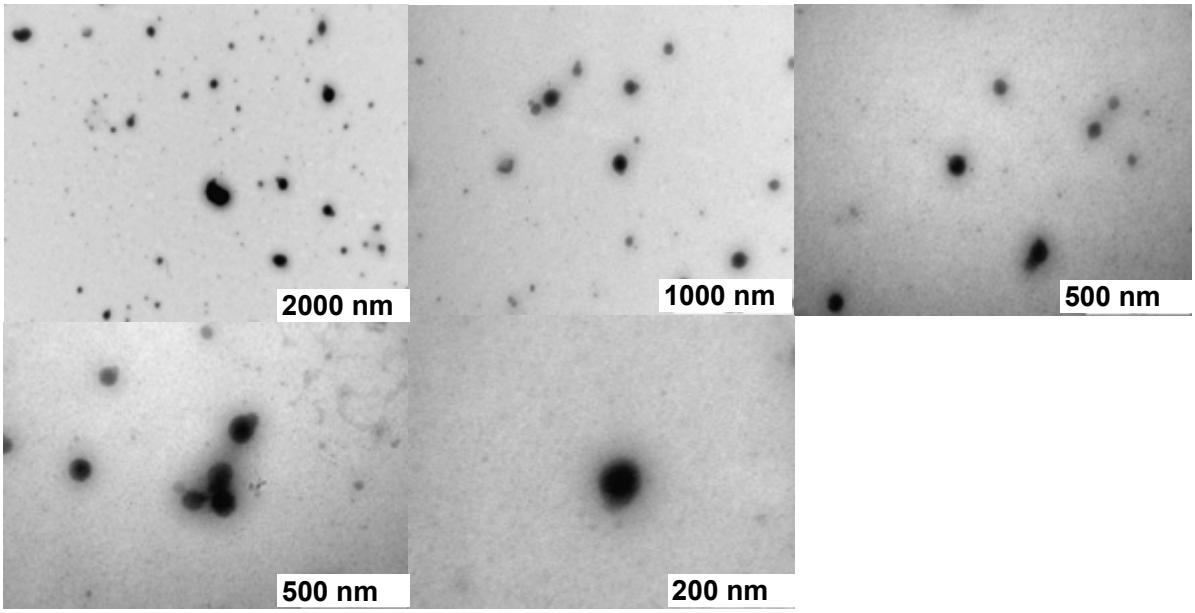


Figure 5.17. TEM images of F18 taken at different scales.

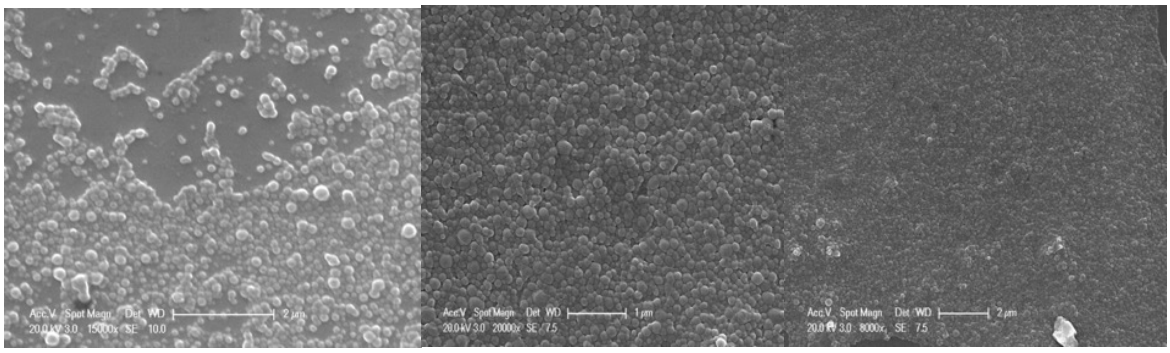


Figure 5.18. SEM images of F2 taken at different scales

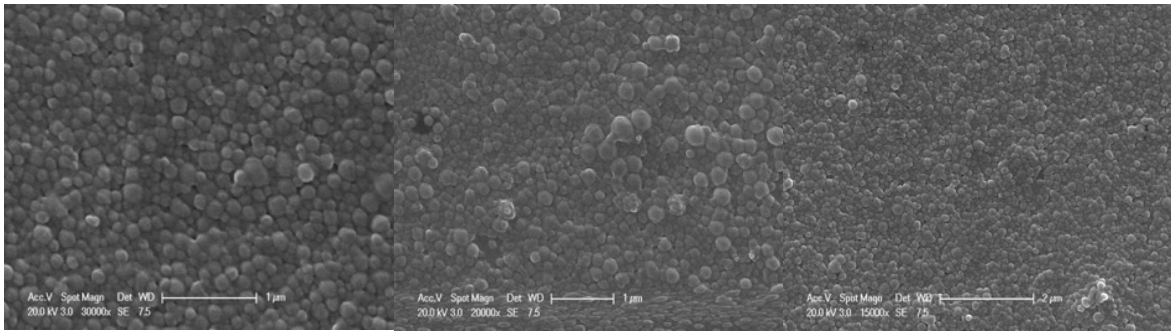


Figure 5.19. SEM images of F15 taken at different scales

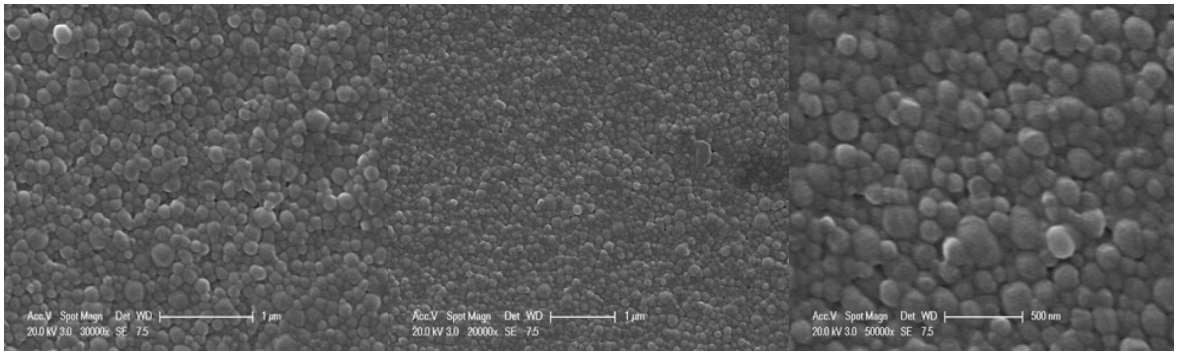


Figure 5.20. SEM images of F18 taken at different scales.

5.4 Discussion

Mathematical modelling is useful to understand the complexity of the release mechanism of NP formulations. In mathematical modelling, the focus is usually on one or two of the most superior driving forces for release (Fu and Kao, 2010b). The present work focuses on 4 different models of release considering the contribution of burst

release, NP degradation-relaxation phases and Fickian diffusion. In the zero-order model, drug release occurs with a constant rate as a function of time and is considered independent of the concentration of the drug. First order drug release is a function of the remaining drug only. The initial step of burst release is described by the first order release model where it considers that no drug is dissolved in the release media at time zero. Whereas, the last step suggests Fickian diffusion as the drug release mechanism (Lucero-Acuña et al., 2019). The final stage of release follows Fickian diffusion when the polymer relaxation time (tr) is greater than the solvent diffusion time (td). Whereas, non Fickian or the anomalous diffusion happens when both tr and td are equal (Grassi and Grassi, 2005). The Higuchi release model is concerned with drug released as a function of the square root of time. A few assumptions are made in the Higuchi model, firstly, the initial concentration of the drug is higher than the drug concentration in the release media. Secondly, sink conditions are met in which the released drug never exceeds 10% of the drug soluble in the release media. Thirdly, drug diffusion occurs with a fixed rate and finally, polymer swelling is minimal (Baishya, 2017). After confirming that the drug is released by diffusion, an essential step to define the pattern of this diffusion is done by using the Korsmeyer-Peppas empirical equation (Singhvi and Singh, 2011). Korsmeyer and Peppas described drug release from polymeric delivery systems using the equation: $Mt/M^{\infty}=kt^{n}$. (Mt/M^{∞}) is the fraction of drug released at time t, k is the kinetic constant, and n is the exponent that correlates to a particular diffusion mechanism which is obtained by plotting Mt/M^{∞} versus time. Korsmeyer-Peppas described release patterns that involve either Fickian diffusion or swelling (Azadi et al., 2015; Carril et al., 2017). Spherical particles follow either a Fickian diffusion if n = 0.43 or swelling if n = 0.85. If n is in-between 0.43 and 0.85, then

diffusion is anomalous which is a combination between the Fickian diffusion and swelling or erosion (Siepmann and Göpferich, 2001). If n is larger than 0.85, then diffusion occurs by erosion (Gao et al., 2013). A summary for n values for spherical particles can be explained in Table 5.3: -

Table 5.3. Release mechanisms for spherical particles given by the n exponent (Sarker Apu et al., 2009)

n values for spherical particles	Mechanism of Drug release
0.43	Fickian Diffusion
0.43<n<0.85	Anomalous Transport
0.85	Case-II Transport
>0.85	Super Case-II Transport

Fickian diffusion only considers the classical diffusion to be the mechanism for drug release. Case II transport considers swelling and relaxation of the delivery system as the only mechanism for drug delivery and is independent of time. Anomalous transport considers both diffusion and swelling/relaxation of the delivery system to be the controlling mechanisms for drug delivery. Super case-II considers release to be managed by the macromolecular relaxation of the polymer chains (Korsmeyer et al., 1983).

The release data in this study fitted all four models, as represented by the high R^2 in table 5.2. All the PCL formulations used in this study exhibited anomalous drug release except F2 that exhibited Fickian diffusion. This could be due to the slow swelling or relaxation of the polymer in addition to the low drug content that makes diffusion the only mechanism of drug release leading to a slower drug release of 15.6 ± 0.96 % over 16 days. High polymer content could hinder the release of the drug especially if the drug is used at low concentration. In addition, high drug loading enhances the release

even if the polymer content is high as in F4 with high polymer content (162 mg) and high drug content (9 mg) exhibiting 34.4 ± 0.12% release over 16 days. This is in accordance with a previous study using PCL microspheres to entrap doxycycline, in which the release was shown to be either Fickian or anomalous depending on the molecular weight of the polymer (Aydin et al., 2015). It is also reported that the acidic pH (5.9) as in cancer environment can enhance the release of drugs from polymeric matrices (Vilar et al., 2012). Acidic pH can also preserve the stability of some drugs depending on their pKa (Mahmoud and McConville, 2021).

As shown in Figure 5.1, the release rate was enhanced to 69.39 ± 0.58 % over 16 days by blending PCL with PLGA, which is due to enhanced hydrophilicity and penetration of water. PLGA is an amorphous polymer with a faster degradation rate than PCL(Makadia and Siegel, 2011). Moreover, the inclusion of PLGA in F18 has increased the magnitude of the surface charge to -32.5 mV which could have had an impact on enhancing the release by avoiding molecules adherence or pore clogging over time. Previous research has also indicated that PLGA and PCL blends had an enhanced hydrophilicity as scaffolds compared to the pure polymers (Pawlik et al., 2019). Other research has demonstrated that PCL and PLGA can form successful blends without chemical reactions involved when fabricated in the form of films (Pawlik et al., 2019).

Amorphous materials are used in pharmaceutical formulations to enhance the dissolution of insoluble drugs and improve their bioavailability. Amorphous domains are prone to enzymatic hydrolysis *in vivo,* however, they have a disadvantage of exhibiting a high molecular energy state which could negatively impact their stability.

Less crystallinity could enable a better release profile of the drugs due to the absence of extensive crystalline chains that hamper drug release (Kamaly et al., 2016). Using PLGA in a previous study has provided a biphasic release pattern starting with the burst release of drug molecules adsorbed on the surface then diffusion from swollen polymer matrix and finally degradation of the polymer that starts slow then becomes fast by action of the acidic degradation products (Fredenberg et al., 2011; Mirakabad et al., 2014). Another study using PLGA exhibited an n value of 0.43, which confirms that swelling was negligible and that diffusion was the dominant release mechanism from these PLGA based systems (Körber, 2010).

In conclusion, polymers that undergo erosion exhibit complexity in their release patterns since the conditions are constantly changing including drug diffusion distance, chemical reactions, boundaries, volume changes, production of oligomers and monomers, development of pores and holes. This in turn complicates the mathematical modelling for drug release (Siepmann and Göpferich, 2001; Siepmann and Peppas, 2001).

The overlay of the DSC thermogram for F2 (Figure 5.3) exhibited an absence of the IRH melting peak which confirms that the drug has lost its crystalline property after being loaded onto PCL, suggesting that the IRH is dissolved in the PCL. Absence of a melting peak could also be an indication of a change to an amorphous state (Kittur et al., 2002). The PCL melting point has decreased from 64.03°C to 56.12°C, suggesting a change in its crystalline structure and the solubility of IRH within its matrix, which did not occur in the physical mixture. On the contrary, there was almost no observed endothermic peak shifts for the PVA in the formulation as compared to the PVA

individual thermogram. Similar research reported that the absence of the endothermic peak of the drug is an indication of its dispersion within the polymer matrix. This also highlights that the polymer and the drug are compatible (Tummala et al., 2015).

By comparing both thermograms of F2 blank NPs and F2 drug loaded NPs, it is quite clear that they look similar due to the absence of the IRH endothermic peak in both formulations suggesting the solubility and/ interaction of the drug within the PCL matrix in F2. This is in accordance with previous research that reported similarity between thermograms of drug loaded and blank NPs concluding the efficient entrapment of the drug (Dimchevska et al., 2017b). Another study reported absence of the endothermic peak for etoposide drug encapsulated in PCL and PLGA 50/50 NPs suggesting complete encapsulation of the drug with limited adsorption on the surface of the NPs (Snehalatha et al., 2008).

A low Tg is an indication of crystallinity which is the case for pure PCL exhibiting Tg of -63.03°C. Whereas, a higher Tg is relevant to the amorphous state of the polymer which is evident for PLGA which has a Tg of 39.03°C.

Polymer miscibility is determined by the Tg, in which fully miscible polymers exhibit a single Tg, whereas partially miscible polymers exhibit 2 Tgs shifted towards each other depending on the composition of the blend and degree of miscibility (Menczel and Prime, 2008). In F18, the miscibility of PCL and PLGA was confirmed by the appearance of a single Tg at 8.43°C and 6.51°C for F18 and its blank respectively (Figure 5.6). The Tm of the PCL was reduced to 52.99°C and 53.05°C for both F18 and blank F18 respectively suggesting amorphization of the PCL by PLGA. Similar to our results, another study highlighted that there was a decline in the Tm of PCL in the

blend compared to pure PCL which was directly proportional to the concentration of the PLGA (Pawlik et al). This has confirmed the miscibility of the two polymers and that PLGA chains could disrupt the crystalline chains of the PCL owing to the higher solubility of PLGA in DCM compared to PCL (Pawlik et al., 2019).

The XRD analysis was used to characterize the physical state of both the PCL and IRH. Pure compounds were analysed individually where they exhibited sharp crystalline peaks. As shown in Figure 5.10 and 5.11, PCL exhibited sharp peaks at 22.74 and 24.84 degrees. Similar patterns for PCL were previously reported (Othman et al., 2016). Whereas IRH exhibited sharp peaks at 8.42, 9,66, 11.20, 12.54, 13.52 and 14.46 degrees.

In F2 the sharp peaks of the IRH disappeared and the PCL crystalline peaks were less intense and broader than the pure PCL confirming change from semi-crystalline to a more amorphous state. Amorphization of the polymer in NP formulations was also confirmed in a former study (Othman et al., 2016). The sharp crystalline peaks at 28.04 and 38.12 degrees in both F2 and its blank respectively were due to the PVA as shown in the individual XRD pattern for PVA (Figure 5.10). Physical mixtures of both PCL and IRH as well as physical mixture of all excipients exhibited sharp peaks for PCL and IRH indicating no interaction between the pure excipients and that they remained in their original crystalline state.

Similar observations were seen in the F18 blend NPs which is in accordance with previous research suggesting that the blending of PCL with other polymers could render the PCL amorphous providing a broad XRD diffraction peak (Balu et al., 2011). Moreover, there was no peak shift which suggests that there was no interaction

between PCL and the rest of the excipients. Similar observation has been reported elsewhere (Ganipineni et al., 2019).

The XRD results confirmed the DSC results where both of the PCL and IRH have lost their crystallinity within the formulations. This could be attributed to the amorphization of the polymer and the solubility of the drug as an amorphous molecular dispersion within the polymer and possible interaction between the PCL and IRH.

Stability of NPs is one of the main obstacles in their advancement within the field of drug delivery. NPs have a large surface area due to their small particle size that allows for a high surface free energy. High free energy makes the NPs highly reactive and prone to agglomeration. PCL is a hard polymer matrix that could soften over time and erode (Allotey-Babington et al., 2018). The large surface area of the NPs results in their high reactivity and tendency to adhere to each other by *van der Waal* forces in order to reduce the free surface energy (Madkour et al., 2019). This results in irregular shaped clusters and aggregation of the NPs which is a common issue in nanomedicine. Formation of aggregates could lead to the clearance of the NPs by the RES limiting their application in drug delivery (Gómez-Gaete et al., 2007). The present results showed that blank NPs had the highest stability in PBS compared to drug loaded NPs over time. This could possibly be due to the absence of the drug which seems to contribute to the agglomeration of the NPs after being released due to its degradation of its lactone form in PBS which makes it more reactive.

In tissue culture media, the charge of the NPs was impacted over time, possibly due to formation of protein corona on the NPs rather than agglomeration. The intravenous application of NPs could lead them to deposit protein corona which is mainly made of

plasma proteins making them more reactive and less stable (Carril et al., 2017). In F18, the size did not increase significantly up to day 3 in tissue culture media. Similar findings reported stability of the size of PCL NPs in tissue culture media for 48 hours (Łukasiewicz et al., 2021). The cell culture media alters the chemical and physical properties of the NPs due to two factors one is adsorption of proteins, and the other is the ionic strength of the media. Low ionic strength could help particles repel from each other and stay apart. Whereas high ionic strength encourages aggregation by *van der Waal* forces (Boström et al., 2001; Edwards and Williams, 2004). High ionic strength is known to compress the electric double layer and reduce the repulsion between particles. Similar results indicated agglomeration in PBS owing to its intermediate ionic strength of 164 mM. Whereas exposure to tissue culture media with low ionic strength as RPMI (152 mM) had less agglomeration and sedimentation of the NPs. Ionic strength is not the only factor that determines the behaviour of the NPs but other factors control their behaviour such as their hydrodynamic size and ligands attached to the surface (Kwon et al., 2010).

One of the approaches used to reverse the aggregation of the NPs is *via* steric stabilization by utilizing polymers or surfactants on the surface of the NPs (Mo et al., 2016). Polymeric stability by using surfactants is abundantly used where it relies on the fact that surfactants reduce the surface tension between the solid surface of the NPs and the liquid medium resulting in less reactivity. The surfactants can have several chemical structures whether negatively charged, positively charged, zwitterionic (charge depends on the pH of the medium) amphoteric or non-ionic (with no net charge) like PVA. The most favourable class of surfactants is the non-ionic as it is the least toxic to the biological membranes(Gagliardi et al., 2019; Rege et al., 2002).

Surfactants can also form a protective layer around NPs to protect them to some extent against degradation by enzymes (Lee et al., 1999). PEGylation is also a widely used approach that reduces the formation of protein corona and extends the half-life of the circulating NPs (Owens and Peppas, 2006).

In conclusion, PCL NPs could provide a sustained release of IRH mostly by anomalous transport over a 16-day period. Blending PCL with PLGA has enhanced the release of IRH up to 69.39%. Also, the blend NPs had a reduced polymer crystallinity as a result of the amorphous PLGA and the drug was solubilized in the NPs confirming proper loading within the polymeric matrix. The PCL and PCL-PLGA blend NPs were more stable in slightly acidic conditions (pH 5.9) and in tissue culture media more than the PBS and pH 3 release media, which makes them suitable for the cancer environment.

The next chapter will examine the behaviour of the PCL and PCL-PLGA blend NPs in the environment of the HGG primary cells.

Chapter 6 BIOLOGICAL CHARACTERIZATION OF THE PCL NPS FOR THEIR HAEMOCOMPATIBILITY, CELLULAR UPTAKE, AND CYTOTOXICTY AGAINST HGG PRIMARY CELLS

6.1 Introduction

6.1.1 Cellular Uptake of NPs and Free Drugs

NPs exert their cytotoxic activity within the cell due to their electrostatic interaction with the cell membrane and subsequent uptake. Such interaction is controlled by several factors including the charge, shape, size, and chemical characteristics of the NPs (Hong et al., 2006; Nel et al., 2006; Leroueil et al., 2008). The EPR effect only permits particles less than 500 nm to traverse cell membrane and reach the tumour microenvironment where they accumulate. Upon systemic administration, larger NPs accumulate in the lungs and are removed *via* the RES system (Petros and Desimone, 2010). Endocytosis is the main route of cellular uptake for NPs (Behzadi et al., 2017), however, NPs can extravasate passively to tumours *via* the EPR effect depending on their size, shape, and charge. The endocytosis route of cellular uptake can be enhanced *via* surface modification (Maeda, 2015; Li et al., 2017). The mechanism of entry of NPs into cells is decisive of their pathways which determine their biodistribution and cytotoxicity. Therefore, the recognition of the routes for cellular uptake of the NPs will help in designing NPs with specific properties that could target tumours (Foroozandeh and Aziz, 2018). Each cell type has a certain phenotype which decides the size of the NPs to be internalized. Cells also express target receptors differently which could favour different internalization modes. More variations could also exist by using primary cells or immortalized cells for testing NP internalization *in vitro* (Albanese et al., 2012a) .

Internalization of drugs into the cells is controlled by several factors including the molecular weight, lipid solubility and ionization state of the drug (Peetla,

Vijayaraghavalu and Labhasetwar, 2013). Drugs can cross the BBB by passing in-between the endothelial cells which is a paracellular pathway or by passing through the endothelial cells by traversing through the luminal and abluminal plasma membranes (Peterson, 2012). The tight junctions of the endothelial cells complicate entry of hydrophilic drugs *via* the paracellular pathway, while lipophilic drugs can translocate through the plasma membrane and enter the cells. Tumours such as glioblastoma may compromise the integrity of the endothelial cells which could be beneficial for the transport of therapeutics into the brain (Peterson, 2012).

6.1.2 NP-induced Apoptotic and Necrotic Cell Death

The dose as well as the physical and chemical properties of the NPs determine their ability to initiate apoptotic and/or necrotic pathways within the cells which could help in the treatment of cancer. Necrosis develops from traumatized cell injury and is regarded as a sudden cell death with loss of control without programmed signals of events (Mohammadinejad et al., 2019). Whereas apoptosis is a programmed cellular death that results in nuclear condensation and fragmentation, membrane blebbing and formation of apoptosis bodies (Wyllie, Kerr and Currie, 1980). Apoptosis is impaired when the production of pro-apoptotic and anti-apoptotic proteins is overwhelmed causing cells to skip natural apoptosis (Wong, 2011). Also, reduced levels of caspases as well as the disruption in the death receptor machinery could enhance apoptosis evasion. Necrosis is morphologically different where it results in electron-lucent cytoplasm, enlargement of the mitochondria and damage of the plasma membrane with minimal effect on the nucleus (Arends and Wyllie, 1991). Clearance of apoptotic cells occurs without an immunogenic response which distinguishes apoptosis from

necrosis (Steinbach and Weller, 2004). In apoptosis, the flip-flop mechanism exposes the phosphatidylserine from the internal to the external side of the plasma membrane which marks the apoptotic cells for phagocytosis by macrophages (Fink and Cookson, 2005).

NPs can cause both apoptosis and necrosis, but a high concentration of NPs can induce necrosis (ÇIFTÇI et al., 2013). High doses of NPs could also stress the endoplasmic reticulum that releases calcium into cytosol during stress, this impairs calcium homeostasis leading to cell death (Ariano et al., 2011). The duration of exposure to NPs also controls the mechanism of cell death by apoptosis or necrosis (Foldbjerg et al., 2009). In some instances, the apoptosis could develop into necrosis leading to confusion during analysis of the leading mechanism of cell death (De Stefano, Carnuccio and Maiuri, 2012). Necrosis *in vitro* could occur as a result of apoptosis, in which apoptotic cells lack the natural phagocytosis that engulf dead cells which causes them to breakdown and appear morphologically as necrotic, which is known as a secondary necrosis process (Ziegler and Groscurth, 2004).

NPs can induce both intrinsic and extrinsic pathways of apoptosis by inducing an oxidative stress leading to the production of reactive oxygen species (ROS) that damage DNA, proteins, mitochondria, and other organelles (Ou et al., 2016). NPs can also induce necrosis by undergoing degradation in the lysosomes and releasing their elements in the cytosol leading to cell damage by necrosis (Mohammadinejad et al., 2019). Moreover, NPs can induce necrosis by triggering inflammation and production of cytokines such as interleukin-6 (IL-6) (Liu et al., 2019). Production of inflammatory cytokines as IL-6 and IL-8 in response to NPs cytotoxic effect has previously been

reported in primary endothelial cells (Bauer et al., 2011). The degree of cytotoxicity of NPs is dependent on their crystallinity, charge, size and composition (Van Loo et al., 2001).

Chemotherapeutic agents are capable of inducing genotoxicity in malignant glioma cells leading to apoptosis. Such mechanism of apoptosis is caspase dependent and involves the release of cytochrome C from the mitochondria. Signalling *via* death receptors is not involved in such mechanism (Glaser and Weller, 2001).

Caspases are crucial proteins that act as initiators and executers of apoptosis, and low levels of caspases signal an impaired apoptotic mechanism (Wong, 2011). Caspases are classified based on their role. Those that participate in immunogenic responses and cytokine regulation are caspase-1, -4, -5, -13, and -14. Whereas, those involved in apoptosis are the initiator caspases (Caspase-2, -8, -9 and -10) that start the process of apoptosis and the effector caspases (Caspase-3, -6 and -7) which function in apoptotic scission of DNA, cellular shrinkage, and plasma membrane blebbing (Shi, 2002). Activation of caspases and DNA fragmentation are mainly exclusive to apoptosis and not observed in necrotic cell death (Proskuryakov, Konoplyannikov and Gabai, 2003).

Apoptosis occurs in Glioblastoma due to high levels of hypoxia, when compared to astrocytomas and anaplastic astrocytomas, which is induced by the high proliferative rate of GBM cells. This could impact the response of malignant cells to radiotherapy or chemotherapy making them more resistant to treatment and difficult to manipulate (Steinbach and Weller, 2004). The level of ATP in cancer cells is known to be higher than normal cells due to the usage of glycolysis during both hypoxic and non-hypoxic

conditions, instead of oxidative phosphorylation (Warburg et al., 1927). Some novel treatments are targeted at inhibiting the hypoxic pathways in tumours (Wouters and Koritzinsky, 2008). Abnormal mitochondrial function could enhance the release of ROS and ATP depletion which develops necrosis (Denecker et al., 2001). ATP depletion is a crucial characteristic of necrosis in which the electron transport chain is impaired leading to dysregulation in the biochemical pathways that activate Na^+-K^+-ATPase and deplete ATP (Padanilam, 2003). However, there is a belief that complete depletion of ATP leads to a different mechanism of cell death termed energy catastrophe, indicating that apoptosis and necrosis still require minimal levels of ATP (Skulachev, 2006).

6.1.3 Haemocompatibility of NPs

NPs administered intravenously and *via* other modes come into direct contact with the blood. Owing to their minute size compared to microparticles, NPs can enter the circulation and cells through their biological reactivity (Matus et al., 2018). NPs can interact with the blood components with certain levels depending on their properties which should be taken into consideration during the design of the NPs for drug delivery (Brash, 2018). The main components of blood that are readily exposed to NP interaction are the red blood cells (RBCs), white blood cells and platelets. These components work in harmony to maintain the haemostasis and any disturbance to their function will result in side effects (de la Harpe et al., 2019). One of those side effects induced by interaction of the NPs with the RBCs is haemolysis, in which the membrane of the RBCs is injured or distorted leading to detrimental effects on the haemostasis (Chen et al., 2015). Haemolysis induced by NPs is related to the structure, shape, size, charge and concentration of the NPs. Some studies highlighted that smaller NPs were more reactive and haemolytic than their larger counterparts (Shang et al., 2014). Other

studies suggested that spherical NPs were haemocompatible and induced no blood clotting or haemolytic activity (Zhang et al., 2008). Also, spherical particles had a better interaction and were internalized better than cylindrical particles into Chinese hamster ovarian (CHO) cells (Zhang et al., 2008). Additionally, Spherical particles have lower interfacial energy due to their low surface per unit volume, this can slow down their drug release compared to non-spherical NPs that have larger surface area leading to rapid drug release (Y. Liu et al., 2012). Positively charged NPs were reported to induce haemolysis and platelet aggregation before being eventually cleared from the circulation (Albanese et al., 2012b). NPs that exist longer in circulation have a better chance of tumour uptake with PEGylation being useful in that regard and was previously exploited in extending the circulation time of spherical NPs (Albanese et al., 2012a; Truong et al., 2015).

6.1.4 IL-6 Protein Expression in Glioma Cells

The GBM environment encompasses a high level of expressed cytokines which are strongly correlated with its proliferation and aggressiveness (Yeung et al., 2013). Among the overexpressed genes that contribute to the invasiveness and lethality of GBMs is IL-6 (Rolhion et al., 2001; Tanabe et al., 2010; Tchirkov et al., 2007). IL-6 is overly expressed in tumours leading to higher proliferation and progression of the disease (Pasi et al., 2010). Some research conducted on transgenic mice has concluded that the deficiency of the IL-6 gene prevented the development of GBM (Weissenberger et al., 2004). Some studies suggested that targeting proinflammatory cytokines could help control the aggressiveness of GBM. However, the necrotic

damage of DNA by chemotherapy or radiotherapy could enhance the production of proinflammatory cytokines (Rodier et al., 2009).

The aim of this chapter was to assess the biological behaviour of HGG cells upon exposure to F2 and F18 NP formulations and their blank counterparts compared to the free IRH. The cellular uptake of the NPs into HGG cells as well as their morphological change, cytotoxicity, mechanism of cytotoxicity and immune response is evaluated in this chapter.

6.2 Materials and Methods

6.2.1 Materials

Alexa Fluor® 488 annexin V/Dead Cell Apoptosis Kit with Alexa® Fluor 488 annexin V and propidium iodide (PI), Rhodamine 123, 4',6-Diamidino-2-Phenylindole (DAPI) and 4% paraformaldehyde solution were purchased from ThermoFisher Scientific (Loughborough, UK). Tissue culture treated coverslips for cell visualization were purchased from Ibidi (Glasgow, UK). Sheep whole blood in Alsever was purchased from Generon (Slough, UK). ATPlite luminescence kit was purchased from PerkinElmer (Beaconsfield, Buckinghamshire, UK). Dulbecco's modified eagle's medium without phenol red was purchased from Sigma-Aldrich (Dorset, Gillingham, UK). Caspase-Glo® 3/7 kit was purchased from Promega (Hampshire, UK). Human IL-6 Duoset ELISA kit was purchased from R&D systems (Abingdon, UK).

6.2.2 Cell Culture of Primary HGG Cells

Primary HGG cells were obtained and maintained according to the method described in Chapter 2, section 2.2.12.

6.2.3 Flow Cytometry Analysis of Cellular Uptake In Primary HGG Cells

500 µL of the cell suspension was seeded onto 24 well plates at a cell density of 50,000 cells per well. Cells were left to adhere and get confluent for 3 days. Cells were then treated with 500 µL of low, medium, and high concentrations of the NP suspensions (F2, F18 and their blank counterparts) as described previously. After the required incubation time (1, 3, 5, 7 and 9 days), cells were washed twice with 500 µL of PBS, then detached with 250 µL of trypsin. Centrifugation occurred at 1500 RPM for 5 minutes at 4°C. Cells were then resuspended in 500 µL of Fluorescence-activated cell sorting (FACS) buffer (PBS), transferred to FACS tubes and kept on ice for immediate analysis using BD LSRFORTESSA X-20 flow cytometer (Flow Cytometry Unit, University of Birmingham, Wokingham, England, UK). The sample was injected into sheath fluid with hydrodynamic focusing to allow single cell analysis. Forward and side scattered light was recorded for each gated event as they pass through laser beam while excluding the region of cell debris. Results were analysed by flowjo software version 10.7.1 (Ashland, USA).

6.2.4 *In Vitro* Cytotoxicity and Morphology of Primary HGG Cells

The cell culture and cytotoxicity of F2, F18 and their blank counterparts was evaluated against primary HGG cells as described in chapter 2, section 2.2.12. The morphology of the cells was observed on days 1, 3, 5, 7, 9 and 11 post treatment using a light microscope at 10X magnification power. Free IRH was used at low, medium and high concentrations equivalent to 0.5, 1 and 10 µM, respectively. The NP formulations were dosed at low, medium, and high concentrations equivalent to 0.5, 1 and 10 µM of encapsulated drug, respectively. Blank NPs were used in equivalent concentrations to the drug loaded NPs.

6.2.5 Imaging of Internalized Nps in Primary HGG Cells by Confocal Microscopy

Cells were seeded on cover slips at a cell density of 10,000 cells / well and left until confluent. The cells were subsequently treated with 800 µL of F2, F18 and their blank counterparts at a low, medium, and high concentrations that were defined previously for the cytotoxicity study for 3 and 5 days. Cells were also treated with fluorescent NPs developed using single emulsion solvent evaporation method with the same formulation parameters as F2, with Rhodamine 123 loaded at 1% (1.62 mg) of the polymer amount. The cells were then spiked with 500 µL of 4% paraformaldehyde for 2 minutes to avoid cell shock by pure paraformaldehyde. Aspiration and cell fixation was then performed using 4% paraformaldehyde solution (diluted in PBS) and incubation occurred for 20 minutes at room temperature. The cells were then rinsed thrice with PBS to remove excess paraformaldehyde. 300 µL of 300 nM of DAPI was added to ensure proper staining of the nucleus with incubation for 5 minutes in the dark. The stain was removed, and the cells were washed thrice with PBS to remove excess stain. The cells were then visualized by z-stacks using Nikon A1R confocal microscope (Nikon, Surrey, UK) at 40X magnification and an excitation and emission of 500 nm/560 nm for rhodamine-123 and 358 nm/461 nm for DAPI. Image processing and visualization were performed using NIS-Elements imaging software (Melville, USA).

6.2.6 Flow Cytometry Analysis of Apoptosis And Necrosis in Primary HGG Cells

Cells were seeded at a cell density of 100,000 cells per well in a 12 well plate in 1.5 mL of media. The cells were left to attach and grow for 3 days. The old media was

replaced with equal volumes of the NP suspensions (F2, F18 and their blank counterparts) and drug solutions and incubated for up to day 5. 2μM of Staurosporine was used as the positive control for apoptosis, while 20% dimethyl sulfoxide (DMSO) was used as the positive control for necrosis. After the incubation period (1, 3 and 5 days), cells were washed twice with PBS, harvested, and then centrifuged at 1500 rpm for 5 minutes at 4°C. The supernatant was discarded, and the cells were re-suspended in 100 μL annexin-binding buffer. 5 μL Alexa Fluor® 488 annexin V and 1 μL of 100 μg/mL PI were mixed each with 100 μL of the cell suspensions and left for 15 minutes at room temperature. Following the incubation period, 400 μL of 1X annexin-binding buffer were added and the solutions were gently mixed and kept on ice for analysis by flow cytometry. The fluorescence emission was measured at 530 nm for Alexa Fluor® 488 and 575 nm for PI using 488 nm excitation.

6.2.7 Caspase Luminescence Assay of Primary HGG Cells

Primary HGG cells were seeded at a cell density of 10,000 cells per well in 96 well white plates. Cells were left to adhere for 3 days and the NP suspensions (F2, F18 and their blank counterparts) and drug solutions were added and the cells incubated for 5 days. 100 μL of Caspase-Glo® 3/7 reagent was added to each well containing either 100 μL of media, negative control cells or treated cells in tissue culture media without phenol red. The wells were gently mixed using a plate shaker at 500 rpm for 30 seconds at room temperature. Then incubation occurred for 10, 60 and 120 minutes before measuring the luminescence using FLUOstar Omega plate reader (BMG LABTECH Ltd, Aylesbury, UK).

6.2.8 ATP Luminescence Assay of Primary HGG Cells

Primary HGG cells were seeded at a cell density of 10,000 cells per well in a 96 well white plates. Cells were left to adhere for 3 days, then the NP suspensions (F2, F18 and their blank counterparts) and drug solutions were added and incubated for 1, 3, 5, 7, 9 and 11 days. All reagents were constituted and incubated at room temperature prior to using. 100 µL of ATPlite 1step reagent solution of ATP was added to the wells containing cells in 100 µL tissue culture media without phenol red and mixed for 2 minutes using an orbital shaker at 700 rpm. Luminescence was measured within 30 minutes of the reaction using FLUOstar Omega plate reader (BMG LABTECH Ltd, Aylesbury, UK).

6.2.9 Haemocompatibility of Selected NP Formulations

To assess the influence of the NP formulations (F2, F18 and their blank counterparts) on haemolysis, erythrocytes were obtained from sheep whole blood. 1 mL of fresh sheep blood was centrifuged at 9500 rpm for 5 minutes, the supernatant containing the lysed cells was discarded and the cell pellet washed in 5 mL of PBS. The PBS wash was repeated until the supernatant was completely clear, then 2% of erythrocyte solution was prepared in PBS and 180 µL added to each well along with 20 µL of the NP suspensions, IRH solutions, negative control and positive control with mixing. Incubation was performed at 37°C for 3 hours and 6 hours followed by plate centrifugation at 1000 rpm for 1 minute. 100 µL of the supernatant was transferred to a fresh flat bottomed 96 well plate and the absorbance at 540 nm recorded using FLUOstar Omega plate reader (BMG LABTECH Ltd, Aylesbury, UK). %Haemolysis was calculated as follows: ((X-Y) / (Z-Y) x 100, where X is the absorbance of the

sample, Y is the background from the PBS (negative control) and Z is the absorbance of 100% lysis from the positive control (10% Triton-X).

6.2.10 Interleukin-6 (IL-6) Protein Expression in Primary HGG Cells

IL-6 protein expression was analysed in the supernatant of primary HGG cells collected at day 3 and 5, using IL-6 Human Duoset ELISA kit. Firstly, the ELISA microplate wells were coated with 100 µL of 2 µg/mL of the capture antibody and incubated at room temperature overnight. The next day, the wells were washed with 200 µL wash buffer 3 times. Then, the plate was blocked by adding 300 µL of reagent diluent per well for one hour. The washing step was then repeated 3 times. Then 100 µL of samples and standards were diluted in reagent diluent and added to the wells for 2 hours of incubation at room temperature. Washing was then repeated 3 times using the wash buffer. The detection antibody was diluted to 50 ng/mL and 100 µL were added to the wells and incubated at room temperature for 2 hours. The washing step was repeated thrice, then 100 µL of 1: 40 diluted streptavidin-horseradish peroxidase (HRP) was added to the wells and incubation occurred for 20 minutes at room temperature away from direct light. Aspiration and washing of the wells were performed three times with wash buffer. 100 µL of substrate solution was added to the wells and the plate was incubated for 20 minutes at room temperature protected from light. Finally, 50 µL of stop solution was added to each well with gentle tapping to ensure thorough mixing and the optical density (OD) was determined at 450 nm using a FLUOstar Omega plate reader (BMG LABTECH Ltd, Aylesbury, UK).

6.2.11 Statistical Analysis

The statistical analysis was carried out with GraphPad Prism, version 9. Two-way ANOVA (Analysis of variance) was used for multiple comparisons between the similar concentrations of the free drug and the nanoparticle formulations with regards to the treatment time. Tukey's post hoc test was carried out in the analysis. The statistical significance was presented as: $p \leq 0.0001$, $p \leq 0.05$. Non-significance was presented for $p > 0.05$. Data were presented as mean (n = 3) ± SD.

6.3 Results

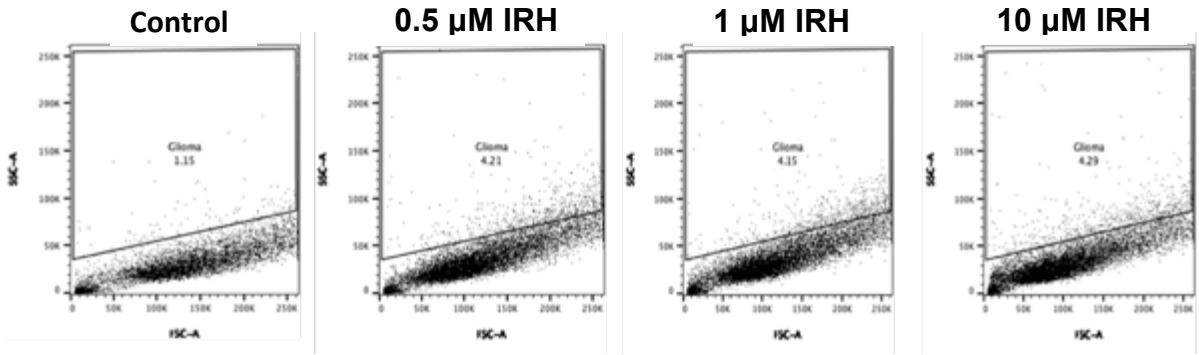
6.3.1 Cellular Uptake

6.3.1.1 Analysis of Cellular Uptake by Flow Cytometry

Figure 6.1 to Figure 6.5 display dot plots of HGG cellular uptake of free IRH and NP formulations assessed over a period of 9 days. As shown in the figures, there was a dose-dependent increase in cellular uptake of the treatments. Figure 6.6 to Figure 6.8 present the intensity of side scattered light (SSC) of cells treated with free IRH and NP formulations. As shown in the figures, there was no significant difference in SSC intensity between cells treated with IRH free drug and the negative control across all days and doses. However, this could be due to insufficient light scattering by the drug molecules within the solution. On day 1, there was a significant difference ($P<0.0001$) between F2 and the IRH treated groups as well as the negative control group across all doses indicating a higher uptake of F2 compared to free IRH (Figure 6.6). The group treated with the highest concentration of F2 had the highest cellular uptake among all

groups. Cellular uptake almost reached a plateau on day 3 and 5 and then was reduced significantly (P<0.0001) on day 7 and 9 compared to day 1 (Figure 6.6). A significant difference (P<0.0001) between the low and high concentrations and/or the medium and high concentrations of F2 treated groups was noticeable on each day. The highest SSC intensity of which was achieved by the highest concentration (Figure 6.6).

A similar trend to the F2 group was observed with the F18 (Figure 6.7) and blank F18 (Figure 6.8) groups in which there was a significant difference between low and medium; and medium and high concentrations across most days (P<0.0001). On day 1, a significant difference (P<0.0001) between F18 and IRH groups; and F18 and negative control groups was obvious across all doses indicating a higher uptake of F18 (Figure 6.7). The highest concentration of F18 also resulted in the highest SSC intensity in the HGG cells (Figure 6.7). However, SSC intensity was reduced significantly (P<0.0001) by day 9 suggesting cytotoxicity of cells that engulfed the particles leaving behind the more viable cells with minimal cellular uptake. The SSC intensity of cells treated with F18 was significantly higher than those treated with F2 on day 1 for all three concentrations (P<0.0001) and continued to be higher on day 5, 7 and 9 for the highest concentration.



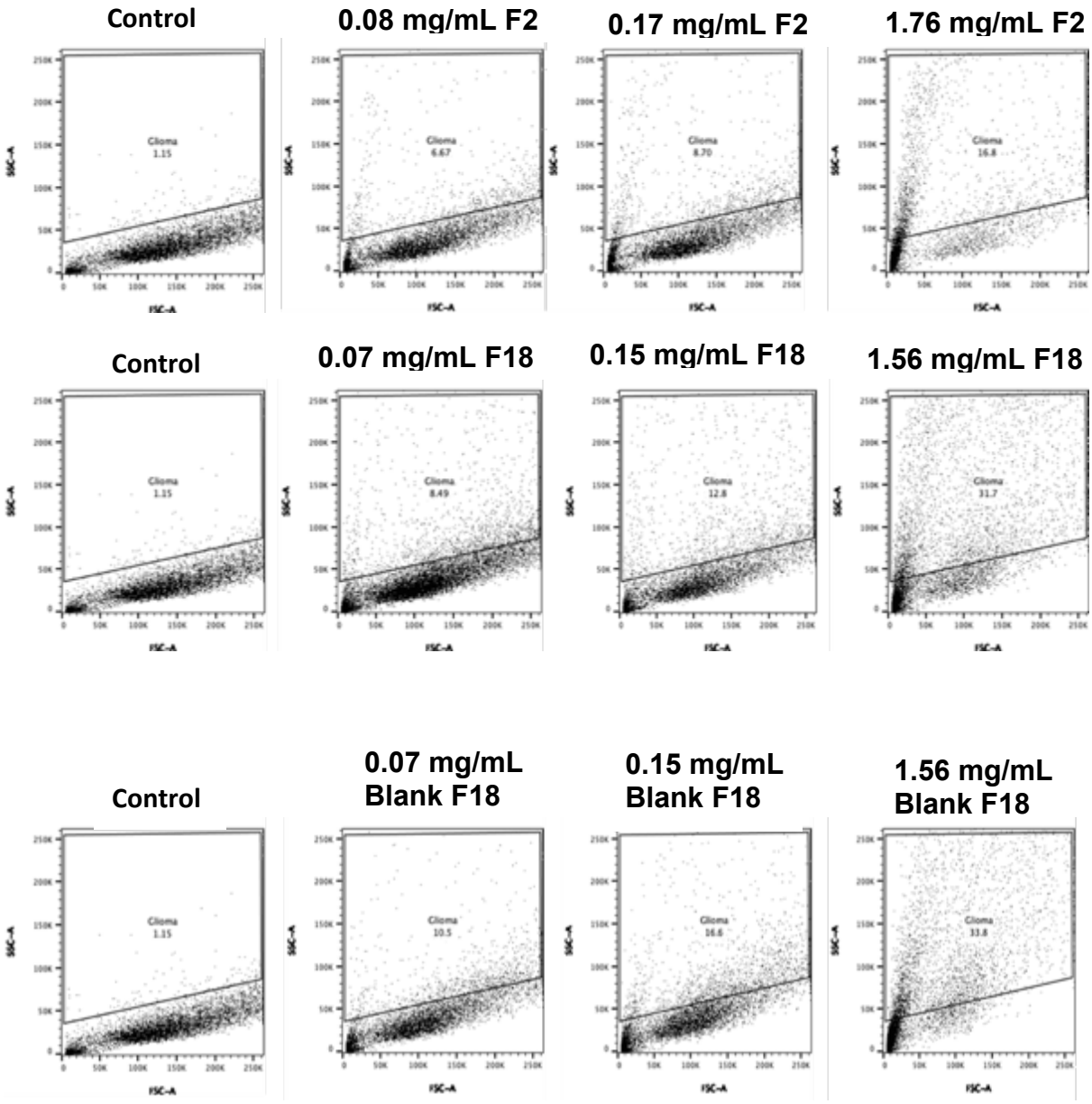
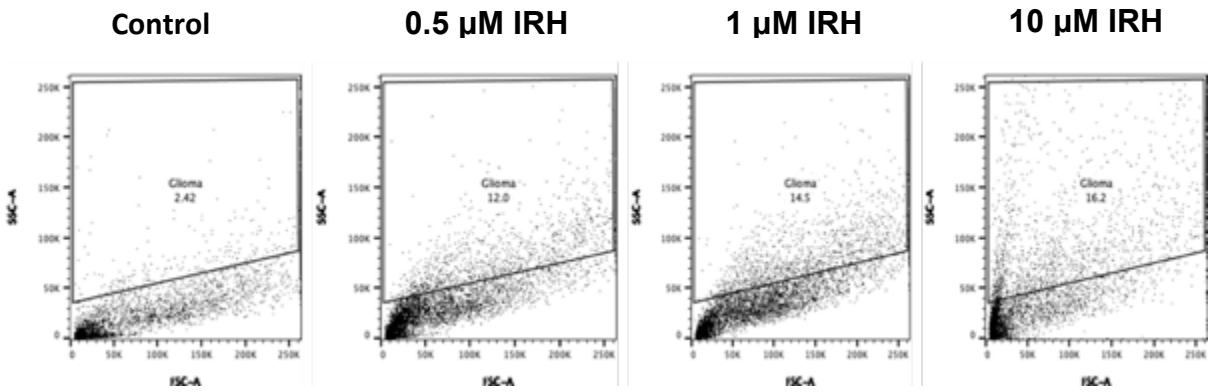


Figure 6.1. HGG cellular uptake of low, medium, and high concentrations of free IRH and NPs after 1 day of treatment.



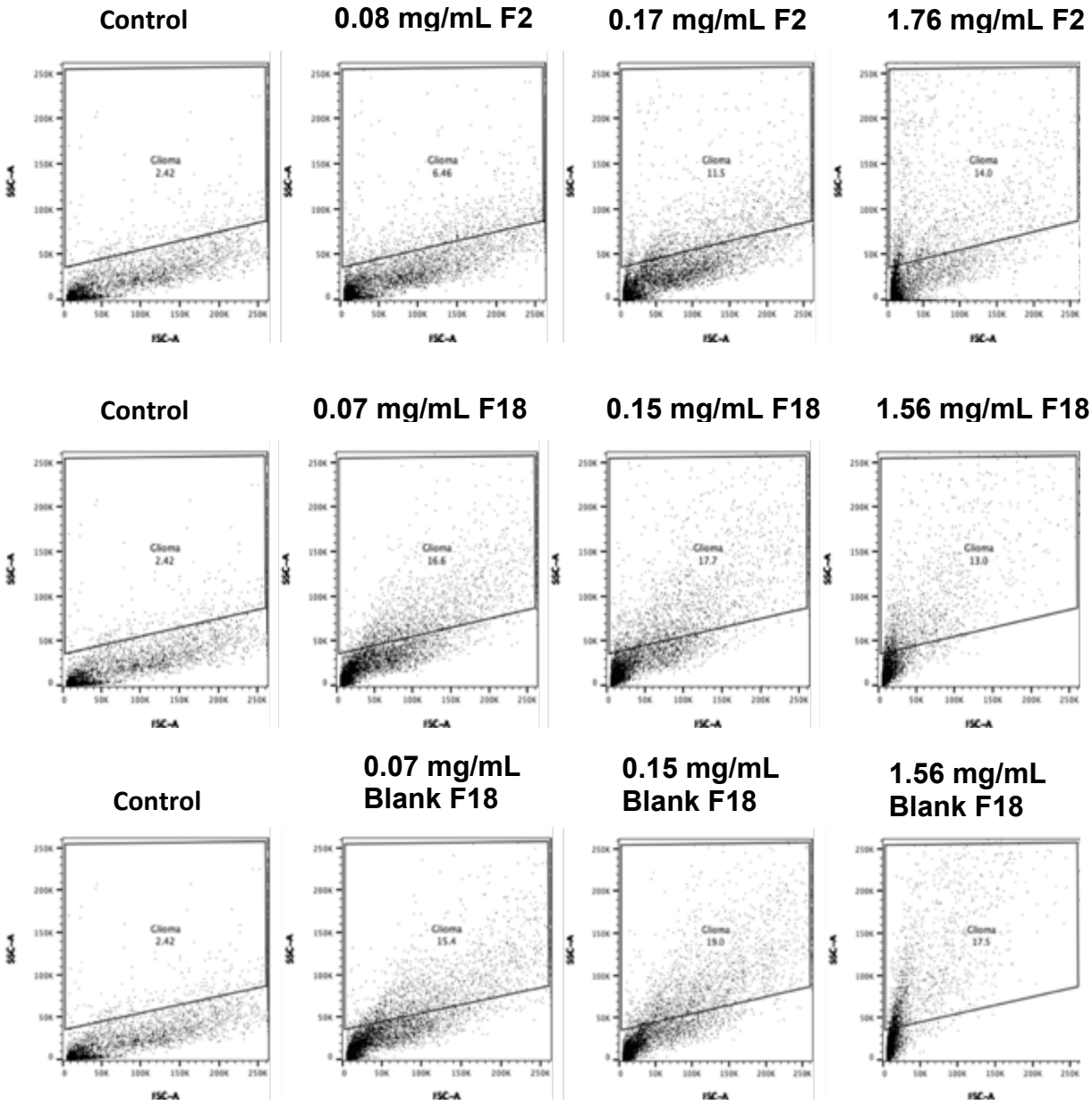
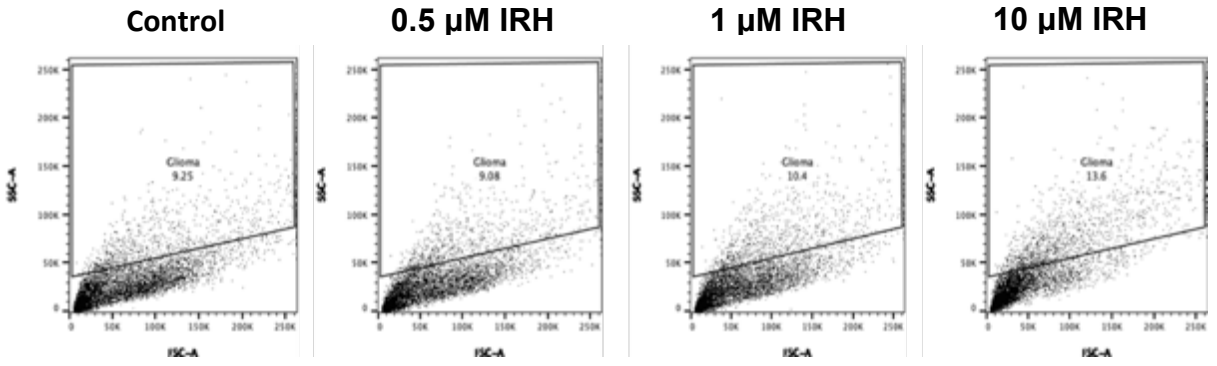


Figure 6.2. HGG cellular uptake of low, medium and high concentrations of free IRH and NPs after 3 days of treatment.



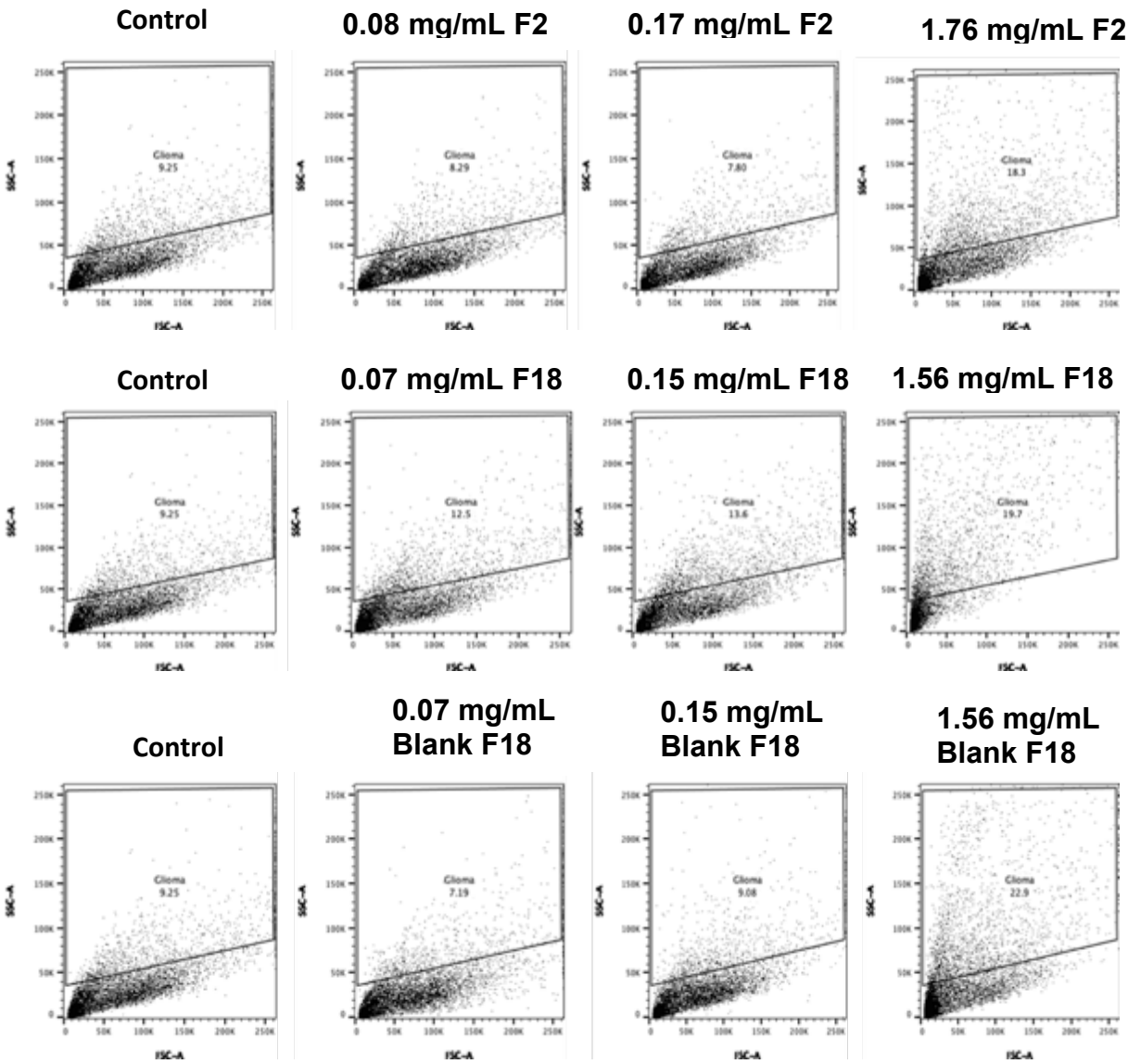
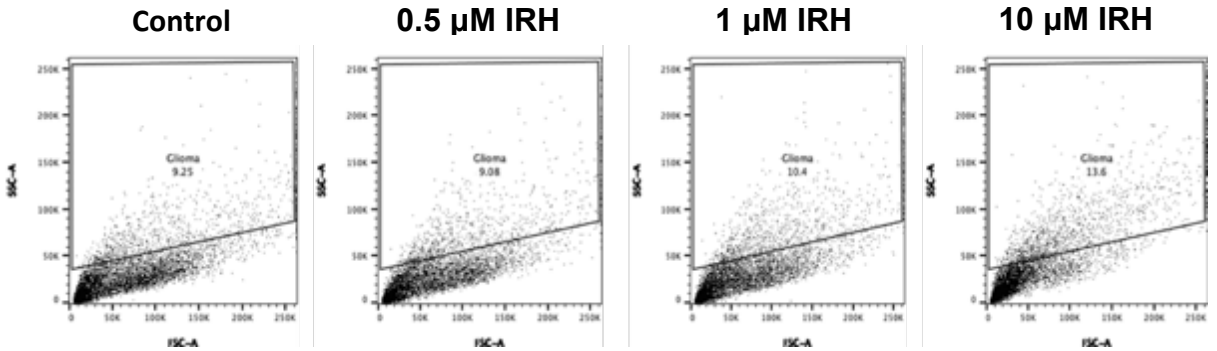


Figure 6.3. HGG cellular uptake of low, medium, and high concentrations of free IRH and NPs after 5 days of treatment.



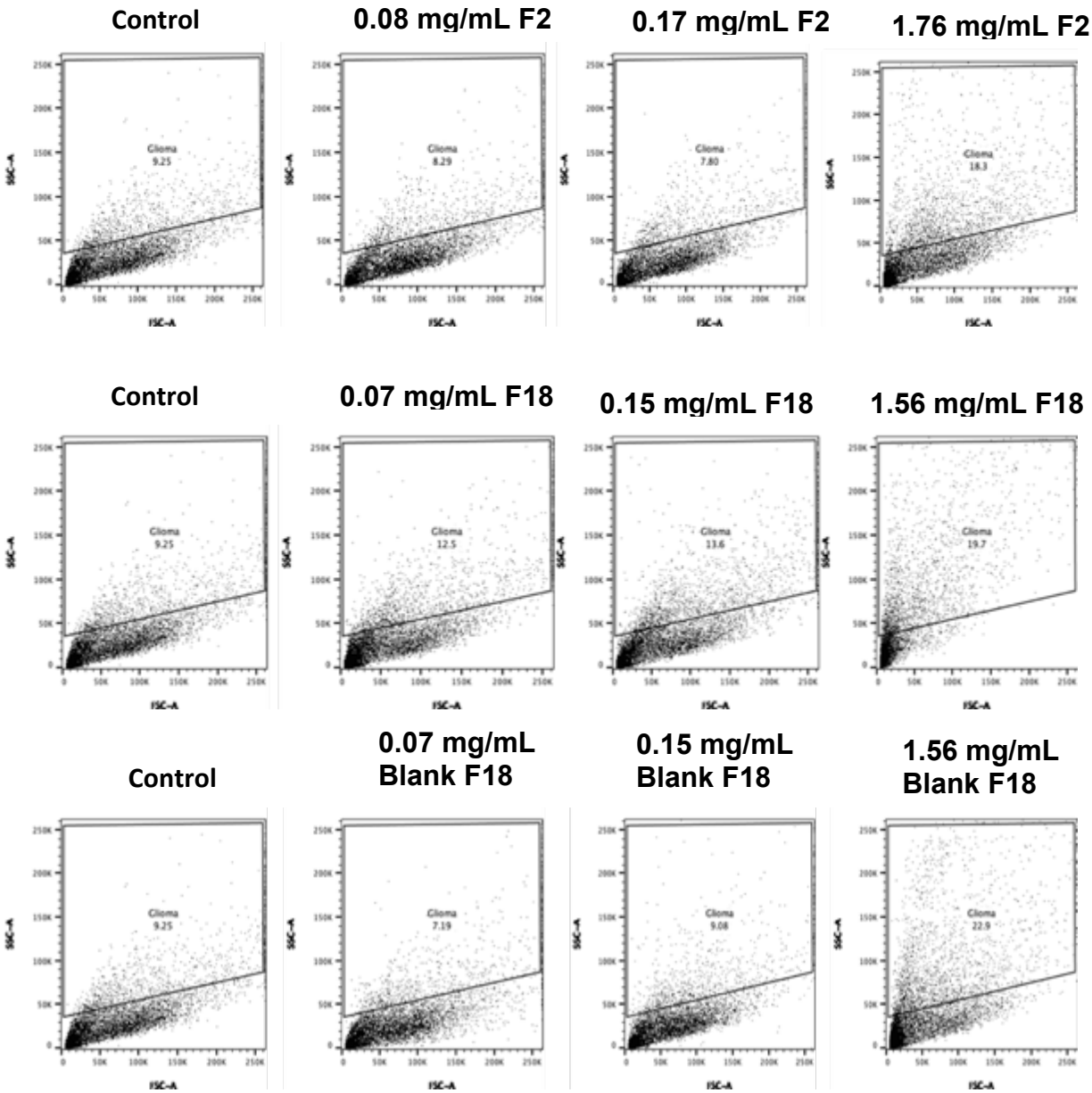


Figure 6.4. HGG cellular uptake of low, medium and high concentrations of free IRH and NPs after 7 days of treatment.

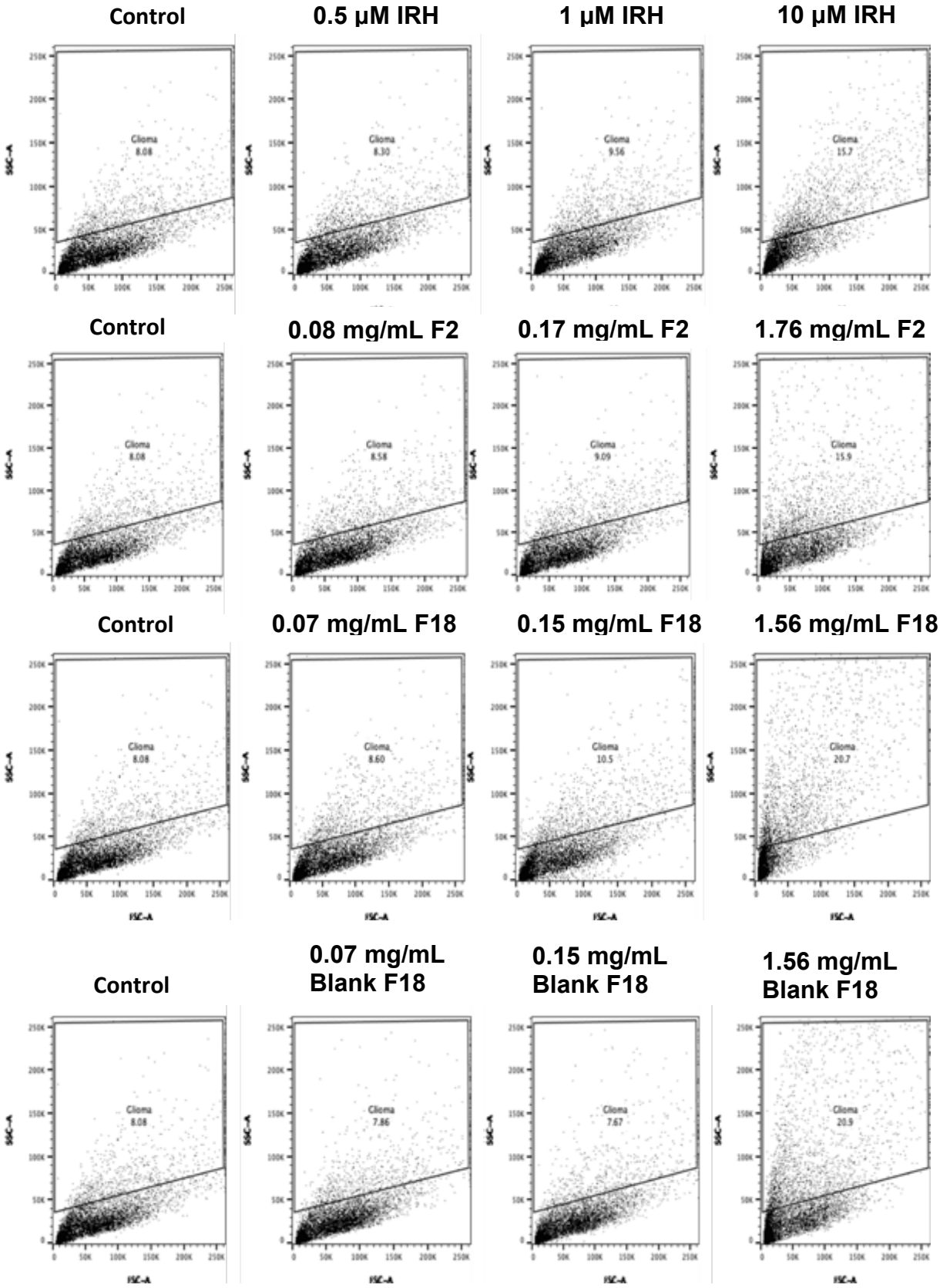


Figure 6.5. HGG cellular uptake of low, medium, and high concentrations of free IRH and NPs after 9 days of treatment.

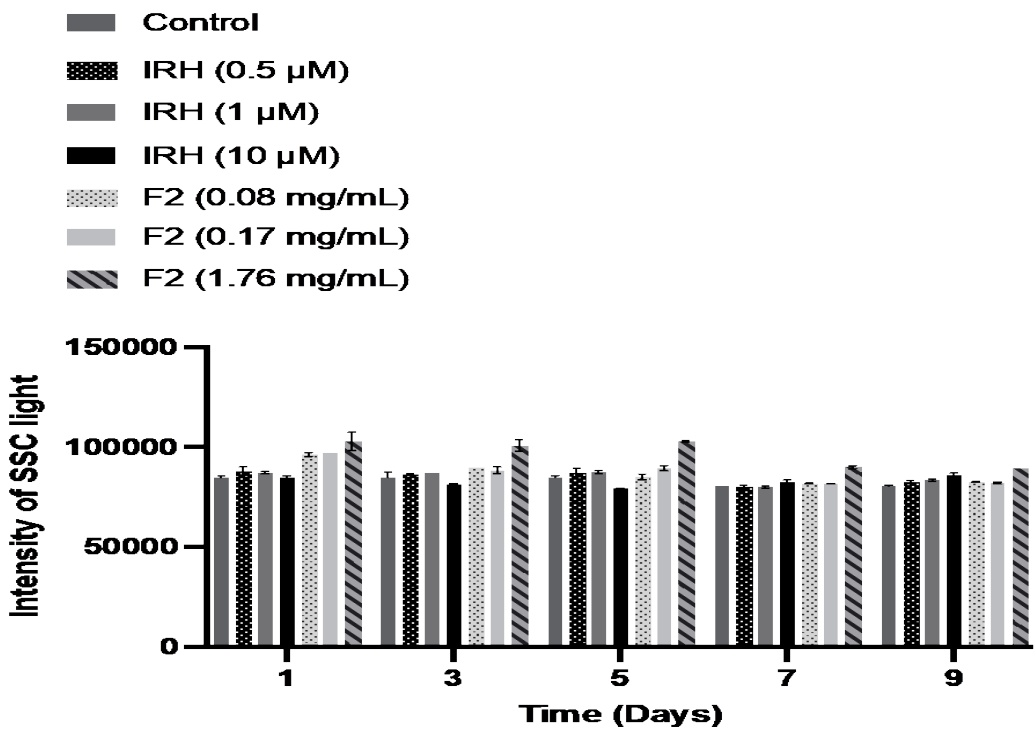


Figure 6.6. SSC intensity of HGG cells treated with low, medium, and high concentrations of free IRH and F2 over 9 days (n=3).

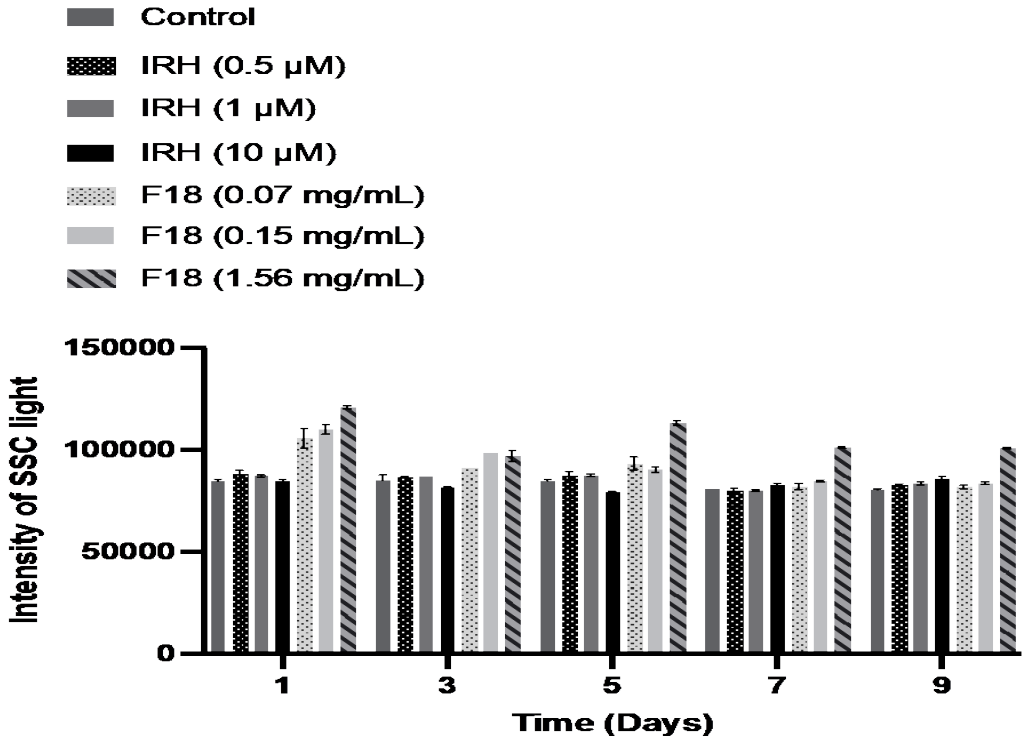


Figure 6.7. SSC intensity of HGG cells treated with low, medium, and high concentrations of free IRH and F18 over 9 days (n=3).

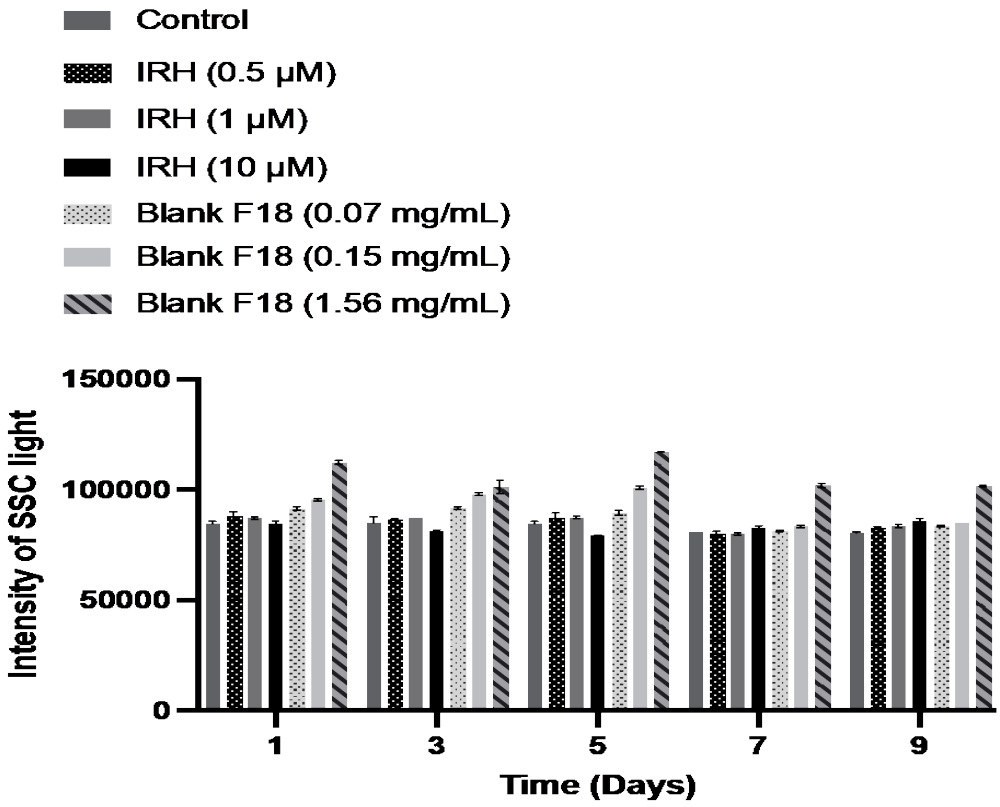


Figure 6.8. SSC intensity of HGG cells treated with low, medium, and high concentrations of free IRH and blank F18 over 9 days (n=3).

6.3.1.2 Analysis of Cellular Uptake by Confocal Microscopy

The subcellular localization of the NPs was assessed by confocal microscopy to determine if the NPs were translocated to the nucleus of the cell, which was stained with DAPI (blue). As shown in Figure 6.9 to Figure 6.14, Rhodamine-123-loaded or IRH-loaded NPs (red) were efficiently internalized by the HGG cells. A volume view 3D image via z-stack of the HGG cells demonstrates that the NPs were localized either inside or surrounding the nucleus.

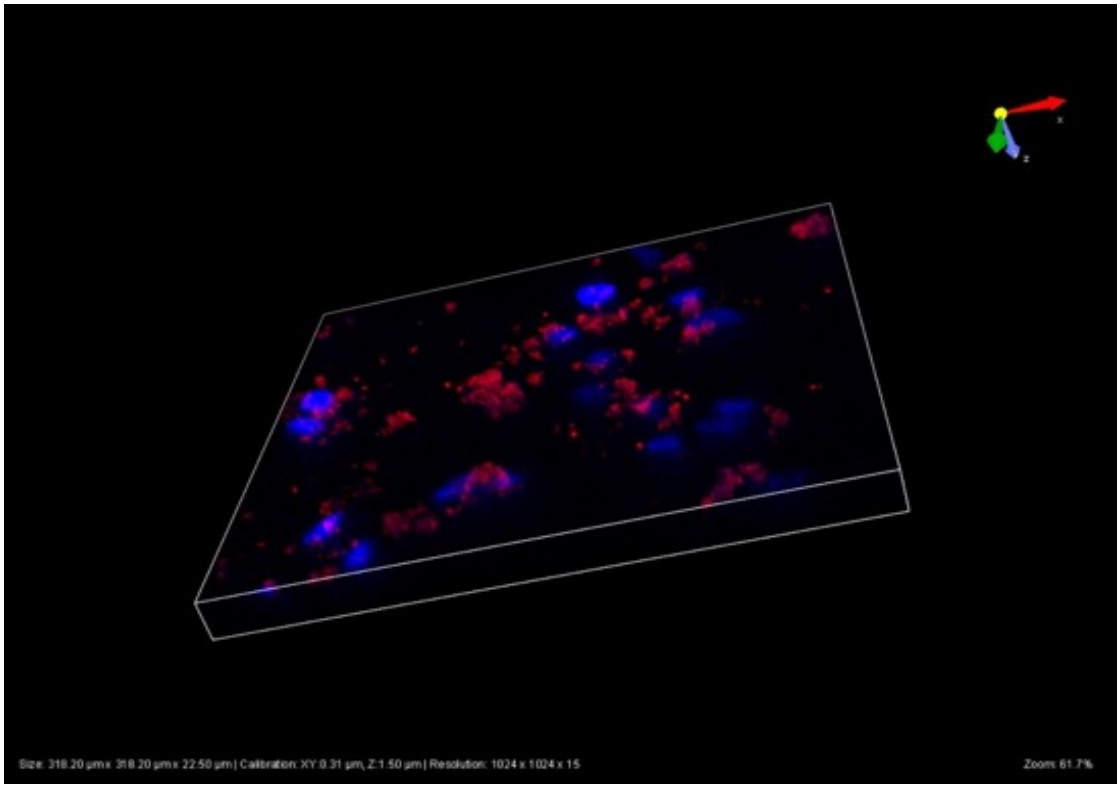


Figure 6.9. Volume view by confocal microscopy showing HGG cells after a 3-day treatment with F2

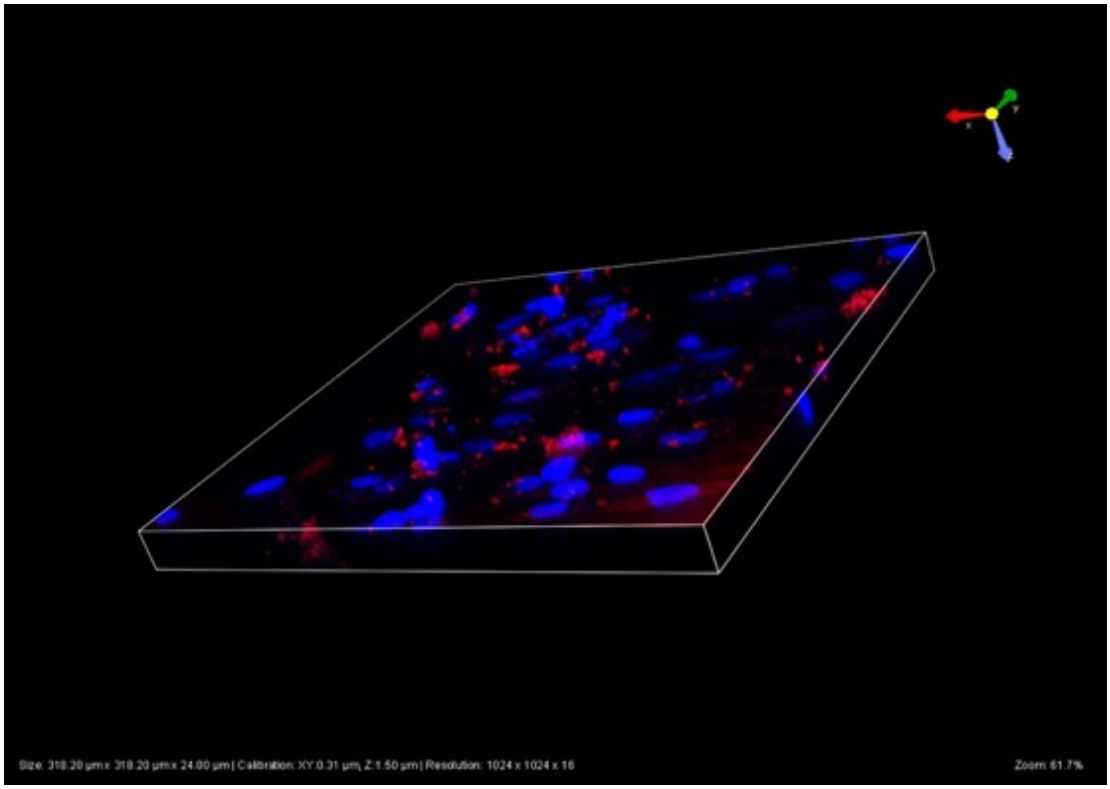


Figure 6.10. Volume view by confocal microscopy showing HGG cells after a 3-day treatment with F18

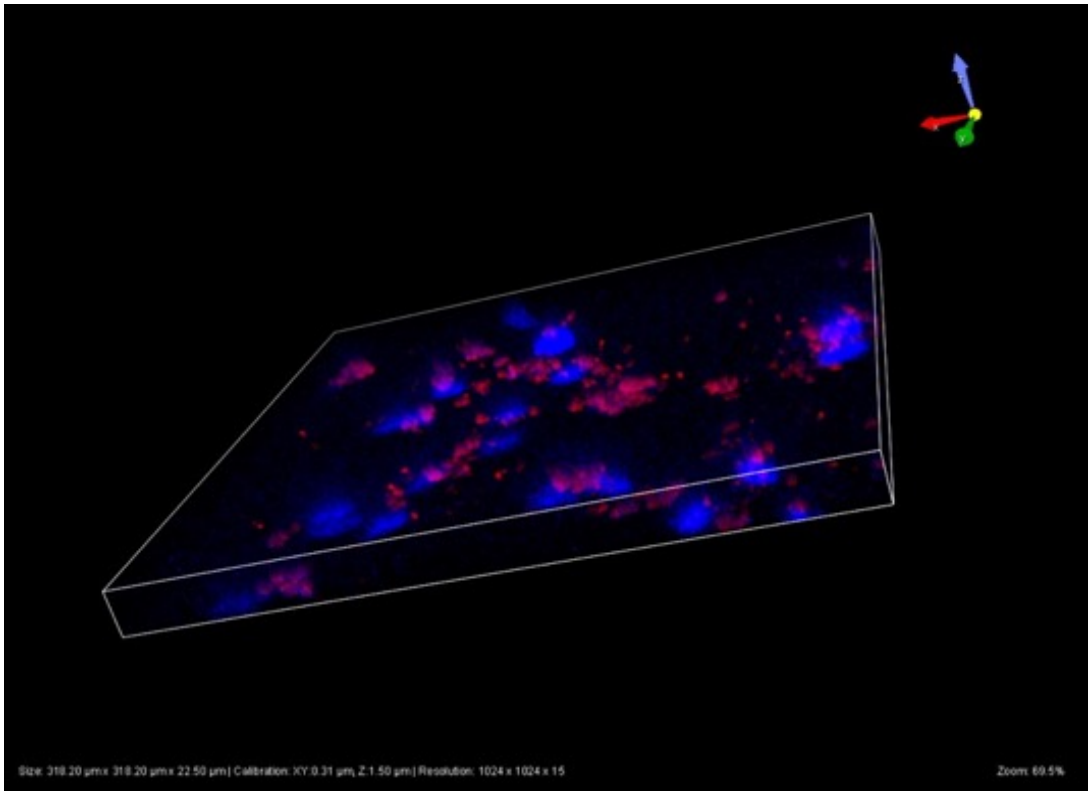


Figure 6.11. Volume view by confocal microscopy showing HGG cells after a 5-day treatment with F2

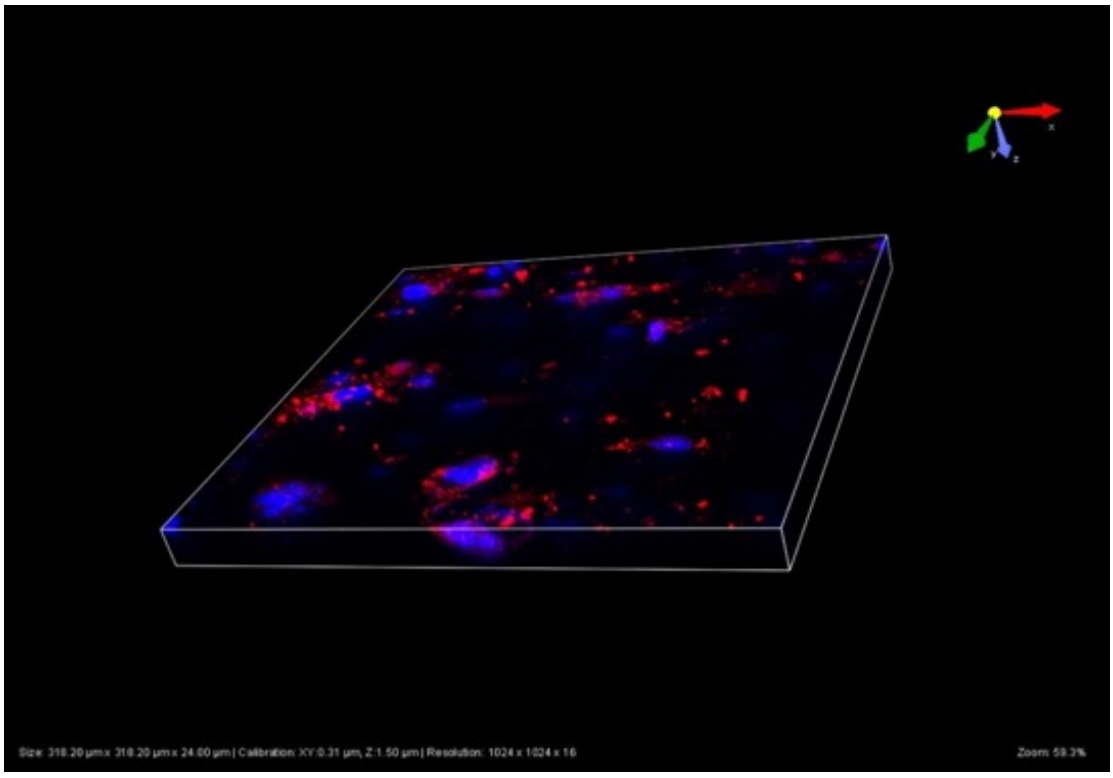


Figure 6.12. Volume view by confocal microscopy showing HGG cells after a 5-day treatment with F18

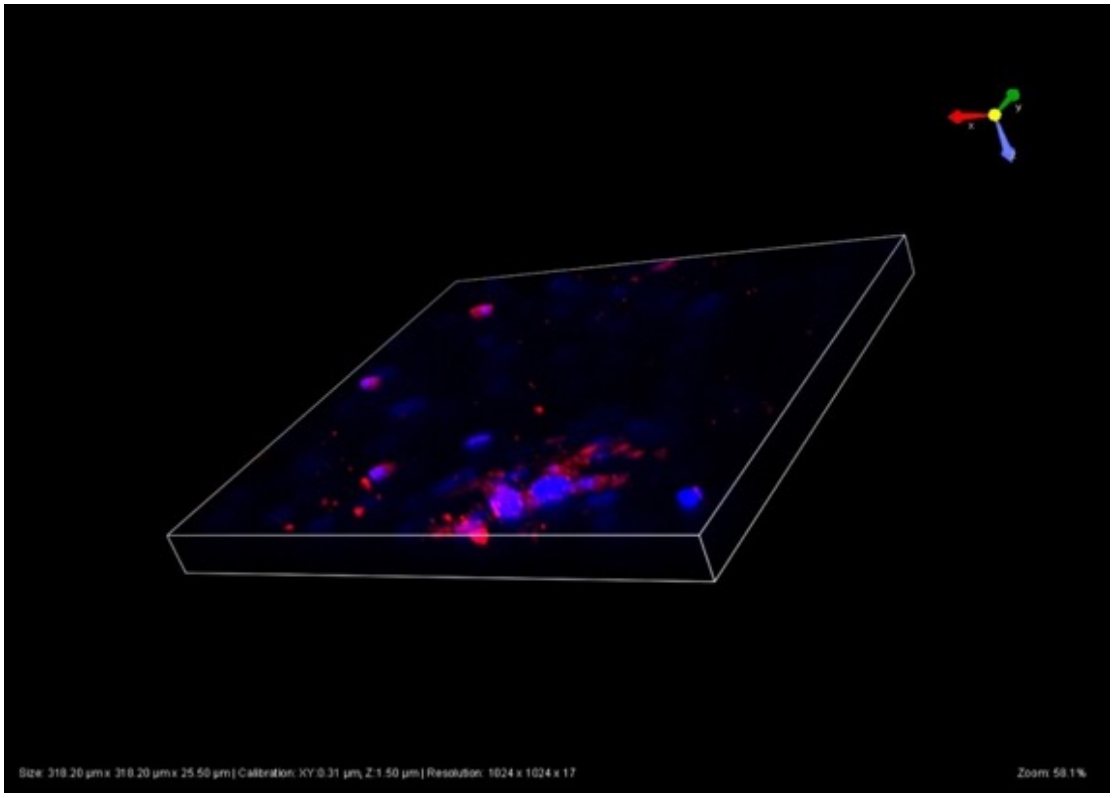


Figure 6.13. Volume view by confocal microscopy showing HGG cells after a 3-day treatment with Rhodamine-123 loaded NPs

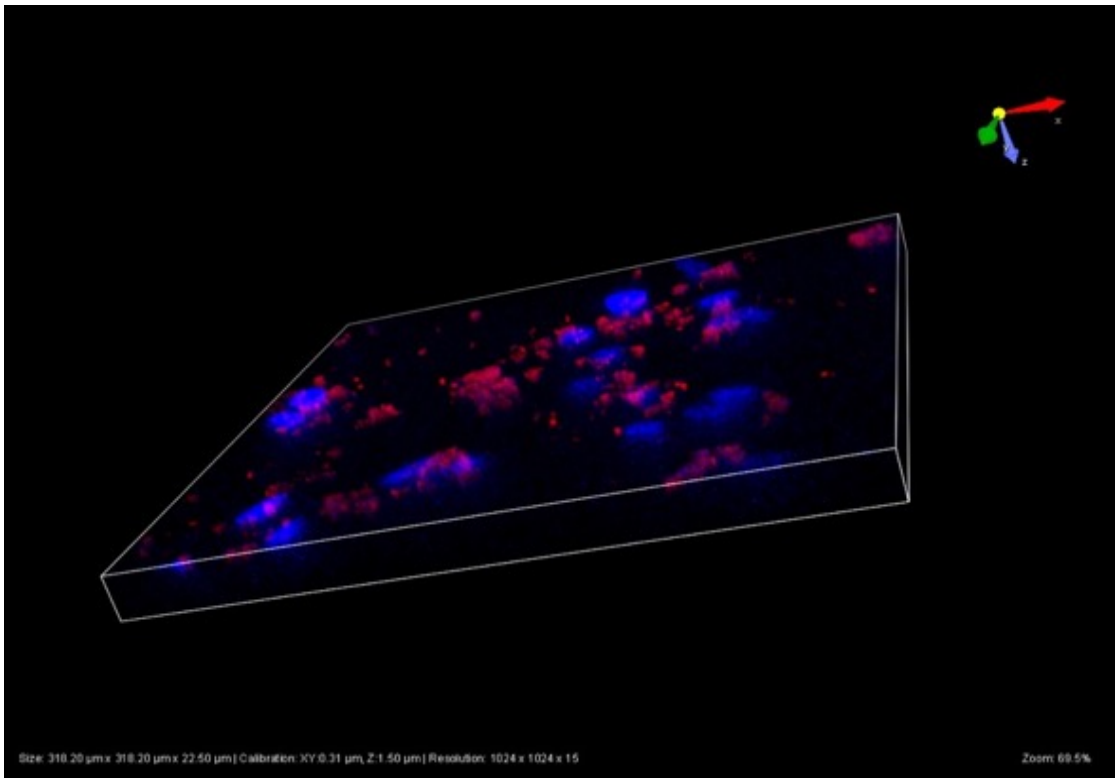


Figure 6.14. Volume view by confocal microscopy showing HGG cells after a 5-day treatment with Rhodamine-123 loaded NPs

6.3.2 Cytotoxicity

The cytotoxic effect of the free IRH, F2 and F18 NPs was determined using primary HGG cells derived from 3 different patients over a period of 11 days. As shown in Figure 6.15, the overall trend of cell cytotoxicity in patient 1 indicated a significantly ($P<0.0001$) higher cytotoxic effect for F2 NPs across all doses and days compared to the negative control and free IRH. By day 11, there was no significant difference between the highest concentrations of IRH and F2 treated cells (Figure 6.15). The greatest cytotoxicity was with F2 and highest dose of free IRH on day 11 reducing viability to less than 20%. While the low and medium concentrations of the free drug achieved 59.20% and 56.13% respectively of cell viability by day 11.

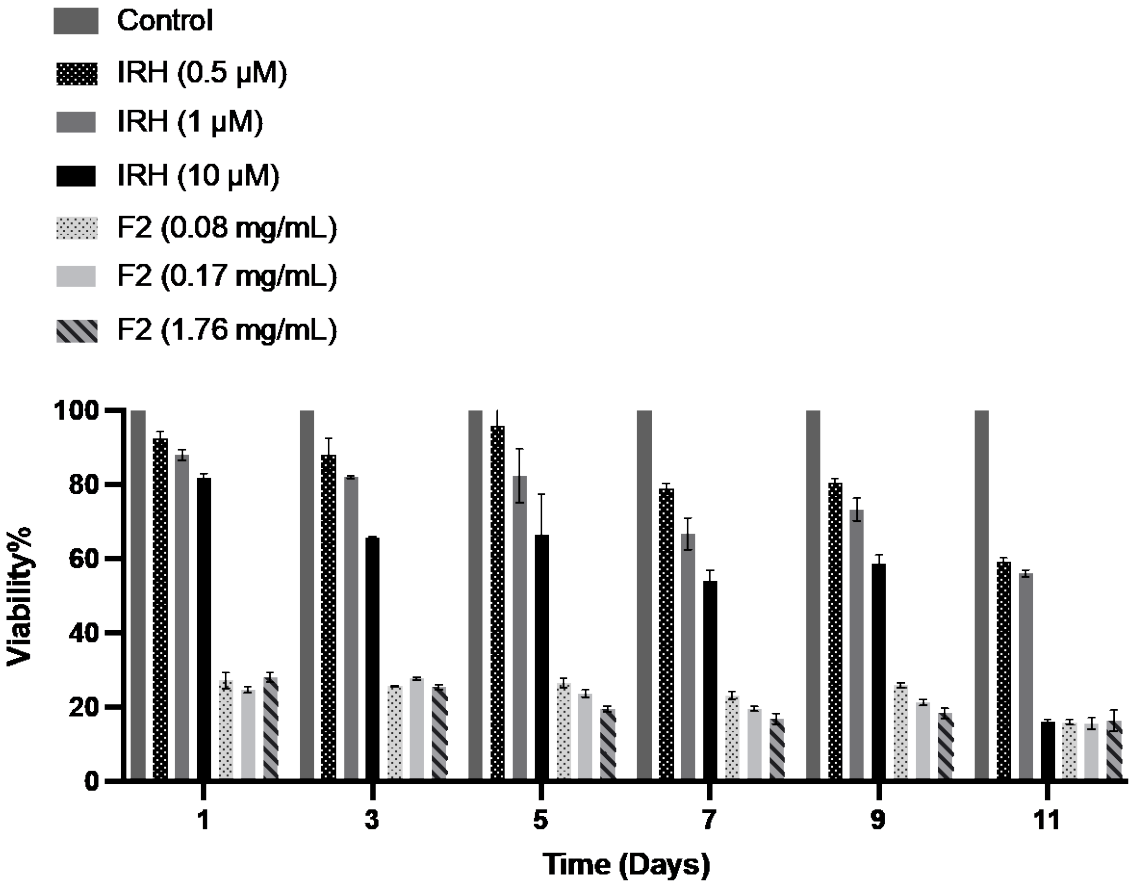


Figure 6.15. Cytotoxicity of free IRH and F2 on primary HGG cells compared to control cells in patient 1 (n=3).

As demonstrated by Figure 6.16, F18 had a significant (P<0.0001) cytotoxic effect across all doses and days compared to the negative control. Furthermore, the cytotoxic effect of F18 against cells derived from patient 1 was significantly (P<0.0001) higher than that of the free drug across days and doses, reducing cell viability to 5.76% for the highest concentration by day 11.

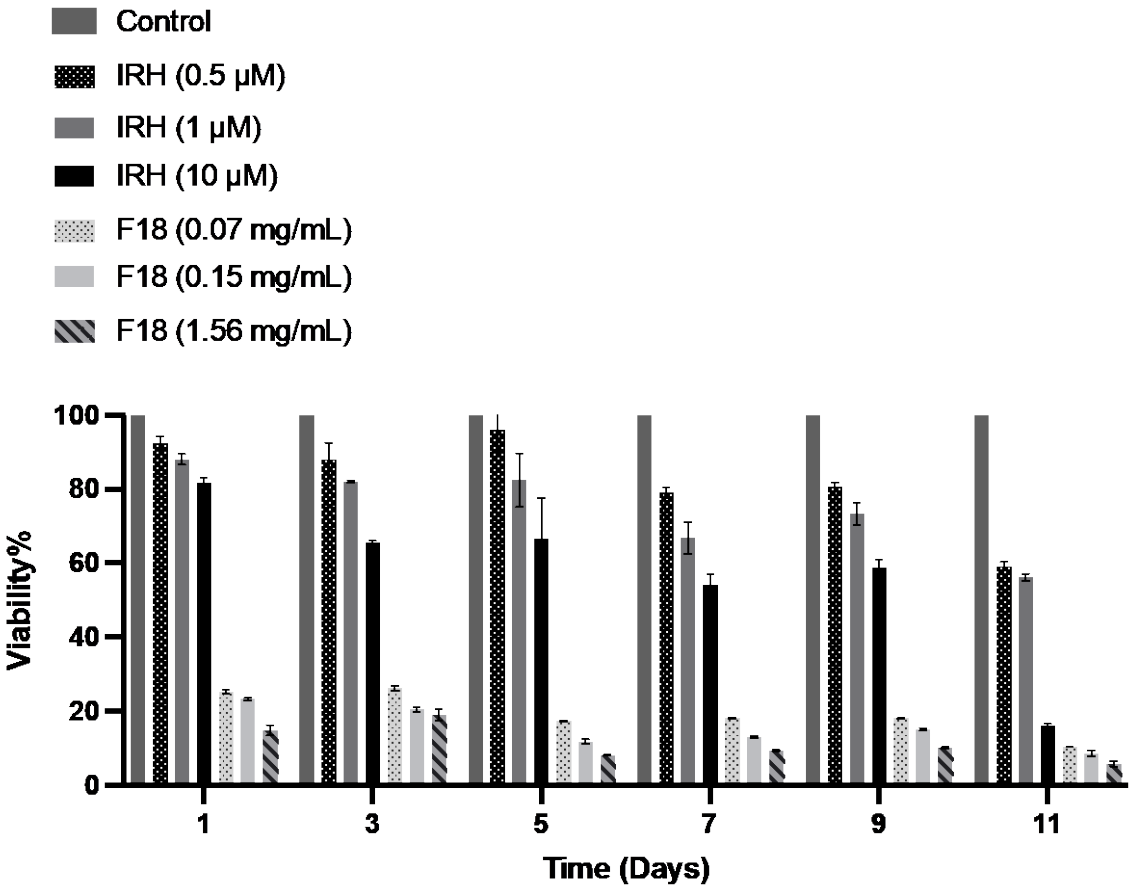


Figure 6.16. Cytotoxicity of free IRH and F18 on primary HGG cells compared to control cells in patient 1 (n=3).

A decreasing trend in cell viability was observed for the Blank F2 NPs on the cells derived from patient 1, which was greater than that achieved with the free IRH and negative control across most days and doses (Figure 6.17). However, by day 11, the cell viability was 40.32% for the highest concentration of the blank NPs compared to

16.14% for the equivalent concentration of free IRH. Additionally, the cells incubated with low and medium concentrations of the blank NPs maintained cell viabilities at 70.14% and 63.72% respectively by day 11 compared to 59.20% and 56.13% respectively for the free IRH.

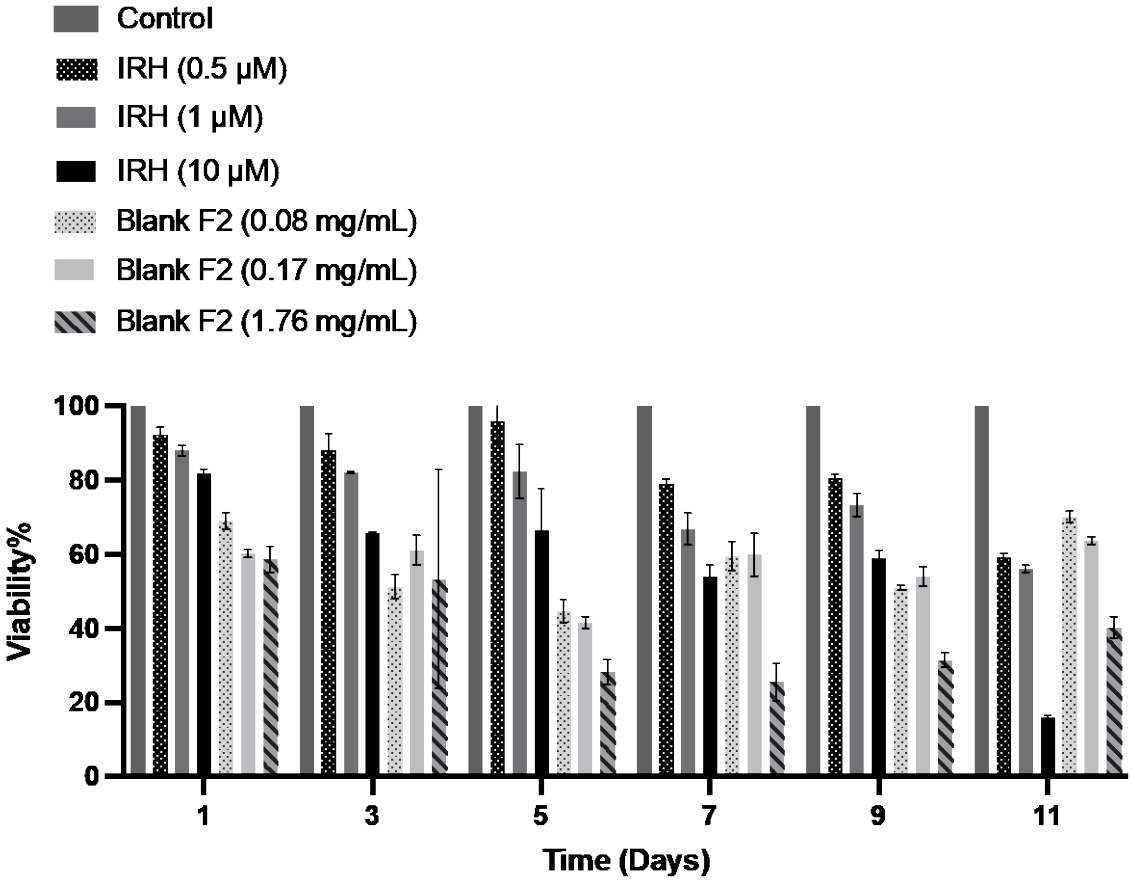


Figure 6.17. Cytotoxicity of free IRH and Blank F2 on primary HGG cells compared to control cells in patient 1 (n=3).

The HGG cells from patient 1 treated with the blank F18 NPs underwent a significant ($P<0.0001$) reduction in cell viability when compared to the cells treated with free IRH and the negative control (Figure 6.18).

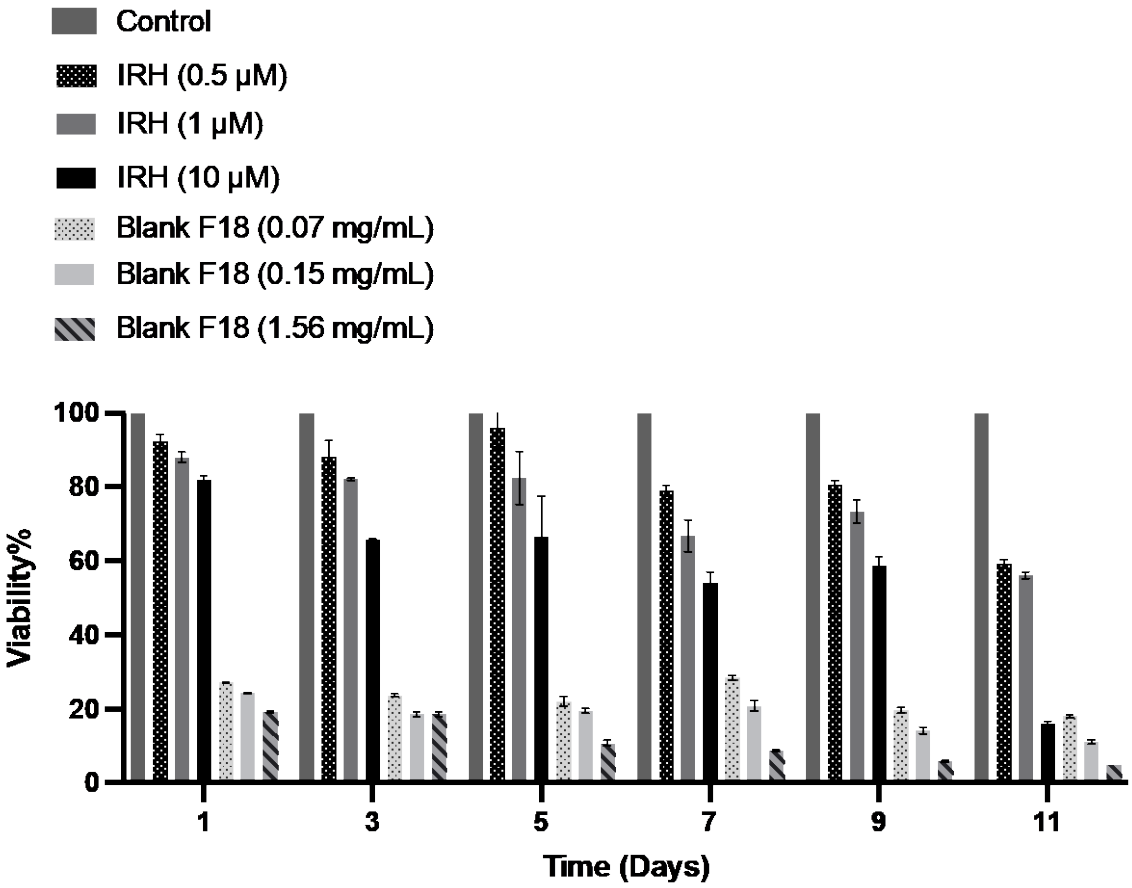


Figure 6.18. Cytotoxicity of free IRH and Blank F18 on primary HGG cells compared to control cells in patient 1 (n=3).

By comparing F2 with their blank counterparts, it was obvious that F2 exerted a significantly ($P<0.0001$) higher cytotoxic effect against HGG cells in patient 1 (Figure 6.19).

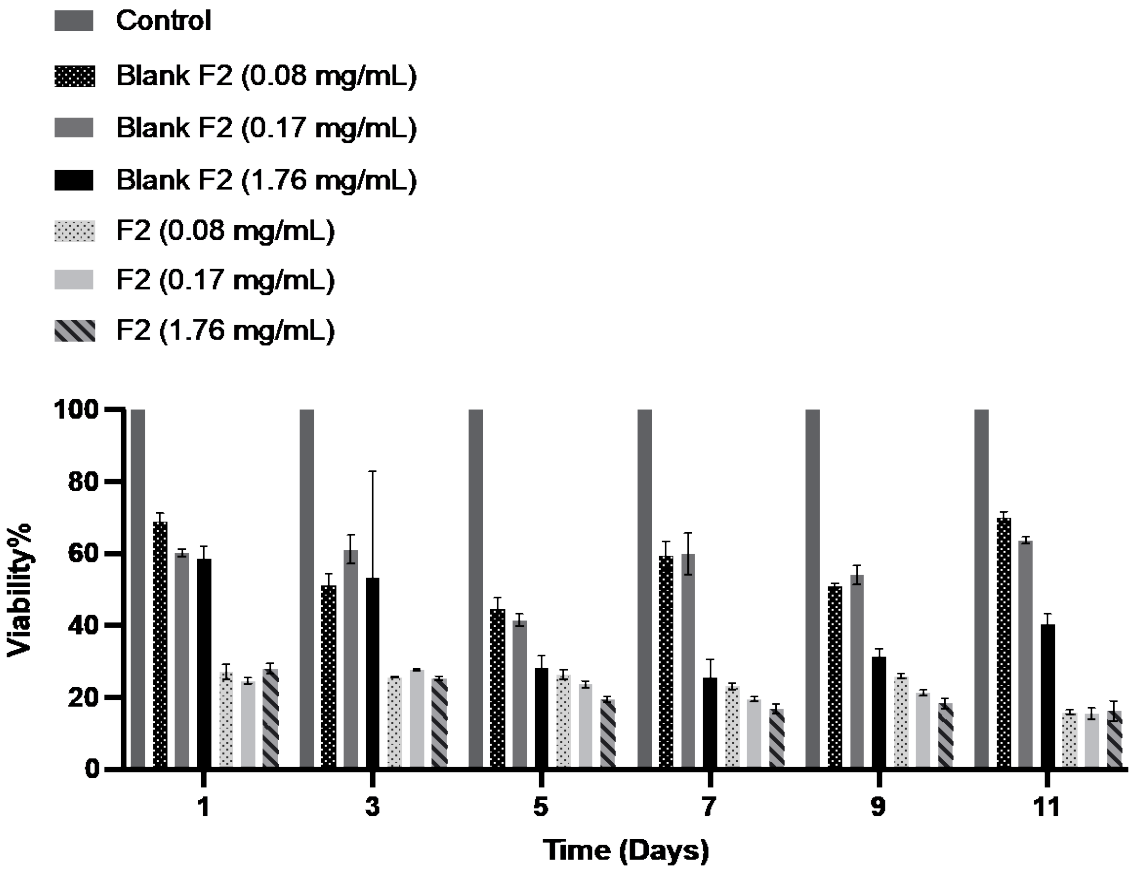


Figure 6.19. Cytotoxicity of Blank F2 and F2 on primary HGG cells compared to control cells in patient 1 (n=3).

There was no significant difference between cells treated with IRH-loaded F18 and blank F18 on day 1 and day 3 across most doses in patient 1 (Figure 6.20). From day 5, the cytotoxicity was significantly ($P<0.0001$) greater for the IRH-loaded F18 for most doses.

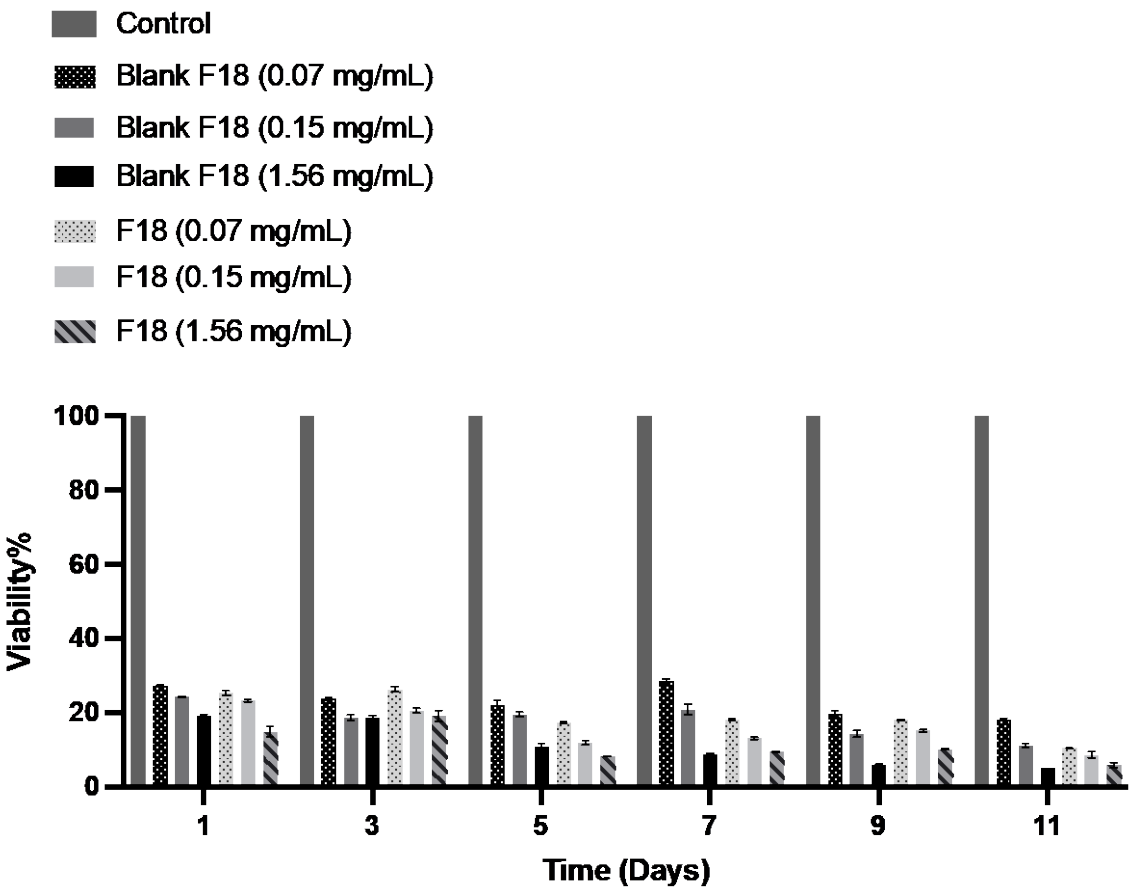


Figure 6.20. Cytotoxicity of Blank F18 and F18 on primary HGG cells compared to control cells in patient 1 (n=3).

In Figure 6.21, F18 and F2 significantly reduced the cell viability in patient 1 although they had a non-significant difference across most doses on day 1 and 3 except for the highest concentration of F18 that was significantly more cytotoxic across all doses and days ($P<0.0001$). From day 5, the cytotoxicity of F18 was significantly greater compared to F2 ($P<0.0001$) across all doses.

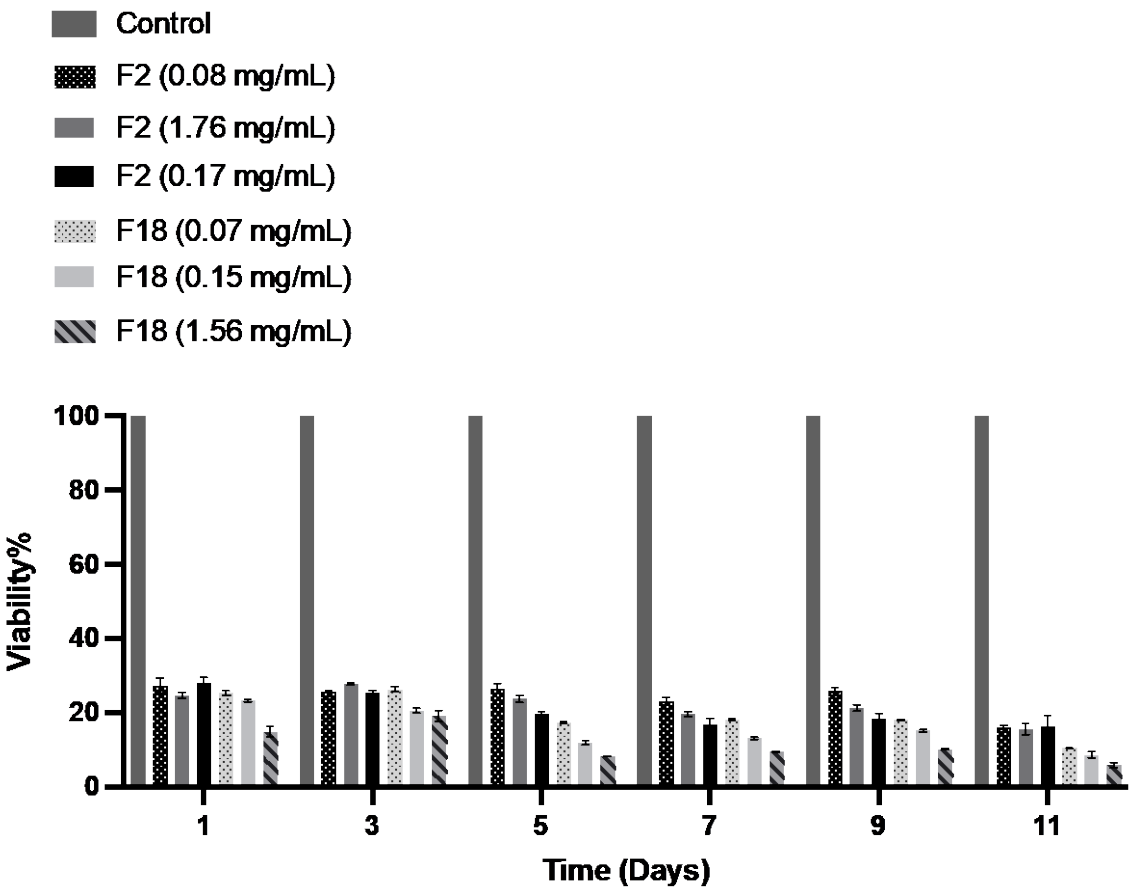


Figure 6.21. Cytotoxicity of F2 and F18 on primary HGG cells compared to control cells in patient 1 (n=3).

The cytotoxicity of the Blank F18 was significantly ($P<0.0001$) higher across all days and doses in patient 1 when compared to blank F2 (Figure 6.22).

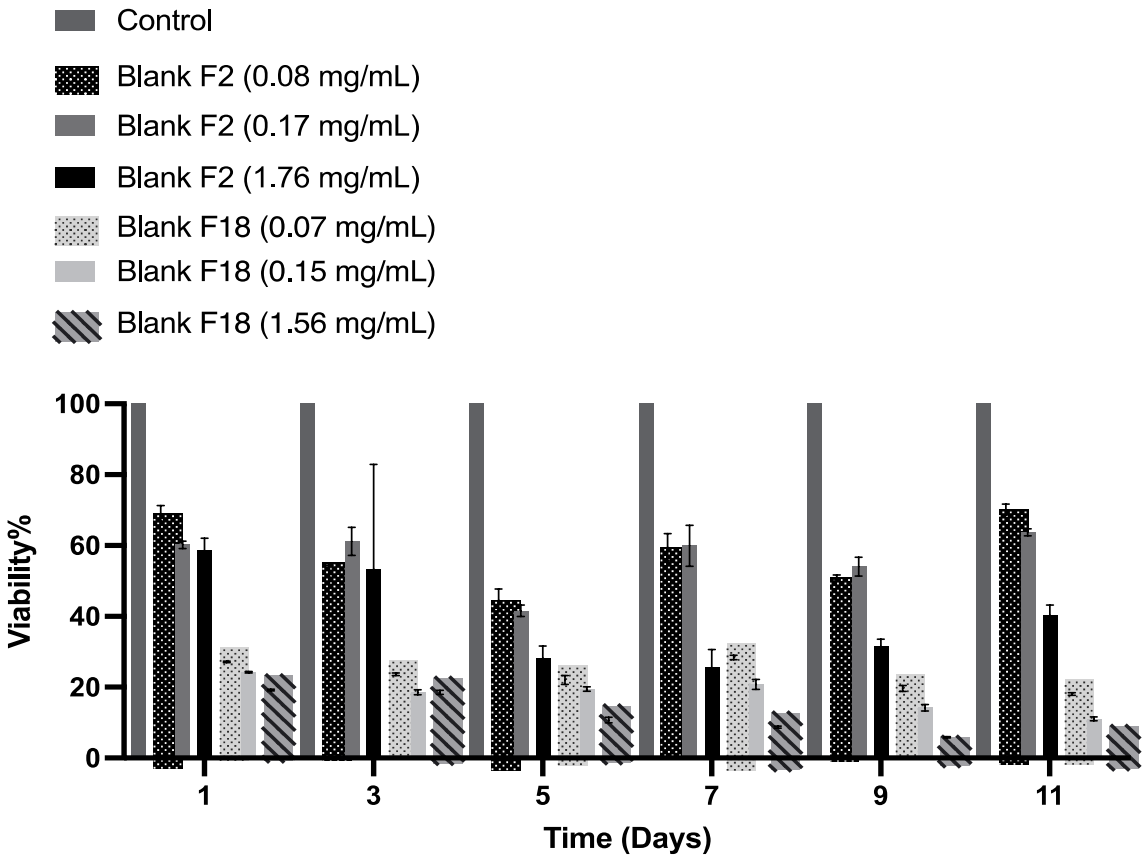


Figure 6.22. Cytotoxicity of Blank F2 and Blank F18 on primary HGG cells compared to control cells in patient 1 (n=3).

In patient 2, F2 and free IRH were significantly more cytotoxic compared to the negative control across all days (Figure 6.23) except for the low concentration of IRH that was non-significant with the control group from day 1 to day 5. However, the free drug was significantly less toxic than F2 across most days and doses ($P<0.0001$). A similar trend to patient 1 was observed in patient 2, in which there was no significant difference between the high concentration of the free drug and F2 by day 11. While, the low and medium concentrations of the free drug maintained 72.27% and 60.50% respectively of cell viability compared to 37.41% and 37.03% respectively of cell viability by F2.

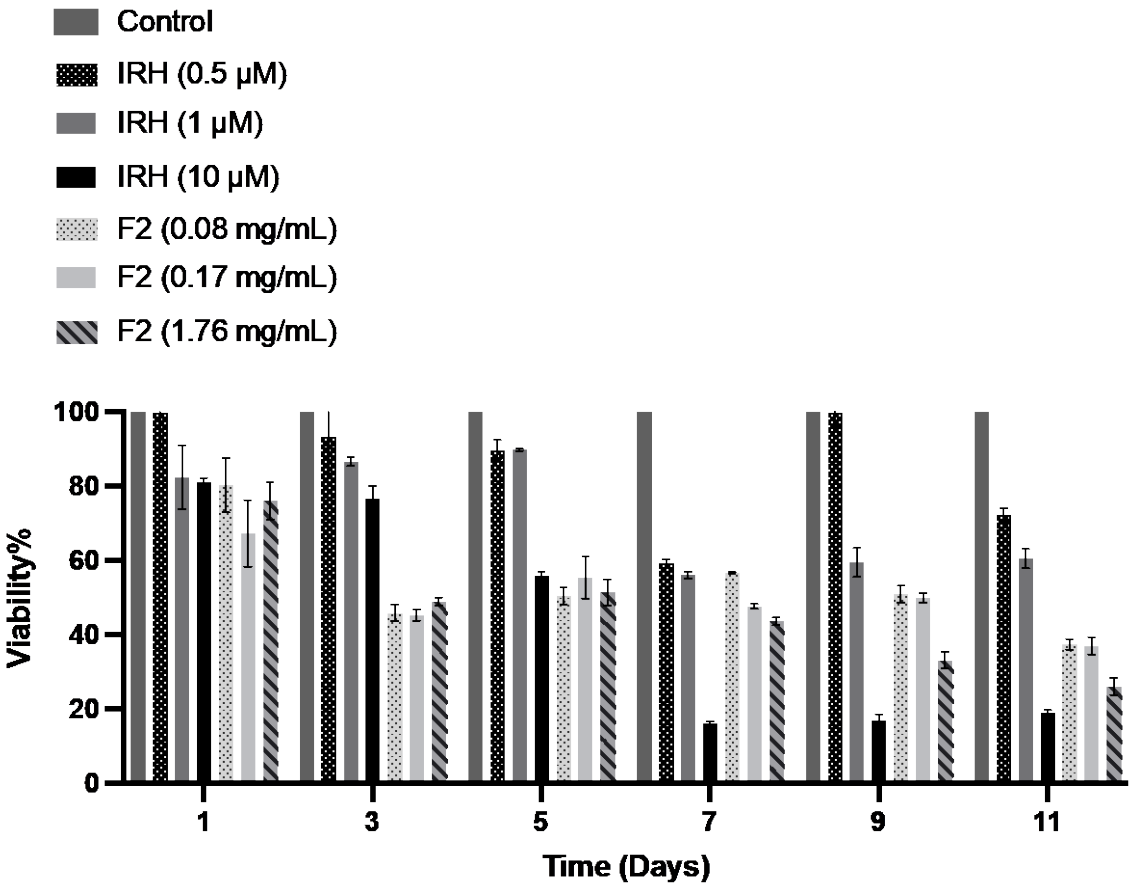


Figure 6.23. Cytotoxicity of free IRH and F2 on primary HGG cells compared to control cells in patient 2 (n=3).

Similar to patient 1, F18 resulted in a significant ($P<0.0001$) increase in cell mortality compared to the free IRH and the negative control across most doses in the HGG cells of patient 2. The lowest cell viability was 4.64%, achieved by the highest concentration of F18 on day 11 (Figure 6.24).

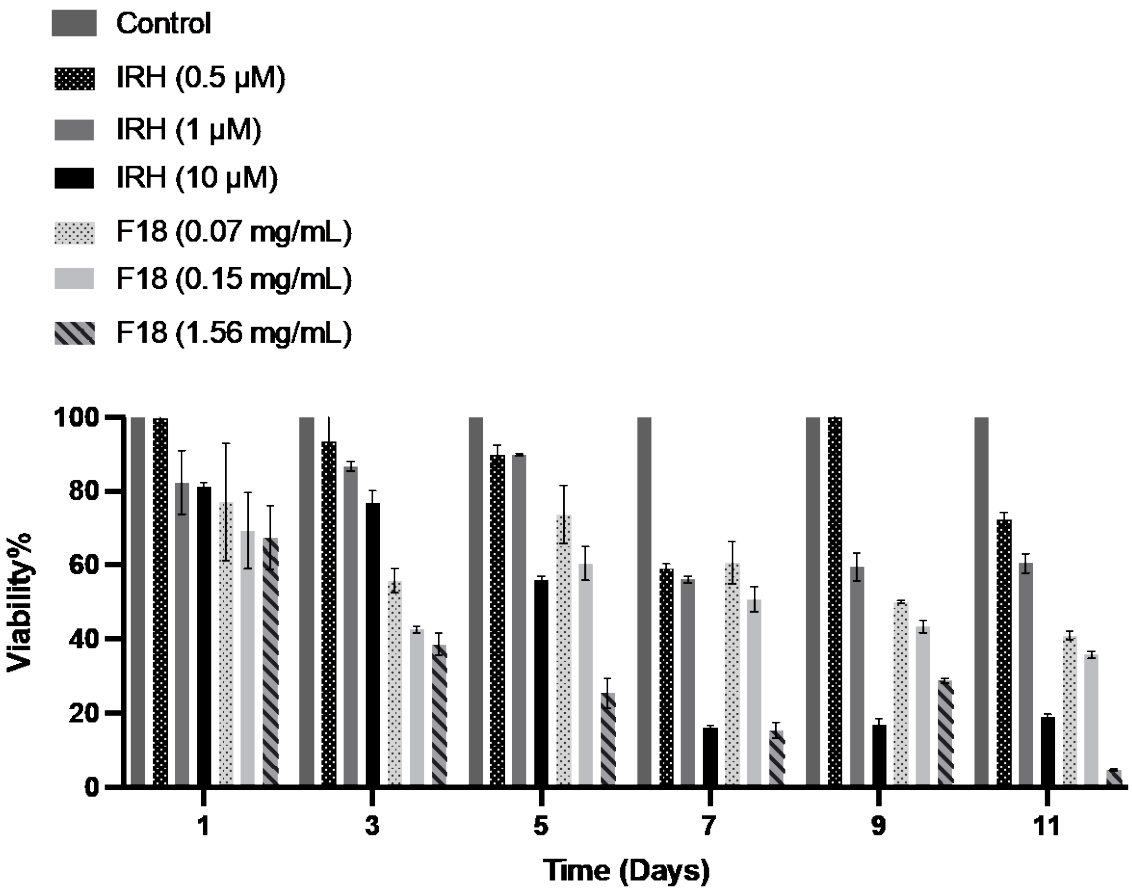


Figure 6.24. Cytotoxicity of free IRH and F18 on primary HGG cells compared to control cells in patient 2 (n=3).

In patient 2, the blank F2 had a cell viability higher than 50% across all days and doses until day 5 where there was a slight reduction in viability before it increased again on day 7. On day 11, the blank F2 maintained cell viability up to 72.68%, 65.66% and 46.48% for the low, medium, and high concentrations respectively as compared to 72.27%, 60.66% and 18.86% for the equivalent concentrations respectively of the free drug (Figure 6.25).

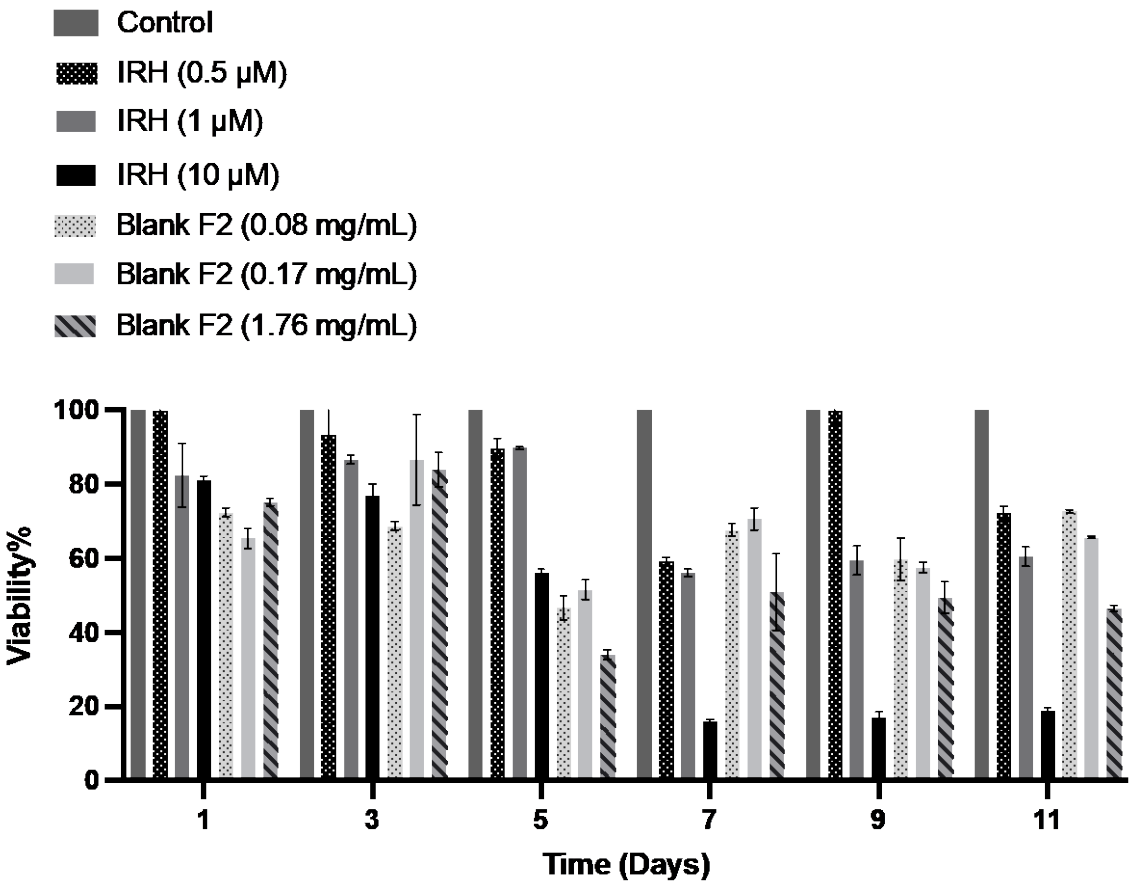


Figure 6.25. Cytotoxicity of free IRH and Blank F2 on primary HGG cells compared to control cells in patient 2 (n=3).

In patient 2, the blank F18 treated group had a higher cell viability compared to patient 1 with the lowest cell viability of 30.48% achieved on day 11 by the highest concentration and compared to 18.86% for the equivalent concentration of free IRH (Figure 6.26).

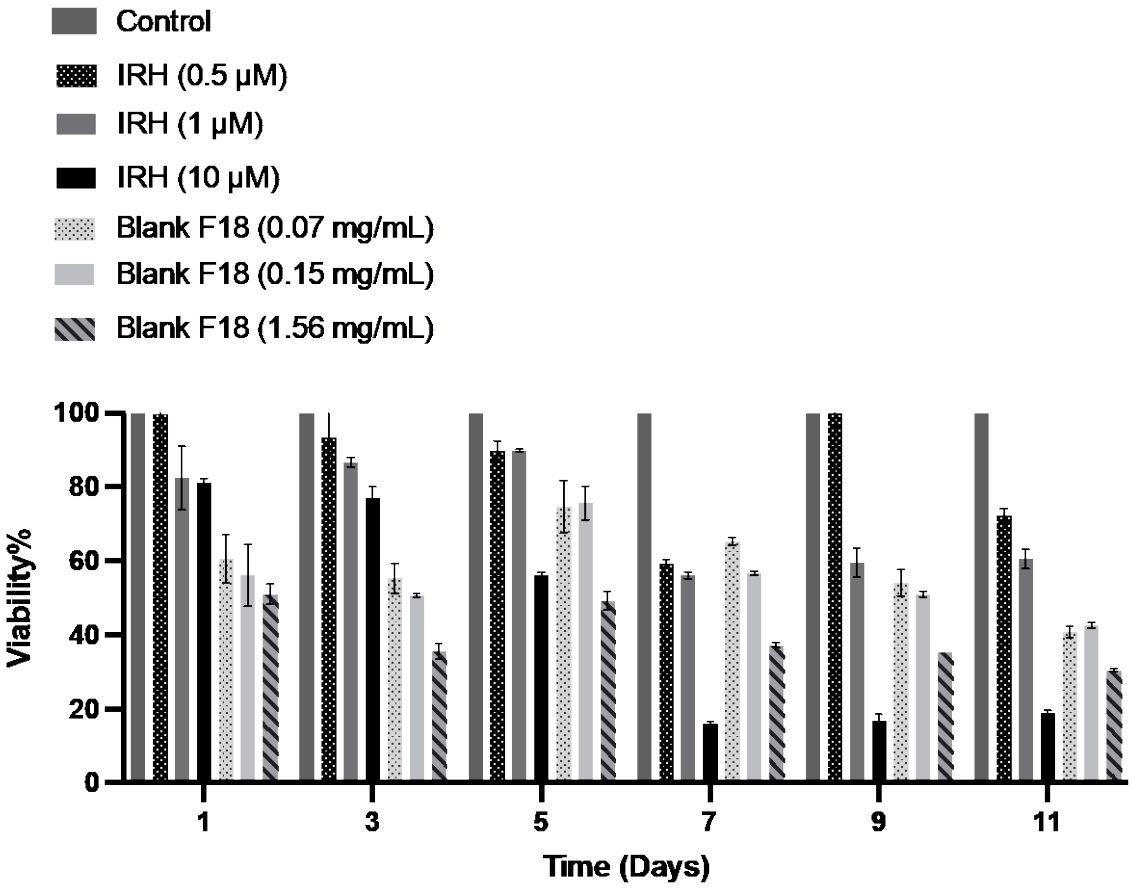


Figure 6.26. Cytotoxicity of free IRH and Blank F18 on primary HGG cells compared to control cells in patient 2 (n=3).

There was no significant difference between IRH-loaded F2 and the blank F2 on cell viability on day 1 for patient 2 (Figure 6.27). However, by day 3, the IRH-loaded F2 NPs started to reduce cell viability more significantly ($P<0.0001$) than the blank F2 across most days and doses (Figure 6.27).

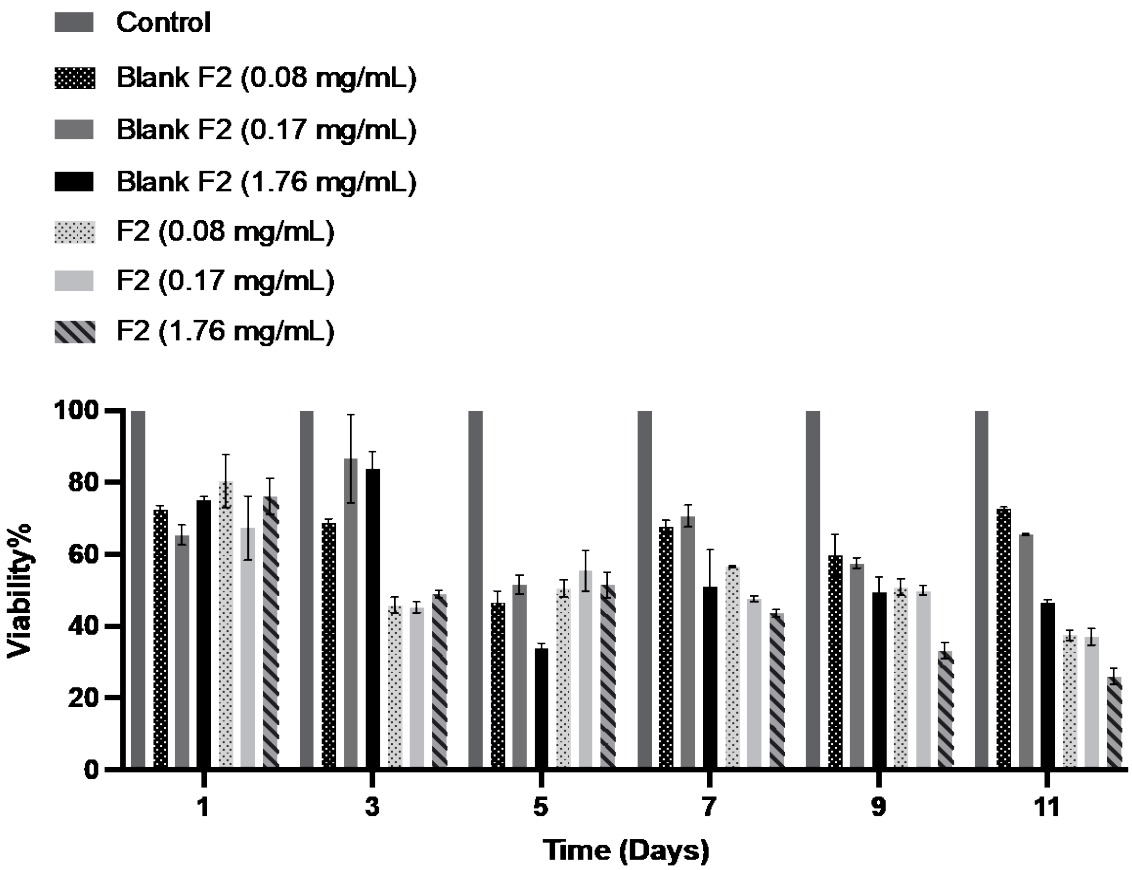


Figure 6.27. Cytotoxicity of Blank F2 and F2 on primary HGG cells compared to control cells in patient 2 (n=3).

The IRH-loaded F18 NPs were more cytotoxic than blank F18 NPs in patient 2 with a significant difference ($P<0.0001$) between the high concentrations of both formulations across most days (Figure 6.28).

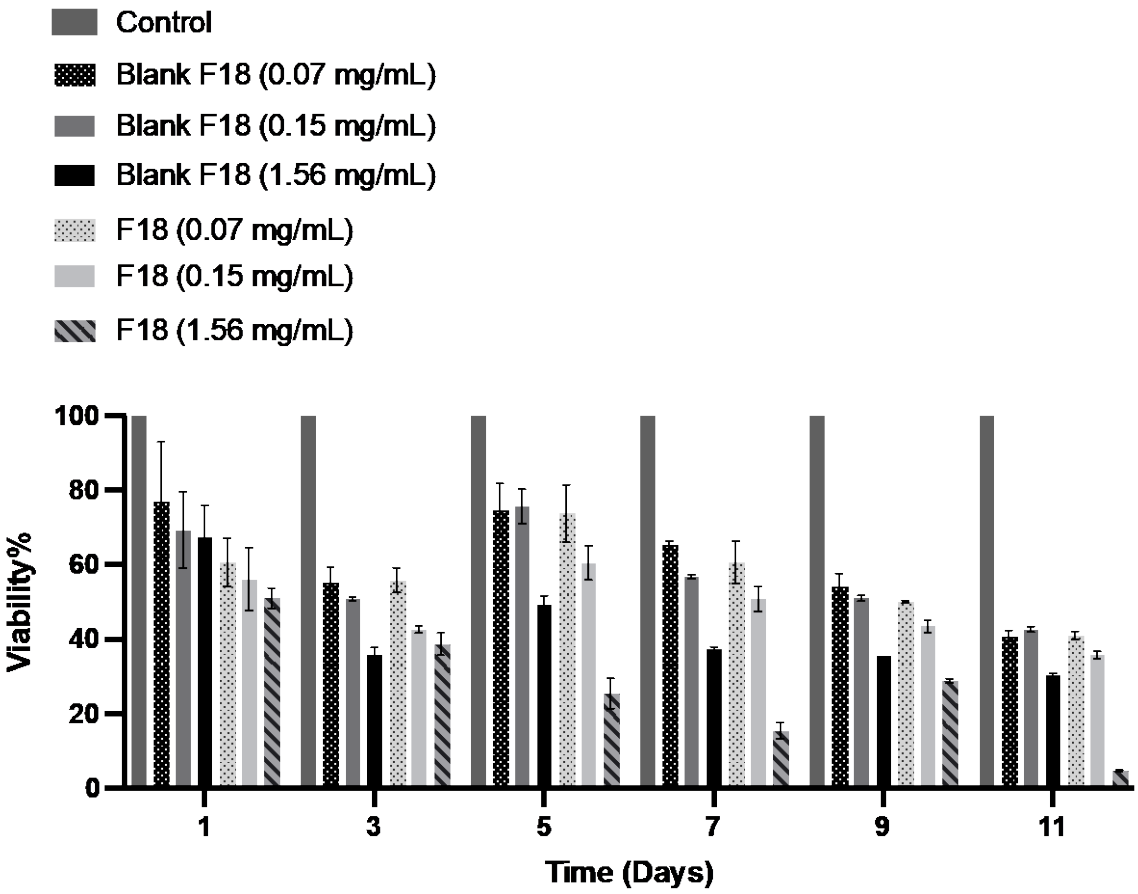


Figure 6.28. Cytotoxicity of Blank F18 and F18 on primary HGG cells compared to control cells in patient 2 (n=3).

Cytotoxicity of the F18 NPs on patient 2 cells was non-significant compared to the F2 NPs. However, the high doses of the F18 NPs were more cytotoxic than F2 from day 3 onward (Figure 6.29).

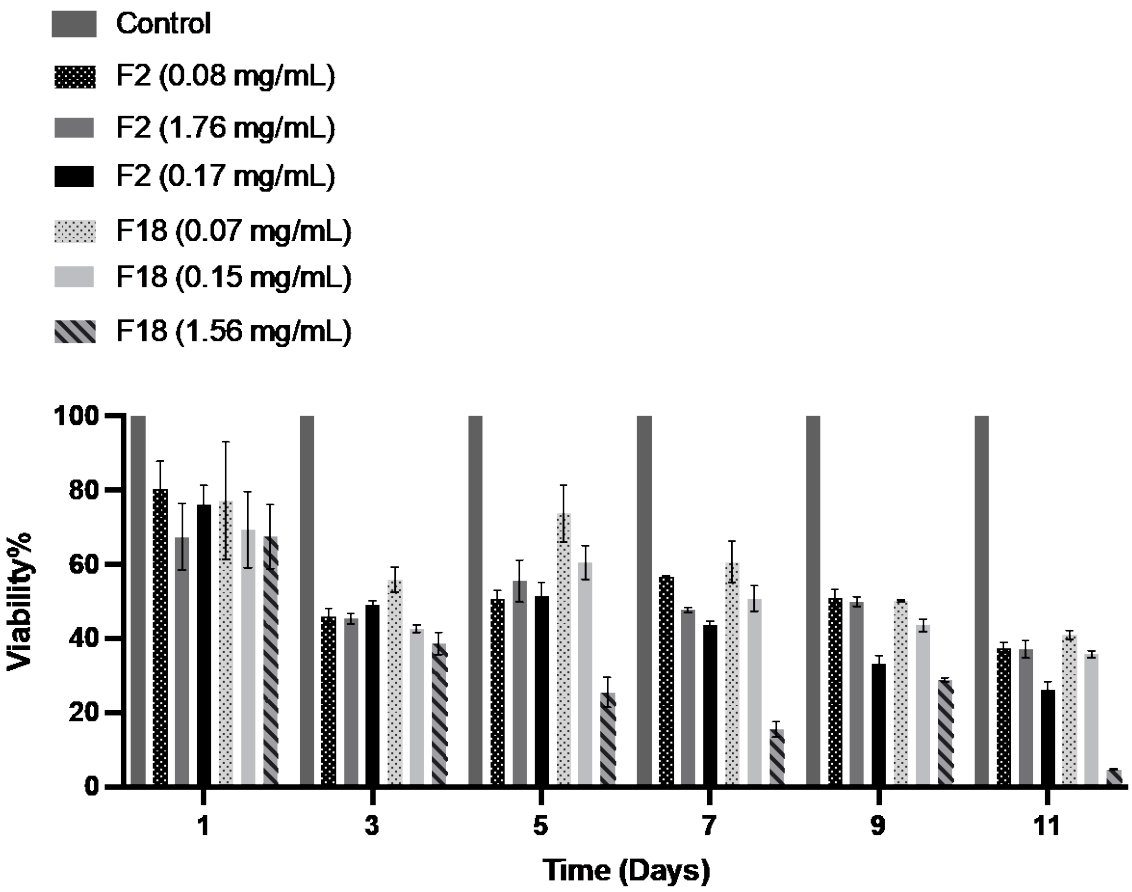


Figure 6.29. Cytotoxicity of F2 and F18 on primary HGG cells compared to control cells in patient 2 (n=3).

Similar to patient 1, the blank F18 NPs were more cytotoxic than the blank F2 NPs for most doses across all days on the patient 2 cells (Figure 6.30).

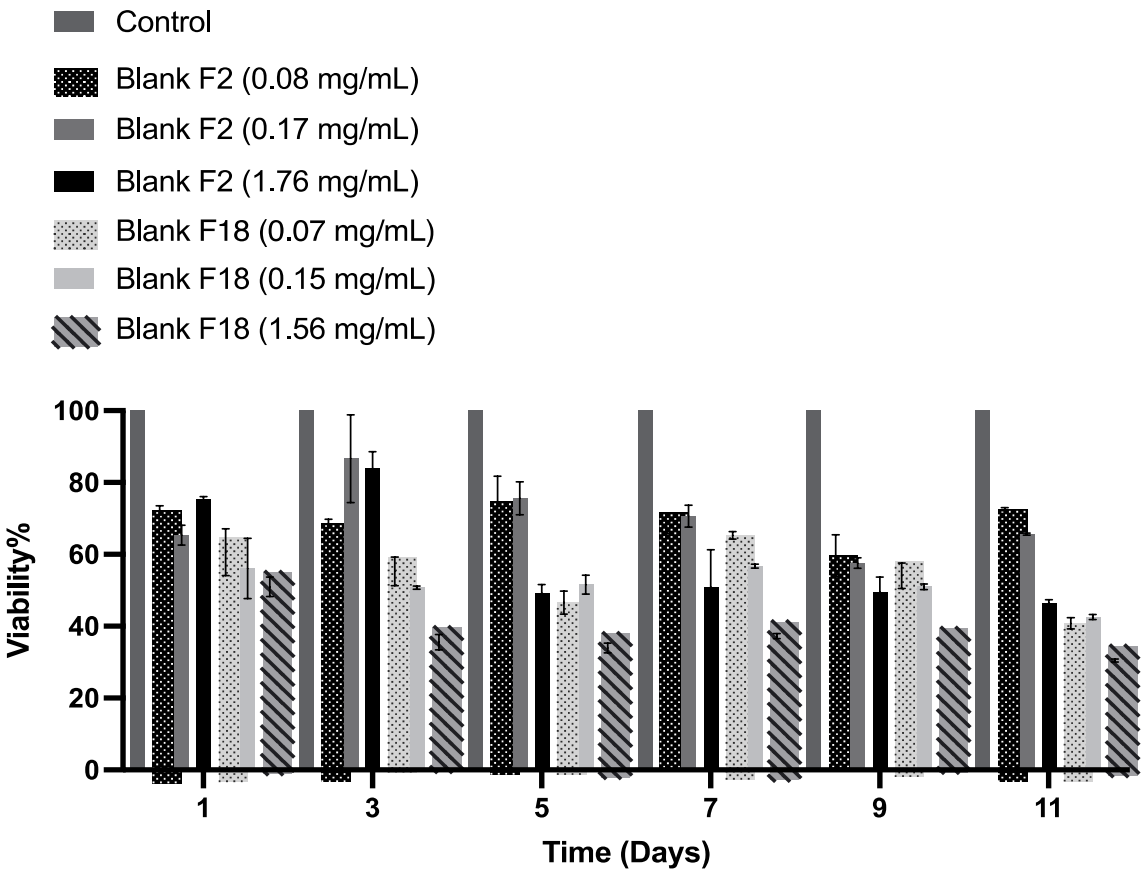


Figure 6.30. Cytotoxicity of Blank F2 and Blank F18 on primary HGG cells compared to control cells in patient 2 (n=3).

As shown in Figure 6.31, there was no significant difference in cytotoxicity of the cells from patient 3 between the F2 NPs and free IRH for the medium and high doses on day 1. On day 3, the F2 NPs were significantly more cytotoxic than free IRH at all doses ($P<0.0001$) as well as the low dose on day 5. From day 9 to day 11, the cytotoxic effect of the free drug was significantly ($P<0.0001$) higher compared to the F2 NPs across all doses reducing cell viability down to 15.25% by day 11 for the highest concentration (Figure 6.31).

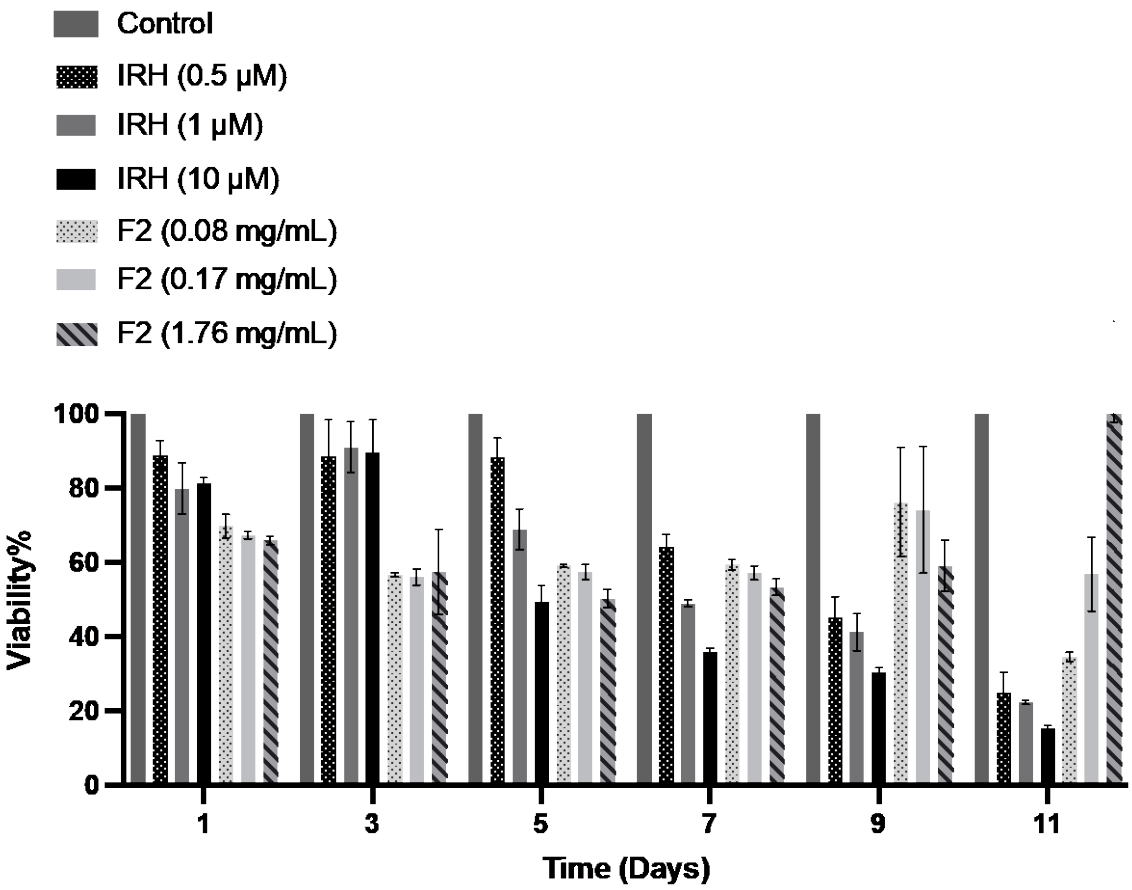


Figure 6.31. Cytotoxicity of free IRH and F2 on primary HGG cells compared to control cells in patient 3 (n=3).

The HGG cells from patient 3 treated with 3 concentrations of the F18 NPs had a greater reduction in cell viability when compared to the free IRH leading to a time dependent cytotoxicity across most doses until day 11. However, the viability increased slightly on day 9 and 11 for the cells treated with the high dose of F18 reaching 27.35% on day 11 compared to 15.25% for the free drug group (Figure 6.32).

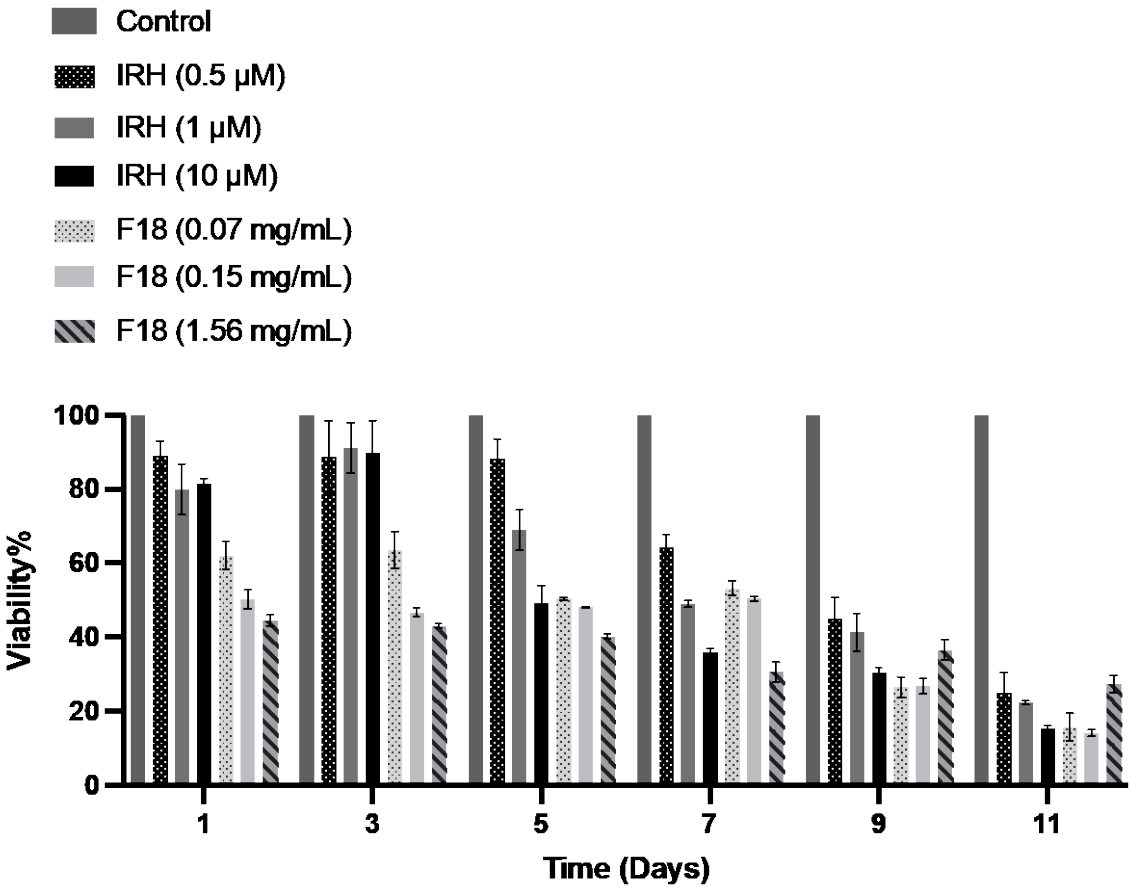


Figure 6.32. Cytotoxicity of free IRH and F18 on primary HGG cells compared to control cells in patient 3 (n=3).

A similar trend to patient 2 was observed in patient 3 in which the blank F2 NPs had greater than 65.00% cell viability until day 5, with the highest concentrations reducing cell viability to 42.91% and to 33.55% on day 7, with the cell viability increasing from day 9. On the other hand, the free IRH reduced the cell viability significantly ($P<0.0001$) by day 11 to 24.87%, 22.30% and 15.25% compared to 74.53%, 68.78% and 50.19% for the blank F2 NPs at the low, medium, and high concentrations respectively (Figure 6.33).

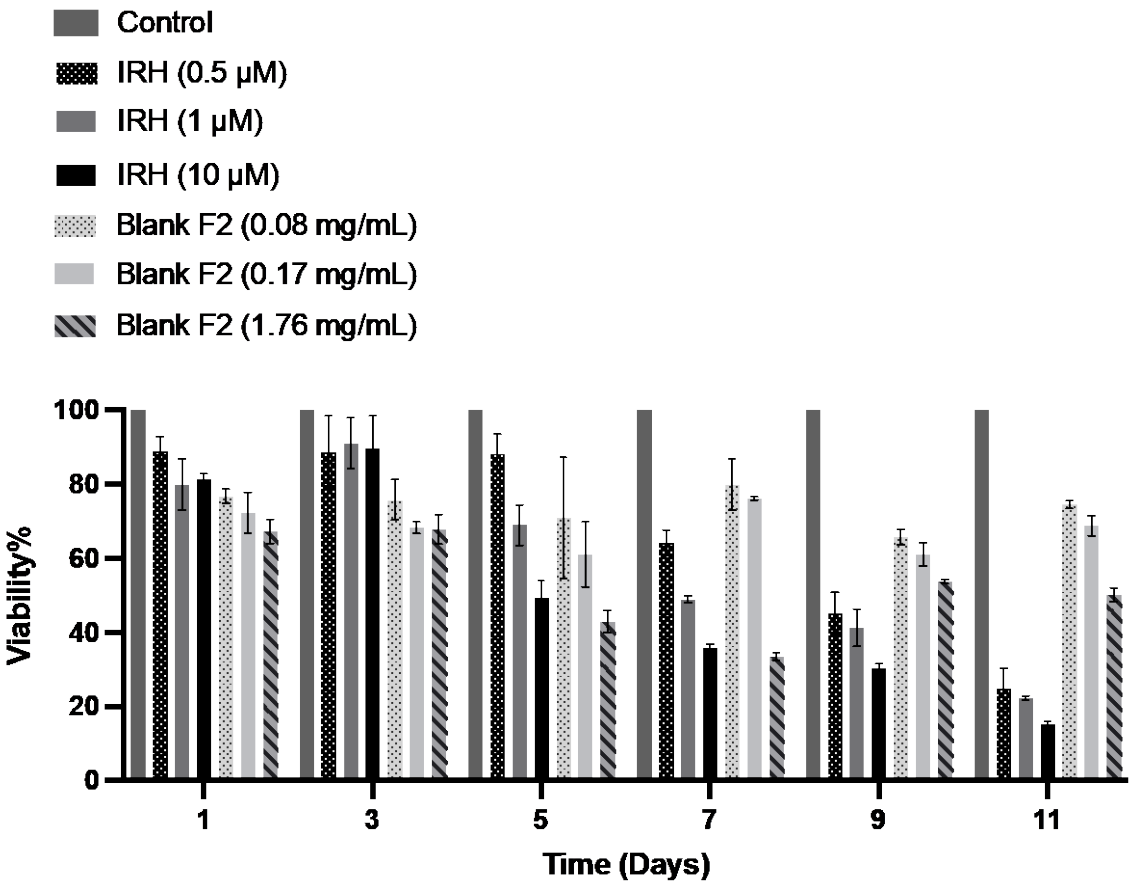


Figure 6.33. Cytotoxicity of free IRH and Blank F2 on primary HGG cells compared to control cells in patient 3 (n=3).

Similar to patient 2, Figure 6.34 shows that the HGG cells from patient 3 had higher cell viabilities when exposed to the blank F18 NPs compared to patient 1. The reduction in viability was dose and time dependent with the lowest viabilities achieved on day 11 reaching 22.53%, 17.92% and 20.60% for the low, medium, and high concentrations respectively (Figure 6.34). This effect was non-significant compared to equivalent concentrations of the free IRH.

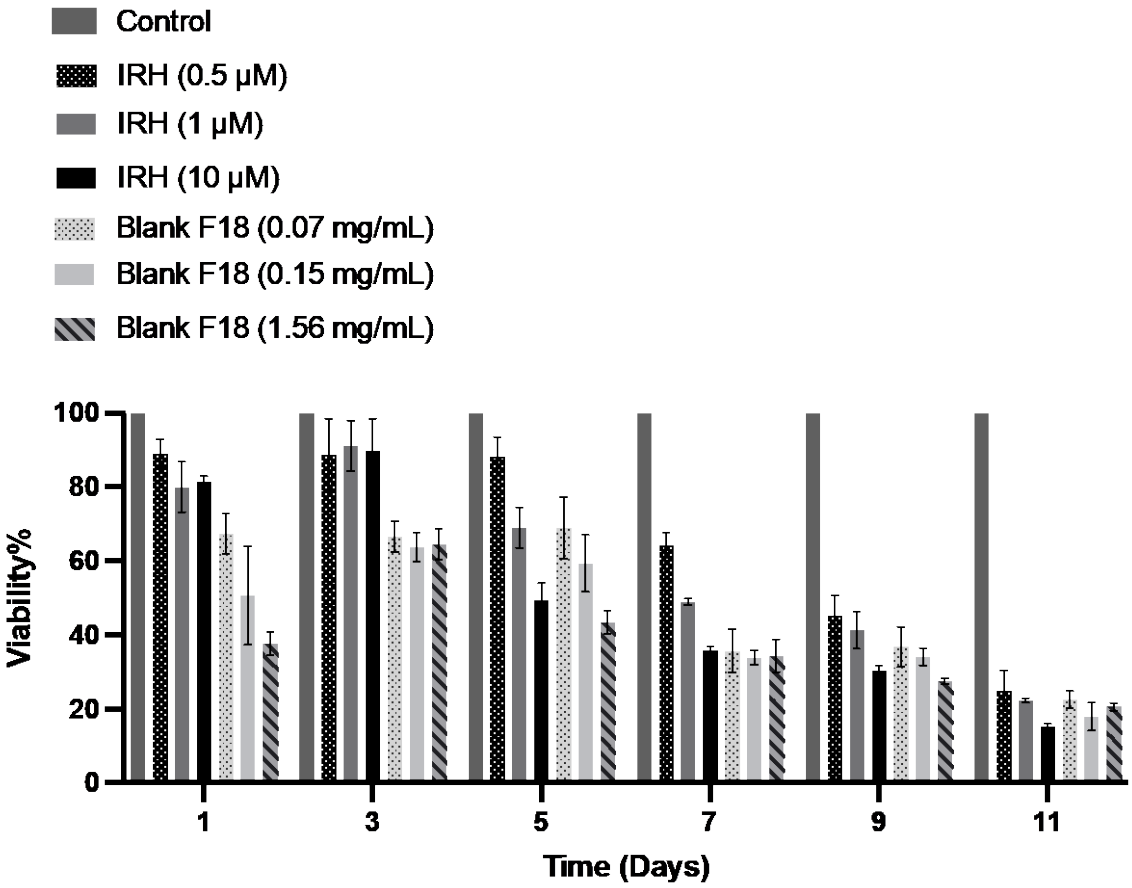


Figure 6.34. Cytotoxicity of free IRH and Blank F18 on primary HGG cells compared to control cells in patient 3 (n=3).

The F2 NPs had a greater reduction on cell viability compared to their blank counterparts across most days and doses in patient 3 (Figure 6.35).

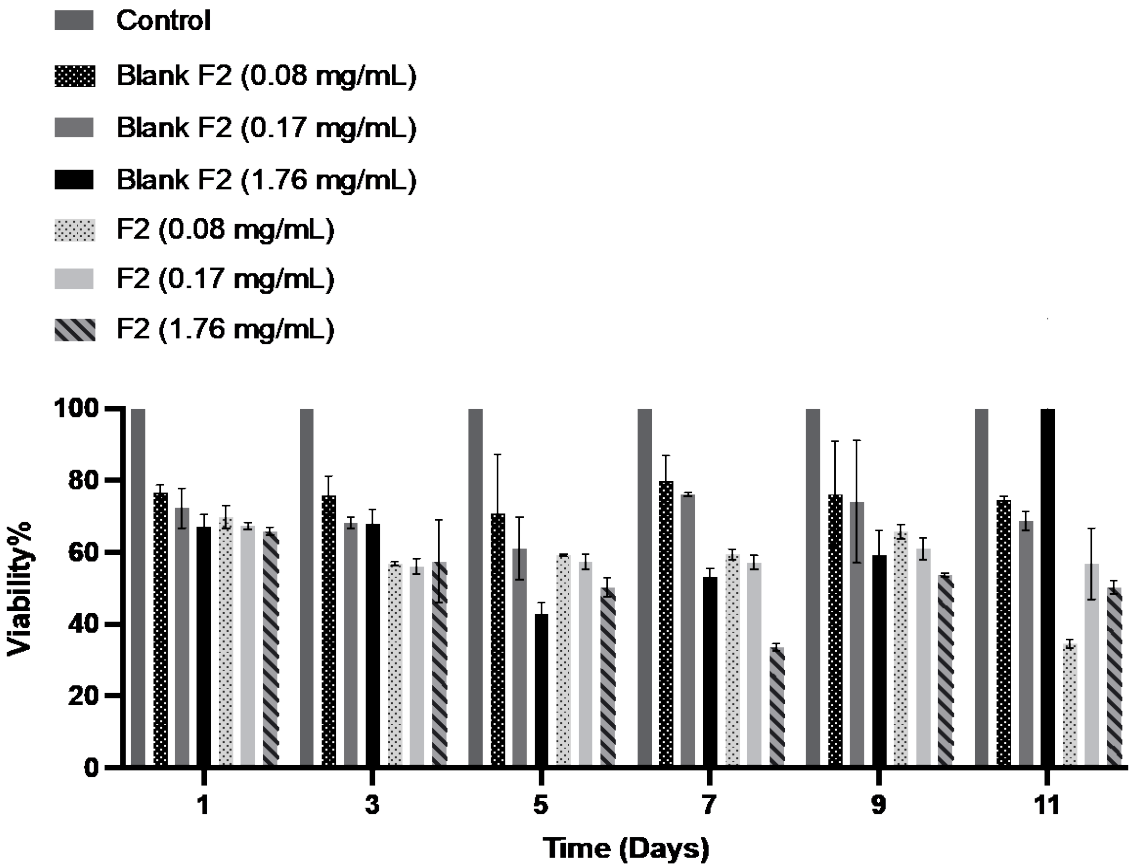


Figure 6.35. Cytotoxicity of F2 and Blank F2 on primary HGG cells compared to control cells in patient 3 (n=3).

Blank F18 NPs had a higher cell viability in patient 3 compared to their IRH-loaded counterparts across most days and doses (Figure 6.36). The cell viability was significantly higher ($P<0.0001$) in blank F18 treated groups at the low dose on day 5 and the medium and high doses for both day 3 and day 7 compared to F18 (Figure 6.36).

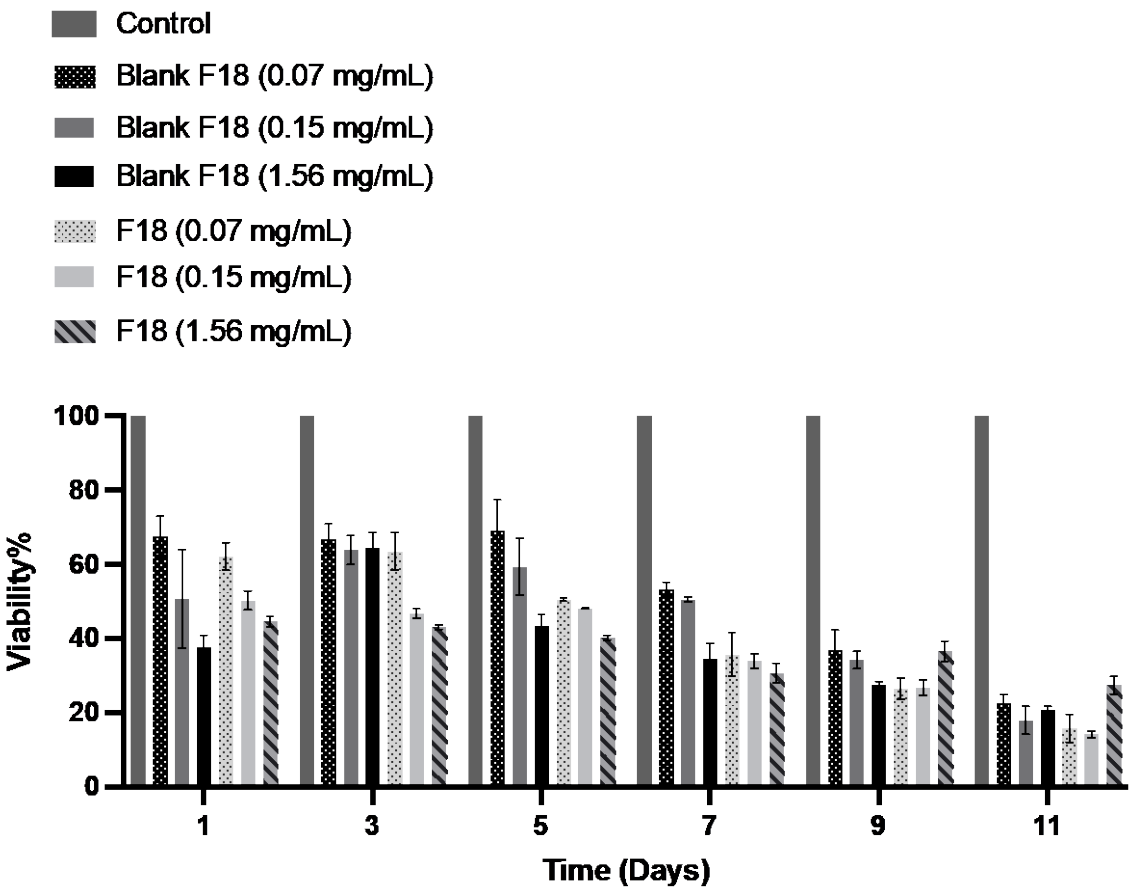


Figure 6.36. Cytotoxicity of F18 and Blank F18 on primary HGG cells compared to control cells in patient 3 (n=3).

F18 exerted a higher cytotoxic effect than F2 against HGG cells obtained from patient 3. The effect was significant on day 1 by the medium (P= 0.01) and high concentrations (P<0.0001). The significance was also shown between the high concentrations on day 7 and all concentrations on day 9 and 11 (P<0.0001) (Figure 6.37).

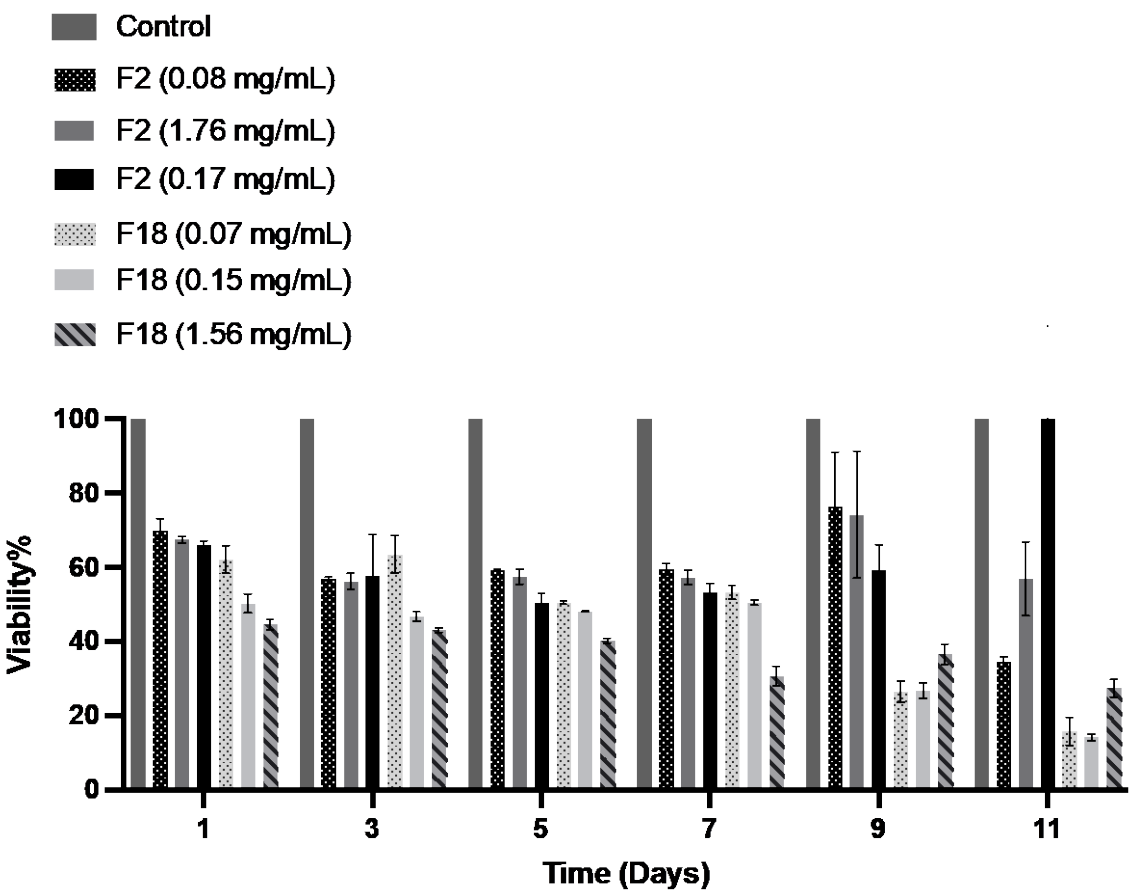


Figure 6.37. Cytotoxicity of F2 and F18 on primary HGG cells compared to control cells in patient 3 (n=3).

In patient 3, there was no significant difference between the blank F2 and blank F18 NPs until day 5 (except for the medium and high concentrations on day 1). From day 7, the blank F18 were significantly more cytotoxic than the blank F2 NPs ($P<0.0001$) (Figure 6.38).

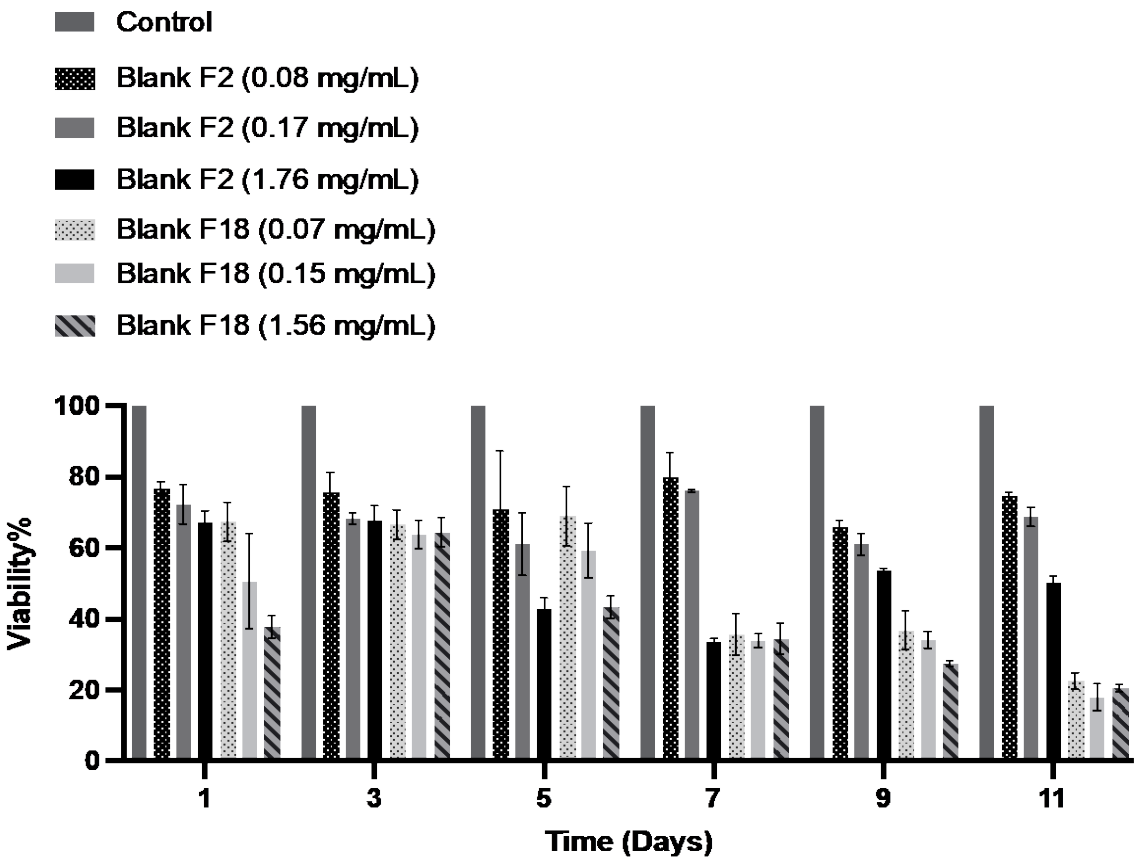


Figure 6.38. Cytotoxicity of Blank F2 and Blank F18 on primary HGG cells compared to control cells in patient 3 (n=3).

6.3.3 Optical Imaging of HGG Cells

The morphology of the cells changed to a more circular and inflated structure when treated with DMSO and staurosporine for 6 hours (Figure 6.40), while the number of attached cells was reduced compared to the negative control (Figure 6.39), which indicates apoptosis and necrosis. By observing the morphology of the cells treated with IRH (Figure 6.41), it is noticeable that the low and medium doses did not induce major morphological changes on day 1 and 3 when compared to the negative control (Figure 6.39). As demonstrated by Figure 6.42 to Figure 6.45, the morphology of the cells treated with all doses of NPs was altered from day 1 to day 11 compared with the negative control, in which the cells showed some circularity and detached from the

flask. This indicates that the NPs had an immediate effect inducing apoptosis and necrosis from day 1.

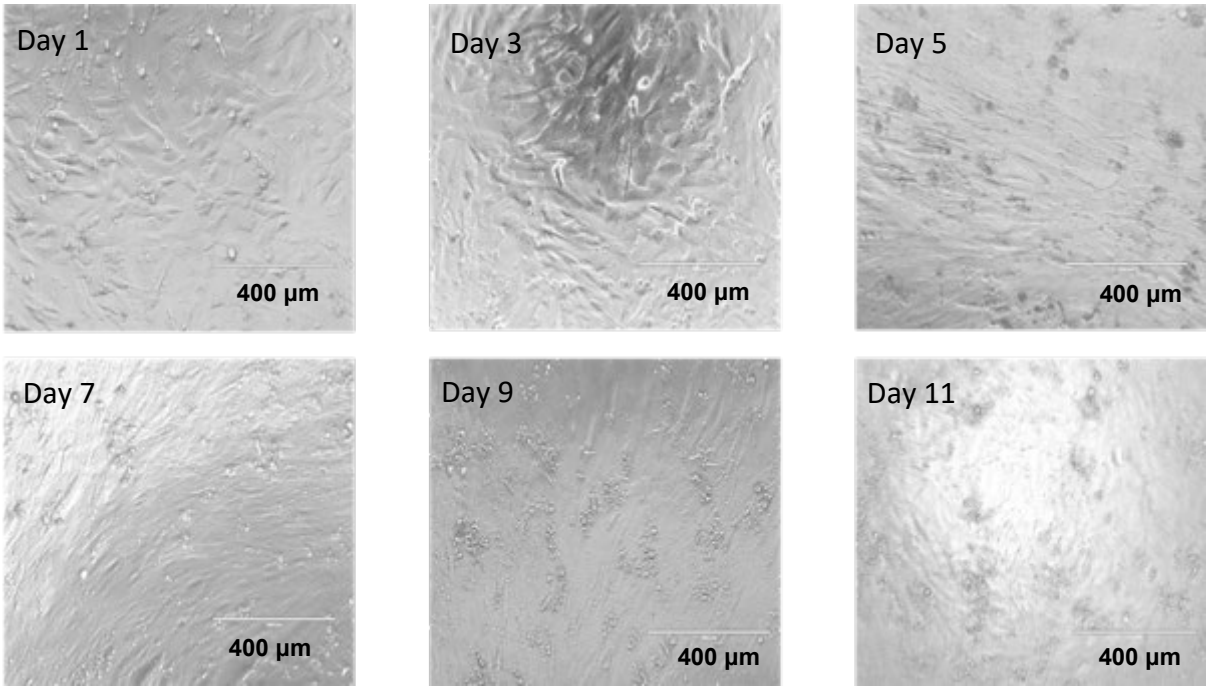


Figure 6.39. Optical imaging of untreated control of primary HGG cells over 11 days period.

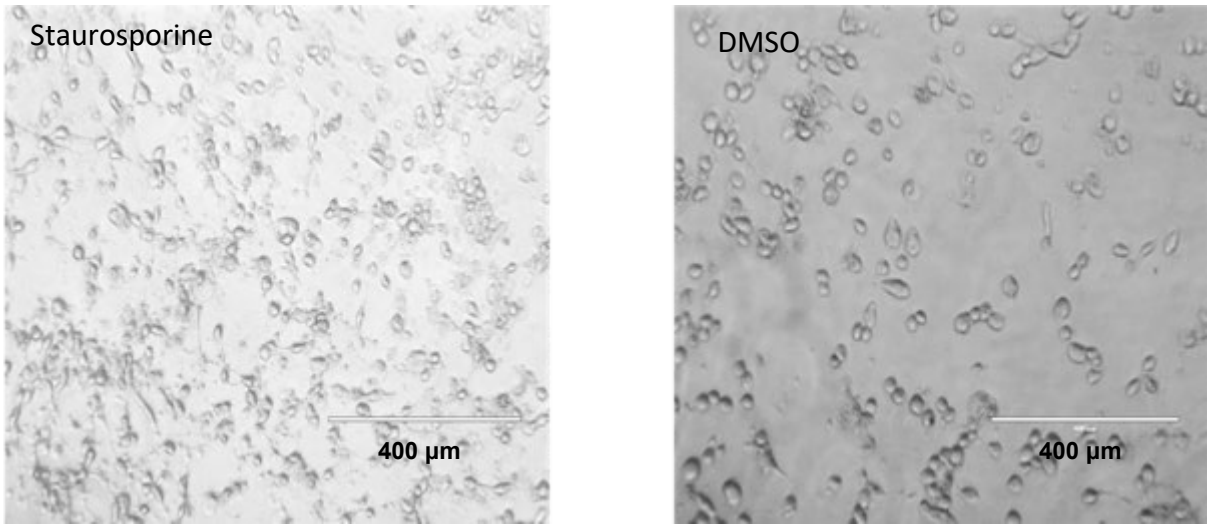
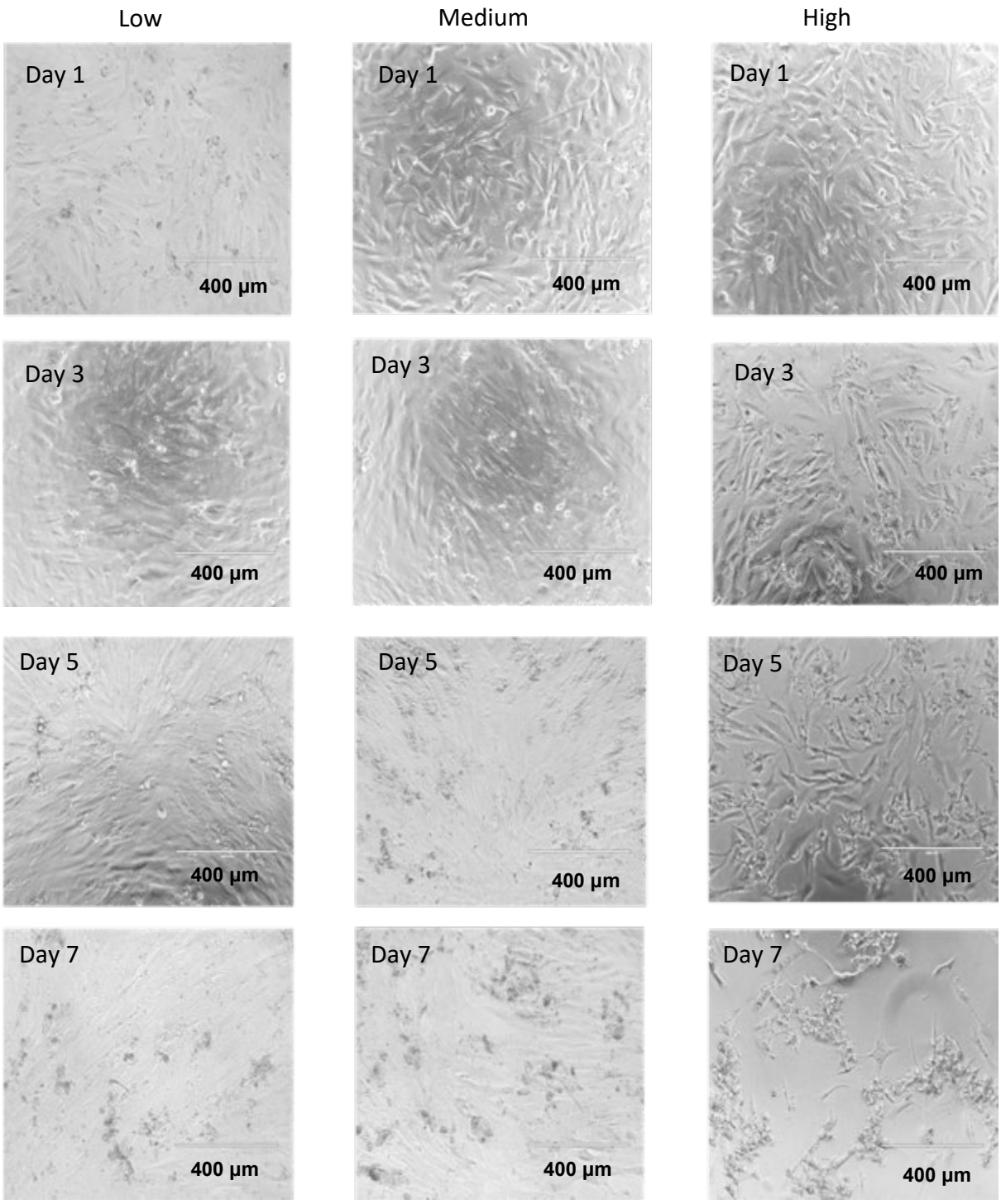


Figure 6.40. Optical imaging of primary HGG cells exposed to 6 hours of 2 µM staurosporine and 20% DMSO.


Low
Medium
High
Day 1
Day 1
Day 1
400 µm
400 µm
400 µm
Day 3
Day 3
Day 3
400 µm
400 µm
400 µm
Day 5
Day 5
Day 5
400 µm
400 µm
400 µm
Day 7
Day 7
Day 7
400 µm
400 µm
400 µm

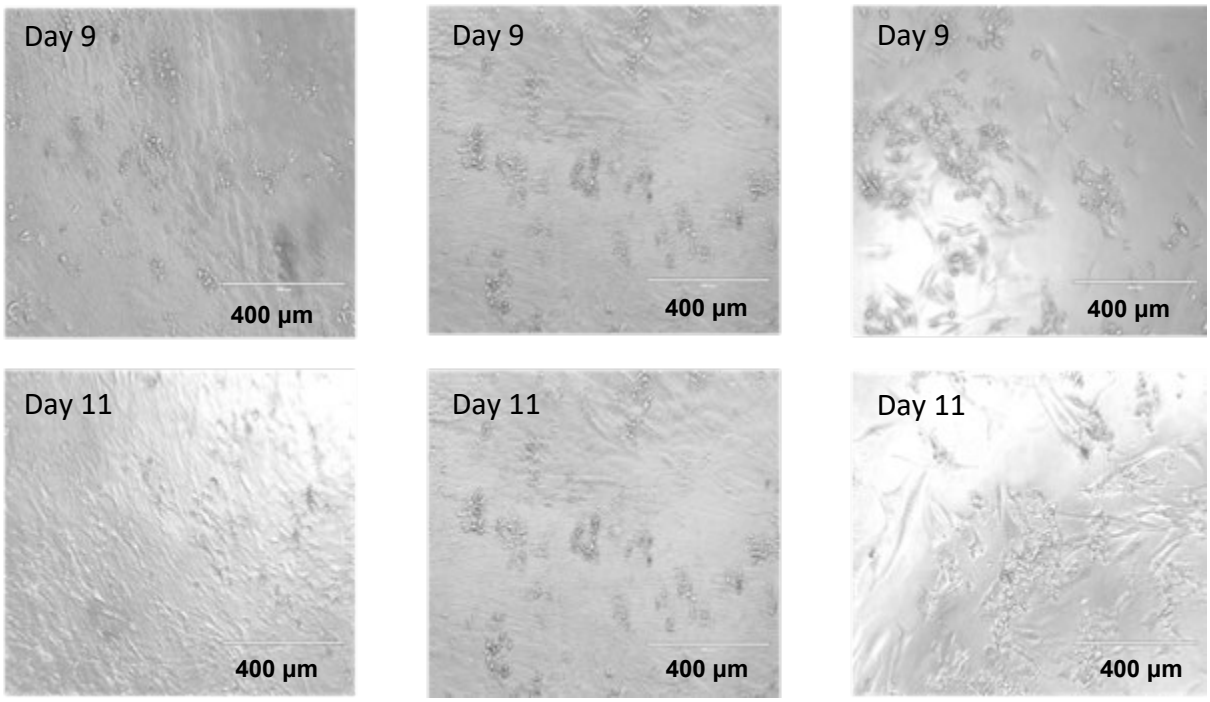
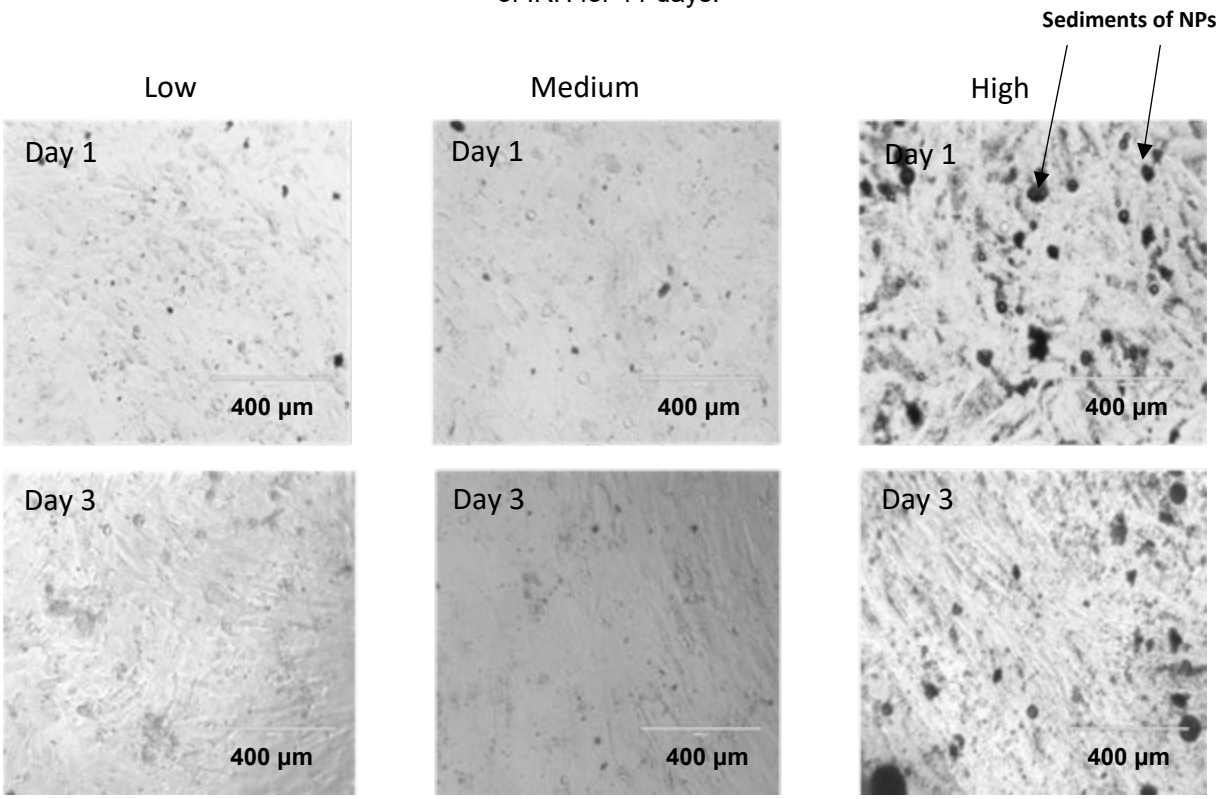


Figure 6.41. Optical imaging of primary HGG cells exposed to low, medium and high concentrations of IRH for 11 days.



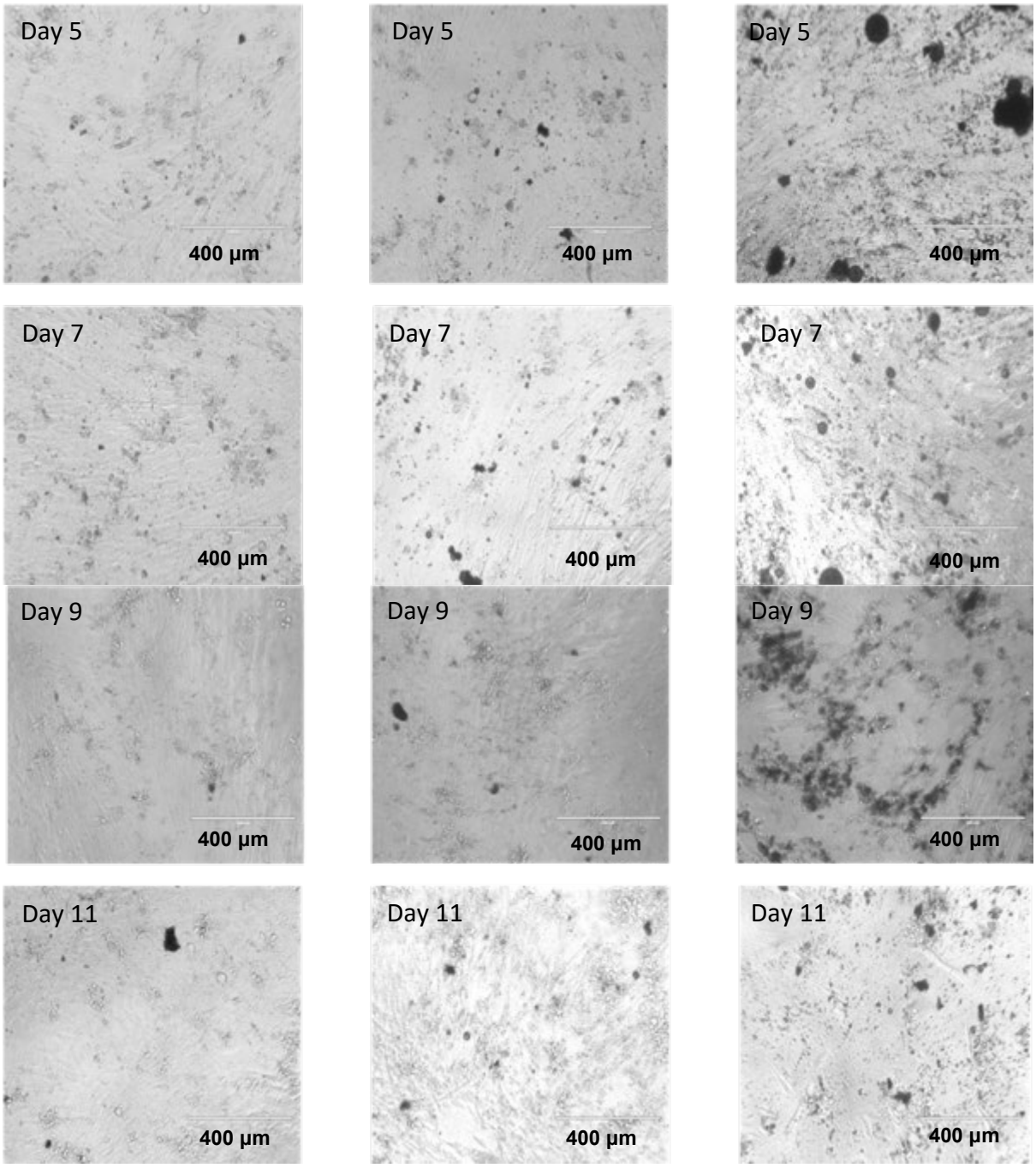
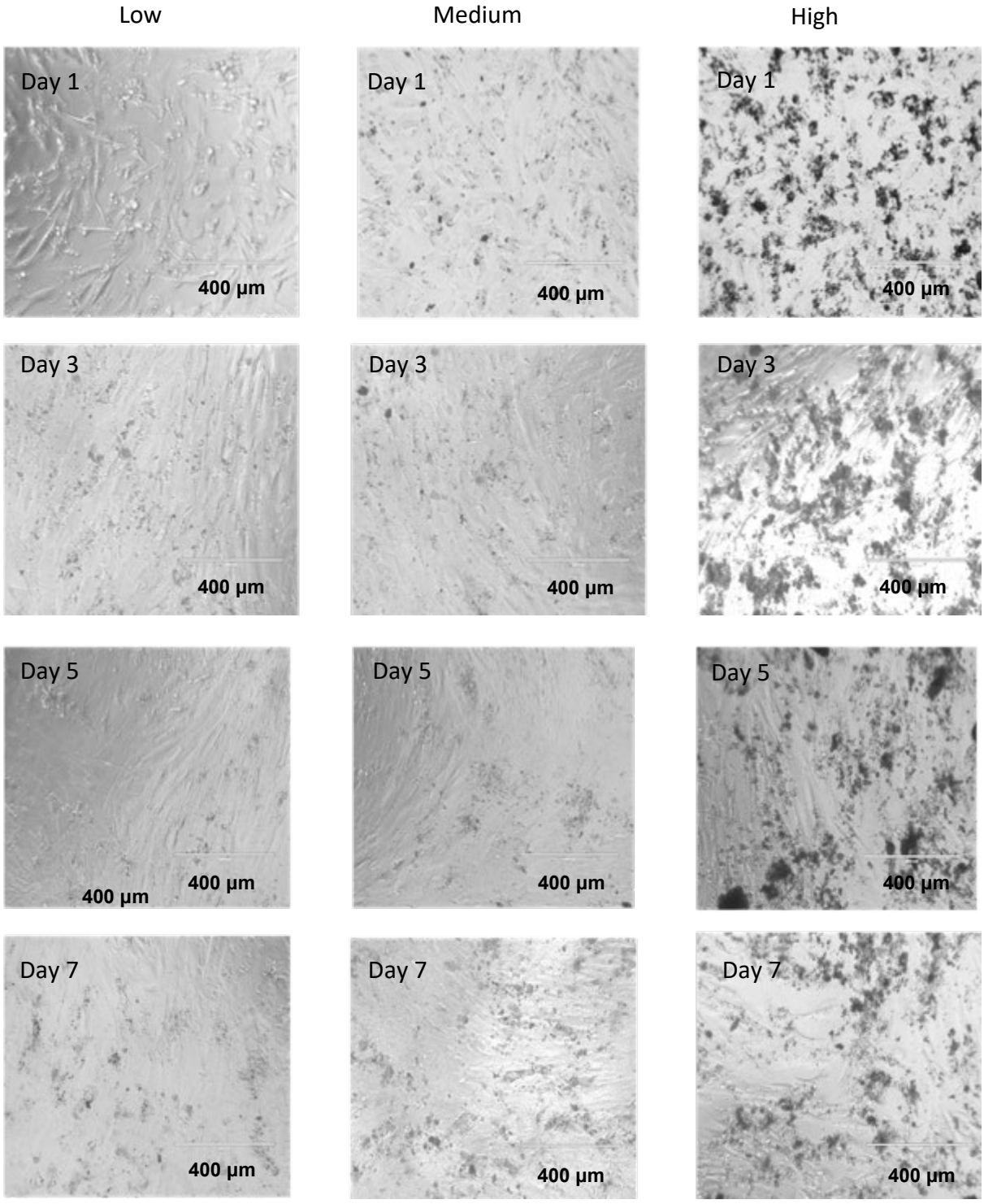


Figure 6.42. Optical imaging of primary HGG cells exposed to low, medium and high concentrations of F2 for 11 days with black areas showing sediments of NPs at high concentration.


Low
Medium
High
Day 1
Day 1
Day 1
400 µm
400 µm
400 µm
Day 3
Day 3
Day 3
400 µm
400 µm
400 µm
Day 5
Day 5
Day 5
400 µm
400 µm
400 µm
400 µm
Day 7
Day 7
Day 7
400 µm
400 µm
400 µm

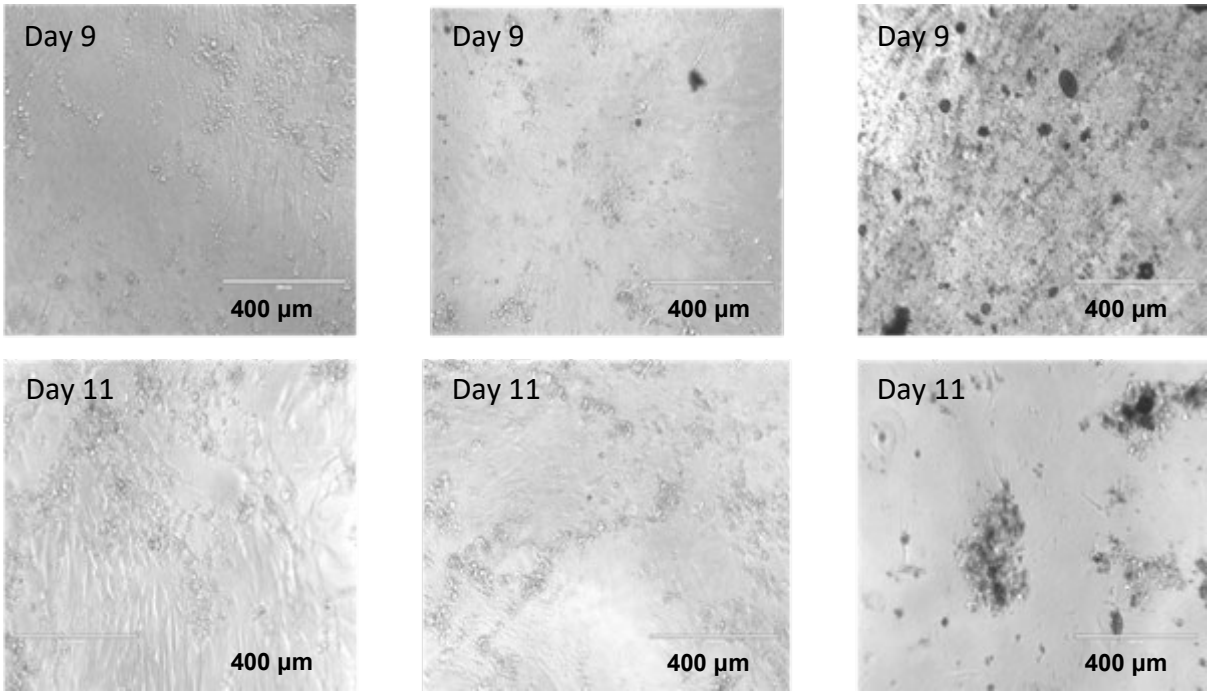
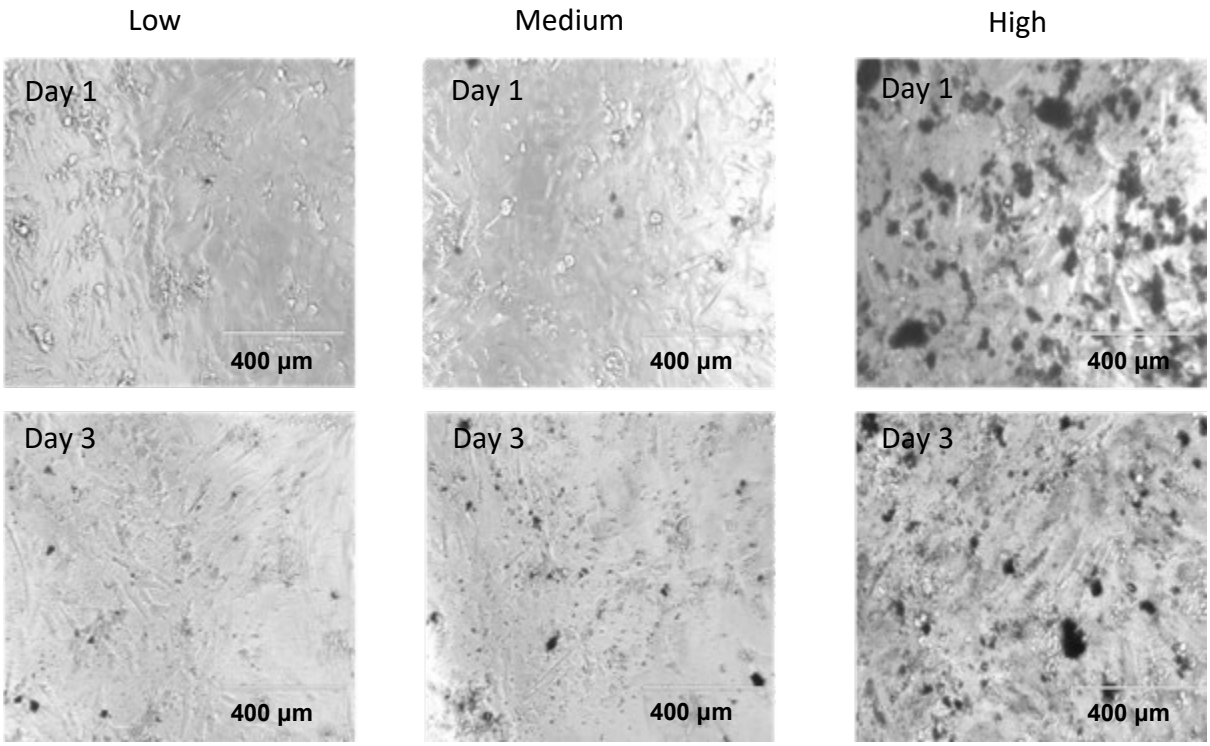


Figure 6.43. Optical imaging of primary HGG cells exposed to low, medium and high concentrations of F18 for 11 days.



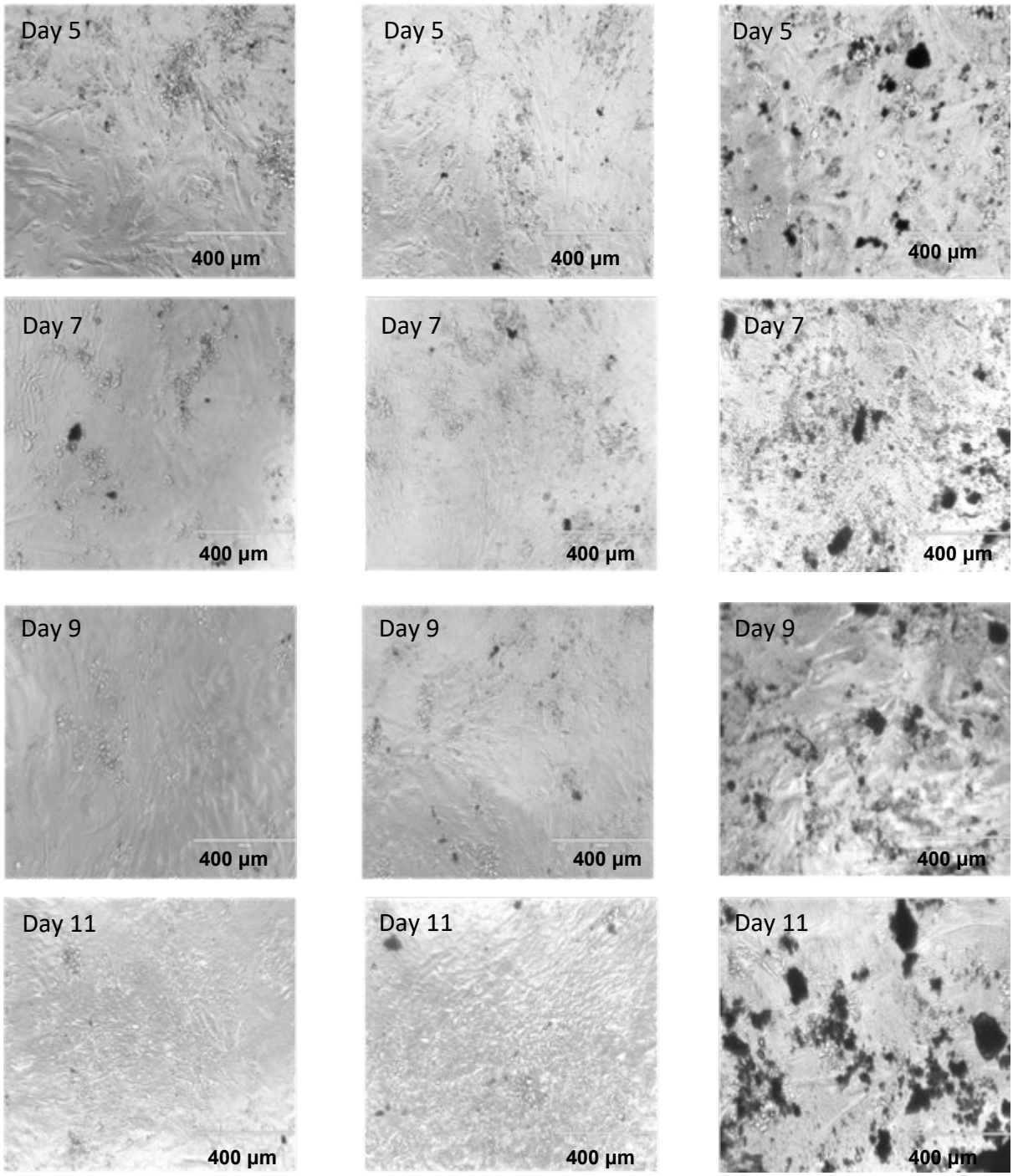
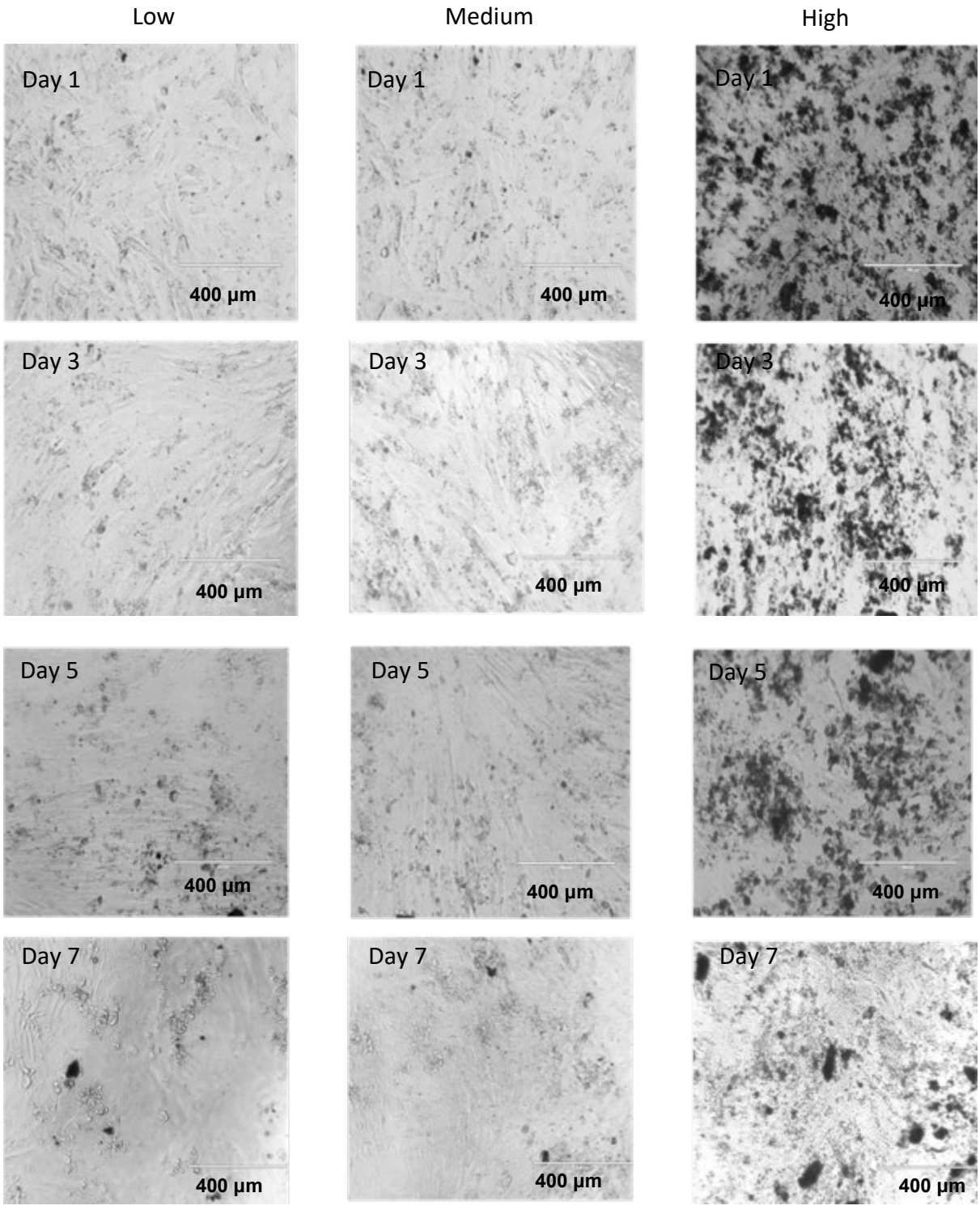


Figure 6.44. Optical imaging of primary HGG cells exposed to low, medium and high concentrations of Blank F2 for 11 days.


Low
Medium
High
Day 1
Day 1
Day 1
400 µm
400 µm
400 µm
Day 3
Day 3
Day 3
400 µm
400 µm
400 µm
Day 5
Day 5
Day 5
400 µm
400 µm
400 µm
Day 7
Day 7
Day 7
400 µm
400 µm
400 µm

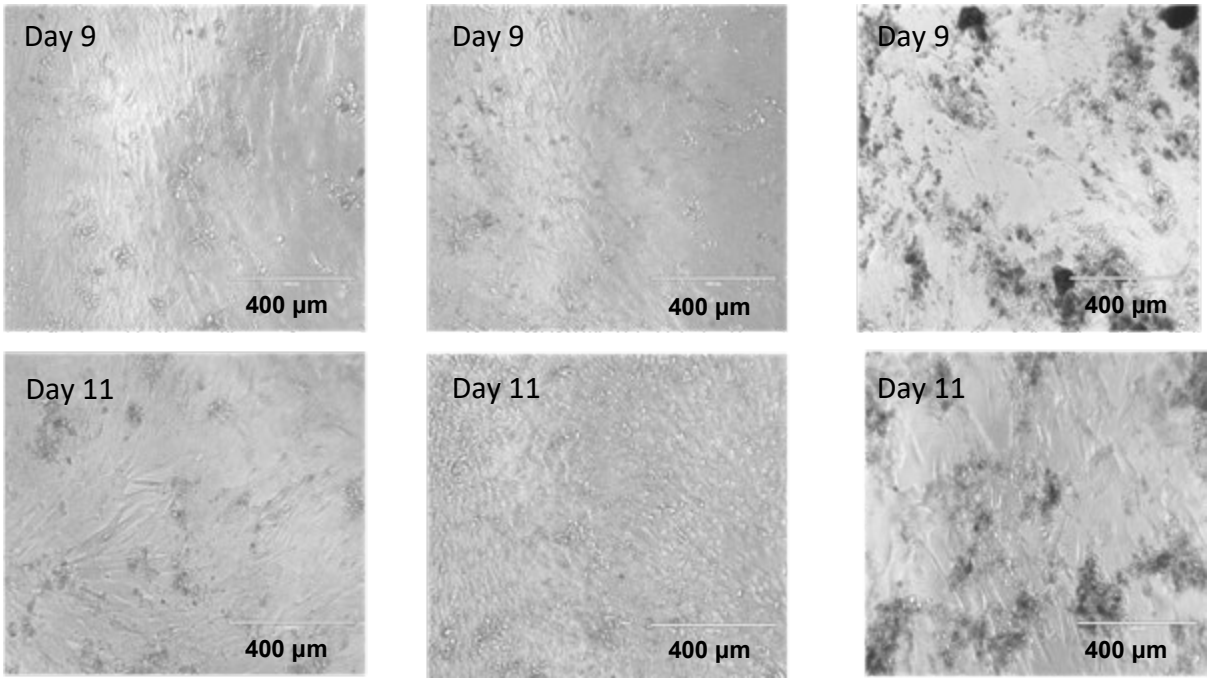


Figure 6.45. Optical imaging of primary HGG cells exposed to low, medium and high concentrations of Blank F18 for 11 days.

6.3.4 Mechanism of Cell Death

The induction of apoptosis and necrosis in primary HGG cells by either free IRH or the NPs was evaluated by flow cytometry using Alexa Fluor 488 Annexin V and PI double staining. The different phases of the cells including viability (annexin V−, PI−), early apoptosis (annexin V+, PI−), late apoptosis (annexin V+, PI+) and necrosis (annexin V−, PI+) are numerically presented in the dot plot quadrants. Values obtained were plotted in bar graphs as an average of 3 replicates. Each formulation was compared to the free IRH, negative and positive controls.

Figure 6.46 to Figure 6.49 display the bar graphs of the HGG cells treated for one day with the free IRH and NP formulations. Compared to the negative control that exhibited 10.96% apoptotic cells, the percentage of cells undergoing both early and late

apoptosis increased from 13.38%, 17.03% and 20.88% for the low, medium and high concentrations respectively of free IRH to 37.63%, 28.22% and 29.45% for the low, medium and high concentrations respectively of the F2 NPs (Figure 6.46).

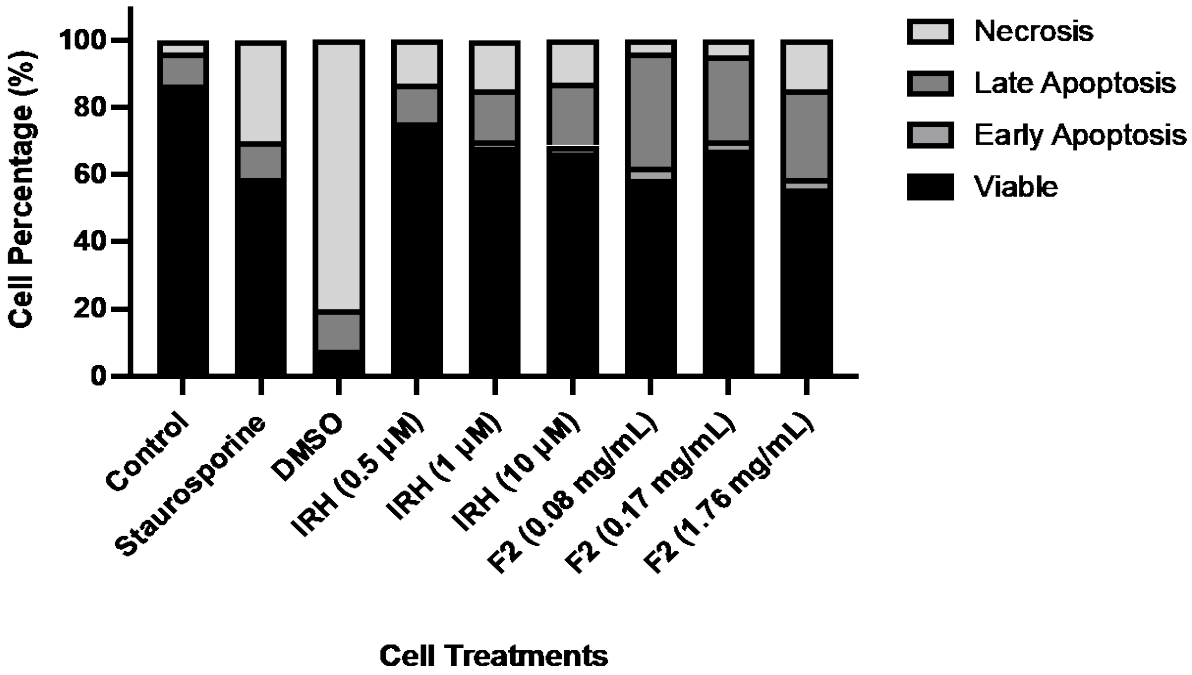


Figure 6.46. Quantification of viable, apoptotic, and necrotic HGG cells exposed to 1-day treatment of IRH and F2 compared to negative and positive controls.

Low, medium, and high concentrations of the F18 NPs resulted in 25.00%, 20.18% and 31.49% of both early and late apoptotic cells respectively (Figure 6.47).

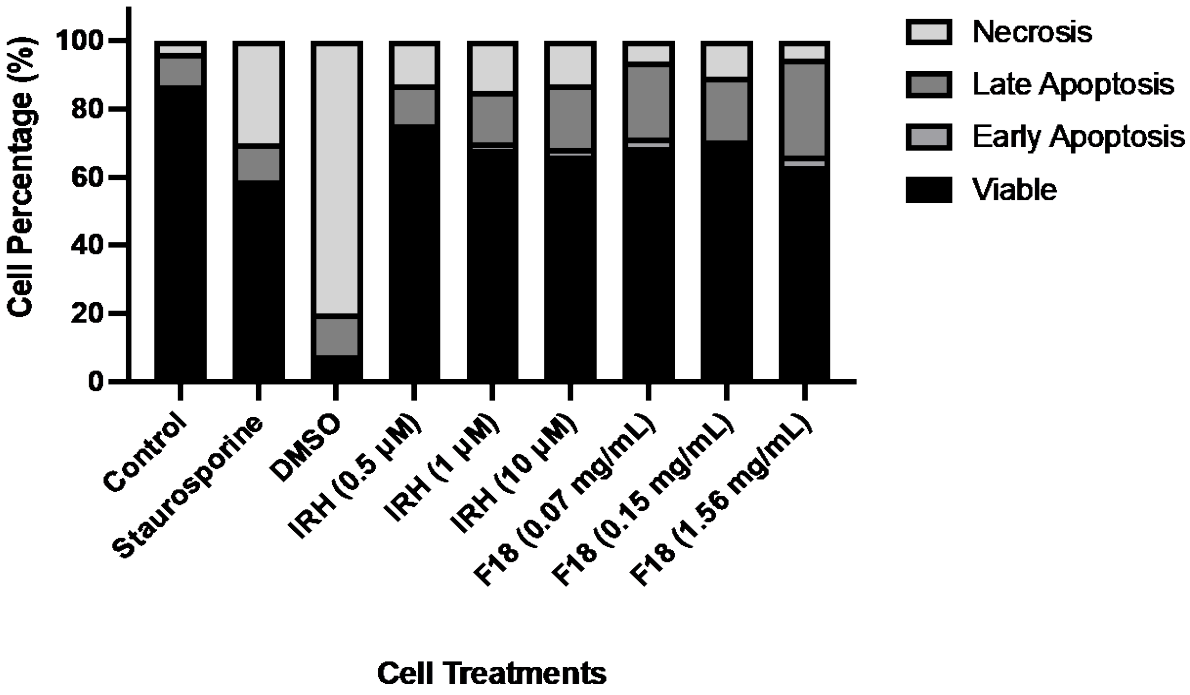


Figure 6.47. Quantification of viable, apoptotic and necrotic HGG cells exposed to 1-day treatment of IRH and F18 compared to negative and positive controls (n=3).

The blank F2 NPs had cell viabilities of 66.09%, 68.51% and 80.30% for the low, medium and high concentrations respectively, while, 15.43%, 13.66% and 10.36% respectively were apoptotic (Figure 6.48).

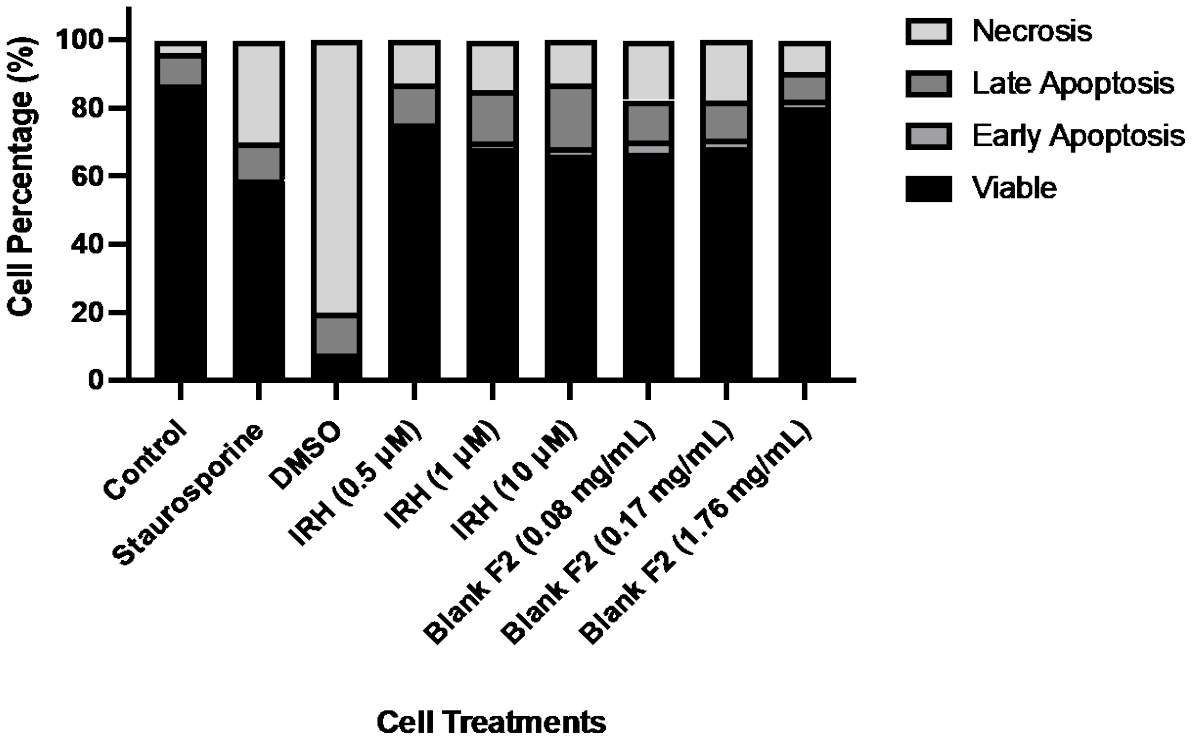


Figure 6.48. Quantification of viable, apoptotic and necrotic HGG cells exposed to 1-day treatment of IRH and blank F2 compared to negative and positive controls (n=3).

Cells treated with low, medium, and high concentrations of blank F18 had a viability of 67.40%, 67.00% and 55.20% respectively. Treatment with the highest concentration of the blank F18 NPs led to 30.90% of necrotic cells, while the remainder of the blank F18 treated groups had less than 15.00% necrosis (Figure 6.49).

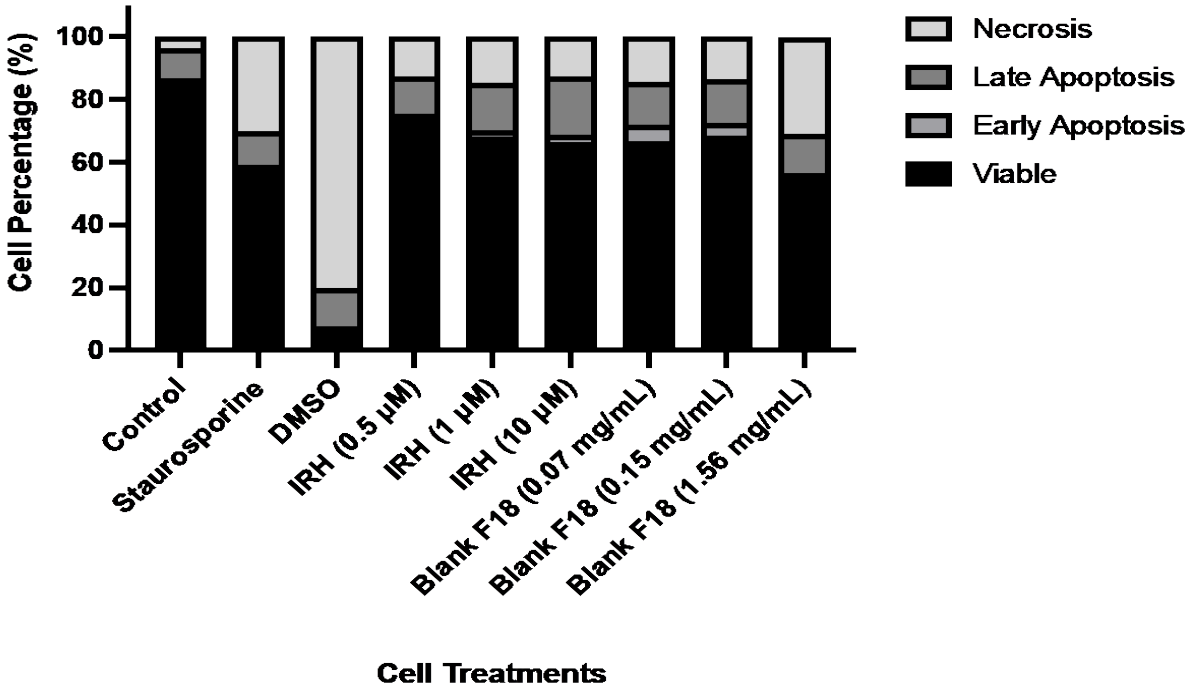


Figure 6.49. Quantification of viable, apoptotic, and necrotic HGG cells exposed to 1-day treatment of IRH and blank F18 compared to negative and positive controls (n=3).

Figure 6.50 to figure 6.53 show that on day 3, IRH treatment resulted in 25.77%, 24.08% and 40.27% of apoptotic cells for the low, medium and high concentrations respectively with 21.60% necrosis at the highest concentration (Figure 6.50). The F2 NPs resulted in 43.53%, 52.30% and 37.67% of the HGG cells being apoptotic after exposure to low, medium, and high concentrations respectively compared to 12.98% of the negative control (Figure 6.50).

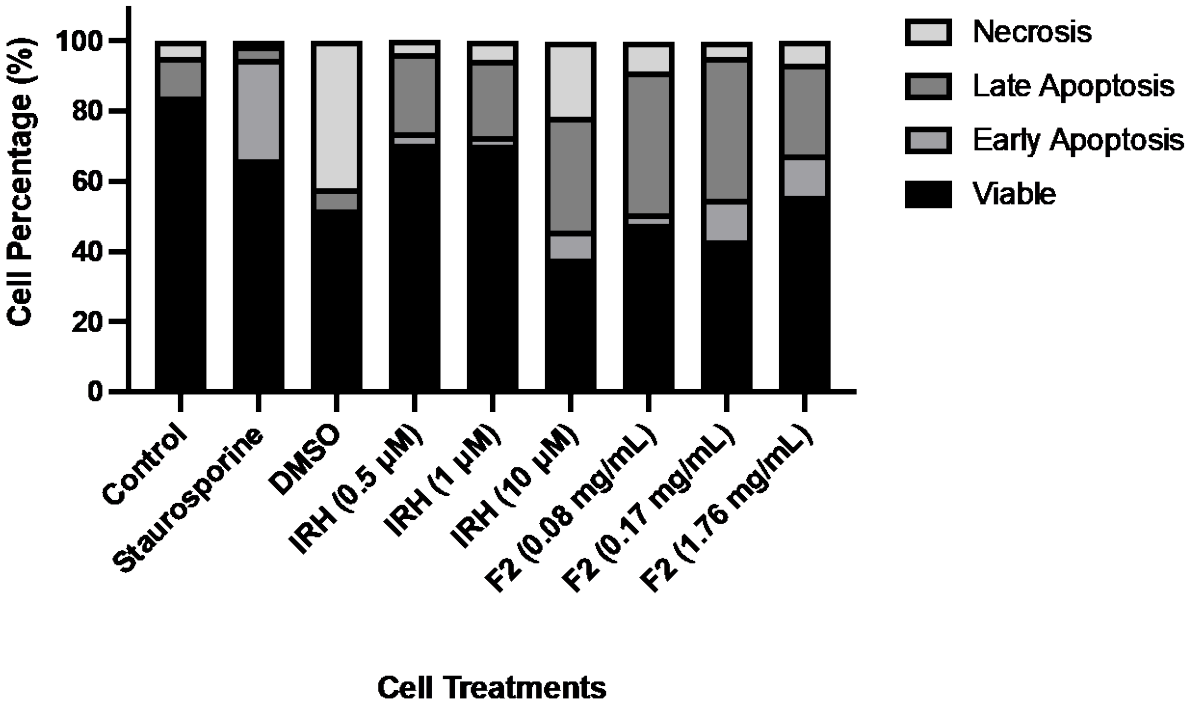


Figure 6.50. Quantification of viable, apoptotic, and necrotic HGG cells exposed to 3-day treatment with IRH and F2 compared to negative and positive controls (n=3).

The F18 NPs produced an apoptotic effect in 12.85%, 18.81% and 36.01% of cells for the low, medium, and high concentrations respectively, while necrosis was induced in less than 15% of the cells (Figure 6.51).

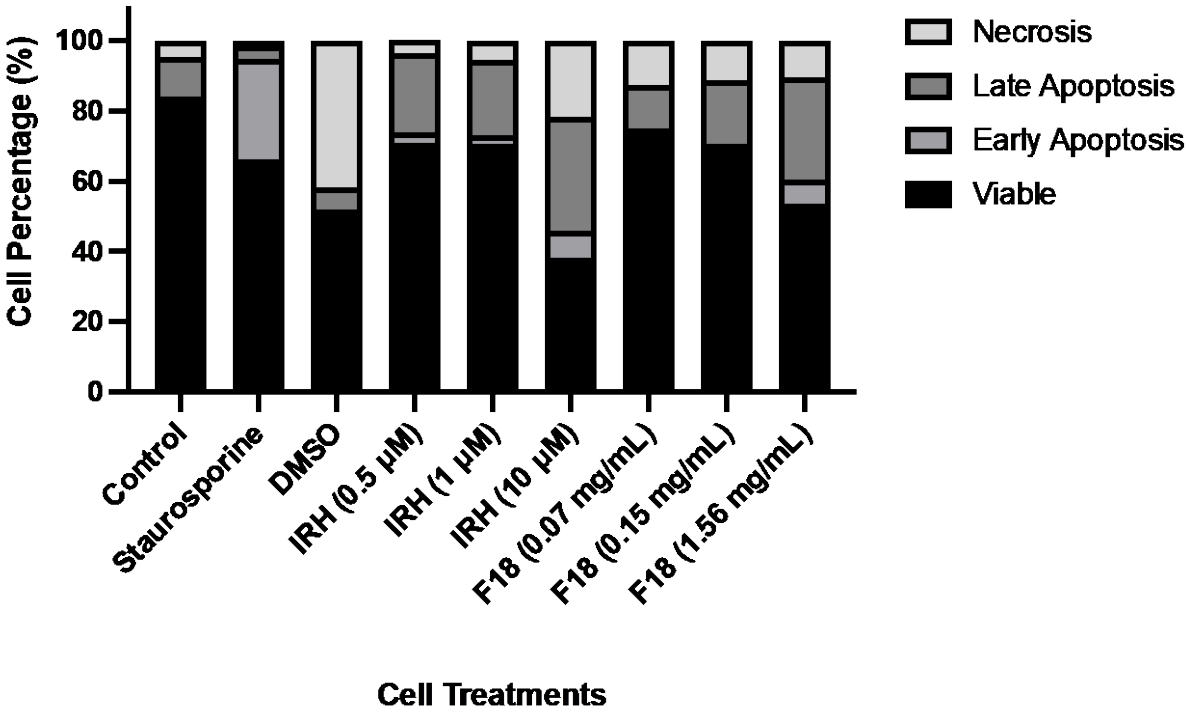


Figure 6.51. Quantification of viable, apoptotic and necrotic HGG cells exposed to 3-day treatment with IRH and F18 compared to negative and positive controls (n=3).

The blank F2 NPs induced less than 20% apoptosis and necrosis at all doses (Figure 6.52).

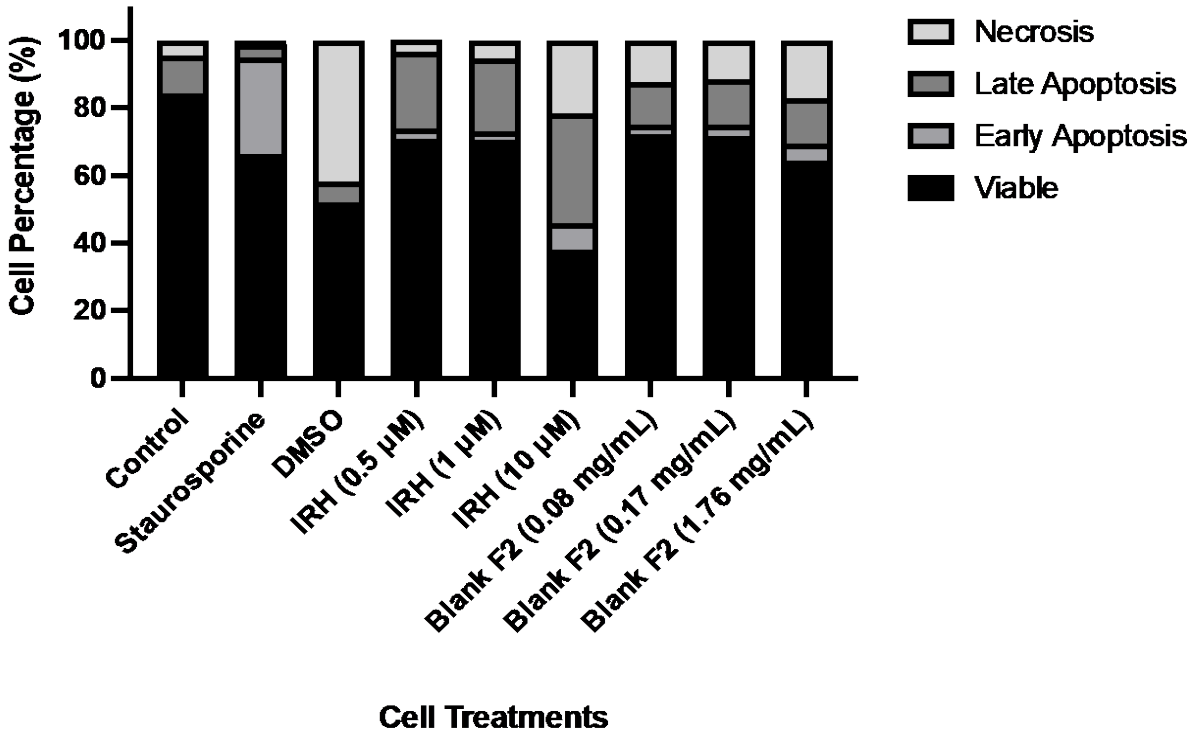


Figure 6.52. Quantification of viable, apoptotic and necrotic HGG cells exposed to 3-day treatment with IRH and blank F2 compared to negative and positive controls (n=3).

The blank F18 NPs induced apoptosis in 22.21%, 18.48% and 27.15% of the cells at the low, medium, and high doses respectively with less than 10% necrosis (Figure 6.53).

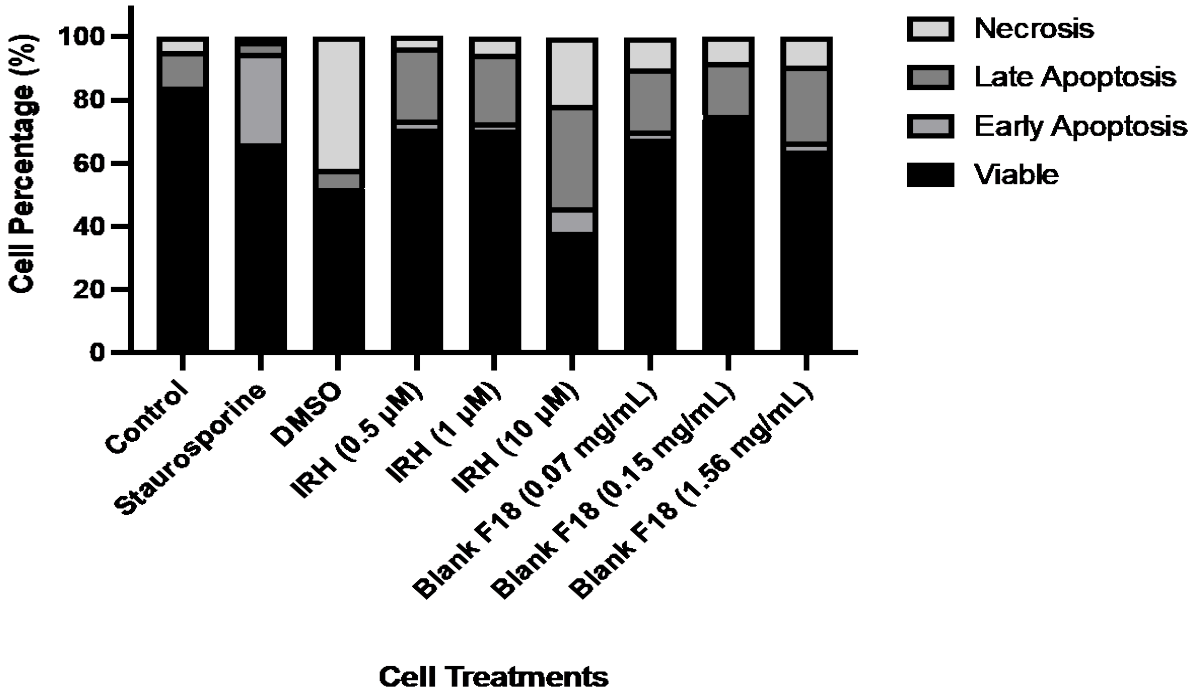


Figure 6.53. Quantification of viable, apoptotic, and necrotic HGG cells exposed to 3-day treatment with IRH and blank F18 compared to negative and positive controls (n=3).

Figure 6.54 to Figure 6.57 show that on day 5, treatment with IRH resulted in more necrotic cells (25.93% and 26.96%) for the low and medium concentrations respectively, while the highest concentration resulted in 92.80% apoptosis (Figure 6.54). The apoptotic effect of cells exposed to the F2 NPs was induced in 45.20%, 55.30% and 62.07% of the cells, while less than 2.00% were necrotic (Figure 6.54).

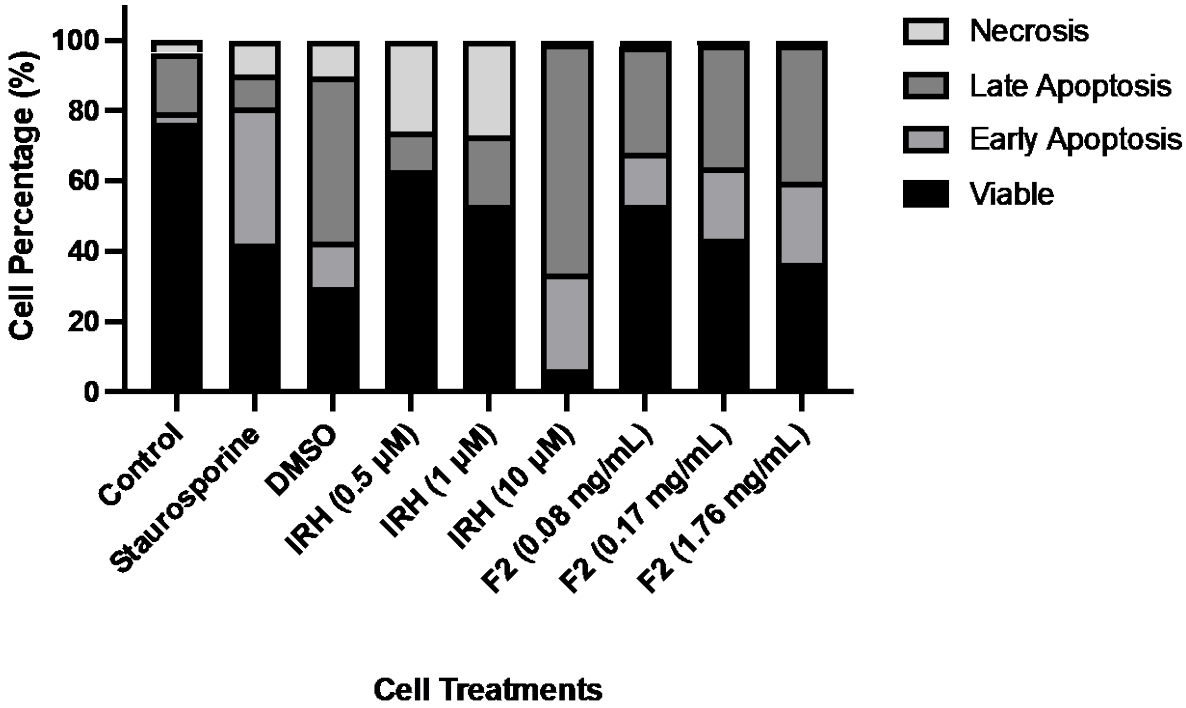


Figure 6.54. Quantification of viable, apoptotic, and necrotic HGG cells exposed to 5-day treatment with IRH and F2 compared to negative and positive controls (n=3).

The F18 NPs resulted in more necrotic cells (31.53 and 29.53%) by day 5 for the low and medium concentrations respectively which demonstrates that apoptosis changed to necrosis at longer incubation periods. The highest concentration had 81.10% apoptotic cells (Figure 6.55).

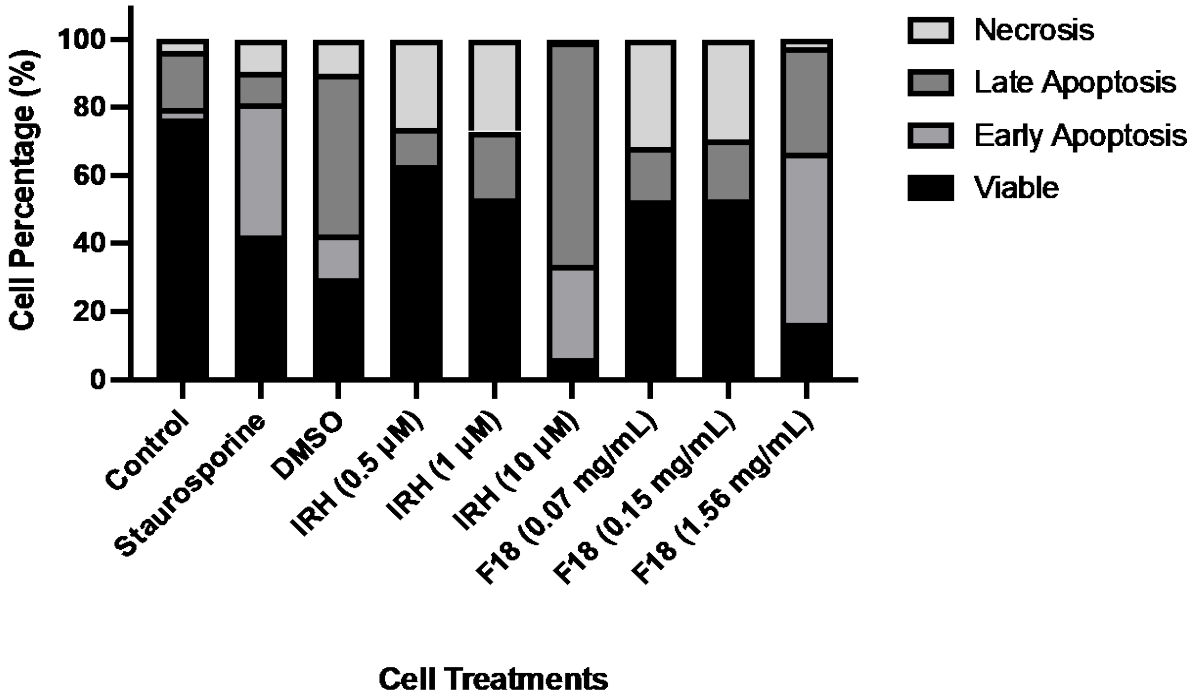


Figure 6.55. Quantification of viable, apoptotic, and necrotic HGG cells exposed to 5-day treatment with IRH and F18 compared to negative and positive controls (n=3).

The blank F2 NPs were less necrotic and less apoptotic than their drug-loaded counterparts by day 5 leading to less than 28.00% apoptosis and less than 15.00% necrosis (Figure 6.56).

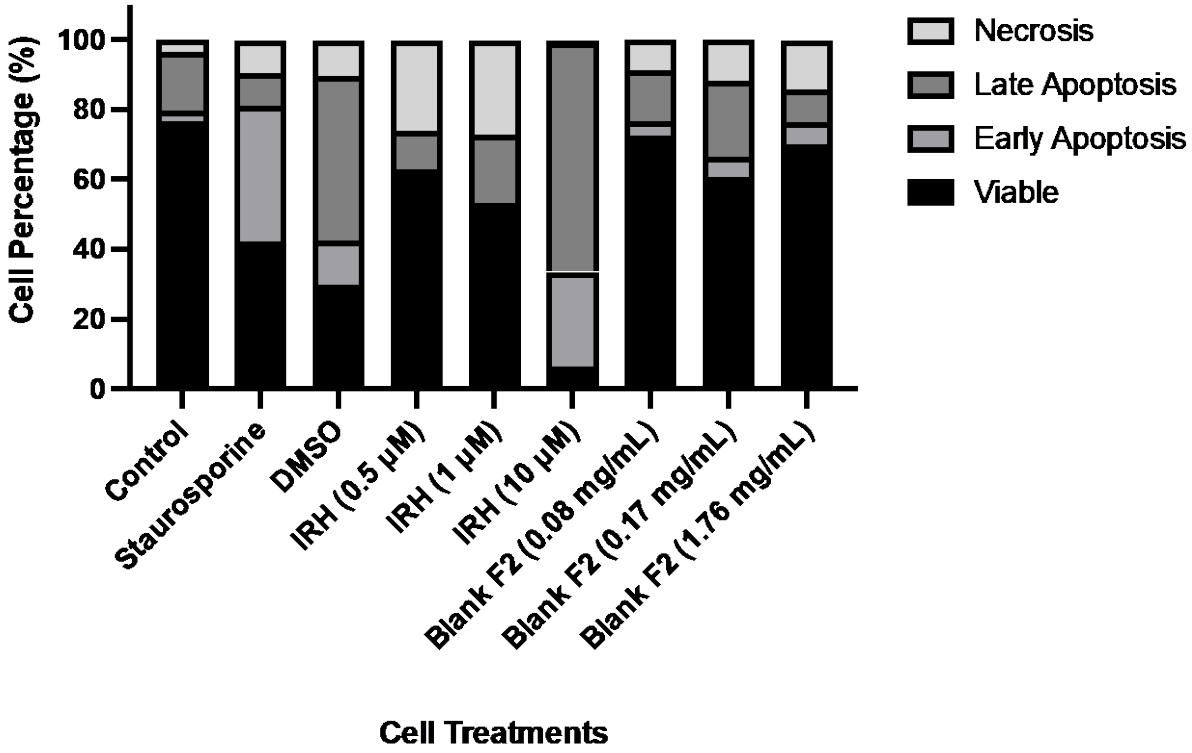


Figure 6.56. Quantification of viable, apoptotic, and necrotic HGG cells exposed to 5-day treatment with IRH and blank F2 compared to negative and positive controls (n=3).

Blank F18 NPs were apoptotic in 24.01% and 82.97% of cells for the medium and high concentrations with necrosis induced in 43.63% at the low concentration (Figure 6.57).

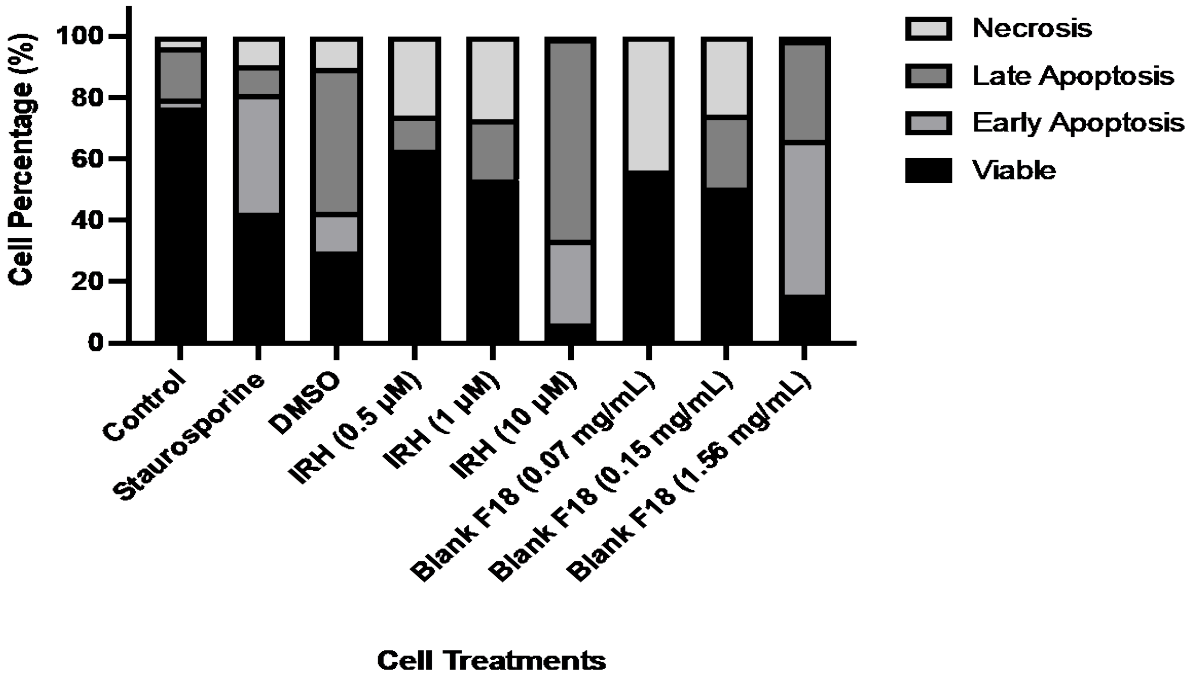


Figure 6.57. Quantification of viable, apoptotic, and necrotic HGG cells exposed to 5-day treatment with IRH and blank F18 compared to negative and positive controls (n=3).

The levels of caspase 3 and 7 were determined after a 5-day incubation period with free IRH and the NP formulations using a luminescence assay which provided the highest values after 10 minutes from the start of the reaction. The reaction is based on the cleavage of proluciferin DEVD substrate by caspase resulting in the production of aminoluciferin which is a substrate of luciferase and ATP that through luciferase reaction produces light (Jue et al., 2005). As shown in Figure 6.58, the level of caspases produced by the cells exposed to the highest concentration of free IRH was significantly ($P<0.0001$) higher than the negative control. The rest of the concentrations did not have a significant difference compared to the negative control. Similarly, as shown in Figure 6.59 to Figure 6.61, the levels of caspases produced by cells incubated with the NP formulations were non-significant compared to the negative control except for the highest concentrations of the F2, F18 and blank F18 NPs, which were significantly ($P<0.0001$) lower than the negative control.

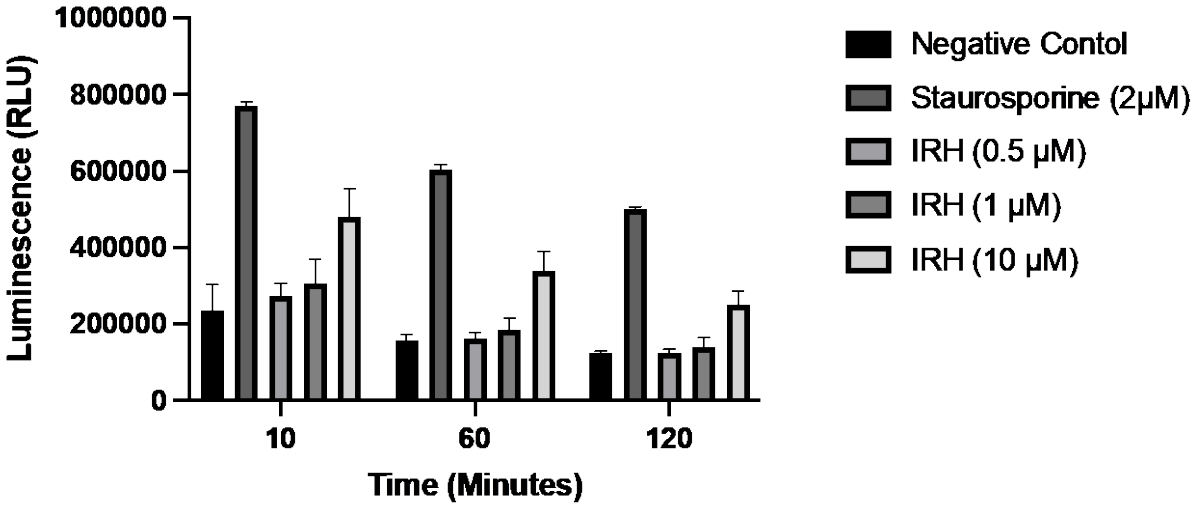


Figure 6.58. Caspase levels induced in HGG exposed to low, medium and high concentrations of IRH compared to positive and negative control expressed by relative light units (RLU) luminescence assay (n=3).

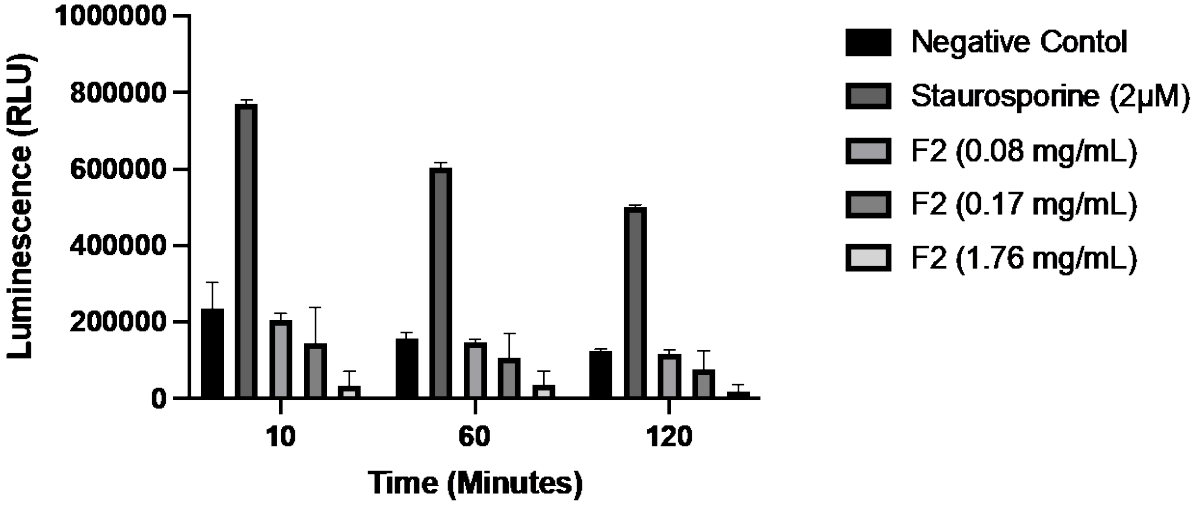


Figure 6.59. Caspase levels induced in HGG exposed to low, medium and high concentrations of F2 compared to positive and negative control expressed by RLU luminescence assay (n=3).

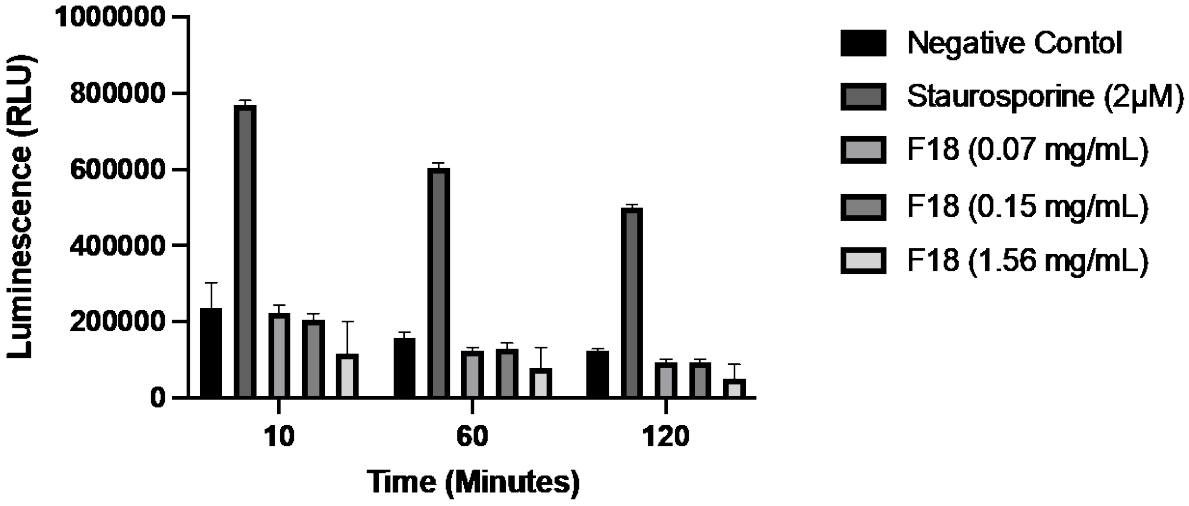


Figure 6.60. Caspase levels induced in HGG exposed to low, medium, and high concentrations of F18 compared to positive and negative control expressed by RLU luminescence assay (n=3).

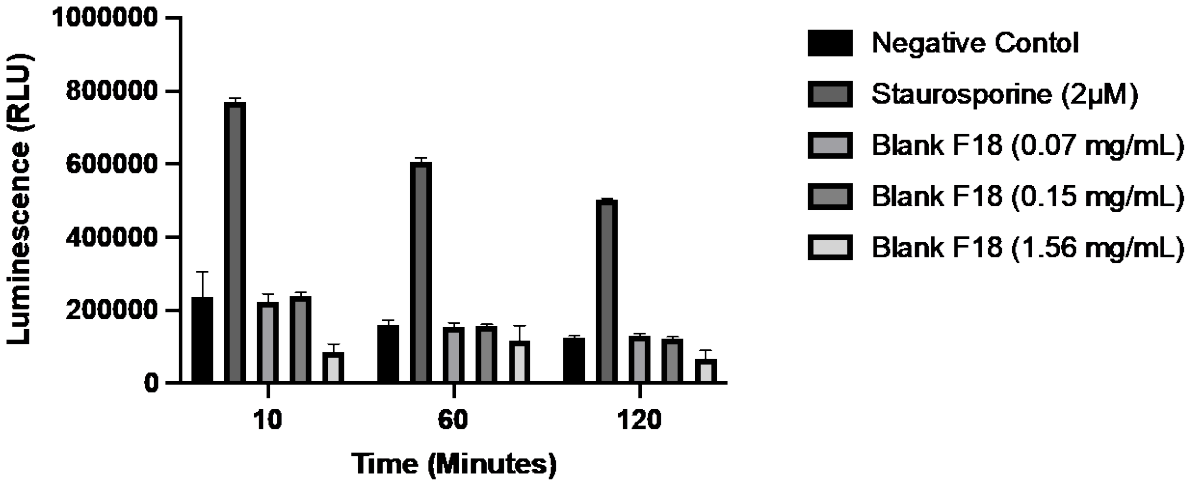


Figure 6.61. Caspase levels induced in HGG exposed to low, medium, and high concentrations of blank F18 compared to positive and negative control expressed by RLU luminescence assay (n=3).

As shown in Figure 6.62 to Figure 6.65, the levels of ATP produced by cells exposed to free IRH and F2 were significantly ($P<0.0001$) lower than that of the negative control on day 1 and day 3. Then, from day 5 onward there was no significant difference in the amount of ATP released by F2 and IRH treated cells compared to untreated cells. Only the highest concentration of F2 significantly ($P<0.0001$) reduced ATP level compared to negative control across most days. Similar trend was observed for cells treated with

F18 and blank F18, with an exception of the highest concentration of F18 which was consistent in reducing the ATP levels significantly (P<0.0001) compared with the negative control and IRH treated groups for all the treatment days. Additionally, the highest concentration of F18 had a stronger effect than F2 on depleting ATP which was significant (P<0.0001) from day 3 onward.

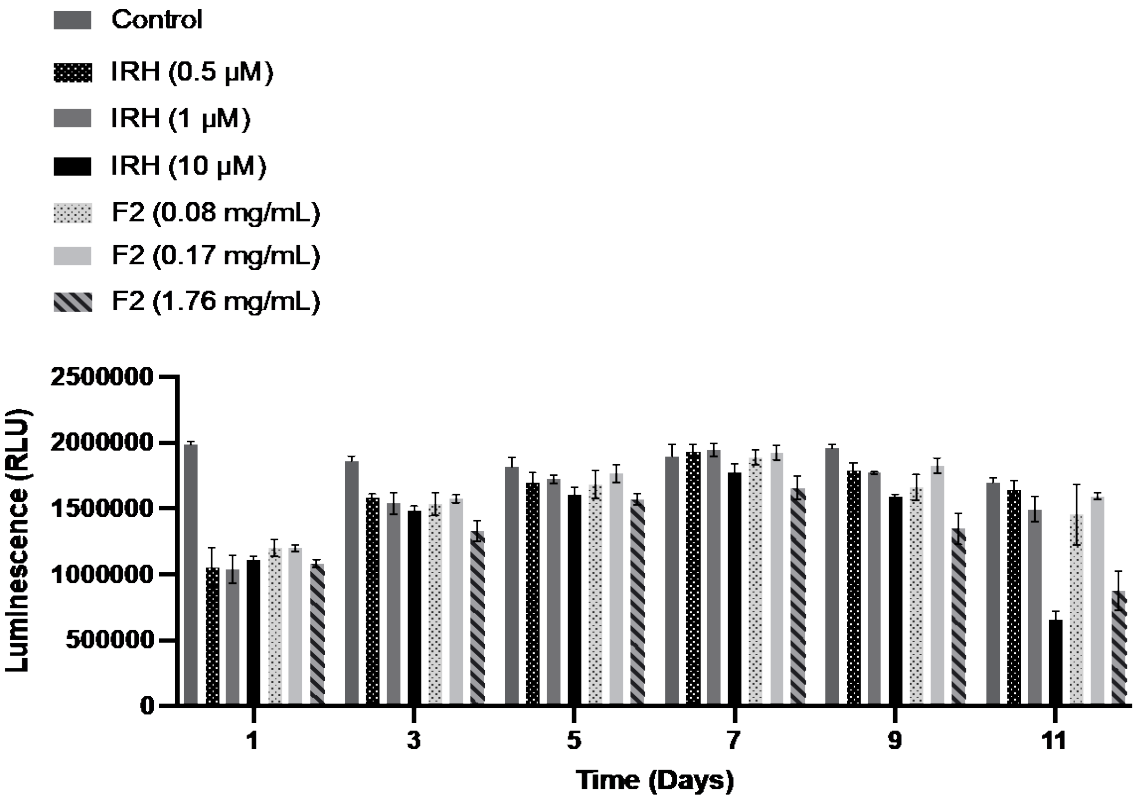


Figure 6.62. ATP levels induced in HGG exposed to low, medium and high concentrations of free IRH and F2 compared to negative control expressed by RLU luminescence assay (n=3).

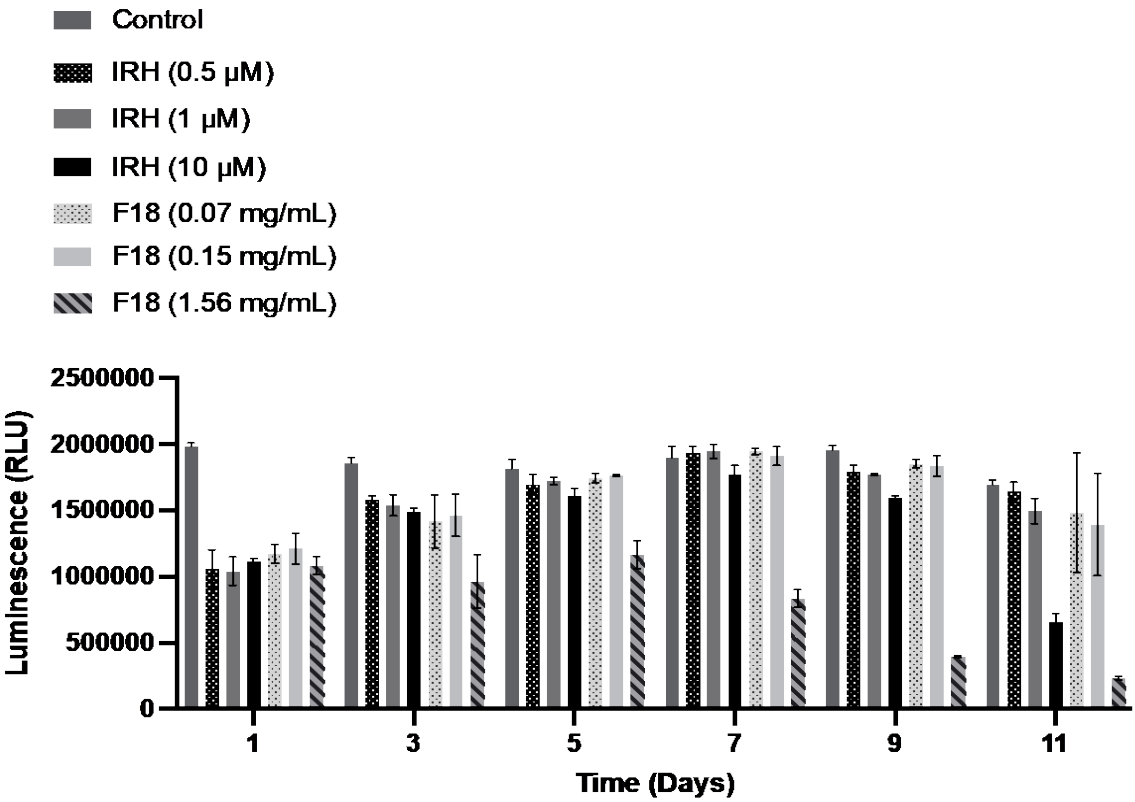


Figure 6.63. ATP levels in HGG cells exposed to low, medium and high concentrations of free IRH and F18 compared to negative control expressed by RLU luminescence assay (n=3).

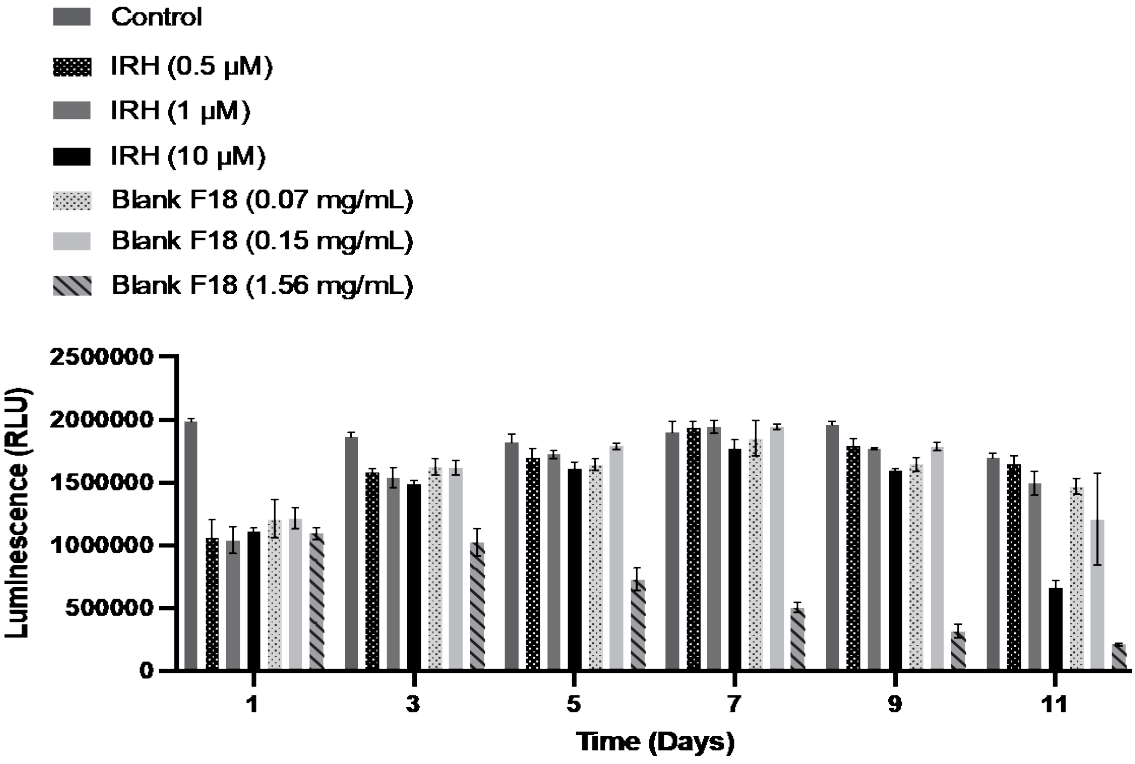


Figure 6.64. ATP levels induced in HGG exposed to low, medium, and high concentrations of free IRH and blank F18 compared to negative control expressed by RLU luminescence assay (n=3).

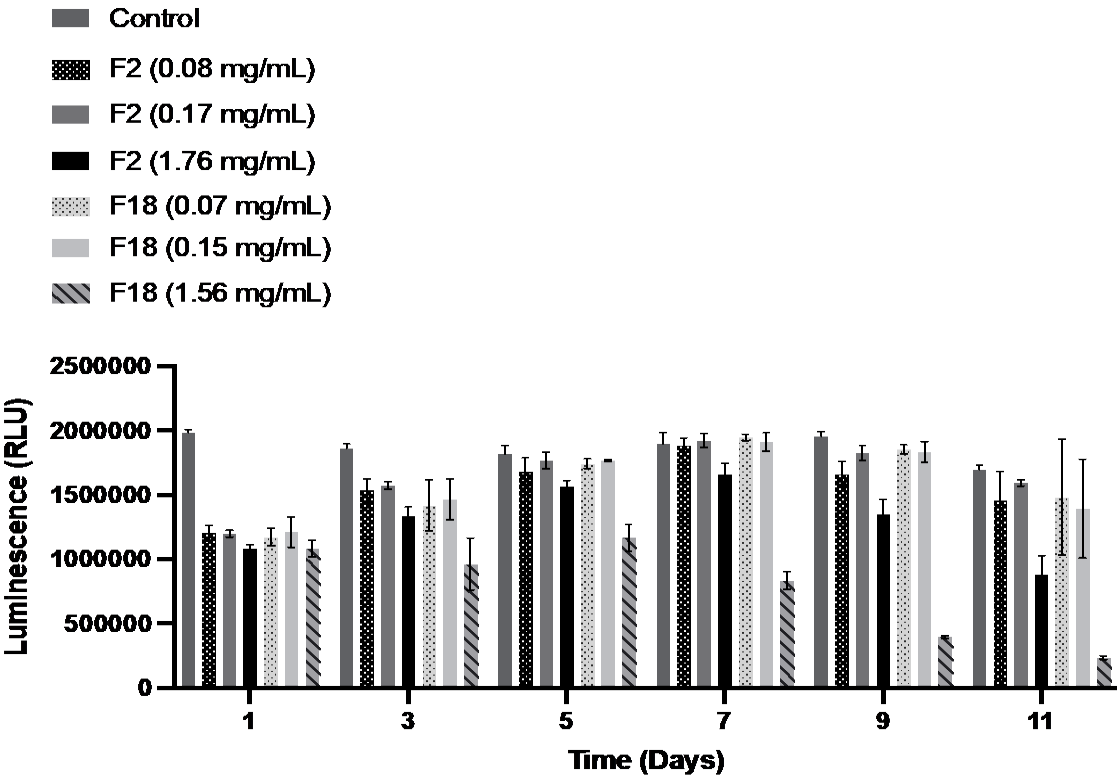


Figure 6.65. ATP levels induced in HGG exposed to low, medium, and high concentrations of F2 compared to F18 expressed by RLU luminescence assay (n=3).

6.3.5 Haemocompatibility

Blood compatibility of the NP formulations was assessed to check their suitability for intravenous administration compared to free IRH. The results, presented in Figure 6.66 to Figure 6.69 highlight that the highest concentration (100 μM) of IRH induced the highest (99.90%) haemolytic effect on the RBCs after 6 hours. On the contrary, the NP formulations induced minimal haemolytic effect (less than 5.00%) on the RBCs.

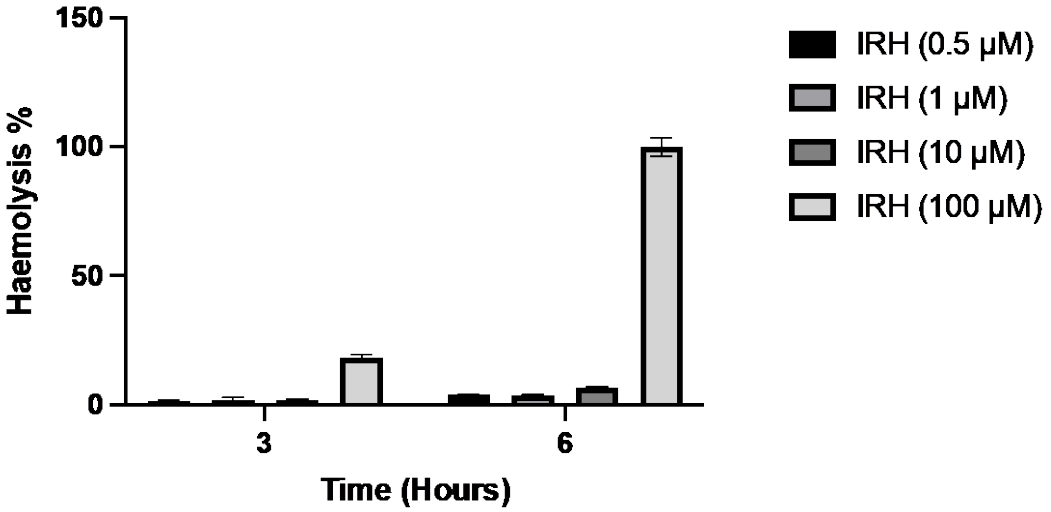


Figure 6.66. Haemolysis induced in RBCs by 0.5, 1, 10 and 100 µM of IRH (n=3).

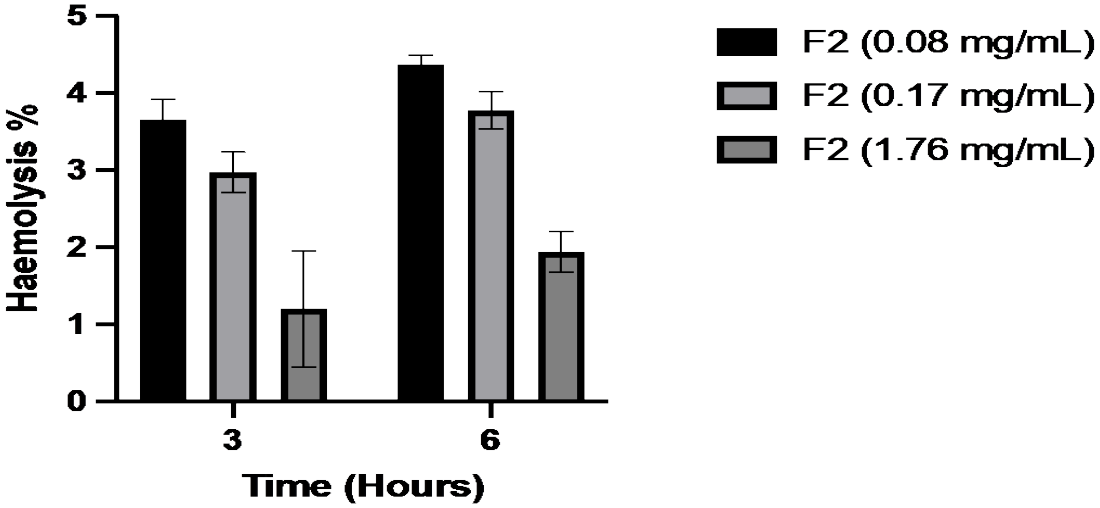


Figure 6.67. Haemolysis induced in RBCs induced by low, medium and high concentrations of F2 (n=3).

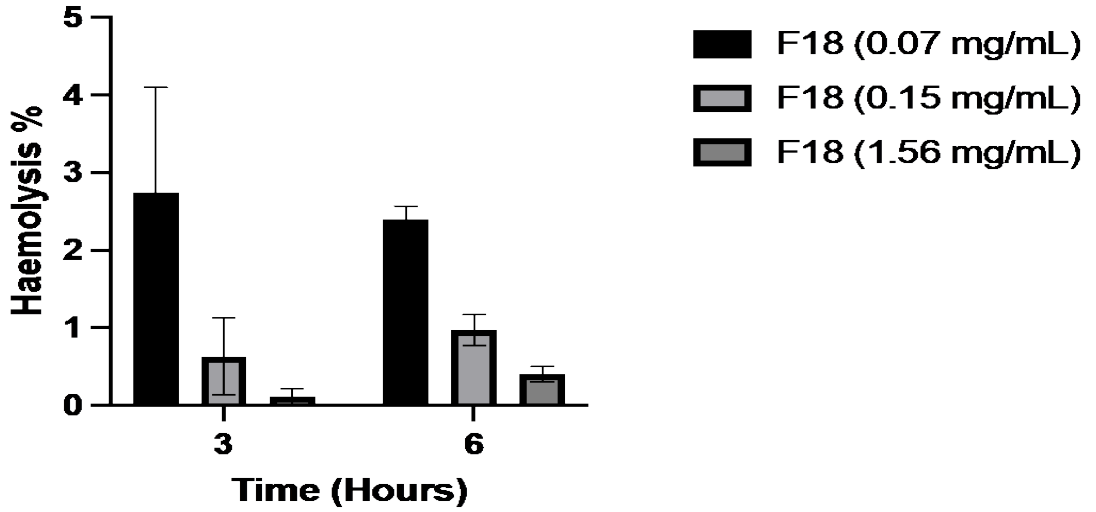


Figure 6.68. Haemolysis induced in RBCs induced by low, medium, and high concentrations of F18 (n=3).

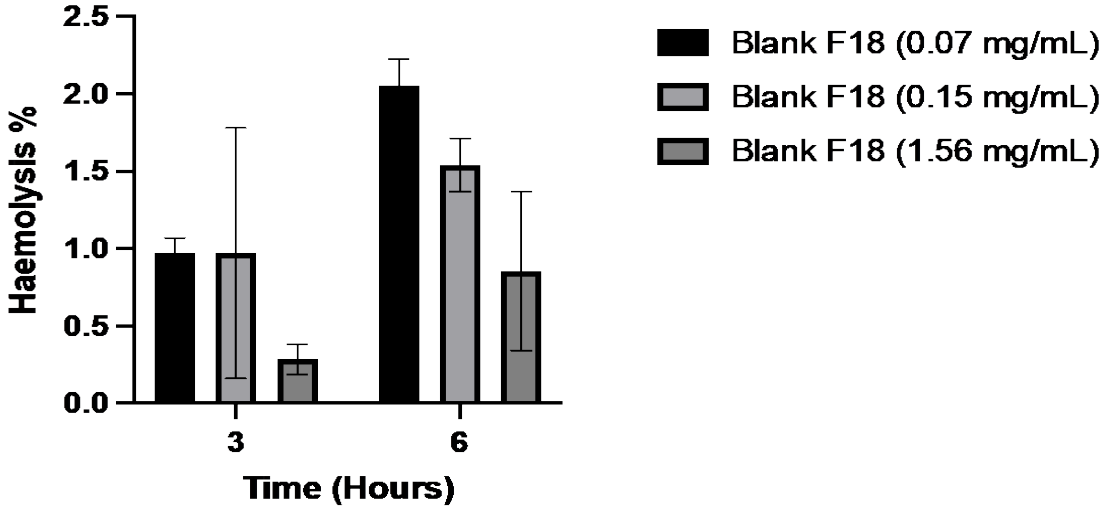


Figure 6.69. Haemolysis induced in RBCs induced by low, medium, and high concentrations of Blank F18 (n=3).

6.3.6 IL-6 Protein Expression

Figure 6.71 to Figure 6.75 demonstrate the difference in IL-6 protein expression in HGG cells treated with free IRH and the NP formulations (F2, F18 and blank F18) at days 3 and 5. The OD of IL-6 standard concentrations is shown in Figure 6.70. IL-6 was expressed the highest in the HGG cells exposed to the highest concentrations of the free IRH and F2 NPs producing concentrations of 909.35 pg/mL and 439.93 pg/mL respectively compared to 326.54 pg/mL for the control group on day 3 (Figure 6.71). The free IRH was significantly ($P<0.0001$) more immunogenic than the F2 NPs at their highest concentrations. The low and medium concentrations of both the free IRH and F2 NPs did not exhibit a significant difference compared to the control group (Figure 6.71). Similarly, treatment with F18 (Figure 6.72) did not induce a significant level of IL-6 when compared to the control group except for the highest concentration that induced an elevated level (548.76 pg/mL) of IL-6 on day 3 which was still significantly ($P<0.0001$) lower than that induced by the free IRH and higher than that of F2 NPs.

On day 5, the level of IL-6 was significantly elevated by treatment with the free IRH peaking at 1312.83 pg/mL for the highest concentration ($P<0.0001$). Whereas, treatment with the F2 NPs continued to induce a downregulation of IL-6 expression by the HGG cells reaching a non-significant difference for most doses with the control group (Figure 6.71). On the other hand, the F18 treatment resulted in a significantly ($P<0.0001$) high expression of IL-6 (844.93 pg/mL) at its highest concentration compared to the negative control, blank F18 (641.63 pg/mL) and F2 (289.99 pg/mL). Such effect was however significantly ($P<0.0001$) lower than that of free IRH at the same concentration (Figure 6.72).

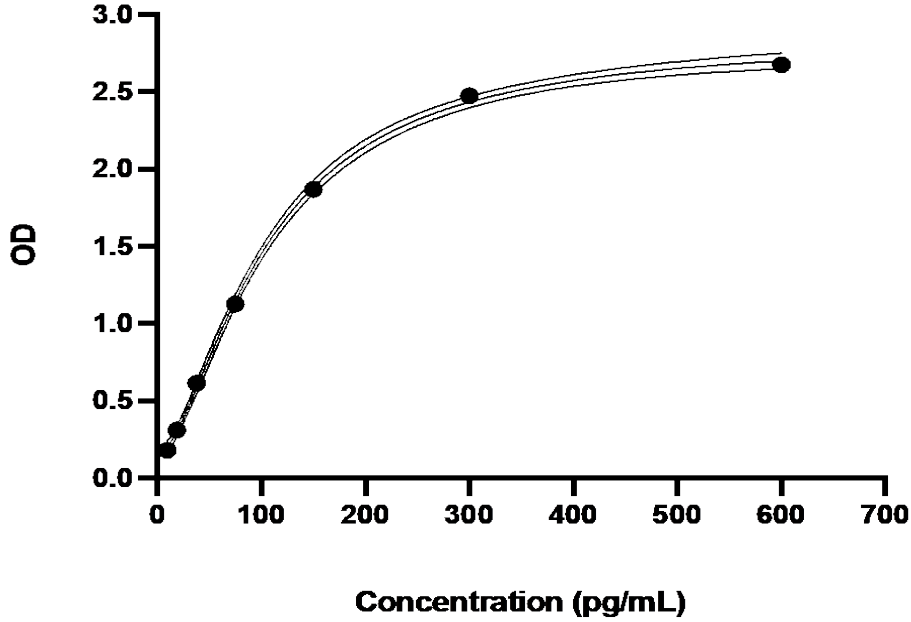


Figure 6.70. OD of IL-6 standard concentrations of human IL-6 (n=3).

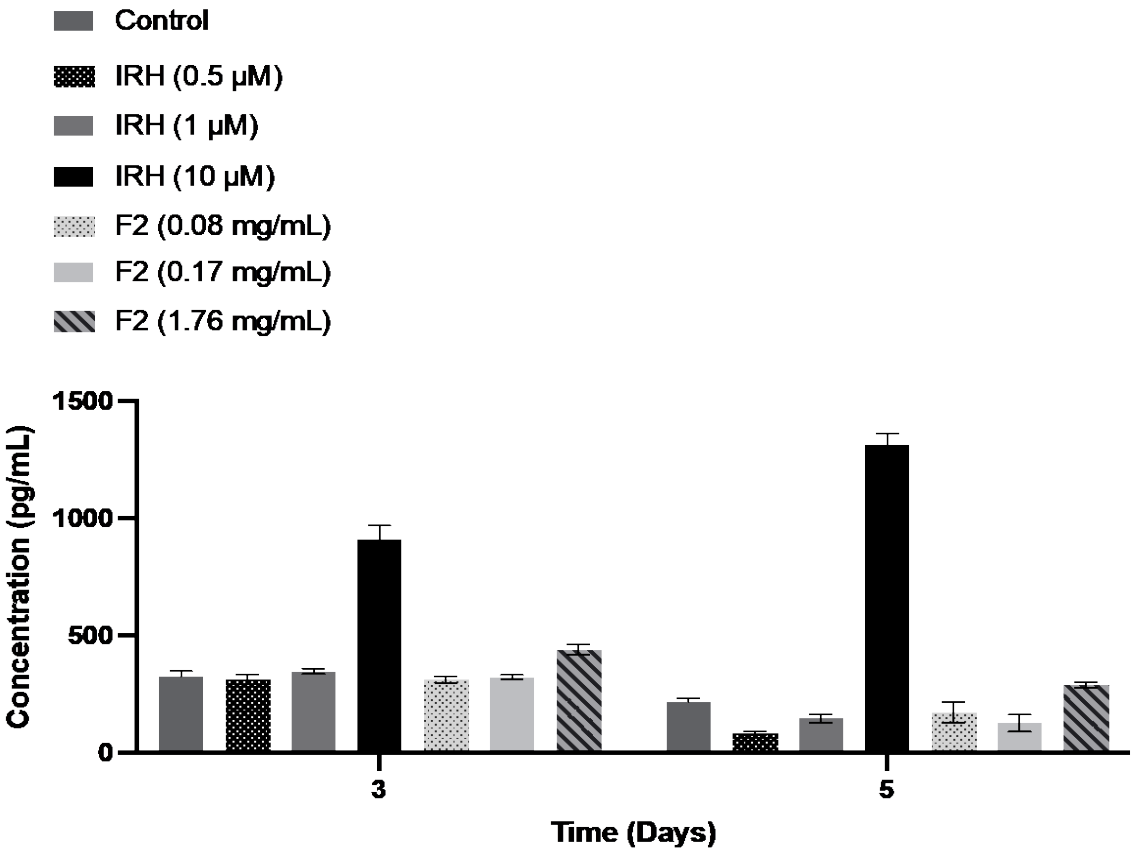


Figure 6.71. Expression of IL-6 in primary HGG cells exposed to low, medium and high concentrations of free IRH and F2 for 3 and 5 days (n=3).

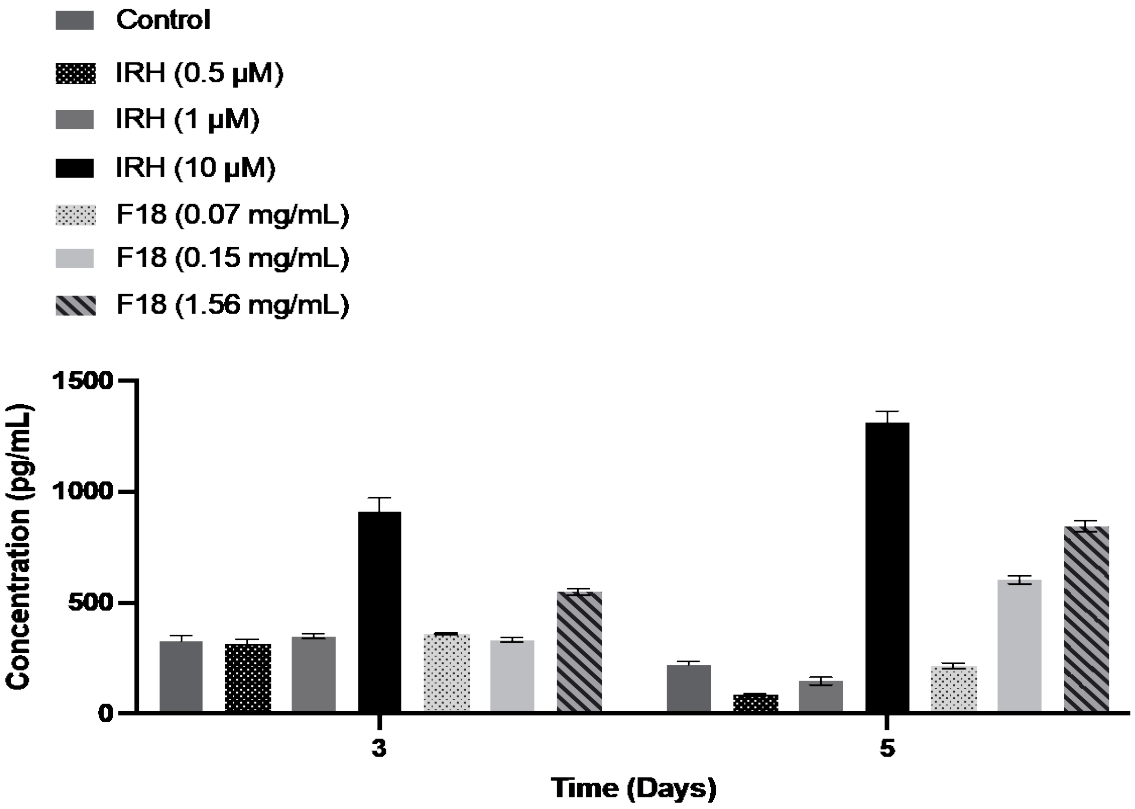


Figure 6.72. Expression of IL-6 in primary HGG cells exposed to low, medium and high concentrations of free IRH and F18 for 3 and 5 days (n=3).

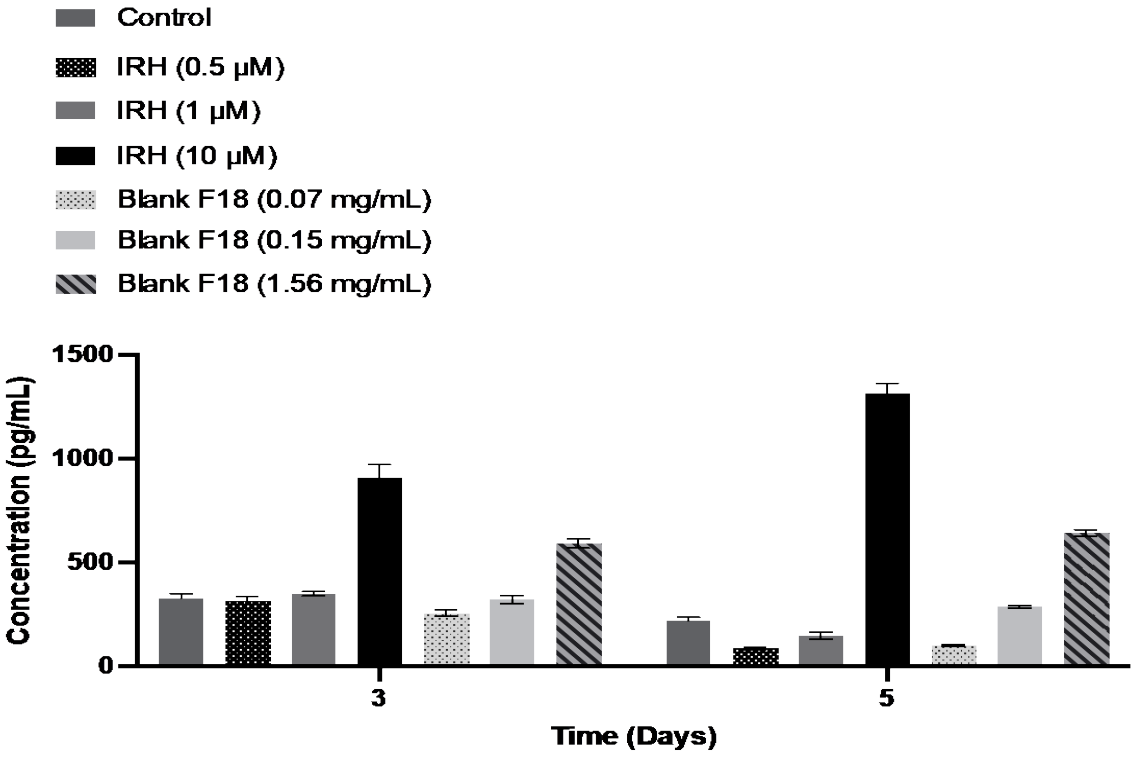


Figure 6.73. Expression of IL-6 in primary HGG cells exposed to low, medium, and high concentrations of free IRH and blank F18 for 3 and 5 days (n=3).

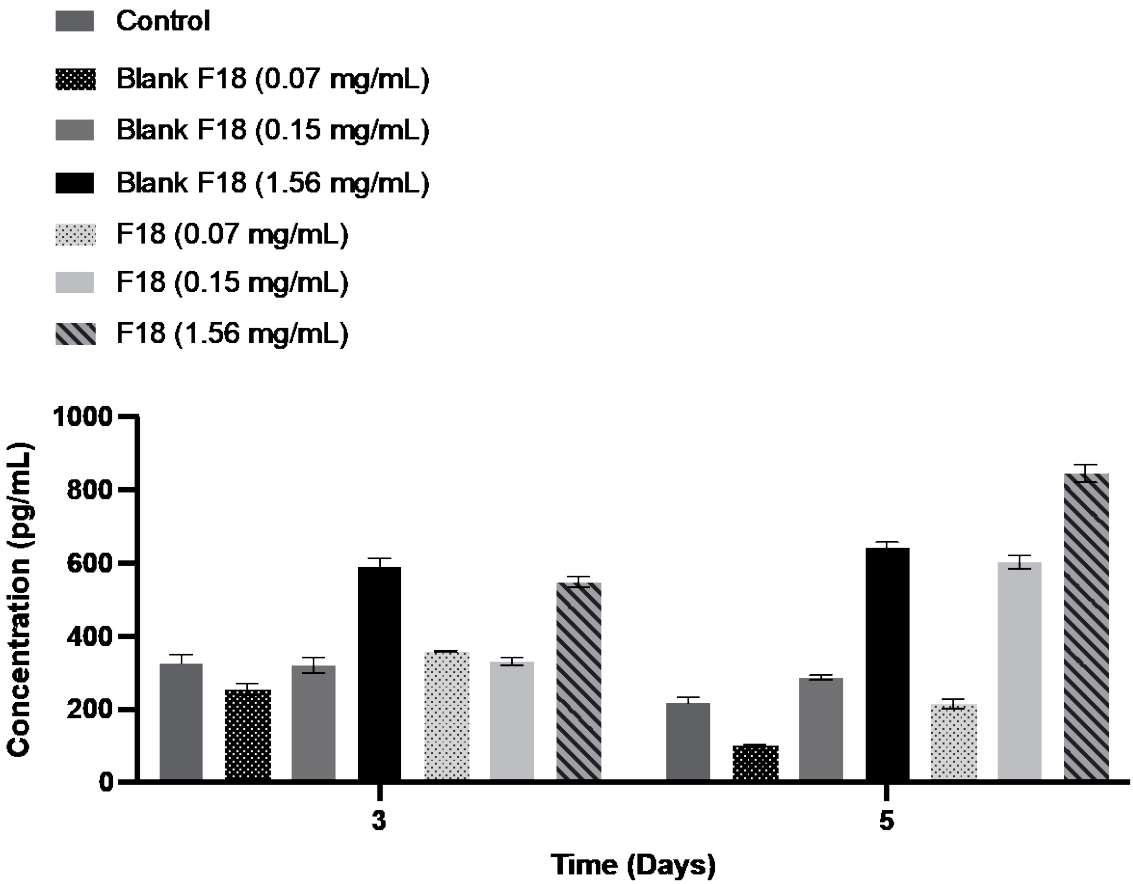


Figure 6.74. Expression of IL-6 in primary HGG cells exposed to low, medium, and high concentrations of F18 and blank F18 for 3 and 5 days (n=3).

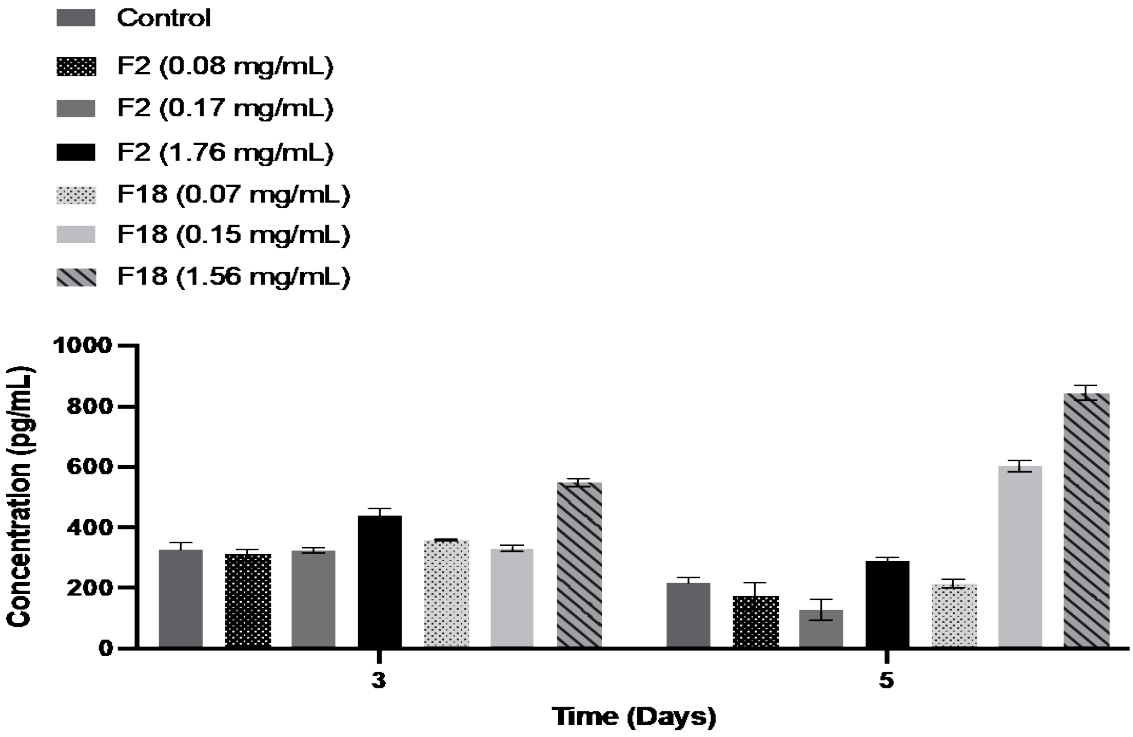


Figure 6.75. Expression of IL-6 in primary HGG cells exposed to low, medium, and high concentrations of F2 and F18 for 3 and 5 days (n=3).

6.4 Discussion

The aim of developing drug loaded carriers is to prevent the unwanted degradation of the drug and avoid its premature action until reaching the target site (Sadat et al., 2016). Our study investigated the cellular uptake of NPs loaded with IRH over a 9-day interval in comparison with the uptake of free IRH. Untreated cells were used as a negative control. Cellular uptake of therapeutics is assessed by monitoring the SSC intensity which increases as a sign of higher cellular complexity and granularity. By evaluating HGG cellular uptake of free IRH and the NP formulations, it was apparent that the SSC intensity of cells treated with the free IRH showed no significant difference compared to the negative control across the entire treatment period. This observation was evident for all 3 concentrations of the free drug. This could be attributed to the hydrophilic nature of the IRH that struggled to passively diffuse across the lipid bilayer of the HGG plasma membrane in high amounts and due to insufficient light scattering by the drug molecules within the solution. On the other hand, PCL and PCL-PLGA blended NPs were transported inside the cells to a greater extent compared to the free drug and negative control. This suggests a different internalization mechanism undertaken by HGG cells to allow the hydrophobic polymeric NPs inside the cells. The internalization was mostly concentration and time dependent until day 5, when a noticeable drop in SSC was recorded indicating that the majority of cells were dead and removed during the analysis and only the live cells that had less internalized particles were analysed showing low SSC intensity.

Drug loaded NPs exhibited better cellular uptake by endocytosis as previously reported, while their mechanism of internalization avoids the P-gp pumps which allows

higher residence inside the tumour (Yoo and Park, 2004). This in turn allows them to be more cytotoxic than the free drug as they trigger different mechanisms of cytotoxicity (Sanna et al., 2011). Likewise, the uptake of a hydrophilic dye by HGG cells was enhanced by loading it onto the hydrophobic PLGA as previously reported (Jain et al., 2014). Another study reported the cellular uptake of PLGA NPs ranging in size from 100 nm to 1 μM that were highly internalized by co-cultured UM-SCC-17A laryngeal cancer cells and THP-1 monocytes/macrophages (Ma et al., 2021). Also, the cellular uptake of radiolabelled PCL and PLGA NPs was higher than free etoposide when intravenously administered into mice (Snehalatha, Venugopal and Saha, 2008). Similarly, PEGylated PLGA NPs were found to be permeated by retinal pigment epithelial cells (ARPE-19) *in vitro* with organelle localization as in mitochondria, endoplasmic reticulum, and lysosomes (Lin et al., 2016).

Similar to the present data, anionic NPs exhibited a significantly better ratio of transport to cell uptake across Caco-2 monolayer cells compared to the positively charged particles of equivalent size despite higher uptake of the positively charged particles (Bannunah et al., 2014). The transport was measured by analysing the basolateral solution at certain time intervals. Cellular uptake occurred for both negatively charged and positively charged NPs. Another study suggested that there was no significant variation between negatively charged and neutral poly (ethylene glycol)-poly (D, L-lactide) block copolymer micelles in blood clearance kinetics following intravenous administration. However, the negatively charged micelles had lower distribution in liver and spleen after 4 hours of administration (Yamamoto et al., 2001). Positively charged NPs could have an enhanced uptake due to adsorption on the negatively charged

plasma membrane (Zhao et al., 2011). However, they develop other issues by forming aggregates with plasma proteins and can be locked in the lung as previously reported (Ishiwata et al., 2000). Exposure of PLGA/PVA NPs to serum containing media did not exhibit a major change in charge which is in consistency with our results (Sadat, Jahan and Haddadi, 2016).

Different routes of endocytosis were reported to mediate the cellular uptake of PLGA NPs, the most prominent of which was the clathrin-independent route (Gao et al., 2009; Gal et al., 2015; Foroozandeh and Aziz, 2018). However, NPs endocytosed via such pathway end up in the lysosomes (Cartiera et al., 2009).

Cell imaging by confocal microscopy could precisely confirm the subcellular localization of drugs and NPs. The data demonstrated the localization of the NPs, either loaded with IRH or Rhodamine 123, around or inside the nucleus, which indicates that the NPs or the IRH could escape lysosomal degradation and enter the nucleus, which is the target for IRH as it interferes with DNA replication preventing cells from multiplying. The mechanism by which PLGA NPs evade lysosomes was previously suggested to be through their electrostatic interaction with the vesicular membrane leading to its destabilization which facilitates the rapid escape of the NPs into the cytosol (Panyam et al., 2002). Additionally, polymeric NPs loaded with doxorubicin were internalized and had an extended residence in the nuclei of HeLa cells compared to the free drug (Han et al., 2012). This could be due to the limitations imposed by the nuclear membrane that allows particles less than 100 nm and 40-45 kDa to passively translocate to the nucleus. Whereas, other molecules may interact

with cytoplasmic factors and create nuclear pore complexes (Görlich and Kutay, 1999). Also, negatively charged NPs made of carboxymethyl chitosan and loaded with Rhodamine B had higher distribution in tumours due to longer residence time in circulation (Alexis et al., 2008b).

The cytotoxicity of the free IRH and NP formulations was evaluated over 11 days against primary HGG cells obtained from 3 different patients. The overall trend in all three patients involved a significant reduction ($P<0.0001$) in cell viability for cells treated with the NP formulations compared to the free IRH and negative control across most doses and days. The highest cytotoxic effect was achieved at day 11, reaching a non-significant difference between the free IRH and drug loaded formulations (F2 and F18). Despite exerting a cytotoxic effect, the free IRH had a lower effect compared to the drug loaded NPs which is due to the hydrophilicity of the drug and its lower permeability across the lipid bilayer as highlighted by the cellular uptake study. This limitation was removed by encapsulating the IRH into hydrophobic NPs. Conversely, the blank F2 NPs had a less cytotoxic effect than the free IRH by day 11 for all patients. Additionally, the blank F2 NPs maintained a higher cell viability compared to their drug loaded counterparts. Similar observations were noted for the blank F18 NPs that were less cytotoxic than the IRH-loaded F18 NPs from day 5 and less cytotoxic than the free IRH on day 7, 9 and 11 for the highest concentration. Our results demonstrate that blank F18 NPs were more cytotoxic than the blank F2 NPs indicating that the blended NPs degrade faster due to the presence of PLGA resulting in cytotoxic degradations products (lactic acid and glycolic acid) or that the PVA was forming a complex structure with both PCL and PLGA which was more toxic to the cells. Similarly, the F18 NPs were significantly ($P<0.0001$) more cytotoxic than the F2 NPs especially towards the

end of the incubation period, indicating that the IRH had greater release from the F18 NPs towards the end of the incubation period due to the degradation of the PLGA. Similar to our results, toxicity of the PLGA and PCL NPs was time-dependent in a study conducted for 6 days on primary retinal vascular endothelial cells (RVEC) and ARPE-19 cells. While PEGylated PLGA NPs exhibited the lowest cytotoxicity on the cells in the same study (Lin et al., 2016). Additionally, it is noteworthy that gravity can lead to a concentration and size dependent sedimentation of the NPs *in vitro* which could result in variations in their cellular response (Cho, Zhang and Xia, 2011; Agarwal et al., 2013; Sahin et al., 2017). Taken together, the cytotoxic effect of all NP formulations could be partially related to the surfactants used, such as PVA, which was previously reported to induce a cytotoxic effect against macrophages when used in formulating PLGA NPs (Grabowski et al., 2016). However, the same study suggested that the toxicity imposed by the surfactants did not involve apoptosis, oxidation or cytokine production and that free surfactant was non-toxic. This issue can be alleviated by designing surfactant free NPs to ensure that cytotoxicity is purely by action of the drug and not the carrier.

Triggering cancer cells to become apoptotic or necrotic is the main goal in the treatment of cancer (Hanurry et al., 2020). Among the primary markers that signal the development of apoptosis is the phosphatidyl serine residues that flip to the external side of the plasma membrane and can be detected by Annexin V fluorophore. The PI associated with Annexin V specifically binds with nucleic acids when the plasma membrane is impaired indicating necrotic cell death (Dos Reis et al., 2019). In this study the percentage of apoptotic and necrotic cells was evaluated after incubation

with blank and drug loaded NP formulations and then compared to the free IRH, negative control and positive control groups. The percentage of live cells decreased consistently for all treatments over time, in which the cells underwent apoptosis and necrosis at different rates. Apoptosis was the dominant pathway of cell death across days for most of the formulations. This is due to the localization of the NPs in the nucleus, as confirmed by confocal imaging, causing disruption to the DNA which triggered apoptosis and inhibited cellular proliferation (Morales-Cruz et al., 2014). Longer incubation periods induced higher apoptosis and necrosis with the highest concentration of free IRH exhibiting the highest apoptotic effect starting at 20.88% on day 1 and increasing to 40.27% on day 3 and 92.89% on day 5. The highest concentration of the F2 NPs exerted the highest apoptotic effect of 29.45%, 37.67% and 62.07% on day 1, 3 and 5 respectively, while the F18 NPs were also apoptotic with their strongest effect induced by the highest dose resulting in 31.49%, 36.01 and 81.10% apoptosis on day 1, 3 and 5 respectively. However, the F18 NPs were more necrotic than the F2 NPs inducing 31.53% and 29.53% necrosis by day 5 for the low and medium concentrations respectively. Furthermore, the blank F18 NPs were more necrotic than the blank F2 NPs inducing 43.63% and 25.80% necrosis compared to 8.75% and 11.76% by blank F2 for the low and medium concentrations by day 5 respectively, while the high concentration of the blank F18 NPs induced 82.97% apoptosis compared to 15.71% for the blank F2 NPs. However, the cells treated with blank F18 NPs were less apoptotic and necrotic on day 1 and 3 compared to day 5, with a range of 55.63% to 73.63% of cell viability, while, the blank F2 NPs had cell viabilities ranging from 64.46% to 80.3% from day 1 to day 5. This indicates that there is a certain apoptosis level above which cells then enter the necrosis phase and die

irreversibly. Thus, the apoptosis/necrosis analysis by flow cytometry confirmed the results of the cytotoxicity and cellular uptake studies indicating that the NP formulations are more efficient in eliciting apoptosis and interrupting cellular proliferation compared to the free IRH except at its highest dose. This is due to the limited internalization of the hydrophilic drug by the HGG cells concluding that improved internalization of therapeutics is a key to effective treatment.

Apoptosis is triggered in cancer cells by chemotherapies via the intrinsic or extrinsic pathway (Fulda and Debatin, 2006). Caspase 3 and 7 were reported to be the main contributors towards the cleavage cascade that occurs during the intrinsic and extrinsic apoptosis. To confirm if the mechanism of apoptosis induced by the NPs was via caspase activation, a luminescence caspase assay was performed to assess the level of caspase 3 and 7 in the HGG cells treated with the free drug and NP formulations. The signal of the luminescence was examined at 3 different time points and was shown to be reduced at longer time points indicating a loss of reaction stability over time. The data demonstrates that the expression of caspases by the HGG cells was higher at day 5 when treated with the free IRH compared to the negative control with a significant difference ($P<0.0001$) observed only at the highest concentration of IRH. With the NP formulations, the caspase levels were either non-significant compared to the free IRH and negative control or were significantly lower ($P<0.0001$) for the highest concentrations of the F2 and blank F18 NPs compared to the negative control group. This indicates that the level of caspases was either reduced faster following apoptotic mortality induced by the NPs as the HGG cells were developing into a necrotic state especially as the level of caspase-3 peaks 3 to 4 hours after the induction of apoptosis

(Elliott and Ravichandran, 2016) or that NPs activated a caspase independent apoptosis. Apoptotic cells that are not engulfed by phagocytes develop into secondary necrosis when the caspase-3 level is low (Beroske et al., 2021).

To further understand the mechanism of cell death induced by the NPs and free drug, the levels of ATP in HGG cells were determined at specific incubation time points using a luminescence assay. The assay measured the RLU of emitted light relevant to the amount of ATP released from the lysed cells after reacting with luciferin and luciferase in the presence of oxygen and magnesium (Frauwirth and Thompson, 2002). Mitochondrial dysfunction during late-stage apoptosis results in ATP depletion which is consumed in the caspases cascade, with further depletion of the ATP occurring during necrosis leading to cell hypoxia (Vanlangenakker et al., 2008). However, cells may develop a resistant defence mechanism by which they increase the rate of glycolysis to produce more ATP in response to genetic toxicity (Zhou et al., 2012). This is in accordance with our data in which the ATP levels of the HGG cells exposed to the free IRH and NPs were significantly ($P<0.0001$) depleted on day 1 compared to the untreated cells which indicates mitochondrial damage. However, the ATP levels recovered on day 3 for all the treated groups due to a higher glycolysis rate as a defence mechanism induced by the cells (Zhou et al., 2011). However, F18 and its blank NPs had the strongest effect, especially at their highest concentration, on depleting the ATP over time. Other reports highlighted the role of blank and drug loaded NPs in bypassing the MDR, demonstrating that the blank NPs effectively depleted the ATP levels in a dose dependent manner (Dong et al., 2009). The mechanism by which NPs bypass cell resistance to treatment is proposed to be due to

their internalization route by endocytosis leading to downregulation of P-gp in addition to altering the signalling pathway involved in caspase dependent apoptosis (Minko et al., 1998; Minko, Kopečková and Kopeček, 2001).

Traditional chemotherapy treatment is known to induce haemolytic anaemia which is a major complication for cancer patients (Groopman and Itri, 1999). The mechanism of haemolysis involves ROS production by oxidative stress or rupture of the cell membrane induced by the chemotherapy (Lin et al., 2019). The FDA has approved the haemolytic assay as a method of evaluating the haemolytic effect of therapeutics administered intravenously (U.S. Department of Health and Human Services Food and Drug Administration Centre for Drug Evaluation and Research FDA, 2005). The results demonstrate that haemolysis was evident for the highest dose (100 μM) of free IRH after 6 hours, inducing almost 100% of haemolytic activity. IRH and oxaliplatin were previously reported to be involved in acute haemolytic anaemia in a case study of advanced colon cancer and liver metastasis (Tam et al., 2019). The RBCs incubated with the NP formulations exhibited minimal haemolytic activity, indicating the biocompatibility of the NPs and their suitability for intravenous administration. As previously highlighted, a haemolytic effect of up to 20% is considered acceptable for polymeric NPs and that PCL polymeric NPs induced minimal haemolysis and were haemocompatible (Kumar et al., 2015). Another study reported that RBCs were intact when they were in contact with polymeric NPs at certain concentrations (da Silva et al., 2019). Cationic polymeric NPs were also reported to exert higher haemolysis compared to negatively charged particles (Sadat, Jahan and Haddadi, 2016).

Multiplication of tumour cells is greatly influenced by inflammation which could have a pro or anti effect against tumours depending on several factors such as the type of immune cells involved, stage of the tumour and cytokines produced. This complex environment is not well explored in HGG compared to other tumour types (Galvão and Zong, 2013). It was previously documented that IL-6 plays a central role towards the development and aggression of primary HGG cells (Zanotto-Filho et al., 2017). HGG tumours contain high levels of IL-6 as a result of immune cells infiltrating into the tumour or by the tumour cells themselves (Hunter and Jones, 2015). IL-6 was reported to exert its role in enhancing the aggression of tumours through inhibiting the process of apoptosis, promoting angiogenesis and inducing chemo resistance via several signalling pathways. IL-6 is a key player in the innate immunity where it stimulates the production of immune cells to start an inflammatory cascade. Therefore, inhibiting IL-6 could be an effective step towards tumour treatment (Liu et al., 2017). Quantification of the level of IL-6 in the supernatant of several HGG cell lines highlighted that expression of IL-6 in HGG cells was much higher than its expression in normal brain tissues (Shan et al., 2015). The concentrations of IL-6 increased significantly with increased malignancy. Further, they found that incubation of U87 and A172 cells with exogenous IL-6 of 100 ng/mL could promote the aggressiveness of the tumour cells (Shan et al., 2015). Another study confirmed that in the absence of IL-6, the tumour was stable in mice (Weissenberger et al., 2004).

The data examines IL-6 protein expression in HGG cells treated with free IRH and the NP formulations for 3 and 5 days. It was apparent that the highest concentrations of

the free IRH and NPs induced the highest expression of IL-6, with highest concentration of free IRN being more immunogenic than the NP formulations.

In conclusion, HGG had a more enhanced cellular uptake of both PCL and PCL-PLGA blend NPs compared to the free IRH, which were confirmed by the confocal microscopy and co-localized within the nuclei. Such enhanced uptake of the NPs has resulted in a higher cytotoxicity profile as compared to free IRH. The blank NPs had mostly preserved the viability; however, they exerted some cytotoxicity against HGG cells, with blank F18 showing more cytotoxicity than blank F2, due to its higher degradation rate and release of acidic products. This was further confirmed by investigating the apoptosis and necrosis mechanisms in cells. It was obvious that the NPs were more apoptotic than the free IRH in a time dependent manner and that the blank NPs induced less apoptotic effect than their drug-loaded counterparts on day 3. On day 5, the IRH induced high apoptosis only at the highest concentration. The percent of necrotic cells increased by all treatments by day 5. Additionally, the caspase levels measured in response to IRH treatment were high compared to the NP treatments indicating a faster apoptotic rate occurring by NPs that was developing into a secondary necrosis or that NPs activated a caspase independent apoptosis. Exposure of the HGG cells to the free IRH and NP formulations has reduced the levels of ATP significantly ($P<0.0001$) on day 1. The NPs showed haemocompatibility and were significantly ($P<0.0001$) less immunogenic than the free IRH as indicated by IL-6 level. The next chapter will examine the behaviour of the PCL and PCL-PLGA blend NPs in the environment of the endothelial cells.

Chapter 7 BIOLOGICAL CHARACTERIZATION OF AN ENDOTHELIAL CELL LINE TREATED WITH DRUG LOADED NPS

7.1 Introduction

7.1.1 BBB and Transendothelial Electrical Resistance (TEER) Measurement

The BBB restricts and regulates entry of molecules from the systemic circulation into the brain. It also functions in maintaining the volume and composition of the brain fluid through its special transport mechanisms. Essential nutrients such as glucose and some amino acids can enter the brain but other toxic molecules and therapeutics are prohibited from entry (Betz and Goldstein, 1986; Strange, 1992).

The BBB consists mainly of endothelial cells which act as a tight boundary that line the brain capillaries. It has two sides; the luminal facing the blood and the abluminal facing the brain. The tight junctions limit the passage of molecules *via* paracellular transport, compared to specific passive or active transport which limits the entry of molecules into the brain. Furthermore, the tight junctions restrict the movement of the membrane proteins between the apical side allowing endocytosis and the basolateral side allowing transcytosis and thus protecting the function of the BBB (Masserini, 2013)Therefore, molecules have to traverse the BBB to enter the brain (Peterson and Hawkins, 2003). Astrocytes contribute to the formation of the tight layer of BBB by secreting paracrine substances enabling the endothelial cells to become compactly adherent while acquiring a polar configuration (Sobue et al., 1999). The tight endothelial barrier has a high electrical resistance greater than 1000 Ω cm^2 with electrolyte transport dependent on transport proteins present in the luminal and abluminal plasma membranes that aid in the transcellular rather than paracellular transport (Hawkins and Davis, 2005b). The presence of the P-gp efflux pump acts as a selective guard that allows the entry of some molecules while preventing the entry of others including drugs (Masserini, 2013).

Pericytes which exist in the basal membrane act by regulating the proliferation of the endothelial cells.

One of the methods used to examine the integrity of the BBB is measuring the TEER of endothelial cells cultured on semipermeable filters with apical and basolateral sides. TEER is measured using chopstick electrodes with one in contact with the lower compartment where the tissue culture media exists and the other in the upper compartment where the endothelial cells are cultured, with the TEER recorded in Ohm x cm^2 (Wilhelm et al., 2011).

There is a body of evidence that prolonged exposure of the normal brain endothelium to the tumour microenvironment of gliomas could alter the structure and functional behaviour of the endothelium. Endothelial cells present in the tumour microenvironment have a faster migration and different proliferation rate than normal endothelial cells (Charalambous et al., 2005). Certain growth factors such as the VEGF produced by the glioma cells participate in the communication between glioma and endothelial cells promoting angiogenesis (Dubois et al., 2014).

Therefore, it is important to assess the effect of NP exposure on the viability, permeability and cytokine expression in endothelial cells to allow effective glioma targeting. This chapter aims at examining the biology of the endothelial cells in response to the free IRH and NP formulations by assessing their TEER, morphology, cytotoxicity, mechanism of cytotoxicity and immune response.

7.2 Materials and Methods

7.2.1 Materials

Endothelial cell culture EndoGRO TM MV supplement kit was purchased from Millipore (Watford, Hertfordshire, UK).

7.2.2 Cell Culture of Endothelial Cell Line

Endothelial cells were grown and maintained in endothelial cell culture kit with the same protocol used for primary HGG cells as described in Chapter 2, Section 2.2.12. Sterile 6.5 mm transwell plates with an 8.0 μm pore size polycarbonate membrane insert, were purchased from Corning (Flintshire, UK)

7.2.3 Flow Cytometry Analysis of Cellular Uptake in Endothelial Cell Line

Cellular uptake analysis in endothelial cells followed the same protocol described in Chapter 6, Section 6.2.3 for primary HGG cells.

7.2.4 *In Vitro* Cytotoxicity and Morphology of Endothelial Cell Line

The cell culture, cytotoxicity and morphology of the NP treatments against endothelial cell line was evaluated as described in Chapter 2, Section 2.2.12 and Chapter 6, Section 6.2.4

7.2.5 Flow Cytometry Analysis of Apoptosis and Necrosis in Endothelial Cell Line

Assessment of apoptosis and necrosis in endothelial cells exposed to free IRH and NP formulations followed the same protocol described in Chapter 6, Section 6.2.7.

7.2.6 BBB Permeability

hCMEC/D3 cells were seeded at a density of 75,000 per well on the apical side of trans-well plates. The cells were allowed to adhere for 72 hours until they reached a maximum resistance. Free IRH and the NP treatments were then added and TEER (Ohm) measured at certain time points (0.5, 1, 2, 4, 6, 24, 48, 72 hours) using EVOM2 and an STX2 electrode (World precision instruments, Hitchin, Hertfordshire, UK).

7.2.7 IL-6 Protein Expression in Endothelial Cell Line

Quantitative analysis of IL-6 in endothelial cells exposed to free IRH and NP formulations followed the same protocol described in Chapter 6, Section 6.2.11.

7.2.8 Statistical Analysis

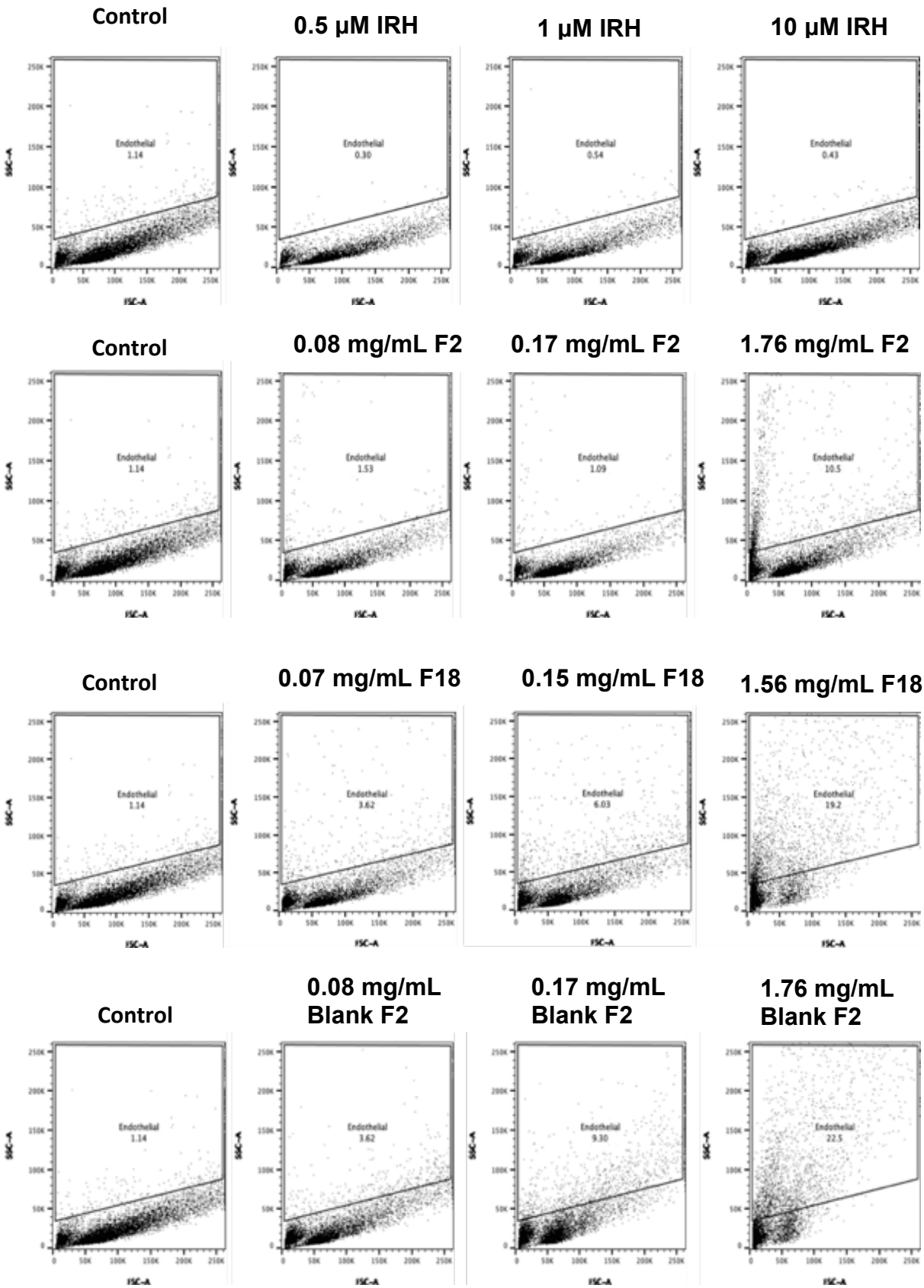
The statistical analysis was carried out with GraphPad Prism, version 9. Two-way ANOVA (Analysis of variance) was used for multiple comparisons between the similar concentrations of the free drug and the nanoparticle formulations with regards to the treatment time. Tukey's post hoc test was carried out in the analysis. The statistical significance was presented as: $p \leq 0.0001$, $p \leq 0.05$. Non-significance was presented for $p > 0.05$. Data were presented as mean (n = 3) ± SD.

7.3 Results

7.3.1 Cellular Uptake Analysis by Dot Plots and SSC Intensity Using Flow Cytometry

Figure 7.1 to Figure 7.3 display dot plots of endothelial cellular uptake of the free IRH and NP formulations assessed after 1, 3 and 5 days. As shown in the dot plots, cell count increased within the gate as the concentration increased indicating more cellular uptake. Figure 7.4 to Figure 7.8 present the intensity of SSC light of endothelial cells exposed to NP formulations compared to the free IRH. There was no significant difference in SSC intensity between free IRH and the negative control treated groups on day 1 (Figure 7.4) which could be due to insufficient light scattering by the drug molecules within the solution and despite showing dose and time dependent increase in gated events. However, the difference was significant ($P<0.0001$) from day 1 to day 5 between the F2 NPs and the free IRH; and the F2 NPs and the negative control groups across all doses indicating higher uptake of the F2 NPs compared to the free IRH.

A similar trend to F2 NPs was observed with the blank F2 and F18 NPs from day 1 to day 5 in which there was a significant difference ($P<0.0001$) in cell granularity compared to the free IRH and negative control across all doses (Figure 7.5 and Figure 7.6). The SSC intensity of the cells treated with the F18 NPs was non-significant compared to those treated with the F2 NPs for all days and concentrations. The blank F18 NPs was significantly ($P<0.0001$) internalized by the cells when compared to the negative control and free IRH. However, the cells exposed to the highest concentration of the blank F18 NPs had a non-significant SSC intensity compared with the negative control from day 3 to day 5 indicating loss of the dead cells that had cellular uptake of the NPs by day 5.


Control
0.5 µM IRH
1 µM IRH
10 µM IRH
Endothelial
1.14
Endothelial
0.30
Endothelial
0.54
Endothelial
0.43
Control
0.08 mg/mL F2
0.17 mg/mL F2
1.76 mg/mL F2
Endothelial
1.14
Endothelial
1.53
Endothelial
1.09
Endothelial
10.5
Control
0.07 mg/mL F18
0.15 mg/mL F18
1.56 mg/mL F18
Endothelial
1.14
Endothelial
3.62
Endothelial
6.03
Endothelial
19.2
Control
0.08 mg/mL Blank F2
0.17 mg/mL Blank F2
1.76 mg/mL Blank F2
Endothelial
1.14
Endothelial
3.62
Endothelial
9.30
Endothelial
22.5
SSC-A
FSC-A

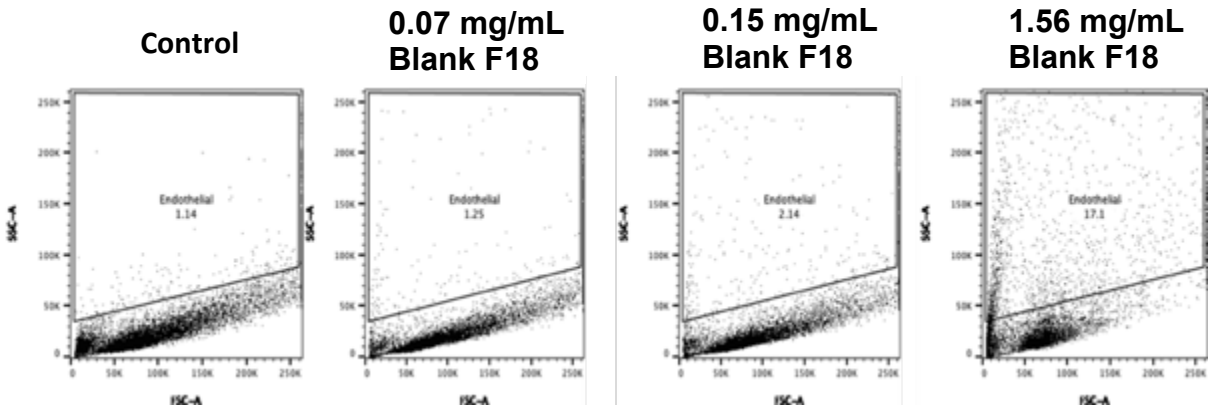
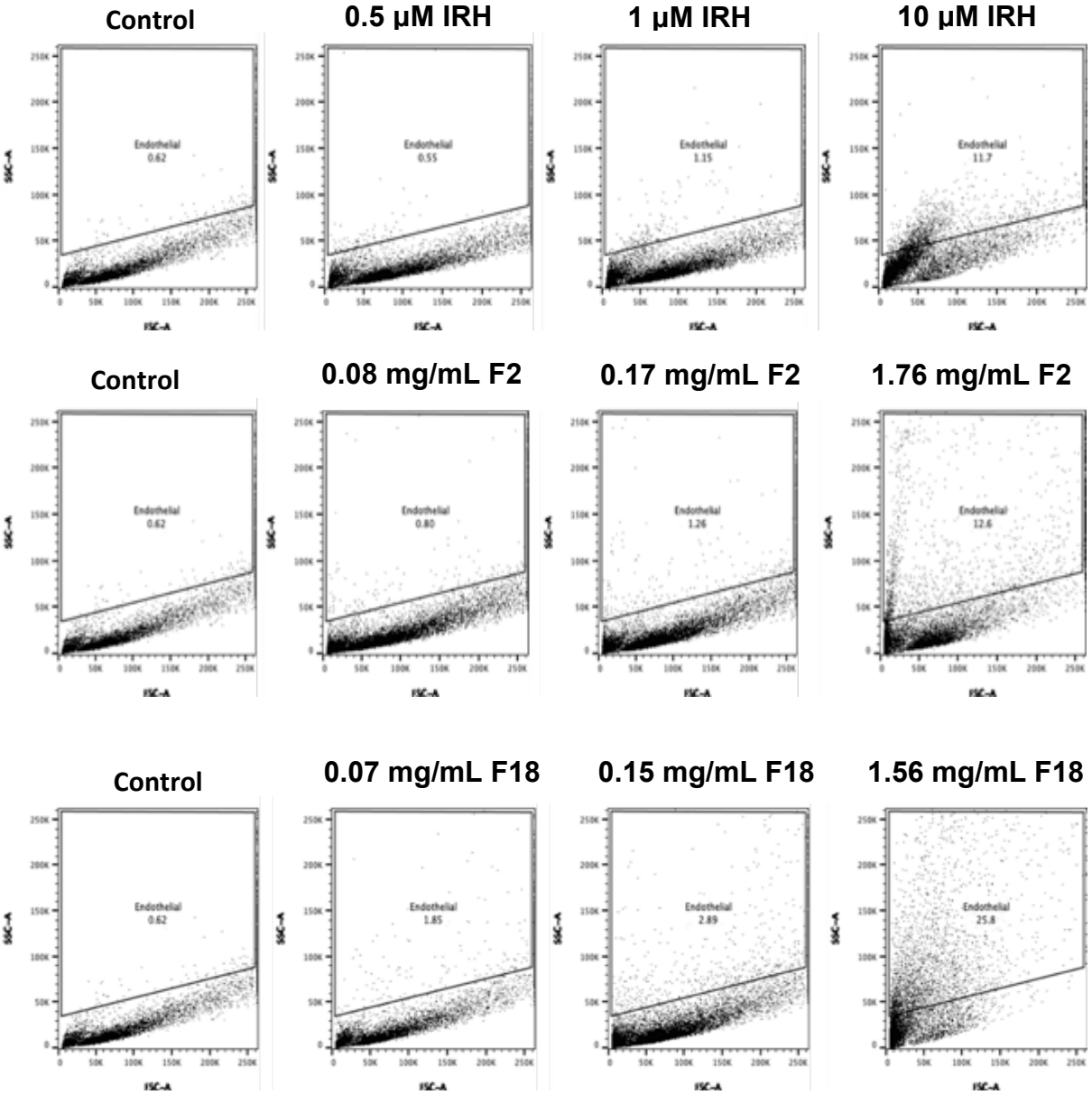


Figure 7.1. Endothelial cellular uptake of low, medium and high concentrations of free IRH and NPs after 1 day of treatment.



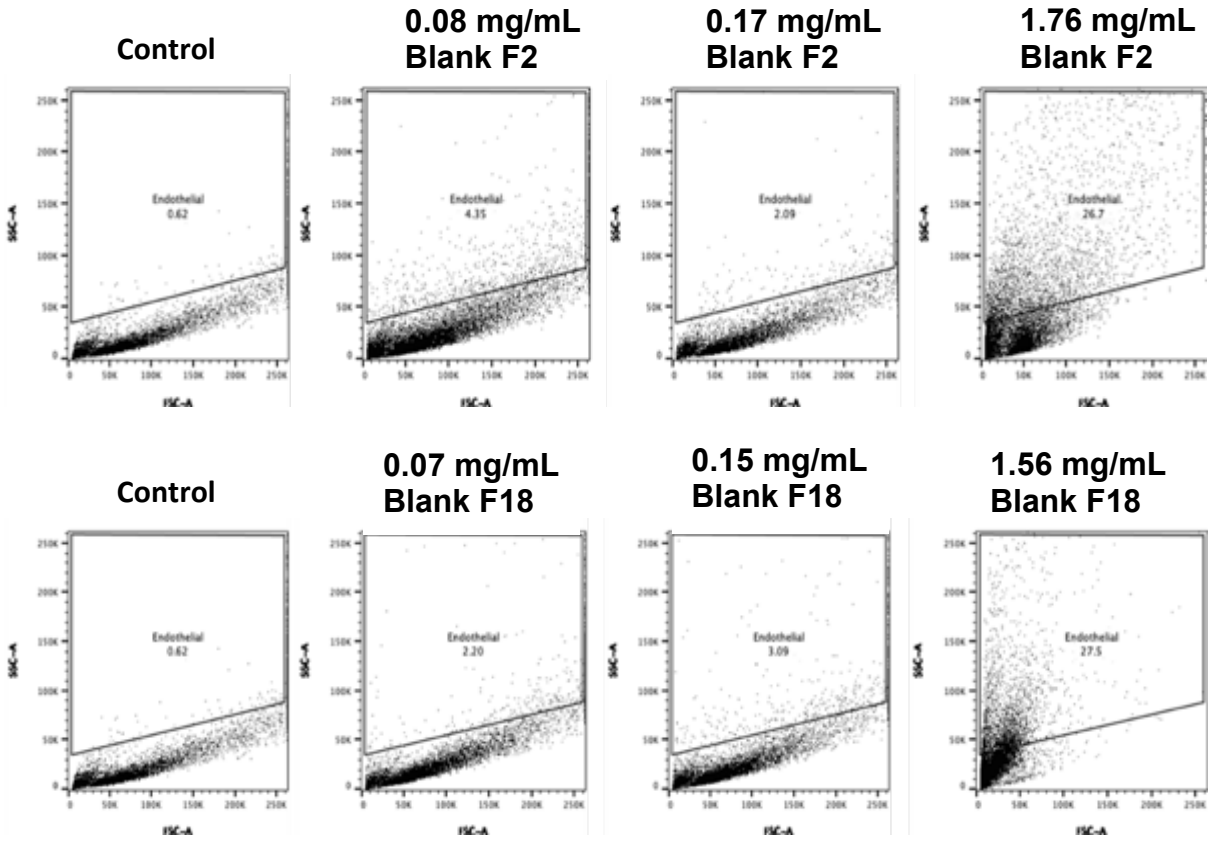
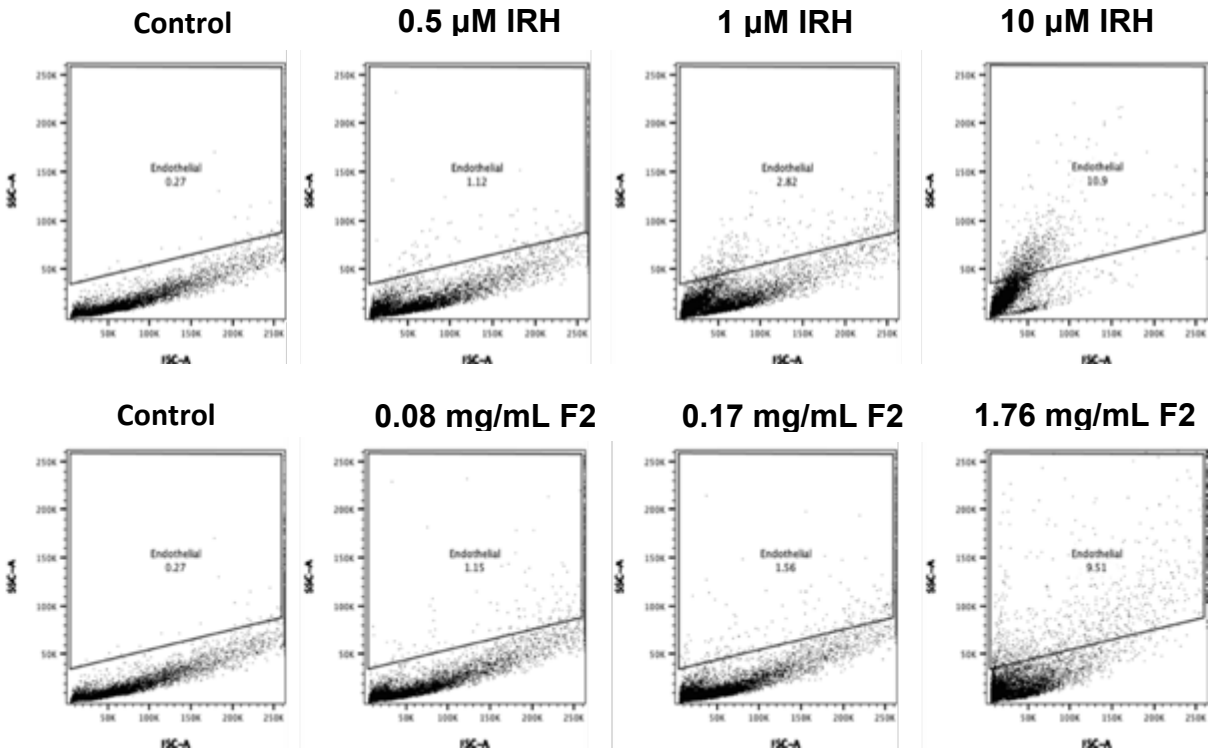


Figure 7.2. Endothelial cellular uptake of low, medium and high concentrations of free IRH and NPs after 3 days of treatment.



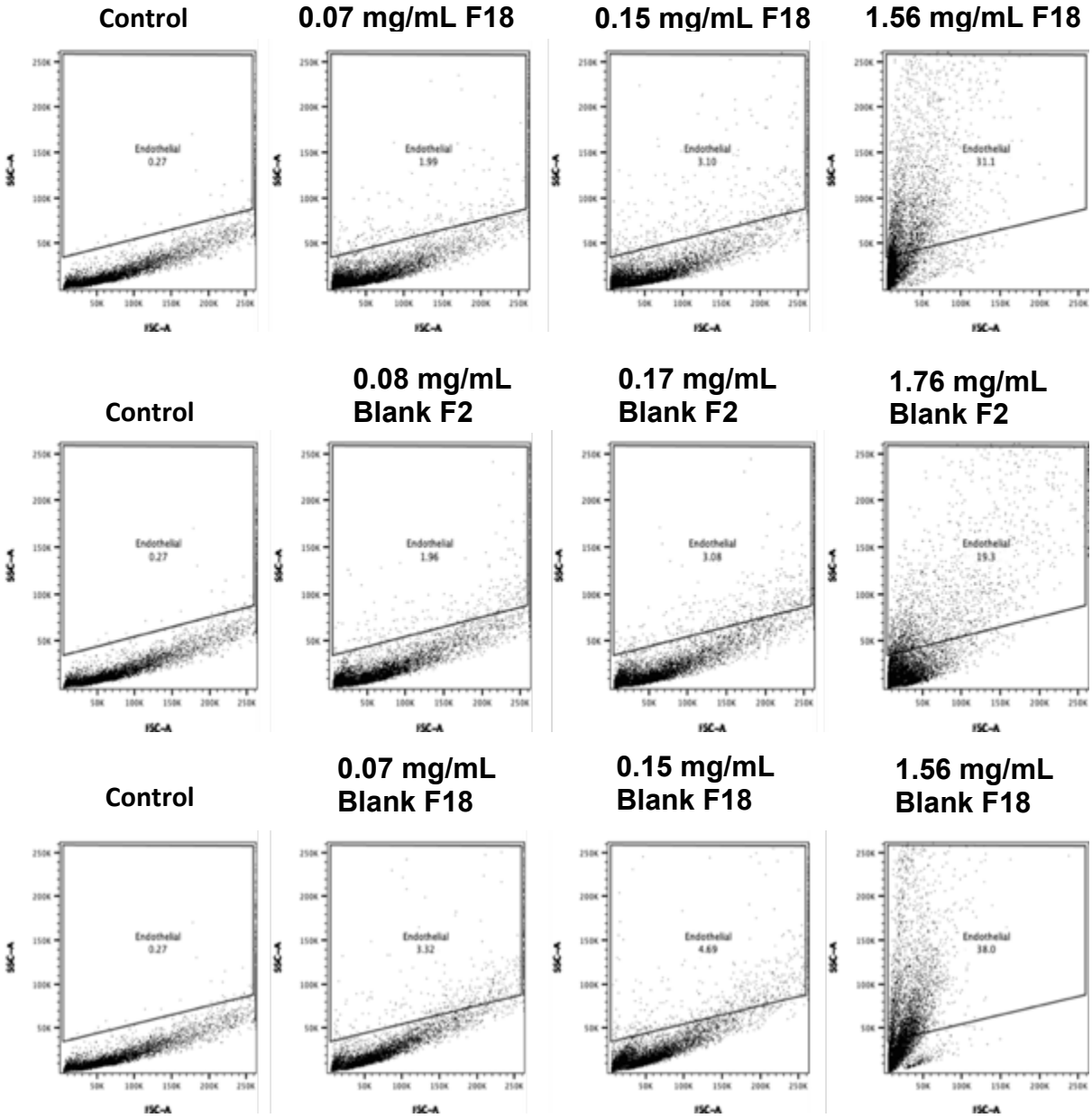


Figure 7.3. Endothelial cellular uptake of low, medium and high concentrations of free IRH and NPs after 5 days of treatment.

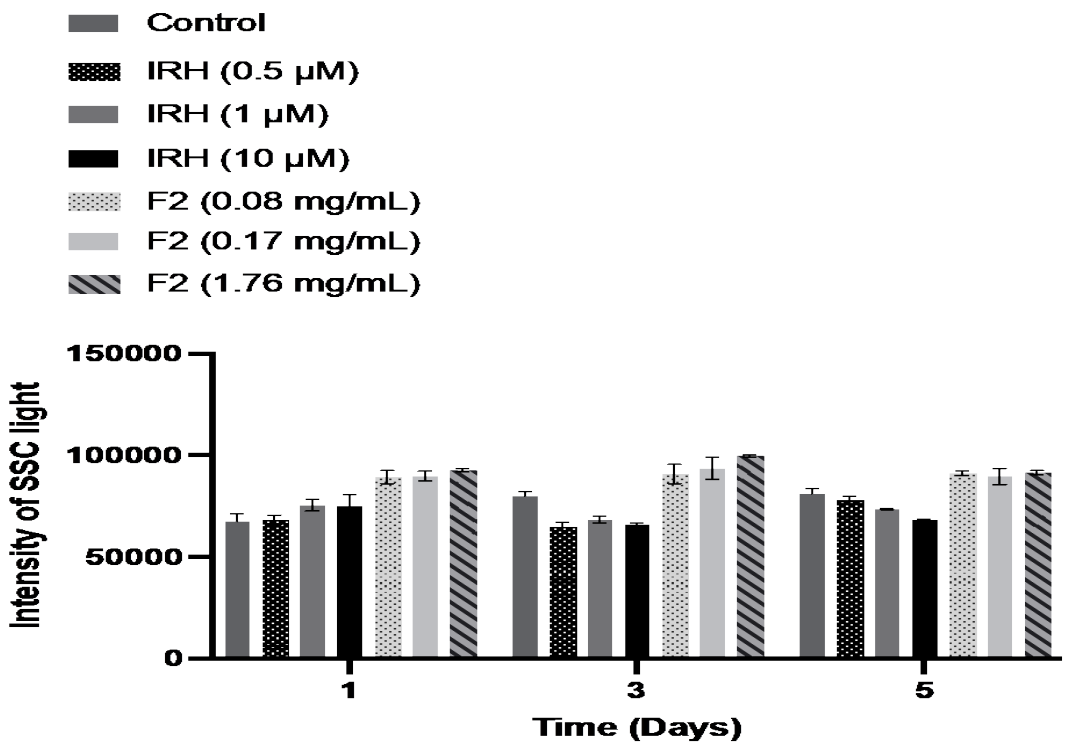


Figure 7.4. SSC light intensity of endothelial cells treated with low, medium and high concentrations of free IRH and F2 over 5 days (n=3).

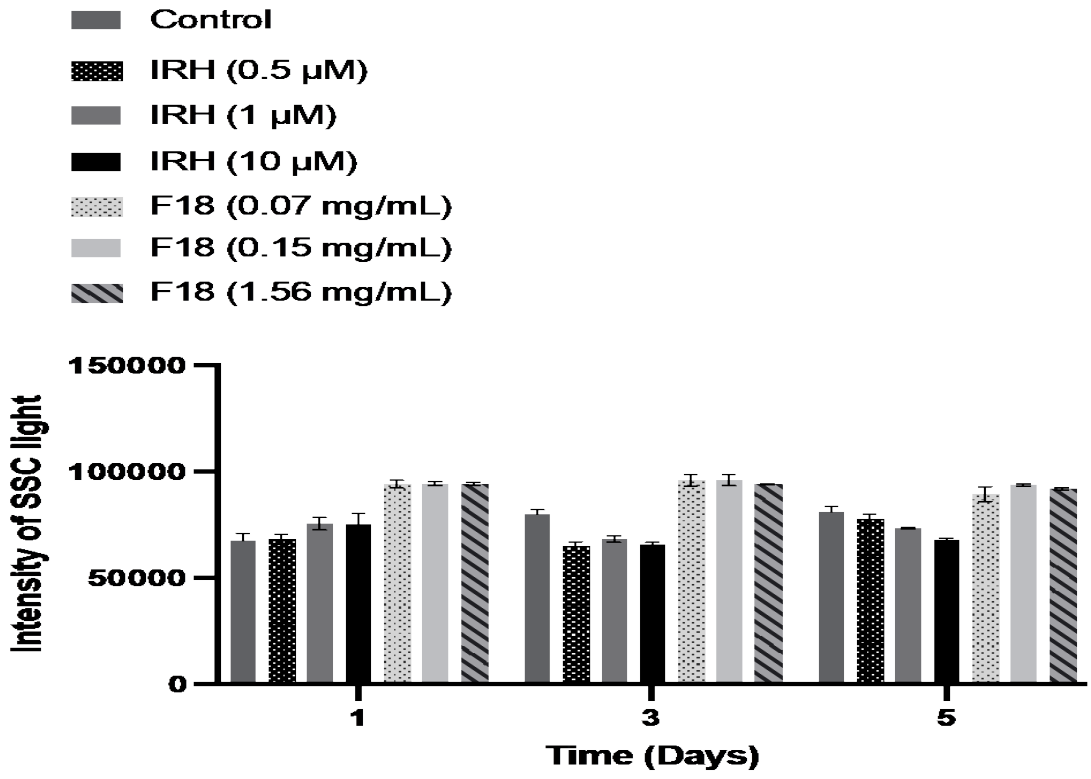


Figure 7.5. SSC light intensity of endothelial cells treated with low, medium and high concentrations of free IRH and F18 over a 5-day period (n=3).

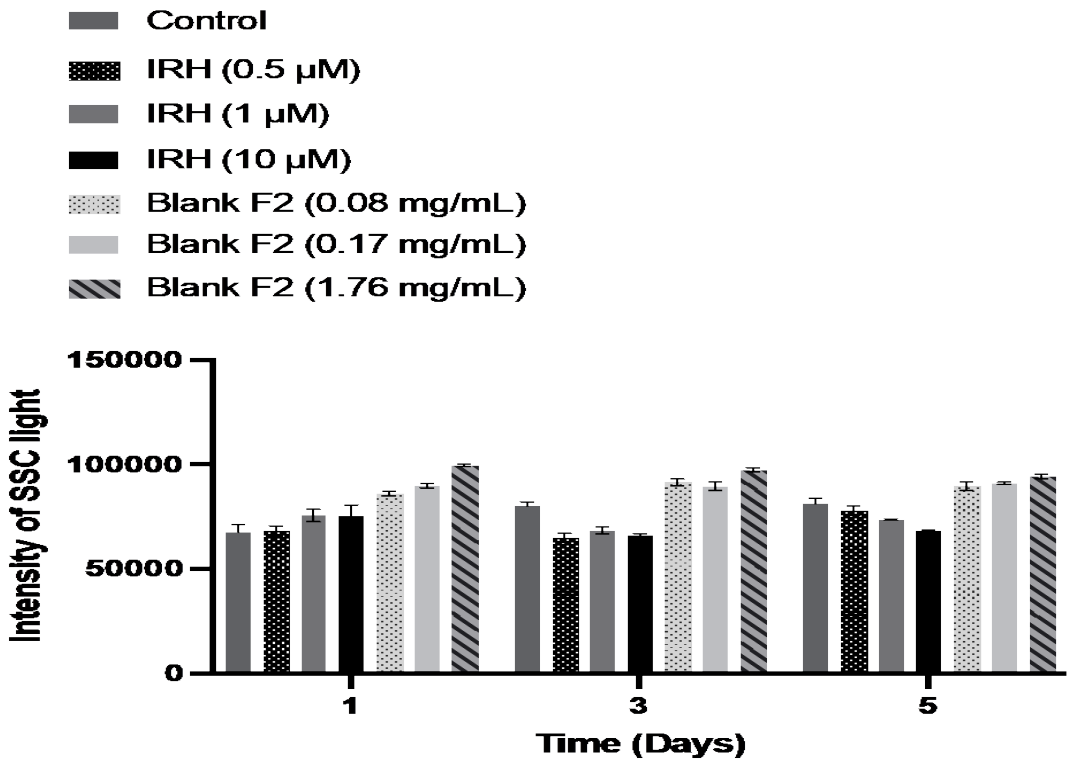


Figure 7.6. SSC light intensity of endothelial cells treated with low, medium and high concentrations of free IRH and blank F2 over 5 days (n=3).

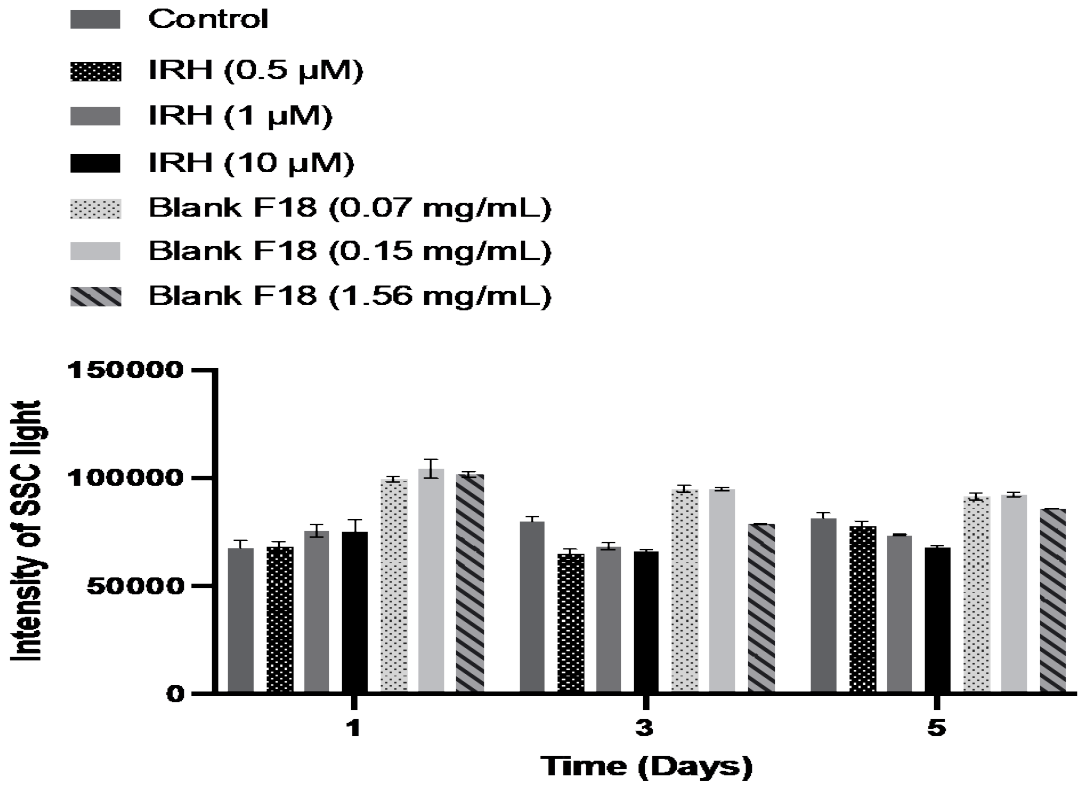


Figure 7.7. SSC light intensity of endothelial cells treated with low, medium and high concentrations of free IRH and blank F18 over 5 days (n=3).

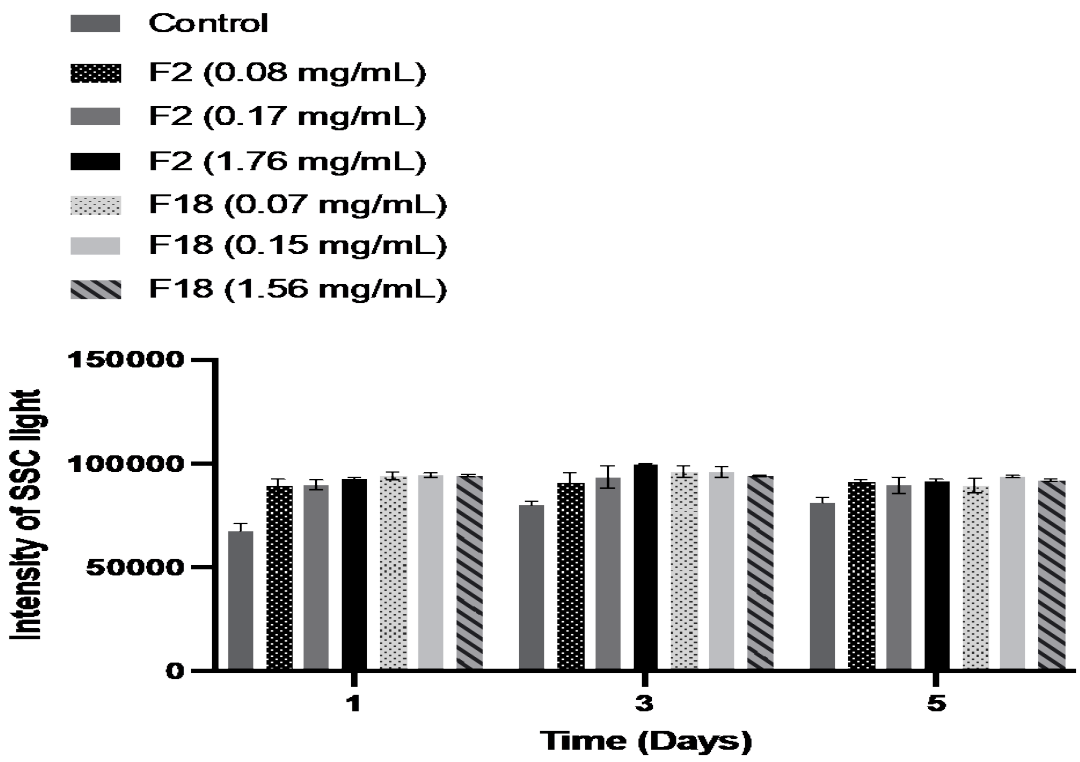


Figure 7.8. SSC light intensity of endothelial cells treated with low, medium and high concentrations of F2 and F18 over 5 days (n=3).

7.3.2 Cytotoxicity

The cytotoxic effect of the free IRH, blank and IRH loaded NPs on endothelial cells was investigated over a period of 11 days. As shown in Figure 7.9, the overall trend of cell cytotoxicity indicated a non-significant difference between the free IRH and negative control from day 1 to day 7 for most doses. However, the highest concentration became significantly toxic from day 3 to day 11 compared to the negative control and F2 NPs ($P<0.0001$). The F2 NPs induced a dose dependent cytotoxicity and the cytotoxic effect started to become significant ($P<0.0001$) when compared to the negative control from day 3 and continued across all doses and days (Figure 7.9). The highest cytotoxic effect (39.27%) was achieved by the highest concentration of the F2 NPs on day 9. However, the highest dose of free IRH reduced cell viability to less

than 5% on day 11, while the low and medium concentrations of the free IRH had cell viabilities of 78.13 and 64.15% respectively by day 11.

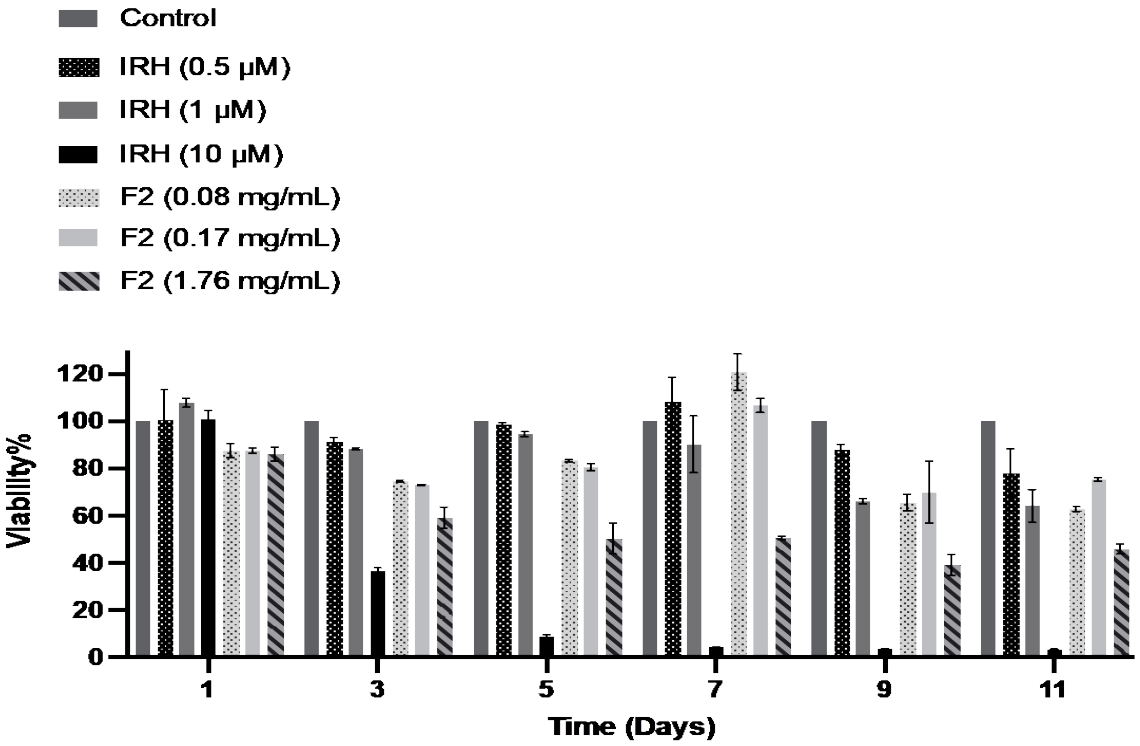


Figure 7.9. Cytotoxicity of free IRH and F2 on endothelial cells compared to control cells (n=3).

Figure 7.10 displays the cytotoxicity of F18 compared to the free IRH and negative control on endothelial cells. The F18 NPs were significantly ($P<0.0001$) more cytotoxic compared to the free IRH and negative control. However, on day 5 the highest concentration of the free IRH was more cytotoxic than the F18 NPs ($P<0.0001$). The highest concentration of the F18 NPs reduced viability to less than 7% by day 11, while, the low and medium concentrations maintained cell viabilities of 60.10% and 64.99% respectively.

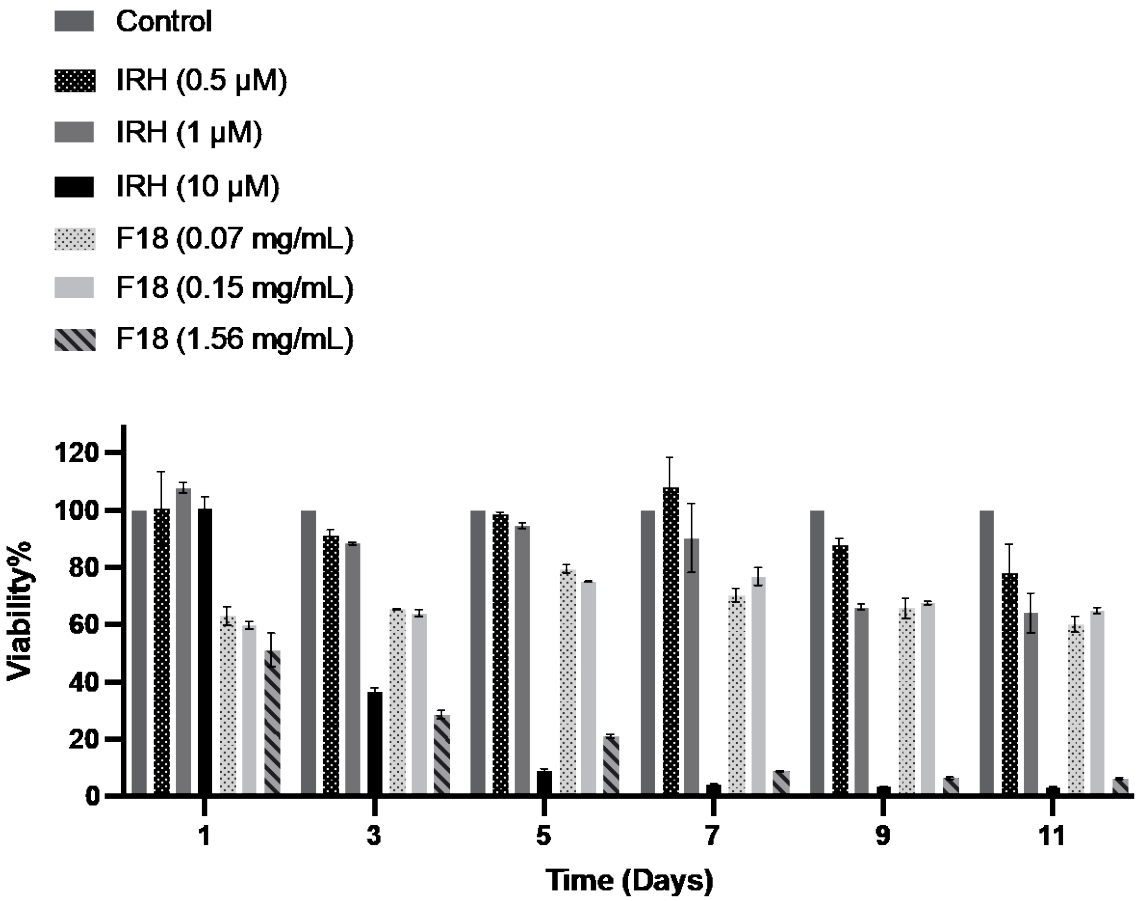


Figure 7.10. Cytotoxicity of free IRH and F18 on endothelial cells compared to control cells (n=3).

The blank F2 treated groups had cell viabilities higher than 70% from day 1 to day 5 at the low and medium doses (Figure 7.11). However, the highest concentration reduced the cell viability from 76.89% on day 1 to less than 5.00% on day 11 which was significantly ($P<0.0001$) lower than the negative control group; and non-significant with the free IRH (Figure 7.11).

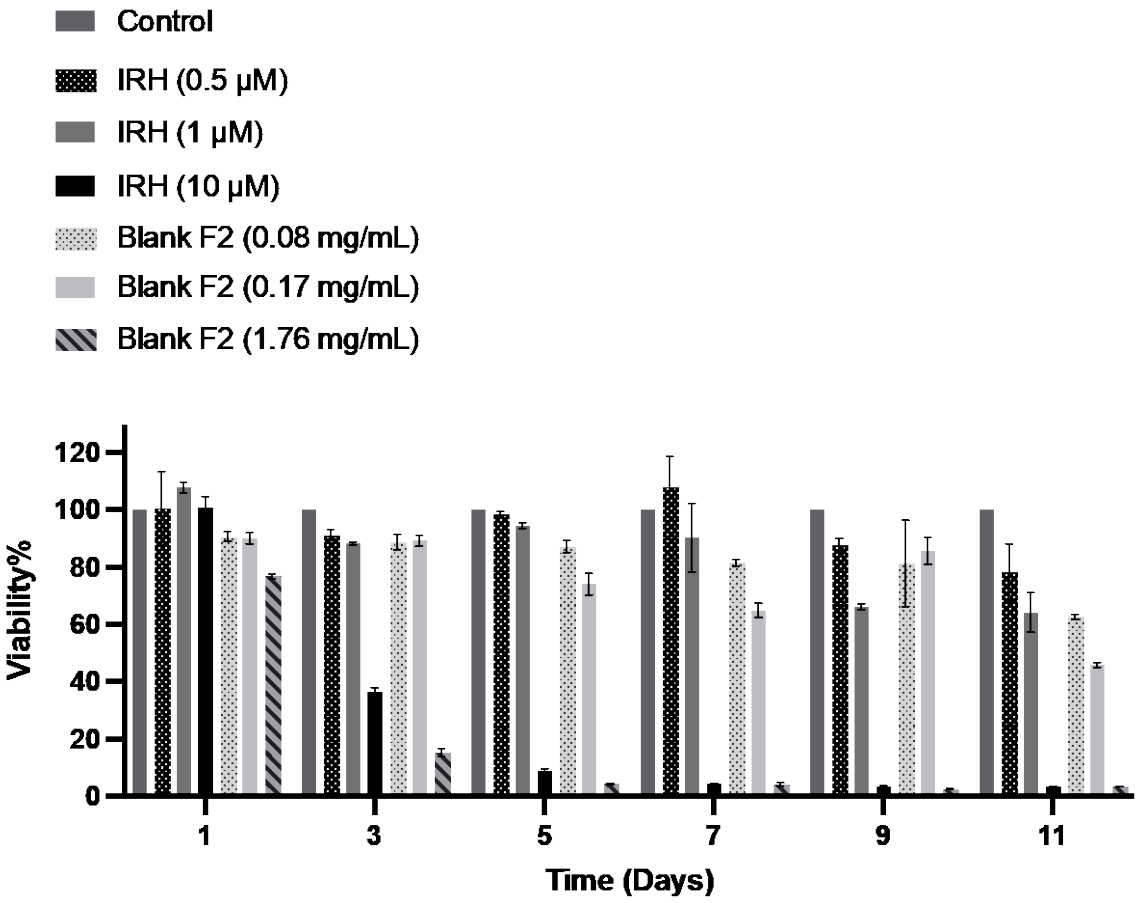


Figure 7.11. Cytotoxicity of free IRH and blank F2 on endothelial cells compared to control cells (n=3).

Figure 7.12 displays the cytotoxicity of the blank F18 NPs compared to the free IRH and negative control. The blank F18 NPs were significantly ($P<0.0001$) more cytotoxic compared to the free IRH and negative control. However, on day 5 the highest concentration of the free IRH was more cytotoxic than the blank F18 NPs. By the end of the incubation period, the blank F18 NPs had greater than 70.00% cell viability (Figure 7.12).

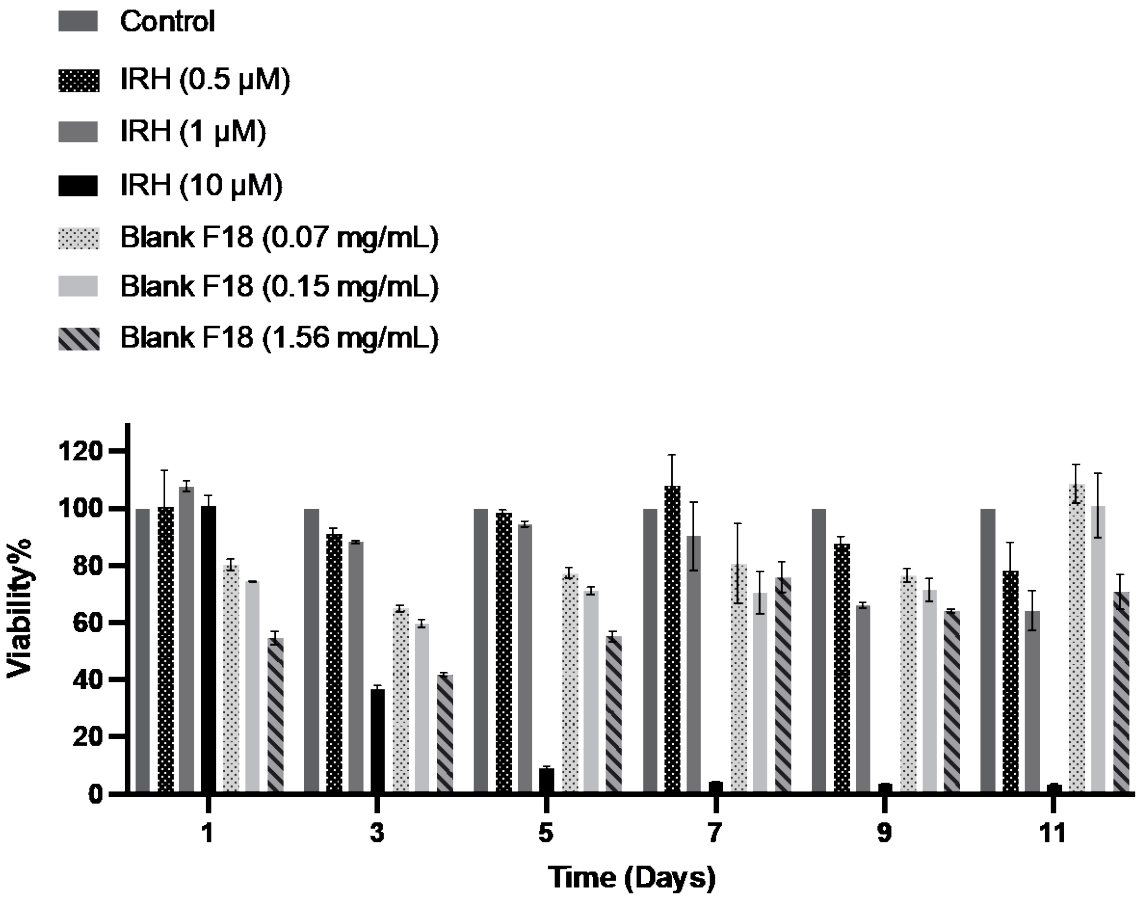


Figure 7.12. Cytotoxicity of free IRH and blank F18 on endothelial cells compared to control cells (n=3).

No significant difference between the blank F2 and IRH-loaded F2 NPs was observed on day 1 (Figure 7.13). However, on day 3, the IRH-loaded F2 NPs appeared to be more cytotoxic than the blank F2 NPs except for the highest concentration, which was maintained until the end of the incubation period. This could be due to higher cellular uptake of the blank F2 NPs compared to their IRH-loaded F2 NPs.

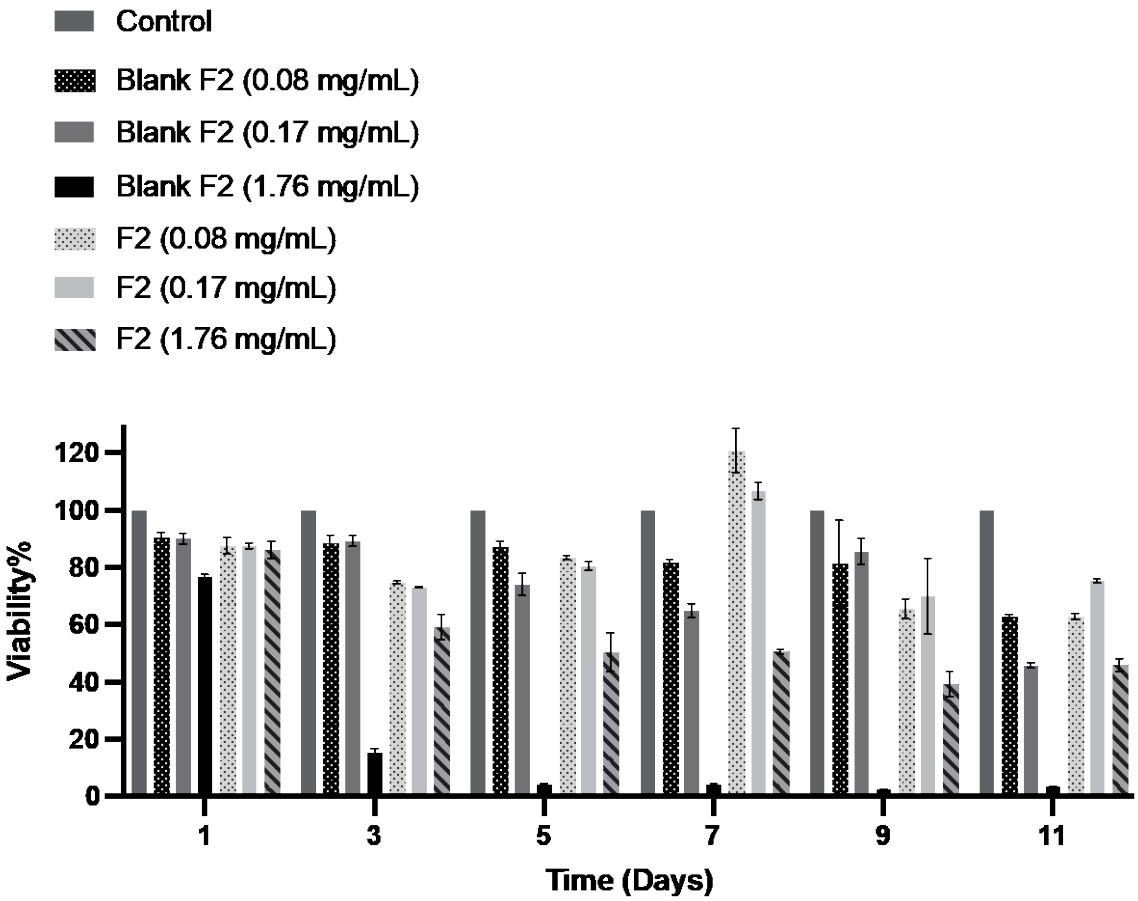


Figure 7.13. Cytotoxicity of F2 and blank F2 on endothelial cells compared to control cells (n=3).

As shown in Figure 7.14, the IRH-loaded F18 NPs were more cytotoxic than the blank F18 NPs with the highest concentration inducing the most significant effect from day 3 ($P= 0.03$) up to the end of the incubation period ($P<0.0001$).

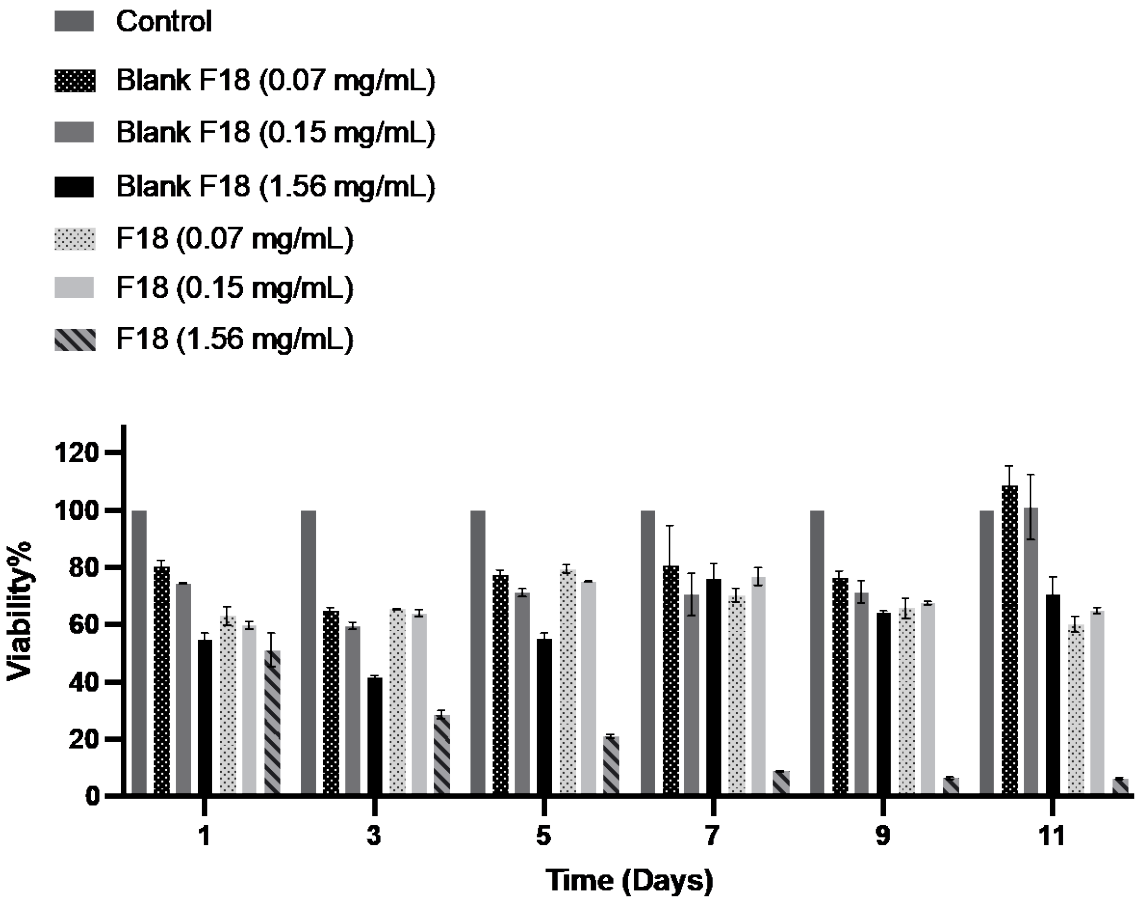


Figure 7.14. Cytotoxicity of F18 and blank F18 on endothelial cells compared to control cells (n=3).

As shown in Figure 7.15, the F18 NPs were more cytotoxic than the F2 NPs. From day 9, the F18 NPs were more significantly cytotoxic ($P<0.0001$) only at its highest concentration which was maintained until day 11.

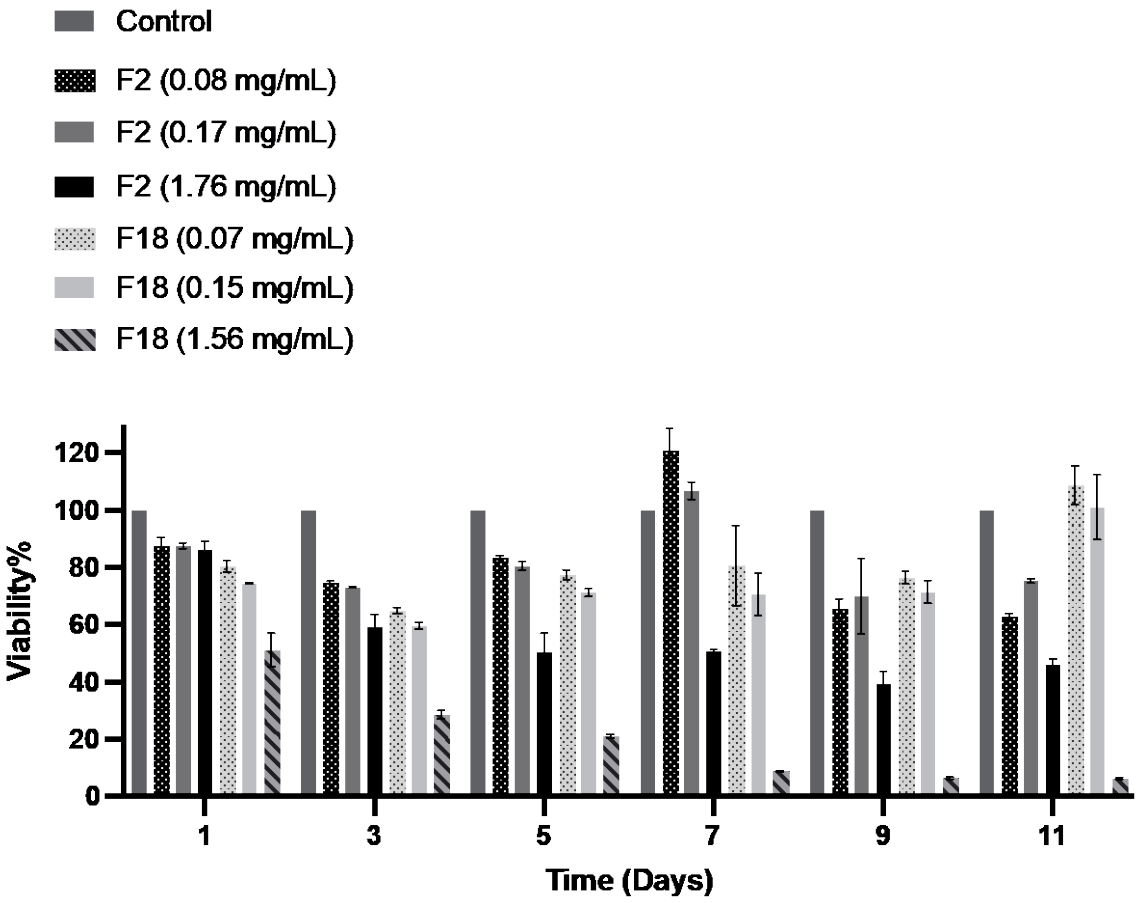


Figure 7.15. Cytotoxicity of F2 and F18 on endothelial cells compared to control cells (n=3).

The cytotoxicity of the blank F2 NPs was lower than the blank F18 NPs at the low and medium concentrations across most days however, the highest concentration of the blank F2 NPs was significantly ($P<0.0001$) more cytotoxic than the blank F18 NPs from day 3 until day 11 (Figure 7.16).

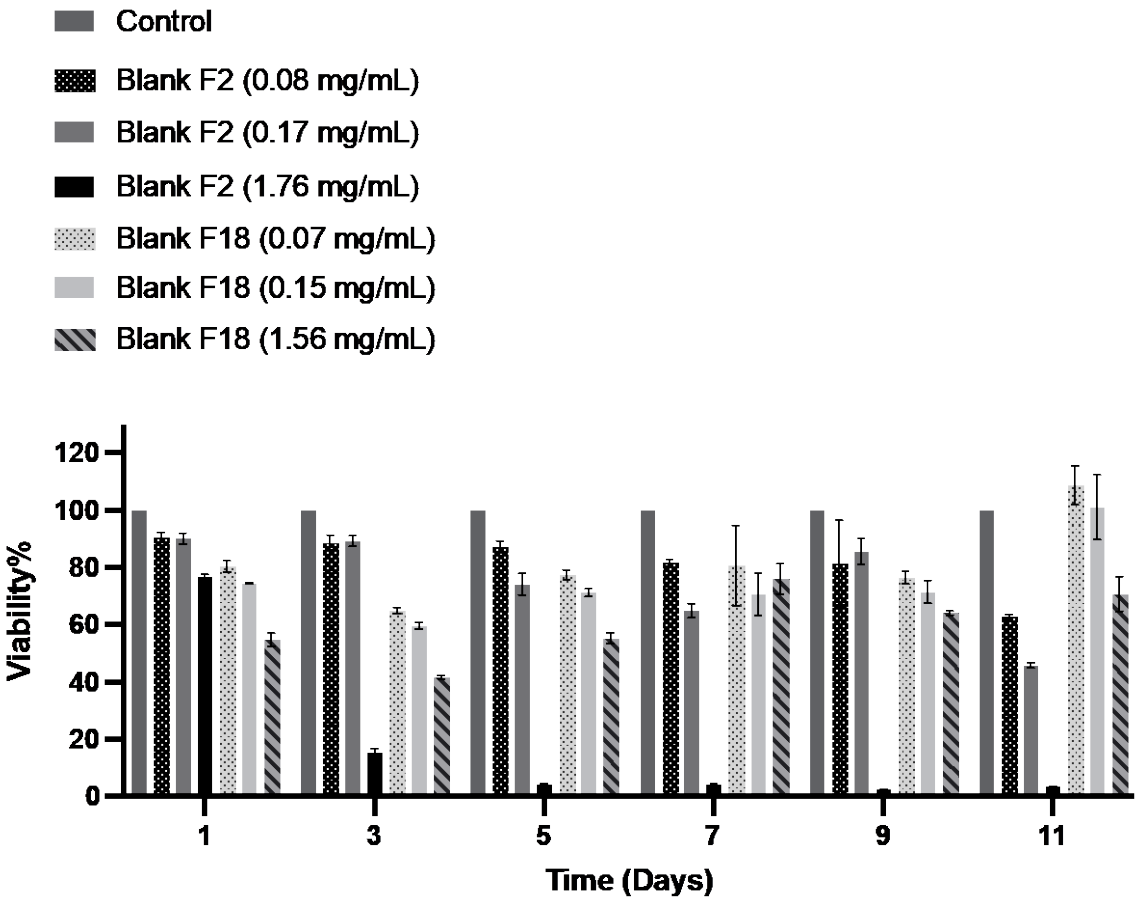


Figure 7.16. Cytotoxicity of blank F2 and blank F18 on endothelial cells compared to control cells (n=3).

7.3.3 Optical Imaging of Endothelial Cells

Figure 7.17 to Figure 7.22 show the shrinkage and swelling of the endothelial cells after exposure to the free IRH and NP formulations compared to the negative control (Figure 7.17). The number of attached cells was reduced by the treatments compared to the negative control, which indicated loss of viability in a dose and time dependent manner.

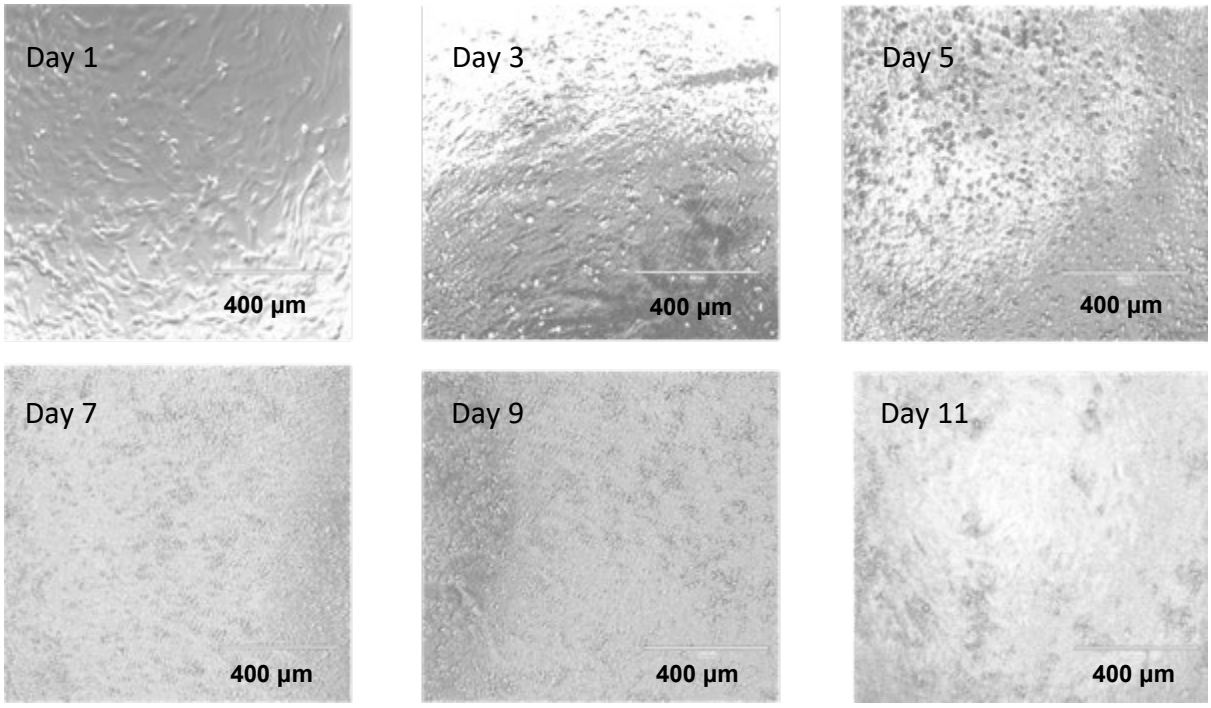
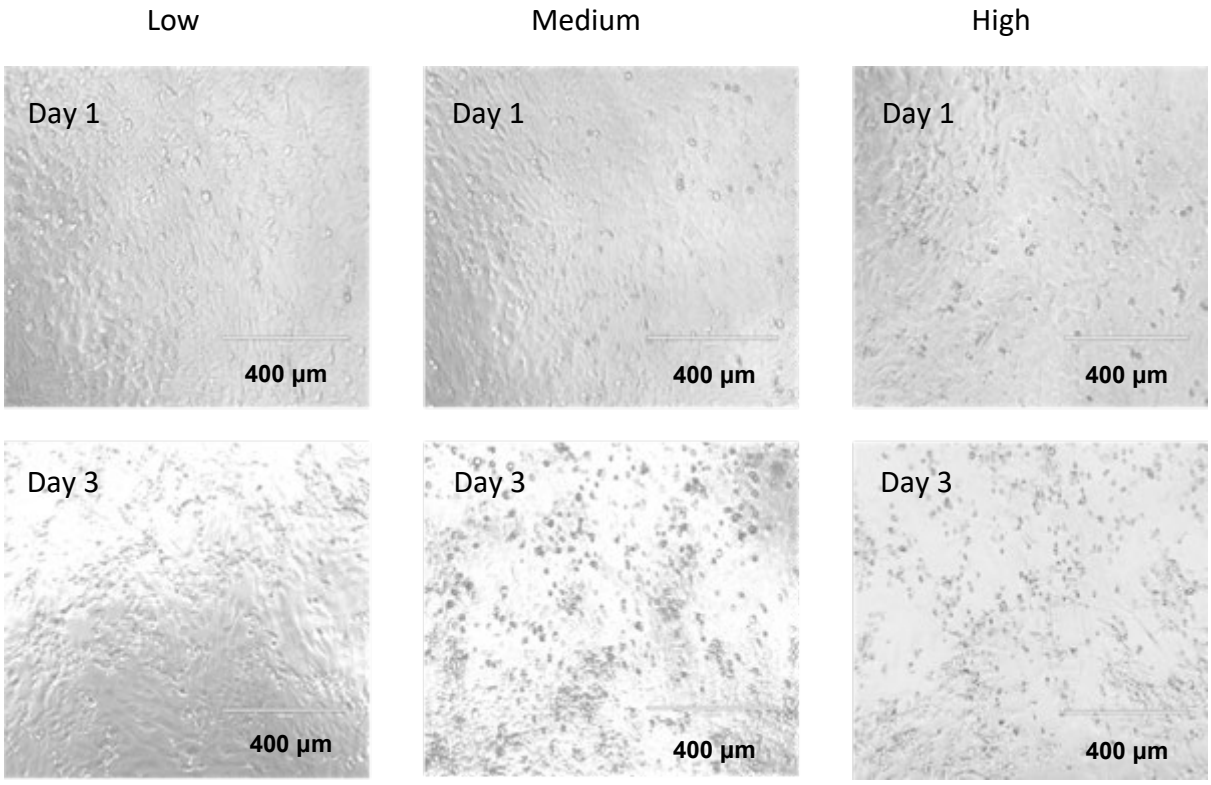


Figure 7.17. Optical imaging of untreated control of endothelial cells over 11 days.



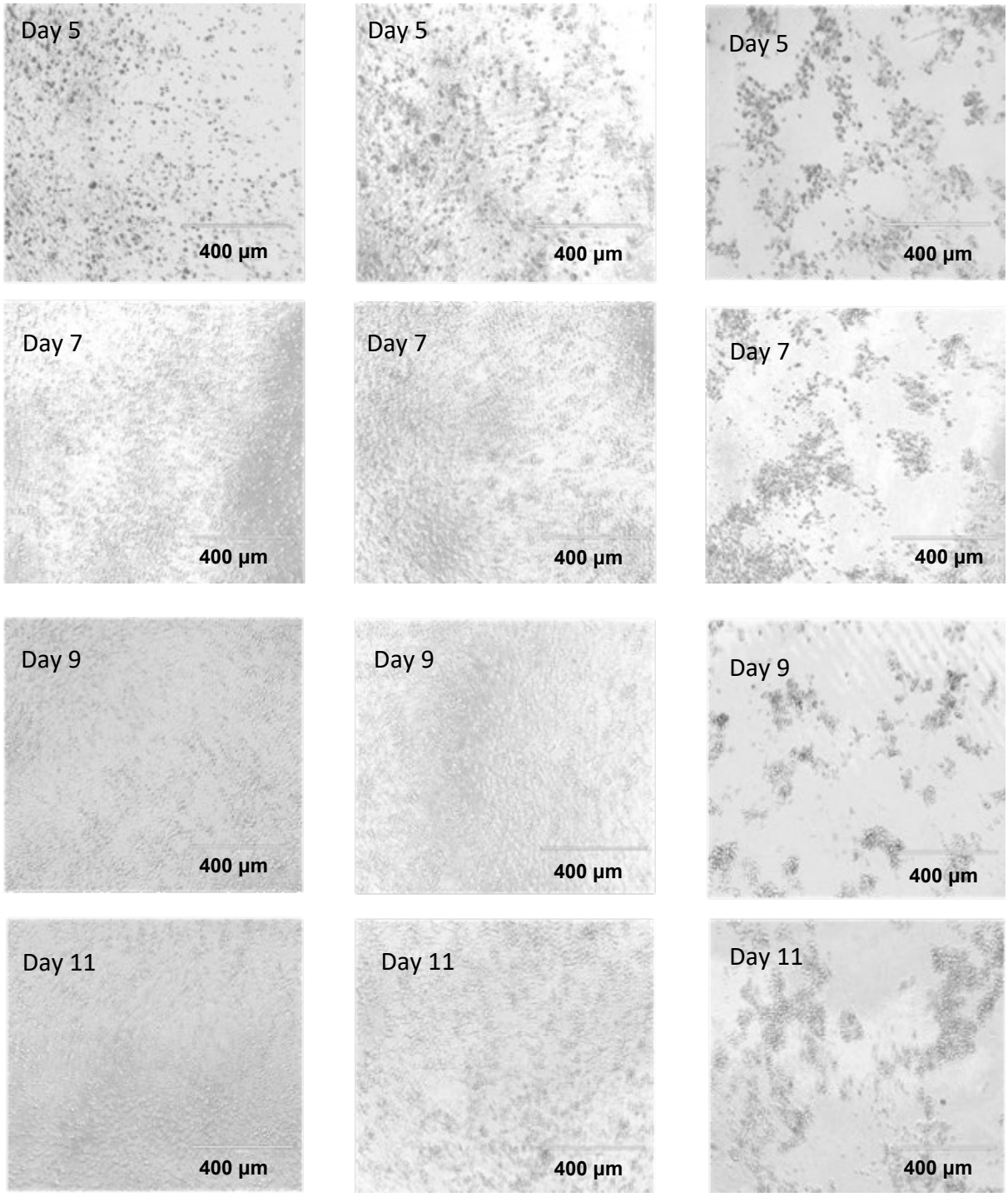
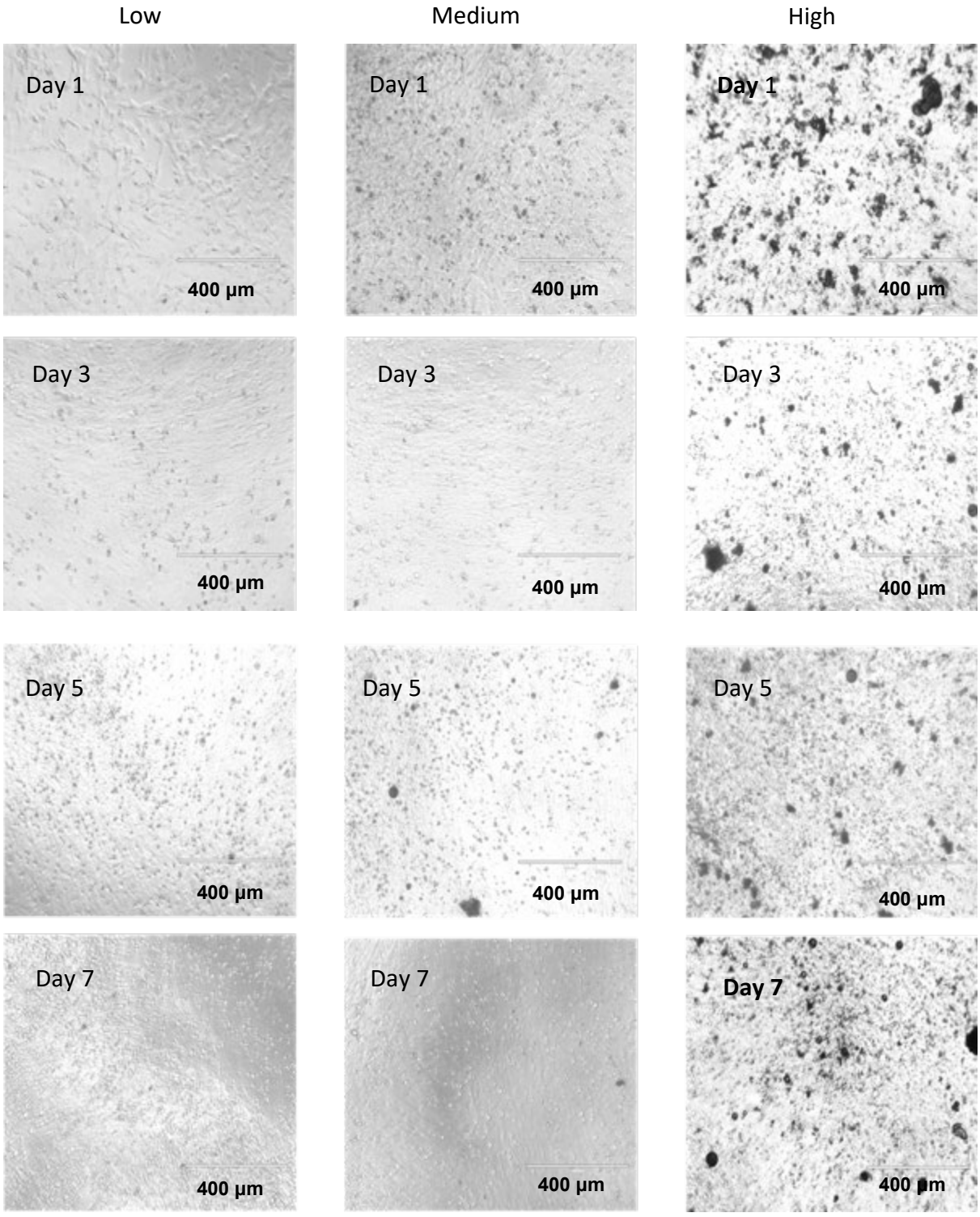


Figure 7.18. Optical imaging of endothelial cells exposed to low, medium and high concentrations of IRH for 11 days.


Low
Medium
High
Day 1
400 µm
Day 1
400 µm
Day 1
400 µm
Day 3
400 µm
Day 3
400 µm
Day 3
400 µm
Day 5
400 µm
Day 5
400 µm
Day 5
400 µm
Day 7
400 µm
Day 7
400 µm
Day 7
400 µm

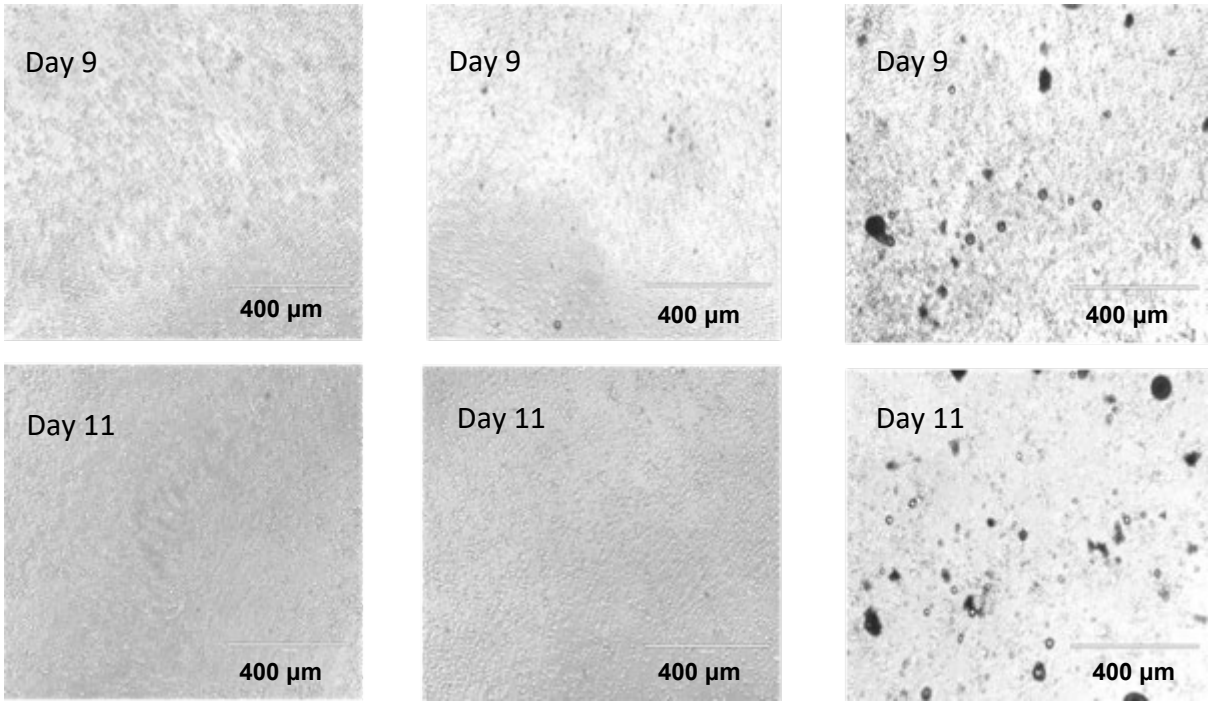
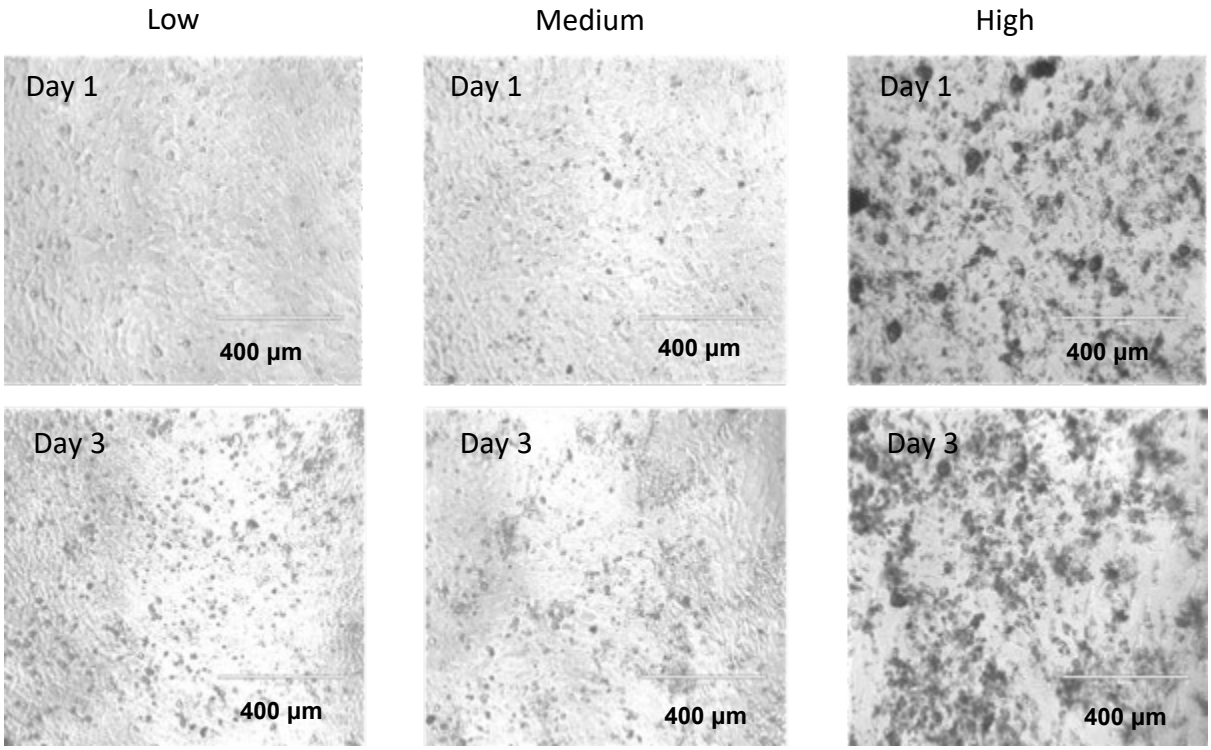


Figure 7.19. Optical imaging of endothelial cells exposed to low, medium and high concentrations of F2 for 11 days.



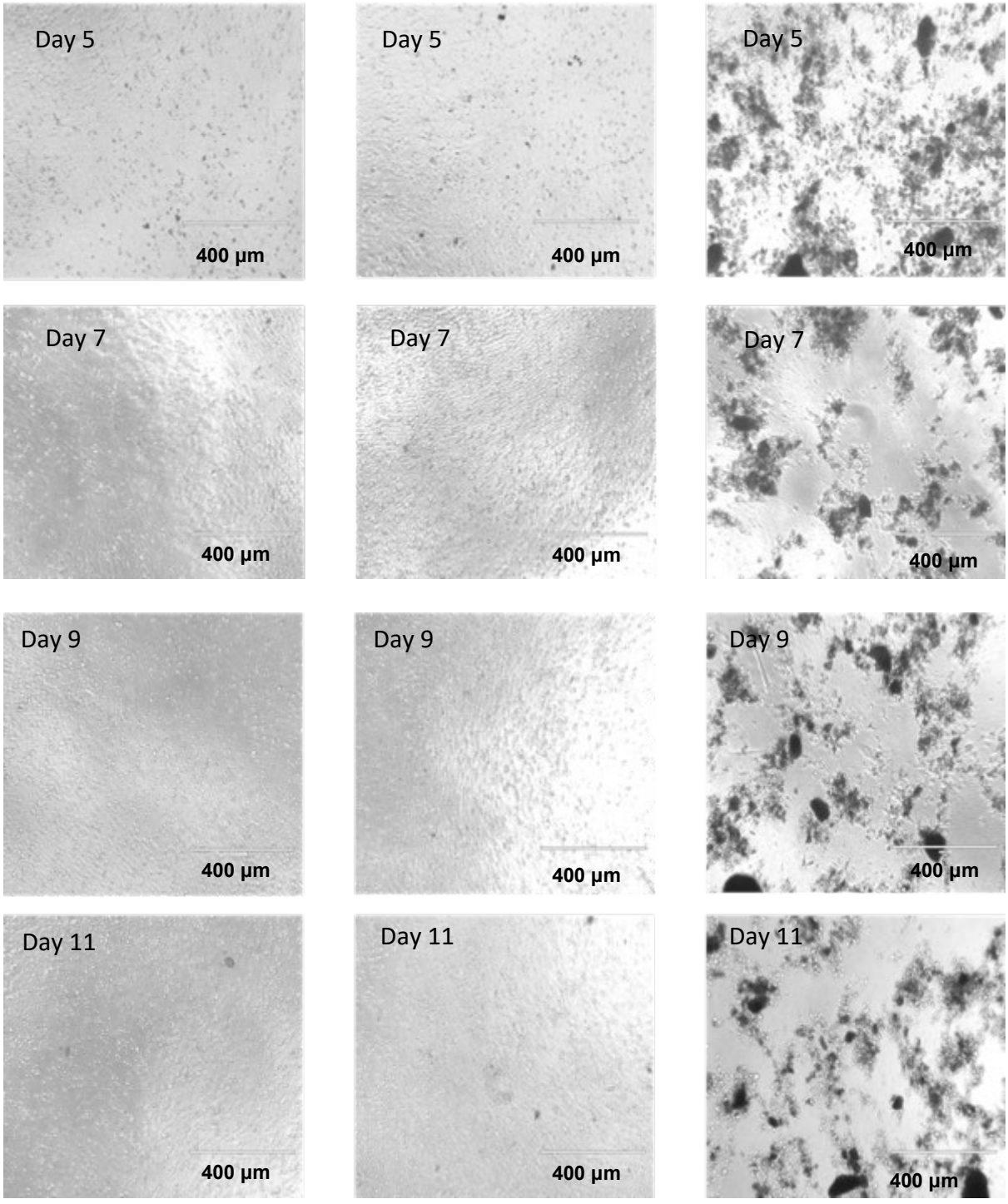
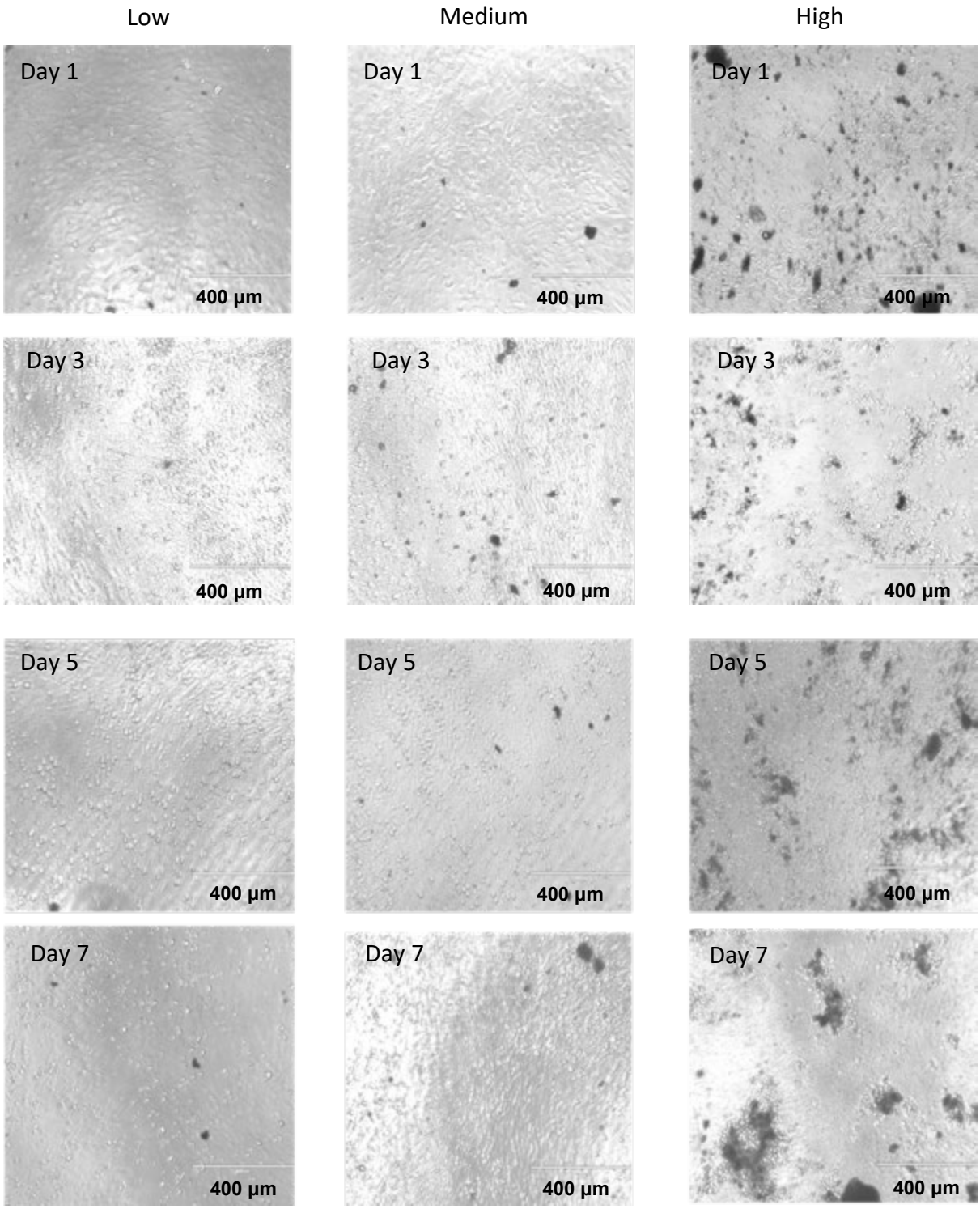


Figure 7.20. Optical imaging of endothelial cells exposed to low, medium and high concentrations of F18 for 11 days.


Low
Medium
High
Day 1
Day 1
Day 1
400 µm
400 µm
400 µm
Day 3
Day 3
Day 3
400 µm
400 µm
400 µm
Day 5
Day 5
Day 5
400 µm
400 µm
400 µm
Day 7
Day 7
Day 7
400 µm
400 µm
400 µm

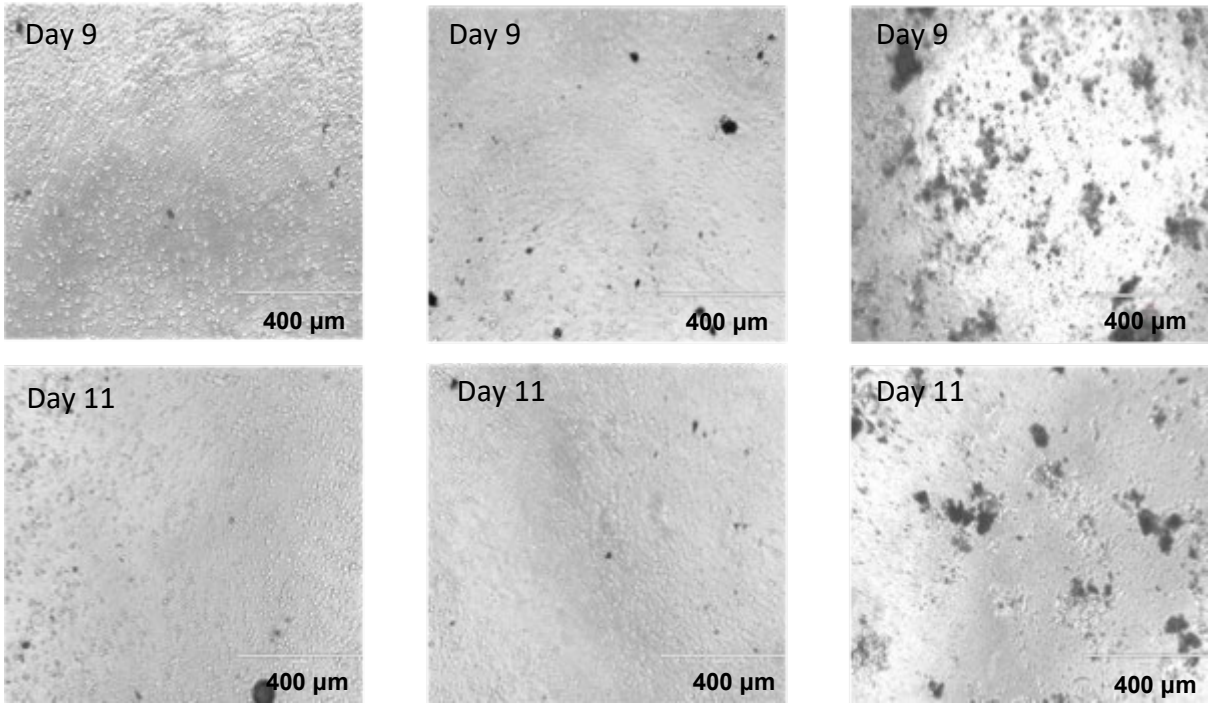
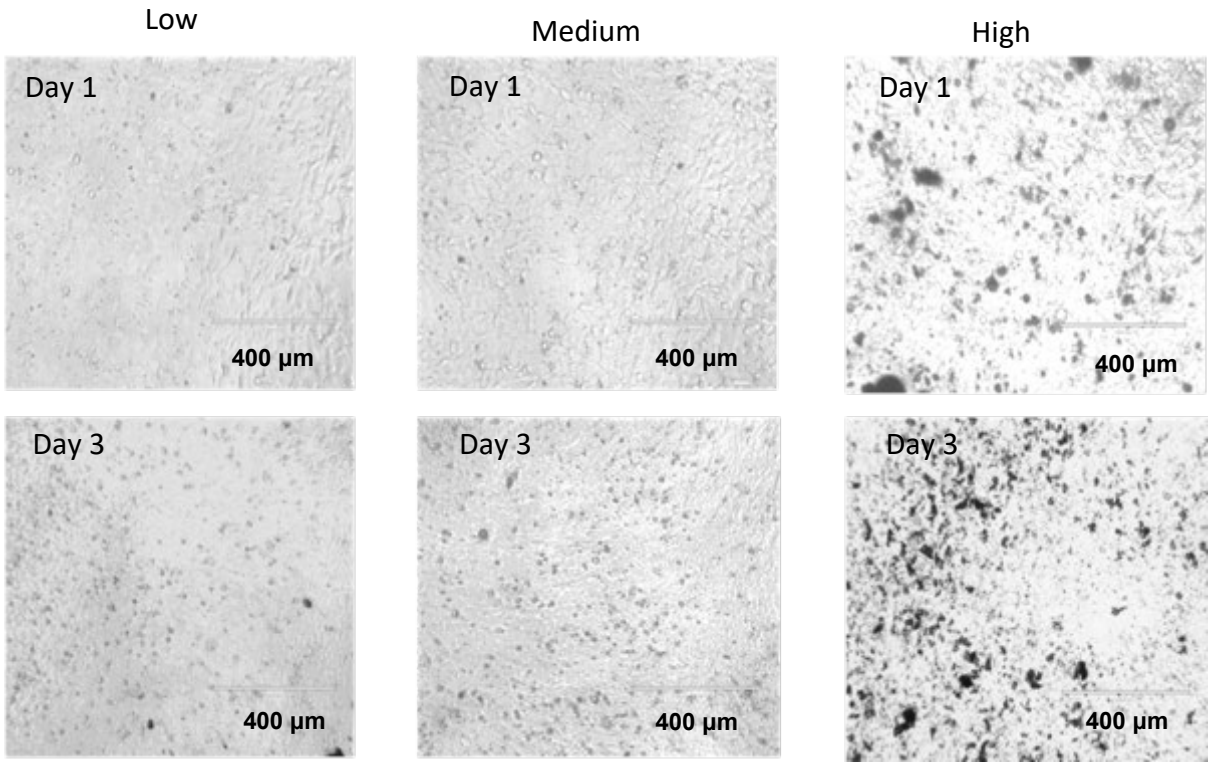


Figure 7.21. Optical imaging of endothelial cells exposed to low, medium and high concentrations of Blank F2 for 11 days.



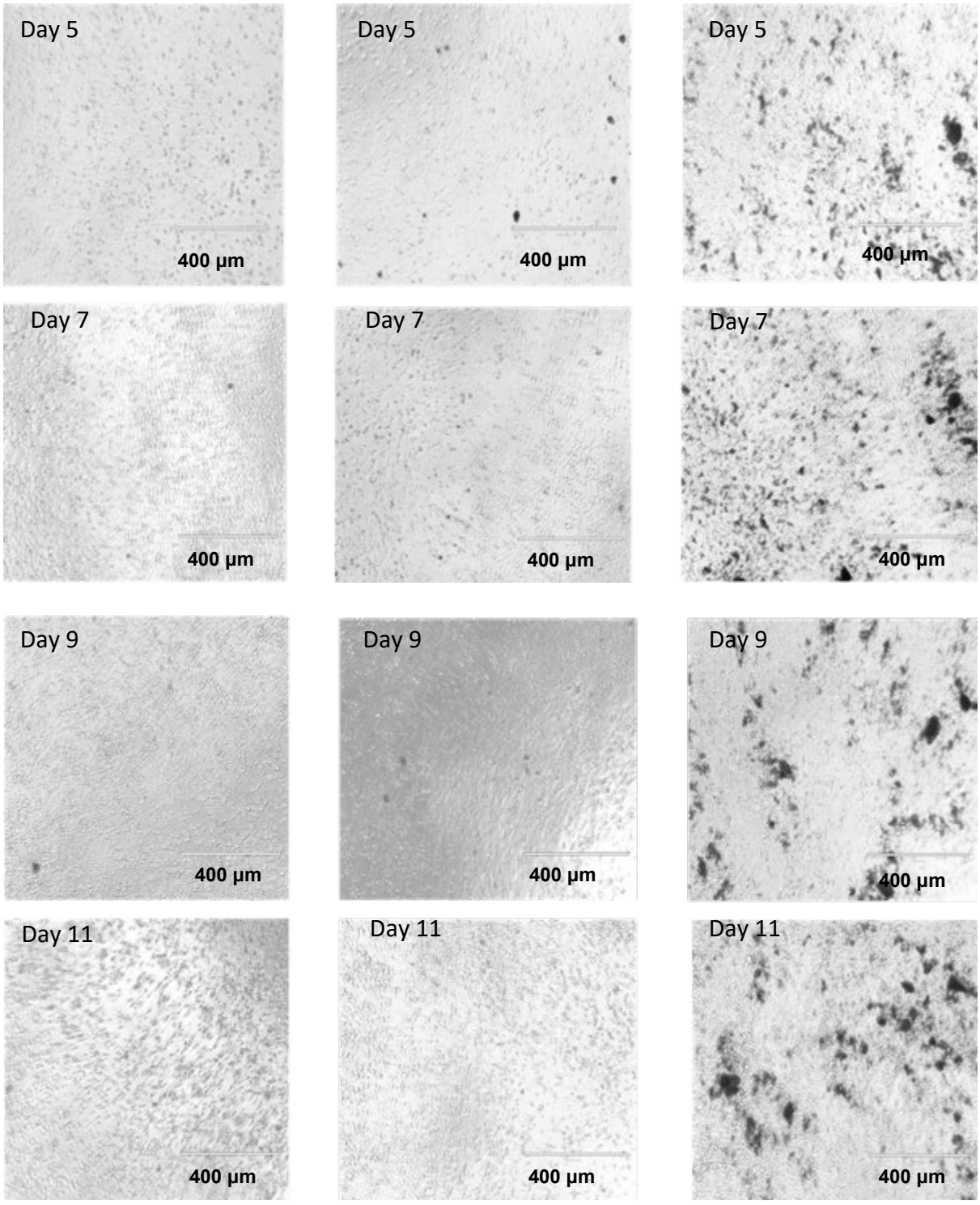


Figure 7.22. Optical imaging of endothelial cells exposed to exposed to low, medium and high concentrations of Blank F18 for 11 days.

7.3.4 Mechanism of Cell Death

Apoptotic and necrotic endothelial cells were analysed by flow cytometry after incubation with the free IRH and NP formulations using Alexa Fluor 488 Annexin V and PI double staining. The dot plots show the quadrants of the different states of the cells including their viability (annexin V−, PI−), early apoptosis (annexin V+, PI−), late apoptosis (annexin V+, PI+) and necrosis (annexin V−, PI+). The percentages of each state are given as a mean of 3 replicates.

Figure 7.23 to Figure 7.26 display the bar graphs for the endothelial cells treated with the free IRH and NP formulations after one day. Compared to the negative control, the free IRH induced minimal apoptosis and necrosis while preserving 93.40%, 83.30% and 91.03% of cell viability for the low, medium and high concentrations respectively (Figure 7.23). Exposure of the cells to the F2 NPs for the same duration of treatment also resulted in minimal apoptosis and necrosis while preserving the cell viability at 84.40%, 85.53% and 84.30% for the low, medium and high concentrations respectively (Figure 7.23).

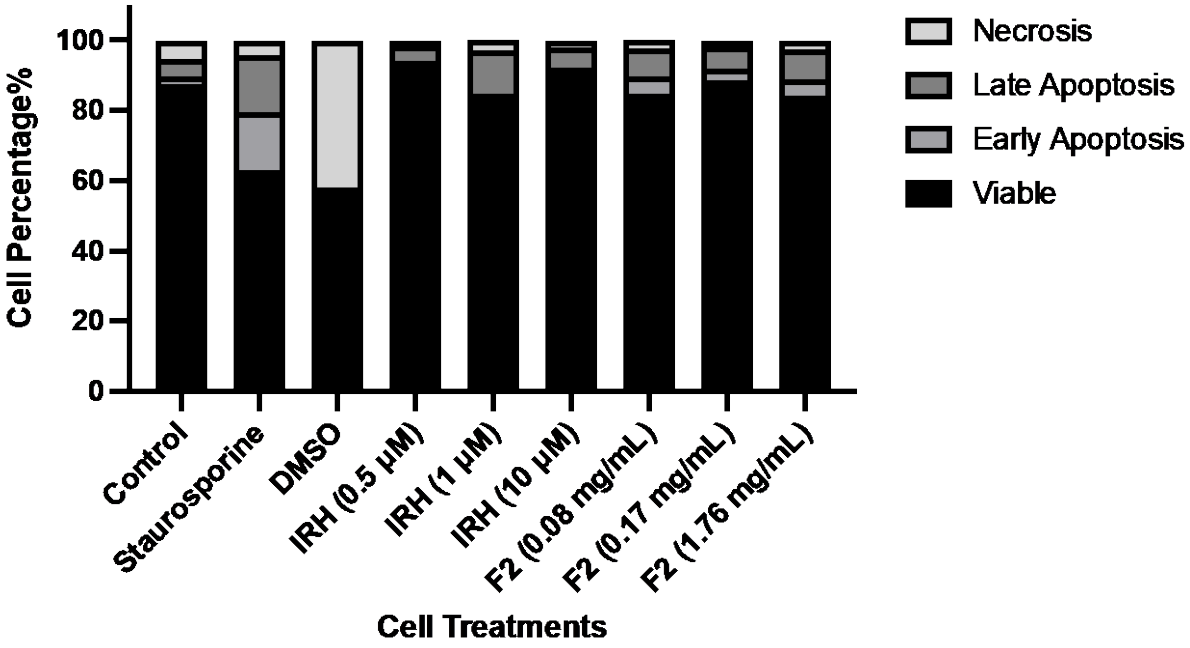


Figure 7.23. Quantification of viable, apoptotic and necrotic endothelial cells exposed to 1-day treatment with IRH and F2 compared to negative and positive controls (n=3).

F18 NPs were more apoptotic and necrotic than the F2 NPs and free IRH from the first day of treatment, reducing cell viability to 82.03%, 76.90% and 60.13% at the low, medium and high concentrations respectively (Figure 7.24).

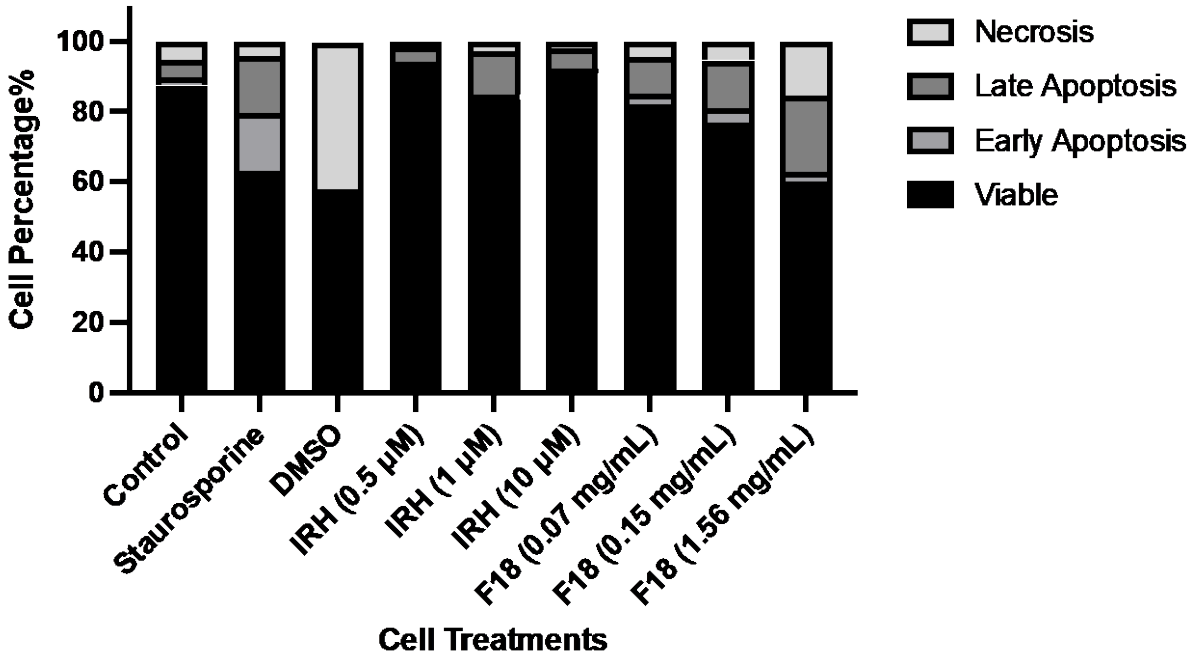


Figure 7.24. Quantification of viable, apoptotic and necrotic endothelial cells exposed to 1- day treatment with IRH and F18 compared to negative and positive controls (n=3).

The blank F2 NPs also preserved 93.90%, 92.73% and 80.16% of the cell viability on day 1 at the low, medium and high concentrations respectively (Figure 7.25).

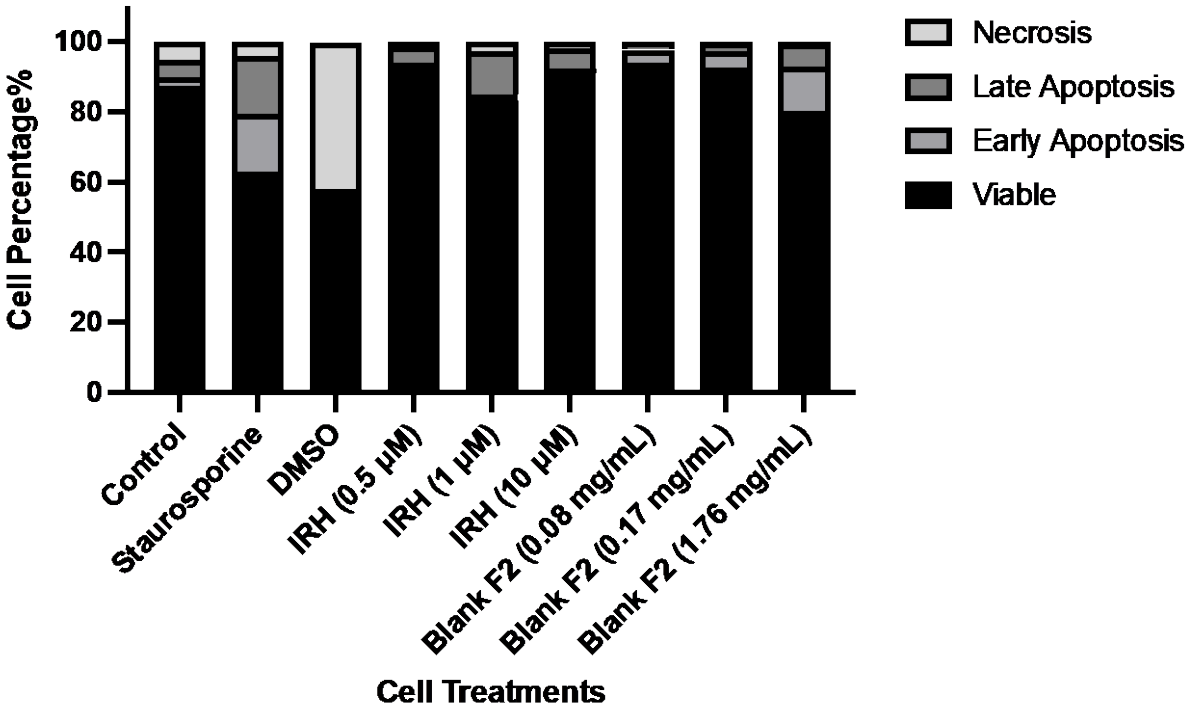


Figure 7.25. Quantification of viable, apoptotic and necrotic endothelial cells exposed to 1-day treatment with IRH and blank F2 compared to negative and positive controls (n=3).

Similarly, blank F18 was apoptotic and necrotic from day 1 reducing viability down to 83.83%, 75.46% and 63.30% by the low, medium and high concentrations respectively (Figure 7.26).

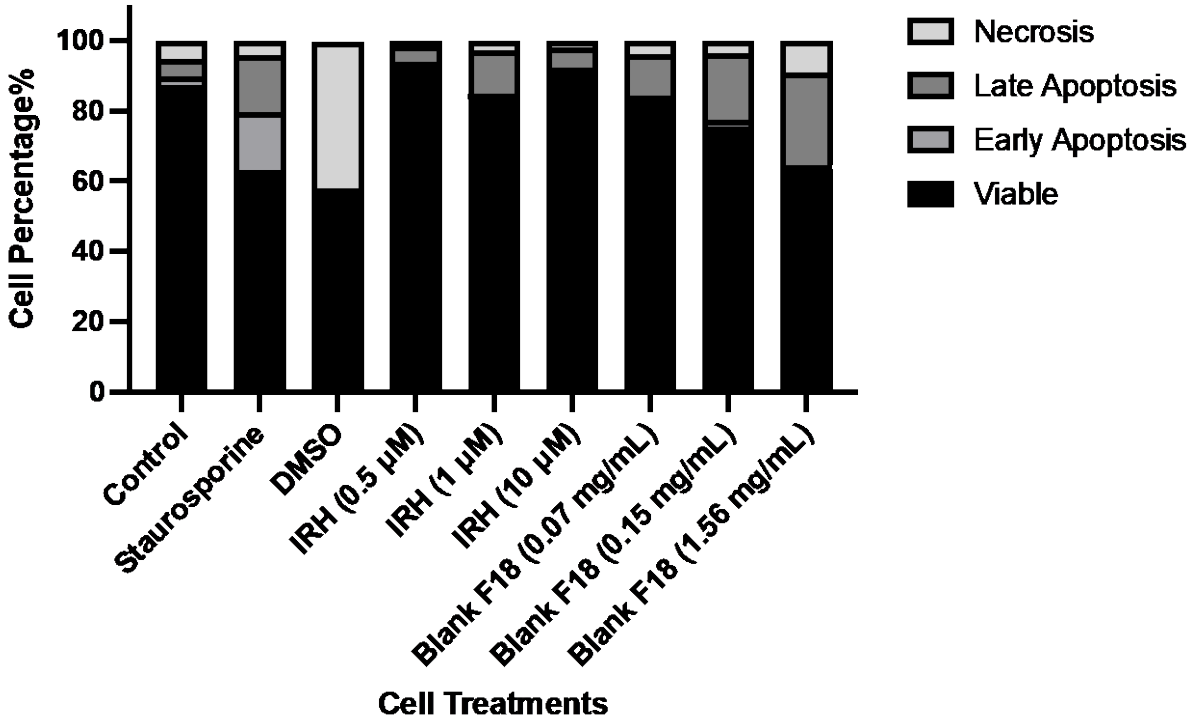


Figure 7.26. Quantification of viable, apoptotic and necrotic endothelial cells exposed to 1- day treatment with IRH and blank F18 compared to negative and positive controls *(n=3)*.

Figure 7.27 to Figure 7.30, display the bar graphs of endothelial cells treated with the free IRH and NP formulations for three days. The highest concentration of the free IRH induced the highest apoptotic effect, reducing cell viability to 28.90% (Figure 7.27). Groups treated with the low and medium IRH concentrations had cell viabilities of 90.00% and 85.00% compared to 92.70% for the negative control (Figure 7.27). The groups treated with F2 NPs had cell viabilities of 91.66%, 91.33% and 85.46% for the low, medium and high concentrations respectively (Figure 7.27).

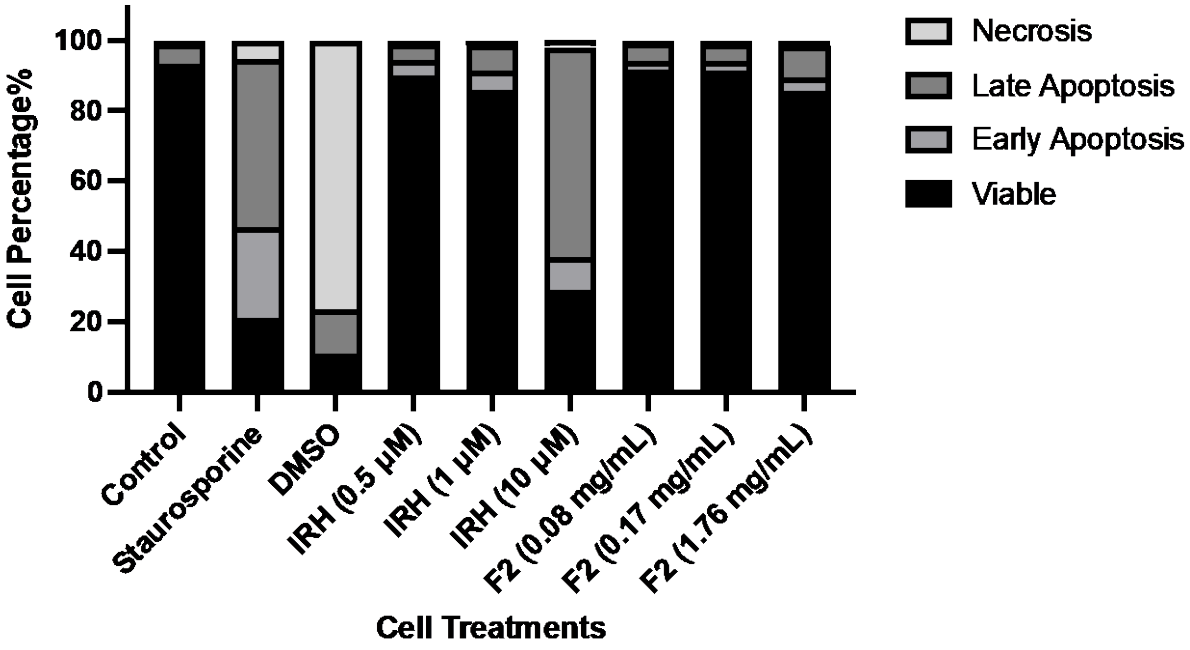


Figure 7.27. Quantification of viable, apoptotic and necrotic endothelial cells exposed to 3-day treatment with IRH and F2 compared to negative and positive controls (n=3).

The highest concentration of the F18 NPs reduced the cell viability to 48.56%, while the groups treated with the low and medium concentrations had higher than 91.00% of cell viabilities (Figure 7.28).

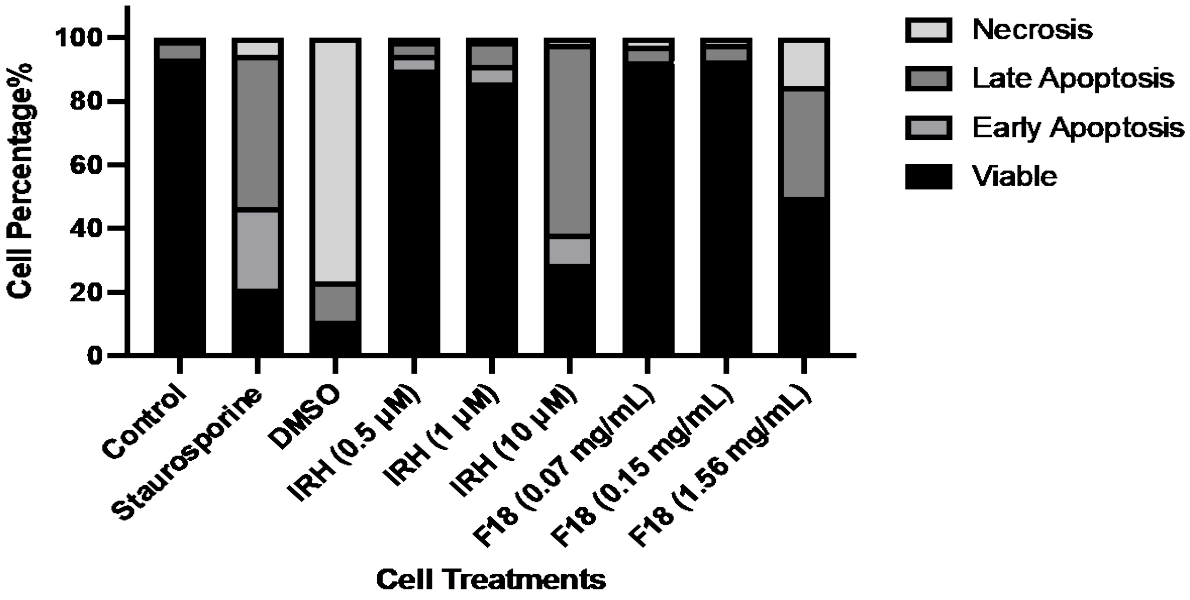


Figure 7.28. Quantification of viable, apoptotic and necrotic endothelial cells exposed to 3-day treatment with IRH and F18 compared to negative and positive controls (n=3).

Surprisingly, the blank F2 NPs induced the highest level of apoptosis in the endothelial cells at the highest concentration reducing cell viability to 8.77% by day 3, while the low and medium concentrations had cell viabilities greater than 82.00% (Figure 7.29).

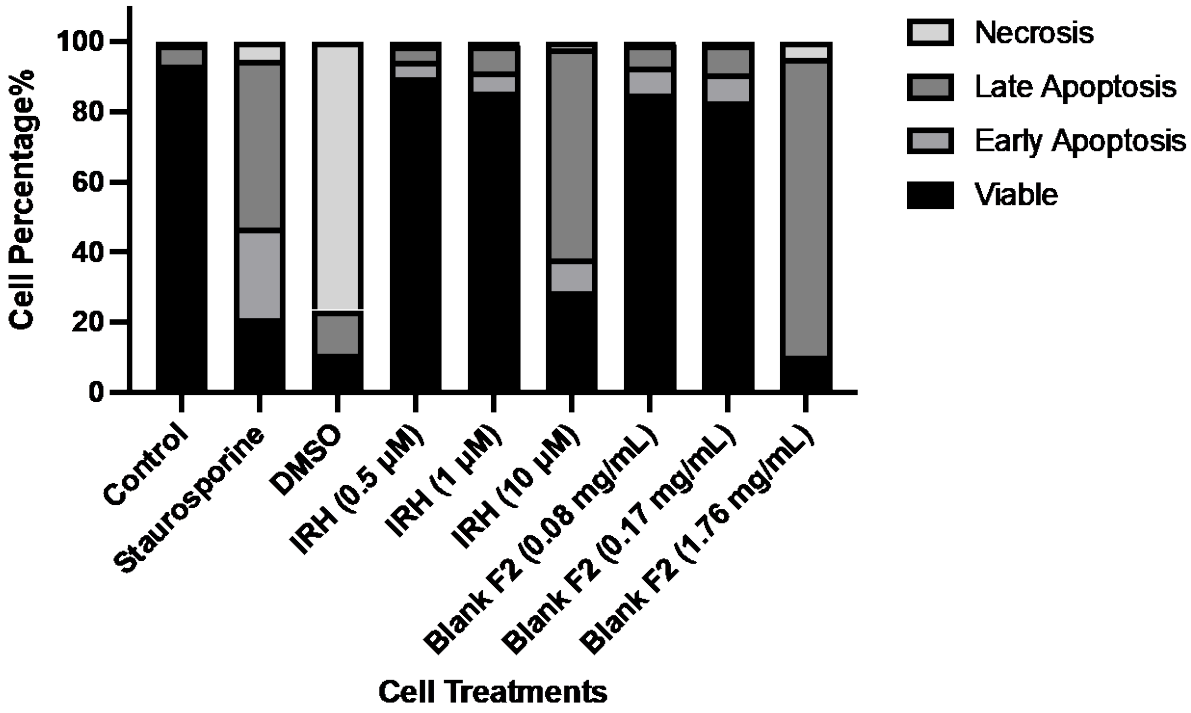


Figure 7.29. Quantification of viable, apoptotic and necrotic endothelial cells exposed to 3-day treatment with IRH and blank F2 compared to negative and positive controls (n=3).

Similarly, groups treated with the blank F18 NPs had higher than 91% cell viabilities for both the low and medium concentrations, with the highest concentration having 76.93% of viable cells (Figure 7.30).

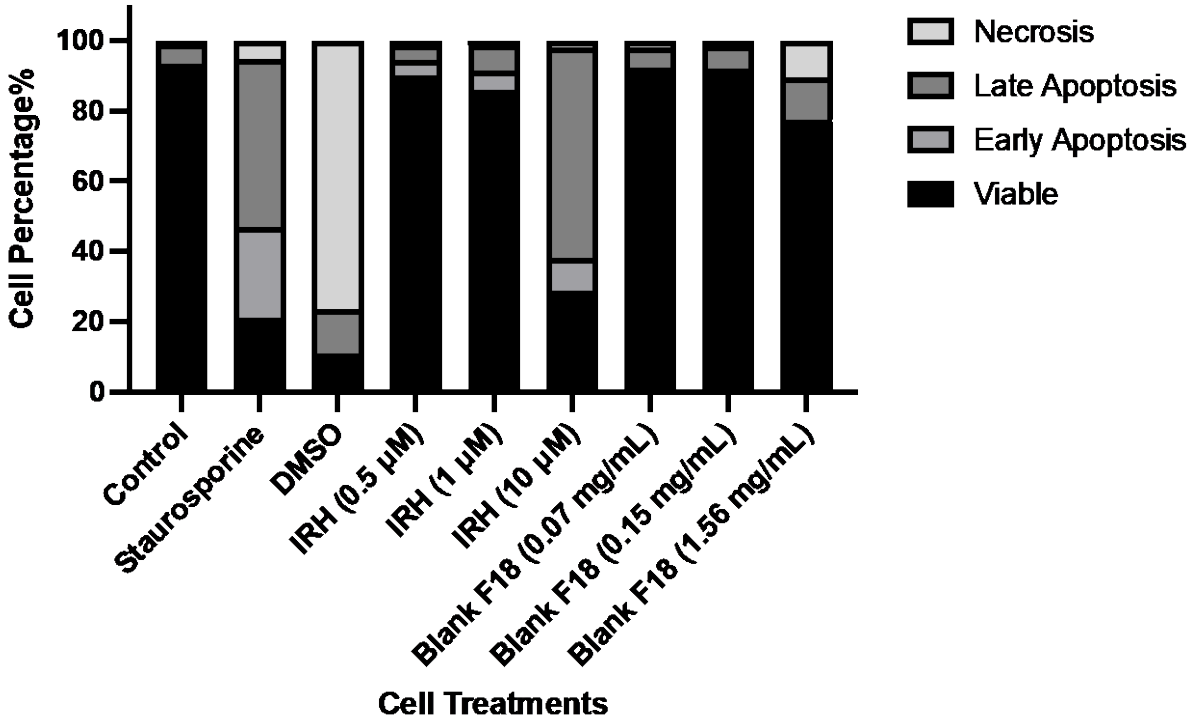


Figure 7.30. Quantification of viable, apoptotic and necrotic endothelial cells exposed to 3-day treatment with IRH and blank F18 compared to negative and positive controls (n=3).

Figure 7.31 to Figure 7.34 demonstrate that the highest concentration of the free IRH continued to increase the level of apoptosis to 63.33%, reducing cell viability to 14.46% at day 5. However, the groups treated with low and medium concentrations had cell viabilities greater than 73.00% at day 5 (Figure 7.31). The groups treated with F2 NPs had cell viabilities of 92.76%, 89.90% and 82.33% at the low, medium and high concentrations respectively at day 5 (Figure 7.31).

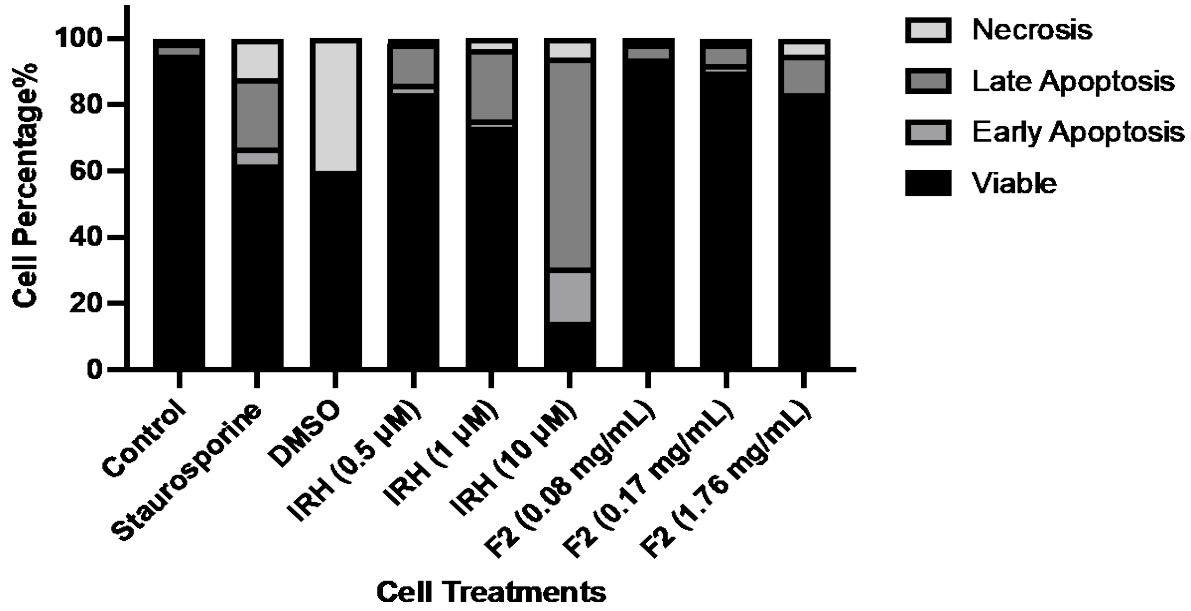


Figure 7.31. Quantification of viable, apoptotic and necrotic endothelial cells exposed to 5-day treatment with IRH and F2 compared to negative and positive controls (n=3).

The highest concentration of the F18 NPs continued reducing the cell viability to 21.23% at day 5, while the groups treated with the low and medium concentrations had cell viabilities of 87.93% and 88.06% respectively (Figure 7.32).

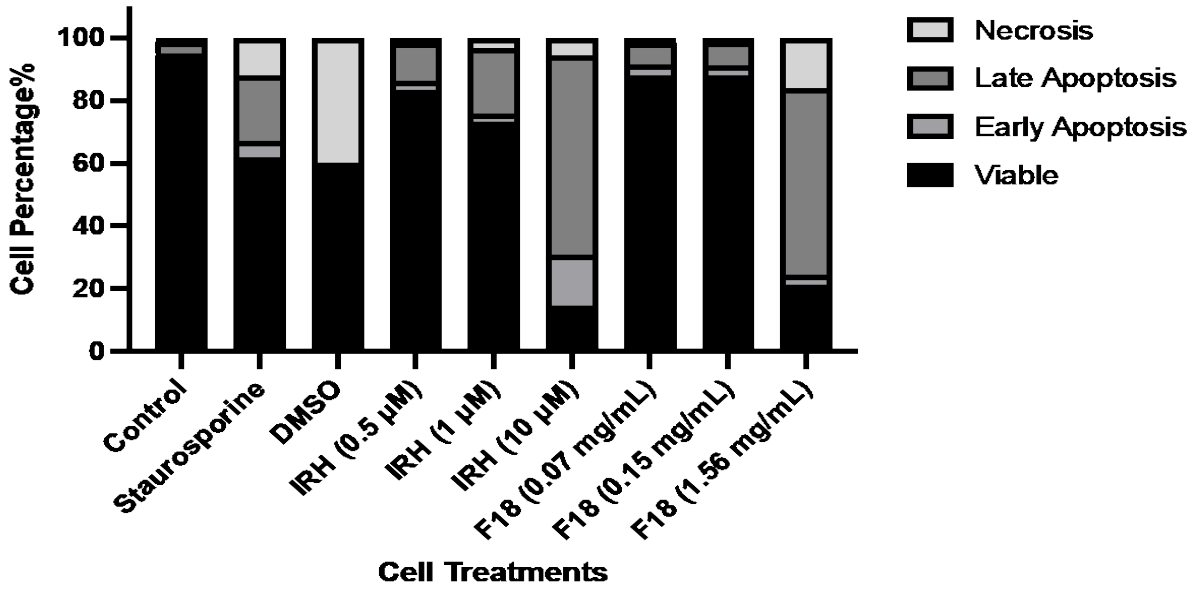


Figure 7.32. Quantification of viable, apoptotic and necrotic endothelial cells exposed to 5-day treatment with IRH and F18 compared to negative and positive controls (n=3).

The blank F2 NPs reduced the cell viability to 9.96% at its highest concentration, while the groups treated with the low and medium concentrations had cell viabilities of 84.26% and 72.30% respectively (Figure 7.33).

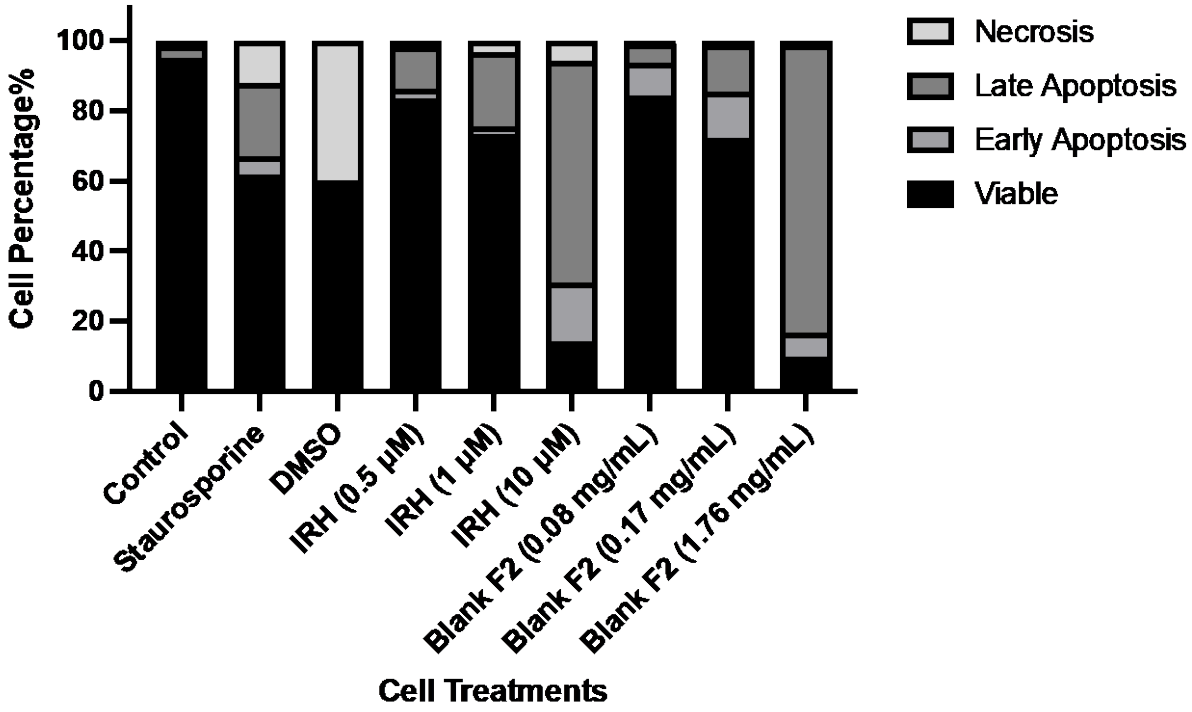


Figure 7.33. Quantification of viable, apoptotic and necrotic endothelial cells exposed to 5-day treatment with IRH and blank F2 compared to negative and positive controls (n=3).

The group treated with the highest concentration of the blank F18 NPs had a cell viability of 73.96% and above 91.00% for its low and medium concentrations respectively (Figure 7.34).

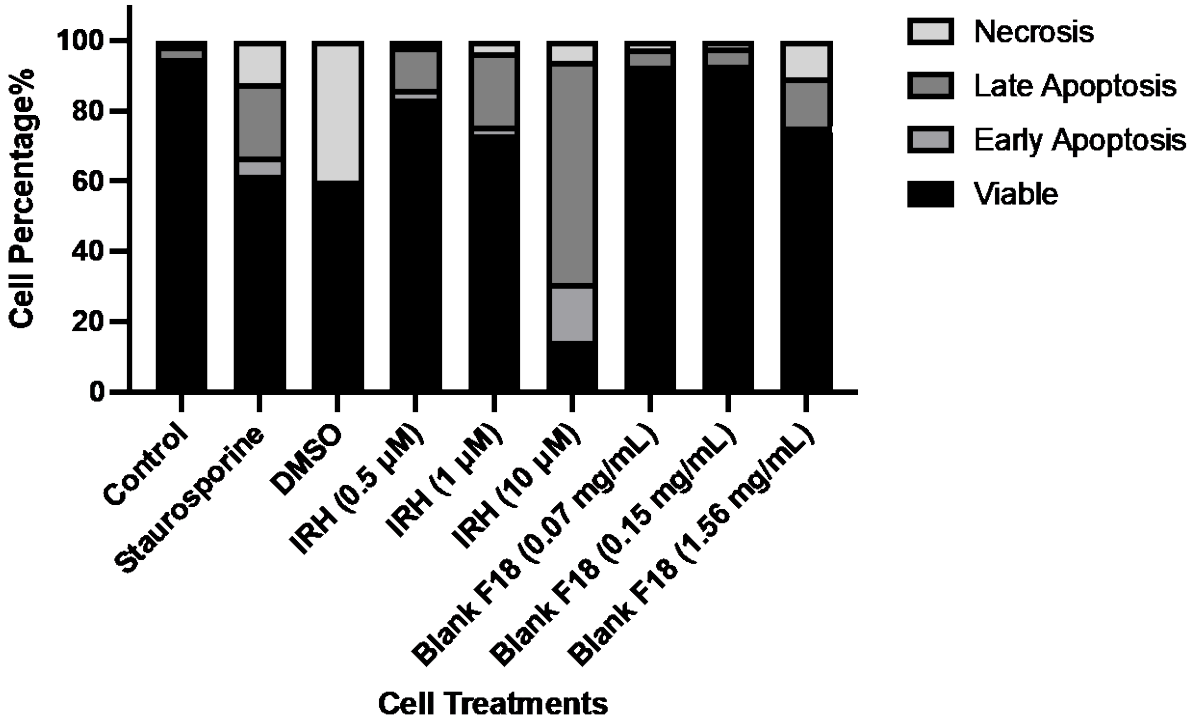


Figure 7.34. Quantification of viable, apoptotic and necrotic endothelial cells exposed to 5-day treatment with IRH and blank F18 compared to negative and positive controls (n=3).

7.3.5 Permeability of BBB

Figure 7.35 to Figure 7.39 present the TEER values of the endothelial cells upon exposure to the free IRH and NPs. The free IRH resulted in a decrease in the TEER value after 24 hours, which was maintained until day 3 (Figure 7.35). This is most likely a result of damage to the endothelial cells, rather than an increase in permeability as we would expect the TEER value to increase as the drug crosses the endothelial cells. Treatment of the endothelial cells with the NP formulations led to a slower and temporary reduction in the TEER value, which was then restored by day 3 showing recovery of the endothelial resistance. This would indicate that the NPs permeated the BBB, but did not damage it.

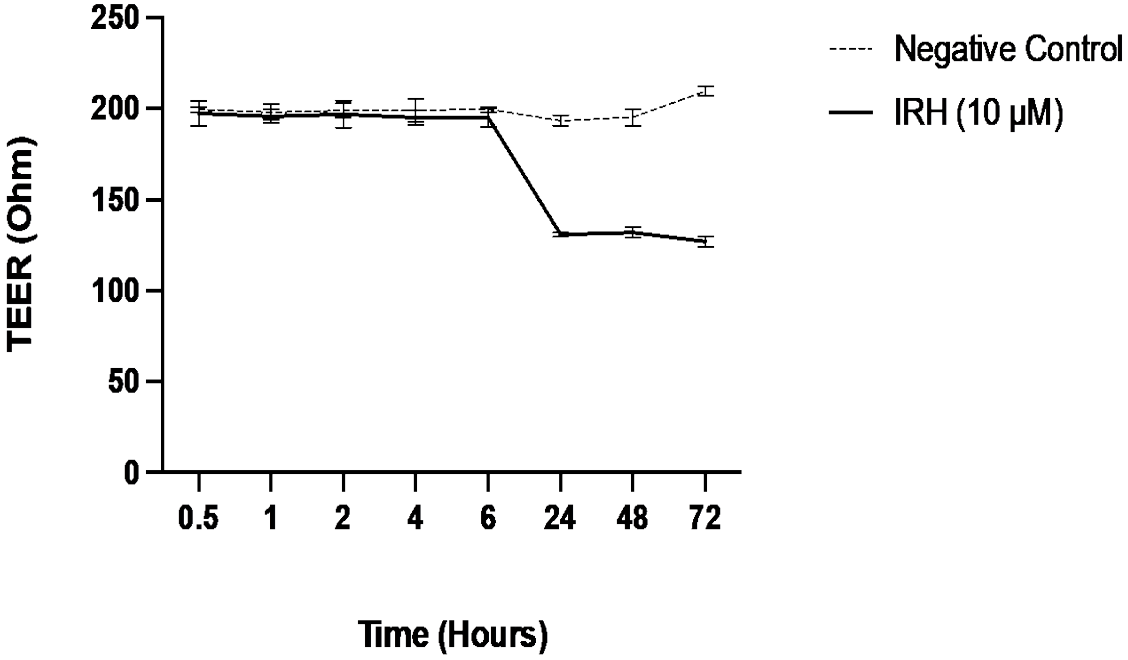


Figure 7.35. Effect of free IRH on TEER of brain endothelial cells (n=3).

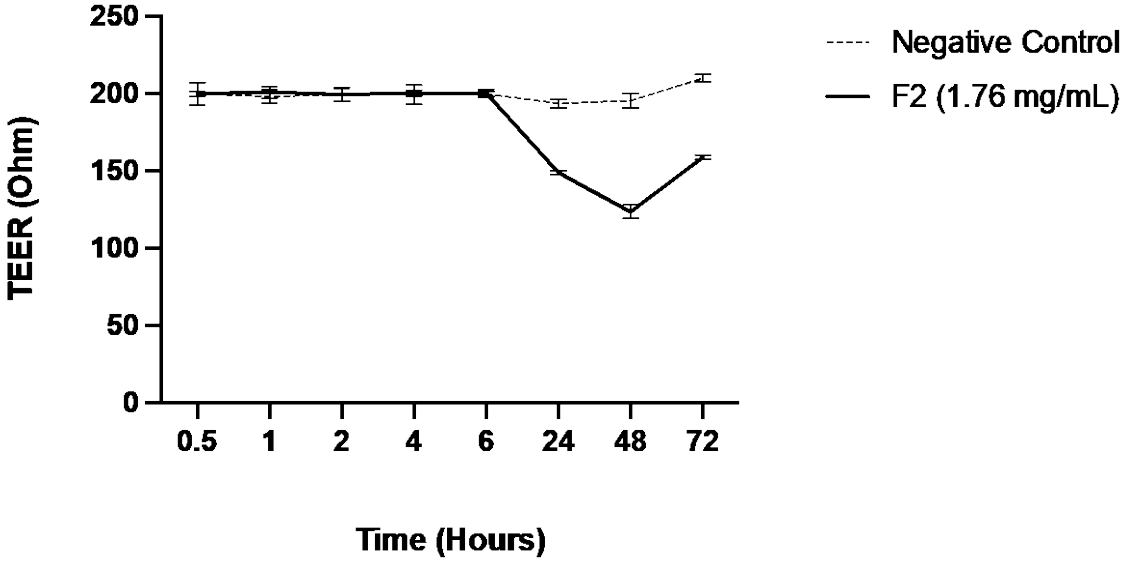


Figure 7.36. Effect of F2 on TEER of brain endothelial cells (n=3).

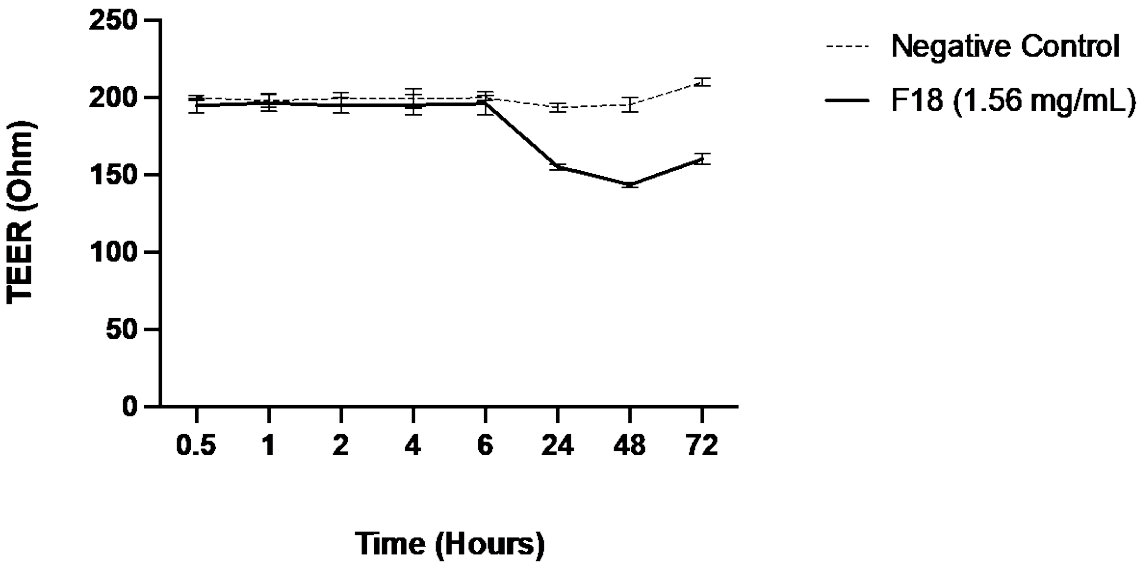


Figure 7.37. Effect of F18 on TEER of brain endothelial cells (n=3).

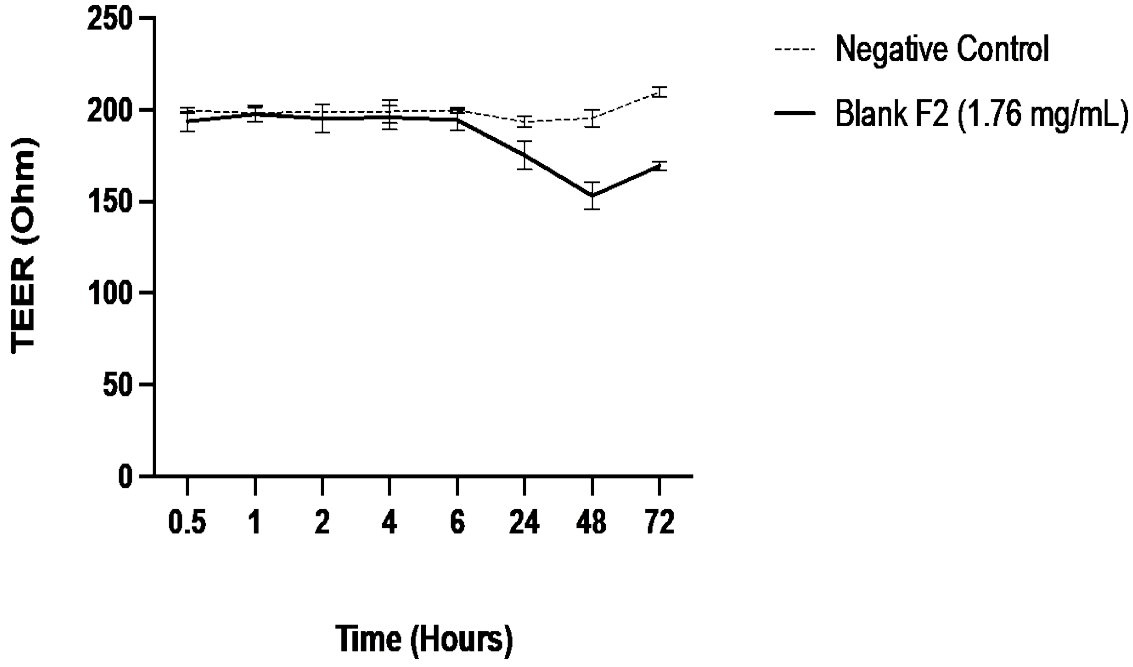


Figure 7.38. Effect of blank F2 on TEER of brain endothelial cells (n=3).

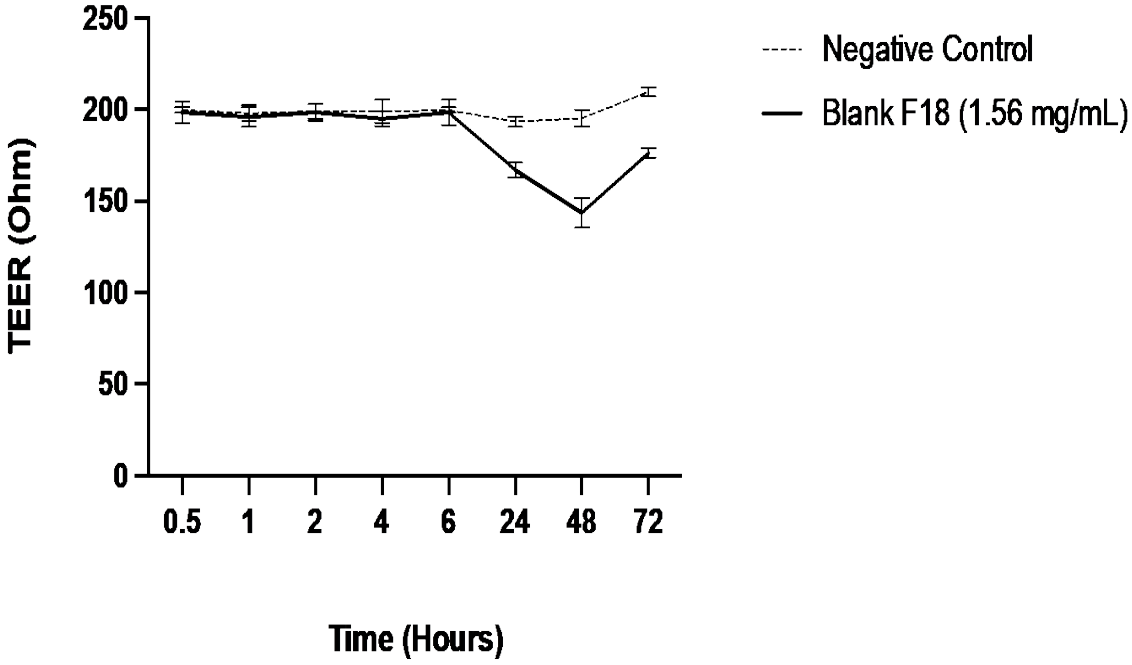


Figure 7.39. Effect of blank F18 on TEER of brain endothelial cells (n=3).

7.3.6 IL-6 Protein Expression

The difference in IL-6 protein expression in endothelial cells treated with the free IRH and NP formulations over 3 and 5 days was investigated. IL-6 was mostly expressed in the endothelial cells exposed to the highest concentrations of the free IRH on day 3 resulting in 1354.71 pg/mL of IL-6 (Figure 7.40), which is significantly ($P<0.0001$) higher than the negative control (106.47 pg/mL). All of the F2 NP concentrations showed a non-significant effect on IL-6 production compared to the negative control on day 3, the highest of which led to the production of 302.96 pg/mL of IL-6 (Figure 7.40). The free IRH was significantly ($P<0.0001$) more immunogenic than the F2 NPs at their highest concentrations. The low and medium concentrations of both the free IRH and F2 did not exhibit a significant difference compared to the control group (Figure 7.40).

On day 5, the level of IL-6 was significantly elevated by treatment with the free IRH peaking at 2977.34 pg/mL for the highest concentration (P<0.0001). Whereas, treatment with the F2 NPs led to 2304.88 pg/mL of IL-6 expressed by endothelial cells compared to 389.26 pg/mL produced by the negative control and 1944.14 pg/mL produced by blank F2 NPs (Figure 7.42). Additionally, the F18 NPs (Figure 7.41) resulted in a significantly (P<0.0001) higher expression of IL-6 (3736.60 pg/mL) compared to the negative control, blank F18 NPs (821.04 pg/mL) (Figure 7.45) and F2 NPs (Figure 7.46).

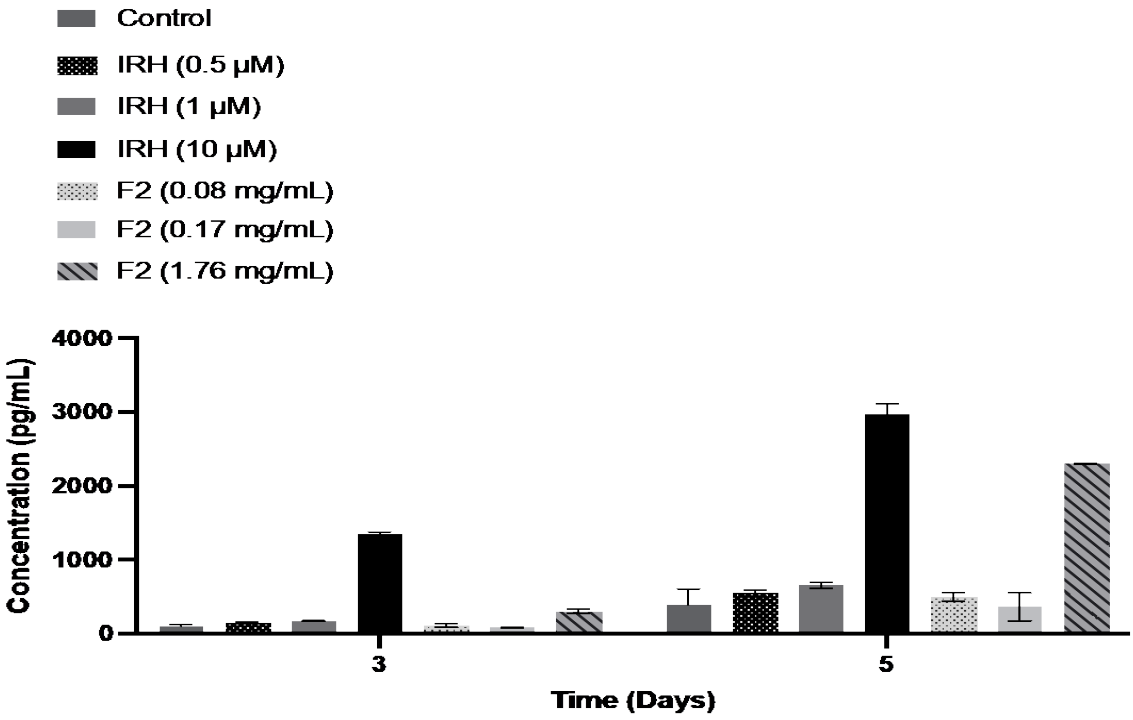


Figure 7.40. Expression of IL-6 in endothelial cells exposed to low, medium and high concentrations of F2 for 3 and 5 days (n=3).

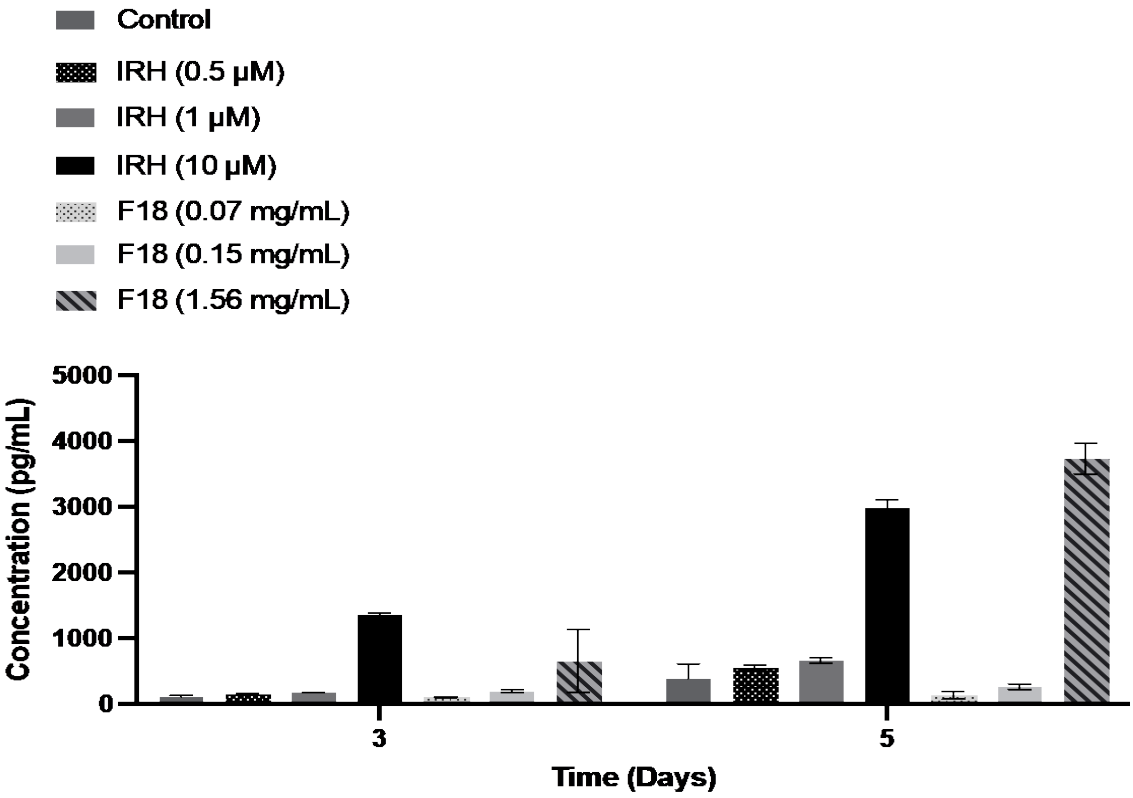


Figure 7.41. Expression of IL-6 in endothelial cells exposed to low, medium and high concentrations of F18 for 3 and 5 days (n=3).

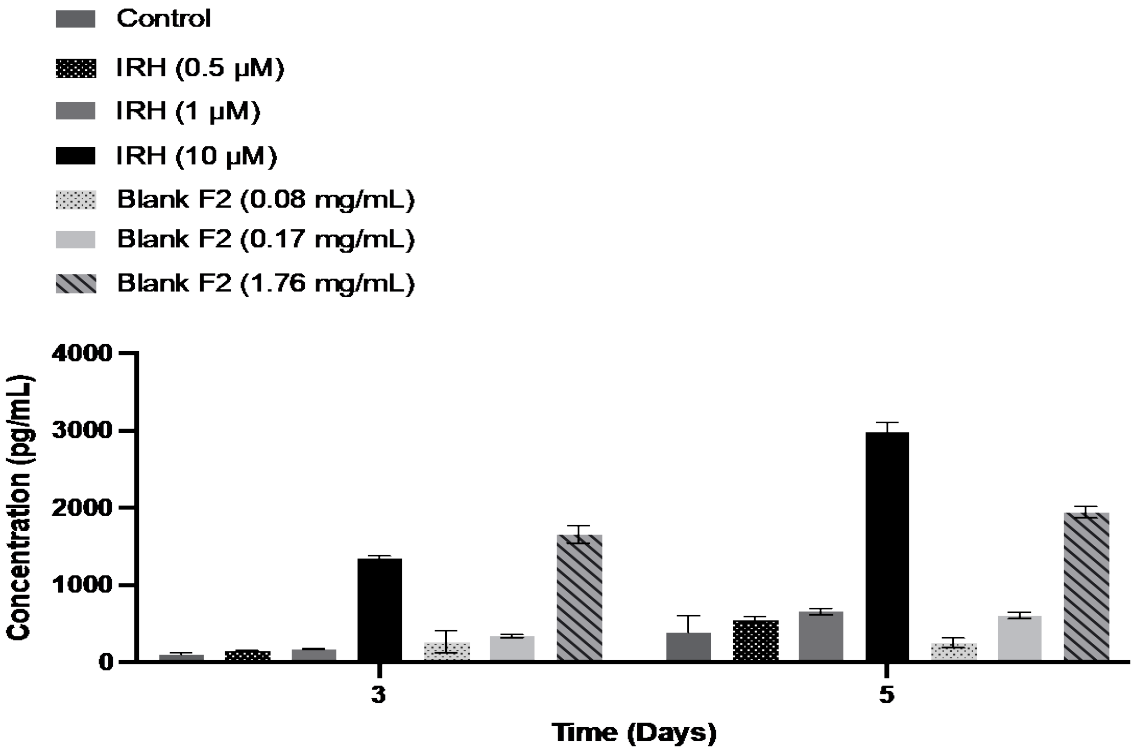


Figure 7.42. Expression of IL-6 in endothelial cells exposed to low, medium and high concentrations of blank F2 for 3 and 5 days (n=3).

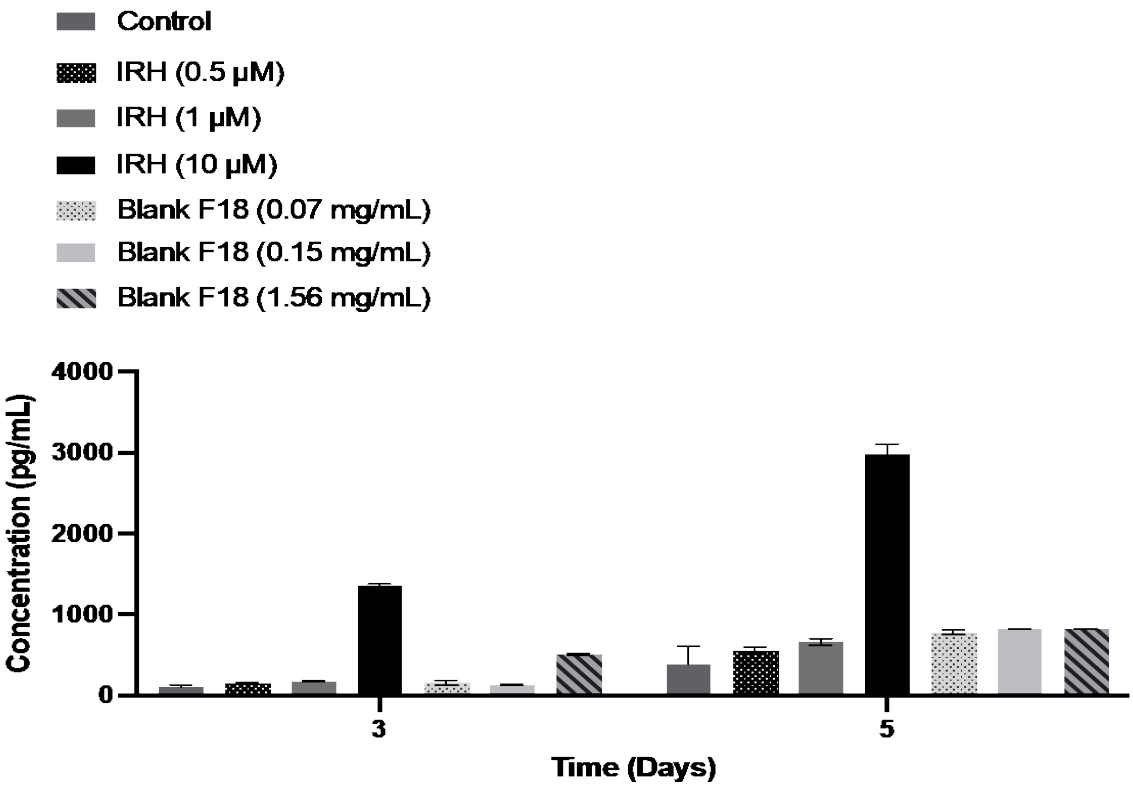


Figure 7.43. Expression of IL-6 in endothelial cells exposed to low, medium and high concentrations of blank F18 for 3 and 5 days (n=3).

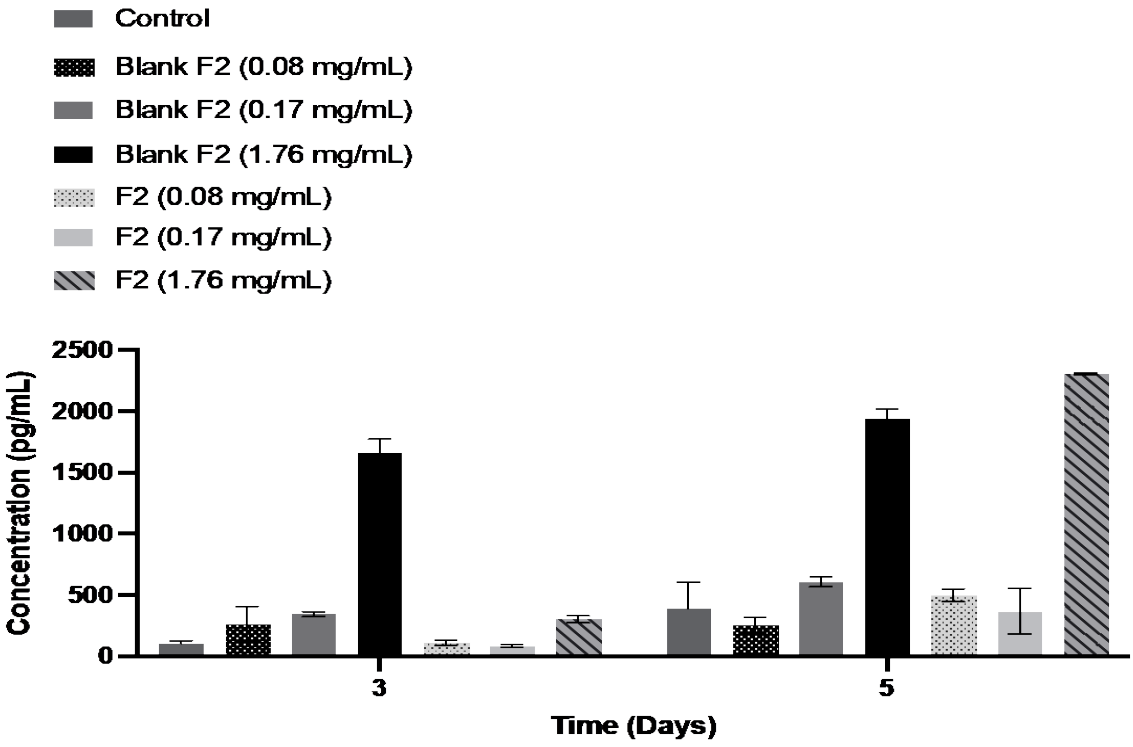


Figure 7.44. Expression of IL-6 in endothelial cells exposed to low, medium and high concentrations of F2 and blank F2 for 3 and 5 days (n=3).

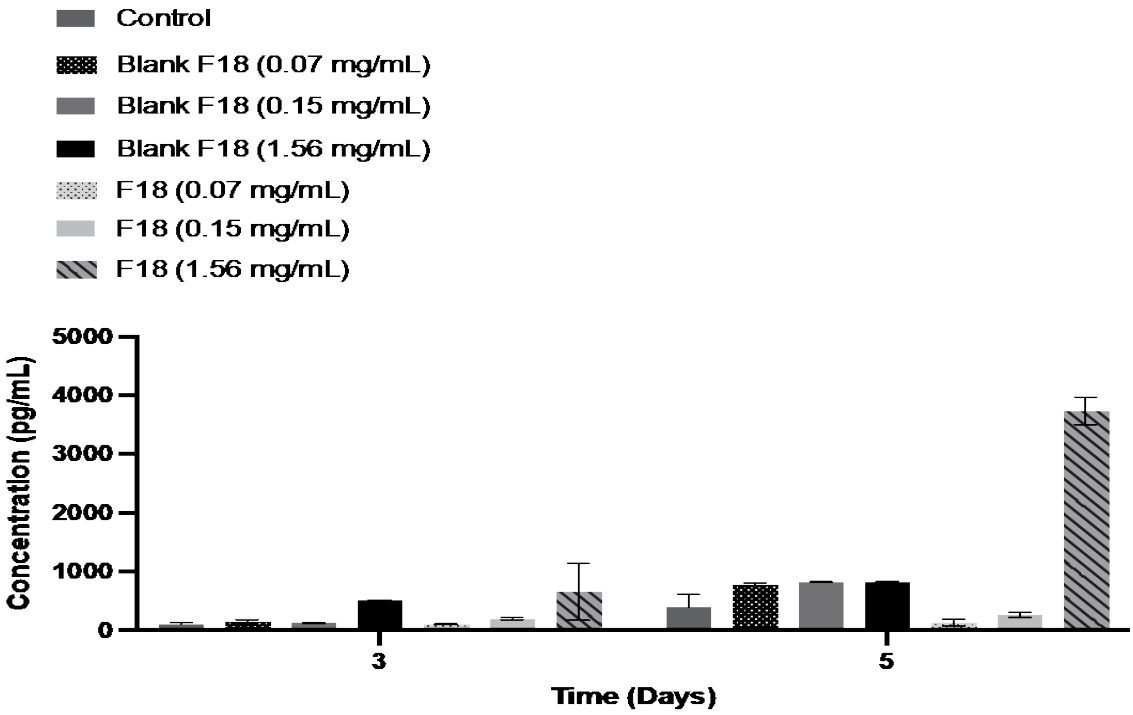


Figure 7.45. Expression of IL-6 in endothelial cells exposed to low, medium and high concentrations of F18 and blank F18 for 3 and 5 days (n=3).

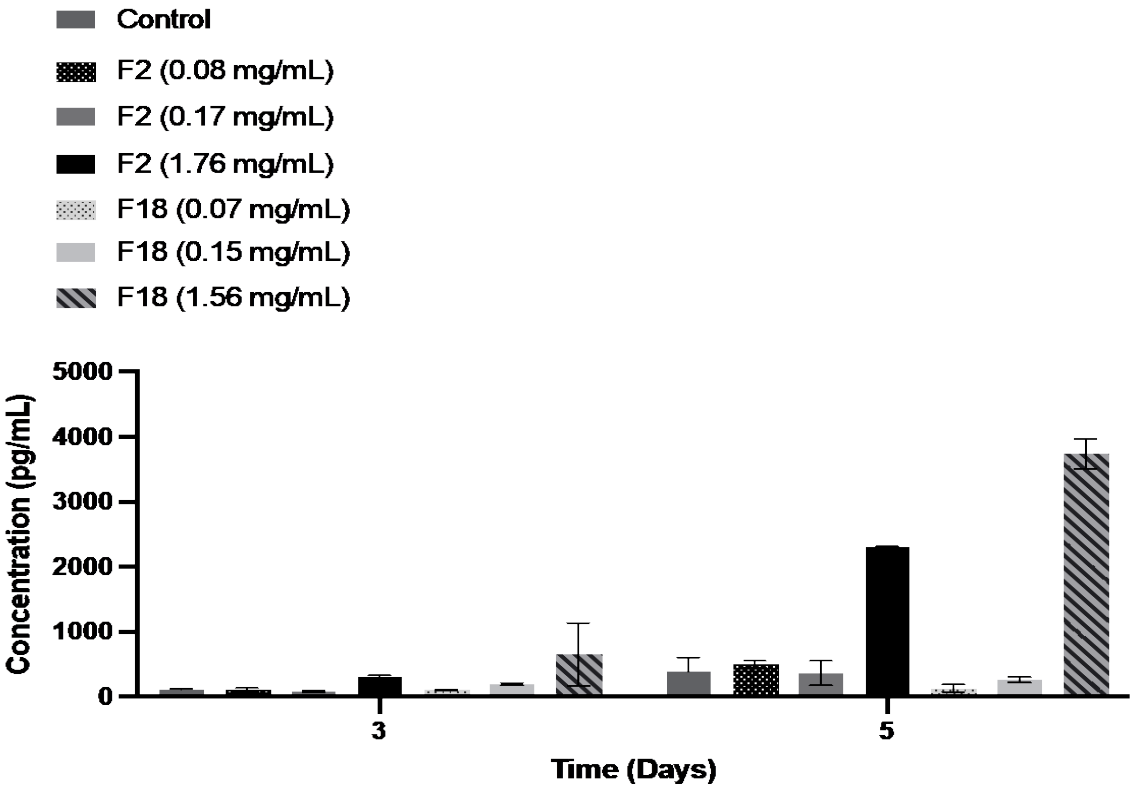


Figure 7.46. Expression of IL-6 in endothelial cells exposed to low, medium and high concentrations of F2 and F18 for 3 and 5 days (n=3).

7.4 Discussion

Brain endothelial cells are crucially involved in the tight structure of the BBB and its selective transport mechanisms which limit the transport of molecules into the brain regardless of their size (Daneman and Prat, 2015; Kniesel and Wolburg, 2000). Cerebral vascular endothelial cells represent a crucial target in the field of drug delivery since they are involved in normal brain function or pathological conditions such as tumour development (Dass and Su, 2010). Therefore, it is necessary to examine the effect of treatments on the viability and integrity of these cells.

The uptake of the NPs by endothelial cells was concentration dependent with a higher uptake of F2, F18, blank F2 and blank F18 NPs compared to the free IRH. Similar observations were reported for the uptake of NPs that occurred in a time and dose dependent pattern in a human umbilical vein endothelial cell line (Davda and Labhasetwar, 2002). Cellular uptake of NPs varies according to cell type, with polarized cells that form monolayers having different uptake pathways and receptors on their apical and basolateral sides compared to confluent cells (Francia et al., 2018). Additionally, endothelial cells of different organs are heterogenous in nature and behave differently in relation to NP uptake and protein expression (Kowalski et al., 2013). In a study comparing different endothelial cells from different sources, the brain endothelium was the tightest and had the lowest uptake. The rate of endocytosis also determines the difference in cellular uptake (Gromnicova et al., 2016).

The cell viability study indicated higher toxicity of the free IRH compared to the F2 NPs at their highest concentrations. The drug loaded NPs were most toxic at their highest concentrations, whereas, the low and medium concentrations maintained some level

of viability of the endothelial cells. The blank NPs were less toxic than their drug-loaded counterparts for most of the doses. Some variations occurred, however, at the highest concentrations due to possible gravitational sedimentation of the NPs as discussed in chapter 6, section 6.4. Similar observations were recorded elsewhere in which low concentration of PLGA NPs exerted mild toxicity on endothelial cells reducing viability to 60-70%. However, at the highest concentration of 1 mg/mL, they were severely toxic to the cells. The same study highlighted that TEER reduction following the uptake of the PLGA NPs was not only related to toxicity and that other contributing factors were involved such as high cellular uptake and particle agglomeration (Onyema et al., 2021).

The TEER was measured in the endothelial cells to evaluate the effect of the free IRH and NP formulations on the monolayer permeability. The cells were left to achieve maximum resistance before adding the treatments. Upon the addition of the free IRH there was a rapid decrease in the TEER value, which persisted until day 3, with no sign of recovery. This type of response is indicative of damage to the endothelial cells with a lack of recovery of the integrity of the BBB. However, with the NPs the decrease in TEER value was gradual across days 1 and 2, with an increase in TERR value at day 3. This is indicative of permeation of the NPs across the BBB without causing permanent damage which demonstrates that the NPs had a limited and temporary effect on the integrity of the BBB. Similar data were previously reported in which PCL NPs and free drug reduced the endothelial integrity for 24 hours before increasing again in a sustained manner demonstrating that a drop in the TEER values could allow the passive transport of solutes through tight junctions of the BBB (Omarch et al., 2019).

Unlike glioma cells, apoptosis is downregulated in endothelial cells (Charalambous et al., 2005). This is in accordance with our data in which the negative control had high cell viability and limited apoptosis. Treatment with the free IRH and NPs had a low impact on inducing apoptosis from day 1 to day 5, except for the highest concentrations of the free IRH and some of the NP formulations, indicating less toxicity imposed on the endothelial cells compared to glioma cells.

The IL-6 proinflammatory cytokine is known to be produced by endothelial cells and the IL-6 receptors are expressed by different brain cells including endothelial cells, astrocytes, microglia and neurons. IL-6 triggers the production of VEGF which enhances angiogenesis increasing the severity of the tumour (Yao et al., 2006). Several studies have reported that upregulation of IL-6 plays a vital role in reducing the permeability of endothelial cells by the expression of tight junction proteins as occludin and claudin-5 which are crucial in maintaining the integrity of the endothelial barrier (Cohen et al., 2013; Desai et al., 2002; Noma et al., 2012). Also, other studies reported that IL-6 is involved in gap formation and increased permeability by rearranging the actin filaments that maintain the integrity of endothelial barriers which is a reversible process upon downregulation of IL-6 (Maruo et al., 1992). Acute vascular permeability resulting from cytokine activation as an inflammatory response is necessary for pathogen disposal and maintenance of tissue. However, extended durations of permeability or vascular leakage can result in tissue damage, impairment in the function of organs and death (Alsaffar et al., 2020). The present data demonstrates that exposure to the highest concentration of free IRH for extended periods of time, led to upregulation of IL-6 from 1354.71 pg/mL on day 3 to 2977.34 pg/mL on day 5. On the other hand, treatment with the NP formulations was

significantly ($P<0.0001$) less immunogenic at their highest concentrations on day 3 but led to higher immunogenicity on day 5 with the highest effect triggered by the F18 NPs due to increased drug release. Conversely, the low and medium concentrations of all the NPs induced a mild increase in IL-6, which suggests that using NPs within certain doses can limit the level immunogenicity.

In conclusion, the endothelial cells had a more enhanced cellular uptake of both PCL and PCL-PLGA blend NPs compared to the free IRH. However, free IRH was more cytotoxic at its highest concentration compared the NP formulations. Also, the effect of the NPs on the endothelial cells was not as intense as it was on glioma cells over time except at the highest concentrations. This effect was also confirmed by analysing the apoptotic and necrotic endothelial cells, where there was minimal effect by the low and medium concentrations of the treatments compared to glioma cells which indicate that the endothelial cells are less susceptible to cytotoxicity by NPs compared to glioma cells. In addition, free IRH was more immunogenic at its highest concentrations than its counterparts of NP formulations and has induced more damage to the endothelial integrity as compared to the NP treatments which was evident by the irreversible TEER by day 3.

Chapter 8 FINAL CONCLUSION, SUMMARY OF FINDINGS AND FUTURE RESEARCH

Malignant gliomas are a lethal class of brain tumours that develop resistance to both chemo and radiation therapies. The BBB provides an extra complexity by limiting access of most therapeutics to the brain. Therefore, the quest for alternative therapies that can bypass the BBB is deemed crucial.

Nanomedicine is a non-invasive approach that is gaining approval from the FDA and popularity in clinics. Among the plethora of NPs, polymeric NPs are gaining more attention due to their advantages compared to other NPs. These include biocompatibility, biodegradability and ease of preparation and functionalization. However, efforts must be exerted in order to optimize the characteristics of NPs. Hydrophobic polymeric NPs are regarded as promising carriers for drugs, owing to their ability to traverse the BBB enhancing the delivery of the drugs to the tumours, especially if targeting over-expressed receptors on the surface of tumours. PEGylation of the Polymeric NPs can also reduce their immunogenicity. Therefore, they can be administered systemically, which is a favourable route for cancer treatment especially for cases of metastasis. However, more efforts are required to enable the design of the drug-loaded NPs with optimum physico-chemical and biological characteristics specific for the target tumour.

PCL is a flexible polymer that possesses several advantages as a drug carrier for sustained delivery of drugs, however its low EE has limited its application. In this research different approaches were employed to enhance the EE of the PCL by lowering its crystallinity and hydrophobicity without affecting its natural properties. One of the approaches was by using the double emulsion solvent evaporation technique and by performing amorphization of the PCL. Addition of electrolytes was also used in

the process and was effective in retaining the drug within the PCL matrix. A sustained release was achieved by the NP formulations prepared with such technique. This study concluded that the most crucial factors were the amorphization of PCL and addition of electrolytes which helped keep the drug entrapped efficiently within the PCL matrix.

The parameters of the most optimum formulation were then used as the center points in BBD of experiment, which aimed at optimising and selecting the most crucial factors necessary for achieving the smallest size, lowest charge and highest EE of the IRH loaded PCL NPs.

It was concluded that the size of the PCL NPs varied mostly as a result of the interaction between the PCL and PVA. The PVA squared concentration was the most influential factor on the zeta potential of the NPs, while the drug amount had the greatest influence on the EE. The most optimized formulation for all three dependent factors was found to be achieved using 61.02 mg PCL, 9 mg IRH and 4.82% PVA which would yield 203.01 nm, -15.81 mV and 82.35% EE.

Another approach to enhance the EE and release of IRH from PCL NPs involved blending the PCL with an amorphous polymer that is less hydrophobic. In this study, a 50:50 polymer blend of PCL: PLGA was developed into drug loaded NPs. BBD was conducted to investigate the levels of the independent factors that control the properties of the dependent variables (size, charge and EE). The BBD of the blend NPs also highlighted that the amount of drug had the greatest impact on the EE. While the polymer amount had the greatest impact on both the size and charge of the blend NPs. The optimum factors were predicted to be achieved by using 162 mg polymer

blend, 8.37 mg IRH and 8% PVA which would yield NPs with a size of 283.06 nm, a charge of -31.54 mV and a 70% EE.

NP formulations with a size less than 300 nm were selected for further physico-chemical characterization. Both PCL and PCL-PLGA blend NPs had a reduced crystallinity of the PCL, effective drug encapsulation and sustained release of the drug over a 16-day period. However, the release from the blend NPs was higher due to the higher solubility and degradation rate of the polymeric blend compared to the individual PCL. In addition, The NP formulations made of PCL and PCL-PLGA blend were spherical in shape with higher stability at pH 5.9, which makes them fit for the purpose of cancer treatment.

Further biological characterization using RBCs and HGG cells concluded that shielding the IRH within the polymeric NPs could alleviate the haemolytic effect of the free drug and enhance both cellular uptake and cytotoxicity compared to the free drug. Confocal microscopy has confirmed the nuclear internalization of the NPs which is the main target for achieving a successful treatment with IRH. The blank PCL NPs were not as toxic as their drug-loaded counterparts. However, the blank blend NPs were more toxic than the blank PCL NPs due to their higher degradation rate and release of lactic and glycolic acids.

Additionally, downregulation of caspase levels following treatment with the NPs could indicate faster apoptotic rate, that was developing into secondary necrosis, than the free drug or that NPs activated a caspase independent apoptosis. A minimal haemolytic effect on RBCs was evident upon exposure to all the NPs which enables them to be safe candidates for intravenous administration.

Expression of IL-6 as a cytokine produced during the inflammation cascade was also examined and was found to be of minimal levels upon exposure of HGG cells to the NP formulations compared to the free IRH which enhanced the upregulation of IL-6 expression.

Further biological characterization using an endothelial cell line as a BBB model has elucidated higher cellular uptake of the NPs compared to the free IRH. Despite inducing cytotoxicity, the NPs were less cytotoxic to the endothelial cells compared to glioma cells, especially when used at their low and medium concentrations. The immunogenicity of all the treatments were also tested on the endothelial cells and the IL-6 was found to be higher expressed upon exposure to the free IRH. The TEER values of the endothelial cells have also highlighted that the free drug was more harmful on the integrity of the cells, while NPs had a temporary effect.

This study demonstrated that both approaches of amorphization and developing polymeric blends could alleviate the crystallinity of the PCL and enhance its EE and release profile. It was concluded that the PCL NPs (F2) could be better candidates for glioma therapy by being less necrotic and by releasing drug at a slower pace than the blend NPs (F18) at physiologic pH. However, an animal study is required to determine whether the blend NPs were naturally necrotic or that the necrosis that occurred *in vitro* was a secondary necrosis developing from apoptosis and lack of the natural phagocytosis present *in vivo*.

Future Research

Further studies are required to determine:

1. The influence of the NPs size on the biological response of glioma and endothelial cells. This could be implemented by designing NPs with various size ranges and studying their biological effect on glioma cells. In this regard, more advanced technologies could be employed to allow better control over size of NPs, such as the microfluidics technology. Also, consideration of reducing the chemical residues used to develop the formulations is encouraged by considering natural alternatives to toxic solvents, for example the supercritical fluid technology that relies on using CO_2 as a solvent for both polymers and drugs at critical temperature and pressure.

2. The optimal factors for controlling drug release from the NPs. BBD can be used in this regard to provide the optimum formulation parameters required to achieve lowest release of drug in physiologic pH and highest release in acidic pH relevant to cancer environment.

3. The route of internalization of the NPs *via* clathrin- or caveolin-mediated endocytosis. This could be investigated by using fluorescent NPs and tracking their localization within the endosomes or caveosomes.

4. The cytotoxic effect of the NPs on normal brain cells after proving cytotoxicity against tumour cells with consideration towards their cellular uptake, cytotoxic mechanism and immunogenicity.

5. The cytotoxic and immunogenic effects of the NPs on experimental animals as a follow up study to further investigate the safety of the NPs before introducing into clinic. These could involve studies of the thrombogenicity, haemolysis, anaphylaxis, as well as screening of cytokine expression *in vivo*. Imaging of the RES organs is also necessary to determine non-specific accumulation of the NPs.

6. The sterility of the NPs and their lack of endotoxins that can negatively impact the efficacy of the treatments.

REFERENCES

Abedalwafa, M., Wang, F., Wang, L., Li, C., 2013. Biodegradable PCL for tissue engineering applications: A review. Reviews on Advanced Materials Science 34, 123–140.

Abraham, J., Mohammed, A.P., Kumar, M.P.A., George, S.C., Thomas, S., 2018. Thermoanalytical Techniques of Nanomaterials. Characterization of Nanomaterials: Advances and Key Technologies 213–236.

Adabi, Mahdi, Naghibzadeh, M., Adabi, Mohsen, Zarrinfard, M.A., Esnaashari, S.S., Seifalian, A.M., Faridi-Majidi, R., Tanimowo Aiyelabegan, H., Ghanbari, H., 2017. Biocompatibility and nanostructured materials: applications in nanomedicine. Artificial Cells, Nanomedicine and Biotechnology 45, 833–842.

Agarwal, R., Singh, V., Jurney, P., Shi, L., Sreenivasan, S. V., Roy, K., 2013. Mammalian cells preferentially internalize hydrogel nanodiscs over nanorods and use shape-specific uptake mechanisms. Proc Natl Acad Sci U S A 110, 17247–17252.

Ahn, H.K., Jung, M., Sym, S.J., Shin, D.B., Kang, S.M., Kyung, S.Y., Park, J.W., Jeong, S.H., Cho, E.K., 2014. A phase II trial of Cremorphor EL-free paclitaxel (Genexol-PM) and gemcitabine in patients with advanced non-small cell lung cancer. Cancer Chemotherapy and Pharmacology 74, 277–282.

Ajiboye, A.L., Trivedi, V., Mitchell, J.C., 2018. Preparation of polycaprolactone nanoparticles via supercritical carbon dioxide extraction of emulsions. Drug Delivery and Translational Research 8, 1790–1796.

Albanese, A., Tang, P.S., Chan, W.C.W., 2012a. The effect of nanoparticle size, shape, and surface chemistry on biological systems. Annual Review of Biomedical Engineering 14, 1–16.

Albanese, A., Tang, P.S., Chan, W.C.W., 2012b. The effect of nanoparticle size, shape, and surface chemistry on biological systems. Annual Review of Biomedical Engineering 14, 1–16.

Alexandrakis, G., Brown, E.B., Tong, R.T., McKee, T.D., Campbell, R.B., Boucher, Y., Jain, R.K., 2004. Two-photon fluorescence correlation microscopy reveals the two-phase nature of transport in tumors. Nature Medicine 10, 203–207.

Alexis, F., Pridgen, E., Molnar, L.K., Farokhzad, O.C., 2008a. Factors affecting the clearance and biodistribution of polymeric nanoparticles. Molecular Pharmaceutics 5, 505–515.

Alexis, F., Pridgen, E., Molnar, L.K., Farokhzad, O.C., 2008b. Factors affecting the clearance and biodistribution of polymeric nanoparticles. Molecular Pharmaceutics 5, 505–515.

Al-Kaysi, R.O., Müller, A.M., Ahn, T.S., Lee, S., Bardeen, C.J., 2005. Effects of sonication on the size and crystallinity of stable zwitterionic organic nanoparticles formed by reprecipitation in water. Langmuir 21, 7990–7994.

Allard, E., Jarnet, D., Vessières, A., Vinchon-Petit, S., Jaouen, G., Benoit, J.P., Passirani, C., 2010. Local delivery of ferrociphenol lipid nanocapsules followed by external radiotherapy as a synergistic treatment against intracranial 9L glioma xenograft. Pharmaceutical Research 27, 56–64.

Allémann, E., Gurny, R., Doelker, E., 1992. Preparation of aqueous polymeric nanodispersions by a reversible salting-out process: influence of process parameters on particle size. International Journal of Pharmaceutics 87, 247–253.

Allen, C., Maysinger, D., Eisenberg, A., 1999. Nano-engineering block copolymer aggregates for drug delivery. Colloids and Surfaces B: Biointerfaces 16, 3–27.

Aller, S.G., Yu, J., Ward, A., Weng, Y., Chittaboina, S., Zhuo, R., Harrell, P.M., Trinh, Y.T., Zhang, Q., Urbatsch, I.L., Chang, G., 2009. Structure of P-glycoprotein reveals a molecular basis for poly-specific drug binding. Science (1979) 323, 1718–1722.

Allotey-Babington, G.L., Nettey, H., D'Sa, S., Braz Gomes, K., D'Souza, M.J., 2018. Cancer chemotherapy: Effect of poloxamer modified nanoparticles on cellular function. Journal of Drug Delivery Science and Technology 47, 181–192.

Alsaffar, H., Martino, N., Garrett, J.P., Adam, A.P., 2020. Interleukin-6 promotes a sustained loss of endothelial barrier function via janus kinase-mediated STAT3 phosphorylation and de novo protein synthesis. American Journal of Physiology - Cell Physiology 314, C589–C602.

Andrade, F., Almeida, A., Rafael, D., Schwartz, S., Sarmento, B., 2018. Micellar-Based Nanoparticles for Cancer Therapy and Bioimaging. Springer.

Angell, C.A., 1988. Structural instability and relaxation in liquid and glassy phases near the fragile liquid limit. Journal of Non-Crystalline Solids 102, 205–221.

Anselmo, A.C., Mitragotri, S., 2019. Nanoparticles in the clinic: An update. Bioengineering & Translational Medicine 4, 10–29.

Arbab-Zavar, M.H., Chamsaz, M., Youssefi, A., Aliakbari, M., 2012. Multivariate optimization on flow-injection electrochemical hydride generation atomic absorption spectrometry of cadmium. Talanta 97, 229–234.

Arends, M.J., Wyllie, A.H., 1991. Apoptosis: Mechanisms and Roles in Pathology. International Review of Experimental Pathology 32, 223–254.

Ariano, P., Zamburlin, P., Gilardino, A., Mortera, R., Onida, B., Tomatis, M., Ghiazza, M., Fubini, B., Lovisolo, D., 2011. Interaction of spherical silica nanoparticles with neuronal cells: Size-dependent toxicity and perturbation of calcium homeostasis. Small 7, 766–774.

Arica, B., Lamprecht, A., 2005. In vitro evaluation of betamethasone-loaded nanoparticles. Drug Development and Industrial Pharmacy 31, 19–24.

Ashby, L.S., Smith, K.A., Stea, B., 2016. Gliadel wafer implantation combined with standard radiotherapy and concurrent followed by adjuvant temozolomide for treatment of newly diagnosed high-grade glioma: A systematic literature review. World Journal of Surgical Oncology 14, 1–15.

Autio, K.A., Dreicer, R., Anderson, J., Garcia, J.A., Alva, A., Hart, L.L., Milowsky, M.I., Posadas, E.M., Ryan, C.J., Graf, R.P., Dittamore, R., Schreiber, N.A., Summa, J.M., Youssoufian, H., Morris, M.J., Scher, H.I., 2018. Safety and Efficacy of BIND-014, a Docetaxel Nanoparticle Targeting Prostate-Specific Membrane Antigen for Patients with Metastatic Castration-Resistant Prostate Cancer: A Phase 2 Clinical Trial. JAMA Oncology 4, 1344–1351.

Aydin, O., Aydin, B., Tezcaner, A., Keskin, D., 2015. Study on physiochemical structure and in vitro release behaviors of doxycycline-loaded PCL microspheres. Journal of Applied Polymer Science 132.

Azadi, A., Rouini, M.R., Hamidi, M., 2015. Neuropharmacokinetic evaluation of methotrexate-loaded chitosan nanogels. International Journal of Biological Macromolecules 79, 326–335.

Baishya, H., 2017. Application of Mathematical Models in Drug Release Kinetics of Carbidopa and Levodopa ER Tablets. Journal of Developing Drugs 06.

Balmayor, E.R., Tuzlakoglu, K., Azevedo, H.S., Reis, R.L., 2009. Preparation and characterization of starch-poly-ε-caprolactone microparticles incorporating bioactive agents for drug delivery and tissue engineering applications. Acta Biomaterialia 5, 1035–1045.

Balu, R., Sampath Kumar, T.S., Ramalingam, M., Ramakrishna, S., 2011. Electrospun polycaprolactone/Poly(1,4-butylene adipate-co-polycaprolactam) blends: Potential biodegradable scaffold for bone tissue regeneration. Journal of Biomaterials and Tissue Engineering 1, 30–39.

Bannunah, A.M., Vllasaliu, D., Lord, J., Stolnik, S., 2014. Mechanisms of nanoparticle internalization and transport across an intestinal epithelial cell model: Effect of size and surface charge. Molecular Pharmaceutics 11, 4363–4373.

Barani, I.J., Larson, D.A., 2015. Radiation Therapy of Glioblastoma BT - Current Understanding and Treatment of Gliomas. Springer.

Barenholz, Y., 2012. Doxil®--the first FDA-approved nano-drug: lessons learned. J Control Release 160, 117–134.

Bartlett, D.W., Su, H., Hildebrandt, I.J., Weber, W.A., Davis, M.E., 2007. Impact of tumor-specific targeting on the biodistribution and efficacy of siRNA nanoparticles measured by multimodality in vivo imaging. Proc Natl Acad Sci U S A 104, 15549–15554.

Batchelor, T.T., Sorensen, A.G., di Tomaso, E., Zhang, W.T., Duda, D.G.G., Cohen, K.S., Kozak, K.R., Cahill, D.P., Chen, P.J., Zhu, M., Ancukiewicz, M., Mrugala, M.M., Plotkin, S., Drappatz, J., Louis, D.N., Ivy, P., Scadden, D.T.T., Benner, T., Loeffler, J.S., Wen, P.Y., Jain, R.K., 2007. AZD2171, a Pan-VEGF Receptor Tyrosine Kinase Inhibitor, Normalizes Tumor Vasculature and Alleviates Edema in Glioblastoma Patients. Cancer Cell 11, 83–95.

Batrakova, E. v., Gendelman, H.E., Kabanov, A. v., 2011. Cell-mediated drug delivery. Expert Opinion on Drug Delivery 8, 415–433.

Bauer, A.T., Strozyk, E.A., Gorzelanny, C., Westerhausen, C., Desch, A., Schneider, M.F., Schneider, S.W., 2011. Cytotoxicity of silica nanoparticles through exocytosis of von Willebrand factor and necrotic cell death in primary human endothelial cells. Biomaterials 32, 8385–8393.

Béduneau, A., Saulnier, P., Benoit, J.P., 2007. Active targeting of brain tumors using nanocarriers. Biomaterials.

Behzadi, S., Serpooshan, V., Tao, W., Hamaly, M.A., Alkawareek, M.Y., Dreaden, E.C., Brown, D., Alkilany, A.M., Farokhzad, O.C., Mahmoudi, M., 2017. Cellular uptake of nanoparticles: Journey inside the cell. Chemical Society Reviews 46, 4218–4244.

Bellavance, M.A., Blanchette, M., Fortin, D., 2008. Recent advances in blood-brain barrier disruption as a CNS delivery strategy. AAPS Journal 10, 166–177.

Bennewitz, M.F., Saltzman, W.M., 2009. Nanotechnology for Delivery of Drugs to the Brain for Epilepsy. Neurotherapeutics 6, 323–336.

Berkland, C., Kipper, M.J., Narasimhan, B., Kim, K., Pack, D.W., 2004. Microsphere size, precipitation kinetics and drug distribution control drug release from biodegradable polyanhydride microspheres. Journal of Controlled Release 94, 129–141.

Beroske, L., Van den Wyngaert, T., Stroobants, S., Van der Veken, P., Elvas, F., 2021. Molecular imaging of apoptosis: The case of caspase-3 radiotracers. International Journal of Molecular Sciences 22, 3948.

Betz, A.L., Goldstein, G.W., 1986. Specialized properties and solute transport in brain capillaries. Annual Review of Physiology VOL. 48, 241–250.

Bhattarai, S.R., Bhattarai, N., Viswanathamurthi, P., Yi, H.K., Hwang, P.H., Kim, H.Y., 2006. Hydrophilic nanofibrous structure of polylactide; fabrication and cell affinity. Journal of Biomedical Materials Research Part A 78A, 247–257.

Binello, E., Germano, I.M., 2011. Targeting glioma stem cells: A novel framework for brain tumors. Cancer Science.

Blanco, E., Shen, H., Ferrari, M., 2015. Principles of nanoparticle design for overcoming biological barriers to drug delivery. Nature Biotechnology 33, 941–951.

Blasberg, R.G., Patlak, C., Fenstermacher, J.D., 1975. Intrathecal chemotherapy: brain tissue profiles after ventriculo cisternal perfusion. Journal of Pharmacology and Experimental Therapeutics 195, 73–83.

Blasi, P., D'Souza, S.S., Selmin, F., DeLuca, P.P., 2005. Plasticizing effect of water on poly(lactide-co-glycolide). Journal of Controlled Release 108, 1–9.

Boström, M., Williams, D.R.M., Ninham, B.W., 2001. Specific Ion Effects: Why DLVO Theory Fails for Biology and Colloid Systems. Physical Review Letters 87, 168103.

Boucher, Y., Baxter, L.T., Jain, R.K., 1990. Interstitial Pressure Gradients in Tissue-isolated and Subcutaneous Tumors: Implications for Therapy. Cancer Research 50, 4478–4484.

Brash, J.L., 2018. Blood compatibility of nanomaterials. Drug Delivery Nanosystems for Biomedical Applications 13–31.

Bray, D., Levin, M.D., Morton-Firth, C.J., 1998. Receptor clustering as a cellular mechanism to control sensitivity. Nature 393, 85–88.

Bregoli, L., Movia, D., Gavigan-Imedio, J.D., Lysaght, J., Reynolds, J., Prina-Mello, A., 2016. Nanomedicine applied to translational oncology: A future perspective on cancer treatment. Nanomedicine: Nanotechnology, Biology, and Medicine 12, 81–103.

Brem, H., Ewend, M.G., Piantadosi, S., Greenhoot, J., Burger, P.C., Sisti, M., 1995. The safety of interstitial chemotherapy with BCNU-loaded polymer followed by radiation therapy in the treatment of newly diagnosed malignant gliomas: Phase I trial. Journal of Neuro-Oncology 26, 111–123.

Budhian, A., Siegel, S.J., Winey, K.I., 2007. Haloperidol-loaded PLGA nanoparticles: Systematic study of particle size and drug content. International Journal of Pharmaceutics 336, 367–375.

Busquets, M.A., Espargaro, A., Sabaté, R., Estelrich, J., 2015. Magnetic nanoparticles cross the blood-brain barrier: When physics rises to a challenge. Nanomaterials 5, 2231–2248.

Cabral, H., Matsumoto, Y., Mizuno, K., Chen, Q., Murakami, M., Kimura, M., Terada, Y., Kano, M.R., Miyazono, K., Uesaka, M., Nishiyama, N., Kataoka, K., 2011. Accumulation of sub-100 nm polymeric micelles in poorly permeable tumours depends on size. Nature Nanotechnology 6, 815–823.

Cairncross, G., Wang, M., Shaw, E., Jenkins, R., Brachman, D., Buckner, J., Fink, K., Souhami, L., Laperriere, N., Curran, W., Mehta, M., 2013. Phase III trial of chemoradiotherapy for anaplastic oligodendroglioma: Long-term results of RTOG 9402. Journal of Clinical Oncology 31, 337–343.

Callewaert, M., Dukic, S., Van Gulick, L., Vittier, M., Gafa, V., Andry, M.C., Molinari, M., Roullin, V.G., 2013. Etoposide encapsulation in surface-modified poly(lactide-co-glycolide) nanoparticles strongly enhances glioma antitumor efficiency. J Biomed Mater Res A 101, 1319–1327.

Calvo, P., Gouritin, B., Chacun, H., Desmaile, D., D'Angelo, J., Noel, J.P., Georgin, D., Fattal, E., Andreux, J.P., Couvreur, P., 2001. Long-circulating pegylated polycyanoacrylate nanoparticles as new drug carrier for brain delivery. Pharmaceutical Research 18, 1157–1166.

Calzolari, A., Larocca, L.M., Deaglio, S., Finisguerra, V., Boe, A., Raggi, C., Ricci-Vitani, L., Pierconti, F., Malavasi, F., de Maria, R., Testa, U., Pallini, R., 2010. Transferrin receptor 2 is frequently and highly expressed in glioblastomas. Translational Oncology 3, 123–134.

Carnevale, J., Ko, A.H., 2016. MM-398 (nanoliposomal irinotecan): Emergence of a novel therapy for the treatment of advanced pancreatic cancer. Future Oncology 12, 453–464.

Carril, M., Padro, D., del Pino, P., Carrillo-Carrion, C., Gallego, M., Parak, W.J., 2017. In situ detection of the protein corona in complex environments. Nature Communications 2017 8:1 8, 1–5.

Cartiera, M.S., Johnson, K.M., Rajendran, V., Caplan, M.J., Saltzman, W.M., 2009. The uptake and intracellular fate of PLGA nanoparticles in epithelial cells. Biomaterials 30, 2790–2798.

Casadó, A., Giuffrida, M.C., Sagristá, M.L., Castelli, F., Pujol, M., Alsina, M.A., Mora, M., 2016. Langmuir monolayers and Differential Scanning Calorimetry for the study of the interactions between camptothecin drugs and biomembrane models. Biochimica et Biophysica Acta - Biomembranes 1858, 422–433.

Cedervall, T., Lynch, I., Lindman, S., Berggård, T., Thulin, E., Nilsson, H., Dawson, K.A., Linse, S., 2007. Understanding the nanoparticle-protein corona using methods to quntify exchange rates and affinities of proteins for nanoparticles. Proc Natl Acad Sci U S A 104, 2050–2055.

Ceschel, G.C., Badiello, R., Ronchi, C., Maffei, P., 2003. Degradation of components in drug formulations: a comparison between HPLC and DSC methods. Journal of Pharmaceutical and Biomedical Analysis 32, 1067–1072.

Chakraborty, C., Sharma, A.R., Sharma, G., Doss, C.G.P., Lee, S.S., 2017. Therapeutic miRNA and siRNA: Moving from Bench to Clinic as Next Generation Medicine. Molecular Therapy - Nucleic Acids 8, 132–143.

Champion, J.A., Katare, Y.K., Mitragotri, S., 2007. Particle shape: A new design parameter for micro- and nanoscale drug delivery carriers. Journal of Controlled Release 121, 3–9.

Chandana, S.R., Movva, S., Arora, M., Singh, T., 2008. Primary brain tumors in adults. American Family Physician 77, 1423–1430.

Chang, J., Jallouli, Y., Kroubi, M., Yuan, X. bo, Feng, W., Kang, C. sheng, Pu, P. yu, Betbeder, D., 2009. Characterization of endocytosis of transferrin-coated PLGA nanoparticles by the blood-brain barrier. International Journal of Pharmaceutics 379, 285–292.

Chang, J.E., Khuntia, D., Robins, H.I., Mehta, M.P., 2007. Radiotherapy and radiosensitizers in the treatment of glioblastoma multiforme. Clinical Advances in Hematology and Oncology 5, 894–915.

Chang, L., Deng, L., Wang, W., Lv, Z., Hu, F., Dong, A., Zhang, J., 2012. Poly(ethyleneglycol)-b-Poly(ε-caprolactone-co-γ-hydroxyl-ε- caprolactone) bearing pendant hydroxyl groups as nanocarriers for doxorubicin delivery. Biomacromolecules 13, 3301–3310.

Chang, T.C., Shiah, H.S., Yang, C.H., Yeh, K.H., Cheng, A.L., Shen, B.N., Wang, Y.W., Yeh, C.G., Chiang, N.J., Chang, J.Y., Chen, L.T., 2015. Phase i study of nanoliposomal irinotecan

(PEP02) in advanced solid tumor patients. Cancer Chemotherapy and Pharmacology 75, 579–586.
Chapman, C.D., Frey, W.H., Craft, S., Danielyan, L., Hallschmid, M., Schiöth, H.B., Benedict, C., 2013. Intranasal treatment of central nervous system dysfunction in humans. Pharmaceutical Research 30, 2475–2484.
Charalambous, C., Hofman, F.M., Chen, T.C., 2005. Functional and phenotypic differences between glioblastoma multiforme-derived and normal human brain endothelial cells. Journal of Neurosurgery 102, 699–705.
Chen, G., Zhang, X., Yang, F., Mu, L., 2010. Disposition of nanoparticle-based delivery system via inner ear administration. Curr Drug Metab 11, 886–897.
Chen, L.Q., Fang, L., Ling, J., Ding, C.Z., Kang, B., Huang, C.Z., 2015. Nanotoxicity of silver nanoparticles to red blood cells: Size dependent adsorption, uptake, and hemolytic activity. Chemical Research in Toxicology 28, 501–509.
Chen, Y., Liu, L., 2012. Modern methods for delivery of drugs across the blood-brain barrier. Advanced Drug Delivery Reviews 64, 640–665.
Cho, E.C., Zhang, Q., Xia, Y., 2011. The effect of sedimentation and diffusion on cellular uptake of gold nanoparticles. Nature Nanotechnology 6, 385–391.
Choi, S.H., Park, T.G., 2002. Synthesis and characterization of elastic PLGA/PCL/PLGA tri-block copolymers. Journal of Biomaterials Science, Polymer Edition 13, 1163–1173.
Chorny, M., Fishbein, I., Danenberg, H.D., Golomb, G., 2002. Lipophilic drug loaded nanospheres prepared by nanoprecipitation: Effect of formulation variables on size, drug recovery and release kinetics. Journal of Controlled Release 83, 389–400.
ÇIFTÇI, H., TÜRK, M., Tamer, U., Karahan, S., Menemen, Y., 2013. Silver nanoparticles: Cytotoxic, apoptotic, and necrotic effects on MCF-7 cells. Turkish Journal of Biology 37, 573–581.
Cohen, S.S., Min, M., Cummings, E.E., Chen, X., Sadowska, G.B., Sharma, S., Stonestreet, B.S., 2013. Effects of Interleukin-6 on the Expression of Tight Junction Proteins in Isolated Cerebral Microvessels from Yearling and Adult Sheep. Neuroimmunomodulation 20, 264–273.
Coombes, A.G.A., Yeh, M.K., Lavelle, E.C., Davis, S.S., 1998. The control of protein release from poly(DL-lactide co-glycolide) microparticles by variation of the external aqueous phase surfactant in the water-in oil-in water method. Journal of Controlled Release 52, 311–320.
Cornago, M., Garcia-Alberich, C., Blasco-Angulo, N., Vall-llaura, N., Nager, M., Herreros, J., Comella, J.X., Sanchis, D., Llovera, M., 2014. Histone deacetylase inhibitors promote glioma cell death by G2 checkpoint abrogation leading to mitotic catastrophe. Cell Death and Disease 5, 1435.
Crotts, G., Park, T.G., 1998. Protein delivery from poly(lactic-co-glycolic acid) biodegradable microspheres: Release kinetics and stability issues. Journal of Microencapsulation 15, 699–713.
Cui, J.H., Goh, J.S., Park, S.Y., Kim, P.H., Lee, B.J., 2001. Preparation and physical characterization of alginate microparticles using air atomization method. Drug Development and Industrial Pharmacy 27, 309–319.

da Silva, J., Jesus, S., Bernardi, N., Colaço, M., Borges, O., 2019. Poly(D, L-lactic Acid) nanoparticle size reduction increases its immunotoxicity. Frontiers in Bioengineering and Biotechnology 7, 137.

Daneman, R., Prat, A., 2015. The blood–brain barrier. Cold Spring Harbor Perspectives in Biology 7, a020412.

Das Neves, J., Amiji, M., Bahia, M.F., Sarmento, B., 2013. Assessing the physical-chemical properties and stability of dapivirine-loaded polymeric nanoparticles. International Journal of Pharmaceutics 456, 307–314.

Dash, T.K., Konkimalla, V.B., 2012. Polymeric modification and its implication in drug delivery: Poly-ε-caprolactone (PCL) as a model polymer. Molecular Pharmaceutics 9, 2365–2379.

Dass, C.R., Su, T., 2010. Delivery of Lipoplexes for Genotherapy of Solid Tumours: Role of Vascular Endothelial Cells. Journal of Pharmacy and Pharmacology 52, 1301–1317.

Davda, J., Labhasetwar, V., 2002. Characterization of nanoparticle uptake by endothelial cells. International Journal of Pharmaceutics 233, 51–59.

Davis, M.E., 2009. The first targeted delivery of siRNA in humans via a self-assembling, cyclodextrin polymer-based nanoparticle: From concept to clinic. Molecular Pharmaceutics.

Davis, M.E., 2013. Tumor treating fields-an emerging cancer treatment modality. Clinical Journal of Oncology Nursing 17, 441–443.

De Boer, A.G., Breimer, D.D., 1998. Cytokines and blood-brain barrier permeability. Progress in Brain Research 115, 425–451.

De Boer, A.G., Gaillard, P.J., 2007. Strategies to improve drug delivery across the blood-brain barrier. Clin Pharmacokinet 46, 553–576.

De Jong, W.H., Borm, P.J.A., 2008. Drug delivery and nanoparticles: Applications and hazards. International Journal of Nanomedicine 3, 133–149.

de la Harpe, K.M., Kondiah, P.P.D., Choonara, Y.E., Marimuthu, T., du Toit, L.C., Pillay, V., 2019. The Hemocompatibility of Nanoparticles: A Review of Cell-Nanoparticle Interactions and Hemostasis. Cells 8.

De Stefano, D., Carnuccio, R., Maiuri, M.C., 2012. Nanomaterials Toxicity and Cell Death Modalities. Journal of Drug Delivery 2012, 1–14.

Dean, M., Fojo, T., Bates, S., 2005. Tumour stem cells and drug resistance. Nature Reviews Cancer 5, 275–284.

Demeule, M., Currie, J.C., Bertrand, Y., Ché, C., Nguyen, T., Régina, A., Gabathuler, R., Castaigne, J.P., Béliveau, R., 2008a. Involvement of the low-density lipoprotein receptor-related protein in the transcytosis of the brain delivery vector Angiopep-2. Journal of Neurochemistry 106, 1534–1544.

Demeule, M., Regina, A., Ché, C., Poirier, J., Nguyen, T., Gabathuler, R., Castaigne, J.P., Béliveau, R., 2008b. Identification and design of peptides as a new drug delivery system for the brain. Journal of Pharmacology and Experimental Therapeutics 324, 1064–1072.

Denecker, G., Vercammen, D., Steemans, M., Vanden Berghe, T., Brouckaert, G., Van Loo, G., Zhivotovsky, B., Fiers, W., Grooten, J., Declercq, W., Vandenabeele, P., 2001. Death receptor-induced apoptotic and necrotic cell death: Differential role of caspases and mitochondria. Cell Death and Differentiation 8, 829–840.

Desai, K.G.H., Olsen, K.F., Mallery, S.R., Stoner, G.D., Schwendeman, S.P., 2010. Formulation and In Vitro-In Vivo Evaluation of Black Raspberry Extract-Loaded PLGA/PLA Injectable

Millicylindrical Implants for Sustained Delivery of Chemopreventive Anthocyanins. Pharmaceutical Research 2010 27:4 27, 628–643.

Desai, T.R., Leeper, N.J., Hynes, K.L., Gewertz, B.L., 2002. Interleukin-6 causes endothelial barrier dysfunction via the protein kinase C pathway. Journal of Surgical Research 104, 118–123.

Dhami, N.K., Pandey, R.S., Jain, U.K., Chandra, R., Madan, J., 2014. Non-aggregated protamine-coated poly(lactide-co-glycolide) nanoparticles of cisplatin crossed blood-brain barrier, enhanced drug delivery and improved therapeutic index in glioblastoma cells: In vitro studies. Journal of Microencapsulation 31, 685–693.

Dimchevska, S., Geskovski, N., Petruševski, G., Chacorovska, M., Popeski-Dimovski, R., Ugarkovic, S., Goracinova, K., 2017a. SN-38 loading capacity of hydrophobic polymer blend nanoparticles: formulation, optimization and efficacy evaluation. Drug Development and Industrial Pharmacy 43, 502–510.

Dimchevska, S., Geskovski, N., Petruševski, G., Popeski-dimovski, R., Ugarkovic, S., Dimchevska, S., Geskovski, N., Petruševski, G., Popeski-dimovski, R., Ugarkovic, S., Goracinova, K., Ugarkovic, S., Goracinova, K., 2017b. SN-38 loading capacity of hydrophobic polymer blend nanoparticles : formulation , optimization and efficacy evaluation 9045.

Dobrovolskaia, M.A., Aggarwal, P., Hall, J.B., McNeil, S.E., 2008. Preclinical studies to understand nanoparticle interaction with the immune system and its potential effects on nanoparticle biodistribution. Molecular Pharmaceutics 5, 487–495.

Dolecek, T.A., Propp, J.M., Stroup, N.E., Kruchko, C., 2012. CBTRUS statistical report: Primary brain and central nervous system tumors diagnosed in the United States in 2005-2009. Neuro-Oncology.

Dong, X., Mattingly, C.A., Tseng, M.T., Cho, M.J., Liu, Y., Adams, V.R., Mumper, R.J., 2009. Doxorubicin and paclitaxel-loaded lipid-based nanoparticles overcome multidrug resistance by inhibiting P-glycoprotein and depleting ATP. Cancer Research 69, 3918–3926.

Dos Reis, L.G., Lee, W.H., Svolos, M., Moir, L.M., Jaber, R., Windhab, N., Young, P.M., Traini, D., 2019. Nanotoxicologic effects of PLGA nanoparticles formulated with a cell-penetrating peptide: Searching for a safe pDNA delivery system for the lungs. Pharmaceutics 11.

Douglas, P., Albadarin, A.B., Sajjia, M., Mangwandi, C., Kuhs, M., Collins, M.N., Walker, G.M., 2016. Effect of poly ethylene glycol on the mechanical and thermal properties of bioactive poly(ε-caprolactone) melt extrudates for pharmaceutical applications. International Journal of Pharmaceutics 500, 179–186.

Downs, M.E., Buch, A., Karakatsani, M.E., Konofagou, E.E., Ferrera, V.P., 2015. Blood-Brain Barrier Opening in Behaving Non-Human Primates via Focused Ultrasound with Systemically Administered Microbubbles. Scientific Reports 5, 15076.

Drummond, D.C., Meyer, O., Hong, K., Kirpotin, D.B., Papahadjopoulos, D., 1999. Optimizing liposomes for delivery of chemotherapeutic agents to solid tumors. Pharmacological Reviews 51, 691–743.

Duan, X., Li, Y., 2013. Physicochemical characteristics of nanoparticles affect circulation, biodistribution, cellular internalization, and trafficking. Small 9, 1521–1532.

Dubois, L.G., Campanati, L., Righy, C., D'Andrea-Meira, I., e Spohr, T.C.L. de S., Porto-Carreiro, I., Pereira, C.M., Balça-Silva, J., Kahn, S.A., DosSantos, M.F., Oliveira, M. de A.R., Ximenes-da-Silva, A., Lopes, M.C., Faveret, E., Gasparetto, E.L., Moura-Neto, V., 2014. Gliomas and the vascular fragility of the blood brain barrier. Frontiers in Cellular Neuroscience 8.

Ebewele, R.O., Raton, B., York, N., 2000. POLYMER SCIENCE AND TECHNOLOGY.

Ebrahimnejad, P., Dinarvand, R., Sajadi, S.A., Atyabi, F., Ramezani, F., Jaafari, M.R., 2009. Preparation and characterization of poly lactide-co-glycolide nanoparticles of SN-38. PDA Journal of Pharmaceutical Science and Technology 63, 512–520.

Edwards, S.A., Williams, D.R.M., 2004. Double Layers and Interparticle Forces in Colloid Science and Biology: Analytic Results for the Effect of Ionic Dispersion Forces. Physical Review Letters 92, 248303.

Ehrlich, M., Boll, W., Van Oijen, A., Hariharan, R., Chandran, K., Nibert, M.L., Kirchhausen, T., 2004. Endocytosis by random initiation and stabilization of clathrin-coated pits. Cell 118, 591–605.

Elliott, M.R., Ravichandran, K.S., 2016. The Dynamics of Apoptotic Cell Clearance. Developmental Cell 38, 147–160.

Ellor, S. V., Pagano-Young, T.A., Avgeropoulos, N.G., 2014. Glioblastoma: Background, standard treatment paradigms, and supportive care considerations. Journal of Law, Medicine and Ethics 42, 171–182.

Esmaeili, F., Ghahremani, M.H., Esmaeili, B., Khoshayand, M.R., Atyabi, F., Dinarvand, R., 2008. PLGA nanoparticles of different surface properties: Preparation and evaluation of their body distribution. International Journal of Pharmaceutics 349, 249–255.

Fadul, C., Wood, J., Thaler, H., Galicich, J., Patterson, R.H., Posner, J.B., 1988. Morbidity and mortality of craniotomy for excision of supratentorial gliomas. Neurology 38, 1374–1379.

Fakheri, F., Alam, A.S., 2016. Application of Box Behnken Experimental Design to Analysis Reaction Conversion of n-Butyl Acetate to n-Butanol. Journal of Advanced Chemical Engineering 4.

Ferrari, M., 2010. Frontiers in cancer nanomedicine: Directing mass transport through biological barriers. Trends in Biotechnology 28, 181–188.

Fink, S.L., Cookson, B.T., 2005. Apoptosis, pyroptosis, and necrosis: Mechanistic description of dead and dying eukaryotic cells. Infection and Immunity 73, 1907–1916.

Fischer, U., Meese, E., 2007. Glioblastoma multiforme: The role of DSB repair between genotype and phenotype. Oncogene 26, 7809–7815.

Fletcher, J.I., Haber, M., Henderson, M.J., Norris, M.D., 2010. ABC transporters in cancer: More than just drug efflux pumps. Nature Reviews Cancer 10, 147–156.

Florence, A.T., Whitehill, D., 1982. The formulation and stability of multiple emulsions. International Journal of Pharmaceutics 11, 277–308.

Foldbjerg, R., Olesen, P., Hougaard, M., Dang, D.A., Hoffmann, H.J., Autrup, H., 2009. PVP-coated silver nanoparticles and silver ions induce reactive oxygen species, apoptosis and necrosis in THP-1 monocytes. Toxicology Letters 190, 156–162.

Foroozandeh, P., Aziz, A.A., 2018. Insight into Cellular Uptake and Intracellular Trafficking of Nanoparticles. Nanoscale Research Letters 13, 1–12.

Fourniols, T., Randolph, L.D., Staub, A., Vanvarenberg, K., Leprince, J.G., Préat, V., Des Rieux, A., Danhier, F., 2015. Temozolomide-loaded photopolymerizable PEG-DMA-based hydrogel for the treatment of glioblastoma. Journal of Controlled Release 210, 95–104.

Francia, V., Aliyandi, A., Salvati, A., 2018. Effect of the development of a cell barrier on nanoparticle uptake in endothelial cells. Nanoscale 10, 16645–16656.
Frauwirth, K.A., Thompson, C.B., 2002. Activation and inhibition of lymphocytes by costimulation. Journal of Clinical Investigation 109, 295–299.
Fredenberg, S., Wahlgren, M., Reslow, M., Axelsson, A., 2011. The mechanisms of drug release in poly(lactic-co-glycolic acid)-based drug delivery systems - A review. International Journal of Pharmaceutics 415, 34–52.
Friedman, H.S., Kerby, T., Calvert, H., 2000. Temozolomide and treatment of malignant glioma. Clinical Cancer Research 6, 2585–2597.
Fu, Y., Kao, W.J., 2010a. Drug release kinetics and transport mechanisms of non-degradable and degradable polymeric delivery systems. Expert Opinion on Drug Delivery 7, 429–444.
Fu, Y., Kao, W.J., 2010b. Drug release kinetics and transport mechanisms of non-degradable and degradable polymeric delivery systems. http://dx.doi.org/10.1517/17425241003602259 7, 429–444.
Fulda, S., Debatin, K.M., 2006. Extrinsic versus intrinsic apoptosis pathways in anticancer chemotherapy. Oncogene 25, 4798–4811.
Fung, L.K., Ewend, M.G., Sills, A., Sipos, E.P., Thompson, R., Watts, M., Colvin, O.M., Brem, H., Saltzman, W.M., 1998. Pharmacokinetics of interstitial delivery of carmustine, 4-hydroperoxycyclophosphamide, and paclitaxel from a biodegradable polymer implant in the monkey brain. Cancer Research 58, 672–684.
Gagliardi, A., Bonacci, S., Paolino, D., Celia, C., Procopio, A., Fresta, M., Cosco, D., 2019. Paclitaxel-loaded sodium deoxycholate-stabilized zein nanoparticles: characterization and in vitro cytotoxicity. Heliyon 5.
Gal, N., Massalha, S., Samuelly-Nafta, O., Weihs, D., 2015. Effects of particle uptake, encapsulation, and localization in cancer cells on intracellular applications. Medical Engineering and Physics 37, 478–483.
Galvão, R.P., Zong, H., 2013. Inflammation and Gliomagenesis: Bi-Directional Communication at Early and Late Stages of Tumor Progression. Current Pathobiology Reports 1, 19–28.
Ganipineni, L.P., Ucakar, B., Joudiou, N., Riva, R., Jérôme, C., Gallez, B., Danhier, F., Préat, V., 2019. Paclitaxel-loaded multifunctional nanoparticles for the targeted treatment of glioblastoma. Journal of Drug Targeting 27, 614–623.
Gao, C., Pan, J., Lu, W., Zhang, M., Zhou, L., Tian, J., 2009. In-vitro evaluation of paclitaxel-loaded MPEG-PLGA nanoparticles on laryngeal cancer cells. Anti-Cancer Drugs 20, 807–814.
Gao, H., Zhang, S., Cao, S., Yang, Z., Pang, Z., Jiang, X., 2014. Angiopep-2 and activatable cell-penetrating peptide dual-functionalized nanoparticles for systemic glioma-targeting delivery. Mol Pharm 11, 2755–2763.
Gao, X., Tao, W., Lu, W., Zhang, Q., Zhang, Y., Jiang, X., Fu, S., 2006. Lectin-conjugated PEG-PLA nanoparticles: Preparation and brain delivery after intranasal administration. Biomaterials 27, 3482–3490.
Gao, Y., Zuo, J., Bou-Chacra, N., Pinto, T.D.J.A., Clas, S.D., Walker, R.B., Löbenberg, R., 2013. In vitro release kinetics of antituberculosis drugs from nanoparticles assessed using a modified dissolution apparatus. BioMed Research International 2013.

Garcia-Garcia, E., Andrieux, K., Gil, S., Couvreur, P., 2005. Colloidal carriers and blood-brain barrier (BBB) translocation: A way to deliver drugs to the brain? International Journal of Pharmaceutics 298, 274–292.

Gaumet, M., Vargas, A., Gurny, R., Delie, F., 2008. Nanoparticles for drug delivery: The need for precision in reporting particle size parameters. European Journal of Pharmaceutics and Biopharmaceutics 69, 1–9.

Gelperina, S., Maksimenko, O., Khalansky, A., Vanchugova, L., Shipulo, E., Abbasova, K., Berdiev, R., Wohlfart, S., Chepurnova, N., Kreuter, J., 2010. Drug delivery to the brain using surfactant-coated poly(lactide-co-glycolide) nanoparticles: influence of the formulation parameters. European journal of pharmaceutics and biopharmaceutics : official journal of Arbeitsgemeinschaft fur Pharmazeutische Verfahrenstechnik e.V 74, 157–163.

Georgieva, J. v., Hoekstra, D., Zuhorn, I.S., 2014. Smuggling drugs into the brain: An overview of ligands targeting transcytosis for drug delivery across the blood–brain barrier. Pharmaceutics 6, 557–583.

Giddings, S.J., Chirgwin, J., Permutt, M.A., 1985. Evaluation of rat insulin messenger RNA in pancreatic and extrapancreatic tissues. Diabetologia 28, 343–347.

Gill, P., Moghadam, T.T., Ranjbar, B., 2010. Differential Scanning Calorimetry Techniques: Applications in Biology and Nanoscience. Journal of Biomolecular Techniques : JBT 21, 167.

Giri, T.K., Choudhary, C., Ajazuddin, Alexander, A., Badwaik, H., Tripathi, D.K., 2013. Prospects of pharmaceuticals and biopharmaceuticals loaded microparticles prepared by double emulsion technique for controlled delivery. Saudi Pharmaceutical Journal 21, 125–141.

Giri, V., Kanodia, S., Giri, O., Sumit, K., 2015. Anti-nicotine vaccine: current status. International Journal of Basic and Clinical Pharmacology 1309–1313.

Glaser, T., Weller, M., 2001. Caspase-dependent chemotherapy-induced death of glioma cells requires mitochondrial cytochrome c release. Biochemical and Biophysical Research Communications 281, 322–327.

Gokce, Y., Cengiz, B., Yildiz, N., Calimli, A., Aktas, Z., 2014. Ultrasonication of chitosan nanoparticle suspension: Influence on particle size. Colloids and Surfaces A: Physicochemical and Engineering Aspects 462, 75–81.

Golden, P.L., Maccagnan, T.J., Pardridge, W.M., 1997. Human blood-brain barrier leptin receptor. Binding and endocytosis in isolated human brain microvessels. Journal of Clinical Investigation 99, 14–18.

Gómez-Gaete, C., Tsapis, N., Besnard, M., Bochot, A., Fattal, E., 2007. Encapsulation of dexamethasone into biodegradable polymeric nanoparticles. Int J Pharm 331, 153–159.

Görlich, D., Kutay, U., 1999. Transport between the cell nucleus and the cytoplasm. Annual Review of Cell and Developmental Biology 15, 607–660.

Gottesman, M.M., Fojo, T., Bates, S.E., 2002. Multidrug resistance in cancer: Role of ATP-dependent transporters. Nature Reviews Cancer 2, 48–58.

Govender, T., Stolnik, S., Garnett, M.C., Illum, L., Davis, S.S., 1999. PLGA nanoparticles prepared by nanoprecipitation: Drug loading and release studies of a water soluble drug. Journal of Controlled Release 57, 171–185.

Grabowski, N., Hillaireau, H., Vergnaud-Gauduchon, J., Nicolas, V., Tsapis, N., Kerdine-Römer, S., Fattal, E., 2016. Surface-modified biodegradable nanoparticles' impact on cytotoxicity

and inflammation response on a co-culture of lung epithelial cells and human-like macrophages. Journal of Biomedical Nanotechnology 12, 135–146.
Grassi, M., Grassi, G., 2005. Mathematical Modelling and Controlled Drug Delivery: Matrix Systems. Current Drug Delivery 2, 97–116.
Gritsenko, P.G., Ilina, O., Friedl, P., 2012. Interstitial guidance of cancer invasion. Journal of Pathology 226, 185–199.
Gromnicova, R., Kaya, M., Romero, I.A., Williams, P., Satchell, S., Sharrack, B., Male, D., 2016. Transport of gold nanoparticles by vascular endothelium from different human tissues. PLoS ONE 11, e0161610.
Groopman, J.E., Itri, L.M., 1999. Chemotherapy-induced anemia in adults: Incidence and treatment. J Natl Cancer Inst 91, 1616–1634.
Gryparis, E.C., Mattheolabakis, G., Bikiaris, D., Avgoustakis, K., 2007. Effect of conditions of preparation on the size and encapsulation properties of PLGA-mPEG nanoparticles of cisplatin. Drug Delivery 14, 371–380.
Gu, F., Zhang, L., Teply, B.A., Mann, N., Wang, A., Radovic-Moreno, A.F., Langer, R., Farokhzad, O.C., 2008. Precise engineering of targeted nanoparticles by using self-assembled biointegrated block copolymers. Proc Natl Acad Sci U S A 105, 2586–2591.
Guterres, S.S., Weiss, V., De Lucca Freitas, L., Pohlmann, A.R., 2000. Influence of benzyl benzoate as oil core on the physicochemical properties of spray-dried powders from polymeric nanocapsules containing indomethacin. Drug Delivery: Journal of Delivery and Targeting of Therapeutic Agents 7, 195–199.
Habgood, M.D., Begley, D.J., Abbott, N.J., 2000. Determinants of passive drug entry into the central nervous system. Cellular and Molecular Neurobiology 20, 231–253.
Hadjidemetriou, M., Al-Ahmady, Z., Mazza, M., Collins, R.F., Dawson, K., Kostarelos, K., 2015. In Vivo Biomolecule Corona around Blood-Circulating, Clinically Used and Antibody-Targeted Lipid Bilayer Nanoscale Vesicles. ACS Nano 9, 8142–8156.
Halder, A., Maiti, S., Sa, B., 2005. Entrapment efficiency and release characteristics of polyethyleneimine- treated or -untreated calcium alginate beads loaded with propranolol-resin complex. International Journal of Pharmaceutics 302, 84–94.
Han, S., Liu, Y., Nie, X., Xu, Q., Jiao, F., Li, W., Zhao, Y., Wu, Y., Chen, C., 2012. Efficient delivery of antitumor drug to the nuclei of tumor cells by amphiphilic biodegradable poly(L - Aspartic Acid-co-Lactic Acid)/DPPE co-polymer nanoparticles. Small 8, 1596–1606.
Hanurry, E.Y., Mekonnen, T.W., Andrgie, A.T., Darge, H.F., Birhan, Y.S., Hsu, W.H., Chou, H.Y., Cheng, C.C., Lai, J.Y., Tsai, H.C., 2020. Biotin-decorated PAMAM g4.5 dendrimer nanoparticles to enhance the delivery, anti-proliferative, and apoptotic effects of chemotherapeutic drug in cancer cells. Pharmaceutics 12.
Haque, S., Md, S., Alam, M.I., Sahni, J.K., Ali, J., Baboota, S., 2012. Nanostructure-based drug delivery systems for brain targeting. Drug Development and Industrial Pharmacy 38, 387–411.
Hart, M.G., Garside, R., Rogers, G., Somerville, M., Stein, K., Grant, R., 2011. Chemotherapy wafers for high grade glioma. Cochrane Database of Systematic Reviews.
Hart, M.G., Garside, R., Rogers, G., Stein, K., Grant, R., 2013. Temozolomide for high grade glioma. Cochrane Database of Systematic Reviews 2013.
Hawkins, B.T., Davis, T.P., 2005a. The blood-brain barrier/neurovascular unit in health and disease. Pharmacological Reviews 57, 173–185.

Hawkins, B.T., Davis, T.P., 2005b. The blood-brain barrier/neurovascular unit in health and disease. Pharmacological Reviews 57, 173–185.

Heesters, M.A.A.M., Wijrdeman, H.K., Struikmans, H., Witkamp, T., Moerland, M.A., 1993. Brain tumor delineation based on CT and MR imaging. Implications for radiotherapy treatment planning. Strahlentherapie und Onkologie.

Hekmatara, T., Bernreuther, C., Khalansky, A.S., Thiesen, A., Weissenberger, J., Matschke, J., Gelperina, S., Kreuter, J., Glatzel, M., 2009. Efficient systemic therapy of rat glioblastoma by nanoparticle-bound doxorubicin is due to antiangiogenic effects. Clinical Neuropathology 28, 153–164.

Hentschel, S.J., Sawaya, R., 2003. Optimizing outcomes with maximal surgical resection of malignant gliomas. Cancer Control 10, 109–114.

Hermanson, G.T., 2013. Bioconjugate Techniques: Third Edition. Bioconjugate Techniques: Third Edition 1–1146.

Hervé, F., Ghinea, N., Scherrmann, J.M., 2008. CNS delivery via adsorptive transcytosis. AAPS Journal 10, 455–472.

Hess, K.R., 1999. Extent of resection as a prognostic variable in the treatment of gliomas. Journal of Neuro-Oncology 42, 227–231.

Hoki, Y., Fujimori, A., Pommier, Y., 1997. Differential cytotoxicity of clinically important camptothecin derivatives in P-glycoprotein-overexpressing cell lines. Cancer Chemotherapy and Pharmacology 40, 433–438.

Holmes, D., 2013. The next big things are tiny. The Lancet Neurology 12, 31.

Ho-Lun, W., Bendayan, R., Rauth, A.M., Hui, Y.X., Babakhanian, K., Xiao, Y.W., 2006. A mechanistic study of enhanced doxorubicin uptake and retention in multidrug resistant breast cancer cells using a polymer-lipid hybrid nanoparticle system. Journal of Pharmacology and Experimental Therapeutics 317, 1372–1381.

Honary, S., Zahir, F., 2013. Effect of zeta potential on the properties of nano-drug delivery systems - A review (Part 2). Tropical Journal of Pharmaceutical Research 12, 265–273.

Hong, S., Leroueil, P.R., Janus, E.K., Peters, J.L., Kober, M.M., Islam, M.T., Orr, B.G., Baker, J.R., Banaszak Holl, M.M., 2006. Interaction of polycationic polymers with supported lipid bilayers and cells: Nanoscale hole formation and enhanced membrane permeability. Bioconjugate Chemistry 17, 728–734.

Hsiang, Y.H., Hertzberg, R., Hecht, S., Liu, L.F., 1985. Camptothecin induces protein-linked DNA breaks via mammalian DNA topoisomerase I, Journal of Biological Chemistry.

Huang, C.F., Yao, G.H., Liang, R.P., Qiu, J.D., 2013. Graphene oxide and dextran capped gold nanoparticles based surface plasmon resonance sensor for sensitive detection of concanavalin A. Biosensors and Bioelectronics 50, 305–310.

Huang, R., Ke, W., Han, L., Liu, Y., Shao, K., Ye, L., Lou, J., Jiang, C., Pei, Y., 2009. Brain-targeting mechanisms of lactoferrin-modified DNA-loaded nanoparticles. Journal of Cerebral Blood Flow and Metabolism 29, 1914–1923.

Hunter, C.A., Jones, S.A., 2015. IL-6 as a keystone cytokine in health and disease. Nature Immunology 16, 448–457.

Huynh, N.T., Morille, M., Bejaud, J., Legras, P., Vessieres, A., Jaouen, G., Benoit, J.P., Passirani, C., 2011. Treatment of 9L gliosarcoma in rats by ferrociphenol-loaded lipid nanocapsules based on a passive targeting strategy via the EPR effect. Pharmaceutical Research 28, 3189–3198.

Huynh, N.T., Passirani, C., Allard-Vannier, E., Lemaire, L., Roux, J., Garcion, E., Vessieres, A., Benoit, J.P., 2012. Administration-dependent efficacy of ferrociphenol lipid nanocapsules for the treatment of intracranial 9L rat gliosarcoma. International Journal of Pharmaceutics 423, 55–62.

Iacob, G., Dinca, E.B., 2009. Current data and strategy in glioblastoma multiforme. J Med Life.

Ishiwata, H., Suzuki, N., Ando, S., Kikuchi, H., Kitagawa, T., 2000. Characteristics and biodistribution of cationic liposomes and their DNA complexes. Journal of Controlled Release 69, 139–148.

Itoh, N., Santa, T., Kato, M., 2015. Rapid evaluation of the quantity of drugs encapsulated within nanoparticles by high-performance liquid chromatography in a monolithic silica column. Analytical and Bioanalytical Chemistry 407, 6429–6434.

Jain, Atul, Jain, Ashay, Garg, N.K., Tyagi, R.K., Singh, B., Katare, O.P., Webster, T.J., Soni, V., 2015. Surface engineered polymeric nanocarriers mediate the delivery of transferrin-methotrexate conjugates for an improved understanding of brain cancer. Acta Biomaterialia 24, 140–151.

Jain, D.S., Athawale, R.B., Bajaj, A.N., Shrikhande, S.S., Goel, P.N., Nikam, Y., Gude, R.P., 2014. Unraveling the cytotoxic potential of Temozolomide loaded into PLGA nanoparticles. DARU, Journal of Pharmaceutical Sciences 22, 18.

Jain, K.K., 2012. Nanobiotechnology-based strategies for crossing the blood-brain barrier. Nanomedicine 7, 1225–1233.

Jain, R.K., 2005. Normalization of tumor vasculature: An emerging concept in antiangiogenic therapy. Science (1979) 307, 58–62.

Jain, S., Mishra, V., Singh, P., Dubey, P.K., Saraf, D.K., Vyas, S.P., 2003. RGD-anchored magnetic liposomes for monocytes/neutrophils-mediated brain targeting. International Journal of Pharmaceutics 261, 43–55.

Jeong, J.-C., Lee, J., Cho, K., 2003. Effects of crystalline microstructure on drug release behavior of poly(epsilon-caprolactone) microspheres. J Control Release 92, 249–58.

Jevševar, S., Kunstelj, M., Porekar, V.G., 2010. PEGylation of therapeutic proteins. Biotechnology Journal 5, 113–128.

Jiang, W., Huang, Y., An, Y., Kim, B.Y.S., 2015. Remodeling Tumor Vasculature to Enhance Delivery of Intermediate-Sized Nanoparticles. ACS Nano 9, 8689–8696.

Jue, J.L., Wang, W., Dicker, D.T., El-Deiry, W.S., 2005. Bioluminescent imaging of TRAIL-induced apoptosis through detection of caspase activation following cleavage of DEVD-aminoluciferin. Cancer Biology and Therapy 4.

Kaasalainen, M., Aseyev, V., von Haartman, E., Karaman, D.Ş., Mäkilä, E., Tenhu, H., Rosenholm, J., Salonen, J., 2017. Size, Stability, and Porosity of Mesoporous Nanoparticles Characterized with Light Scattering. Nanoscale Research Letters 12.

Kamaly, N., Xiao, Z., Valencia, P.M., Radovic-Moreno, A.F., Farokhzad, O.C., 2012. Targeted polymeric therapeutic nanoparticles: Design, development and clinical translation. Chemical Society Reviews 41, 2971–3010.

Kamaly, N., Yameen, B., Wu, J., Farokhzad, O.C., 2016. Degradable Controlled-Release Polymers and Polymeric Nanoparticles: Mechanisms of Controlling Drug Release. Chemical Reviews 116, 2602–2663.

Kang, J., Schwendeman, S.P., 2007. Pore closing and opening in biodegradable polymers and their effect on the controlled release of proteins. Molecular Pharmaceutics 4, 104–118.

Kastin, A.J., Pan, W., Maness, L.M., Banks, W.A., 1999. Peptides crossing the blood-brain barrier: Some unusual observations. Brain Research 848, 96–100.

Kaufmann, J.K., Chiocca, E.A., 2014. Glioma virus therapies between bench and bedside. Neuro-Oncology 16, 334–351.

Ke, X., Ng, V.W.L., Ono, R.J., Chan, J.M.W., Krishnamurthy, S., Wang, Y., Hedrick, J.L., Yang, Y.Y., 2014. Role of non-covalent and covalent interactions in cargo loading capacity and stability of polymeric micelles. Journal of Controlled Release 193, 9–26.

Kelkar, S.S., Reineke, T.M., 2011. Theranostics: Combining imaging and therapy. Bioconjugate Chemistry 22, 1879–1903.

Khajeh, M., Ghanbari, M., 2011. Optimization of Microwave-Assisted Extraction Procedure to Determine Metal in Fish Muscles Using Box-Behnken Design. Food Analytical Methods 4, 431–436.

Khayata, N., Abdelwahed, W., Chehna, M.F., Charcosset, C., Fessi, H., 2012. Preparation of vitamin e loaded nanocapsules by the nanoprecipitation method: From laboratory scale to large scale using a membrane contactor. International Journal of Pharmaceutics 423, 419–427.

Kim, T.Y., Kim, D.W., Chung, J.Y., Shin, S.G., Kim, S.C., Heo, D.S., Kim, N.K., Bang, Y.J., 2004. Phase I and pharmacokinetic study of Genexol-PM, a Cremophor-free, polymeric micelle-formulated paclitaxel, in patients with advanced malignancies. Clinical Cancer Research 10, 3708–3716.

Kirpotin, D.B., Drummond, D.C., Shao, Y., Shalaby, M.R., Hong, K., Nielsen, U.B., Marks, J.D., Benz, C.C., Park, J.W., 2006. Antibody targeting of long-circulating lipidic nanoparticles does not increase tumor localization but does increase internalization in animal models. Cancer Research 66, 6732–6740.

Kirtane, A.R., Abouzid, O., Minahan, D., Bensel, T., Hill, A.L., Selinger, C., Bershteyn, A., Craig, M., Mo, S.S., Mazdiyasni, H., Cleveland, C., Rogner, J., Lee, Y.A.L., Booth, L., Javid, F., Wu, S.J., Grant, T., Bellinger, A.M., Nikolic, B., Hayward, A., Wood, L., Eckhoff, P.A., Nowak, M.A., Langer, R., Traverso, G., 2018. Development of an oral once-weekly drug delivery system for HIV antiretroviral therapy. Nature Communications 9, 1–12.

Kittur, F.S., Harish Prashanth, K. V., Udaya Sankar, K., Tharanathan, R.N., 2002. Characterization of chitin, chitosan and their carboxymethyl derivatives by differential scanning calorimetry. Carbohydrate Polymers 49, 185–193.

Kniesel, U., Wolburg, H., 2000. Tight junctions of the blood-brain barrier. Cellular and Molecular Neurobiology 20, 57–76.

Koffie, R.M., Farrar, C.T., Saidi, L.J., William, C.M., Hyman, B.T., Spires-Jones, T.L., 2011. Nanoparticles enhance brain delivery of blood-brain barrier-impermeable probes for in vivo optical and magnetic resonance imaging. Proc Natl Acad Sci U S A 108, 18837–18842.

Koleske, J.V., 1978. Blends Containing Poly(ε-caprolactone) and Related Polymers. Polymer Blends 369–389.

Koo, B.K., Lim, H.S., Song, R., Yoon, M.J., Yoon, K.J., Moon, J.S., Kim, Y.W., Kwon, M.C., Yoo, K.W., Kong, M.P., Lee, J., Chitnis, A.B., Kim, C.H., Kong, Y.Y., 2005. Mind bomb 1 is essential for generating functional Notch ligands to activate Notch. Development 132, 3459–3470.

Koo, Y.E.L., Reddy, G.R., Bhojani, M., Schneider, R., Philbert, M.A., Rehemtulla, A., Ross, B.D., Kopelman, R., 2006. Brain cancer diagnosis and therapy with nanoplatforms. Advanced Drug Delivery Reviews 58, 1556–1577.

Körber, M., 2010. PLGA Erosion: Solubility- or Diffusion-Controlled? Pharmaceutical Research 2010 27:11 27, 2414–2420.

Korsmeyer, R.W., Gurny, R., Doelker, E., Buri, P., Peppas, N.A., 1983. Mechanisms of solute release from porous hydrophilic polymers. International Journal of Pharmaceutics 15, 25–35.

Kostaras, X., Cusano, F., Kline, G.A., Roa, W., Easaw, J., 2014. Use of dexamethasone in patients with high-grade glioma: A clinical practice guideline. Current Oncology 21, 493–503.

Kowalski, P.S., Lintermans, L.L., Morselt, H.W.M., Leus, N.G.J., Ruiters, M.H.J., Molema, G., Kamps, J.A.A.M., 2013. Anti-VCAM-1 and anti-E-selectin SAINT-O-somes for selective delivery of siRNA into inflammation-activated primary endothelial cells. Molecular Pharmaceutics 10, 3033–3044.

Koziara, J.M., Lockman, P.R., Allen, D.D., Mumper, R.J., 2004. Paclitaxel nanoparticles for the potential treatment of brain tumors. Journal of Controlled Release 99, 259–269.

Kreuter, J., 1978. Nanoparticles and nanocapsules--new dosage forms in the nanometer size range. Pharmaceutica Acta Helvetiae 53, 33–39.

Kreuter, J., 2001. Nanoparticulate systems for brain delivery of drugs. Adv Drug Deliv Rev 47, 65–81.

Kreuter, J., Alyautdin, R.N., Kharkevich, D.A., Ivanov, A.A., 1995. Passage of peptides through the blood-brain barrier with colloidal polymer particles (nanoparticles). Brain Research 674, 171–174.

Kumar, A., Ahuja, A., Ali, J., Baboota, S., 2016. Curcumin-loaded lipid nanocarrier for improving bioavailability, stability and cytotoxicity against malignant glioma cells. Drug Delivery 23, 214–229.

Kumar, A., Lale, S. V., Naz, F., Choudhary, V., Koul, V., 2015. Synthesis and biological evaluation of dual functionalized glutathione sensitive poly(ester-urethane) multiblock polymeric nanoparticles for cancer targeted drug delivery. Polymer Chemistry 6, 7603–7617.

Kuo, Y.C., Chen, Y.C., 2015. Targeting delivery of etoposide to inhibit the growth of human glioblastoma multiforme using lactoferrin- and folic acid-grafted poly(lactide-co-glycolide) nanoparticles. International Journal of Pharmaceutics 479, 138–149.

Kuskov, A.N., Voskresenskaya, A.A., Goryachaya, A. v., Shtilman, M.I., Spandidos, D.A., Rizos, A.K., Tsatsakis, A.M., 2010. Amphiphilic poly-N-vinylpyrrolidone nanoparticles as carriers for non-steroidal anti-inflammatory drugs: Characterization and in vitro controlled release of indomethacin. International Journal of Molecular Medicine 26, 85–94.

Kwon, D., Lee, S.H., Kim, J., Yoon, T.H., 2010. Dispersion, fractionation and characterization of sub-100nm P25 TiO2 nanoparticles in aqueous media. Toxicology and Environmental Health Sciences 2010 2:1 2, 78–85.

Labhasetwar, V., Song, C., Humphrey, W., Shebuski, R., Levy, R.J., 1998. Arterial uptake of biodegradable nanoparticles: Effect of surface modifications. Journal of Pharmaceutical Sciences 87, 1229–1234.

Laine, A.L., Huynh, N.T., Clavreul, A., Balzeau, J., Béjaud, J., Vessieres, A., Benoit, J.P., Eyer, J., Passirani, C., 2012. Brain tumour targeting strategies via coated ferrociphenol lipid nanocapsules. European Journal of Pharmaceutics and Biopharmaceutics 81, 690–693.

Lamprecht, A., Ubrich, N., Yamamoto, H., Schäfer, U., Takeuchi, H., Lehr, C.M., Maincent, P., Kawashima, Y., 2001. Design of rolipram-loaded nanoparticles: Comparison of two preparation methods. Journal of Controlled Release 71, 297–306.

Lapointe, S., Perry, A., Butowski, N.A., 2018. Primary brain tumours in adults. The Lancet 392, 432–446.

Lee, H.J., Engelhardt, B., Lesley, J., Bickel, U., Pardridge, W.M., 2000. Targeting rat anti-mouse transferrin receptor monoclonal antibodies through blood-brain barrier in mouse. Journal of Pharmacology and Experimental Therapeutics 292, 1048–1052.

Lee, J.E., Kim, M.G., Jang, Y.L., Lee, M.S., Kim, N.W., Yin, Y., Lee, J.H., Lim, S.Y., Park, J.W., Kim, J., Lee, D.S., Kim, S.H., Jeong, J.H., 2018. Self-assembled pegylated albumin nanoparticles (Span) as a platform for cancer chemotherapy and imaging. Drug Delivery 25, 1570–1578.

Lee, S.C., Oh, J.T., Jang, M.H., Chung, S. il, 1999. Quantitative analysis of polyvinyl alcohol on the surface of poly(D,L-lactide-co-glycolide) microparticles prepared by solvent evaporation method: Effect of particle size and PVA concentration. Journal of Controlled Release 59, 123–132.

Leroueil, P.R., Berry, S.A., Duthie, K., Han, G., Rotello, V.M., McNerny, D.Q., Baker, J.R., Orr, B.G., Holl, M.M.B., 2008. Wide varieties of cationic nanoparticles induce defects in supported lipid bilayers. Nano Letters 8, 420–424.

Li, B., Li, Q., Mo, J., Dai, H., 2017. Drug-loaded polymeric nanoparticles for cancer stem cell targeting. Frontiers in Pharmacology 8, 51.

Li, J., Feng, L., Fan, L., Zha, Y., Guo, L., Zhang, Q., Chen, J., Pang, Z., Wang, Y., Jiang, X., Yang, V.C., Wen, L., 2011. Targeting the brain with PEG-PLGA nanoparticles modified with phage-displayed peptides. Biomaterials 32, 4943–4950.

Li, M.K., Fogler, H.S., 1978. Acoustic emulsification. Part 2. Breakup of the large primary oil droplets in a water medium. Journal of Fluid Mechanics 88, 513–528.

Lin, H., Yue, Y., Maidana, D.E., Bouzika, P., Atik, A., Matsumoto, H., Miller, J.W., Vavvas, D.G., 2016. Drug delivery nanoparticles: Toxicity comparison in retinal pigment epithelium and retinal vascular endothelial cells. Seminars in Ophthalmology 31, 1–9.

Lin, H.C., Chuang, C.H., Cheng, M.H., Lin, Y.C., Fang, Y.P., 2019. High potency of SN-38-loaded bovine serum albumin nanoparticles against triple-negative breast cancer. Pharmaceutics 11.

Liu, H., Zhang, M., Dong, X., Liu, Y., Hao, Y., Wang, Y., 2019. Necrostatin-1 protects against ischemia/reperfusion injury by inhibiting receptor-interacting protein 1 in a rat flap model. Journal of Plastic, Reconstructive and Aesthetic Surgery 72, 194–202.

Liu, J., Yu, M., Zhou, C., Yang, S., Ning, X., Zheng, J., 2013. Passive tumor targeting of renal-clearable luminescent gold nanoparticles: Long tumor retention and fast normal tissue clearance. J Am Chem Soc 135, 4978–4981.

Liu, M., Zhang, J., Shan, W., Huang, Y., 2014. Developments of mucus penetrating nanoparticles. Asian Journal of Pharmaceutical Sciences 10, 275–282.

Liu, Q., Li, R., Zhu, Z., Qian, X., Guan, W., Yu, L., Yang, M., Jiang, X., Liu, B., 2012. Enhanced antitumor efficacy, biodistribution and penetration of docetaxel-loaded biodegradable nanoparticles. International Journal of Pharmaceutics 430, 350–358.

Liu, Q., Yu, S., Li, A., Xu, H., Han, X., Wu, K., 2017. Targeting interlukin-6 to relieve immunosuppression in tumor microenvironment. Tumor Biology 39.

Liu, Y., Tan, J., Thomas, A., Ou-Yang, D., Muzykantov, V.R., 2012. The shape of things to come: Importance of design in nanotechnology for drug delivery. Therapeutic Delivery 3, 181–194.

Liu, Z., Robinson, J.T., Tabakman, S.M., Yang, K., Dai, H., 2011. Carbon materials for drug delivery & cancer therapy. Materials Today 14, 316–323.

Lochhead, J.J., Thorne, R.G., 2012. Intranasal delivery of biologics to the central nervous system. Advanced Drug Delivery Reviews 64, 614–628.

Lollo, G., Vincent, M., Ullio-Gamboa, G., Lemaire, L., Franconi, F., Couez, D., Benoit, J.P., 2015. Development of multifunctional lipid nanocapsules for the co-delivery of paclitaxel and CpG-ODN in the treatment of glioblastoma. International Journal of Pharmaceutics 495, 972–980.

Louis, D.N., Perry, A., Reifenberger, G., von Deimling, A., Figarella-Branger, D., Cavenee, W.K., Ohgaki, H., Wiestler, O.D., Kleihues, P., Ellison, D.W., 2016. The 2016 World Health Organization Classification of Tumors of the Central Nervous System: a summary. Acta Neuropathologica.

Loureiro, J.A., Gomes, B., Coelho, M.A.N., do Carmo Pereira, M., Rocha, S., 2014. Targeting nanoparticles across the blood-brain barrier with monoclonal antibodies. Nanomedicine 9, 709–722.

Lovely, M.P., Stewart-Amidei, C., Arzbaecher, J., Bell, S., Maher, M.E., Maida, M., Mogensen, K., Nicolaseau, G., 2014. Care of the adult patient with a brain tumor. Journal of Neuroscience Nursing 46, 367–369.

Lucero-Acuña, A., Gutiérrez-Valenzuela, C.A., Esquivel, R., Guzmán-Zamudio, R., 2019. Mathematical modeling and parametrical analysis of the temperature dependency of control drug release from biodegradable nanoparticles. RSC Advances 9, 8728–8739.

Łukasiewicz, S., Mikołajczyk, A., Błasiak, E., Fic, E., Dziedzicka-Wasylewska, M., 2021. Polycaprolactone Nanoparticles as Promising Candidates for Nanocarriers in Novel Nanomedicines. Pharmaceutics 13, 191.

Ma, L.J., Niu, R., Wu, X., Wu, J., Zhou, E., Xiao, X.P., Chen, J., 2021. Quantitative evaluation of cellular internalization of polymeric nanoparticles within laryngeal cancer cells and immune cells for enhanced drug delivery. Nanoscale Research Letters 16.

Maaz, A., Abdelwahed, W., Tekko, I.A., Trefi, S., 2015. Influence of nanoprecipitation method parameters on nanoparticles loaded with gatifloxacin for ocular drug delivery. IJASR International Journal of Academic Scientific Research 3, 1–12.

MacKenzie, D.J., 1926. A Classification of the Tumours of the Glioma Group on a Histogenetic Basis With a Correlated Study of Prognosis. Canadian Medical Association Journal 16, 872.

Madkour, M., Bumajdad, A., Al-Sagheer, F., 2019. To what extent do polymeric stabilizers affect nanoparticles characteristics? Advances in Colloid and Interface Science 270, 38–53.

Maeda, H., 2015. Toward a full understanding of the EPR effect in primary and metastatic tumors as well as issues related to its heterogeneity. Advanced Drug Delivery Reviews 91, 3–6.

Mahapatro, A., Singh, D.K., 2011. Biodegradable nanoparticles are excellent vehicle for site directed in-vivo delivery of drugs and vaccines. J Nanobiotechnology.

Mahmoud, B.S., Alamri, A.H., McConville, C., 2020. Polymeric Nanoparticles for the Treatment of Malignant Gliomas. Cancers (Basel) 12.

Mahmoud, B.S., McConville, C., 2021. Development and Optimization of Irinotecan-Loaded PCL Nanoparticles and Their Cytotoxicity against Primary High-Grade Glioma Cells. Pharmaceutics 2021, Vol. 13, Page 541 13, 541.

Makadia, H.K., Siegel, S.J., 2011. Poly Lactic-co-Glycolic Acid (PLGA) as Biodegradable Controlled Drug Delivery Carrier. Polymers (Basel) 3, 1377–1397.

Malikmammadov, E., Tanir, T.E., Kiziltay, A., Hasirci, V., Hasirci, N., 2018. PCL and PCL-based materials in biomedical applications. Journal of Biomaterials Science, Polymer Edition 29, 863–893.

Malinovskaya, Y., Melnikov, P., Baklaushev, V., Gabashvili, A., Osipova, N., Mantrov, S., Ermolenko, Y., Maksimenko, O., Gorshkova, M., Balabanyan, V., Kreuter, J., Gelperina, S., 2017. Delivery of doxorubicin-loaded PLGA nanoparticles into U87 human glioblastoma cells. International Journal of Pharmaceutics 524, 77–90.

Mallipeddi, R., Rohan, L.C., 2010. Nanoparticle-based vaginal drug delivery systems for HIV prevention. Expert Opinion on Drug Delivery 7, 37–48.

Mandal, T.K., 1995. The influence of binding solvents on drug release from hydroxypropyl methylcellulose tablets. Drug Development and Industrial Pharmacy 21, 1389–1397.

Mao, S., Shi, Y., Li, L., Xu, J., Schaper, A., Kissel, T., 2008. Effects of process and formulation parameters on characteristics and internal morphology of poly(d,l-lactide-co-glycolide) microspheres formed by the solvent evaporation method. European Journal of Pharmaceutics and Biopharmaceutics 68, 214–223.

Marks, J.A., Wegiel, L.A., Taylor, L.S., Edgar, K.J., 2014. Pairwise polymer blends for oral drug delivery. Journal of Pharmaceutical Sciences 103, 2871–2883.

Maruo, N., Morita, I., Shirao, M., Murota, S.I., 1992. IL-6 increases endothelial permeability in vitro. Endocrinology 131, 710–714.

Mason, T.J., 1996. Advances in bioclimatology. Volume 4, Advances in bioclimatology. Volume 4. Jai Press LTD.

Masood, F., 2016. Polymeric nanoparticles for targeted drug delivery system for cancer therapy. Materials Science and Engineering C.

Masserini, M., 2013. Nanoparticles for Brain Drug Delivery. ISRN Biochemistry 2013, 1–18.

Matsumura, Y., Hamaguchi, T., Ura, T., Muro, K., Yamada, Y., Shimada, Y., Shirao, K., Okusaka, T., Ueno, H., Ikeda, M., Watanabe, N., 2004. Phase I clinical trial and pharmacokinetic evaluation of NK911, a micelle-encapsulated doxorubicin. British Journal of Cancer 91, 1775–1781.

Matus, M.F., Vilos, C., Cisterna, B.A., Fuentes, E., Palomo, I., 2018. Nanotechnology and primary hemostasis: Differential effects of nanoparticles on platelet responses. Vascular Pharmacology 101, 1–8.

McKee, T.D., Grandi, P., Mok, W., Alexandrakis, G., Insin, N., Zimmer, J.P., Bawendi, M.G., Boucher, Y., Breakefield, X.O., Jain, R.K., 2006. Degradation of fibrillar collagen in a human melanoma xenograft improves the efficacy of an oncolytic herpes simplex virus vector. Cancer Research 66, 2509–2513.

Mei, Q., Luo, P., Zuo, Y., Li, J., Zou, Q., Li, Y., Jiang, D., Wang, Y., 2018a. Formulation and in vitro characterization of rifampicin-loaded porous poly (ε-caprolactone) microspheres for sustained skeletal delivery. Drug Design, Development and Therapy 12, 1533–1544.

Mei, Q., Luo, P., Zuo, Y., Li, J., Zou, Q., Li, Y., Jiang, D., Wang, Y., 2018b. Formulation and in vitro characterization of rifampicin-loaded porous poly (ε-caprolactone) microspheres for sustained skeletal delivery. Drug Design, Development and Therapy 12, 1533–1544.

Mellman, I., 1996. Endocytosis and molecular sorting. Annual Review of Cell and Developmental Biology 12, 575–625.

Menczel, J.D., Prime, R.B., 2008. Thermal Analysis of Polymers: Fundamentals and Applications. Thermal Analysis of Polymers: Fundamentals and Applications 1–688.

Meyers, J.D., Doane, T., Burda, C., Basilion, J.P., 2013. Nanoparticles for imaging and treating brain cancer. Nanomedicine 8, 123–143.

Miele, Evelina, Spinelli, G.P., Miele, Ermanno, Tomao, F., Tomao, S., 2009. Albumin-bound formulation of paclitaxel (Abraxane® ABI-007) in the treatment of breast cancer. International Journal of Nanomedicine 4, 99–105.

Miller, D.S., 2015. Regulation of ABC transporters at the blood-brain barrier. In: Clinical Pharmacology and Therapeutics. Elsevier, pp. 395–403.

Minko, T., Kopečková, P., Kopeček, J., 2001. Preliminary evaluation of caspases-dependent apoptosis signaling pathways of free and HPMA copolymer-bound doxorubicin in human ovarian carcinoma cells. Journal of Controlled Release 71, 227–237.

Minko, T., Kopečková, P., Pozharov, V., Kopeček, J., 1998. HPMA copolymer bound adriamycin overcomes MDR1 gene encoded resistance in a human ovarian carcinoma cell line. Journal of Controlled Release 54, 223–233.

Mirakabad, F.S.T., Nejati-Koshki, K., Akbarzadeh, A., Yamchi, M.R., Milani, M., Zarghami, N., Zeighamian, V., Rahimzadeh, A., Alimohammadi, S., Hanifehpour, Y., Joo, S.W., 2014. PLGA-based nanoparticles as cancer drug delivery systems. Asian Pacific Journal of Cancer Prevention 15, 517–535.

Mo, S., Shao, X., Chen, Y., Cheng, Z., 2016. Increasing entropy for colloidal stabilization. Scientific Reports 2016 6:1 6, 1–7.

Moghimi, Seyed Moein, Hunter, Alan Christy, Moghimi, S Moein, Hunter, A Christy, Murray, J.C., 2001. Long-Circulating and Target-Specific Nanoparticles: Theory to Practice.

Mohammadinejad, R., Moosavi, M.A., Tavakol, S., Vardar, D.Ö., Hosseini, A., Rahmati, M., Dini, L., Hussain, S., Mandegary, A., Klionsky, D.J., 2019. Necrotic, apoptotic and autophagic cell fates triggered by nanoparticles. Autophagy 15, 4–33.

Mohammady, H., Dinarvand, ; Rassoul, Mehdi, ;, Manesh, E., Ebrahimnejad, P., 2016. Encapsulation of irinotecan in polymeric nanoparticles: Characterization, release kinetic and cytotoxicity evaluation. Nanomed. J 3, 159–168.

Moore, D.C., 2016. Drug-induced neutropenia: A focus on rituximab-induced late-onset neutropenia, P and T.

Mora-Huertas, C.E., Fessi, H., Elaissari, A., 2010. Polymer-based nanocapsules for drug delivery. International Journal of Pharmaceutics 385, 113–142.

Morales-Cruz, M., Figueroa, C.M., González-Robles, T., Delgado, Y., Molina, A., Méndez, J., Morales, M., Griebenow, K., 2014. Activation of caspase-dependent apoptosis by intracellular delivery of cytochrome c-based nanoparticles. Journal of Nanobiotechnology 12, 1–11.

Mosallaei, N., Jaafari, M.R., Hanafi-Bojd, M.Y., Golmohammadzadeh, S., Malaekeh-Nikouei, B., 2013. Docetaxel-loaded solid lipid nanoparticles: Preparation, characterization, in vitro, and in vivo evaluations. Journal of Pharmaceutical Sciences 102, 1994–2004.

Mutsaers, S.E., Papadimitriou, J.M., 1988. Surface charge of macrophages and their interaction with charged particles. Journal of Leukocyte Biology 44, 17–26.

Nandhakumar, S., Dhanaraju, M.D., Sundar, V.D., Heera, B., 2017. Influence of surface charge on the in vitro protein adsorption and cell cytotoxicity of paclitaxel loaded poly(ε-caprolactone) nanoparticles. Bulletin of Faculty of Pharmacy, Cairo University 55, 249–258.

Nel, A., Xia, T., Mädler, L., Li, N., 2006. Toxic potential of materials at the nanolevel. Science (1979) 311, 622–627.

Nicholson, J.W., 2006. The chemistry of polymers 177.

Niwa, T., Takeuchi, H., Hino, T., Kunou, N., Kawashima, Y., 1993. Preparations of biodegradable nanospheres of water-soluble and insoluble drugs with D,L-lactide/glycolide copolymer by a novel spontaneous emulsification solvent diffusion method, and the drug release behavior. Journal of Controlled Release 25, 89–98.

Niwa, T., Takeuchi, H., Hino, T., Kunou, N., Kawashima, Y., 1994. In vitro drug release behavior of D, L-lactide/glycolide copolymer (PLGA) nanospheres with nafarelin acetate prepared by a novel spontaneous emulsification solvent diffusion method. Journal of Pharmaceutical Sciences 83, 727–732.

Nobs, L., Buchegger, F., Gurny, R., Allémann, E., 2004. Current methods for attaching targeting ligands to liposomes and nanoparticles. Journal of Pharmaceutical Sciences 93, 1980–1992.

Noma, H., Funatsu, H., Mimura, T., 2012. Vascular endothelial growth factor and interleukin-6 are correlated with serous retinal detachment in central retinal vein occlusion. Current Eye Research 37, 62–67.

Norden, A.D., Wen, P.Y., 2006. Glioma therapy in adults. Neurologist 12, 279–292.

Öcal, H., Arica-Yegin, B., Vural, I., Goracinova, K., Çaliş, S., 2014. 5-Fluorouracil-loaded PLA/PLGA PEG-PPG-PEG polymeric nanoparticles: Formulation, in vitro characterization and cell culture studies. Drug Development and Industrial Pharmacy 40, 560–567.

Omarch, G., Kippie, Y., Mentor, S., Ebrahim, N., Fisher, D., Murilla, G., Swai, H., Dube, A., 2019. Comparative in vitro transportation of pentamidine across the blood-brain barrier using polycaprolactone nanoparticles and phosphatidylcholine liposomes. Artificial Cells, Nanomedicine and Biotechnology 47, 1428–1436.

Omuro, A., DeAngelis, L.M., 2013. Glioblastoma and other malignant gliomas: A clinical review. JAMA - Journal of the American Medical Association 310, 1842–1850.

On, N., Miller, D., 2014. Transporter-Based Delivery of Anticancer Drugs to the Brain: Improving Brain Penetration by Minimizing Drug Efflux at the Blood-Brain Barrier. Current Pharmaceutical Design 20, 1499–1509.

Onyema, H.N., Berger, M., Musyanovych, A., Bantz, C., Maskos, M., Freese, C., 2021. Uptake of polymeric nanoparticles in a human induced pluripotent stem cell-based blood–brain barrier model: Impact of size, material, and protein corona. Biointerphases 16, 021004.

Ortiz, R., Prados, J., Melguizo, C., Arias, J.L., Adolfina Ruiz, M., Álvarez, P.J., Caba, O., Luque, R., Segura, A., Aránega, A., 2012. 5-fluorouracil-loaded poly(ε-caprolactone) nanoparticles combined with phage E gene therapy as a new strategy against colon cancer. International Journal of Nanomedicine 7, 95–107.

Ostrom, Q.T., Gittleman, H., Fulop, J., Liu, M., Blanda, R., Kromer, C., Wolinsky, Y., Kruchko, C., Barnholtz-Sloan, J.S., 2015. CBTRUS statistical Report: primary brain and central nervous

system tumors diagnosed in the United States in 2008-2012. Neuro-Oncology 17, iv1–iv62.
Ostrom, Q.T., Gittleman, H., Liao, P., Rouse, C., Chen, Y., Dowling, J., Wolinsky, Y., Kruchko, C., Barnholtz-Sloan, J., 2014. CBTRUS statistical report: Primary brain and central nervous system tumors diagnosed in the United States in 2007–2011. Neuro-Oncology 16, iv1–iv63.
Othman, R., Vladisavljević, G.T., Nagy, Z.K., Holdich, R.G., 2016. Encapsulation and Controlled Release of Rapamycin from Polycaprolactone Nanoparticles Prepared by Membrane Micromixing Combined with Antisolvent Precipitation. Langmuir 32, 10685–10693.
Ou, L., Song, B., Liang, H., Liu, J., Feng, X., Deng, B., Sun, T., Shao, L., 2016. Toxicity of graphene-family nanoparticles: A general review of the origins and mechanisms. Particle and Fibre Toxicology 13, 1–24.
Owens, D.E., Peppas, N.A., 2006. Opsonization, biodistribution, and pharmacokinetics of polymeric nanoparticles. Int J Pharm 307, 93–102.
Padanilam, B.J., 2003. Cell death induced by acute renal injury: A perspective on the contributions of apoptosis and necrosis. American Journal of Physiology - Renal Physiology 284.
Pal, T., Paul, S., Sa, B., 2011. Polymethylmethacrylate Coated Alginate Matrix Microcapsules for Controlled Release of Diclofenac Sodium. Pharmacology & Pharmacy 02, 56–66.
Panyam, J., Zhou, W., Prabha, S., Sahoo, S.K., Labhasetwar, V., 2002. Rapid endo-lysosomal escape of poly(DL-lactide- co glycolide) nanoparticles: implications for drug and gene delivery . The FASEB Journal 16, 1217–1226.
Parikh, V., Gumaste, S.G., Phadke, S., 2018. Effect of the Interaction Between an Ionic Surfactant and Polymer on the Dissolution of a Poorly Soluble Drug. AAPS PharmSciTech 19, 3040–3047.
Park, J.H., Lee, S., Kim, J.H., Park, K., Kim, K., Kwon, I.C., 2008. Polymeric nanomedicine for cancer therapy. Progress in Polymer Science (Oxford) 33, 113–137.
Parrish, K.E., Cen, L., Murray, J., Calligaris, D., Kizilbash, S., Mittapalli, R.K., Carlson, B.L., Schroeder, M.A., Sludden, J., Boddy, A. V., Agar, N.Y.R., Curtin, N.J., Elmquist, W.F., Sarkaria, J.N., 2015. Efficacy of PARP inhibitor rucaparib in orthotopic glioblastoma xenografts is limited by ineffective drug penetration into the central nervous system. Molecular Cancer Therapeutics 14, 2735–2743.
Pasi, F., Facoetti, A., Nano, R., 2010. IL-8 and IL-6 bystander signalling in human glioblastoma cells exposed to gamma radiation. Anticancer Research 30, 2769–2772.
Paul, D.R., 1995. Polymer-polymer interactions 67, 977–984.
Paw, I., Carpenter, R.C., Watabe, K., Debinski, W., Lo, H.W., 2015. Mechanisms regulating glioma invasion. Cancer Letters 362, 1–7.
Pawlik, J., Łukowicz, K., Cholewa-Kowalska, K., Osyczka, A.M., 2019. New insights into the PLGA and PCL blending: physico-mechanical properties and cell response. Materials Research Express 6, 085344.
Pearson, R.M., Juettner, V. V., Hong, S., 2014. Biomolecular corona on nanoparticles: a survey of recent literature and its implications in targeted drug delivery. Frontiers in Chemistry 0, 108.
Peer, D., Karp, J.M., Hong, S., Farokhzad, O.C., Margalit, R., Langer, R., 2007. Nanocarriers as an emerging platform for cancer therapy. Nature Nanotechnology.

Peetla, C., Vijayaraghavalu, S., Labhasetwar, V., 2013. Biophysics of cell membrane lipids in cancer drug resistance: Implications for drug transport and drug delivery with nanoparticles. Advanced Drug Delivery Reviews 65, 1686–1698.

Peterson, D.R., 2012. Blood–Brain Barrier. eLS.

Peterson, D.R., Hawkins, R.A., 2003. Transport studies using membrane vesicles. Methods Mol Med 89, 233–247.

Petri, B., Bootz, A., Khalansky, A., Hekmatara, T., Müller, R., Uhl, R., Kreuter, J., Gelperina, S., 2007. Chemotherapy of brain tumour using doxorubicin bound to surfactant-coated poly(butyl cyanoacrylate) nanoparticles: Revisiting the role of surfactants. Journal of Controlled Release 117, 51–58.

Petros, R.A., Desimone, J.M., 2010. Strategies in the design of nanoparticles for therapeutic applications. Nature Reviews Drug Discovery 9, 615–627.

Petty, M.A., Lo, E.H., 2002. Junctional complexes of the blood-brain barrier: Permeability changes in neuroinflammation. Progress in Neurobiology 68, 311–323.

Phillips, H.S., Kharbanda, S., Chen, R., Forrest, W.F., Soriano, R.H., Wu, T.D., Misra, A., Nigro, J.M., Colman, H., Soroceanu, L., Williams, P.M., Modrusan, Z., Feuerstein, B.G., Aldape, K., 2006. Molecular subclasses of high-grade glioma predict prognosis, delineate a pattern of disease progression, and resemble stages in neurogenesis. Cancer Cell 9, 157–173.

Pinto Reis, C., Neufeld, R.J., Ribeiro, A.J., Veiga, F., 2006. Nanoencapsulation I. Methods for preparation of drug-loaded polymeric nanoparticles. Nanomedicine 2, 8–21.

Pistel, K.F., Kissel, T., 2000. Effects of salt addition on the microencapsulation of proteins using W/O/W double emulsion technique. Journal of Microencapsulation 17, 467–483.

Pluen, A., Boucher, Y., Ramanujan, S., McKee, T.D., Gohongi, T., Di Tomaso, E., Brown, E.B., Izumi, Y., Campbell, R.B., Berk, D.A., Jain, R.K., 2001. Role of tumor-host interactions in interstitial diffusion of macromolecules: Cranial vs. subcutaneous tumors. Proc Natl Acad Sci U S A 98, 4628–4633.

Pollauf, E.J., Pack, D.W., 2006. Use of thermodynamic parameters for design of double-walled microsphere fabrication methods. Biomaterials 27, 2898–2906.

Proskuryakov, S.Y., Konoplyannikov, A.G., Gabai, V.L., 2003. Necrosis: A specific form of programmed cell death? Experimental Cell Research 283, 1–16.

Qin, J., Chen, D.W., Hu, H., Cui, Q., Qiao, M.X., Chen, B., 2007. Surface modification of RGD-liposomes for selective drug delivery to monocytes/neutrophils in brain. Chemical and Pharmaceutical Bulletin 55, 1192–1197.

Rabanel, J.M., Aoun, V., Elkin, I., Mokhtar, M., Hildgen, P., 2012. Drug-Loaded Nanocarriers: Passive Targeting and Crossing of Biological Barriers, Current Medicinal Chemistry.

Rajinikanth, P.S., Sankar, C., Mishra, B., 2003. Sodium alginate microspheres of metoprolol tartrate for intranasal systemic delivery: Development and evaluation. Drug Delivery: Journal of Delivery and Targeting of Therapeutic Agents 10, 21–28.

Ramalho, M.J., Loureiro, J.A., Coelho, M.A.N., Pereira, M.C., 2019. Factorial design as a tool for the optimization of plga nanoparticles for the co-delivery of temozolomide and o6-benzylguanine. Pharmaceutics 11.

Ramalho, M.J., Sevin, E., Gosselet, F., Lima, J., Coelho, M.A.N., Loureiro, J.A., Pereira, M.C., 2018. Receptor-mediated PLGA nanoparticles for glioblastoma multiforme treatment. International Journal of Pharmaceutics 545, 84–92.

Ravi, P.R., Vats, R., Dalal, V., Gadekar, N., Aditya, N., 2015. Design, optimization and evaluation of poly-ε-caprolactone (PCL) based polymeric nanoparticles for oral delivery of lopinavir. Drug Development and Industrial Pharmacy 41, 131–140.

Re, F., Gregori, M., Masserini, M., 2012. Nanotechnology for neurodegenerative disorders. Nanomedicine: Nanotechnology, Biology, and Medicine 8, S51–S58.

Rege, B.D., Kao, J.P.Y., Polli, J.E., 2002. Effects of nonionic surfactants on membrane transporters in Caco-2 cell monolayers. Eur J Pharm Sci 16, 237–246.

Retamal Marín, R.R., Babick, F., Lindner, G.G., Wiemann, M., Stintz, M., 2018. Effects of sample preparation on particle size distributions of different types of silica in suspensions. Nanomaterials.

Rodier, F., Coppé, J.P., Patil, C.K., Hoeijmakers, W.A.M., Muñoz, D.P., Raza, S.R., Freund, A., Campeau, E., Davalos, A.R., Campisi, J., 2009. Persistent DNA damage signalling triggers senescence-associated inflammatory cytokine secretion. Nature Cell Biology 11, 973–979.

Rodrigueza, W. V., Haydn Pritchard, P., Hope, M.J., 1993. The influence of size and composition on the cholesterol mobilizing properties of liposomes in vivo. BBA - Biomembranes 1153, 9–19.

Rolhion, C., Penault-Llorca, F., Kémény, J.L., Lemaire, J.J., Jullien, C., Labit-Bouvier, C., Finat-Duclos, F., Verrelle, P., 2001. Interleukin-6 overexpression as a marker of malignancy in human gliomas. Journal of Neurosurgery 94, 97–101.

Ruggiero, A., Villa, C.H., Bander, E., Rey, D.A., Bergkvist, M., Batt, C.A., Manova-Todorova, K., Deen, W.M., Scheinberg, D.A., McDevitt, M.R., 2010. Paradoxical glomerular filtration of carbon nanotubes. Proc Natl Acad Sci U S A 107, 12369–12374.

Sadat, S.M.A., Jahan, S.T., Haddadi, A., 2016. Effects of Size and Surface Charge of Polymeric Nanoparticles on <i>in Vitro</i> and <i>in Vivo</i> Applications. Journal of Biomaterials and Nanobiotechnology 07, 91–108.

Sah, H.K., Toddywala, R., Chien, Y.W., 1995. Biodegradable microcapsules prepared by a W/O/W technique: Effects of shear force to make a primary w/o emulsion on their morphology and protein release. Journal of Microencapsulation 12, 59–69.

Sahin, A., Esendagli, G., Yerlikaya, F., Caban-Toktas, S., Yoyen-Ermis, D., Horzum, U., Aktas, Y., Khan, M., Couvreur, P., Capan, Y., 2017. A small variation in average particle size of PLGA nanoparticles prepared by nanoprecipitation leads to considerable change in nanoparticles' characteristics and efficacy of intracellular delivery. Artificial Cells, Nanomedicine and Biotechnology 45, 1657–1664.

Salame, P.H., Pawade, V.B., Bhanvase, B.A., 2018. Characterization Tools and Techniques for Nanomaterials. Nanomaterials for Green Energy 83–111.

Saltiel, C., Chen, Q., Manickavasagam, S., Schadler, L.S., Siegel, R.W., Menguc, M.P., 2004. Identification of the dispersion behavior of surface treated nanoscale powders. Journal of Nanoparticle Research 6, 35–46.

Salvati, A., Pitek, A.S., Monopoli, M.P., Prapainop, K., Bombelli, F.B., Hristov, D.R., Kelly, P.M., Åberg, C., Mahon, E., Dawson, K.A., 2013. Transferrin-functionalized nanoparticles lose their targeting capabilities when a biomolecule corona adsorbs on the surface. Nature Nanotechnology 8, 137–143.

Sanna, V., Roggio, A.M., Posadino, A.M., Cossu, A., Marceddu, S., Mariani, A., Alzari, V., Uzzau, S., Pintus, G., Sechi, M., 2011. Novel docetaxel-loaded nanoparticles based on

poly(lactide-co-caprolactone) and poly(lactide-co-glycolide-co-caprolactone) for prostate cancer treatment: Formulation, characterization, and cytotoxicity studies. Nanoscale Research Letters 6, 260.

Saraiva, C., Praça, C., Ferreira, R., Santos, T., Ferreira, L., Bernardino, L., 2016. Nanoparticle-mediated brain drug delivery: Overcoming blood-brain barrier to treat neurodegenerative diseases. Journal of Controlled Release 235, 34–47.

Saran, R., Robinson, B., Abbott, K.C., Agodoa, L.Y.C., Bragg-Gresham, J., Balkrishnan, R., Dietrich, X., Eckard, A., Eggers, P.W., Gaipov, A., Gillen, D., Gipson, D., Hailpern, S.M., Hall, Y.N., Han, Y., He, K., Herman, W., Heung, M., Hirth, R.A., Hutton, D., Jacobsen, S.J., Jin, Y., Kalantar-Zadeh, K., Kapke, A., Kovesdy, C.P., Lavallee, D., Leslie, J., McCullough, K., Modi, Z., Molnar, M.Z., Montez-Rath, M., Moradi, H., Morgenstern, H., Mukhopadhyay, P., Nallamothu, B., Nguyen, D. V., Norris, K.C., O'Hare, A.M., Obi, Y., Park, C., Pearson, J., Pisoni, R., Potukuchi, P.K., Rao, P., Repeck, K., Rhee, C.M., Schrager, J., Schaubel, D.E., Selewski, D.T., Shaw, S.F., Shi, J.M., Shieu, M., Sim, J.J., Soohoo, M., Steffick, D., Streja, E., Sumida, K., Tamura, M.K., Tilea, A., Tong, L., Wang, D., Wang, M., Woodside, K.J., Xin, X., Yin, M., You, A.S., Zhou, H., Shahinian, V., 2018. US Renal Data System 2017 Annual Data Report: Epidemiology of Kidney Disease in the United States. Am J Kidney Dis 71, A7.

Sarkaria, J.N., Hu, L.S., Parney, I.F., Pafundi, D.H., Brinkmann, D.H., Laack, N.N., Giannini, C., Burns, T.C., Kizilbash, S.H., Laramy, J.K., Swanson, K.R., Kaufmann, T.J., Brown, P.D., Agar, N.Y.R., Galanis, E., Buckner, J.C., Elmquist, W.F., 2018. Is the blood-brain barrier really disrupted in all glioblastomas? A critical assessment of existing clinical data. Neuro-Oncology 20, 184–191.

Sarker Apu, A., Pathan, A.H., Shrestha, D., Kibria, G., Jalil, R.-U., 2009. Investigation of In vitro Release Kinetics of Carbamazepine from Eudragit ® RS PO and RL PO Matrix Tablets, Tropical Journal of Pharmaceutical Research.

Sathornsumetee, S., Rich, J.N., Reardon, D.A., 2007. Diagnosis and treatment of high-grade astrocytoma. Neurol Clin 25, 1111–1139.

Scaringi, C., Agolli, L., Minniti, G., 2018. Technical advances in radiation therapy for brain tumors. Anticancer Research 38, 6041–6045.

Schlachetzki, F., Zhu, C., Pardridge, W.M., 2002. Expression of the neonatal Fc receptor (FcRn) at the blood-brain barrier. Journal of Neurochemistry 81, 203–206.

Schröder, U., Sabel, B.A., 1996. Nanoparticles, a drug carrier system to pass the blood-brain barrier, permit central analgesic effects of i.v. dalargin injections. Brain Research 710, 121–124.

Scott, J., Tsai, Y.Y., Chinnaiyan, P., Yu, H.H.M., 2011. Effectiveness of radiotherapy for elderly patients with glioblastoma. International Journal of Radiation Oncology Biology Physics 81, 206–210.

Seremeta, K.P., Chiappetta, D.A., Sosnik, A., 2013. Poly(ε-caprolactone), Eudragit® RS 100 and poly(ε-caprolactone)/Eudragit® RS 100 blend submicron particles for the sustained release of the antiretroviral efavirenz. Colloids Surf B Biointerfaces 102, 441–449.

Shan, Y., He, X., Song, W., Han, D., Niu, J., Wang, J., 2015. Role of IL-6 in the invasiveness and prognosis of glioma. Int J Clin Exp Med 8, 9114–20.

Shang, L., Nienhaus, K., Nienhaus, G.U., 2014. Engineered nanoparticles interacting with cells: Size matters. Journal of Nanobiotechnology 12, 1–11.

Shao, K., Huang, R., Li, J., Han, L., Ye, L., Lou, J., Jiang, C., 2010. Angiopep-2 modified PE-PEG based polymeric micelles for amphotericin B delivery targeted to the brain. Journal of Controlled Release 147, 118–126.

Shapiro, W.R., Green, S.B., Burger, P.C., Mahaley, M.S., Selker, R.G., VanGilder, J.C., Robertson, J.T., Ransohoff, J., Mealey, J., Strike, T.A., Pistenmaa, D.A., 1989. Randomized trial of three chemotherapy regimens and two radiotherapy regimens in postoperative treatment of malignant glioma. Journal of Neurosurgery 71, 1–9.

Sharma, N., Madan, P., Lin, S., 2016. Effect of process and formulation variables on the preparation of parenteral paclitaxel-loaded biodegradable polymeric nanoparticles: A co-surfactant study. Asian Journal of Pharmaceutical Sciences 11, 404–416.

Shen, Y., Sun, W., Zhu, K.J., Shen, Z., 2000. Regulation of biodegradability and drug release behavior of aliphatic polyesters by blending.

Shenoy, D.B., Amiji, M.M., 2005. Poly(ethylene oxide)-modified poly(ε-caprolactone) nanoparticles for targeted delivery of tamoxifen in breast cancer. International Journal of Pharmaceutics 293, 261–270.

Shi, J., Xiao, Z., Kamaly, N., Farokhzad, O.C., 2011. Self-assembled targeted nanoparticles: Evolution of technologies and bench to bedside translation. Accounts of Chemical Research.

Shi, M., Yang, Y.Y., Chaw, C.S., Goh, S.H., Moochhala, S.M., Ng, S., Heller, J., 2003. Double walled POE/PLGA microspheres: encapsulation of water-soluble and water-insoluble proteins and their release properties. Journal of Controlled Release 89, 167–177.

Shi, Y., 2002. Mechanisms of caspase activation and inhibition during apoptosis. Molecular Cell 9, 459–470.

Shityakov, S., Förster, C., 2014. In silico predictive model to determine vector-mediated transport properties for the blood-brain barrier choline transporter. Advances and Applications in Bioinformatics and Chemistry 7, 23–36.

Shrivastava, A., 2018. Introduction to Plastics Engineering. Introduction to Plastics Engineering 1–16.

Shuai, X., Ai, H., Nasongkla, N., Kim, S., Gao, J., 2004. Micellar carriers based on block copolymers of poly(ε-caprolactone) and poly(ethylene glycol) for doxorubicin delivery. Journal of Controlled Release 98, 415–426.

Siepmann, J., Göpferich, A., 2001. Mathematical modeling of bioerodible, polymeric drug delivery systems. Adv Drug Deliv Rev 48, 229–247.

Siepmann, J., Peppas, N.A., 2001. Mathematical modeling of controlled drug delivery. Advanced Drug Delivery Reviews 48, 137–138.

Silva, C.O., Pinho, J.O., Lopes, J.M., Almeida, A.J., Gaspar, M.M., Reis, C., 2019. Current Trends in Cancer Nanotheranostics: Metallic, Polymeric, and Lipid-Based Systems. Pharmaceutics 11.

Simpson, J.R., Horton, J., Scott, C., Curran, W.J., Rubin, P., Fischbach, J., Isaacson, S., Rotman, M., Asbell, S.O., Nelson, J.S., Weinstein, A.S., Nelson, D.F., 1993. Influence of location and extent of surgical resection on survival of patients with glioblastoma multiforme: Results of three consecutive radiation therapy oncology group (RTOG) clinical trials. International Journal of Radiation Oncology, Biology, Physics 26, 239–244.

Sindhu, R., Binod, P., Pandey, A., 2015. Microbial Poly-3-Hydroxybutyrate and Related Copolymers. Industrial Biorefineries and White Biotechnology 575–605.

Singh, C., Purohit, S., Pandey, B.L., Singh, M., 2014. Review 4, 96–104.
Singhvi, G., Singh, M., 2011. Review: In-vitro Drug Release Characterisation Models. International Journal of Pharmaceutical Studies and Research 2, 77–84.
Sinha, V.R., Bansal, K., Kaushik, R., Kumria, R., Trehan, A., 2004. Poly-ϵ-caprolactone microspheres and nanospheres: an overview. International Journal of Pharmaceutics 278, 1–23.
Skarlatos, S., Yoshikawa, T., Pardridge, W.M., 1995. Transport of [125I]transferrin through the rat blood-brain barrier. Brain Research 683, 164–171.
Skulachev, V.P., 2006. Bioenergetic aspects of apoptosis, necrosis and mitoptosis. Apoptosis 11, 473–485.
Snehalatha, M., Venugopal, K., Saha, R.N., 2008. Etoposide-Loaded PLGA and PCL Nanoparticles I: Preparation and Effect of Formulation Variables. http://dx.doi.org/10.1080/10717540802174662 15, 267–275.
Sobue, K., Yamamoto, N., Yoneda, K., Hodgson, M.E., Yamashiro, K., Tsuruoka, N., Tsuda, T., Katsuya, H., Miura, Y., Asai, K., Kato, T., 1999. Induction of blood-brain barrier properties in immortalized bovine brain endothelial cells by astrocytic factors. Neuroscience Research 35, 155–164.
Song, C.X., Labhasetwar, V., Murphy, H., Qu, X., Humphrey, W.R., Shebuski, R.J., Levy, R.J., 1997. Formulation and characterization of biodegradable nanoparticles for intravascular local drug delivery. Journal of Controlled Release 43, 197–212.
Soo Choi, H., Liu, W., Misra, P., Tanaka, E., Zimmer, J.P., Itty Ipe, B., Bawendi, M.G., Frangioni, J. V., 2007. Renal clearance of quantum dots. Nature Biotechnology 25, 1165–1170.
Sriamornsak, P., Thirawong, N., Korkerd, K., 2007. Swelling, erosion and release behavior of alginate-based matrix tablets. European Journal of Pharmaceutics and Biopharmaceutics 66, 435–450.
Steinbach, J.P., Weller, M., 2004. Apoptosis in gliomas: Molecular mechanisms and therapeutic implications. Journal of Neuro-Oncology 70, 245–254.
Steiniger, S.C.J., Kreuter, J., Khalansky, A.S., Skidan, I.N., Bobruskin, A.I., Smirnova, Z.S., Severin, S.E., Uhl, R., Kock, M., Geiger, K.D., Gelperina, S.E., 2004. Chemotherapy of glioblastoma in rats using doxorubicin-loaded nanoparticles. International Journal of Cancer 109, 759–767.
Strange, K., 1992. Regulation of solute and water balance and cell volume in the central nervous system. Journal of the American Society of Nephrology 3, 12–27.
Stupp, R., Hegi, M.E., van den Bent, M.J., Mason, W.P., Weller, M., Mirimanoff, R.O., Cairncross, J.G., 2006. Changing Paradigms—An Update on the Multidisciplinary Management of Malignant Glioma. The Oncologist 11, 165–180.
Stupp, R., Mason, W.P., van den Bent, M.J., Weller, M., Fisher, B., Taphoorn, M.J.B., Belanger, K., Brandes, A.A., Marosi, C., Bogdahn, U., Curschmann, J., Janzer, R.C., Ludwin, S.K., Gorlia, T., Allgeier, A., Lacombe, D., Cairncross, J.G., Eisenhauer, E., Mirimanoff, R.O., 2005. Radiotherapy plus Concomitant and Adjuvant Temozolomide for Glioblastoma. New England Journal of Medicine 352, 987–996.
Stupp, R., Roila, F., 2009. Malignant glioma: ESMO clinical recommendations for diagnosis, treatment and follow-up. Ann Oncol 20 Suppl 4.
Stupp, R., Taillibert, S., Kanner, A.A., Kesari, S., Steinberg, D.M., Toms, S.A., Taylor, L.P., Lieberman, F., Silvani, A., Fink, K.L., Barnett, G.H., Zhu, J.J., Henson, J.W., Engelhard, H.H.,

Chen, T.C., Tran, D.D., Sroubek, J., Tran, N.D., Hottinger, A.F., Landolfi, J., Desai, R., Caroli, M., Kew, Y., Honnorat, J., Idbaih, A., Kirson, E.D., Weinberg, U., Palti, Y., Hegi, M.E., Ram, Z., 2015. Maintenance therapy with tumor-Treating fields plus temozolomide vs temozolomide alone for glioblastoma a randomized clinical trial. JAMA - Journal of the American Medical Association 314, 2535–2543.

Stupp, R., Wong, E.T., Kanner, A.A., Steinberg, D., Engelhard, H., Heidecke, V., Kirson, E.D., Taillibert, S., Liebermann, F., Dbalý, V., Ram, Z., Villano, J.L., Rainov, N., Weinberg, U., Schiff, D., Kunschner, L., Raizer, J., Honnorat, J., Sloan, A., Malkin, M., Landolfi, J.C., Payer, F., Mehdorn, M., Weil, R.J., Pannullo, S.C., Westphal, M., Smrcka, M., Chin, L., Kostron, H., Hofer, S., Bruce, J., Cosgrove, R., Paleologous, N., Palti, Y., Gutin, P.H., 2012. NovoTTF-100A versus physician's choice chemotherapy in recurrent glioblastoma: A randomised phase III trial of a novel treatment modality. European Journal of Cancer 48, 2192–2202.

Stylianopoulos, T., Poh, M.Z., Insin, N., Bawendi, M.G., Fukumura, D., Munn, L.L., Jain, R.K., 2010. Diffusion of particles in the extracellular matrix: The effect of repulsive electrostatic interactions. Biophysical Journal 99, 1342–1349.

Sugano, M., Egilmez, N.K., Yokota, S.J., Chen, F.A., Harding, J., Huang, S.K., Bankert, R.B., 2000. Antibody targeting of doxorubicin-loaded liposomes suppresses the growth and metastatic spread of established human lung tumor xenografts in severe combined immunodeficient mice. Cancer Research 60, 6942–6949.

Szakács, G., Paterson, J.K., Ludwig, J.A., Booth-Genthe, C., Gottesman, M.M., 2006. Targeting multidrug resistance in cancer. Nature Reviews Drug Discovery 5, 219–234.

Tam, E.L., Draksharam, P.L., Park, J.A., Sidhu, G.S., 2019. Acute Immune-Mediated Thrombocytopenia due to Oxaliplatin and Irinotecan Therapy. Case Reports in Oncological Medicine 2019, 1–5.

Tanabe, K., Matsushima-Nishiwaki, R., Yamaguchi, S., Iida, H., Dohi, S., Kozawa, O., 2010. Mechanisms of tumor necrosis factor-α-induced interleukin-6 synthesis in glioma cells. Journal of Neuroinflammation.

Tang, Z.G., Rhodes, N.P., Hunt, J.A., 2007. Control of the domain microstructures of PLGA and PCL binary systems: Importance of morphology in controlled drug release. Chemical Engineering Research and Design 85, 1044–1050.

Tanyildizi, M.S., Özer, D., Elibol, M., 2005. Optimization of α-amylase production by Bacillus sp. using response surface methodology. Process Biochemistry 40, 2291–2296.

Tchirkov, A., Khalil, T., Chautard, E., Mokhtari, K., Véronèse, L., Irthum, B., Vago, P., Kémény, J.L., Verrelle, P., 2007. Interleukin-6 gene amplification and shortened survival in glioblastoma patients. British Journal of Cancer 96, 474–476.

Thakkar, J.P., Dolecek, T.A., Horbinski, C., Ostrom, Q.T., Lightner, D.D., Barnholtz-Sloan, J.S., Villano, J.L., 2014. Epidemiologic and molecular prognostic review of glioblastoma. Cancer Epidemiology Biomarkers and Prevention 23, 1985–1996.

Tian, G., Yin, W., Jin, J., Zhang, X., Xing, G., Li, S., Gu, Z., Zhao, Y., 2014. Engineered design of theranostic upconversion nanoparticles for tri-modal upconversion luminescence/magnetic resonance/X-ray computed tomography imaging and targeted delivery of combined anticancer drugs. Journal of Materials Chemistry B 2, 1379–1389.

Tinca, A.L., Iurian, S., Rus, L.M., Porfire, A., Tefas, L.R., 2020. Development and characterization of curcumin-loaded polycaprolactone nanoparticles by Design of Experiments. Romanian Journal of Pharmaceutical Practice 13, 127–138.

Tipduangta, P., Belton, P., Fábián, L., Wang, L.Y., Tang, H., Eddleston, M., Qi, S., 2016. Electrospun Polymer Blend Nanofibers for Tunable Drug Delivery: The Role of Transformative Phase Separation on Controlling the Release Rate. Molecular Pharmaceutics 13, 25–39.

Tomasetti, C., Li, L., Vogelstein, B., 2017. Stem cell divisions, somatic mutations, cancer etiology, and cancer prevention. Science (1979) 355, 1330–1334.

Truong, N.P., Whittaker, M.R., Mak, C.W., Davis, T.P., 2015. The importance of nanoparticle shape in cancer drug delivery. Expert Opinion on Drug Delivery 12, 129–142.

Tummala, S., Satish Kumar, M.N., Prakash, A., 2015. Formulation and characterization of 5-Fluorouracil enteric coated nanoparticles for sustained and localized release in treating colorectal cancer. Saudi Pharmaceutical Journal 23, 308–314.

Turnbull, D., 1969. Under What Conditions Can A Glass Be Formed? Contemporary Physics 10, 473–488.

Unagolla, J.M., Jayasuriya, A.C., 2018. Drug transport mechanisms and in vitro release kinetics of vancomycin encapsulated chitosan-alginate polyelectrolyte microparticles as a controlled drug delivery system. European Journal of Pharmaceutical Sciences 114, 199–209.

U.S. Department of Health and Human Services Food and Drug Administration Center for Drug Evaluation and Research FDA, 2005. Guidance for Industry Nonclinical Studies for the Safety Evaluation of Pharmaceutical Excipients. FDA Guidance 12.

Valle, J.W., Armstrong, A., Newman, C., Alakhov, V., Pietrzynski, G., Brewer, J., Campbell, S., Corrie, P., Rowinsky, E.K., Ranson, M., 2011. A phase 2 study of SP1049C, doxorubicin in P-glycoprotein-targeting pluronics, in patients with advanced adenocarcinoma of the esophagus and gastroesophageal junction. Investigational New Drugs 29, 1029–1037.

Van De Ven, H., Paulussen, C., Feijens, P.B., Matheeussen, A., Rombaut, P., Kayaert, P., Van Den Mooter, G., Weyenberg, W., Cos, P., Maes, L., Ludwig, A., 2012. PLGA nanoparticles and nanosuspensions with amphotericin B: Potent in vitro and in vivo alternatives to Fungizone and AmBisome. Journal of Controlled Release 161, 795–803.

Van Den Bent, M.J., Afra, D., De Witte, O., Ben Hassel, M., Schraub, S., Hoang-Xuan, K., Malmström, P.O., Collette, L., Piérart, M., Mirimanoff, R., Karim, A.B.M.F., 2005. Long-term efficacy of early versus delayed radiotherapy for low-grade astrocytoma and oligodendroglioma in adults: The EORTC 22845 randomised trial. Lancet 366, 985–990.

Van Loo, G., Schotte, P., Van Gurp, M., Demol, H., Hoorelbeke, B., Gevaert, K., Rodriguez, I., Ruiz-Carrillo, A., Vandekerckhove, J., Declercq, W., Beyaert, R., Vandenabeele, P., 2001. Endonuclease G: A mitochondrial protein released in apoptosis and involved in caspase-independent DNA degradation. Cell Death and Differentiation 8, 1136–1142.

Van Tellingen, O., Yetkin-Arik, B., De Gooijer, M.C., Wesseling, P., Wurdinger, T., De Vries, H.E., 2015. Overcoming the blood-brain tumor barrier for effective glioblastoma treatment. Drug Resistance Updates 19, 1–12.

Vanlangenakker, N., Berghe, T., Krysko, D., Festjens, N., Vandenabeele, P., 2008. Molecular Mechanisms and Pathophysiology of Necrotic Cell Death. Current Molecular Medicine 8, 207–220.

Varma, M.V.S., Kaushal, A.M., Garg, A., Garg, S., 2004. Factors affecting mechanism and kinetics of drug release from matrix-based oral controlled drug delivery systems. American Journal of Drug Delivery 2, 43–57.

Vauthier, C., Bouchemal, K., 2009. Methods for the Preparation and Manufacture of Polymeric Nanoparticles. Pharmaceutical Research 26, 1025–1058.

Verhaak, R.G.W., Hoadley, K.A., Purdom, E., Wang, V., Qi, Y., Wilkerson, M.D., Miller, C.R., Ding, L., Golub, T., Mesirov, J.P., Alexe, G., Lawrence, M., O'Kelly, M., Tamayo, P., Weir, B.A., Gabriel, S., Winckler, W., Gupta, S., Jakkula, L., Feiler, H.S., Hodgson, J.G., James, C.D., Sarkaria, J.N., Brennan, C., Kahn, A., Spellman, P.T., Wilson, R.K., Speed, T.P., Gray, J.W., Meyerson, M., Getz, G., Perou, C.M., Hayes, D.N., 2010. Integrated Genomic Analysis Identifies Clinically Relevant Subtypes of Glioblastoma Characterized by Abnormalities in PDGFRA, IDH1, EGFR, and NF1. Cancer Cell 17, 98–110.

Verreault, M., Wehbe, M., Strutt, D., Masin, D., Anantha, M., Walker, D., Chu, F., Backstrom, I., Kalra, J., Waterhouse, D., Yapp, D.T., Bally, M.B., 2015. Determination of an optimal dosing schedule for combining Irinophore C™ and temozolomide in an orthotopic model of glioblastoma. Journal of Controlled Release 220, 348–357.

Vijaya Ramesh, D., 2009. Comparison of oil-in-oil, water-in-oil-in-water and melt encapsulation techniques for the preparation of controlled release B12 poly (ε-caprolactone) microparticles. Trends in Biomaterials and Artificial Organs 23, 21–33.

Vilar, G., Tulla-Puche, J., Albericio, F., 2012. Polymers and drug delivery systems. Curr Drug Deliv 9, 367–394.

Vleeschouwer, S. de, Bergers, G., 2017. Glioblastoma: To Target the Tumor Cell or the Microenvironment? Glioblastoma 315–340.

von Roemeling, C., Jiang, W., Chan, C.K., Weissman, I.L., Kim, B.Y.S., 2017. Breaking Down the Barriers to Precision Cancer Nanomedicine. Trends in Biotechnology 35, 159–171.

Vonarbourg, A., Passirani, C., Saulnier, P., Benoit, J.P., 2006. Parameters influencing the stealthiness of colloidal drug delivery systems. Biomaterials 27, 4356–4373.

Wagner, J.R., Mount, E.M., Giles, H.F., 2013. Extrusion: The Definitive Processing Guide and Handbook: Second Edition. Extrusion: The Definitive Processing Guide and Handbook: Second Edition 1–620.

Wahl, M., Unterberg, A., Baethmann, A., Schilling, L., 1988. Mediators of blood-brain barrier dysfunction and formation of vasogenic brain edema. Journal of Cerebral Blood Flow and Metabolism 8, 621–634.

Walid, M., 2008. Prognostic Factors for Long-Term Survival after Glioblastoma. The Permanente Journal 12, 45.

Walker, R.A., 1978. Significance of α-subunit HCG demonstrated in breast carcinomas by the immunoperoxidase technique. Journal of Clinical Pathology 31, 245–249.

Wang, Z.H., Wang, Z.Y., Sun, C.S., Wang, C.Y., Jiang, T.Y., Wang, S.L., 2010. Trimethylated chitosan-conjugated PLGA nanoparticles for the delivery of drugs to the brain. Biomaterials 31, 908–915.

Warburg, O., Wind, F., Negelein, E., 1927. The metabolism of tumors in the body. Journal of General Physiology 8, 519–530.

Webster, R., Didier, E., Harris, P., Siegel, N., Stadler, J., Tilbury, L., Smith, D., 2007. PEGylated proteins: Evaluation of their safety in the absence of definitive metabolism studies. Drug Metabolism and Disposition 35, 9–16.

Wei, H., Song, J., Li, H., Li, Y., Zhu, S., Zhou, X., Zhang, X., Yang, L., 2013. Active loading liposomal irinotecan hydrochloride: Preparation, in vitro and in vivo evaluation. Asian Journal of Pharmaceutical Sciences 8, 303–311.

Weissenberger, J., Loeffler, S., Kappeler, A., Kopf, M., Lukes, A., Afanasieva, T.A., Aguzzi, A., Weis, J., 2004. IL-6 is required for glioma development in a mouse model. Oncogene 23, 3308–3316.

Wen, P.Y., Schiff, D., Kesari, S., Drappatz, J., Gigas, D.C., Doherty, L., 2006. Medical management of patients with brain tumors. Journal of Neuro-Oncology 2006 80:3 80, 313–332.

West, K., Otto, S., 2005. Reversible Covalent Chemistry in Drug Delivery. Current Drug Discovery Technologies 2, 123–160.

Wick, W., Hartmann, C., Engel, C., Stoffels, M., Felsberg, J., Stockhammer, F., Sabel, M.C., Koeppen, S., Ketter, R., Meyermann, R., Rapp, M., Meisner, C., Kortmann, R.D., Pietsch, T., Wiestler, O.D., Ernemann, U., Bamberg, M., Reifenberger, G., Von Deimling, A., Weller, M., 2009. NOA-04 randomized phase III trial of sequential radiochemotherapy of anaplastic glioma with Procarbazine, Lomustine, and Vincristine or Temozolomide. Journal of Clinical Oncology 27, 5874–5880.

Wicki, A., Witzigmann, D., Balasubramanian, V., Huwyler, J., 2015. Nanomedicine in cancer therapy: Challenges, opportunities, and clinical applications. Journal of Controlled Release.

Wilhelm, I., Fazakas, C., Krizbai, I.A., 2011. In vitro models of the blood-brain barrier [WWW Document]. Acta Neurobiologiae Experimentalis. URL https://pubmed.ncbi.nlm.nih.gov/21499332/ (accessed 11.5.21).

Wilson, B., 2009. Brain targeting PBCA nanoparticles and the blood-brain barrier. Nanomedicine 4, 499–502.

Wilson, T.A., Karajannis, M.A., Harter, D.H., 2014. Glioblastoma multiforme: State of the art and future therapeutics. Surgical Neurology International 5, 64.

Winer, J.L., Kim, P.E., Law, M., Liu, C.Y., Apuzzo, M.L.J., 2011. Visualizing the future: Enhancing neuroimaging with nanotechnology. World Neurosurgery 75, 626–637.

Wohlfart, S., Khalansky, A.S., Gelperina, S., Maksimenko, O., Bernreuther, C., Glatzel, M., Kreuter, J., 2011. Efficient chemotherapy of rat glioblastoma using doxorubicin-loaded PLGA nanoparticles with different stabilizers. PLoS ONE 6, 19121.

Wong, C., Stylianopoulos, T., Cui, J., Martin, J., Chauhan, V.P., Jiang, W., Popovíc, Z., Jain, R.K., Bawendi, M.G., Fukumura, D., 2011. Multistage nanoparticle delivery system for deep penetration into tumor tissue. Proc Natl Acad Sci U S A 108, 2426–2431.

Wong, H.L., Wu, X.Y., Bendayan, R., 2012. Nanotechnological advances for the delivery of CNS therapeutics. Advanced Drug Delivery Reviews 64, 686–700.

Wong, R.S.Y., 2011. Apoptosis in cancer: From pathogenesis to treatment. Journal of Experimental and Clinical Cancer Research 30, 1–14.

Woodruff, M.A., Hutmacher, D.W., 2010. The return of a forgotten polymer - Polycaprolactone in the 21st century. Progress in Polymer Science (Oxford) 35, 1217–1256.

Wouters, B.G., Koritzinsky, M., 2008. Hypoxia signalling through mTOR and the unfolded protein response in cancer. Nature Reviews Cancer 8, 851–864.

Wu, J., Ding, D., Ren, G., Xu, X., Yin, X., Hu, Y., 2009. Sustained delivery of endostatin improves the efficacy of therapy in Lewis lung cancer model. Journal of Controlled Release 134, 91–97.

Wu, J., Lee, A., Lu, Y., Lee, R.J., 2007. Vascular targeting of doxorubicin using cationic liposomes. International Journal of Pharmaceutics 337, 329–335.

Wyllie, A.H., Kerr, J.F.R., Currie, A.R., 1980. Cell Death: The Significance of Apoptosis. International Review of Cytology 68, 251–306.

Xin, H., Jiang, X., Gu, J., Sha, X., Chen, L., Law, K., Chen, Y., Wang, X., Jiang, Y., Fang, X., 2011. Angiopep-conjugated poly(ethylene glycol)-co-poly(ε-caprolactone) nanoparticles as dual-targeting drug delivery system for brain glioma. Biomaterials 32, 4293–4305.

Xin, H., Sha, X., Jiang, X., Zhang, W., Chen, L., Fang, X., 2012. Anti-glioblastoma efficacy and safety of paclitaxel-loading Angiopep-conjugated dual targeting PEG-PCL nanoparticles. Biomaterials 33, 8167–8176.

Xiong, X.B., Lavasanifar, A., 2011. Traceable multifunctional micellar nanocarriers for cancer-targeted co-delivery of MDR-1 siRNA and doxorubicin. ACS Nano 5, 5202–5213.

Yamamoto, Y., Nagasaki, Y., Kato, Y., Sugiyama, Y., Kataoka, K., 2001. Long-circulating poly(ethylene glycol)-poly(D,L-lactide) block copolymer micelles with modulated surface charge. Journal of Controlled Release 77, 27–38.

Yan, L., Shen, J., Wang, J., Yang, X., Dong, S., Lu, S., 2020. Nanoparticle-Based Drug Delivery System: A Patient-Friendly Chemotherapy for Oncology. Dose-Response 18.

Yao, J.S., Zhai, W., Young, W.L., Yang, G.Y., 2006. Interleukin-6 triggers human cerebral endothelial cells proliferation and migration: The role for KDR and MMP-9. Biochemical and Biophysical Research Communications 342, 1396–1404.

Yeung, Y.T., McDonald, K.L., Grewal, T., Munoz, L., 2013. Interleukins in glioblastoma pathophysiology: Implications for therapy. British Journal of Pharmacology 168, 591–606.

Yi, X., Manickam, D.S., Brynskikh, A., Kabanov, A. V., 2014. Agile delivery of protein therapeutics to CNS. Journal of Controlled Release 190, 637–663.

Yoo, H.S., Park, T.G., 2004. Folate-receptor-targeted delivery of doxorubicin nano-aggregates stabilized by doxorubicin-PEG-folate conjugate. Journal of Controlled Release 100, 247–256.

Yu, A.S., Hirayama, B.A., Timbol, G., Liu, J., Diez-Sampedro, A., Kepe, V., Satyamurthy, N., Huang, S.C., Wright, E.M., Barrio, J.R., 2013. Regional distribution of SGLT activity in rat brain in vivo. American Journal of Physiology - Cell Physiology 304, C240.

Yuan, Y., Choi, K., Choi, S.-O., Kim, J., 2018. Early stage release control of an anticancer drug by drug-polymer miscibility in a hydrophobic fiber-based drug delivery system. RSC Advances 8, 19791–19803.

Zanotto-Filho, A., Gonçalves, R.M., Klafke, K., de Souza, P.O., Dillenburg, F.C., Carro, L., Gelain, D.P., Moreira, J.C.F., 2017. Inflammatory landscape of human brain tumors reveals an NFκB dependent cytokine pathway associated with mesenchymal glioblastoma. Cancer Letters 390, 176–187.

Zhang, B., Sun, X., Mei, H., Wang, Y., Liao, Z., Chen, J., Zhang, Q., Hu, Y., Pang, Z., Jiang, X., 2013. LDLR-mediated peptide-22-conjugated nanoparticles for dual-targeting therapy of brain glioma. Biomaterials 34, 9171–9182.

Zhang, B., Wang, H., Liao, Z., Wang, Y., Hu, Yue, Yang, J., Shen, S., Chen, J., Mei, H., Shi, W., Hu, Yu, Pang, Z., Jiang, X., 2014. EGFP-EGF1-conjugated nanoparticles for targeting both neovascular and glioma cells in therapy of brain glioma. Biomaterials 35, 4133–4145.

Zhang, D., Mehler, M.F., Song, Q., Kessler, J.A., 1998. Development of bone morphogenetic protein receptors in the nervous system and possible roles in regulating trkC expression. Journal of Neuroscience 18, 3314–3326.

Zhang, K., Fang, H., Chen, Z., Taylor, J.S.A., Wooley, K.L., 2008. Shape effects of nanoparticles conjugated with cell-penetrating peptides (HIV Tat PTD) on CHO cell uptake. Bioconjugate Chemistry 19, 1880–1887.

Zhang, L., Yang, M., Wang, Q., Li, Y., Guo, R., Jiang, X., Yang, C., Liu, B., 2007. 10-Hydroxycamptothecin loaded nanoparticles: Preparation and antitumor activity in mice. Journal of Controlled Release 119, 153–162.

Zhang, T.T., Li, W., Meng, G., Wang, P., Liao, W., 2016. Strategies for transporting nanoparticles across the blood-brain barrier. Biomaterials Science 4, 219–229.

Zhang, X., Chen, G., Wen, L., Yang, F., Shao, A.L., Li, X., Long, W., Mu, L., 2013. Novel multiple agents loaded PLGA nanoparticles for brain delivery via inner ear administration: In vitro and in vivo evaluation. European Journal of Pharmaceutical Sciences 48, 595–603.

Zhang, Y., Pardridge, W.M., 2001. Rapid transferrin efflux from brain to blood across the blood-brain barrier. Journal of Neurochemistry 76, 1597–1600.

Zhao, F., Zhao, Ying, Liu, Y., Chang, X., Chen, C., Zhao, Yuliang, 2011. Cellular uptake, intracellular trafficking, and cytotoxicity of nanomaterials. Small 7, 1322–1337.

Zhou, Y., Tozzi, F., Chen, J., Fan, F., Xia, L., Wang, J., Gao, G., Zhang, A., Xia, X., Brasher, H., Widger, W., Ellis, L.M., Weihua, Z., 2012. Intracellular ATP levels are a pivotal determinant of chemoresistance in colon cancer cells. Cancer Research 72, 304–314.

Zhou, Yunfei, Zhou, Yan, Shingu, T., Feng, L., Chen, Z., Ogasawara, M., Keating, M.J., Kondo, S., Huang, P., 2011. Metabolic alterations in highly tumorigenic glioblastoma cells: preference for hypoxia and high dependency on glycolysis. J Biol Chem 286, 32843–32853.

Ziegler, U., Groscurth, P., 2004. Morphological features of cell death. News in Physiological Sciences.

Zielińska, A., Ferreira, N.R., Feliczak-Guzik, A., Nowak, I., Souto, E.B., 2020. Loading, release profile and accelerated stability assessment of monoterpenes-loaded solid lipid nanoparticles (SLN). Pharmaceutical Development and Technology 25, 832–844.

Zugasti, M.E., Zornoza, A., Del Mar Goi, M., Isasi, J.R., Vlaz, I., Martn, C., Snchez, M., Martnez-Ohrriz, M.C., 2009. Influence of soluble and insoluble cyclodextrin polymers on drug release from hydroxypropyl methylcellulose tablets. Drug Development and Industrial Pharmacy 35, 1264–1270.

Zweers, M.L.T., Grijpma, D.W., Engbers, G.H.M., Feijen, J., 2003. The Preparation of Monodisperse Biodegradable Polyester Nanoparticles with a Controlled Size. Journal of Biomedical Materials Research - Part B Applied Biomaterials 66, 559–566.